

TECTONIC-MAGMATIC CONTROLS ON VOLCANISM, RIFTING, AND
VOLATILE RELEASE

A Dissertation

Presented in Partial Fulfillment of the Requirements for the

Degree of Doctorate of Philosophy

with a

Major in Geology

in the

College of Graduate Studies

University of Idaho

by

James D. Muirhead

Major Professor: Simon A. Kattenhorn, Ph.D.

Committee Members: Dennis Geist, Ph.D.; John Watkinson, Ph.D.; Eric Mittelstaedt, Ph.D.

Department Administrator: Mickey Gunter, Ph.D.

April 2016

AUTHORIZATION TO SUBMIT DISSERTATION

The thesis of James D. Muirhead, submitted for the degree of Doctorate of Philosophy with a major in Geology and titled, "Tectonic-magmatic controls on volcanism, rifting, and volatile release", has been reviewed in final form. Permission, as indicated by the signatures and dates given below, is now granted to submit final copies to the College of Graduate Studies for approval.

Major Professor: _____ Date: _____
Simon A. Kattenhorn, Ph.D.

Committee Members: _____ Date: _____
Dennis J. Geist, Ph.D.

_____ Date: _____
A. John Watkinson, Ph.D.

_____ Date: _____
Eric Mittelstaedt, Ph.D.

Department
Administrator: _____ Date: _____
Mickey E. Gunter, Ph.D.

ABSTRACT

This dissertation examines the interplay between tectonic and magmatic processes that influence the nature of volcanically active regions. In particular, I address how faulting, fluid transport, and magma intrusion interact in a variety of settings, including continental rifts, large igneous provinces (LIPs), and monogenetic volcanic fields.

In the East African Rift (EAR), I combine structural measurements and field observations with geochronology, geochemistry, and seismicity data to investigate how continental breakup initiates and evolves. Analyses of volcanic cone lineaments illustrate variations in the geometries and distributions of dike intrusions along the rift. In early stage basins (<10 Ma), upper crustal dikes are confined to transfer zones – then, as rifting progresses (>10 Ma), dikes begin to accommodate extension along the entire length of the basin.

Measurements of diffuse gas flux in the EAR demonstrate that significant volumes of magmatic CO₂ (>4 Mt yr⁻¹) are rising along faults from upper mantle/lower crustal magma bodies. Over the entire EAR, this *tectonic degassing* (~71±33 Mt yr⁻¹) contributes significantly to Earth's natural CO₂ budget. Moreover, the release of magmatic volatiles assists strain localization and the development of new rift segmentation within existing half-graben depressions. Newly developing segments become kinematically linked with existing rift segments through the reactivation of rift-oblique basement fabrics. Resulting transverse faults postdate rift-parallel fault systems, indicating that preexisting weaknesses play a critical role at all stages of rift development.

A regional synthesis of sill-fed dikes of the Ferrar LIP, Antarctica, and field and remote-sensing analysis of the Hopi Buttes volcanic field, Arizona, highlights the role of interconnected dike-sill systems in feeding eruptions. Measurements reveal a previously unrecognized feeder system to LIP eruptions—analogous to a “cracked lid” atop a sill network—that may be the archetypal model for LIPs that intrude sedimentary basins undergoing negligible regional extension. At Hopi Buttes, several characteristic shallow feeder systems are identified: (1) dike-dominated, (2) sill-dominated, and (3) interconnected dike-sill networks. Dike-fed eruptions are common, but sills also modulate the flow of magma toward and away from eruptive conduits, providing a novel mechanism for lateral vent migration and changes in magma-water ratios that lead to explosive volcanism.

ACKNOWLEDGEMENTS

After studying in the US for four years across four different states there's inevitably a long list of people to thank. Firstly, my advisor Simon, who despite geographical constraints, has provided unwavering support, mentorship, and meticulous scientific scrutiny over the last four years. This project has given me a unique opportunity to study in some of the most coveted field locations and interact with an amazing group of scientists – I couldn't be happier that you took me on as a student and supported me to do this work.

Committee members. John has always been good for a yarn, and has provided pearls of structural geology wisdom. Eric generously gave his time to help me model continental rifting... watch this space. Dennis has provided great support throughout and warmly welcomed Alexa and me to the Potato State.

The wider research team. Cindy Ebinger has been an amazing source of support over these last four years, whether it's discussing science, analyzing data, or helping us get into the field. Tobias Fischer and Hyunwoo Lee, thanks for a memorable field season in Kenya and Tanzania. James White, once again a dependable ally in the battle for dike-sill feeder systems, with notable support from Michael Ort and Giuseppe Re. Julie Rowland continued on the good work. Giulia (Giules) Airoldi, we're still going strong! Sara Mana, Brent Turrin, and Sarah Stamps timed it to perfection. Nicolas Le Corvec is always good for a discussion about intrusions. Edwin Dindi, Remigius Gamma, Benson Onguso, Korres, Matt Blakeslee, Nicole Thomas and Melania Maqway all provided immense help in the field. Gladys Kianji, I doubt the field work would have been possible without your assistance.

Research support came from the NSF EAR Tectonics Program, and the Fulbright New Zealand and Ministry of Science and Innovation Award. Aerial photographs of Kenya-Tanzania were provided by the Polar Geospatial Center, University of Minnesota. Aster GDEM is a product of METI and NASA. GeoPRISMS has provided invaluable support to attend workshops and discuss continental rifting. The Tanzania COSTECH and Kenyan National Council for Science and Technology granted research permits, with assistance from Majura Songo and Norbert Opiyo-Akech. Great support was also provided by the good people at Fulbright NZ and the International Institute of Education, including Kelly Bonin, Laurie Stevens, Jacqueline Sindoni, Allyson Martinez, and Kara Wood. Lindsae Blue and Joanna Mossop provided support during my initial grant application. The local Navajo people and the Prosser family kindly allowed access to field areas in the Hopi Buttes. Field work in the Navajo Nation was conducted under a Permit from the Navajo Nation Minerals Department. Any persons wishing to conduct geological investigations on the Navajo Nation must first apply for and receive a Permit from the Navajo Nation Minerals Department, P.O. Box 1910, Window Rock, Arizona 86515, and Telephone Number (928) 871-6587.

The people who have graciously gone out of their way to welcome me at their departments in the second half of this PhD. Ramon Arrowsmith and Amanda Clarke went above and beyond. The ASU crew would not be complete though without Dom, Emily, Fabrizio, Christy, Duane, and Loyc. Max Ruldoph, Ashley Streig, Ben Perkins, Adam Booth, John Bershaw, and Martin Streck in particular warmly welcomed me at Portland State University. And my adopted PSU office mates - Hillary, Max and Jon.

Tyrone Rooney, Dave Sherrod, Karen Harpp, Juliet Biggs, Larry Mastin, Dave Sherrod, Craig Magee, Cindy Werner, Christelle Wauthier, Pilar Villamor, and Alex Guth

have all provided invaluable discussions that contributed to this work. Tyrone Rooney in particular has provided his generous advice and help over the years. Thanks to Katie Cooper for stepping in with a moments notice as a proxy committee member. Alexander Weinstein helped compile CRAFTI earthquake data. Steve and Kerstin shared in the best volcano-climb of the PhD. Then there are the journal reviewers and editors for Chapters 2, 3, 6, and 7 of this dissertation, including Nicholas Arndt, Nick Schofield, Amy Witchurch, Valerio Acocella, Thorsten Becker, Bernard Marty, Richard Ernst, Bob Holdsworth, Nicolas Le Corvec, Derek Keir, Giovanni Chiodini, Steffi Burchadt, and Mike Poland.

From the University of Idaho, thanks to Mickey Gunter and Debbie Jensen for their support over the years. Not to be forgotten are the University of Idaho grad students(!), particularly Tom, Erika, Matt, Darin, Kristina, Courtney, Marian, Brady, Emma, Aaron, Daisuke, Alex, Jeff, Emily W, and Emily M, who have helped me more than they probably even realize (well, some probably do), and shared in some great memories. Also, Erika, Tom, Emily B, and Courtney, thanks for a bed to sleep in during visits to Moscow. The Terminal Morons, Alex, Jeff, Matt, and Darin, for garage rock.

Thanks to Mum and Dad. Without you nothing is possible. And adopted parents, Terry, Karen, Tracy, Len and Lynne for their love and support.

Alexa. I couldn't imagine a more inspiring, loving person to share these experiences with. Discussions, debates, fieldwork, editing, and making every day more enjoyable than the last - every page of this thesis has been enriched by your contributions. You've supported me on another great adventure together, with many more to come.

TABLE OF CONTENTS

AUTHORIZATION TO SUBMIT	ii
ABSTRACT.....	iii
ACKNOWLEDGEMENTS	v
TABLE OF CONTENTS.....	viii
LIST OF FIGURES	xv
LIST OF TABLES	xix
CHAPTER 1: INTRODUCTION	1
1.1 Continental rifts.....	4
1.1.1 Magma-poor vs volcanic rifted margins	6
1.1.2 Understanding rift initiation and evolution	8
1.2 Large igneous provinces.....	9
1.3 Monogenetic volcanic fields	11
1.4 Thesis aims and structure.....	13
CHAPTER 2: UPPER CRUSTAL DIKING IN THE EAST AFRICAN RIFT	17
2.1 Abstract	17
2.2 Introduction	18
2.3 Regional setting.....	21
2.4 Study areas	24
2.4.1 The North Tanzanian Divergence	24
2.4.2 The Naivasha-Nakuru basin and Main Ethiopian Rift.....	24
2.4.3 Virunga province.....	25
2.5 Methods.....	26

2.5.1 Definition of cone trends.....	28
2.6 Results	31
2.6.1 The Kenya Rift and North Tanzanian Divergence.....	31
2.6.2 Comparative locations in the East African Rift	34
2.7 Discussion	38
2.7.1 Limitations of the analysis	38
2.7.2 Tectono-magmatic controls on dike orientations.....	39
2.7.6 Magmatic architecture of transfer zones: implications for magma-driven rifting ...	43
2.7.7 Variations in dike patterns across the East African Rift	46
2.8 Conclusions	49
2.9 Supporting information	49
2.9.1 Stress fields induced by pressurized magma chambers	49
2.9.2 Stress rotations induced by mechanical interactions between rift segments.....	53
2.10 Supporting methods	55
2.10.1 Observational methods: deducing cone lineaments	55
2.10.2 Analytical methods: creation of vent alignments.....	56
2.10.3 Defining cone field boundaries	59
2.10.4 Cone fields	62
CHAPTER 3: MAGMATIC CO ₂ RELEASE IN EAST AFRICA.....	64
3.1 Abstract	64
3.2 Introduction	65
3.3 Methods.....	67
3.4 Results	68

3.5 Discussion	71
3.5.1 Source of the mantle-derived CO ₂ in the Magadi and Natron basins	71
3.5.2 Estimating CO ₂ flux along the Eastern rift	72
3.5.3 Continental rifting and the global CO ₂ budget.....	73
3.6 Conclusions	74
3.7 Supporting information	75
3.7.1 Definition of tectonic degassing	75
3.7.2 Definition of structural zones.....	76
3.7.4 Estimating CO ₂ flux	76
3.7.5 Sources of CO ₂ in the Magadi-Natron basin.....	81
3.8 Supporting methods	83
3.8.1 CO ₂ gas accumulation chamber method.	83
3.8.2 Field sampling strategy	83
3.8.3 Laboratory analyses of gas compositions and C isotopes.....	84
3.8.4 Analysis of broadband seismic data.....	85
CHAPTER 4: EVOLUTION OF EARLY-STAGE CONTINENTAL RIFTING.....	89
4.1 Abstract	89
4.2 Introduction	90
4.3 Rift basin development in the Eastern rift of the EAR	94
4.4 Methods.....	99
4.4.1 Strain calculations	101
4.4.2 Measuring fault lengths, throws, and slip rates.....	105
4.5 Results	108

4.5.1 General observations	108
4.5.2 Geochronology of volcanic units and fault slip rates	113
4.5.3 Fault statistics of intra-rift fault populations	115
4.5.4 Fault-related extensional strain	116
4.5.5 Estimating flexure of the border fault hanging wall	121
4.5.6 Distribution of springs and their geochemistry	123
4.6 Discussion	126
4.6.1 Fault evolution during early-stage continental rifting	127
4.6.2 Source of spring waters in the Natron and Magadi basins	136
4.6.3 Controls on fault system evolution	139
4.6.4 Conceptual model	145
4.7 Conclusions	147
4.8 Supporting information	149
4.8.1 Supplemental Map	149
4.8.2 Modelling extensional strain from hanging wall flexure	149
4.8.3 Modelled extension rates of the Magadi and Natron basins	151
4.9 Supporting methods	152
4.9.1 Natron and Magadi springs: sampling and analytical methods	152
4.9.2 $^{40}\text{Ar}/^{39}\text{Ar}$ dating of Magadi and Natron volcanics	154
CHAPTER 5: REACTIVATION OF PREEXISTING STRUCTURES	157
5.1 Abstract	157
5.2 Introduction	158
5.3 Transverse faulting in the Magadi basin	162

5.4 Field observations and remote-sensing analysis	166
5.4.1 Methods.....	166
5.4.2 General structure	169
5.4.2 Fault kinematic indicators from field observations.....	175
5.5 Discussion	177
5.5.1 Kinematics and timing of faulting in the Kordjya system	177
5.5.2 An alternative model for transverse faulting.....	180
5.6 Conclusions	191
CHAPTER 6: ROLE OF SILLS IN FEEDING FLOOD BASALT ERUPTIONS	193
6.1 Abstract	193
6.2 Introduction	194
6.3 Review of intrusion dynamics of the Ferrar LIP.....	197
6.4 Methods.....	204
6.5 Results	206
6.6 Discussion	207
6.6.1 Did the inferred Ferrar dike-fissure network feed the flood basalts?.....	207
6.6.2 Additional ascent through conduits and roof collapse	210
6.6.3 The cracked lid.....	211
6.6.4 When does the cracked lid arise?	213
6.6.5 Applications to active volcanic systems	215
6.7 Conclusions	216
CHAPTER 7: SHALLOW FEEDER SYSTEMS TO MONOGENETIC ERUPTIONS	218
7.1 Abstract	218

7.2 Introduction	219
7.3 Background	221
7.4 Methods.....	224
7.4.1 Terminology	224
7.4.2 Field measurements and remote sensing.....	226
7.5 Results	229
7.5.1 Broad-scale arrangement of dikes, transgressive sills, and pyroclastic massifs	229
7.5.2 Field observations of intrusive complexes.....	234
7.6 Discussion	238
7.6.1 The intrusive-eruptive transition at southern Hopi Buttes	238
7.6.2 Transporting magma to eruption: the role of dikes vs. sills.....	240
7.6.3 Transgressive sills in monogenetic fields	242
7.6.4 Implications for other volcanic fields	245
7.7 Conclusions	248
7.8 Supporting information	250
7.8.1 Estimating surface uplift from shallow sill intrusion.....	250
7.9 Supporting methods	252
7.9.1 Length tolerance for eruptive center alignments.....	252
CHAPTER 8: SYNTHESIS.....	255
8.1 Summary of key findings.....	255
8.2 Future perspectives.....	261
REFERENCES.....	264
APPENDIX A	310

APPENDIX B311

APPENDIX C318

APPENDIX D316

APPENDIX E365

APPENDIX F.....366

LIST OF FIGURES

Figure 1.1 Distribution of Earth's continents and passive margins	6
Figure 1.2. Simplified illustration of the structure of rifted margins	7
Figure 1.3. Distribution of the East African Rift	8
Figure 2.1. Annotated DEM of the African continent	22
Figure 2.2. Rose diagrams of all data.....	25
Figure 2.3. DEM image of the North Tanzanian Divergence	26
Figure 2.4. Google Earth images of volcanic cones.....	29
Figure 2.5. Data from the North Tanzanian Divergence.....	32
Figure 2.6. Data from the South Natron field	33
Figure 2.7 Data from the Arusha field	35
Figure 2.8. Data from the Naivasha-Nakuru basin	36
Figure 2.9. Data from the Boset magmatic segment.....	37
Figure 2.10. Data from the Virunga Province.....	38
Figure 2.11. Local stress state in the Ngorongoro Volcanic Highlands.....	44
Figure 2.12. Conceptual illustration of shallow dike networks in transfer zones	45
Figure 2.13. Distribution of cones and their trends.....	47
Figure 2.14. Two-dimensional elastic models of a pressurized hole	51
Figure 2.15. Moving average analyses in the South Natron and Arusha fields.....	52
Figure 2.16. Two-dimensional elastic model of interacting rift segments.....	54
Figure 2.17. Classification of cone morphologies	57
Figure 2.18. Criteria for defining vent alignments.....	58
Figure 2.19. Distribution of cones in the North Tanzanian Divergence	60

Figure 2.20. Distribution of cones in the North Tanzanian Divergence and Kenya Rift.....	61
Figure 3.1. Distribution of CO ₂ flux samples and seismicity	66
Figure 3.2. Carbon isotope compositions and CO ₂ concentrations.....	69
Figure 3.3. Summary of CO ₂ fluxes.....	70
Figure 3.4. Distribution of fault zones, hanging wall sediments, and footwall lavas	77
Figure 3.5. Diffuse CO ₂ flux data from 7 transects	79
Figure 3.6. Histograms of CO ₂ flux.	80
Figure 3.7. CRAFTI seismic network.....	87
Figure 3.8. Depths of CRAFTI earthquakes	88
Figure 4.1. Magadi and Natron basins	93
Figure 4.2. Conceptual model for the development of rift basins.....	96
Figure 4.3. Field images from the Natron and Magadi basins	100
Figure 4.4. Examples of fault profiles.....	101
Figure 4.5. Simplified cross-sectional depiction of a normal fault.....	102
Figure 4.6. Summary plots of remotely-acquired fault data	106
Figure 4.7. Distribution of fault traces in the Natron-Magadi region	112
Figure 4.8. Rift-normal distribution of fault-related strain	119
Figure 4.9. Modeled deflections from border faulting.....	121
Figure 4.10. Distribution of springs and plots of geochemical data.	124
Figure 4.11. Summary of strain data from this study.....	134
Figure 4.12. Model of evolving structural relief and water/sediment catchments.....	137
Figure 4.13. Distribution of basin lakes in North Tanzania and the Kenya rift.....	138
Figure 4.14. Conceptual model of evolving fault-strain and fluid systems	146

Figure 4.15. Plates and plate boundaries throughout East Africa	153
Figure 5.1. Distribution of major rift faults across East Africa	159
Figure 5.2. Existing structural data from the Magadi Basin.	164
Figure 5.3. Photos of structural features mapped in the field	167
Figure 5.4. Map of the Kordjya fault system	168
Figure 5.5. Elevation profile of the main Kordjya fault.....	170
Figure 5.6. Distribution of springs along the Kordjya fault.....	171
Figure 5.7. Fault throw along rift-parallel segments.....	173
Figure 5.8. Left-curving tip zones on rift-parallel faults.....	174
Figure 5.9. Field measurements of joints and faults	176
Figure 5.10. Kinematics of rift-parallel faults.....	178
Figure 5.11. Timing of faulting in the Magadi basin	181
Figure 5.12. Kinematics of the Kordjya fault system	182
Figure 5.13. Tectonic-magmatic evolution of the Magadi basin and Kordjya fault.	187
Figure 6.1. Relative volumes of the components of the Ferrar LIP	197
Figure 6.2. Areas of South Victoria Land examined	198
Figure 6.3. Photos of Ferrar LIP intrusions.	201
Figure 6.4. Kinematics of sill-fed dikes	202
Figure 6.5. Google Earth images of Ferrar dikes	205
Figure 6.6. Frequency histograms of dike lengths, widths, and dips	206
Figure 6.7. Frequency histograms of dike strikes	207
Figure 6.8. End-member, shallow feeder systems for flood basalt provinces.	211
Figure 7.1. Geological map of the southern Hopi Buttes.....	222

Figure 7.2. Simplified stratigraphy of the Hopi Buttes.....	223
Figure 7.3. Field photos of Hopi Buttes intrusive features	226
Figure 7.4. Example of a pyroclastic massif deposit	227
Figure 7.5. Criteria for detecting alignments	229
Figure 7.6. Structural data in the southern Hopi Buttes.....	231
Figure 7.7. Thin sill intrusion in the Chinle Formation.	232
Figure 7.8. Sill margin at Crown Butte.....	233
Figure 7.9. Structural map of northwest Jagged Rocks	233
Figure 7.10. Dike intruding a pyroclastic massif structure	235
Figure 7.11. Structural map of Crown Butte.....	236
Figure 7.12. Transgressive sills at Crown Butte	237
Figure 7.13. Structural map of Crescent Rocks	239
Figure 7.14. Oblique view of intrusive structures at Crescent Rocks.....	239
Figure 7.15. Formation of a saucer-shaped sill	244
Figure 7.16. Flexural uplift of a sill-roof.	252
Figure 7.17. Eruptive center densities and distributions	254

LIST OF TABLES

Table 2.1. Summary of structural data.....	29
Table 3.1. CO ₂ fluxes, mean CO ₂ concentrations and δ ¹³ C data	68
Table 4.1. ⁴⁰ Ar/ ³⁹ Ar ages for faulted volcanic rocks.....	109
Table 4.2. Summary of the general distribution of fault-strain.....	118
Table 4.3. Composition of spring samples.....	125
Table 4.4. Summary of strains accommodated by intra-rift and border faults	129
Table 4.5. Comparison of border extension rates and slip rates	133
Table 6.1. Simplified stratigraphy of South Victoria Land, Antarctica.	200
Table 7.1. Definition of terms	225
Table 7.2. Summary of dike and transgressive sill dimensions	232

CHAPTER 1: INTRODUCTION

Volcano-tectonic systems are responsible for the growth of lithosphere, buildup of mountains, and rifting of continents. They produce hazardous volcanic eruptions and earthquakes, release mantle-derived gases that modulate Earth's climate, and provide natural resources such as rare-earth minerals and hydrothermal energy. Over the past few decades, the research community has increasingly emphasized that the observed complexity of volcano-tectonic systems results from not one or two primary drivers, but from dynamic feedbacks among many processes—particularly among regional tectonics, inherited crustal weaknesses, magma intrusion, and volatile release (Buck, 2004; Ebinger, 2005; Rowland et al., 2010; Rowland and Simmons, 2012; Wright et al., 2012). Understanding how these interrelated processes operate and evolve is of fundamental importance to both hazards resilience and access to valuable resources.

To investigate tectonic-magmatic interactions, we require an understanding of the subsurface architecture of volcanically active regions. However, the inaccessibility of magma plumbing systems limits our ability to visualize their geometry, depth extent, and relationship to fault networks. As a result, volcanic systems are often viewed through the lens of igneous geology and petrology – which typically envisages the buoyant rise magma through sub-vertical dikes extending upward from deep magma reservoirs directly underlying volcanoes (Tibaldi, 2015, and references therein). However, a fuller picture emerges at the intersection of volcanology-petrology, structural geology, and geophysical methods that illuminate active magma pathways in the subsurface. More specifically, this includes considering field observations of exposed intrusions in the context of geophysical (e.g., seismic tomography; Keranen et al., 2004; Keir et al., 2009a), geochemical (e.g., magma geochemistry, mineral

diffusion modelling; Rooney et al., 2011; Cooper et al., 2012; Barker et al., 2016), geodetic (e.g., InSAR; Biggs et al., 2009a; Wauthier et al., 2013), and volcano-structural observations (e.g., volcanic lineament analyses; Condit and Connor, 1996) of both active and inactive volcanic-tectonic systems.

Recently, interdisciplinary studies have revealed a spectrum of complexly interconnected magma networks in extensional tectonic settings. At volcanically active rifts (e.g., Taupo Rift, New Zealand), dikes can intrude laterally for 10s to possibly even 100s of kilometers, and can link magma systems with >50 km horizontal separations (Rowland et al., 2007; Biggs et al., 2016). These diking events are triggered by magma replenishment from below (i.e, the mantle) or from changes in the tectonic stress state in the upper crust (Buck et al., 2006; Rowland et al., 2010; Allan et al., 2012; Barker et al., 2016; Biggs et al., 2016). The intrusions themselves may accommodate 100s of years of accumulated extensional strain and drive static stress changes that initiate shallow (<10 km) normal faulting. Dike intrusion thus plays a key role in controlling rift basin architecture and surface topography (Buck et al., 2005; Rowland et al., 2007; Pinzuti et al., 2010; Wright et al., 2012). Intrusive swarms at spreading ridge centers in Iceland also exhibit varying geometrical arrangements, such as radial dike or cone sheet patterns (Gudmundsson, 1995a; Paquet et al., 2007). However, it is currently unknown how the geometries of upper crustal dike networks vary within continental rift settings as they evolve through time, even in well-studied and volcanically active areas like the East African Rift.

Seismic reflection and field studies of sill complexes also illustrate that magma can travel within interconnected sill networks for upwards of 12 kilometers vertically (Cartwright and Hansen, 2006), and for 100s to even 1000s of kilometers laterally (Aspler et al., 2002;

Leat, 2008; Magee et al., 2016). In support of these assertions, geodetic and seismicity data from the 2010 Eyjafjallajökull eruption, Iceland, show that magma traversed a network of sills that extended to the base of the crust (~20 km; Sigmundsson et al., 2010; Tarasewicz et al., 2012). Some authors even suggest that interconnected sill complexes, rather than giant dikes, can feed flood basalts, although such claims are currently contested (cf., Larsen and Marcussen, 1992; Hald and Tegner, 2000; Cartwright and Hansen, 2006).

Volatiles released from these subsurface magma systems may also interact with tectonic systems and assist continental rift processes. Fluids are known to mechanically weaken lithosphere through increases in pore fluid pressures (Sibson, 2000; Reyners et al., 2007) and hydration mineral reactions (Harte, 1983; Menzies, 1983; Moore and Rymer, 2007). Earthquake swarms signaling brittle failure in the crust and upper mantle have been detected beneath cratonic lithosphere in the East African Rift, and interpreted as the rise of volatiles through the plate (Seno and Saito, 1994; Lindenfeld et al., 2012; Albaric et al., 2014). However, the volumes of fluids released from magma bodies in extensional rift systems, and the role these fluids play in strain localization, is yet to be resolved.

In this dissertation, I examine a broad range of volcanic-tectonic systems, including continental rifts, large igneous provinces, and monogenetic volcanic fields (Fig. 1.1). The purpose of this work is to investigate how structural and magmatic processes interact in complex and interesting ways to control the nature of faulting, magmatic strain accommodation, fluid transport, and eruption. More specifically, I address the following topics:

1. How do the orientations and spatial occurrences of upper crustal dike networks vary over the course of continental rift evolution?
2. What is the volume of fault-controlled magmatic CO₂ released along the East African Rift, and the role of magmatic volatiles in driving rift basin development?
3. How do preexisting structures affect faulting and strain localization during rift initiation and evolution?
4. What is the typical geometrical arrangement of LIP feeder systems and are sill networks capable of feeding voluminous lava eruptions?
5. What processes govern the intrusive architecture of monogenetic fields, and how does their development affect eruptive style and vent location?

Below, I introduce the various tectonic-magmatic settings investigated in this dissertation, and summarize the salient points motivating each topic.

1.1 Continental rifts

Continental rifts are zones of tectonic extension, often accompanied by magmatism. Extensional tectonic forces at continental rift settings are primarily accommodated by a combination of normal faulting and dike intrusion in the upper crust, and ductile thinning and magmatism at lower crustal levels (Buck, 1991; Ebinger and Casey, 2001; Ebinger, 2005; Behn et al., 2006; Corti, 2009). Examples of active continental rifts include the Basin and Range (USA), Taupo (New Zealand), Baikal (Russia), Rio Grande (USA), and East African rifts (Fig. 1.1). Some continental rifts undergo stretching and strain localization to the point of continental breakup, transitioning to seafloor spreading to create new oceanic lithosphere.

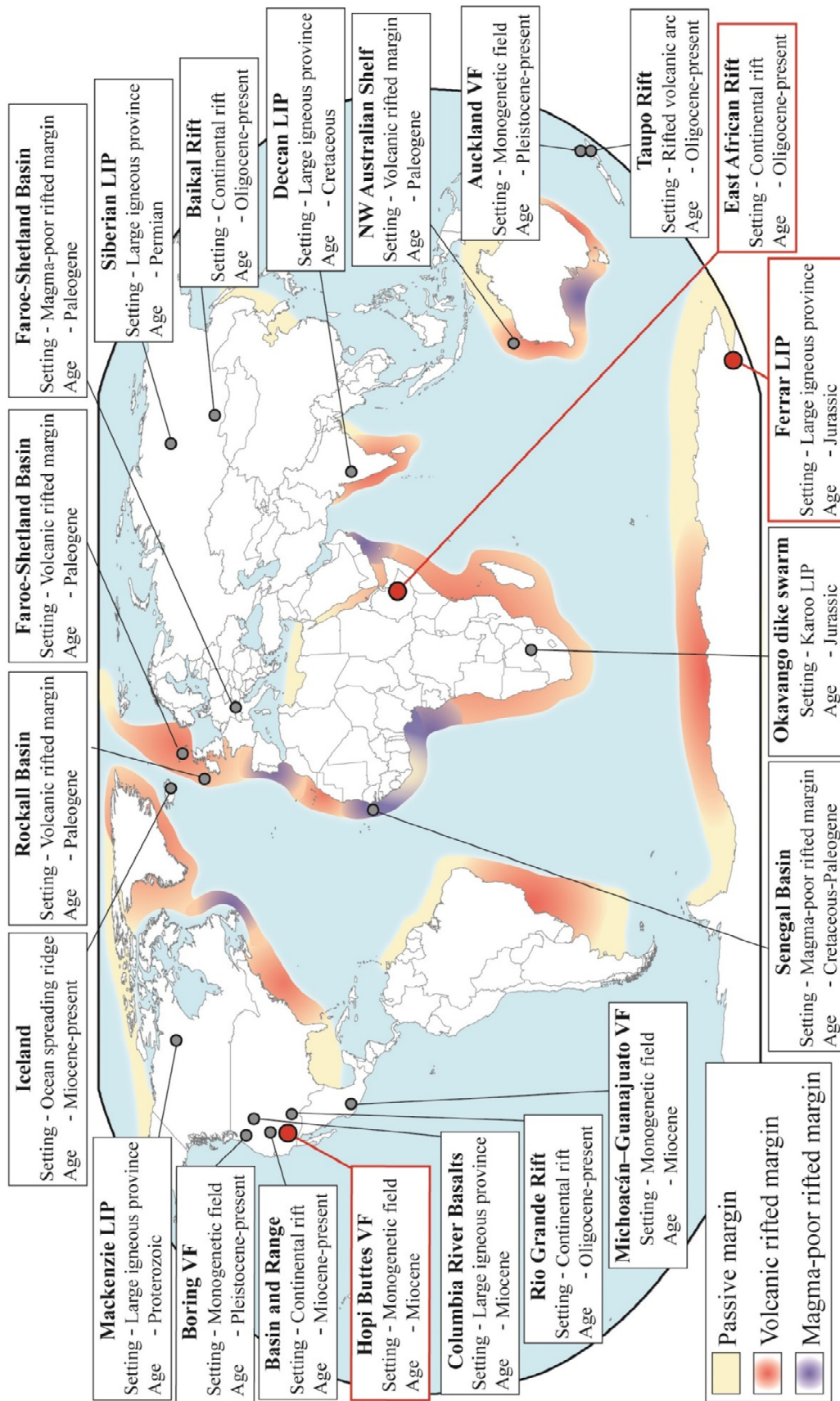


Figure 1.1. (previous page). Distribution of Earth's continents (white), and passive margins (color gradients) modified from Magee et al. (2016). Also shown are the locations of volcanic and magma-poor rifted margins, continental rifts, large igneous provinces, and monogenetic fields discussed in Section 1. The target sites for this dissertation are shown as red-filled circles. VF = volcanic field. LIP = large igneous province.

Once seafloor spreading initiates, the continental rift zone becomes a passive margin, like those observed today along the eastern margins of North and South America (Fig 1.1). These margins eventually subside below sea level as the lithosphere cools post-rifting.

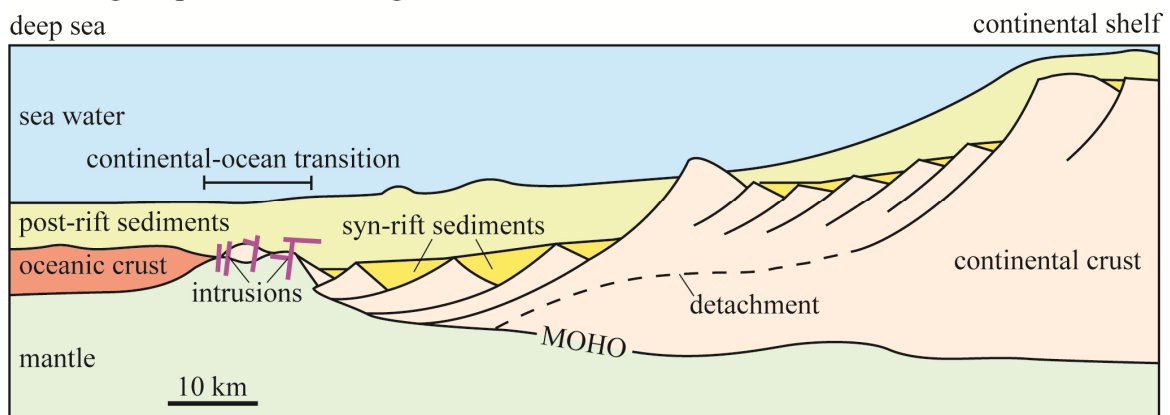
1.1.1 Magma-poor vs volcanic rifted margins

Much of the geological record of continental rifting comes from seismic reflection and field studies of passive margins (O'Reilly et al., 1996; Eldholm et al., 2000; Whitmarsh et al., 2001; Manatschal, 2004; Masini et al., 2011; Franke, 2013). Two end-member margin types are recognized: volcanic rifted margins and magma-poor rifted margins (Franke, 2013) (Fig. 1.2). Magma-poor rifted margins are characterized by extensive zones (>100 km wide) of rotated fault blocks and fault surfaces that may extend to the base of the continental crust (Whitmarsh et al., 2001). They do not have significant syn-rift volcanism, although magmatism does become prevalent after continental breakup has taken place (Franke, 2013). Examples include the Alpine-Tethys Margin (central Europe) and the Senegal basin (offshore NW Africa) (Manatschal, 2004; Hansen et al. 2008).

In contrast, volcanic rifted margins are characterized by widespread syn-rift magmatism (Eldholm et al., 2000). The normal fault systems are less widespread compared to their magma-poor counterparts, occurring in zones ~50-100 km wide (Franke, 2013). Fault development occurs coevally with magma intrusion and volcanism. These margins commonly have seaward-dipping reflectors in seismic reflection data, interpreted as tilted syn-rift lavas

(Eldholm et al., 2000). They also contain anomalously high lower-crustal seismic velocities (often above 7.3 m s^{-1}) over a $\sim 50 \text{ km}$ -wide zone immediately inboard of the continent-ocean transition (Fig. 1.2) (Eldholm et al., 2000; Franke, 2013). These high velocity zones have been attributed to the emplacement of lower crustal magma bodies (Eldholm et al., 2000; White et al., 2008), serpentinization of mantle lithosphere (Lundin and Doré, 2011) and, in rare instances, inherited high-grade metamorphic rocks (Ebbing et al., 2006). Examples of volcanic rifted margins include the Rockall and Faroe-Shetland basins (offshore UK), and NW Australian shelf (Falvey and Mutter, 1981; O'Reilly et al., 1996).

A Magma-poor Rifted Margin



B Volcanic Rifted Margin

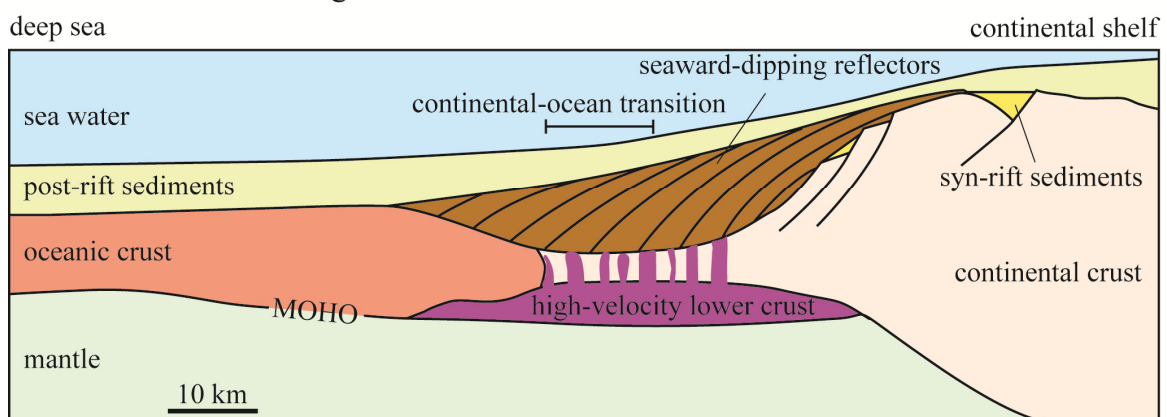


Figure 1.2. Simplified illustration of the structure of magma-poor (A) and volcanic (B) rifted margins modified from Franke (2013).

1.1.2 Understanding rift initiation and evolution: the East African Rift

The volcanically active Eastern rift (also known as the eastern branch) of the East African Rift (EAR) is analogous to volcanic rifted margins (Figs. 1.1 and 1.3), and is often referred to as a *magma-rich* rift setting (Ebinger et al., 2013). Geophysical studies indicate significant volumes of magma in the lower crustal (Mechie et al., 1997). Riftward-dipping lava sequences in evolved rift basins in Ethiopia show similarities to seaward-dipping reflectors seen along rifted margins (Eldholm et al., 2000; Wolfenden et al., 2004; Le Gall et al., 2011; Corti et al., 2015). Seismic tomography and xenolith studies suggest that rifting in the EAR initiated in thick (>100 km) continental lithosphere (Ritsema et al., 1998; Chesley et al., 1999; Vauchez et al., 2005), with strain localizing along the boundary between the Archean Tanzanian Craton and Proterozoic Mozambique Belt rocks (McConnell, 1972; Rosendahl, 1987; Daly et al., 1989).

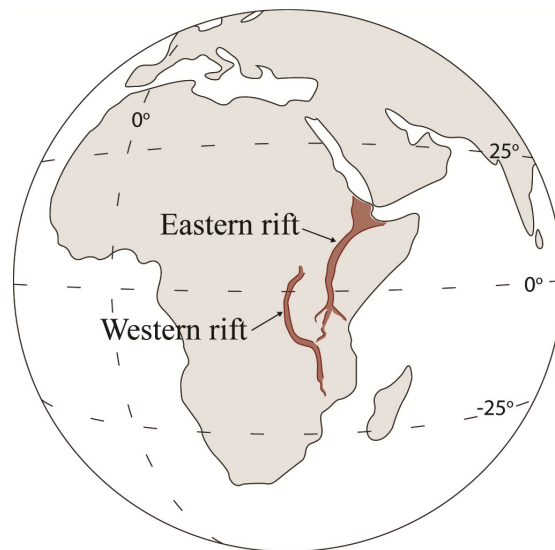


Figure 1.3. Distribution of the East African Rift across Africa. Brown polygons refer to the general area of recent rift-related extension and magmatism, with the Eastern and Western rift arms also annotated. These rift sectors have also been referred to previously as the eastern and western branches (e.g., Rosendahl et al., 1987; Koptev et al., 2015).

The Eastern rift of the EAR has been a focus area for studies of rift initiation in thick, strong, continental crust (Ebinger, 2005). The key issue here is that extensional forces related to lithospheric uplift above hot mantle plumes are theoretically too weak to rupture crust >30 km thick (Buck et al., 2006) – so how does the rifting process get started? In the EAR, rifting has been accompanied by significant volcanism, including the flood basalt eruptions of the Ethiopian Traps (Hofmann et al., 1997; Ebinger and Sleep, 1998; George et al., 1998; Pik et al., 2006). With magmatism comes volatile release at depth (Gerlach, 1989; Hilton et al., 2011; de Moor et al., 2013a,b), which weakens the crust and drives faulting at mid- to lower-crustal levels (Seno and Saito, 1994; Lindenfeld et al., 2012; Albaric et al., 2014). Large rift-bounding faults also appear to localize along preexisting basement shear zones (Smith and Mosley, 1993; Katumwehe et al., 2015a). Collectively, these studies suggest that rifting in East Africa requires the assistance of magmatism, magmatic volatile release, and preexisting weaknesses. Understanding the contributions of each of these processes over the course of continental rift evolution is fundamental to our understanding of how extensional plate boundaries develop, and how early-stage (<10 Ma) continental rifting initiates in thick lithosphere.

1.1 Large igneous provinces

Large igneous provinces (LIPs) represent the most voluminous magmatic events in Earth's history (Coffin and Eldholm, 1994; Ernst et al., 2005; Coffin et al., 2006; Bryan and Ernst, 2008; Bryan and Ferrari, 2013). The volume of erupted lavas ($>10^4 \text{ km}^3$) and associated gas emissions (1000s of Mt yr^{-1} of SO_2) (Self et al., 2006), combined with the recognized links between LIPs and continental breakup (Hooper, 1990; Courtillot et al., 1999), point to their global tectonic and climatic importance (Ernst, 2014). LIPs are also responsible for the

episodic generation of new crust. For example, during Siberian Traps volcanism at ~250 Ma, more than 1% of Earth's land surface was covered by fresh volcanic rock (Renne and Basu, 1991).

LIPs are defined by Bryan and Ernst (2008) as magmatic provinces with areal extents $>10^5 \text{ km}^2$, volumes $>10^5 \text{ km}^3$, and lifespans of up to ~50 million years. The province must occur within the same intraplate tectonic settings and/or have geochemical affinities, and be characterized by igneous pulse(s) of short duration (~1–5 Myr) that are responsible for a significant portion ($\geq 75\%$) of the total igneous material emplaced. In this sense, magma-rich continental rifts may also be classified as LIPs. In the case of the East African Rift, erupted volumes are certainly large enough (e.g., the $>2 \times 10^6 \text{ km}^3$ Ethiopian Traps; Courtillot et al., 1999), and thus the system has been referred to by some authors as the Afro-Arabia LIP (e.g., Baker et al., 1996; Courtillot et al., 1999; Bryan and Ernst, 2008).

Magma transport from the upper mantle/lower crust in LIPs is traditionally thought to occur through swarms of giant dikes (Ernst et al., 1995; Thordarson and Self, 1996, 1998; Ernst et al., 2001; Coffin et al., 2006). As such, studies have primarily focused on continental-scale magma transport dynamics within giant dike swarms, such as the Mackenzie (Canada) and Okavango (southern Africa) dike swarms (Ernst and Baragar, 1992; Baragar et al., 1996; Aubourg et al., 2008). Many flood basalts eruptions (e.g., Columbia River and Deccan Trap basalts; Thordason and Self, 1996; Ray et al., 2007) are thought to be fed by similar swarms of long ($>100 \text{ km}$), subparallel dikes. However, some LIPs show evidence for the emplacement of volumetrically significant sills in the shallow crust (depths $<4 \text{ km}$), such as the Karoo and Siberian LIPs (Naldrett et al., 1995; Chevallier and Woodford, 1999). Seismic reflection surveys of LIPs within volcanic rifted margins also reveal interconnected sills that

extend up to 12 km vertically in the upper crust (Cartwright and Hansen, 2006; Rohrman, 2013). These recent observations have provided a conceptual shift in our understanding of the role of sills in LIP magma transport (Magee et al., 2016), which were previously viewed solely as sites of magma emplacement and storage (cf., Francis, 1982; Coffin et al., 2006; Cartwright and Hansen, 2006). Currently, the role that sills play in magma transport for LIPs is therefore poorly constrained, and it is debated whether interconnected sill complexes, in addition to giant dike swarms, feed voluminous lava eruptions (cf., Larsen and Marcussen, 1992; Hald and Tegner, 2000; Cartwright and Hansen, 2006).

1.2 Monogenetic volcanic fields

Simply stated, a monogenetic volcano is a small-volume ($<1 \text{ km}^3$) scoria cone or maar-crater, which generally forms over a single eruptive episode lasting months to years (Wood, 1980; Connor and Conway, 2000; Kereszturi and Németh, 2012; McGee et al., 2012; Albert et al., 2016). Notable recent examples include the eruptions of the Parícutin (1943–1952 AD) and Jorullo volcanoes (1759–1774 AD) of the Michoacán–Guanajuato volcanic field in Mexico (Foshag and Gonzalez-Reyna, 1956; Johnson et al., 2008; Albert et al., 2016). By comparison, polygenetic volcanoes such as stratovolcanoes or calderas tend to have much longer lifespans (tens to hundreds of thousands of years), over which numerous eruptive events (typically >100 s) produce eruptive volumes $>100 \text{ km}^3$ – examples include Mount St. Helens, Vesuvius, Taupo, and Kilauea (Carey and Sigurdsson, 1987; Ryan, 1988; Priest, 1990; Wilson et al., 1995).

The volume of material produced during eruptions in monogenetic fields (no more than a few km^3 ; Allen and Smith, 1994; Kereszturi and Németh, 2012; Albert et al., 2016) has

been historically smaller than those produced during explosive eruptions at polygenetic volcanoes (e.g., $\sim 30 \text{ km}^3$ during the 1815 Tambora eruption, Indonesia; Self et al., 2004) and fissure eruptions in magma-rich rift systems ($\sim 15 \text{ km}^3$ during the 1783-1784 Laki eruption, Iceland; Thordarson et al., 1996). However, a disproportionate number of major cities are built directly on monogenetic fields, including Mexico City (Mexico), Auckland (New Zealand), and Portland (Oregon). It is clear that a monogenetic eruption of any size would have significant economic and societal impacts in these densely populated areas. Historically, monogenetic eruptions have had durations on the order of months to a few years (Albert et al., 2016), and are known to vary in style and scale over the course of a single, ongoing event (Houghton et al. 1999; Ort and Carrasco-Nunez 2009; McGee et al. 2012; Valentine and Cortés 2013). Understanding how intrusive-extrusive systems develop and interact during these volcanic crises is of considerable importance to hazards mitigation.

Monogenetic fields consist of tens to thousands of monogenetic volcanoes within the same intraplate setting (Connor and Condit, 1996; Németh and Martin, 2007; Le Corvec et al., 2013a). The term ‘monogenetic field’ itself has been criticized due to its loose application in the literature (cf., Sheth and Cañón-Tapia, 2015; Albert et al., 2016). It is often confused with volcanic fields, which can consist of a combination of monogenetic and polygenetic volcanoes (Cañón-Tapia, 2016). Furthermore, the volume of a monogenetic (single) eruption can vary greatly (up to 100s of km^3 ; Self et al., 2008)—therefore, some authors advocate the phrase ‘diffuse volcanic field’ to distinguish monogenetic fields from lava fields (i.e., flood basalts) produced during LIP volcanism (Sheth and Cañón-Tapia, 2015).

In this dissertation, a monogenetic field is defined as an area of diffuse (low-density), mafic volcanism, comprising small-volume monogenetic volcanoes in the same intraplate

tectonic setting. It is interesting to note that the East African Rift frequently produces monogenetic eruptions, forming small volcanic cones and fissure-fed lavas (e.g., Casey et al., 2006; Ebinger, 2010; Smets et al., 2010). However, the cone fields described in the EAR in this dissertation (Chapter 2) do not comprise a monogenetic field *sensu stricto* because the magma volumes are so large (e.g., Mechie et al., 1997; Keranen et al. 2004; Kendall et al., 2005; Keir et al., 2010, 2011a; Ebinger et al., 2010; Smets et al., 2010; Wauthier et al., 2013; Guth, 2015) that the overall system would be better classified as an LIP (Bryan and Ernst, 2008). The term monogenetic field, as it is used in Chapter 7, instead applies to the diffuse volcanic fields of Sheth and Canon-Tapia (2015), such as the Auckland (New Zealand) and Boring volcanic fields (Oregon, USA) (McGee et al., 2012; Fleck et al., 2014).

1.4 Thesis aims and structure

The five main topics outlined earlier are addressed in six chapters. Each is briefly summarized below, with a description of co-author contributions (not including advisor contributions).

Chapter 2: This chapter is based on a paper published during the completion of this dissertation (Muirhead, J. D., Kattenhorn, S. A., Le Corvec, N., 2015, Varying styles of magmatic strain accommodation across the East African Rift: Geochemistry, Geophysics, Geosystems, v. 16, p. 2775-2795, doi:10.1002/2015GC005918). It covers the first regional analysis of the distribution and orientation of upper crustal dikes across the East African Rift, inferred from volcanic cone morphometry and alignments. For this study, I performed remote-sensing mapping (from aerial photos and Google Earth imagery) of >1000 volcanic cones and craters, with accompanying clustering, morphometric, and alignment analyses. I analyzed and

compared these structural patterns with the distribution and geometries of normal fault systems and existing fault plane solutions. N. Le Corvec assisted with the use of a Matlab script for creating alignments and provided comments on the paper.

Chapter 3: This chapter is based on a paper published during the completion of this dissertation (Lee, H., Muirhead, J.D., Fischer, T.P., Ebinger, C.J., Kattenhorn, S.A., Sharpe, Z.D., Kianji, G., 2016, Massive and prolonged deep carbon emissions associated with continental rifting: *Nature Geoscience*, v. 9, p. 145-149, doi:10.1038/ngeo2622). It provides the first investigation of magmatic CO₂ degassing through rift-wide fault systems in the East African Rift. The ~20 day field study (June to July, 2014) was planned and performed by myself and collaborators T. Fischer and H. Lee, with additional field assistance from G. Kianji in the Magadi basin, Kenya. I created fault maps from aerial imagery, which were used to plan the target sites. Along with H. Lee and T. Fischer, I collected CO₂ flux data using a soil accumulation chamber, and gas samples for isotope analyses. After the completion of field work, H. Lee analyzed carbon isotope data at the University of New Mexico, while I compiled and analyzed the CO₂ flux data for spatial comparisons with fault structure. Seismicity data were analyzed and provided by C. Ebinger. The paper was written primarily by myself and H. Lee. T. Fischer, C. Ebinger, and Z. Sharpe provided comments to the manuscript, and C. Ebinger wrote the seismicity methods section, which I edited (Section 3.8.4).

Chapter 4: This chapter is an unpublished study investigating the distribution of upper crustal faulting in the 3 Ma Natron and 7 Ma Magadi basins using quantitative fault-strain analyses and new ⁴⁰Ar/³⁹Ar dates of volcanic deposits. For this study, I collected fault data and sampled volcanic rocks in Kenya and Tanzania during ~50 days of field work in

June 2012, July 2013, and June-July 2014. Field work assistance was provided by E. Dindi and G. Kianji (University of Nairobi). I mapped >1000 normal faults in the Natron and Magadi basins and undertook fault-strain analyses. These results were compared with regional extensional strain from: (1) GPS modelling (calculations and analyses performed by D. S. Stamps of Virginia Polytechnic Institute and State University); and (2) the distribution and geochemical signature of observed hot springs (geochemical data provided by H. Lee and T. Fischer of University of New Mexico). $^{40}\text{Ar}/^{39}\text{Ar}$ dating was performed by S. Mana (Columbia University) and B. Turrin (Rutgers University).

Chapter 5: This chapter provides a revised field and remote-sensing analysis of the mechanics of faulting along the transverse Kordjya fault of the Magadi basins. It is the first study to illustrate the important role of transverse fault structures in assisting the tectonic-magmatic evolution of rift basins in Kenya, and the EAR generally. I collected structural data during ~35 days of field work in the Magadi basin, Kenya, in July 2013, and June-July 2014. I also analyzed and mapped the fault system remotely, using aerial photography and Shuttle Radar Topography Mission data.

Chapter 6: This chapter is based on a paper published during the completion of this dissertation (Muirhead, J. D., Airoidi, G., White, J.D.L., Rowland, J.V., 2014, Cracking the lid: Sill-fed dikes are the likely feeders of flood basalt eruptions: *Earth and Planetary Science Letters*, v. 406, p. 187-197, doi:10.1016/j.epsl.2014.08.036). This study provides the first complete catalogue of the dimensions and distribution of regionally exposed sill-fed dike intrusions of the Ferrar LIP in South Victoria Land, Antarctica. These data were used to analyze the tectonic-magmatic environment during Ferrar LIP emplacement, as well as the ability for sill networks to feed eruptions at the surface. I compiled the data from previously

published maps and new mapping of the region from Google Earth satellite imagery. Photos in Figs. 6.3 and 6.4 were collected during two field seasons, one from December 2006 to January 2007, and other in December, 2008. Co-authors G. Airoidi, J. White, and J. Rowland were involved during fieldwork in the region from 2006-2008 and provided comments on the manuscript.

Chapter 7: This chapter is based on a paper published during the completion of this dissertation (Muirhead, J.D., Van Eaton, A.R., Re, G., White, J.D.L., Ort, M.H., 2016, Monogenetic volcanoes fed by interconnected dikes and sills in the Hopi Buttes volcanic field, Navajo Nation, USA: *Bulletin of Volcanology*, v. 78, p. 1-16, doi: 10.1007/s00445-016-1005-8). This study provides the first regional analysis of dike, sill, and conduit feeder systems in the Hopi Buttes volcanic field, Arizona, revealing a variety of shallow feeder systems to monogenetic fields. Field data for this study were collected by A. Van Eaton and myself, with assistance from J. White, G. Re, and M. Ort, during field work in April, October, and November, 2014 (20 days total). I also measured intrusions from Google Earth imagery, and analyzed the remote-sensing data along with data collected in the field. I wrote the paper, with comments and contributions from all the co-authors.

CHAPTER 2: UPPER CRUSTAL DIKING IN THE EAST AFRICAN RIFT

Chapter based on: Muirhead, J. D., Kattenhorn, S. A., Le Corvec, N., 2015, Varying styles of magmatic strain accommodation across the East African Rift: Geochemistry, Geophysics, Geosystems, v. 16, p.2775-2795, doi:10.1002/2015GC005918.

2.1 Abstract

Observations of active dike intrusions provide present day snapshots of the magmatic contribution to continental rifting. However, unravelling the contributions of upper crustal dikes over the timescale of continental rift evolution is a significant challenge. To address this issue, the morphologies and alignments of >1,500 volcanic cones are analyzed to infer the distribution and trends of upper crustal dikes in various rift basins across the East African Rift (EAR). Cone lineament data reveal along-axis variations in the distribution and geometries of dike intrusions as a result of changing tectono-magmatic conditions. In younger (<10 Ma) basins of the North Tanzanian Divergence, dikes are largely restricted to zones of rift-oblique faulting between major rift segments, referred to here as transfer zones. Cone lineament trends are highly variable, resulting from the interplay between (1) the regional stress field, (2) local magma-induced stress fields, and (3) stress rotations related to mechanical interactions between rift segments. Similar cone lineament trends are found in transfer zones in the western branch of the EAR, such as the Virunga Province, Democratic Republic of the Congo. The distributions and orientations of upper crustal dikes in the Eastern rift of the EAR vary during continental rift evolution. In early-stage rifts (<10 Ma), upper crustal dikes play a limited role in accommodating extension, as they are confined to areas in and around transfer

zones. In evolved rift basins (>10 Ma) in Ethiopia and the Kenya Rift, rift-parallel dikes accommodate upper crustal extension along the full length of the basin.

2.2 Introduction

The role of dike intrusions in driving continental breakup is at the center of a long-standing controversy that is fundamental to our understanding of plate tectonics (Sengor and Burke, 1978; White and McKenzie, 1989; Ernst et al., 2005; Havlin et al., 2013). Similar to large earthquakes, dike-driven rifting episodes can accommodate centuries of extensional stresses accumulated along divergent plate boundaries (Wright et al., 2012; Ebinger et al., 2013). Furthermore, if a steady supply of magma is available, dike intrusion will become the preferred mode of strain accommodation (Buck, 2004, 2006), thereby deactivating the large border faults that flank many rift systems (Ebinger and Casey, 2001; Wolfenden et al., 2004).

Investigating the 3-D magmatic architecture of continental rifts is critical to our broader understanding of magma-driven, plate tectonic processes (Keranen et al., 2004; Wright et al., 2012). Numerical models investigating the mechanical effects of diking to rift processes often depict simplified two-dimensional cross sections of rift basins parallel to the extension direction (e.g., Buck et al., 2005; Behn et al., 2006; Behn and Ito, 2008). Such studies implicitly assume that all dikes intrude rift-parallel along the rift axis. However, exposures of intrusive swarms at some rift settings (e.g., Iceland) reveal complex 3-D geometries, with both the abundance and orientations of intrusions varying spatially along rift axes (Paquet et al., 2007). If geometrically and spatially complex dike networks are present in continental rifts, then the mechanisms for accommodating extension (tectonic vs magmatic) will vary along-axis. For example, when upper crustal dikes are focused into confined

locations along-axis, magmatism will only partially accommodate extension, with normal faulting acting as the primary mode of strain accommodation across the remaining parts of the rift (e.g., Central vs Northern Taupo Volcanic Zone) (Rowland et al., 2010). Furthermore, complex dike patterns (e.g., cones sheets, radial diking) may indicate that dike orientations are controlled by local perturbations in the tectono-magmatic stress regime (e.g., pressurized magma chambers) (Gudmundsson, 1998), rather than the regional extensional stress field.

Much of our understanding of the contribution of dikes to continental rifting comes from geodetic and seismological observations of dike intrusion events (Einarsson, 1991; Calais et al., 2008; Wright et al., 2006, 2012). In particular, the 2005-2010 Afar rifting crisis in Ethiopia provided insights into dike intrusion processes occurring in evolved rift segments in the triple junction between the Red Sea, Gulf of Aden, and East African rifts (Wright et al., 2012). At least 13 dikes intruded the Dabbahu-Manda Hararo rift along the full 65 km-length of the rift segment. These dikes propagated laterally at depths of 1-10 km, sourced from a magma reservoir near the center of the rift segment (Ayele et al., 2009; Grandin et al., 2010; Ebinger et al., 2010). Based on these observations, it is likely that the internal architecture of rift segments in Ethiopia is rife with long sub-parallel dikes (Keir et al., 2005, 2006; Kendall et al., 2005; Bastow et al., 2010; Keir et al., 2011a; Mazzarini et al., 2013a, b).

Less is known, however, about the magmatic architecture of East African Rift (EAR) basins over the course of their evolution. Dike-rifting events in early-stage portions of the rift (<10 Ma) are relatively rare. Two dikes were recorded in the Natron basin (Tanzania) in 2007, however, their lengths were short (<10 km) and the intrusions were locally confined to Oldoinyo Lengai volcano (Calais et al., 2008; Biggs et al., 2013). Consequently, it is

unknown whether these events represent a basin-wide mode of strain accommodation in the ~120 km-long Natron rift segment (Foster et al., 1997).

Consistent with other magma-rich rift settings, such as in Iceland (Gudmundsson, 1995) and the Taupo Volcanic Zone, New Zealand (Wilson et al., 1995; Rowland et al., 2010), the regional tectonic stress field is expected to be the primary control on dike geometries in the EAR. However, other tectono-magmatic processes could lead to dike and fault orientations that deviate locally from those controlled by the regional tectonic stress state, including:

- (1) *Intrusion into pre-existing weaknesses*: Dikes that intrude into zones of pre-existing fractures may mimic the orientations of those fracture sets. This plays a particularly important role when pre-existing fracture planes are normal to the least compressive stress (σ_3) (Delaney et al., 1986; Jolly and Sanderson, 1997; Le Corvec et al., 2013b).
- (2) *Local magmatic stress fields*: Emplacement of dikes and sills below volcanic centers results in the formation of pressurized magma chambers and cylindrical conduits that can locally perturb the regional stress field (Muller and Pollard, 1977; Gudmundsson, 1998; Bistacchi et al., 2012; Muirhead et al., 2012) (see Section 2.8.1). In these instances, high magma pressures locally rotate the principal stress directions, resulting in the formation of cone sheets and/or radial dike intrusions (Muller and Pollard, 1977; Gudmundsson, 1995a; Airoidi et al., 2011).
- (3) *Volcano edifice loading*: Radial diking can also be promoted by stress perturbations related to the load of an overlying volcanic edifice (Pinel and

Jaupart, 2003; Hurwitz et al., 2009; Roman and Jaupart, 2014; Le Corvec et al., 2015).

- (4) *Rift segment interactions*: The regional stress field can be locally perturbed by the mechanical interaction of adjacent rifts and en echelon faults and fracture segments (Pollard and Aydin, 1984; Olson and Pollard, 1991; Morewood and Roberts, 1997; Tentler, 2003) (see Section 2.8.2). Within the interaction zone between structural segments (i.e., transfer zones), principal stresses rotate to produce faults and dikes exhibiting rift-oblique trends that act to link rift segments (e.g., the Okataina Domain of the Taupo Volcanic Zone, New Zealand) (Rowland and Sibson, 2001).

The studies described above provide a conceptual framework for interpreting complex dike patterns at continental rift settings. This paper addresses variations in upper crustal dike patterns across the EAR by analyzing the morphologies, alignments and spatial distributions of volcanic cones. Local- and basin-scale dike patterns are compared with fault populations and regional extension directions to understand the different tectono-magmatic processes influencing dike orientations. By comparing results between rift basins across the EAR, varying mechanisms of magmatic strain accommodation can be inferred, with implications for the evolving role of magmatism during continental rifting.

2.3 Regional setting

The East African Rift is an example of active continental breakup (Fig. 2.1), forming a divergent boundary between the Nubian and Somalian plates of Africa (Chorowicz, 2005). The entire rift system is >3,000 km long, consisting of discrete rift basins ~100 km long and 10s of km wide (Rosendahl, 1987; Ebinger and Scholz, 2012). Rift basins are mechanically

linked by zones (areas ranging from 10^2 - 10^3 km²) of rift-oblique faulting (Ebinger, 1989; Koehn et al., 2010), defined here as *transfer zones* (Chorowicz, 1989; Corti et al., 2002a, b). Rift basins in the central parts of the EAR occur at the eastern and western edges of the Tanzanian Craton, thereby dividing the EAR into eastern and western branches (Fig. 2.1).

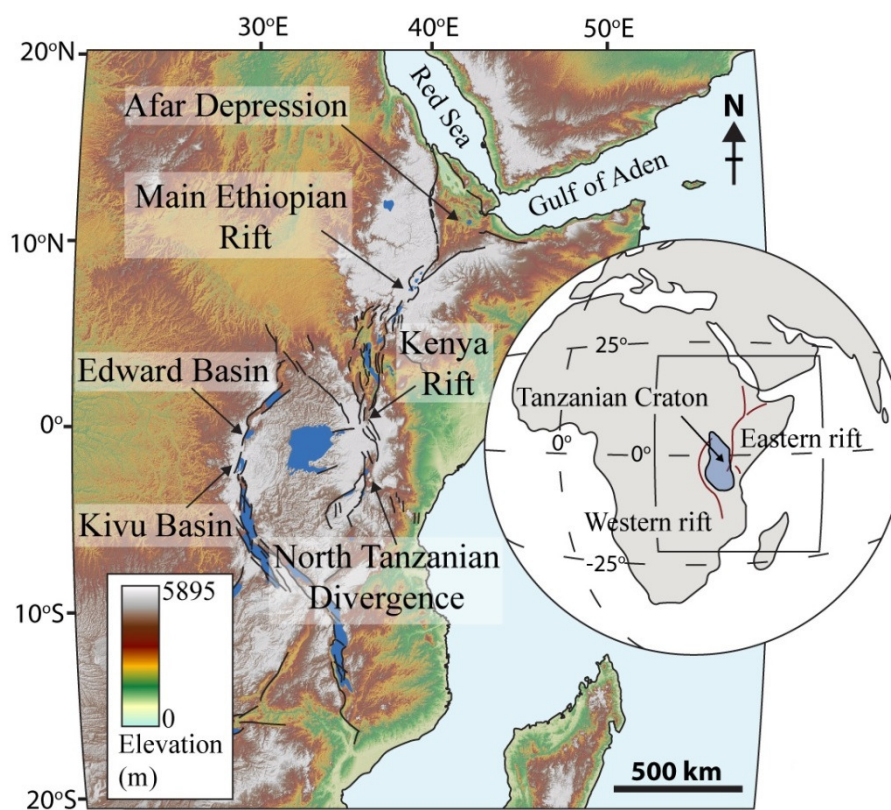


Figure 2.1. Annotated DEM image (90 m SRTM) of the eastern portion of the African continent. Faults (black lines) are from Ebinger (1989) and Chorowicz (2005). Major lakes are colored blue in the DEM, and commonly occur in deep rift basins. Inset globe simplifies the overall extent of the Eastern and Western rifts of the EAR and the inferred extent of the Tanzanian Craton from Corti (2009) and Morley (2010).

Initiation of the EAR is commonly attributed to dynamic stresses related to a mantle upwelling and associated volcanism (Ebinger and Sleep, 1998; Pik et al., 2006; Halldorsson et al., 2014; Stamps et al., 2014), with voluminous eruptions occurring at ~30 Ma (Hofmann et al., 1997). Following this volcanic event, rifting began in the Gulf of Aden, Red Sea, and East

African Rift (Hughes et al., 1991; Wolfenden et al., 2005). Although rifts in the Gulf of Aden and Red Sea have evolved into ocean spreading centers, continental rifting in East Africa has progressed relatively slowly. In the Afar Depression, the system has transitioned to incipient seafloor spreading; however, from the Main Ethiopian Rift southward, continental breakup is in an earlier stage of development (Ebinger, 2005).

Along-strike variability in the age of rift basins in the Eastern rift of the EAR allows us to compare rift architecture and basin structure at different stages of rift evolution (Hayward and Ebinger, 1996; Ebinger and Casey, 2001). The greater proportion of the African superplume is also situated below the Eastern rift (Mulibo and Nyblade, 2013 a, b). Geochemical and numerical modelling studies demonstrate that the African superplume has increased ambient mantle temperatures (up to 1,450°C in Ethiopia) and driven adiabatic decompression melting of rising plume material (Rooney et al., 2012; Ferguson et al., 2013; Koptev et al., 2015). Greater volumes of melt are therefore generated at lower extension rates in the Eastern rift compared to the Western rift (Ferguson et al., 2013). This disparity results in significant differences in the volume of erupted materials, with comparatively rapid strain localization and rift development in the Eastern rift segments (Baker et al., 1972; Kampunzu et al., 1998; Nyblade et al., 2000; Koptev et al., 2015). With these differences in mind, the following terminology is used to differentiate between the ages of basins as well as the relative degree of plume influence. Basins in the Eastern rift are defined as *magmatic rifts*, whereas *magma-poor rifts* define those occurring in the Western rift. *Evolved rifts* are >10 Ma, whereas *immature rifts* are <10 Ma. The main focus of this study is the magmatic architecture of basins in the Eastern rift in Kenya and Tanzania with comparison to select parts of the EAR.

2.4 Study areas

2.4.1 The North Tanzanian Divergence: immature, magmatic rifting

The North Tanzanian Divergence represents an early-stage (<7 Ma) of continental rifting in close proximity to the African superplume (Le Gall et al., 2008; Mulibo and Nyblade, 2013a, b) (box C, Fig. 2.2). Following Le Gall et al. (2008), this area extends from the ~60 km-wide Natron-Magadi basin southward into a ~300 km-wide, faulted zone containing the Eyasi, Manyara, and Pangani rift basins (Fig. 2.3). Located in the middle of this region is a 200 km-wide, magmatic transfer zone, known as the Ngorongoro-Kilimanjaro Volcanic Belt (Le Gall et al., 2008; Delcamp et al., 2016) (Fig. 2.3). Additional volcanism occurs off-axis of the North Tanzanian Divergence in the Chyulu Hills region (Haug and Strecker, 1995; Isola et al., 2014) (Fig. 2.3).

2.4.2 The Naivasha-Nakuru basin and Main Ethiopian Rift: evolved, magmatic rifting

Examples of evolved, magmatic rifts include the Boset magmatic segment in the Adama basin of the Main Ethiopian Rift (Box A, Fig. 2.2) and Naivasha-Nakuru basin of the Kenya Rift (box B, Fig. 2.2). Syn-rift growth of sedimentary sequences suggests faulting first initiated at Boset at ~10.6 Ma (Wolfenden et al., 2004). The structural characteristics of monogenetic volcanic fields are well documented for the Main Ethiopian Rift (Korme et al., 1997; Mazzarini, 2004; Corti et al., 2013; Mazzarini et al., 2013b), and this study targets only the youngest vents (<0.65 Ma) in the Boset magmatic segment (Keranen et al., 2004; Abebe et al., 2007). The Naivasha-Nakuru basin exhibits bimodal volcanism, consisting of five silicic volcanic centers, some of which are actively deforming (Biggs et al., 2009b), and three

basaltic fields containing cones that are <0.5 Ma (Macdonald et al., 2008; Macdonald and Baginski, 2009).

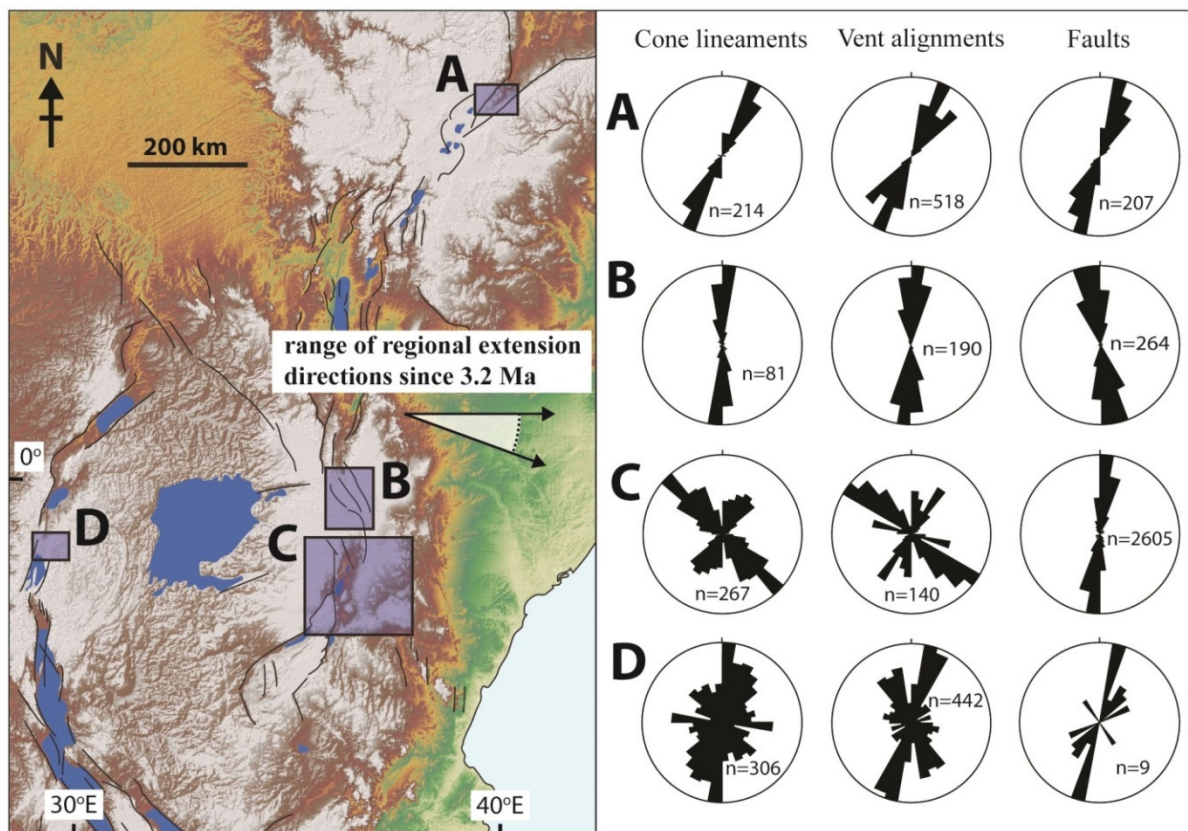


Figure 2.2. Rose diagrams of all cone lineament, vent alignment, and fault strike data collected in this study. The fault strike data (both border faults and intra-rift faults) are length-weighted. Letters refer to (A) the Boset magmatic segment, (B) Naviasha-Nakuru basin, (C) North Tanzanian Divergence, and (D) Virunga Province.

2.4.3 Virunga province: evolved, magma-poor rifting

The Virunga province is the most volcanically active region in the EAR (Smets et al., 2010, 2014; Wadge and Burt, 2011), despite being situated in the overall magma-poor, Western rift (box D, Fig. 2.2). This province is in a transfer zone linking the Edward and Kivu basins (Corti et al., 2002a; Ebinger and Furman, 2003). InSAR studies in this region have

detected a number of dike intrusions in the last 20 years, with some dikes extending from the Virunga province southward into the northern part of the Kivu basin (Wauthier et al., 2012, 2013).

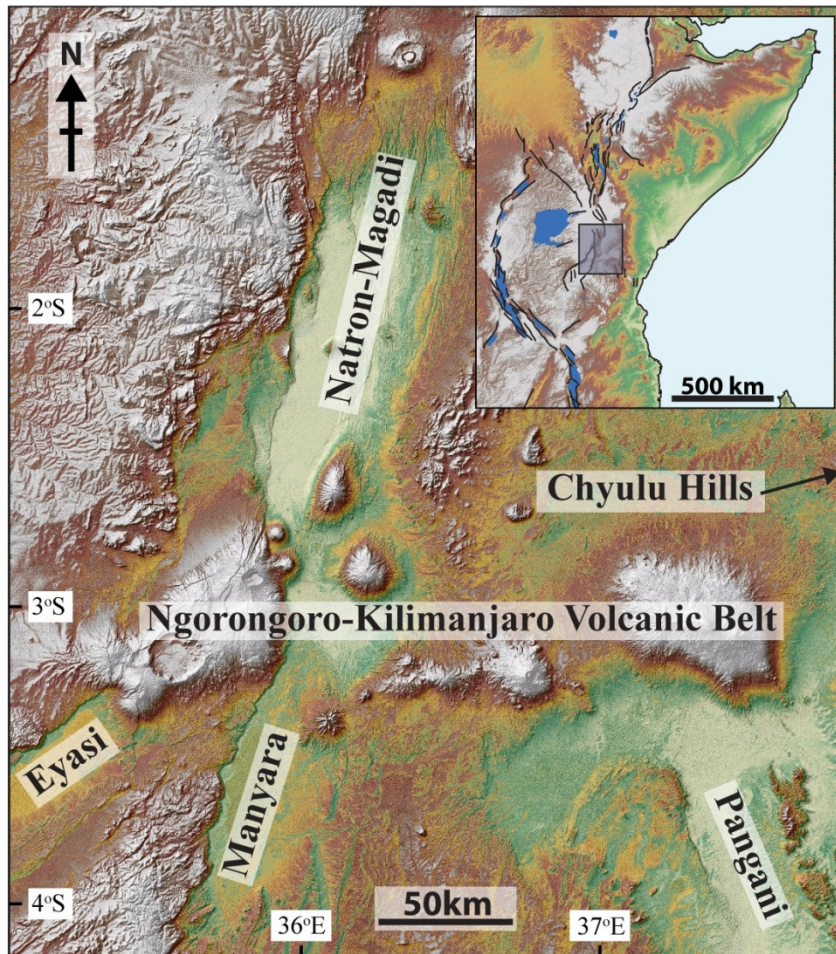


Figure 2.3. DEM image (90 m SRTM) showing rift basins of the North Tanzanian Divergence.

2.5 Methods

Volcanic features, such as scoria cones, tuff cones, fissures, and maar craters, are the expression of a magmatic intrusion that reached the surface. They are typically thought to be fed by dikes (Delaney and Pollard, 1982; Kiyosugi et al., 2012), which form as near-planar,

magma-filled cracks oriented in a direction either normal to σ_3 (Anderson, 1951; Rubin, 1995; Rivalta et al., 2015), or, in some instances, parallel to pre-existing structures (Le Corvec et al., 2013a, b). Studies of eroded monogenetic volcanic fields show a strong correlation between the density of volcanic conduits and the density of upper crustal dikes (Kiyosugi et al., 2012). Given this association between eruptive vents and dikes, studies in the EAR commonly use cone densities to investigate the distribution of the upper crustal dike networks (Mazzarini, 2004; Mazzarini et al., 2013a; Keir et al., 2015), whereas cone elongations and alignments provide clues to the orientations of these intrusions (Le Corvec et al., 2013a; Chapter 7).

In this study, the morphologies of monogenetic volcanic cones are used to infer the orientations of upper crustal dikes, using the observational and analytical techniques described in detail in the supporting information (see Section 2.9). Morphometric features, such as elongate cone/crater geometries and breakouts (Tibaldi, 1995) are determined by tracing the idealized shape of monogenetic cones using high resolution aerial images (0.5 m resolution) and Google Earth satellite imagery (1-2 m resolution) (Paulsen and Wilson, 2010; Bonali et al., 2011). If specific criteria are met (outlined in the Section 2.9.2), the trend of the long axis is recorded, described throughout this paper as the *cone lineament*, and inferred to reflect the strike of the dike that fed the volcanic cone (Fig. 2.4). Secondly, the cone lineament data are supplemented by *vent alignment* analyses (i.e., best-fit lines between groups of 3 cones) using the linear regression algorithm and MATLAB script of Le Corvec et al. (2013a).

These volcanic cone analyses are compared with structural analyses of fault patterns for each area of interest (Fig. 2.2; Table 2.1; Appendix A). Rose plots illustrating fault data are length-weighted throughout this chapter (Fig. 2.2).

2.5.1 Definition of cone trends

Cone lineaments are described in this study as extension-normal, extension-oblique, or radial. Cone ages vary anywhere from 2.25 Ma to present (Table 2.1). Therefore, to compare these data to the regional stress state of the EAR, I have considered a range of extension directions over the last ~3.2 million years inferred from geodetic, seismic, and geological studies (e.g., Bosworth and Strecker, 1997; Korme et al., 1997; Chu and Gordon, 1999; Horner-Johnson et al., 2005; Stamps et al., 2008; Saria et al., 2014). *Extension-normal* cones are defined as trending perpendicular ($\pm 10^\circ$) to the modeled N90-110° extension direction, or regional σ_3 , over the last 3.2 Ma. Conversely, *extension-oblique* groups trend greater than $\pm 10^\circ$ to the regional σ_3 without exhibiting a distinct radial pattern. Within the *radial* group, trends converge into a common area when projected as a straight line away from the center point of the volcanic cone. These radial patterns have been observed in dike swarms constituting the shallow plumbing (<2 km paleo-depth) of eroded volcanic fields, including Spanish Peaks (Muller and Pollard, 1977), and the Ferrar large igneous province (Airoldi et al., 2012), and are also seen in fissure arrays on active volcanic islands (e.g., Fernandina volcano, Galapagos) (Chadwick and Howard, 1991). Brändle et al. (1991) describe a mathematical approach for identifying radial swarms and locating their convergence centers, termed the method of maximum intersections. In this study, dike orientations inferred from cone lineaments and vent alignments are taken as straight lines, with the intersection of each line taken as the center of the radial swarm. However, not all intersections are considered

valid. For example, following the methods of Ancochea et al. (2008), I have ignored intersections between: (1) closely spaced cones, <4000 m apart, and (2) cone lineaments at <math><15^\circ</math> angles to each other.

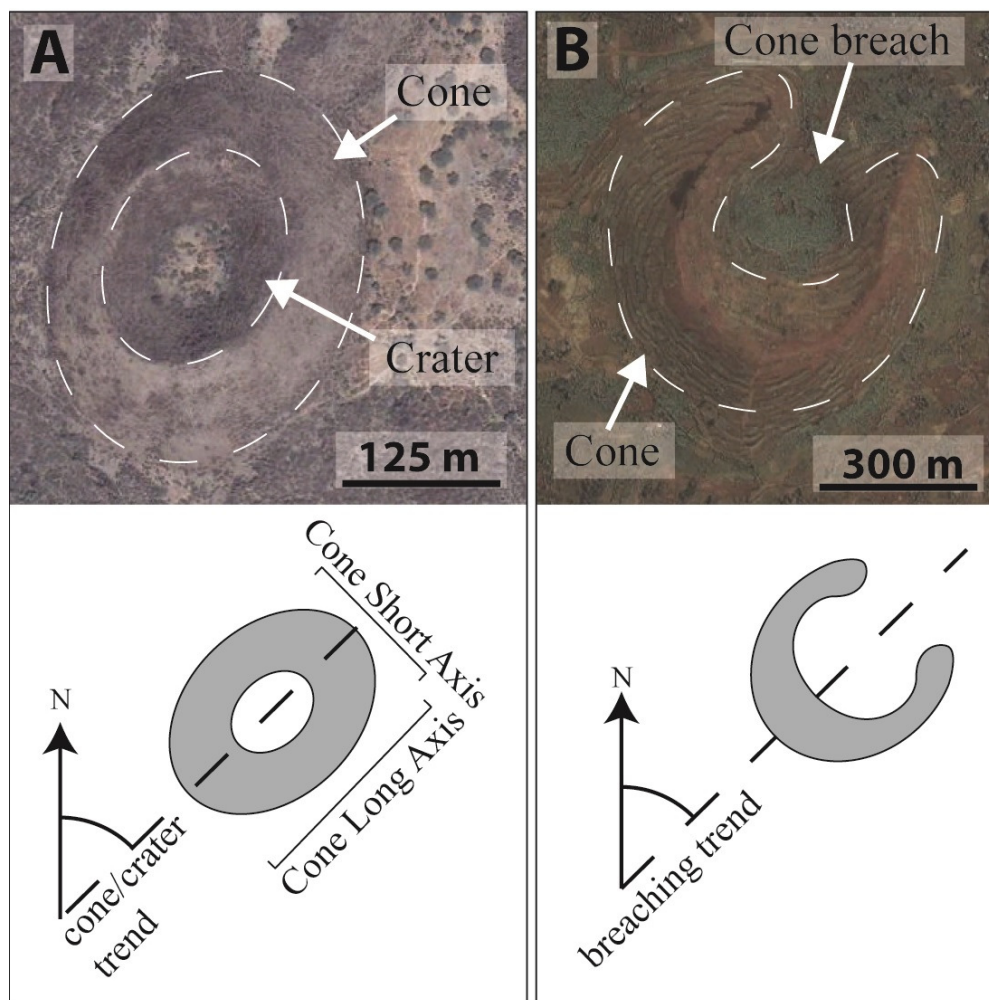


Figure 2.4. Google Earth image of a volcanic cone from the Boset segment outlining the cone and crater shape. Shown below is an illustration of a lineament trend from an elongate cone or crater. B: Google Earth image of a breached cone (Tibaldi, 1995) in the Virunga Province. Shown below is an illustration of the measured breaching trend.

Table 2.1 (next page). Summary of structural data presented in this study. “Observed mean NN” and “Expected mean NN” refer to nearest neighbor analyses both observed and modeled (Poisson distribution) for all cones in each field. Cone and rift basin ages are from: (1) Foster et al. (1997); (2) MacIntyre et al. (1974), Wilkinson et al. (1986); (3) Crossley (1979); (4) Smith (1994), George et al. (1998), Nyblade and Brazier (2002); (5) Ebinger

(1989), Kampunzu et al. (1998); (6) Wolfenden et al. (2004); (7) Hillaire-Marcel et al. (1986), Keller et al. (2006), Mattson and Tripoli (2011), Sherrod et al. (2013); (8) Nonnotte et al. (2008), Le Gall et al. (2008); (9) Baker and Mitchell (1976), Baker et al. (1988); (10) Mollet et al. (2008); (11) Macdonald et al. (2008), Macdonald and Baginski (2009); (12) Rogers et al. (1998), Smets et al. (2010); (13) Abebe et al. (2007). No faults were observed or documented for the Kilimanjaro field (*).

Field	North Tanzanian Divergence							Boset Segment
	South Natron	Arusha	Kilimanjaro	Natron-Magadi	Ngorogoro Volcanic Highlands	Naivasha-Nakuru	Virunga Province	
Age of faulting/rifting (Ma)	3 (1)	<2.2 (2)	N/A (*)	7-3 (1,3)	<3 (1)	15-12 (4)	11-10 (5)	11 (6)
Cone ages (Ma)	<0.35 (7)	<2.2 (2)	<1.0 (8)	<0.8 (9)	<2.25 (10)	<0.5 (11)	<0.2 (12)	<0.65 (13)
Rift branch	eastern	eastern	eastern	eastern	eastern	eastern	western	eastern
Basin type	immature, magmatic	immature, magmatic	immature, magmatic	immature, magmatic	immature, magmatic	mature, magmatic	mature, magmatic	mature, magmatic
Structural location	transfer zone	transfer zone	transfer zone	central axis	transfer zone	central axis	transfer zone	central axis
Number of cones	267	344	250	19	15	118	389	258
Area (convex hull) (m²)	1.52E9	6.74E9	3.87E9	2.74E9	1.07E8	2.05E9	2.79E9	6.00E8
Cone density (cones/km²)	0.176	0.051	0.0646	0.00693	0.14	0.0576	0.139	0.43
Observed mean NN (m)	966	1605	1445	N/A	N/A	1174	872	378
Expected mean NN (Poisson) (m)	1193	2213	1966	N/A	N/A	2083	1331	763
N.o. of cone lineaments	110	66	88	1	2	81	306	214
Mean strike of cone lineaments	029°	157°	142°	N/A	N/A	000°	014°	028°
N.o. of vent alignments	82	26	32	N/A	N/A	190	442	518
Mean strike of vent alignments	025°	145°	140°	N/A	N/A	003°	178°	032°
N.o. of fault segments	155	226	N/A	2157	58	264	9	201
Cumulative fault length (km)	630	1321	N/A	6583	635	1057	222	372
Mean fault strike (length-weighted)	010°	167°	N/A	007°	038°	173°	N/A	023°

2.6 Results

2.6.1 The Kenya Rift and North Tanzanian Divergence

The sections of the North Tanzanian Divergence and Kenya Rift analyzed in this study are sub-divided into 6 vent fields based on the general rift structure and the spatial distribution of vents (Table 2.1; Fig. 2.5; see Section 2.9.3 and 2.9.4). Two fields, the Natron-Magadi and Ngorongoro Volcanic Highlands, have few observable cones. The Kilimanjaro field (area 5 in Fig. 2.5) contains no observable faults, and exhibits NW-SE striking, extension-oblique cone lineaments (142° mean strike). These results are consistent with structural trends described in previous studies (Dawson, 2008; Nonnotte et al., 2008; Tibaldi et al., 2014). The overall NW-SE trend is comparable to the Chyulu Hills region (Fig. 2.3) and the Arusha field (area 4, Fig. 2.5) (Isola et al., 2014).

Cone lineament trends in the South Natron and Arusha fields (areas 2 and 4 in Fig. 2.5) are more variable than the Kilimanjaro field. For example, the South Natron field exhibits two distinct clusters exhibiting NNE-SSW and ESE-WNW trends (Fig. 2.6). The NNE-SSW striking lineaments show extension-normal orientations. These cones align subparallel with the orientation of the July 2007 dike intrusion deduced by Calais et al. (2008), as well as the mean fault orientation (010° , Fig. 2.6). The second ESE-WNW trending cone set aligns subparallel to a second dike intrusion in late-2007, near the eastern flank of Oldoinyo Lengai (Biggs et al., 2013).

The observed ~ESE-WNW cone lineament trend in the South Natron field seems counter-intuitive given that these cones align subparallel (rather than normal) to the regional extension direction. To investigate the controls on these contrasting alignments, cones were

sub-divided into two groups. In Figure 2.6a, those trending within 025° of the strike of the 2007 dike intrusion (027°) (Calais et al., 2008) are colored red, whereas those trending between 052° and 182° are colored green. Cones trending $052 - 182^\circ$ cluster locally in the southernmost 12 km of the South Natron field, within 18 km of the summit of Oldoinyo Lengai volcano. Conversely, the 72 cones trending between 002 and 052° occur in the northernmost 50 km of the South Natron field. The occurrence of locally clustered,

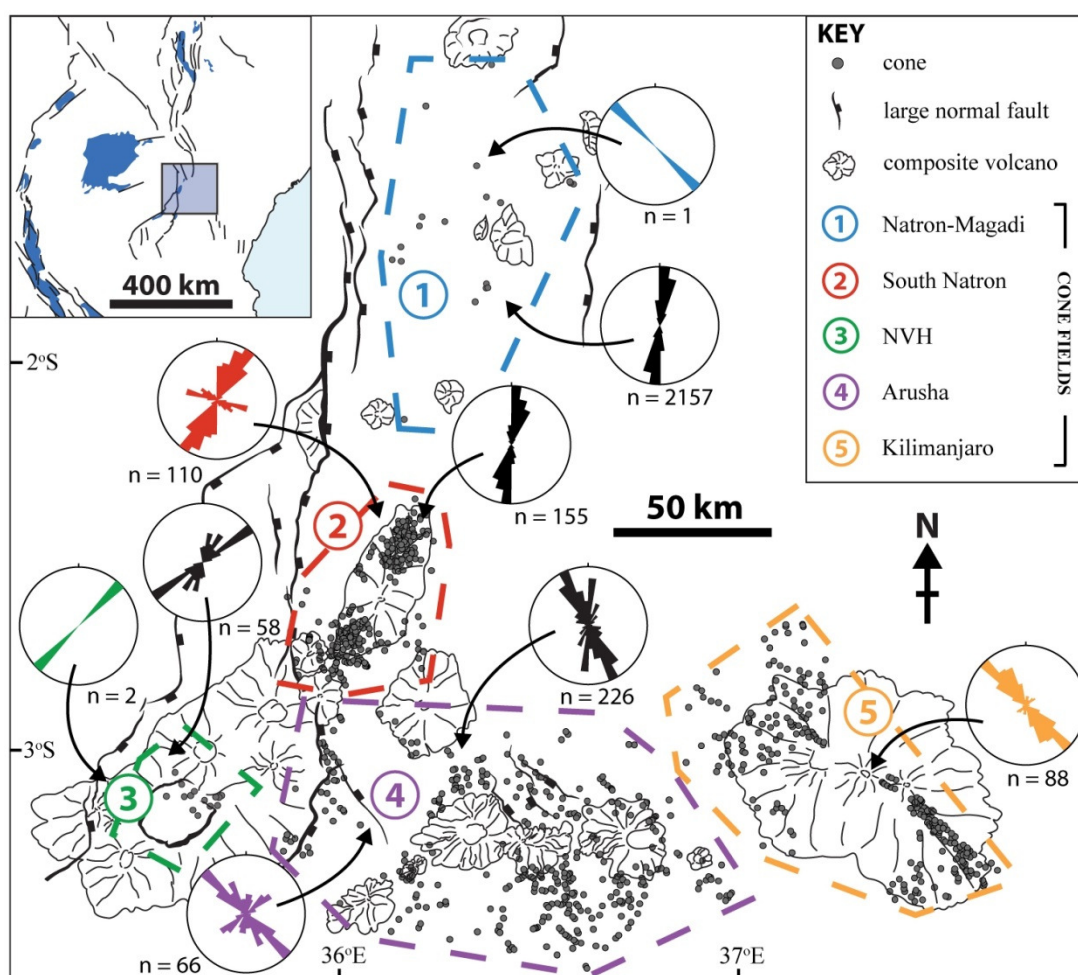


Figure 2.5. Rose diagrams of cone (colored rose diagrams) and fault (black rose diagrams) data from the North Tanzanian Divergence. The area has been sub-divided into cone fields (dashed boxes) based on fault structure and the general distribution of cones. NVH = Ngorongoro Volcanic Highlands. All fault data are length-weighted.

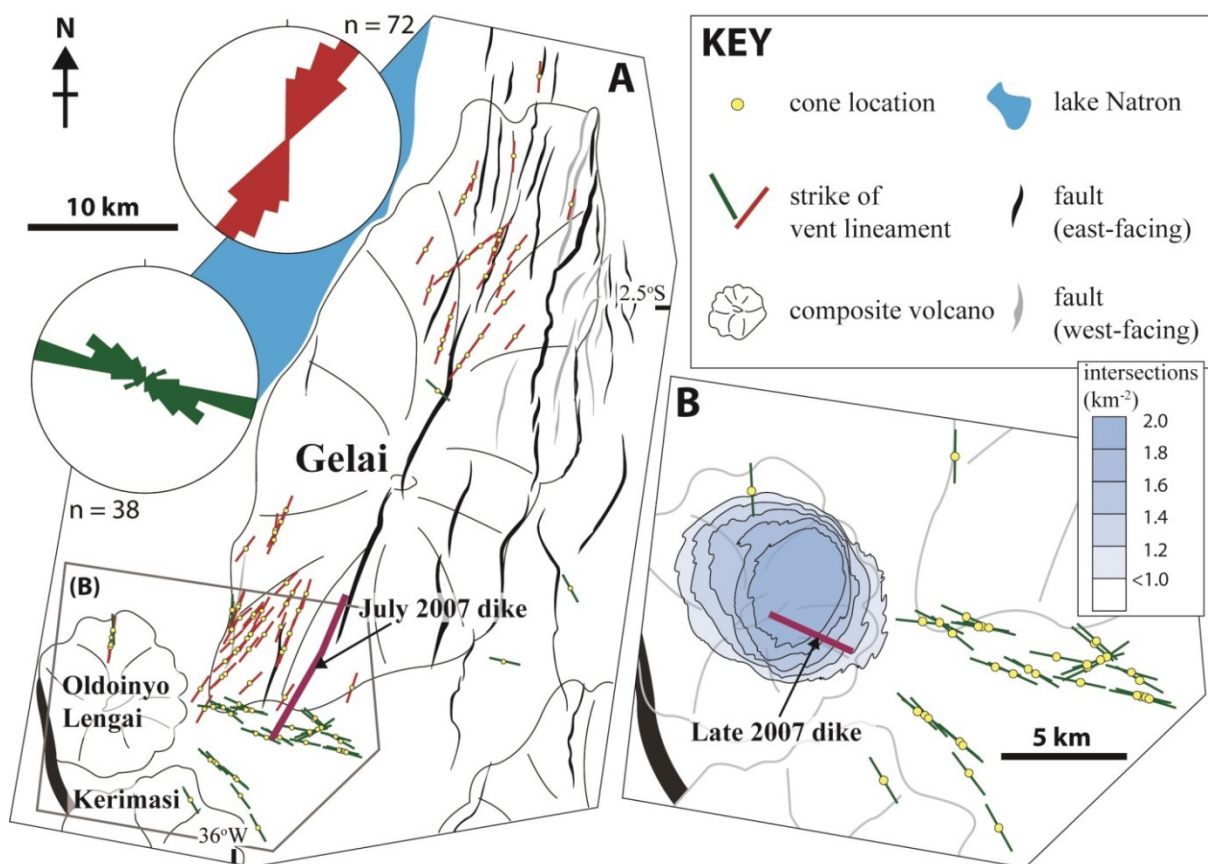


Figure 2.6. A: Cone lineament data from the South Natron field (area 2 in Fig. 2.5). Only the locations of cones exhibiting identifiable lineaments are shown. B: Zone of maximum intersections for cone lineaments with 052 - 182° trends. Intersections cluster around Oldoinyo Lengai volcano

~ESE-WNW trending cones in the vicinity of Oldoinyo Lengai highlight a potential magmatic stress control on cone orientations (e.g., Gudmundsson, 1998). This hypothesis was tested by constructing the area of maximum intersections (e.g., Ancochea et al., 2008), which is centered on Oldoinyo Lengai (Fig. 2.6b). Although these cones do not exhibit the full range of orientations expected for a radial swarm, the correspondence between maximum intersections and the location of Oldoinyo Lengai suggests that this volcano has, in part, affected the orientations of volcanic cones in the South Natron field.

Cone lineament trends in the Arusha field (area 4 in Fig. 2.5) also exhibit considerable variability. In general, the Arusha field marks a distinct change in the mean orientation of cone lineaments from north (South Natron: 027° mean strike) to south (Arusha: 157° mean strike) in the North Tanzania Divergence. The 157° mean NW-SE cone trend is subparallel to the mean fault orientation (167°) (Fig. 2.7a). An additional radial cone pattern is also observed in the vicinity of the active Meru volcano, as illustrated in the maximum intersections analysis presented in Figure 2.7b for cones <40 km from Mt Meru (see also Fig. 2.15).

In contrast to the North Tanzanian Divergence, cones are observed along the full length of the Naivasha-Nakuru basin of the Kenya Rift (Fig. 2.8). In general, cone lineaments here exhibit consistent extension-normal orientations (000° mean trend). These cones roughly align with intra-rift faults (179° mean trend) and faults on the rift borders (170° mean trend).

2.6.2 Comparative locations in the East African Rift: Virunga Province and Boset segment

Cone lineaments in the Boset segment exhibit consistent extension-normal orientations (028° mean trend). These lineaments align with local faults (Fig. 2.9) and shear-wave splitting lineations deduced by Kendall et al. (2005). Volcanic cones are present along the entire Boset segment with no significant deviations in the cone lineament trend. These data are consistent with cone lineament studies in the Main Ethiopian Rift by Korme et al. (1997) and Corti et al. (2013).

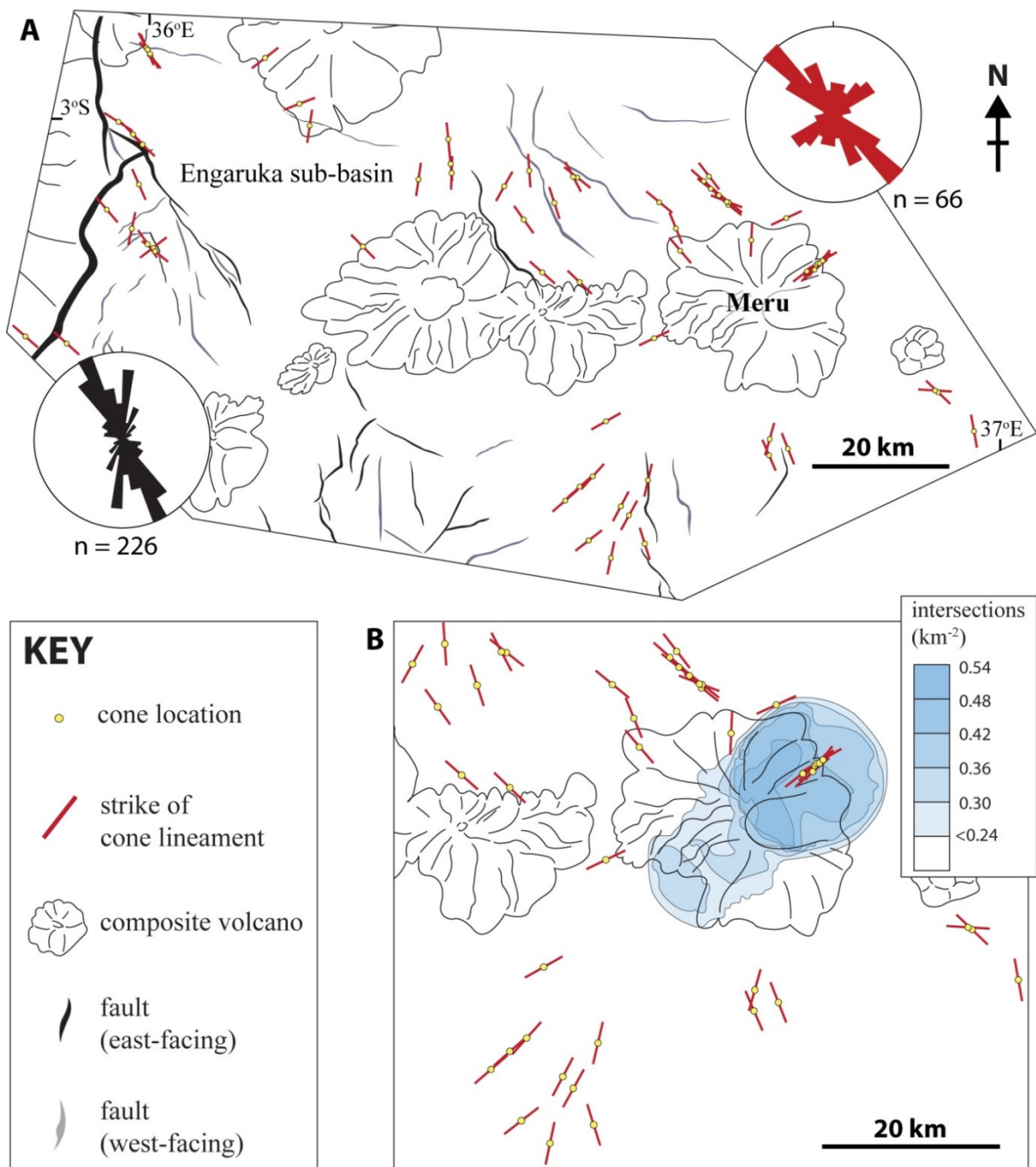


Figure 2.7. A: Cone lineament (red rose diagram) and fault orientation (black rose diagram) data from the Arusha field (area 4 in Fig. 2.5). Only the locations of cones exhibiting identifiable lineaments are presented. Fault data are length-weighted. B: Zone of maximum intersections for cones <40 km from the summit of Mt Meru.

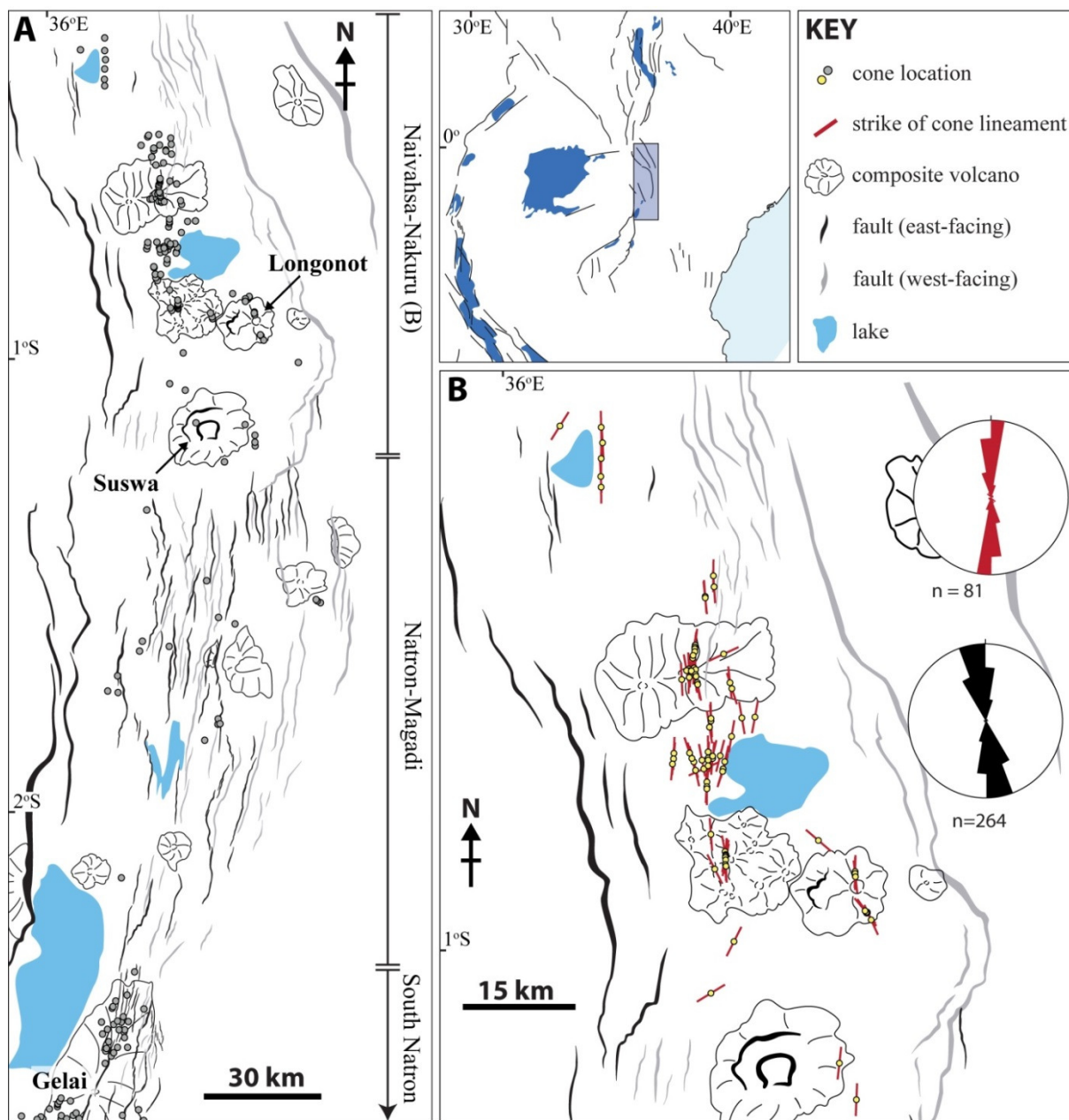


Figure 2.8. A: Locations of monogenetic cones from the Naivasha-Nakuru basin to the South Natron field. B: Cone lineament (red rose diagram) and fault orientation (black rose diagram) data from the Naivasha-Nakuru basin. Only the locations of cones exhibiting identifiable lineaments are presented. Fault data are length-weighted.

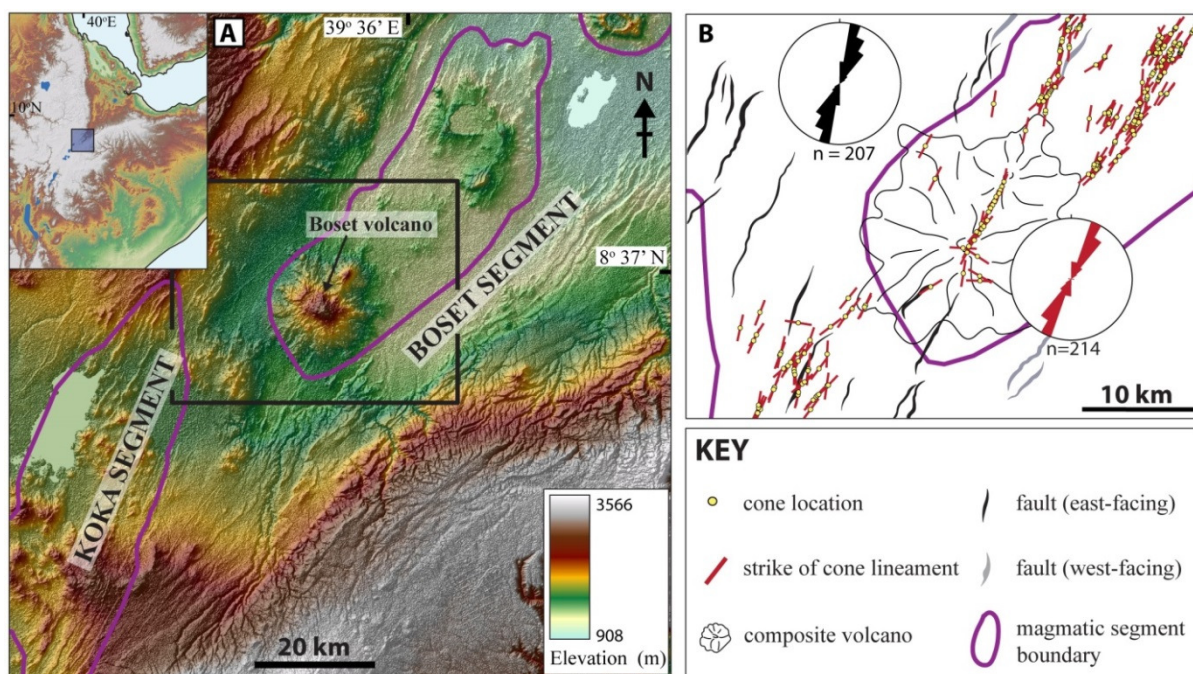


Figure 2.9. A: Aster DEM image of the northern Main Ethiopian Rift. The boundaries for the magmatic segments are from Keranen et al. (2004). Black box shows location of map in B. B: Cone lineament (red rose diagram) and fault orientation (black rose diagram) data for the Boset magmatic segment in this study. Only the locations of cones exhibiting identifiable lineaments are presented. Fault data are length-weighted.

Cone lineament data for the Virunga Province in the Western rift of the EAR exhibit considerable complexity (Fig. 2.10). In the southern 30 km of the field, cones have primarily extension-normal orientations (018° mean trend). In the vicinity of the Nyamuragira and Nyiragongo volcanoes, the trends are variable and exhibit radial patterns. In the eastern part of the field, vent orientations are primarily extension-normal (028° mean trend). This structural variability was noted by previous authors (Smets et al., 2010; Wadge and Burt, 2011; Wauthier et al., 2013; Tibaldi et al., 2014), who related dike and fissure orientations to local magmatic overpressures, pre-existing structures, volcano topography and the far-field extensional tectonic environment.

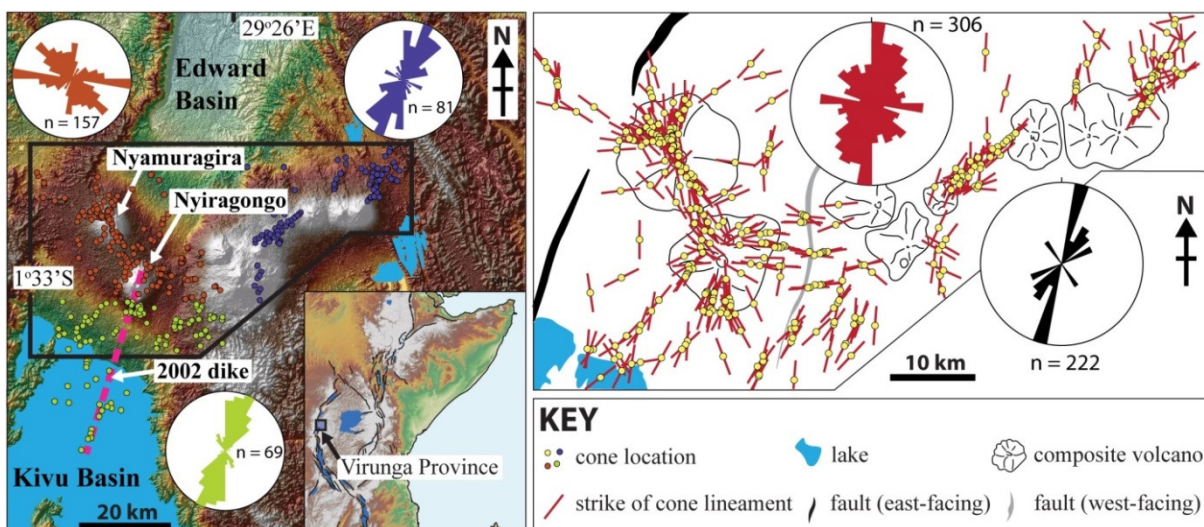


Figure 2.10. A: Locations of cones in the Virunga Province. Rose diagrams show cone lineament trends, with different colors corresponding to cones in the southern (green), northern (orange), and eastern (purple) sections of the Virunga Province. B: Locations and orientations of cones exhibiting identifiable lineaments. Red rose diagram shows cone lineaments (this study). Black rose diagram shows fault orientations from Wadge and Burt (2011). Fault data are length-weighted.

2.7 Discussion

2.7.1 Limitations of the analysis

Studies of volcanic cone geometries provide a limited view of an underlying intrusive system. For example, only the present state of the cone distributions and morphologies can be obtained (Le Corvec et al., 2013a), and older cones are likely to have been eroded and covered by lavas and/or sediments. Sparse age dating in most volcanic fields also limits robust assessment of intrusion variability over time (Condit and Connor, 1996; Negrete-Aranda et al., 2010). Furthermore, volcanic cones only give the orientations of dikes that erupted at the surface, and not necessarily the shallowly-arrested or deeper intrusions. Therefore, the geometry of volcanic feeders may be more complex than what is measured from surface exposures – examples include vents that overlie shallowly-dipping cone sheets

or sill-fed dike intrusions (Galland et al., 2009; Magee et al., 2013a; Muirhead et al., 2014; refer also to Chapter 7).

Despite these limitations, the dike orientations inferred from this study are in close agreement with geophysical and geodetic studies of active diking in these areas, including the 2007 Natron and 2002 Nyiragongo dike intrusions (Calais et al., 2008; Wauthier et al., 2012; Biggs et al., 2013) (Figs. 2.6 and 2.10a). This similarity suggests that the analysis provides a reasonable picture of the EAR's contemporary magmatic architecture.

2.7.2 Tectono-magmatic controls on dike orientations in the Kenya Rift and North Tanzanian Divergence

The orientations of faults and cone lineaments in the Kenya Rift and North Tanzanian Divergence reflect the role of various tectono-magmatic forces described in the introduction. These include, in addition to the regional stress state, (1) pre-existing weaknesses, (2) local magma overpressures, (3) volcanic edifice loading and (4) basin segment interactions.

Extension-normal dikes: influence of the regional stress state

Extension-normal cone lineaments are observed in the South Natron field and along the central axis of the Naivasha-Nakuru basin (Fig. 2.8). These cones align with the orientations of fault structures, and are normal to the regional σ_3 direction. It is inferred that extension-normal cones represent aligned swarms of dikes, with orientations controlled by the regional extensional stress field. As these basins comprise abundant fault and dike systems oriented normal to the regional σ_3 , many of the dikes could potentially be focused along pre-existing structures (Le Corvec et al., 2013b), as is interpreted for interacting fissures and

faults in magmatic rifts in the Reykjanes Peninsula, Iceland (Jenness and Clifton, 2009), and the Main Ethiopian Rift (Casey et al., 2006; Mazzarini, 2013b).

Cones are, however, rarely observed on top of 0.8-1.4 Ma lavas along the central axis of the Natron-Magadi basin (Baker and Mitchell, 1976; Baker et al., 1988) (Figs. 2.5 and 2.8). This observation suggests that dike-driven rifting is either relatively infrequent or rarely results in surface eruptions. In contrast, in the Naivasha-Nakuru basin, extension-normal cone lineaments are observed along the full length of the basin; hence, extension-normal dike rifting may be the primary mode of magmatic strain accommodation in this part of the Kenya Rift.

Radial dikes: the role of magma overpressure

Radial cone lineaments are observed in the South Natron and Arusha fields, with the area of maximum intersections occurring in the vicinity of active volcanoes (i.e., Oldoinyo Lengai and Meru; Figs. 2.6 and 2.7). Given that the age of the cones forming these radial patterns also overlaps with the ages of the volcanic edifices (Wilkinson et al., 1986; Roberts, 2002; Sherrod et al., 2013; Mana et al, 2015), it is likely that these geometries are primarily related to local stress fields induced by shallow crustal magma chambers below the volcanic centers (e.g., Muller and Pollard, 1977; Bistachhi et al., 2013). An alternative hypothesis is that the radial pattern results from volcano loading (Tibaldi et al., 2014). However, in South Natron, cones forming the Oldoinyo Lengai radial group (Fig. 2.6b) are also observed on and around the slopes of the inactive, 1.0-1.2 Ma Kerimasi and Gelai volcanoes (Mana et al, 2015). The effect of edifice loading from these volcanoes appears to have had little to no influence on these cone lineaments – instead of exhibiting trends that converge on the volcano

edifice and trend parallel to the downslope direction (e.g., Roman and Jaupart, 2014), cones on the southern flank of Gelai and northeastern flank of Kerimasi trend sub-perpendicular to the downslope direction and converge on the summit of Oldoinyo Lengai (Fig. 2.6).

Baer et al. (2008) highlight the NNE migration of the July 2007 dike intrusion as evidence of a dike fed laterally away from a ~3 km-deep (i.e., Petibon et al., 1998; Biggs et al., 2013) magma chamber below Oldoinyo Lengai volcano. Lateral propagation of radial dikes as far as 18 km from the volcano could be additionally assisted by stress gradients induced by the Oldoinyo Lengai edifice load (Hurwitz et al. 2009; Roman and Juapart, 2014). However, geochemical and petrologic data imply that a shallow crustal magma chamber did not laterally source all dikes in the South Natron field. For example, Mattsson et al. (2013) show that cones in the inferred radial swarm have primarily melilitite (67% of sampled cones) and nephelinite compositions (29%). Settling velocity estimates of mantle inclusions observed in melilitites require these magmas to ascend from the upper mantle in 1-2 days, whereas nephelinites show evidence for fractional crystallization and thus greater residence times at shallow crustal depths (Mattsson, 2012; Mattsson et al., 2013). Consequently, it is unlikely that all cones forming radial patterns in the South Natron field were fed by dikes propagating laterally away from Oldoinyo Lengai; some were instead fed directly from a mantle source. Based on these observations, the radial cone patterns in the North Tanzanian Divergence reflect two possible scenarios of intrusion: (1) dikes propagate upward from mantle depths, then rotate in the vicinity of a pressurized magma chamber in the shallow sub-surface (e.g., at ~3 km depth); and (2) high magma pressures in a shallow crustal magma reservoir result in chamber failure and radial diking away from the source, with lateral propagation promoted further by the effects of volcanic edifice loads.

Extension-oblique dikes and faults: pre-existing structures or stress rotations?

The presence of NW-SE trending, extension-oblique cone lineaments in the North Tanzanian Divergence (areas 4 and 5 in Fig. 2.5) can be explained as the result of either (1) dikes intruding pre-existing, transverse structures (Le Corvec et al., 2013a, b), and/or (2) local rotations of σ_3 from rift segment interactions (Pollard and Aydin, 1984). The Proterozoic basement in Kenyan and Tanzanian regions of the EAR contains NW-SE striking shear zones, which are aligned locally with recently active, transverse faults (Smith and Mosley, 1993; Le Turdu et al., 1999; Le Gall et al., 2008; Kattenhorn et al., 2013). This observation has led authors to infer that faults and dikes exploit this structural fabric under the current ESE-WNW extension direction (Smith and Mosley, 1993; Haug and Strecker, 1995; Le Turdu et al., 1999; Isola et al., 2014).

In contrast with these studies, fault and cone lineament data may also reflect local rotations of σ_3 within the Ngorongoro-Kilimanjaro Volcanic Belt away from the present-day, WNW-ESE regional extension direction (Stamps et al., 2008; Saria et al., 2014) (areas 3-5, Fig. 2.5; Fig. 2.11). Fault kinematics from previous seismic and structural studies, in conjunction with fault and cone lineament data from this study, support this hypothesis (Fig. 2.11). For example, fault plane solutions indicate NW-SE extension from Oldoinyo Lengai into the Ngorongoro Volcanic Highlands (Calais et al., 2008; Delvaux and Barth, 2010), consistent with the NE-SW striking faults and cones in this study. Existing fault plane solutions around the Arusha field, although sparse, suggest a component of NE-SW extension (Delvaux and Barth, 2010) (Fig. 2.11), which would result in the observed NW-SE fault and cone lineament trends. Extension directions deduced from fault striations on NW-SE striking

faults near the Engaruka sub-basin (Fig. 2.7a) and the northernmost portion of the Manyara basin also support a similar NE-SW extension direction (Ring et al., 2005).

These stress rotations are likely the product of the mechanical interaction of the Natron basin with the Eyasi and Pangani basins (Fig. 2.11; see also Fig. 2.16). For example, an interaction between the Natron and Pangani basins would result in a local counterclockwise rotation of σ_3 (Pollard and Aydin, 1984), consistent with the NW-SE striking cone and fault structures in the Arusha field (Fig. 2.11). Similarly, the NW-SE extension in the Ngorongoro Volcanic Highlands (Fig. 2.11) could result from an interaction between the Eyasi and Natron basins. Although basement weaknesses may have additionally been reactivated under these modified stress environments (e.g., Isola et al., 2014), the mechanical interaction between rift basin segments is inferred here to exert a first-order control on the observed structural fabrics.

2.7.6 Magmatic architecture of transfer zones: implications for magma-driven rifting

The results of this study, in combination with remote-sensing studies of modern-day intrusion events (Calais et al., 2008; Wauthier et al., 2012; Biggs et al., 2013; Wauthier et al., 2013), can be incorporated into a conceptual model of the magmatic architecture of transfer zones in rift basins (Fig. 2.12). Stress fields induced by magma reservoirs produce radial dikes, whereas extension-oblique dike intrusions form from the mechanical interaction between segmented rift basins. Extension-normal dikes occur at the boundary between transfer zones and the “distal ends” of rift basins, where their orientations are controlled by the regional extensional stress field (Fig. 2.12).

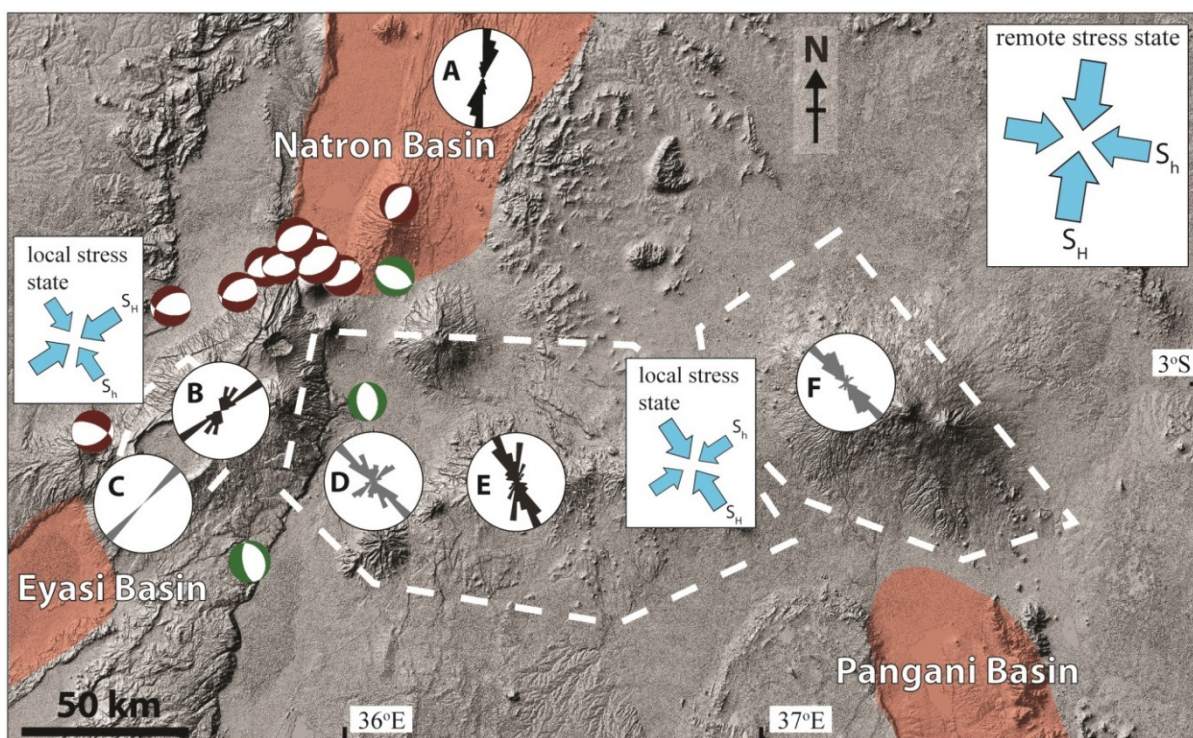


Figure 2.11. Interpretation of the local stress state in the Ngorongoro Volcanic Highlands (area 3 in Fig. 2.5), Arusha (area 4 in Fig. 2.5) and Kilimanjaro fields (area 5 in Fig. 2.5) of the Ngorongoro-Kilimanjaro Volcanic Belt, based on fault and cone lineament orientations and earthquake focal mechanisms. Focal mechanism data are from the Global CMT catalog (Appendix A). Focal mechanisms are colored based on earthquake location and the strikes of fault and auxiliary planes. Focal mechanisms with NW-SE striking faults are colored green. Those colored brown have NE-SW fault strikes and occur from the flanks of Oldoinyo Lengai southwest to the Eyasi Basin. The black focal mechanism occurs north of the Gelai summit, and strikes NNW-SSE, sub-perpendicular to the modeled plate motion vector (Stamps et al., 2008; Saria et al., 2014). Rose plots represent fault (black) and cone lineament (grey) data from this study from South Natron (A), the Ngorongoro Volcanic Highlands (B and C), Arusha (D and E), and Kilimanjaro fields (F). S_H and S_h represent the greatest and least horizontal compressive stresses, respectively.

Modern-day InSAR observations of dike intrusions support these interpretations.

Wauthier et al. (2013) describe a 15-year history of dike intrusions in the vicinity of Nyamuragira (Virunga Province), occurring from 1996 to 2010. Dike intrusions in the vicinity of Nyamuragira's magma reservoir showed considerable variability in their orientations, producing a semi-radial pattern, although some dikes exhibited shallow dips. The late-2007 dike intrusion on the western side of Oldoinyo Lengai also matches the radial pattern inferred

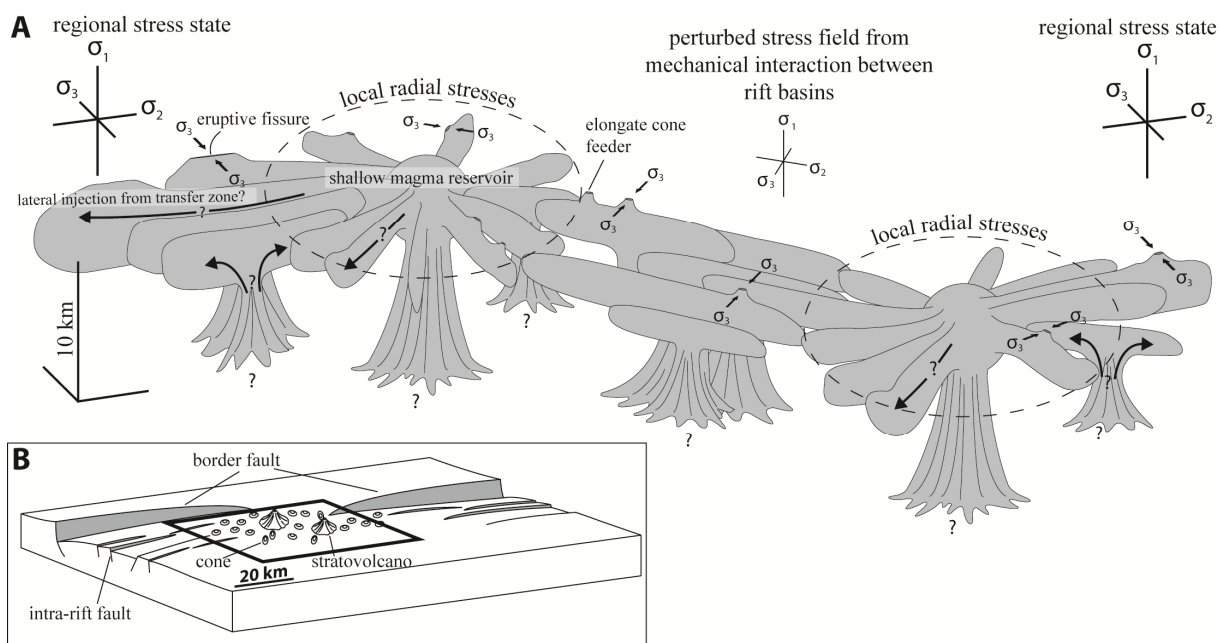


Figure 2.12. A: 3-D conceptual illustration of shallow dike networks in transfer zones in this study. The strikes of intrusions are controlled by variations in the stress state within the transfer zone. Extension-normal dikes, with orientations controlled by the regional stress state, intrude the distal ends of the rift basins. Zones of shallow magma storage, situated below active volcanoes, create a local magmatic stress field responsible for the formation of radial dikes. These shallow magma reservoirs are assumed to be fed from below. Extension-oblique dikes form under a rotated stress field driven by the mechanical interaction between adjacent rift segments. Erupted dikes are either fed laterally from shallow magma reservoirs or ascend from mantle depths. The ascent path of magma below the upper few kilometers of the crust cannot be constrained from the data presented in this study. B: Inset showing the structural location (transfer zone) of the volcanic cones fed by the dike network presented in A (region indicated by box).

in this study (Fig. 2.6b). Examples of extension-normal intrusions in the vicinity of transfer zones include the ~10 km-long, 2007 Natron (Calais et al., 2008) and ~20 km-long, 2002 Nyiragongo dike intrusions (Wauthier et al., 2012). Like the extension-normal cones observed in this study (Figs. 2.6a and 2.10a), the 2002 Nyiragongo dike extended southward from the transfer zone 10 km into the northern end of the Kivu Basin (Wauthier et al., 2012). A potential implication is that the injection of extension-normal, upper crustal dikes laterally from transfer zones into the rift axis may facilitate magmatic rifting in both magma-poor and immature magmatic rifts of the EAR, albeit localized to the distal ends of these basins.

Furthermore, the focusing of magma within transfer zones suggests that dike intrusion, rather than tectonic faulting, may be the preferred mode of upper crustal strain accommodation within these structural settings (Rowland et al., 2010).

2.7.7 Variations in dike patterns across the East African Rift

Cone lineament data presented in this study reveal that the geometries and distribution of upper crustal dikes vary between magma-rich and magma-poor rifts across the EAR, and over the course of rift evolution (Fig. 2.13). For example, evolved magmatic rifts (the Naivasha-Nakuru basin and Boset segment) in the Eastern rift exhibit extension-normal cone lineament trends along their entire lengths. Despite the presence of active volcanic centers in these regions (e.g., Boset volcano), the radial patterns observed in the North Tanzanian Divergence and Virunga Province are not present. These observations suggest that extension-normal, upper crustal dikes accommodate regional extension across the full length of evolved rift basins of the Eastern rift. This assertion is supported by modern day seismicity and InSAR observations of the 2004 and 2008 diking in the Erta Ale segment (Nobile et al., 2012; Pagli et al., 2012), and the 2005-2010 Dabbahu-Manda Hararo rifting event (Ebinger et al., 2010). During these rifting episodes, dikes intruded rift-parallel along the length of the central axis of these basins. Despite the inferred presence of multiple magma reservoirs at depth (Keir et al., 2009b; Pagli et al., 2012), no local radial patterns were observed in the dike populations. One exception is the 2000 dike intrusion by the Ayelu volcano in the northern Main Ethiopian Rift, which exhibited a 122° , rift-oblique trend. The orientation of this intrusion was interpreted by Keir et al. (2011b) to reflect the NE-oriented African-Arabian extension responsible for opening of the Red Sea, although radial stresses resulting from magma overpressures or volcanic edifice loading were not completely ruled out.

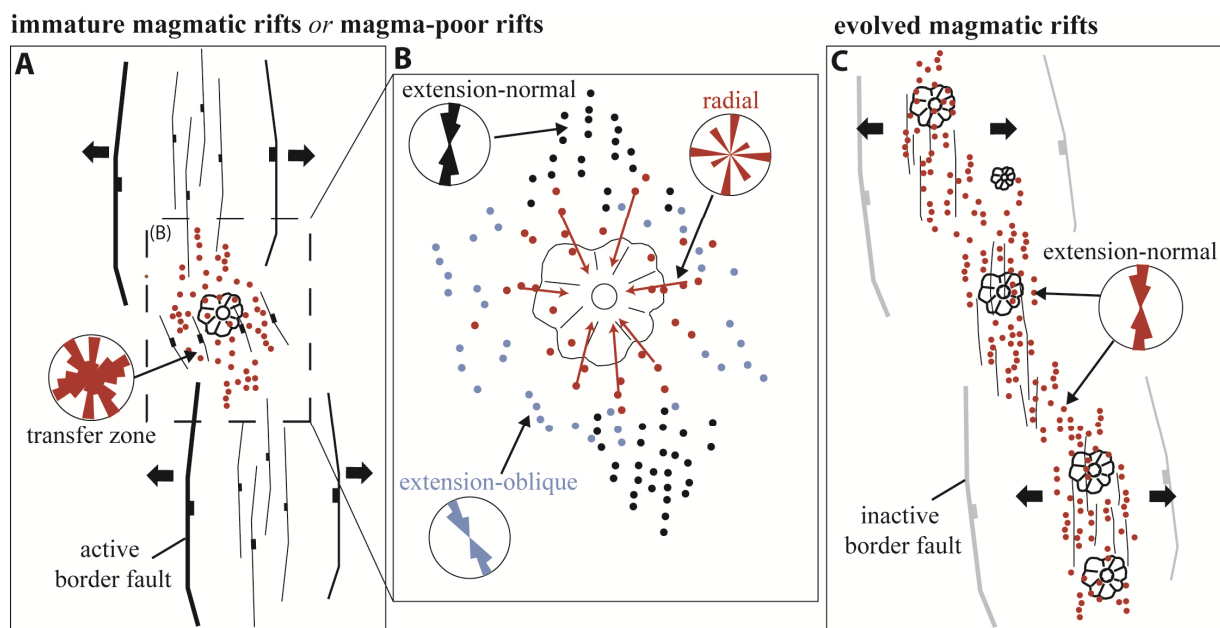


Figure 2.13. Schematic representation of the distribution of cones and their trends in this study. Rose diagrams provide a conceptual example of the expected cone lineament trends in the different structural settings. Black arrows in A and B represent the regional extension direction (E-W in this example). A: Immature magmatic rifts and magma-poor rifts. Cones (red circles) focus in transfer zones and the distal tips of basins. B: The range of cone trends distributed within transfer zones in immature magmatic rifts and magma-poor rifts. Extension-normal cones (black circles, black rose diagram) occur near the boundary between the transfer zone and the distal tip of the basin. Extension-oblique cones (blue circles, blue rose diagram) occur across the entire transfer zone. Their orientations are controlled by stresses related to the mechanical interaction between rift segments, as well as inherited crustal structure, which together also control the orientation of faults within the transfer zone. Radial cones (red circles, red rose diagram) occur in the vicinity of volcanoes with orientations related to local, magmatically perturbed stresses. C: Distribution of extension-normal cone lineament trends along evolved magmatic rifts. In evolved magmatic rifts, strain focuses into magmatic segments (Keranen et al., 2004), and cone lineament trends provide no evidence for radial diking and mechanical interactions between basin segments in potential transfer zones.

In contrast to evolved magmatic rifts, magma-poor rifts in the Western rift of the EAR and immature magmatic rifts in the Eastern rift exhibit spatial variations in both the occurrence and orientation of upper crustal dikes (Fig. 2.13). Consistent with previous experimental and geological studies (e.g., Rosendahl, 1987; Ebinger, 1989; Corti et al., 2002a, b), the flux of magma from depth in these basins appears spatially variable, with magma preferentially drawn into transfer zones. The central portions of these basins may, however,

experience punctuated phases of dike-fed eruptions over time scales of perhaps 10^5 years (Ebinger et al., 2013), to produce lavas such as the 0.8-1.4 Ma Magadi trachytes or the 1.0-1.2 Ma Gelai volcanics of the Magadi and Natron basins, respectively (Baker and Mitchell, 1976; Mana et al., 2015). However, in the interim (i.e., 0.8 Ma – Present), cones are rarely observed along the central axes of these basins (e.g., Area 1, Fig. 2.5). Recent observations of dike intrusions within these areas (e.g., July 2007 Natron dike) (Calais et al., 2008) thus only reflect the local importance of dike-driven rifting to particular structural zones (i.e., transfer zones), rather than illustrating a basin-wide mode of upper crustal strain accommodation.

Previous studies have also highlighted variations in the distribution of magmatism among rift basins in the East African Rift (Baker et al., 1971; Kampunzu et al., 1998; Wolfenden et al., 2004; Rooney et al., 2007, 2014). In the Main Ethiopian Rift in particular, linear belts of volcanic cones are observed both within rifts and along rift margins (Korme et al., 1997; Mazzarini, 2004; Corti, 2009; Rooney, 2010). Volcanic cones in the central Main Ethiopian Rift become progressively younger towards the rift axis (WoldeGabriel et al., 1990; Wolfenden et al., 2004; Rooney et al., 2014). Some authors have suggested that magmatism may migrate from the rift borders to the central axis as continental rifts evolve (Ebinger, 2005), although studies in the Arabian margin of the Red Sea Rift show that magma-driven rifting can occur along rift margins even after the onset of sea-floor spreading (Pallister et al., 2010). Along-strike variations in cone density are observed in the Main Ethiopia Rift, and attributed to melt focusing resulting from steep gradients along the lithosphere-asthenosphere boundary (Keir et al., 2015). In contrast with these studies, results presented here not only demonstrate that the density of upper crustal dikes varies spatially within rift basins, but dike orientations also vary as a result of changing tectono-magmatic conditions.

2.8 Conclusions

Cone lineament data presented in this study reveal spatial variations in the distribution and geometries of upper crustal dike intrusions across rift basins in the East African Rift. Upper crustal diking in the North Tanzania Divergence is focused in a transfer zone. Dike intrusions here rarely occur along the central axis of rift basins (e.g., Natron-Magadi basin), suggesting that dikes play a limited role in accommodating upper crustal extension in this part of the rift. Transfer zones in the EAR exhibit complex dike geometries that can be attributed to local stress fields related to pressurized magma chambers and mechanical interactions between rift segments, in addition to the regional stress field. These transfer zones may contribute to the rifting process by sourcing upper crustal dikes that propagate laterally into the tips of rift basins.

The distributions and orientations of upper crustal dikes in the Eastern rift of the EAR vary over the timescale of continental rift evolution. During early-stage rifting (<10 Ma), surface-breaching dikes are confined to areas in and around transfer zones, whereas dikes in evolved rift basins accommodate upper crustal extension along the full length of the basin. These time-evolving complexities need to be considered in numerical and analog modeling studies investigating the mechanical effects of dike intrusion on rift initiation and continental rift development.

2.9 Supporting information

2.9.1 Stress fields induced by pressurized magma chambers

The stress conditions involved in the generation of radial dike patterns may be modeled in two-dimensions as a pressurized hole in an elastic body subject to a biaxial remote

stress field (Muller and Pollard, 1977; Baer and Reches, 1991; Koenig and Pollard, 1998). Some modeling studies also include additional stress sources, such as an overlying volcanic load (e.g., Pinel and Juapart, 2003; Hurwitz et al., 2009; Le Corvec et al., 2015). The presence of a pressurized hole, or magma chamber, perturbs the local stress field (Fig. 2.14). This perturbation results in a radial stress pattern, where the greatest compressive stress (σ_1) rotates around the chamber such that the strike of σ_1 everywhere converges on the center of the chamber. The magnitude of this local stress perturbation is dependent on magma chamber radius (R), internal magma pressure (P) and the remote differential stress ($\sigma_{11} - \sigma_{22}$) (Fig. 2.14a). If R and P remain constant, the magnitude of the stress perturbation decreases with increasing differential stress values (Fig. 2.14b-d).

This study describes a number of radial dike patterns in the East African Rift (EAR), possibly reflecting these modeled effects. Figure 15 shows a moving average analysis of the radial dike swarms in the North Tanzanian Divergence. Note the change in the mean orientations in the NE, SE, SW and NW sectors around the Oldoinyo Lengai and Meru volcanoes. Around Meru, dikes in the NE and SW sectors exhibit ~NE-SW striking trends, whereas dikes in the NW and SE sectors exhibit ~NW-SE trends, indicative of a radial pattern. This radial trend prevails for cone lineaments both near the volcano (<25 km from the volcano summit), as well as those as far as 40 km from the summit. Radial swarms may also be differentiated using the method of maximum intersections (Ancochea et al. 2008), shown in Figures 2.6 and 2.7.

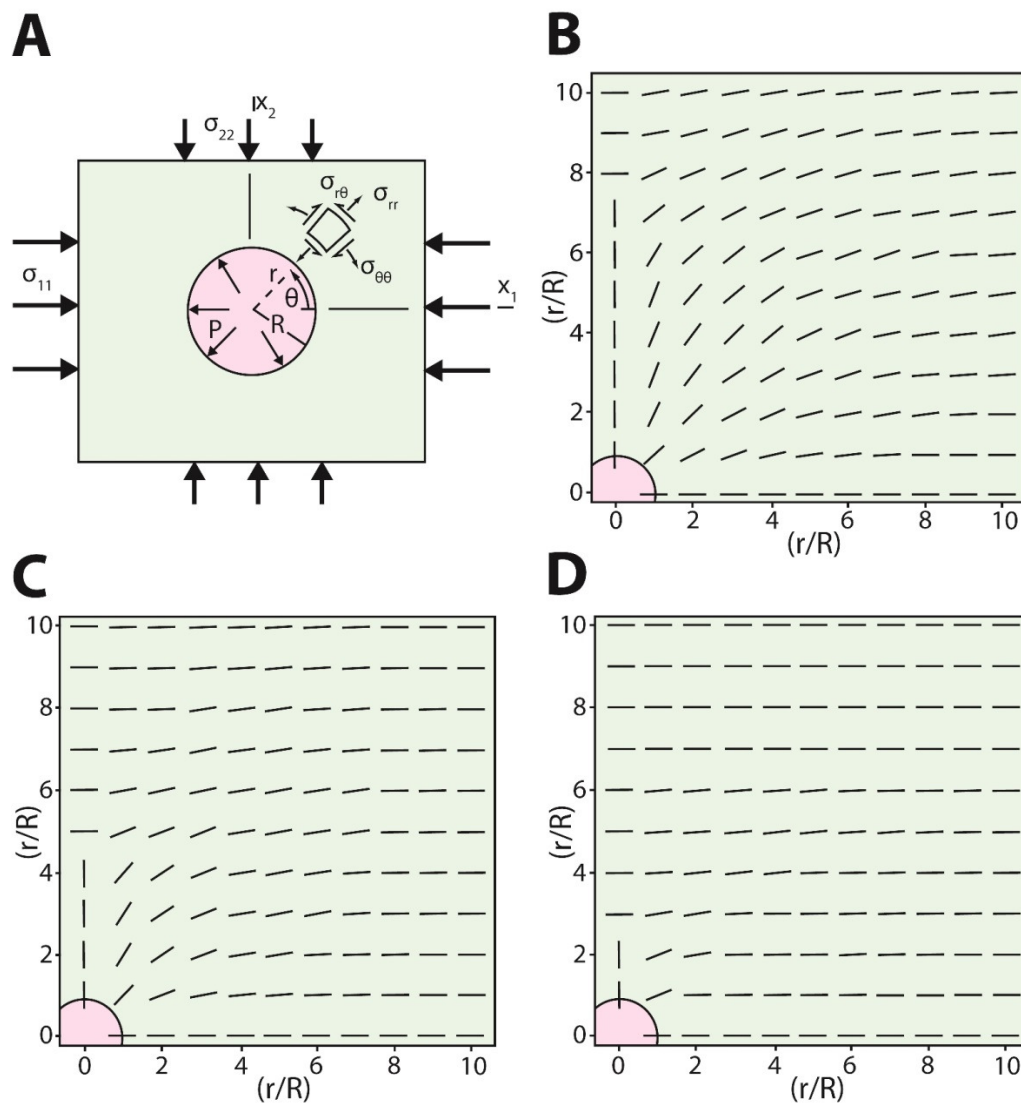


Figure 2.14. Two-dimensional elastic models of a pressurized hole (magma chamber) in an elastic plate, modified from Koenig and Pollard (1998). A: Idealization of the model setup. Pink circle represents the pressurized hole (magma chamber) with radius, R , and internal pressure, P . The hole is subject to remote biaxial loading from a least (σ_{22}) and greatest (σ_{11}) compressive stress. θ and r indicate the polar coordinate system, the origin of which is located at the center of the hole. B-D: Calculated stress trajectories resulting from a pressurized magma chamber. Black ticks at each grid point represent the local orientation of σ_1 . In each example, internal magma pressure (100 MPa) and chamber diameter (normalized to 1) are held constant, while the remote stress difference is varied from 2 to 10 to 20 MPa in B, C and D, respectively. Analytical solutions for these models are provided in Koenig and Pollard (1998).

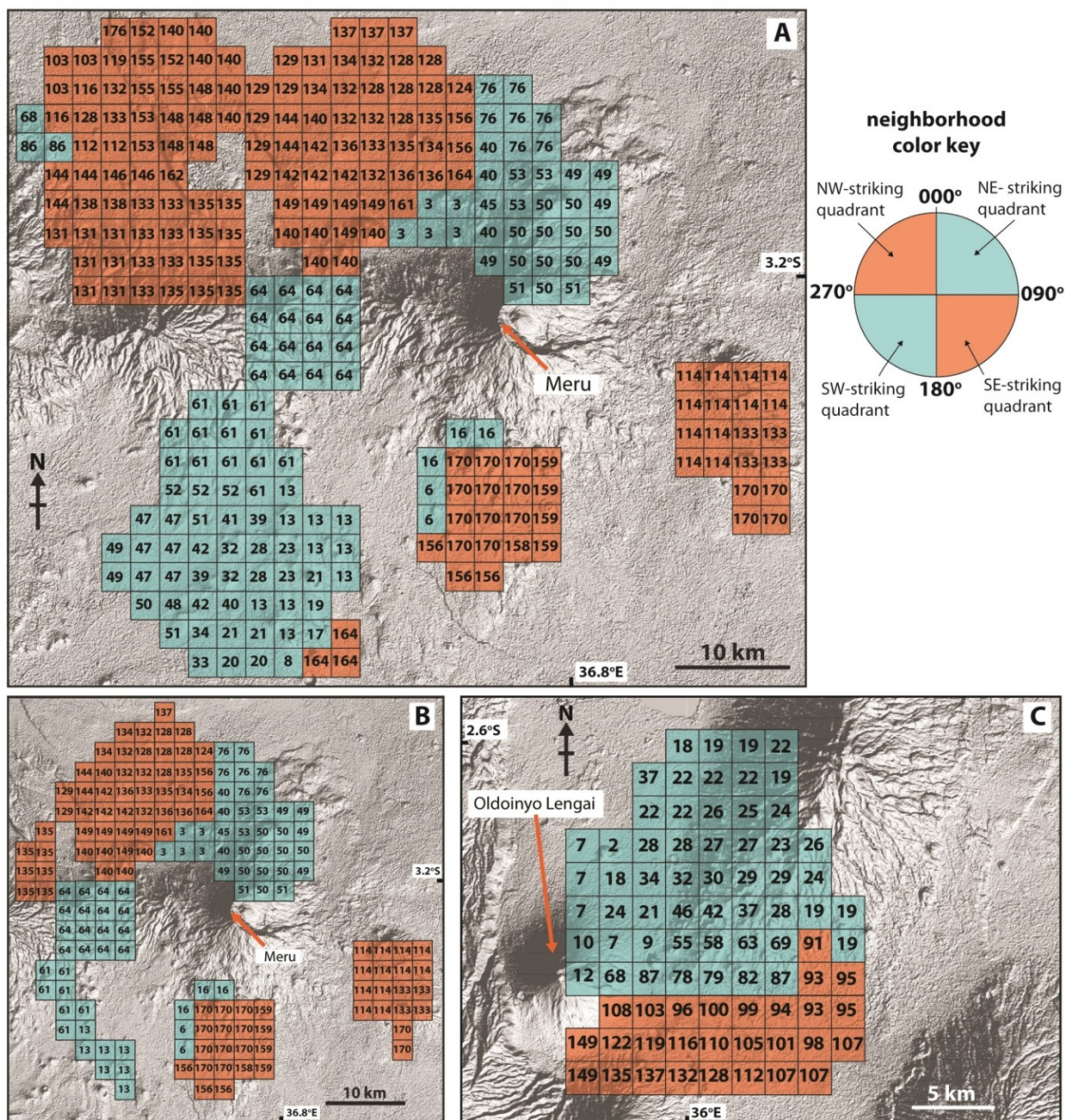


Figure 2.15. Moving average analyses of dike trends in the South Natron and Arusha fields. The analysis was performed in ArcGIS v. 10.3 and involves non-overlapping neighborhoods (2.5 x 2.5 km in size) and a search radius of 6 km. Neighborhoods colored blue contain cone lineaments with mean strike values in NE and SW quadrants (i.e., 000-090° and 180-270°, respectively). Neighborhoods colored red contain cone lineaments with mean strike values in SE and NW quadrants (i.e., 090-180° and 270-360°, respectively). A: Moving average analysis of cone lineaments in the Arusha field for neighborhoods within 40 km of the summit of Meru volcano. B: Same analysis as in A, except that only neighborhoods within 25 km of the summit are presented. C: Analysis of mean strike values of cones in the South Natron field for neighborhoods within 22 km of the summit of Oldoinyo Lengai. Note that in each analysis the mean orientations of cone lineaments varies depending on the position around the volcano. Cones in NE and SW quadrants also show ~NE-SW striking lineaments. Those in SE and NW quadrants exhibit ~SE-NW striking lineaments. These geometries are consistent with a radial pattern.

2.9.2 Stress rotations induced by mechanical interactions between rift segments

Field, analog, and numerical modeling studies show that the lateral growth of en-echelon structural segments, whether joints, faults, dikes or rifts, is accompanied by stress interactions between adjacent segments (Pollard and Aydin, 1984). In some instances, these stress interactions may cause the lateral ends of segments to rotate, forming two interlocking hooks (Pollard et al., 1982; Olson and Pollard, 1991; Thomas and Pollard, 1993; Tentler, 2003; Koehn et al., 2008). The interaction zone where these rotations occur is located in the area between segment ends (Fig. 2.16b and c) (Pollard and Aydin, 1984). This behavior is inferred to be scale-invariant, occurring in brittle material over at least 11 orders of magnitude in length scale, from micro-cracks to mid-ocean ridge or continental rift segments (Pollard and Aydin, 1984; Tentler, 2003; Koehn et al., 2010). The size of these interaction zones thus scales with the size of the interacting structural segments. For macro-scale fractures tens of meters in length, these interaction zones will be on the order of 10^{-1} to 10^0 m² (Pollard et al., 1982; Pollard and Aydin, 1984). For continental rift basins 100s of km in length, such as the EAR, these interaction zones, commonly termed transfer zones, may occupy areas of 10^2 to 10^3 km² (Ebinger, 1989; Koehn et al., 2010; Corti, 2012).

En echelon structural segments in extensional settings may be modeled in two-dimensions as two offset slits (mode I fractures) in an elastic medium subject to remote tensile stresses acting normal to the slit walls (Pollard and Aydin, 1984; Gudmundsson, 1995b) (Fig. 2. 16a). Early-stage continental rift segments have been modeled previously as underlapping segments (Pollard and Aydin, 1984) (Fig. 2.16a and b), as would be appropriate for the Natron and Pangani basins shown in Figure 16c. High stress concentrations form at the tips of mode I fractures subjected to an external tensile stress field (Olson and Pollard, 1989).

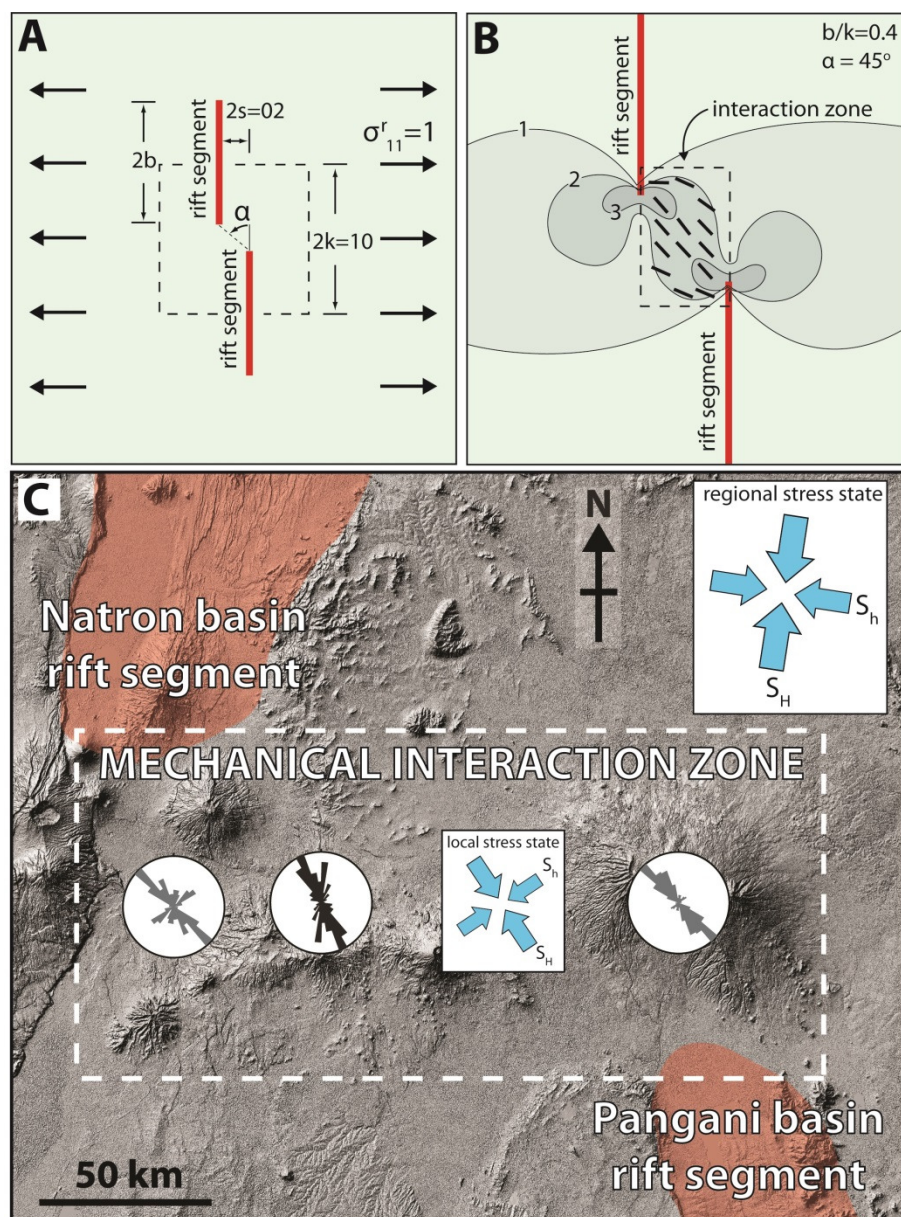


Figure 2.16. Two-dimensional elastic model of interacting rift segments, modified from Pollard and Aydin (1984). A: Geometry and boundary conditions for two rift segments subject to orthogonal extension. The model considers rift segment length ($2b$), segment spacing ($2k$) and segment separation ($2s$). The remote tectonic stress (tensile) normal to the rift is $\sigma_{11}^r=1$ and α represents the angle between the rift segment ends with respect to the strike of the rift. B: Contour map of maximum shear stress ($(\sigma_1 - \sigma_2)/2$) and stress orientations (black ticks represent the orientation of the greatest compressive stress) for left-stepping, underlapping rift segments ($\alpha = 45^\circ$) subject to far-field tension. Stress magnitudes are normalized to the ambient shear stress. The highest stress occurs near the segment tips and within the interaction zone between the rift segments (dashed box), where the orientations of the principal stresses are locally rotated in a counter-clockwise sense. Analytical solutions applied in this model are provided in Pollard and Aydin [1984]. C: Example of underlapping, left-stepping rift segments in the North Tanzanian Divergence. Dike (grey rose plots) and fault data (black rose plot) are from this study. These data show a counter-clockwise rotation of the principal stresses away from the regional stress field, consistent with the model results in B.

In the case of two offset fracture or rift segments, stress fields generated at the respective segment tips interact and locally reorient the principal stress directions (Pollard and Aydin, 1984; Gudmundsson 1995b). This stress reorientation causes fracture segments to divert from their original propagation paths, and in some instances form the characteristic interlocking hook shapes between segment ends (Pollard et al., 1982; Tentler, 2003). For the two underlapping, left-stepping segments modeled in Fig. 2.16b, the interaction between segments results in a counter-clockwise rotation of the horizontal principal stresses. The dike and fault orientations observed in the interaction zone (transfer zone) between the left-stepping Natron and Pangani rift segments (Fig. 2.16c) are consistent with this modeled interaction and resulting stress rotation. A similar counter-clockwise stress rotation is inferred for the Rwenzori transfer zone between the left-stepping Lake Albert and Lake Edward rift basins of the EAR, based on fault kinematic and numerical modeling data (Koehn et al., 2008, 2010). This type of stress modification in the interaction zone between segments has been described in a number of studies as a “mechanical interaction” between rift/fracture segments (Pollard et al., 1982; Pollard and Aydin, 1984; Olsen and Pollard, 1991; Crider and Pollard, 1998); hence, the same terminology is adopted in this work.

2.10 Supporting methods

2.10.1 Observational methods: deducing cone lineaments

Monogenetic volcanic cones were mapped using aerial photography (0.5 m resolution) and Google Earth satellite imagery (1-2 m resolution), supplemented by published maps (Roberts, 2002; Dawson, 2008; Wauthier, 2011; Smets et al., 2014) (see Appendix A). Following Paulsen and Wilson (2010), the idealized shapes (circular to elliptical) of cones and

craters were determined and each cone was classified as a cone, cleft cone, linear fissure, or crater (Fig. 2.17). As the resolution of the imagery (0.5-2.0 m) is an order of magnitude greater than the typical dimensions of the monogenetic cones (30-1000 m radii), the reliability of the cone morphology is not affected by image resolution. The reliability of the shape of each cone was nonetheless ranked (1 = probable; 2 = likely; 3 = unknown) depending on the degree of observable erosion and the likelihood that the cone morphology was affected by wind direction rather than a possible dike-feeder. The cone was considered to produce a lineament if it had a reliability ranking of 1 or 2 and a cone or crater axial ratio (long axis to short axis) >1.2 , which is the minimum ratio required to define lineaments from Paulsen and Wilson (2010). If these criteria were met, the trend of the long axis of the cone was recorded and interpreted to mimic the dike that fed the cone (Tibaldi, 1995; Korme et al., 1997; Bonali et al., 2011). If both the cone base and cone crater exhibited an axial ratio >1.2 , the long axis direction of the crater was used in the analysis. In addition to using cone and crater elongations, the breaching direction (Fig. 2.4) was used as a direct indicator of feeder dike orientation (i.e., Tibaldi, 1995), as well as the strike of volcanic fissures (Fig. 2.17). Throughout this paper these features are described as *cone lineaments*, and are inferred to reflect the strike of the dike that fed the volcanic cone (Fig. 2.17).

2.10.2 Analytical methods: creation of vent alignments

In addition to identifying cone lineaments, alignment analyses were performed on groups of 3 cones using the linear regression algorithm and MATLAB script of Le Corvec et al. (2013a). For these analyses, each alignment must satisfy a certain “width” and “length” tolerance (Fig. 2.18). A width tolerance of 50 m was applied, which is within the width tolerance for “A grade” alignments of Paulsen and Wilson (2010) (125 m). The length

tolerance of the alignment depended on the observed distribution of cones within each field, where the mean distance between cones within the alignment had to be less than the expected mean distance between cones from a Poisson distribution (Table 2.1).

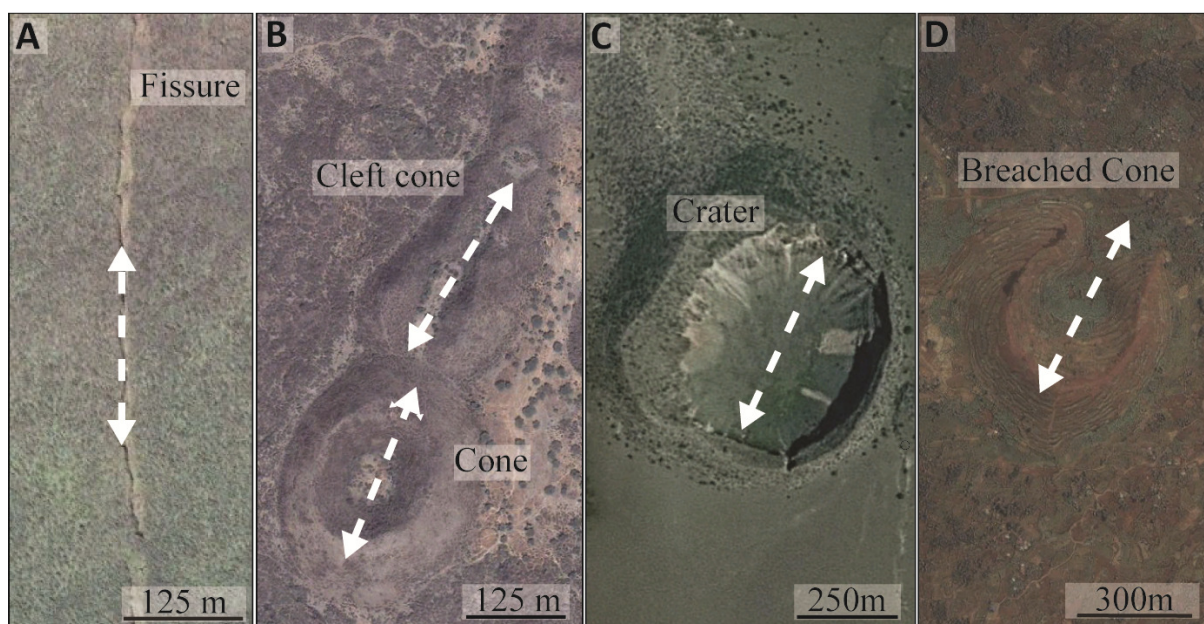


Figure 2.17. Example images from Google Earth representing the classification of cone morphologies used to determine cone lineaments from the Virunga Province (A and D), Boset segment (B), and South Natron (C). Double-sided arrows show the orientation of the cone lineaments for each cone based on fissure orientation (A), crater elongation (B & C), and breaching direction (D).

Following Paulsen and Wilson (2010), the reliability of each alignment was then verified by assessing cone lineaments produced by cones present within each alignment (Fig. 2.18). In this case, there must be a cone present within the alignment that has a cone lineament trend within 15° of the alignment trend for the alignment to be considered. As such, each vent alignment satisfied the reliability criteria for vent alignments defined by Paulsen and Wilson (2010). In this study, if these criteria were met, the trend of the alignment was recorded, and any cones present within the alignment that did not exhibit a cone lineament

trend (i.e. have an axial ratio <1.2 and/or a reliability rating of 3) were ascribed a cone lineament trend that matched the alignment. Alignments analyzed in each field are outlined in Appendix A. Throughout this paper, these features are described as *vent alignments* and are distinct from cone lineaments, as they represent a structural alignment between 3 points (e.g., Le Corvec et al., 2013a) rather than the orientation of a feeder dike below a single cone (e.g., Bonalli et al., 2011).

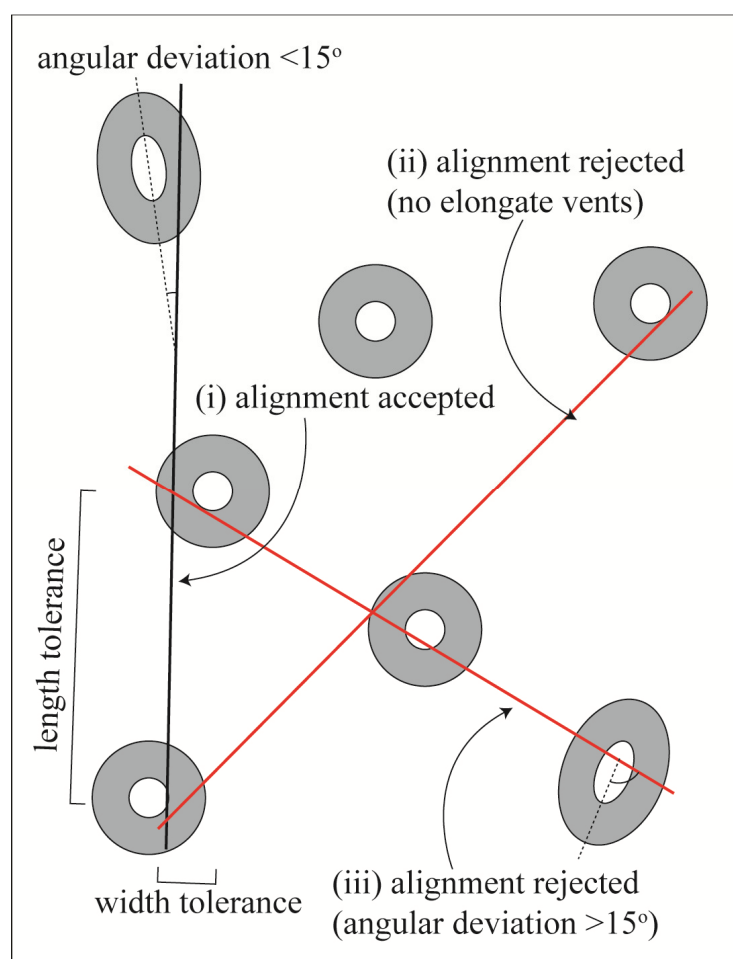


Figure 2.18. Schematic demonstration of the criteria for defining vent alignments, modified from Le Corvec et al. (2013a). The alignment represented by the black line (i) is accepted for analysis because it contains a cone with a lineament trend that has an angular deviation $<15^\circ$ from the trend of the alignment. The red alignments are rejected on the basis that they have no cone with a reliable lineament (ii) or, alternatively, have a cone with a lineament that is $>15^\circ$ to the trend of the vent alignment (iii).

2.10.3 Defining cone field boundaries in the North Tanzanian Divergence and Kenya Rift

Boundaries delineating cone fields analyzed in the North Tanzanian Divergence and Kenya Rift in this study have not been previously specified, in part due to an incomplete catalog of geochemical data and ages for most cones. Similar problems occur in the EAR as a result of sparse geochemical sampling (e.g., Main Ethiopian Rift: Mazzarini, 2007), as well as in cone fields elsewhere (e.g., Baja California, Mexico: Germa et al., 2013). Monogenetic fields are, therefore, often grouped using statistical methods, such as agglomerative hierarchical clustering (Mazzarini, 2004; Mazzarini et al., 2013b) or kernel density estimations (Connor and Connor, 2009; Germa et al., 2013). Volcanic cone groupings in the North Tanzanian Divergence in this study did not depend solely on density estimations (Figs. 2.19 and 2.20). This is because the distribution of cones appears to be affected by large volcanic edifices (composite volcanoes) and areas of high sediment input, possibly creating artificial clusters. For example, a distinct scarcity of cones was observed in the 1.2 Ma Engaruka (sub-)basin (Fig. 2.19a); cones erupted into this depression are likely buried by rapidly accumulating sediments in the subsiding basin. Dikes intersecting volcanic edifices are also more likely to erupt on the lower flanks rather than the volcano summit and, in these instances, cones may form clusters on the lower flanks of volcanoes (Pinel et al., 2004; Gaffney and Damjanac, 2006; Kervyn et al., 2009) (Fig. 2.20a).

As the analysis addressed the variability in cone lineament and vent alignment data across different structural locations in the North Tanzanian Divergence and Kenya Rift, boundaries were approximated based on general rift structure and the spatial distribution of vents (Figs. 2.19 and 2.20). Cones within the defined groups exhibit distinct trends that align locally with fault structures (Fig. 2.5), and therefore validate the approach.

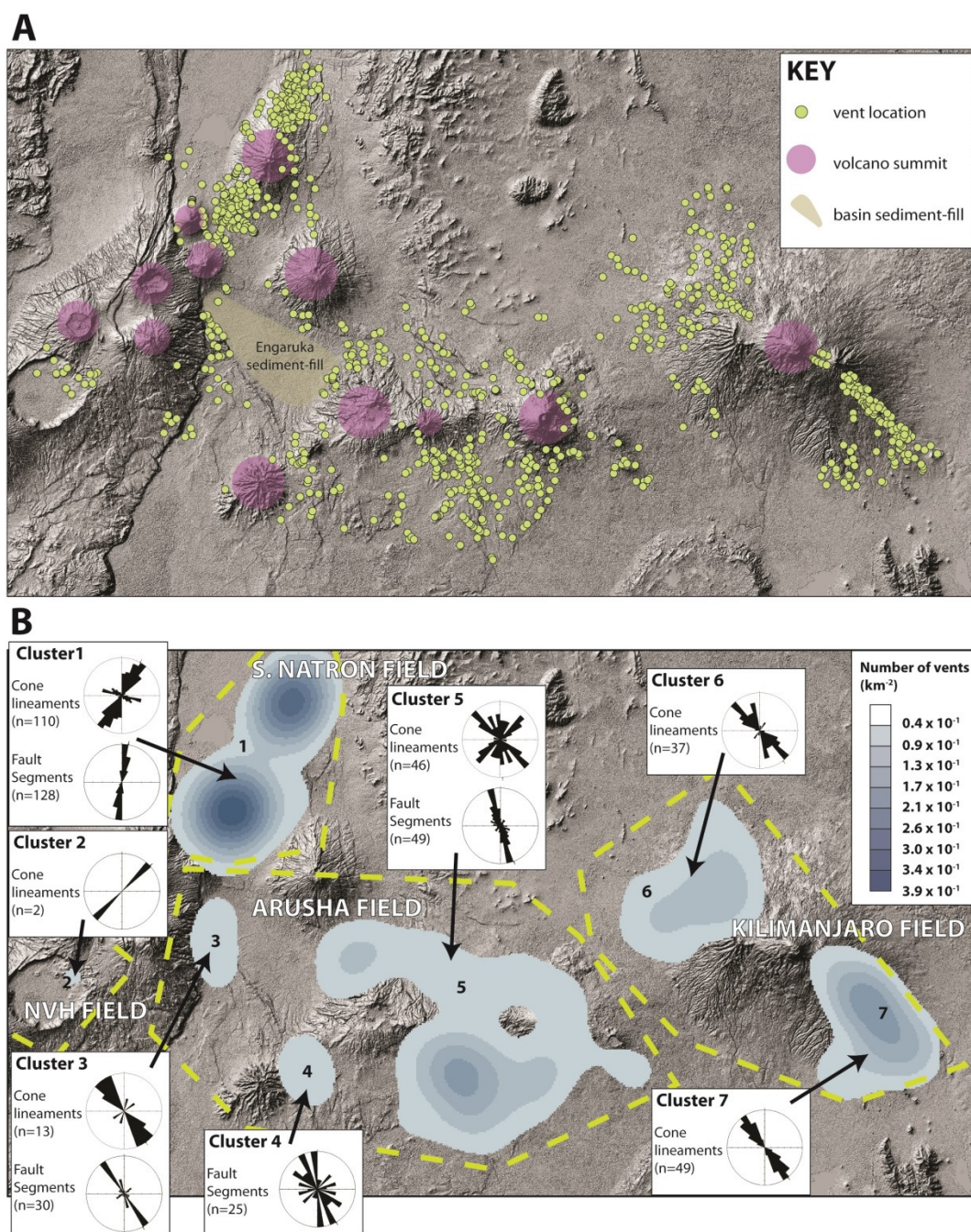


Figure 2.19. A: Distribution of monogenetic cones in the North Tanzanian Divergence shown on an Aster DEM hillshade map. Note how the cones are largely absent near the summits of stratovolcanoes (transparent purple) and in the Engaruka Basin (transparent brown). B: Kernel density plots of North Tanzanian Divergence cones performed in Arc GIS v.10 using a 15 km search radius. Rose plots are of fault segment and cone lineament trends in the 7 computed clusters. NVH corresponds to Ngorongoro Volcanic Highlands.

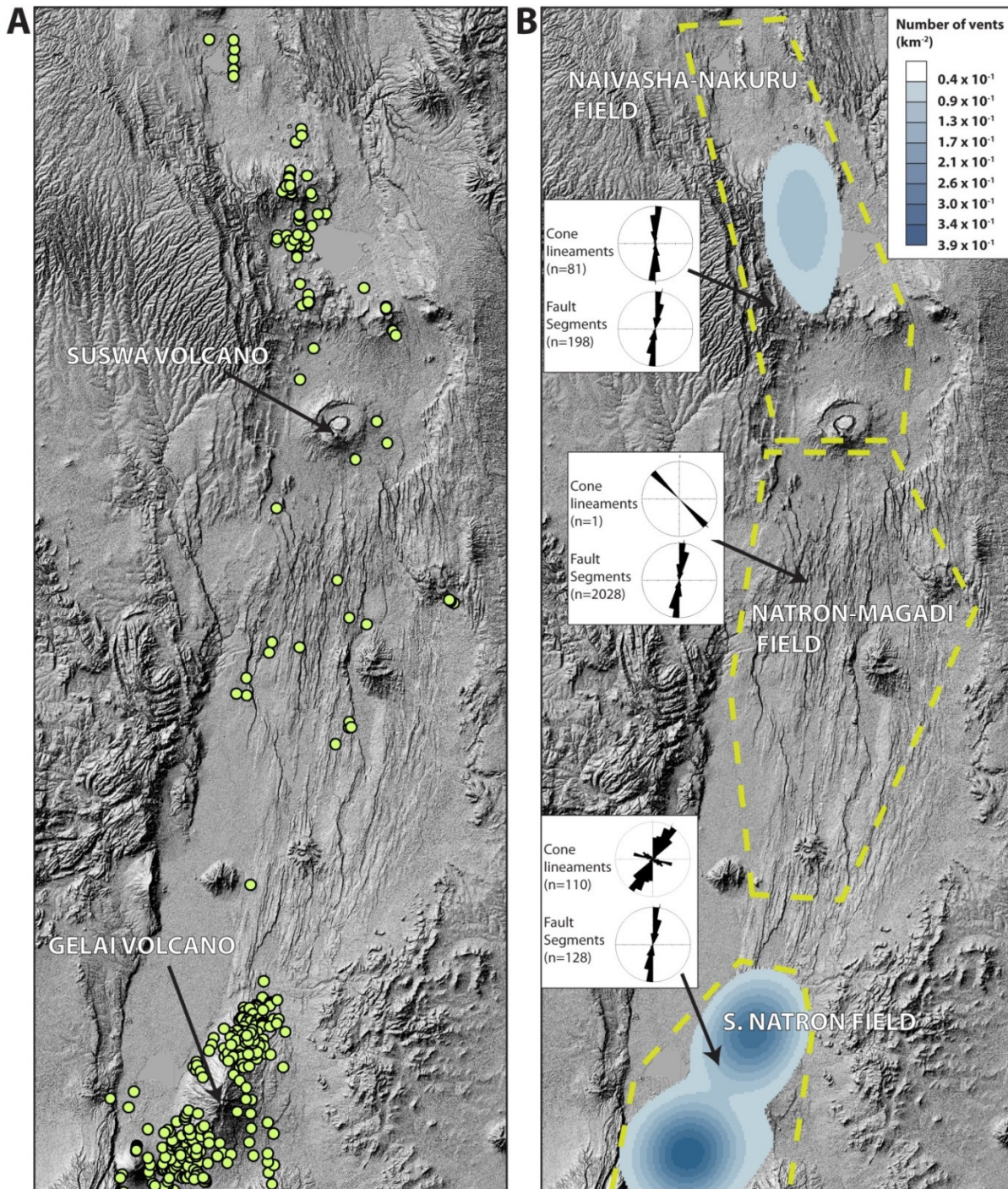


Figure 2.20. A: Distribution of monogenetic cones in the North Tanzanian Divergence and Kenya Rift shown on an Aster DEM hillshade map. B: Kernel density plots performed in Arc GIS v.10 using a 15 km search radius. Rose plots are of fault segment and cone lineament trends in each field.

2.10.4 Cone fields in the North Tanzanian Divergence and Kenya Rift

The sections of the North Tanzanian Divergence and Kenya Rift analyzed in this study were divided into 6 cone fields: Naivasha-Nakuru, Natron-Magadi, South Natron, Arusha, Ngorongoro Volcanic Highlands, and Kilimanjaro (Figs. 2.19 and 2.20; Fig. 2.5). The Natron-Magadi field was delineated based on a distinct lack ($n=19$) of monogenetic cones over a ~130 km-long section from Gelai volcano in the south to Suswa volcano in the north (Fig. 2.20a). North of the Natron-Magadi field are volcanic cones of the Naivasha-Nakuru field. The Naivasha-Nakuru basin represents a distinct magmatic-tectonic province (Kenya peralkaline province) of the Kenya Rift (MacDonald and Baginski, 2009), comprising a series of actively deforming composite volcanoes and silicic centers (e.g., Suswa, Longonot, Menegai) (Biggs et al., 2009b). The transition from the Natron-Magadi field north into the Naivasha-Nakuru field is marked by an increase in the number of cones ($n=118$) north of Suswa volcano, which exhibit significant clustering in the center of the field (Fig. 2.20b). The South Natron field (cluster 1 in Fig. 2.19b) has a greater number of cones ($n=267$) and extends rift-parallel across the southernmost ~40 km of the Natron Basin into the northernmost ~10 km of the Ngorongoro-Kilimanjaro Volcanic Belt. Here, cone lineaments and faults exhibit primarily spreading-normal orientations (029° and 011° mean strike, respectively), and also align sub-parallel with the orientation of the 2007 Natron dike (027° strike: Calais et al., 2008). It also contains a unique group of cones with a mean ESE-WNW trend that, on closer inspection, forms a sub-radial pattern (section 2.6.1). A small group of cones ($n=15$) ~50 km southwest of the South Natron field exhibit a NE-SW cone lineament trend, and form the Ngorongoro Volcanic Highlands field (cluster 2 in Fig. 2.19b). East of this field are three clusters of cones (clusters 3, 4 and 5 in Fig. 2.19b), all of which exhibit a

NW-SE trend and are surrounded by NW-SE trending faults. Based on the similar structural trends observed in these clusters, they have been grouped into a single cone field, called the Arusha field. The final cone field delineated in this study is the Kilimanjaro field (clusters 6 and 7 in Fig. 2.19b). This field consists of cones on or around the flanks of Kilimanjaro volcano. These cones exhibit a NW-SE cone lineament trend. Unlike the Arusha field, no faults are identifiable in Google Earth imagery in the Kilimanjaro field.

CHAPTER 3: FAULT-CONTROLLED MAGMATIC CO₂ RELEASE IN EAST AFRICA

Chapter based on: Lee, H., Muirhead, J.D., Fischer, T.P., Ebinger, C.J., Kattenhorn, S.A., Sharpe, Z.D., Kianji, G., 2016, Massive and prolonged deep carbon emissions associated with continental rifting: *Nature Geoscience*, v. 9, p. 145-149, doi:10.1038/ngeo2622.

3.1 Abstract

Carbon from Earth's interior is thought to be released to the atmosphere mostly via degassing of CO₂ from active volcanoes. CO₂ can also escape along faults away from active volcanic centers, but such tectonic degassing is poorly constrained. Measurements of diffuse soil CO₂, combined with carbon isotopic analyses, were used in this study to quantify the flux of CO₂ through fault systems away from active volcanoes in the East African Rift (EAR). From these analyses it is estimated that about 4 megatons per year of mantle-derived CO₂ is released from the Magadi and Natron basins, at the border between Kenya and Tanzania. Seismicity at depths of 15 to 30 km implies that extensional faults in this region may penetrate the lower crust, and it is suggested that CO₂ is transferred from upper mantle or lower crustal magma bodies along these deep faults. Extrapolation of measurements to the entire Eastern rift of the EAR implies a CO₂ flux on the order of tens of Mt yr⁻¹, comparable to emissions from the entire mid-ocean ridge system of 53 to 97 Mt yr⁻¹. Results from this study suggest that widespread continental rifting and super-continent breakup could produce massive, long-term CO₂ emissions and contribute to prolonged greenhouse conditions like those of the Cretaceous.

3.2 Introduction

Emissions of mantle-derived CO₂ are thought to be sourced primarily at volcanic centers, where it is currently estimated that ~90% of Earth's natural CO₂ is released through active degassing of volcanic plumes or passive, diffuse emissions around volcanic edifices, mid-ocean ridges, and volcanic lakes (Marty and Tolstikhin, 1998; Pérez et al., 2011; Burton et al., 2013; Kagoshima et al., 2015). One major source of discrepancy in global flux estimates relates to sparse sampling of diffuse CO₂ flux in fault systems away from volcanic centres (Seward and Kerrick, 1996). These areas of tectonic degassing (e.g., Apennines, Italy; Chiodini et al., 2004) exhibit high surface CO₂ fluxes sourced from deep magma bodies, yet have no expression of recently active volcanism (e.g., composite volcanoes or calderas, see also Section 3.7.1). Although magma-rich continental rifts (e.g., East African and Rio Grande rifts) represent prime targets to test and quantify this mode of CO₂ transfer, gross estimates of CO₂ flux within areas of tectonic degassing are currently restricted to only a few localities globally (Italy and Pacific Rim; Seward and Kerrick, 1996; Chiodini et al., 2004). Consequently, global CO₂ flux estimates from natural systems are likely underestimated (Seward and Kerrick, 1996).

The East African Rift (EAR) is the world's largest active continental rift, comprising distinct western and eastern sectors with a cumulative length of >3,000 km (Ebinger and Scholz, 2012) (Fig. 1). Active volcanoes in the EAR emit large volumes of CO₂, such as Nyiragongo ($\geq 3.4 \text{ Mt yr}^{-1}$; Sawyer et al., 2008) and Oldoinyo Lengai (2.42 Mt yr^{-1} ; Brantley and Koepenick, 1995), and significant amounts of CO₂ are stored in large anoxic lakes (e.g., Lake Kivu; Pasche et al., 2011). Fault systems dissecting active volcanic centers in the EAR (e.g., Aluto complex, Ethiopia) have been shown to provide local pathways through which

CO₂-rich fluids are transported from shallowly degassing magma chambers (Hutchison et al., 2015). However, earthquake swarms spanning the crustal depth range, interpreted as the release and rise of CO₂-rich fluids through faults, are also observed in EAR basins away from active volcanic centers (e.g., Albertine basin; Lindenfeld et al., 2012). Despite these findings, no study has tested the volumetric capacity of rift-wide fault systems in the EAR to transport deeply-derived CO₂. This study provides strong evidence that significant volumes of CO₂, likely sourced from upper mantle and/or lower crustal magma bodies, are emitted through fault systems positioned away from active volcanic centers in the EAR.

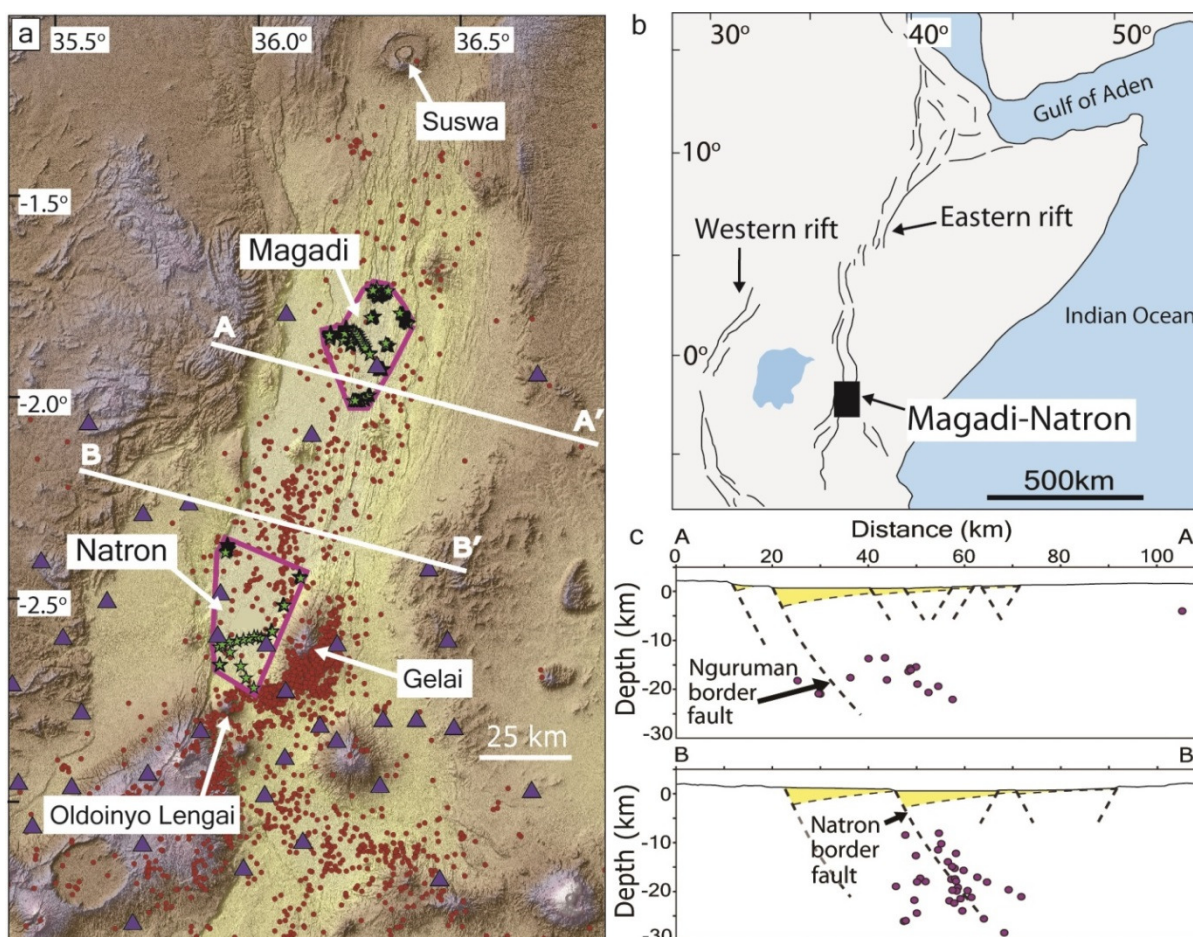


Figure 3.1. Distribution of CO₂ flux samples and seismicity. A: SRTM map of the Magadi-Natron basin. Active volcanic centers (Suswa, Gelai, and Oldoinyo Lengai) are annotated. Green stars show CO₂ measurements locations. Red circles show earthquake epicenters from the CRAFTI seismic network (purple triangles). B:

Location of the study area. C: Cross-sections from A-A' and B-B' in A. Purple circles represent earthquake foci 2 km from each section. Yellow fill represents basin sediments (Birt et al., 1997; Ebinger et al., 1997). Border faults are projected to lower crustal seismicity using surface and seismic observations.

3.3 Methods

The volume of CO₂ released diffusively at any volcanic-tectonic setting can be estimated from soil CO₂ flux measurements, whereas CO₂ sources (e.g., mantle and/or biogenic) may be characterized by carbon isotope compositions (Lewicki and Brantley, 2000; Chiodini et al., 2008). Diffuse CO₂ emissions were measured within fault populations in the Magadi and Natron basins at the Kenya-Tanzania border (Fig. 3.1 and Table 3.1). Diffuse CO₂ flux was measured with an accumulation chamber (Chiodini et al., 2008) at the base of fault scarps (termed here fault zones) and compared with background values in hanging walls and footwalls across horst and graben structures (see also Sections 3.7.2 and 3.7.3). Gas samples were collected by diverting gas from the chamber into pre-evacuated glass vials during flux measurements (Parks et al., 2013). These samples were analyzed in the laboratory for $\delta^{13}\text{C-CO}_2$ (‰) and CO₂ concentrations, and compared with samples collected on Oldoinyo Lengai, an active volcano at the southern terminus of the Natron basin (Fig. 3.1a). Seismicity data were collected on the 38-station CRAFTI broadband seismic array (refer to Section 3.8.4).

Table 3.1. CO₂ fluxes, mean CO₂ concentrations and δ¹³C from the Magadi-Natron basin.

		area (km ²)	mean flux (g m ⁻² d ⁻¹)	total flux (t d ⁻¹)	annual flux (Mt yr ⁻¹)	CO ₂ (ppm)	δ ¹³ C-CO ₂ (‰ vs. PDB)
Magadi	Fault zones	72.9	36.6 ± 11.0	2,672 ± 804	0.98 ± 0.29	1,056 ± 581	-7.8 ± 1.3
	Background	334.6	4.9 ± 1.9	1,650 ± 649	0.61 ± 0.24	789 ± 209	-8.1 ± 1.4
	Sum	407.5		4,327 ± 1453	1.59 ± 0.53		
Natron	Fault zones	33.1	17.2 ± 5.0	570 ± 166	0.21 ± 0.06	944 ± 158	-8.1 ± 2.0
	Background	540.9	11.4 ± 6.6	6,176 ± 3592	2.25 ± 1.31	837 ± 108	-8.5 ± 1.3
	Sum	574.0		6,746 ± 3758	2.46 ± 1.37		
Total		981.5			4.05 ± 1.90	929 ± 386	-8.0 ± 1.3

Fluxes are ± 95% confidence. Mean values of CO₂ concentrations and δ¹³C are ± 1σ. Fault zones occur adjacent to fault scarps, extending outward on the downthrown side a distance equal to the maximum throw. Faults were mapped from aerial photos and throws were estimated using a measured throw/length ratio of 0.0061. Background values represents the combined CO₂ flux from hanging walls (downthrown sediments) and footwalls (uplifted lavas) measured from aerial photos and LandSat imagery, and validated in the field. See also Figure 3.4 and Tables B1 and B2 in Appendix B.

3.4 Results: Carbon isotope and CO₂ flux data from faults of the Magadi-Natron region

Carbon isotope compositions indicate a strong mantle contribution to the observed CO₂ (Fig. 3.2). Measured δ¹³C-CO₂ values range from -3.8 to -11.7‰ with a mean value of -8.0±1.3‰ (Table 3.1), and 78% of values fall within the mantle range (-6.5±2.5‰; Sano and Marty, 1995). All δ¹³C-CO₂ values are distinctively heavier than biogenic δ¹³C values from soil CO₂ studies along transform plate boundaries elsewhere, such as the San Andreas fault (-21.6‰ to -23.7‰; Lewicki and Brantley, 2000). Although two samples have similar δ¹³C-CO₂ values (-3.8‰ and -4.3‰, respectively) to fumaroles on Oldoinyo Lengai volcano (-2.36‰ to -4.01‰; Fischer et al., 2009), they are within the range of isotope values from mantle-derived CO₂ collected in volcanic and geothermal areas in the Kenya rift (-1.7‰ to -

6.9‰; Darling et al., 1995). CO₂ concentrations of analyzed samples (< 0.4%) are lower than typical magmatic and hydrothermal gases (0.5%-11.9%; Fischer et al., 2009), which may be attributed to dilution of mantle-derived CO₂ by air during diffuse degassing (Fig. 3.2). For example, following the approach of Parks et al. (2013), plots of δ¹³C and CO₂ concentrations fit on a mantle-air mixing line (Fig. 3.2). Samples with lighter δ¹³C values (< -9‰) are possibly affected by minor contributions of biogenic CO₂ to a predominantly mantle-derived CO₂ and air mixture.

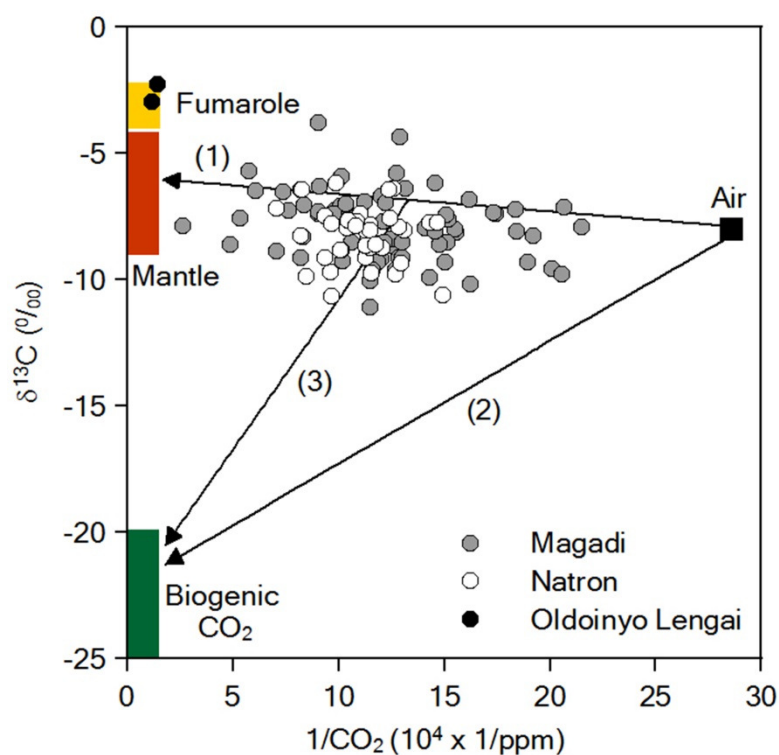


Figure 3.2. Carbon isotope compositions and concentrations of diffuse CO₂ in the Magadi-Natron basin. δ¹³C-CO₂ vs the reciprocal of CO₂ concentration (x10⁴). Mantle δ¹³C values (red box) are -6.5±2.5‰ (Sano and Marty, 1995). δ¹³C values of fumaroles (yellow bar) are from Fischer et al. (2009). Biogenic CO₂ (green bar) ranges from -20‰ to -25‰ of δ¹³C (Lewicki and Brantley, 2000). Values for air (Lewicki and Brantley, 2000) are represented by the black square. Arrows show mixing lines between mantle and air (1), biogenic CO₂ and air (2), and mixtures of mantle/air and biogenic CO₂ (3).

An elevated CO₂ flux in fault zones of the Magadi and Natron basins (Table 3.1; Fig. 3.3) provides strong evidence that faults act as permeable pathways that facilitate the ascent of the deeply-derived CO₂ (refer also to Section 3.7.3). Mean values of diffuse CO₂ flux in fault zones of the Magadi and Natron study areas ($36.6 \pm 11.0 \text{ g m}^{-2} \text{ d}^{-1}$ and $17.2 \pm 5.0 \text{ g m}^{-2} \text{ d}^{-1}$, respectively) are higher than background values in graben sediments and uplifted rift lavas (Table 3.1). The highest individual CO₂ flux measurements (up to $533.5 \text{ g m}^{-2} \text{ d}^{-1}$) occur along large faults (throws >150 m), which occasionally exhibit aligned hot springs along them (Fig. 3.3a). Some of these large faults bound the >2-km-deep rift basins (Birt et al., 1997; Foster et al., 1997) and are underlain by lower crustal earthquake swarms (Fig. 3.1).

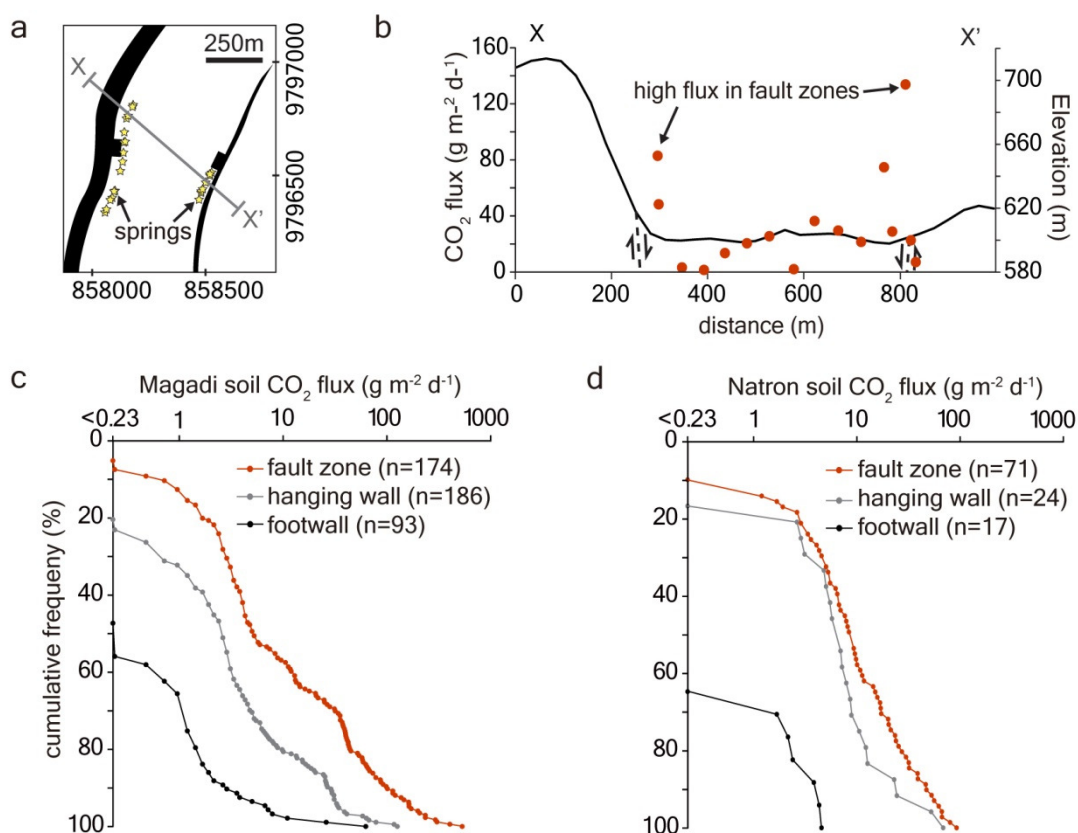


Figure 3.3. Summary of CO₂ fluxes throughout the Magadi-Natron basin. A: Simplified structural map of a faulted graben in Magadi basin (coordinate system is UTM 36S). Black lines represent faults and yellow stars the location of springs. B: Cross-section (X-X' in a) showing the distribution of CO₂ flux (red circles). C & D: Cumulative frequency plots of diffuse CO₂ flux from all transects across faulted grabens in the study area.

Hanging wall represents downthrown sediments, footwalls are uplifted lavas, and fault zones occur adjacent to fault scarps, extending outward on the downthrown side a distance equal to the maximum throw (see section 3.7.2).

Diffuse CO₂ flux from tectonic degassing in the Magadi and Natron basin study areas equates to estimated CO₂ outputs of $1.59 \pm 0.53 \text{ Mt yr}^{-1}$ and $2.46 \pm 1.37 \text{ Mt yr}^{-1}$, respectively (Table 3.1) (refer also to Section 3.7.4). These values represent tectonic degassing of mantle-derived CO₂ through fault systems away from active volcanic centers, and thus omit CO₂ flux values from volcanoes at the northern (Suswa) and southern (Oldoinyo Lengai) extents of the Magadi-Natron region. The combined study area represents only ~10% of the entire 9,200 km², pervasively faulted Natron and Magadi basins; therefore, our flux values represent a conservative minimum estimate for the study region. Despite this cautious approach, the total CO₂ flux from tectonic degassing along fault systems in the Magadi-Natron region is an order of magnitude greater than the mean diffuse CO₂ flux of reported historically active volcanoes (0.21 Mt yr^{-1} ; Burton et al., 2013). However, it is important to note that diffuse CO₂ flux occurs passively over wide areas, and thus CO₂ contributions from diffuse degassing at many volcanoes may be underestimated as a result of sparse sampling and the large study areas required to accurately constrain flux.

3.5 Discussion

3.5.1 Source of the mantle-derived CO₂ in the Magadi and Natron basins

CO₂ is extracted from the mantle by the generation and ascent of magma. It exsolves from magma during cooling, crystallization, and decompression. Where extensional fracture systems exist, as in rift zones, exsolved CO₂ has a permeable network through which it may

rise to the surface (Reyners et al., 2007; Lindenfeld et al., 2012; Burton et al., 2013). Seismic and magnetotelluric studies provide evidence for volumetrically significant accumulations of magma trapped within the crust and upper mantle beneath the Eastern rift (Birt et al., 1997; Keranen et al., 2004). These magma bodies provide the likely source for massive CO₂ emissions. Although CO₂ in the Magadi-Natron basin may in part be sourced by upper crustal dikes (e.g., Calais et al., 2008), the flux of CO₂ is significant, and requires degassing from the large magma volumes in the crust and mantle (see also Section 3.7.5). The association of mantle-derived CO₂ and fault zones provides compelling evidence that CO₂ released from these intrusions into rift-wide fault systems rivals degassing at rift volcanoes. These assertions are further supported by lower crustal earthquakes in the region, which are shown at some rift settings to represent the transport of volatiles exsolved from upper mantle (Reyners et al., 2007; Lindenfeld et al., 2012) and/or lower crustal intrusions (Keir et al., 2009a). Well-located seismicity occurs at depths of 20-27 km and in some instances can be projected along subsurface border faults (Albaric et al., 2014) (Fig. 3.1). Steep, rift-parallel zones of lower crustal to near-surface earthquakes beneath the central Magadi and Natron basins may also mark zones of repeated dike intrusion within incipient magmatic segments (e.g., Keranen et al., 2004) (Fig. 3.1), providing a potential source for massive CO₂ emissions through rift-wide fault systems.

3.5.2 Estimating CO₂ flux along the Eastern rift

Although CO₂ flux from tectonic degassing in the Magadi and Natron basins may be higher than other sectors, the growing evidence of CO₂ degassing from even the magma-poor Albertine system (Lindenfeld et al., 2012) suggests the process may apply to other EAR basins. These considerations imply that faults in the EAR likely contribute a significant

portion of CO₂ to the global budget. CO₂ flux data from Magadi and Natron may be used to make first-order estimates of the total CO₂ flux from tectonic degassing in the Eastern rift (see also Section 3.7.4). The ~184 x 50 km Magadi-Natron basin emits a minimum of 4.05 ± 1.90 Mt yr⁻¹ of diffuse CO₂ over its areal extent (Table 3.1), equating to a mean 4.4×10^2 t km⁻² yr⁻¹. If this flux were to be applied to the 3,240 x 50 km Eastern rift (Ebinger and Scholz, 2012), it would equate to a value of 71 ± 33 Mt yr⁻¹ of CO₂, which could potentially increase the global flux from natural systems (637 Mt yr⁻¹; Burton et al., 2013) by 11% to 708 Mt yr⁻¹. Although this total CO₂ flux represents only degassing along fault systems away from volcanic centers, it is still of the same order as the total CO₂ output from mid-ocean ridges (53 - 97 Mt yr⁻¹; Marty and Tolstikhin, 1998; Kagoshima et al., 2015). The significance of these flux estimates highlights the important contributions of the East African Rift to the deep carbon cycle, as well as the potential role of deeply-derived fluids in assisting rift processes generally (e.g., lower crustal faulting; Lindenfeld et al., 2012; Albaric et al., 2014). However, further diffuse CO₂ surveys across fault systems in Tanzania, Kenya and Ethiopia are required to test whether our flux estimates can be confidently applied to the entire Eastern rift.

3.5.3 Continental rifting and the global CO₂ budget

Understanding the causes of atmospheric CO₂ variations over geologic timescales is important for reconstructing Earth's climate. For example, baseline greenhouse conditions of the Cretaceous to early Paleogene were characterized by 4-8 times higher $p\text{CO}_2$ than the Holocene, requiring a 2-2.8 times increase in global CO₂ input to the atmosphere (Lee et al., 2013). The exact cause of this increase is poorly constrained, although it has been linked previously to increased rates in arc and/or flood basalt volcanism (Kidder and Worsley, 2010; Lee et al., 2013). CO₂ emission estimates from tectonic degassing in the EAR (tens of Mt yr⁻¹)

show that long-lived (> 5 Myr), magma-assisted rifting could produce 10^4 Gt Myr⁻¹ of CO₂, after an initial spike of ~ 1 Gt yr⁻¹ associated with flood basalt eruptions (Courtillot et al., 1999; Self et al., 2006). During the Cretaceous and Paleogene, widespread flood basalt volcanism and continental breakup events occurred in association with the Greenland (60-53 Ma), Deccan (65-60 Ma), and Parana (138-125 Ma) large igneous provinces (Courtillot et al., 1999). Based on estimates from this study, each of these rifting events would be the equivalent of doubling current mid-ocean ridge CO₂ emissions and releasing 10^4 Gt Myr⁻¹ of greenhouse gases over the lifetime of rifting. Although this may not be sufficient to achieve the required 4-8 times increase in atmospheric CO₂ compared to the Holocene, widespread continental rift formation, like the recently proposed ubiquitous continental arc volcanism (Lee et al., 2013), provides a compelling and previously unquantified source of massive, long-term CO₂ input to the atmosphere.

3.6 Conclusions

This study provides the first evidence of volumetrically significant emissions of mantle-derived CO₂ along rift-wide fault systems in the East African Rift. Elevated diffuse CO₂ flux in the vicinity of faults provides strong evidence that these faults act as permeable pathways that facilitate the ascent of the deeply-derived CO₂. Carbon isotope compositions indicate a strong mantle contribution to the observed CO₂. Magma bodies situated in the lower crust and/or upper mantle, which have been imaged across the Eastern rift from both seismic and magnetotelluric studies, provide the likely source for these massive CO₂ emissions. Seismicity at depths of 15 to 30 km implies that some extensional faults in this region may penetrate the lower crust, and it is suggested that CO₂ is transferred from upper mantle or lower crustal magma bodies along these deep faults.

Diffuse CO₂ flux from tectonic degassing in the Magadi and Natron basin study areas equates to estimated CO₂ outputs of $1.59 \pm 0.53 \text{ Mt yr}^{-1}$ and $2.46 \pm 1.37 \text{ Mt yr}^{-1}$, respectively, which is an order of magnitude greater than the mean diffuse CO₂ flux of reported historically active volcanoes (0.21 Mt yr^{-1} ; Burton et al., 2013). Extrapolating these flux values to the entire Eastern rift equates to $71 \pm 33 \text{ Mt yr}^{-1}$ of CO₂, which would increase the global flux from natural systems (637 Mt yr^{-1} ; Burton et al., 2013) by 11% to 708 Mt yr^{-1} . Although this total CO₂ flux represents only degassing along fault systems away from volcanic centers in the EAR, it is still of the same order as the total CO₂ output from mid-ocean ridges. Result from the EAR show that long-lived, magma-assisted rifting could produce 10^4 Gt Myr^{-1} of CO₂. Widespread continental rift formation and supercontinent breakup provides a compelling and previously unquantified source of massive, long-term CO₂ input to the atmosphere.

3.7 Supporting information

3.7.1 Definition of tectonic degassing

The term tectonic degassing was coined by Burton et al. (2013), and can be used to differentiate mantle-derived CO₂ degassing at active volcanic centers (e.g., composite volcanoes, caldera complexes) from areas that are not directly affected by volcanism at the surface. CO₂ released from tectonic degassing is sourced from the mantle (e.g., Apennines, Italy; Chiodini et al., 2004) and ascends the crust through fault networks before reaching the surface in areas away from any observable volcanoes. Therefore, three specific criteria must be met under a tectonic degassing model: (1) the CO₂ must have a magmatic (i.e., mantle-derived) signature; (2) the CO₂ must ascend through the crust along faults and fractures; and (3) the CO₂ must reach the surface away from volcanic centers (e.g., composite volcanoes).

3.7.2 Definition of structural zones from field-based analyses and aerial mapping

The highest CO₂ flux is observed in the Magadi-Natron region in the vicinity of faults, in a zone extending outward from the base of the fault scarp over a distance equal to the fault throw (*fault zone* in Figs. 3.3, 3.4 and 3.5). Permeable sediments in faulted grabens also exhibited higher flux values than those observed in impermeable lavas in uplifted footwalls. Based on these observations, CO₂ flux measurements were subdivided into three categories based on sample location relative to fault structure and surface geology. These structural categories include: (1) *fault zones*, defined as the area directly adjacent to the fault scarp and extending outward on the downthrown side of the fault to a distance equal to the maximum throw; (2) *hanging walls*, the downthrown side of the fault excluding the fault zone and characterized by sedimentary fill; and (3) *footwalls*, the uplifted side of the fault comprising primarily rift lavas with a thin veneer of sediments in places (Fig. 3.4).

3.7.4 Estimating CO₂ flux in the Magadi-Natron basin and Eastern rift of the EAR

Although CO₂ gas emits diffusely over the 982 km² study area in the Magadi-Natron basin, there are clear differences in flux within the three structural zones defined above (Figs. 3.3 and 3.5). To account for these observed variations, total flux was calculated within each of the defined zones by multiplying the area of each zone by its mean CO₂ flux (Table 3.1, and Table B2 of Appendix B). These values were then summed to calculate total diffuse CO₂ flux in the study area. The areas occupied by downthrown graben sediments and uplifted trachyte lavas on the hanging walls and footwalls of faults, as well as fault traces (Fig. 3.4), were mapped from aerial photography (0.5 m resolution), Landsat 7 false color imagery (15 m resolution) and the Aster GDEM v.2 (30 m resolution), and validated in the field. Applying the method of Cowie et al. (1993), fault throw (T) was estimated from the throw-length

scaling relationship within the Magadi-Natron fault population using $T = \gamma L$ (eq. 3.1), where L is fault length and γ is the throw/length coefficient. This study used a γ of 0.0061 for faults of the Magadi-Natron basin, which was estimated from 30 faults measured from the Aster GDEM v.2 and aerial photography (0.5 m resolution). This value of γ is similar to dilation normal fault systems forming in rift lavas in Iceland (0.006; Angelier et al., 1997). The area of

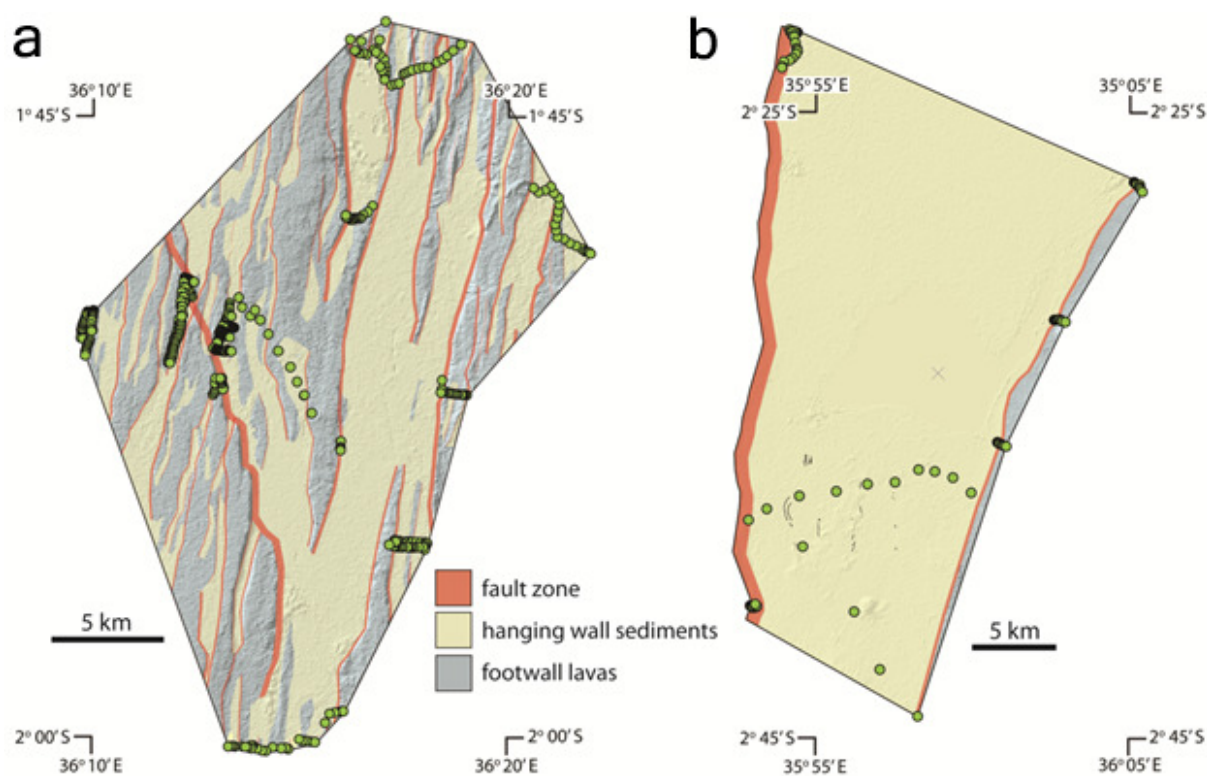


Figure 3.4. Areal distributions of fault zones, hanging wall sediments, and footwall lavas in the Magadi (A) and Natron (B) basin study areas. Structural zones are overlain on an Aster GDEM v.2 hillshade. Locations of CO₂ flux measurements are presented as green circles. Small faults (10s to 100s of meters long) and short gaping fissures (10s of meters long) mapped in the field by Sherrod et al. (2013) are presented as black lines.

the fault zone for each fault was then calculated by multiplying the fault length by fault throw calculated using equation 3.1.

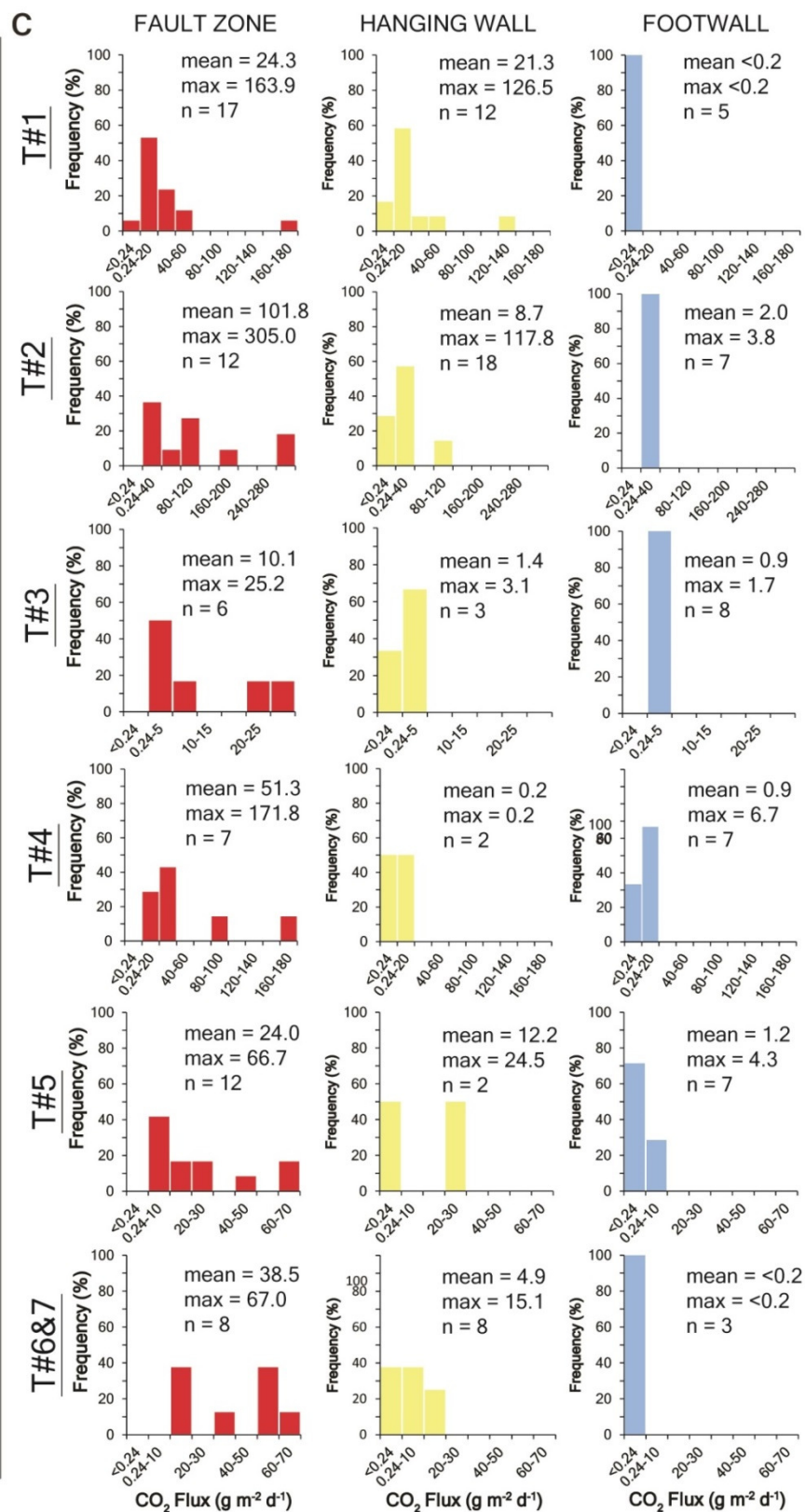
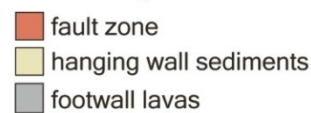
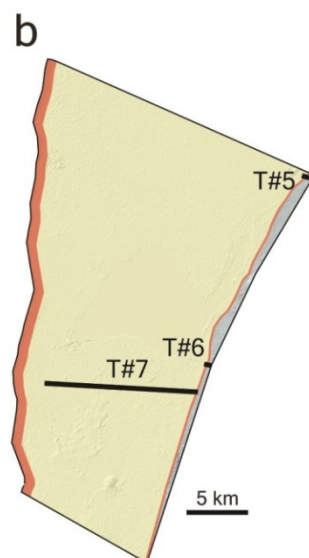
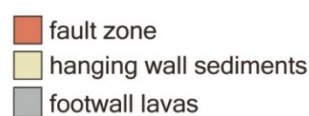
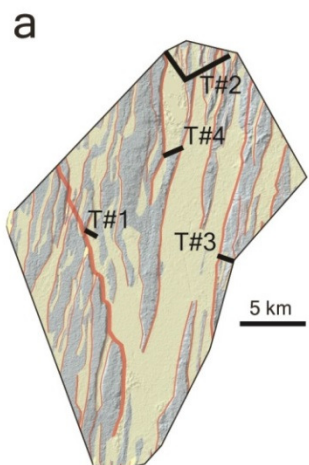


Figure 3.5 (previous page). Diffuse CO₂ flux data from 7 transects across the Natron-Magadi basin. A & B: General location of each transect in the Magadi (A) and Natron (B) study areas. Transect numbers (e.g., T#1, T#2) correspond to transect numbers of histograms in (C). Coordinates of study areas and sample locations are shown in Fig. 3.4. C: Histograms of diffuse CO₂ flux in fault zones (red), hanging walls (yellow), and footwalls (blue) from the transects shown in (A) and (B). Units for mean and max values are g m⁻² d⁻¹.

Uncertainties in our flux estimates are reported as the standard error of the sample distributions. Previous field studies of diffuse CO₂ degassing used a densely-sampled grid over comparatively smaller areas, collecting ~10-100 samples per km² (Werner and Cardellini, 2006; Chiodini et al., 2008) compared to ~1 per km² collected for this work. However, the current study area is 1 to 2 orders of magnitude larger than those of previous studies and was, therefore, comparatively sparsely sampled (565 measurements over 982 km²). The diffuse CO₂ flux is also clearly influenced by fault structure and permeability of the substrate (Fig. 3.3). These two factors limit the application of existing methods of geostatistical analysis (for example SGeMS) used to quantify total CO₂ flux (Deutsch and Journal, 1998; Werner and Cardellini, 2006; Chiodini et al., 2008). For these reasons, it is inferred that the “structural-area method” outlined above currently provides the most robust estimate of total CO₂ flux for the study site. It is, however, challenging to estimate the extent to which the collected flux data represents a fair distribution of CO₂ flux in the defined structural zones. A conservative estimate of total flux has therefore been used for the entire Magadi-Natron basin. Essentially, the calculated CO₂ output of 4.05 Mt yr⁻¹ accounts for CO₂ flux over only ~10% of the 9,200 km² Magadi-Natron basin (combined study area = 982 km²; Fig. 3.4), but this amount has been conservatively assumed to represent the total flux across the entire Magadi-Natron basin. In this study, the basin length is defined as the distance from Oldoinyo Lengai to Suswa volcano (184 km long), and basin width is defined as the distance from the western border fault system to the eastern edge of the faulted monoclinical flexure in

the hanging wall of the half-graben structure (50 km wide; Foster et al., 1997). Assuming a total CO₂ flux of 4.05 Mt yr⁻¹ for the 9,200 km² Magadi-Natron basin equates to a minimum value of flux per unit area of 4.4×10^2 t km⁻² yr⁻¹. This conservative value is one to two orders of magnitude lower than typical flux per unit area estimates of tectonic degassing in smaller ($\sim 10^1$ km²), geothermal regions elsewhere (Morner and Etiope, 2002), yet the total flux is significant compared to flux values from historically active volcanoes (Fig. 3.6a).

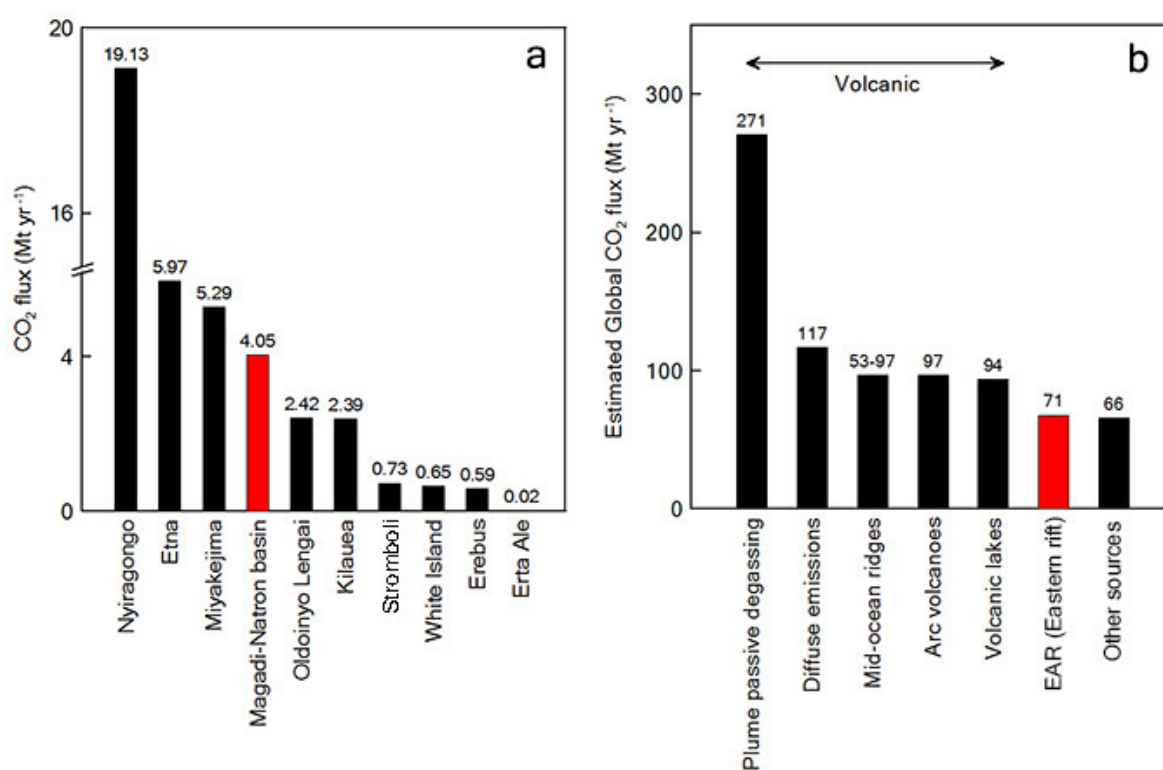


Figure 3.6. Histograms of CO₂ flux. a. Annual CO₂ flux from tectonic degassing in the Magadi-Natron basin and a selection of volcanoes worldwide. Flux estimates from Burton et al. (2013). b. CO₂ flux from tectonic degassing in the EAR (Eastern rift) compared with global estimates from volcanoes and other sources (tectonic, hydrothermal, or inactive volcanic). Flux estimates from Marty and Tolstikhin (1998), Pérez et al. (2011), Burton et al. (2013), and Kagoshima et al. (2015).

The minimum CO₂ flux calculated for the Magadi-Natron basin may be used to extrapolate an estimate of CO₂ flux for the entire Eastern rift of the EAR. Applied rift dimensions are in accordance with Ebinger and Scholz (2012), and define the Eastern rift to include rift basins from the Afar depression southward to the Kilombero rift over a total area of 3,240 × 50 km. By extrapolating CO₂ flux per unit area from the Magadi-Natron basin (4.4 × 10² t km⁻² yr⁻¹) across the Eastern rift, a number of assumptions about the nature of magmatism, faulting, and fluid migration in this rift sector are made. First, it is assumed that strain accommodation proceeds in a similar manner across the Eastern rift via dike intrusion and faulting. Second, plate spreading is accommodated across the full width of rift basins, as suggested by the distribution of seismicity observed across the Eastern rift (Nyblade et al., 1996; Hollnack and Stangl, 1998; Ibs-von Seht et al., 2001; Keir et al., 2006, 2009; Belachew et al., 2011) (Fig. 1). Third, it is assumed that the faulted basins are underlain by zones of magma intrusion, as detected in geophysical imaging, and detection of active intrusions (Keller et al., 1994; Birt et al., 1997; Ibs-von Seht et al., 2001; Keranen et al., 2004; Calais et al., 2008; Keir et al., 2009a; Belachew et al., 2011). Fourth, it is assumed that fluids exsolved from these crustal and upper mantle magma bodies migrate through permeable fault zones, which is supported by fluid-driven lower crustal and upper mantle earthquakes observed in the Albertine rift basin (Lindenfeld et al., 2012) and in magmatic rifts elsewhere (e.g., Taupo Rift, New Zealand; Reyners et al., 2007).

3.7.5 Sources of CO₂ in the Magadi-Natron basin

CO₂ is removed from the mantle by the generation and ascent of magma. It exsolves from magma during cooling, crystallization and decompression, before rising through lithosphere along fractured, permeable pathways (Geissler et al., 2005; Burton et al., 2013).

Seismic and magnetotelluric studies along the Eastern rift provide evidence for volumetrically significant accumulations of magma at depth (Keller et al., 1994; Birt et al., 1997; Ibs-von Seht et al., 2001; Keranen et al., 2004; Kendall et al., 2005; Whaler and Hautot, 2006; Keir et al., 2009a). This magma is the likeliest source of the mantle-derived CO₂ measured at the surface. The possible location of the CO₂ source (upper crust, lower crust, or upper mantle) in the Magadi-Natron basin is discussed below based on previous work and the lower crustal seismicity presented in this study.

Upper crust. Although two shallow dike intrusions (< 10 km deep) have been detected by InSAR and temporary seismic arrays in the Magadi-Natron basin in the last 20 years (Hollnack and Stangl, 1998; Ibs-von Seht et al., 2001; Biggs et al., 2009a), the volume of these intrusions is too small to supply the estimated 4.05 Mt yr⁻¹ of CO₂. For example, assuming that the 2.4 m-wide, 7 km-long and 4 km-high 2007 Natron dike (Calais et al., 2008; Biggs et al., 2009a) consisted of 1 wt% CO₂ and had a density of 3000 kg m⁻³, it would have sourced only 2 Mt of CO₂ to the Magadi-Natron basin 7 years prior to the current survey. Based on analogy to other rift sectors (e.g., Main Ethiopian Rift; Keranen et al., 2004; Keir et al., 2009a), the primary CO₂ is thus likely sourced from lower crustal and mantle lithosphere magma bodies.

Lower crust and Upper mantle. Anomalously low uppermost mantle (Pn) velocities across the Magadi sector of the Kenya Rift can be explained by a zone of ~5% partial melt (Keller et al., 1994; Birt et al., 1997). CO₂ may exsolve from magmas in the partial melt zone, and then travel vertically through faults in a strong, mafic lower crust, resulting in the observed deep seismicity (e.g., Kennedy et al., 1997; Lindenfeld et al., 2012; Albaric et al., 2014). Alternatively, lower crustal seismicity could also be caused by active magma intrusion

(Keir et al., 2009a) and volatile-driven hydraulic fracturing along the margins of modern dike and sill intrusions (Albaric et al., 2014), or in some places represent detachment faulting (Mulibo and Nyblade, 2009).

3.8 Supporting methods

3.8.1 CO₂ gas accumulation chamber method.

The diffuse CO₂ flux survey was performed using the accumulation chamber method described in detail by (Chiodini et al., 1998). The study used an EGM-4 CO₂ Gas Analyzer (PP Systems), which has a cylindrical chamber with a volume of $1.18 \times 10^{-3} \text{ m}^3$, and an infra-red gas analyzer with a measurement range of 0 to 30,000 ppm and <1% error. For each field measurement, the accumulation chamber was pressed firmly into the ground (~2 cm deep) to form a tight seal. Diffuse CO₂ flux was then calculated in the field based on changes in CO₂ concentration (ppm) through time over a 120 second time period.

3.8.2 Field sampling strategy

Owing to the large number of fault systems and eruptive centers in the 184 km-long, 50 km-wide Magadi-Natron basin system, a modified version of the dense grid sampling approach for small sample areas (1-20 km²; Werner and Cardellini, 2006; Chiodini et al., 2008) was applied. In contrast to these previous studies, the analyses focused on understanding CO₂ flux with respect to the location of visible faults (see also Section 3.7.2). Where access allowed, CO₂ flux measurements were taken along 500 m to 4,000 m-long transects either parallel or perpendicular to fault strike, with sample spacing varying between 20 m and 200 m depending on the length of the transect. In addition to targeting faults, broad transects (4,000 m to 20,000 m long) were taken across the Magadi and Natron basins, with

sample spacing between 400 m and 4,000 m. In total, 565 flux measurements were taken over the 960 km² survey area during 18 days of field work in June and July, 2014.

3.8.3 Laboratory analyses of gas compositions and C isotopes.

In total 115 gas samples were collected, each with an accompanying duplicate sample, for isotope analyses in the Magadi-Natron basin and on Oldoinyo Lengai volcano (Table B4 in Appendix B). CO₂ concentrations and $\delta^{13}\text{C}$ values were assessed using the method of Parks et al. (2013). A T-shaped connector, attached to the gas analyzer, was used to divert gas into pre-evacuated Labco 12 ml Borosilicate Vials during flux measurements. CO₂ concentrations in the vials were determined at the University of New Mexico by a Gow-Mac series G-M 816 Gas Chromatograph (GC) and a Pfeiffer Quadrupole Mass Spectrometer (QMS), which has a mass range from 0 to 120 amu. The Volcanic and Geothermal Fluid Analysis Laboratory (University of New Mexico) has a combination system of GC and QMS that enables measurement of gas species at the same time. Relative abundances of CO₂, CH₄, H₂, Ar+O₂, N₂, and CO in the vials were measured on the GC using a He carrier gas. Gas species were separated on the GC using a Hayes Sep pre-column and 5Å molecular sieve columns. A discharge ionization detector was used for CO₂, CH₄, H₂, Ar+O₂, N₂ and CO, respectively (Giggenbach and Goguel, 1989). He, Ar, O₂, and N₂ in the vials were also analyzed for their relative abundances on the QMS with a secondary electron multiplier detector in dynamic mode. These data were processed using the Quadstar software, which corrects possible mass interferences (de Moor et al., 2013a). Combining the data from GC and QMS, the relative abundances of CO₂, CH₄, H₂, Ar, O₂, N₂ and CO were acquired. The $\delta^{13}\text{C}$ -CO₂ values were measured by Isotope Ratio Mass Spectrometer (Finnigan Delta XL) with a gas bench and auto-sampler at the Center for Stable Isotopes, University of New Mexico. The $\delta^{13}\text{C}$ -CO₂

values are presented as per mil (‰) against the standard, Pee Dee belemnite (PDB). Only $\delta^{13}\text{C-CO}_2$ values that have higher peak amplitudes of mass 44 (906 to 10,111mV) than blank tests (average of 805mV) were taken. Using the Oztech isotope ratio reference gas, the standard error of analyses is $\pm 0.2\text{‰}$ (1σ).

3.8.4 Analysis of broadband seismic data

Continuous waveforms from the 38-station CRAFTI (Continental Rifting in Africa: Fluid-Tectonic Interaction) broadband seismic array and GEOFON stations KMBO and KIBK in Kenya were analyzed using the Seismic Handler Motif (SHM) program (Stammler, 1993) (Fig. 3.7). P- and S-wave arrival times were picked manually on Butterworth filtered (1-10 Hz) vertical and horizontal components. P phase arrival times were assigned quality factors of 0, 1, 2 or 3 according to estimated measurement errors of 0.05s, 0.1s, 0.15s, and 0.3s, respectively. S-wave quality factors of 0, 1, 2, and 3 were assigned to arrivals with estimated measurement errors of 0.1s, 0.175s, 0.25s, and 0.3s, respectively. Only events with a minimum of 6 phases, including at least 3 P-arrivals, were used in the locations; most events had 20 or more phases. The initial locations of earthquakes were found assuming the local velocity model of Albaric et al. (2010) and using a hypoinverse absolute location algorithm (Klein, 1978). Progressive GPS timing failures at 32 sites led to changing the network in January and February, 2013 and then a gap between March and January, 2014. Data used in this study (3,274 events) span January 13 to February 28, 2013, and December 15, 2013 to November 1, 2014. Excluding a few mine blast events and earthquakes at Oldoinyo Lengai volcano, earthquakes are tectonic with impulsive P- and S-arrivals and peak frequencies $> 5\text{Hz}$. Earthquakes presented along profiles A-A' and B-B' represent a small, representative proportion of Magadi-Natron data set, consistent with depth histograms of all Natron and

Magadi basin earthquakes, which show significant population at depths between 15 and 27 km (Fig. 3.8). A subset of these earthquakes was relocated using a 3D tomography model of the study area (Roecker et al., 2015). Depth histograms for earthquakes in the Natron and Magadi basins (excluding Gelai volcano) and those relocated from the 3D tomography model show no systematic variations (Fig. 3.8). The same earthquakes were re-located using the double difference algorithm of Roecker et al. (2015). Double difference locations for earthquakes along A-A' and B-B' have formal position errors of ≤ 1.5 km and depth errors ≤ 3.9 km determined by singular value decomposition (errors increase with depth), with additional but small errors associated with 3D velocity variations. Local magnitudes range between 1 and 4.5.

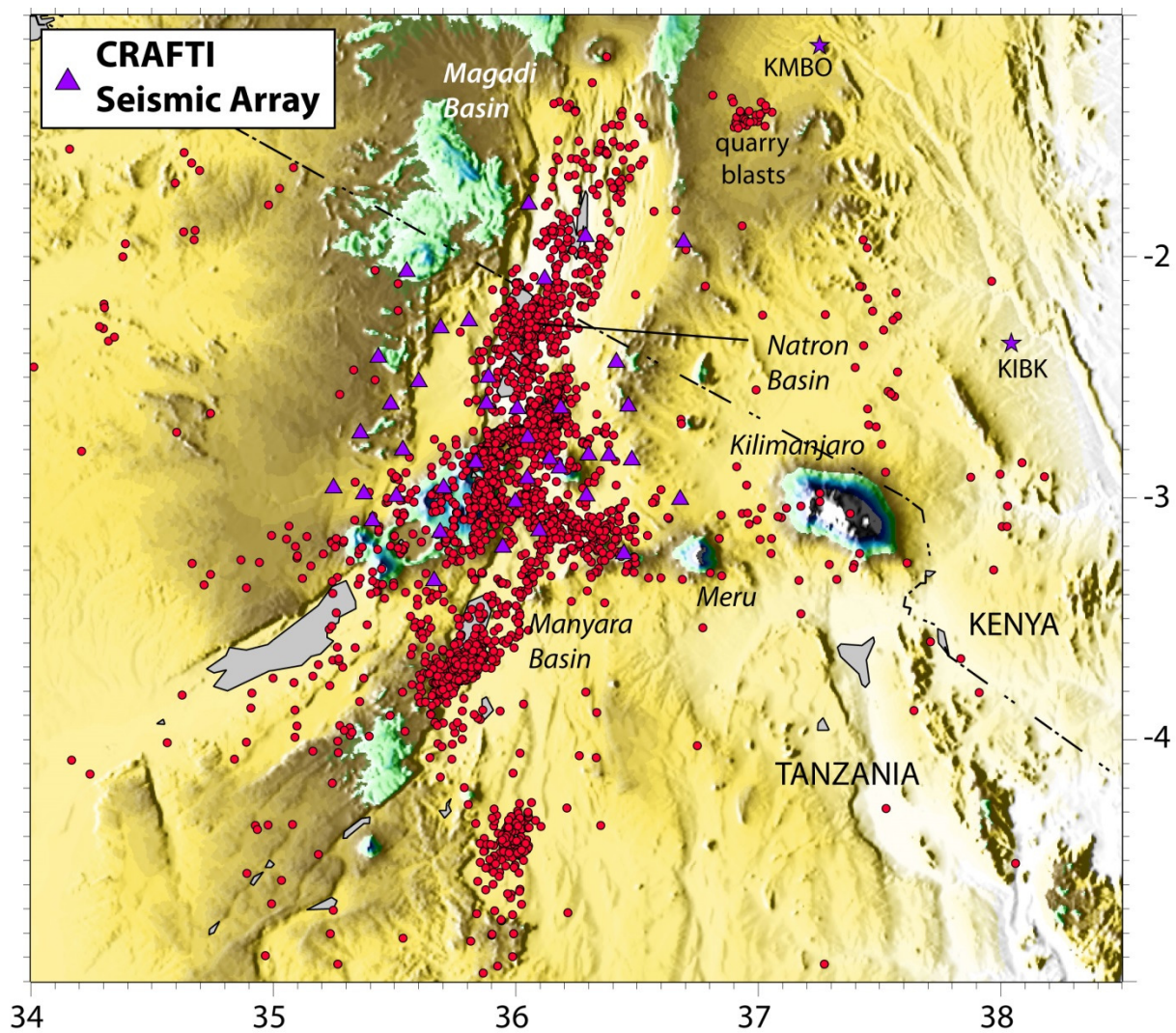


Figure 3.7. CRAFTI seismic network (purple triangles) and GEOFON stations KIBK and KMBO (purple stars) also used in event locations (red circles).

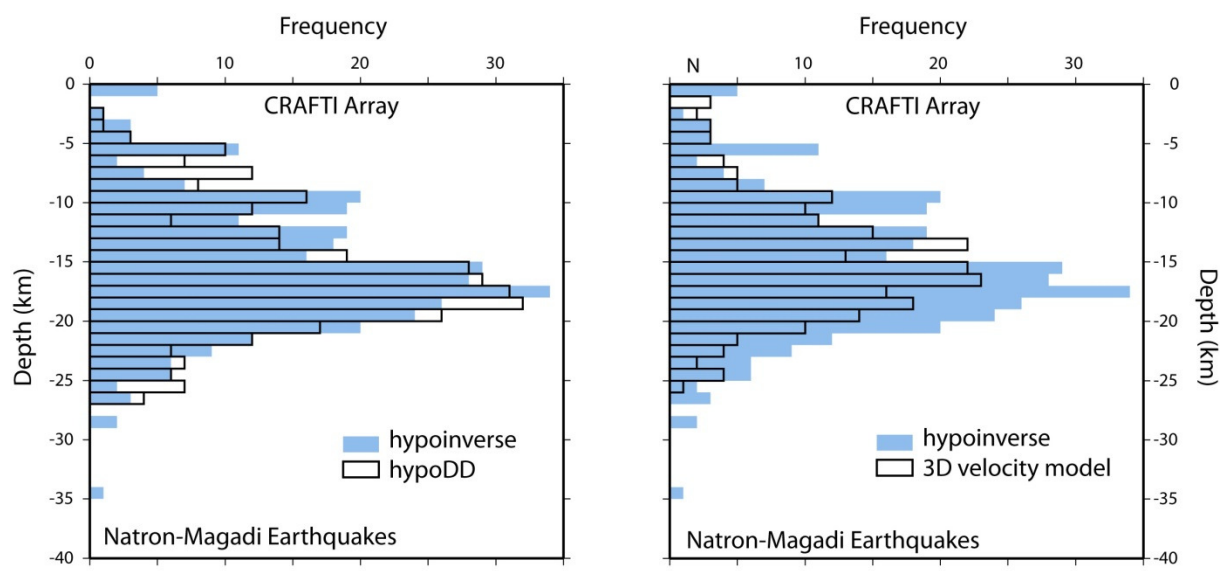


Figure 3.8. Histograms comparing depths of CRAFTI earthquakes in the Natron and Magadi basins (excluding Gelai earthquakes). Earthquakes located using hypoinverse are compared to those relocated using the double-difference algorithm (left) and a sub-set relocated in the 3D tomographic inversion (right). The pattern of depth distributions show little variation between methods, demonstrating a significant set of earthquakes in the lower crust (>15 km) along the length of the Natron and Magadi basins.

CHAPTER 4: EVOLUTION OF FAULTING AND MAGMATIC VOLATILE SYSTEMS DURING EARLY-STAGE CONTINENTAL RIFTING

4.1 Abstract

During the development of continental rifts, strain accommodation shifts from border faults to intra-rift faults. This transition represents a critical process in the evolution of rift basins in the East African Rift (EAR), resulting in the focusing of strain and, ultimately, continental breakup. An analysis of fault and fluid systems in the <7 Ma Natron and Magadi basins (Kenya-Tanzania border) reveals the transition as a complex interaction between plate flexure, magma emplacement, and magmatic volatile release. Rift basin development was investigated by analyzing fault systems, lava chronology, and geochemistry of spring systems. Results show that strain in the 3 Ma Natron basin is primarily accommodated along the border fault, whereas results from the 7 Ma Magadi basin reveal a transition to intra-rift fault dominated strain accommodation. The focusing of strain into a system of intra-rift faults in Magadi also occurred without oblique-style rifting, as is observed in Ethiopia, and border fault hanging wall flexure can account for only a minor portion of faulting along the rift axis (~12% or less). Instead, areas of high upper crustal strain coincide with the presence of hydrothermal springs that exhibit carbon isotopes and N₂-He-Ar abundances indicating mixing between mantle-derived (magmatic) fluids and air saturated water.

By comparing the distribution of fault-related strain and zones of magmatic fluid release in the 3 Ma Natron and 7 Ma Magadi basins, a conceptual model for the evolution of early-stage rifting is presented. In the first 3 million years, border faults accommodate the

majority of regional extension ($1.24\text{-}1.78\text{ mm yr}^{-1}$ in Natron at a slip rate ranging $1.93\text{-}3.56\text{ mm yr}^{-1}$), with a significant portion of intra-rift faulting (38-96%) driven by flexure of the border fault hanging wall. Fluids released from deep magma bodies ascend along the border fault and then outward into nearby faults forming in the flexing hanging wall. By 7 million years, there is reduction in the amount of extension accommodated along the border fault ($0.40\text{-}0.66\text{ mm yr}^{-1}$ in Magadi at a slip rate ranging $0.62\text{-}1.32\text{ mm yr}^{-1}$), and regional extension is primarily accommodated in the intra-rift fault population ($1.34\text{-}1.60\text{ mm yr}^{-1}$), with an accompanying transition of magmatic volatile release into the rift center. The focusing of magma toward the rift center and concomitant release of magmatic fluids into the flexing hanging wall provides a previously unrecognized mechanism that may help to weaken crust and assist the transition to intra-rift dominated strain accommodation. It is concluded that the flow of magmatic fluids within fault systems likely plays an important role in weakening lithosphere and focusing upper crustal strain in early-stage EAR basins prior to the establishment of magmatic segments, like those present in the Main Ethiopian Rift further north.

4.2 Introduction

The initiation of continental breakup is fundamental to plate tectonic theory, yet the combination and relative importance of processes driving breakup remain largely enigmatic. The tectonic forces driving continental rift initiation (e.g., gravitational potential energy, mantle convection; Coblenz and Sandiford, 1994; Bird et al., 2008; Stamps et al., 2015) are theoretically too small to rupture thick lithosphere, particularly in the absence of tractions provided by boundary forces acting on the sides of lithospheric plates (e.g., slab-pull) (Buck, 2004; Stamps et al., 2014). However, some continental rift zones are also sites of

asthenospheric and lithospheric heating (e.g., Kenya Rift; Rooney et al., 2012) that may pre-date rifting (Courtillet et al., 1999; Campbell, 2005), with subsequent tectonic thinning commonly accompanied by decompression melting and the rise of volatiles and magma through the lithosphere (McKenzie and Bickle, 1988; White and McKenzie, 1989; Geissler et al., 2005; Chapter 3). Therefore, intrusion of magma and volatiles is thought to play a major role in the continental rifting process (Buck, 2004; Reyner et al., 2007; Lindenfeld et al., 2012; Rowland and Simmons, 2012; Ebinger et al., 2013).

The buoyancy of magma enables dike intrusions at continental rift settings to ascend from melt generation zones in the mantle toward the surface (Buck, 2004). Dike opening accommodates extensional strain, while the transfer of heat from intrusions weakens the crust locally (e.g., Buck, 2004; Calais et al., 2008; Bialas et al., 2010; Daniels et al., 2014). The rise of magmatic volatiles from mantle depths may also assist rifting. These fluids are hypothesized to mechanically weaken lithosphere through increases in pore fluid pressure (Sibson, 2000; Reyner et al., 2007) and hydration mineral reactions (Moore and Rymer, 2007). Earthquake swarms signaling brittle failure in the lower crust and upper mantle have been detected beneath cratonic lithosphere in the East African Rift (EAR), and interpreted as the rise of fluids through the plate (Lindenfeld et al., 2012; Albaric et al., 2014; Chapter 3). Soil CO₂ flux and carbon isotope data collected in a companion study (Lee et al., 2016) from the Natron basin, Tanzania, and Magadi basin, Kenya, support these interpretations, revealing that mantle-derived CO₂ ascends to the surface along deeply penetrating faults in parts of the EAR (Chapter 3).

The early-stage (<10 Ma) development of continental rift basins is recorded in extensional fault systems observed at the surface. For many continental rifts, active

deformation is concentrated in graben or asymmetric half-graben depressions with accompanying syn-rift sedimentation and volcanic resurfacing (Baker and Mitchell, 1976; Baker, 1986; Rosendahl, 1987; Scholz et al., 1990; Gawthorpe and Leeder, 2000; Ebinger and Scholz, 2012). Sedimentary cover often conceals fault scarps, resulting in uncertainty regarding the geometry and kinematics of fault populations, as well as calculations of bulk strain and time-averaged extension rates. Although these difficulties arise in many parts of the EAR, faults are well-exposed in some basins in Ethiopia and the Kenya Rift (Fig. 4.1B) (Le Turdu et al., 1999; Gupta and Scholz, 2000; Manighetti et al., 2001; Vetel et al., 2005; Agostini et al., 2011a). Well exposed fault systems in the Kenya Rift include the Kino Sogo Fault Belt of the Turkana basin (Vetel et al., 2005), the Maji-Moto fault system of the Baringo basin (Le Turdu et al., 1999; Le Gall et al., 2000), and faults of the Magadi basin (Baker, 1958, 1963; Baker and Mitchell, 1976; Le Gall et al., 2008). A common feature of these fault systems is that they formed in young volcanic units (~3 Ma or younger) with limited sedimentary cover (Baker and Wohlenberg, 1971; Vetel et al., 2005). Despite covering earlier-formed faults, widespread lavas also provide constraints on the accumulated fault strain since the time of their emplacement (Baker and Mitchell, 1976; Baker et al., 1988; Vetel et al., 2005; Le Gall et al., 2008). Therefore, these locations have served as focus sites for studies addressing the growth and kinematics of fault systems in the Kenya Rift of the EAR (Le Turdu et al., 1999; Morley, 1999; Le Gall et al., 2000; Vetel et al., 2005; Le Gall et al., 2008).

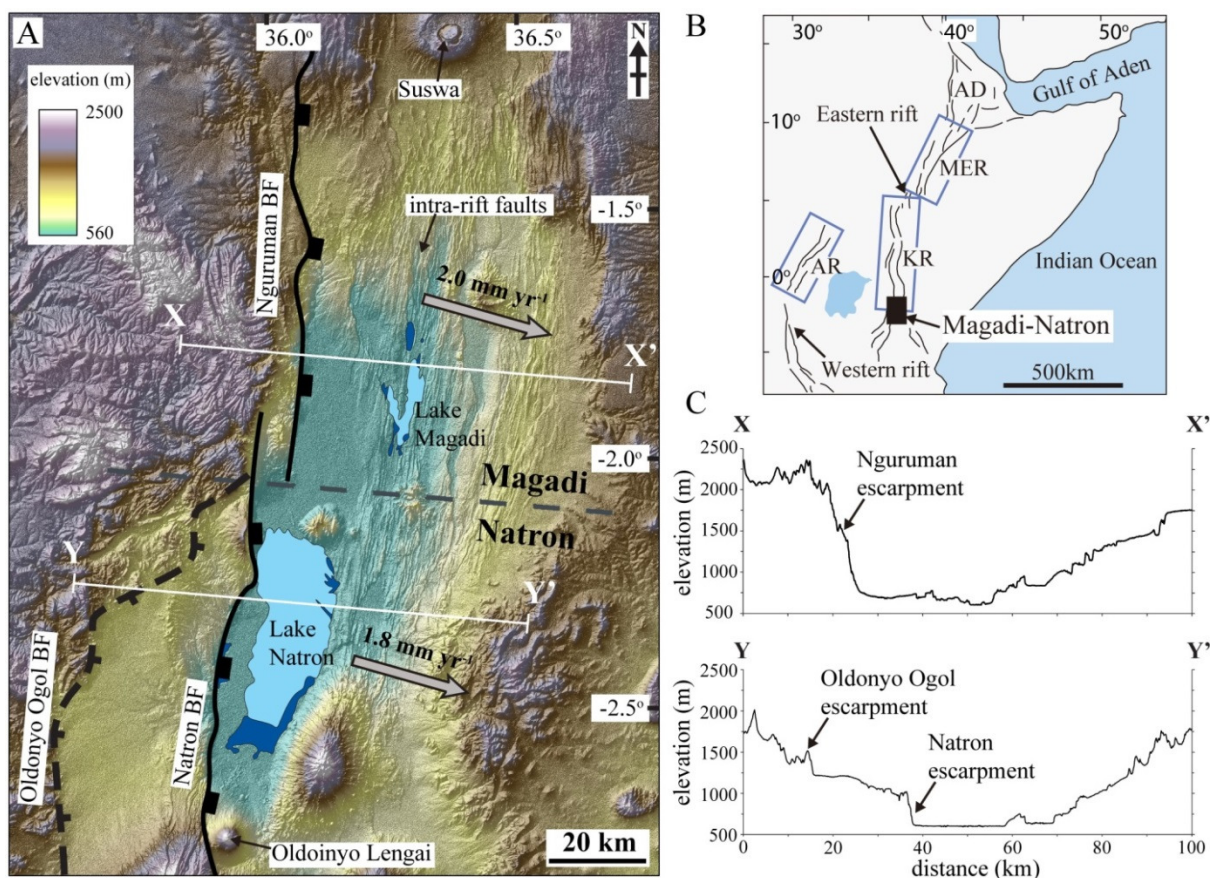


Figure 4.1. (A) Simplified map of the Magadi and Natron basins on a 30 m-resolution SRTM digital elevation model. Active volcanoes (Suswa and Oldoinyo Lengai) at the northern and southern terminus of the basins are annotated. Bold black lines indicate active border faults (BF). Dashed black line shows the now extinct Oldoinyo Ogol fault: an early border fault of the Natron basin (Foster et al., 1997). Dashed grey line shows the inferred boundary between the Magadi and Natron basins based on the northern termination of the Oldoinyo Ogol fault and southern termination of the Nguruman border fault of the Magadi basin. Dark blue polygons show the distribution of permanent spring waters in the rift basin lakes, whereas light blue polygons indicate ephemeral lake waters. Extension rates and directions in the center of each basin (grey arrows) were calculated from the kinematic model of Saria et al. (2014) (see Section 4.8.3). Profiles X-X' in Magadi and Y-Y' in Natron are shown in C. (B) Map of the northeastern part of the African continent, showing the distribution of major fault structures (black lines) in the Western and Eastern rifts of the EAR. Black box shows the location of the Magadi and Natron basins in A. Also annotated are the general locations of the Afar Depression (AD), Main Ethiopian Rift (MER), Kenya Rift (KR) and Albertine Rift (AR). (C) Elevation profiles (10 × vertical exaggeration) through the Magadi (X-X') and Natron (Y-Y') basins.

By comparing fault systems in basins of different ages across the Eastern rift, we can infer how upper crustal strain is distributed within rifts as they evolve through time (Hayward and Ebinger, 1996; Ebinger, 2005; Corti, 2009; Agostini et al., 2011a). Similarly, geophysical

and geochemical studies along the Eastern rift provide insights into how magma and volatile systems assist rift basin development (Birt et al., 1997; Ebinger and Casey, 2001; Pik et al., 2006; Albaric et al., 2014; Halldórsson et al., 2014; Keir et al., 2015). This study uses fault population data and lava chronology to investigate the evolution of fault-related strain, specifically during early-stage rifting (<10 Ma) in the well-exposed fault systems of the 3 Ma Natron and 7 Ma Magadi basins (Fig. 4.1). These data are examined alongside recently-acquired spring geochemistry to investigate the role of magmatic volatile release in rift basin evolution. It is shown that areas of high fault strain coincide with zones of magmatic volatile release, revealing for the first time a strong link between the evolution of upper crustal strain and release of fluids from deep magma bodies in the EAR.

4.3 Rift basin development in the Eastern rift of the EAR

The EAR forms a >3,000-km-long zone of individual rift basins ~100 km long and 10s of km wide (Fig. 4.1B). It is the type example of active continental breakup occurring through extensional faulting, magmatism, and ductile thinning of lithosphere. Rifting in the central parts of the EAR occurs at the eastern and western edges of the Tanzanian craton, dividing the system into distinct Eastern and Western rifts (Koptev et al., 2015).

Faulting in the Eastern rift initiated ~25 Ma in north Kenya and Ethiopia (Ebinger et al., 2000). Geological and geophysical investigations of rift basins of different ages in the Eastern rift have highlighted major shifts in fault and magma systems during basin development (Hayward and Ebinger, 1996; Ebinger and Casey, 2001; Ebinger, 2005; Corti, 2009) (Fig. 4.2). In early-stage basins (<10 Ma), strain is focused along rift-bounding faults (termed border faults), which are often 100s of km long and can accrue >1000 m of throw.

Flexure of a downthrown border fault hanging wall produces extensional strains (Vening Meinesz, 1950; Lavier et al., 2000; Cowie et al., 2005), which can manifest as smaller intra-rift faults that are typically tens of kilometers long with tens to hundreds of meters of throw (McClay and Ellis, 1987; Imber et al., 2003; Ebinger et al., 2005; Corti, 2009). Over the course of rift evolution, the locus of strain migrated away from border faults into these developing intra-rift fault systems (Hayward and Ebinger, 1996; Wolfenden et al., 2004; Cort, 2009). For evolved basins in the Eastern rift (>10 Ma), strain migrated into en echelon magmatic segments in the center of the rift, with dimensions roughly 60 km by 20 km (Ebinger et al., 2001; Keranen et al., 2004). Deformation in these magmatic segments manifests at the surface as slip along intra-rift faults (Rowland et al., 2007; Corti, 2009). At deeper levels of the crust (~5-20 km), strain is primarily accommodated through swarms of rift-parallel dikes (Keir et al., 2006; Wright et al., 2012).

The transition from border fault to intra-rift fault dominated strain accommodation is a critical process to focus strain as continental rifts evolve toward proto-spreading ridges (Corti, 2009). However, the timing and magmatic-tectonic processes controlling this transition are debated. Evidence of extensive diking below magmatic segments from shear-wave splitting and seismic tomography highlights an active magmatic influence on rift basin development (Keranen et al., 2004; Keir et al., 2005; Kendall et al., 2005; Bastow et al., 2010; Keir et al., 2011a). The transition to intra-rift faulting in these segments is also accompanied by extensive volcanism in the rift center, often manifesting as rift-parallel chains of scoria cones and eruptive fissures (Rooney et al., 2010, 2014; Keir et al., 2015; Mazzarini et al., 2016; Chapter 2). Recent fault slip events on intra-rift faults in the Afar depression and the Natron basin, Tanzania, coincide with the emplacement of rift-parallel dikes, suggesting favorable stress

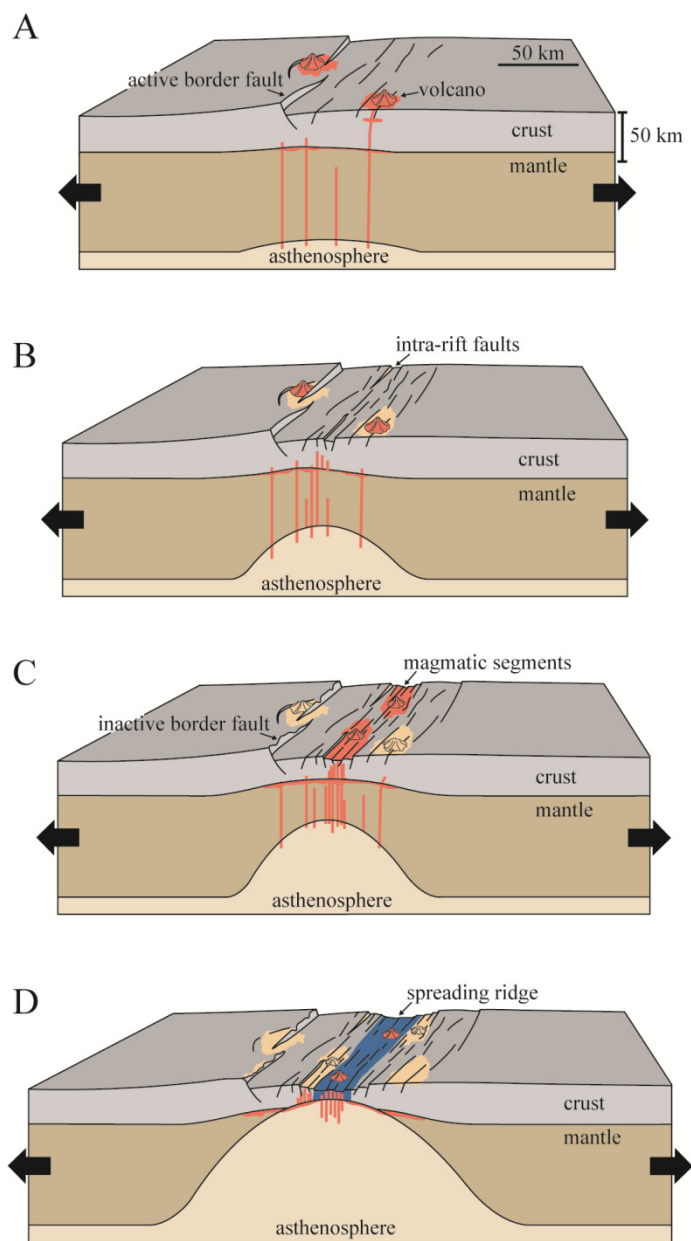


Figure 4.2. Current conceptual model for the development of rift basins in the Eastern rift, modified from Ebinger (2005) and Corti (2009). (A) Within 5 million years of the onset of rifting, the lithosphere thins through brittle (faulting) and ductile deformation. Brittle strain focuses on border faults, which may initiate on preexisting shear zones (McConnell et al., 1972; Daly et al., 1989). Slip along the border fault causes the crust to flex, forming a linear basin. Strain in the lower crust is accommodated through ductile thinning. Asthenosphere begins to rise in response to thinning lithosphere, causing heat transfer and decompression melting to produce magmas that intrude lithosphere as dikes (red) or accrete along the crust-mantle boundary. Fluids released from magmas may alter and even melt rocks near the base of the crust. Magmatism that reaches the surface primarily forms volcanoes along the rift margins. (B) ~5-10 million years after rift initiation, brittle strain begins to focus on smaller intra-rift faults in the rift center, driven either by magmatism (Keir et al., 2006) or oblique rifting (Corti, 2008), with a contribution from plate flexure (Lavie et al., 2000). Ongoing lithospheric thinning leads to further upwelling of asthenosphere and generation of greater melt volumes (which may or may not erupt at the surface). Faulting in the upper crust is thus accompanied by dike intrusions fed from these melt sources, which

heat and weaken lithosphere. Strain in the lower crust is accommodated through magmatic intrusion and ductile thinning. (C) Continued magmatism along the rift axis results in the development of narrow zones of intense magmatism in the rift center, called magmatic segments, after ~10-15 million years. Dike intrusions and related faulting within these segments accommodate the majority of strain in the upper crust, rendering border faults inactive. Strain in the lower crust is accommodated through magmatism and ductile thinning. (D) Nascent spreading ridges, much like those seen in the Afar Depression (e.g., Asal Rift; Stein et al., 1991; Ebinger and Casey, 2001), are initiated. Magma injection along the rift axis creates new oceanic lithosphere (dark blue) as continental crust is replaced by a thin, mafic igneous material.

conditions for intra-rift faulting are achieved during diking events (Rubin and Pollard, 1988; Rowland et al., 2007; Baer et al., 2008; Calais et al., 2008; Belachew et al., 2013).

Other authors suggest that the initiation of intra-rift faulting is a product of oblique continental rifting, and occurs independent of magmatic processes below the rift center (Corti, 2008). For example, in the Main Ethiopian Rift, the earlier formed (> 2 Ma) large border faults trend oblique to the regional extension direction (up to 45°; Keir et al., 2015), whereas younger intra-rift faults (~2 Ma to present) trend normal to the regional extension (Bonini et al., 1997; Agostini et al., 2011a). Oblique continental rifting in the Main Ethiopian Rift has been previously attributed to changes in the relative motions between the Somalian and Nubian plates, where an initial Mio-Pliocene phase of ~NW-SE extension was followed by Quaternary ~E-W extension (e.g., Bonini et al., 1997; Boccaletti et al., 1999; Wolfenden et al., 2004). The resulting change in plate kinematics produced sinistral motions on the earlier formed NE-SW-trending border faults, and drove the formation of N-S-trending intra-faults (Bonini et al., 1997; Corti et al., 2003). Alternatively, oblique rifting in the Main Ethiopian Rift may not require changes in far-field plate motions, but reactivation of preexisting lithospheric weaknesses trending oblique to the regional extension direction (Corti, 2008; Agostini et al., 2009, 2011b). Analog investigations of rift-oblique extension under this model show that the earliest stages of basin development are still characterized by oblique-slip on

border faults, and then followed by a second stage of dip-slip motion within intra-rift faults, that group into discrete populations arranged en echelon in the rift center (Clifton et al., 2000, 2001; Corti, 2008; Agostini et al., 2011b). These experimental results are consistent with fault patterns in the Wonji fault belt of the Main Ethiopian Rift (Gibson, 1969; Chorowicz et al., 1994; Bonini et al., 1997; Boccaletti et al., 1998; Agostini et al., 2011a; Corti et al., 2013). The experiments suggest that the transition to intra-rift faulting may be driven by an upwelling asthenosphere that (1) imposes upward bending forces on the lithosphere that restrict slip on border faults, and (2) drives outward flow of an overlying (thinning) lower crust, which leads to shear stresses acting on the base of the brittle crust below the rift center (Corti, 2008; Agostini et al., 2009). In the context of these models, the development of intra-rift fault systems may predate magmatism, and uprising of warm mantle and enhanced melt production occurred in areas of focused lithospheric thinning below intra-rift fault systems (Corti, 2008, 2009) to produce the magmatic segments imaged geophysically below the rift (Keranen et al., 2004).

The studies described here highlight a fundamental question related to the magmatic-tectonic processes controlling continental rifting. Does rift basin architecture evolve in response to changes in plate kinematics and oblique rifting, or is it controlled by deeper processes, such as decompression melting and enhanced magma production below the rift? Early-stage rifts actively transitioning from border fault to intra-rift fault dominated strain accommodation represent prime targets to investigate processes controlling rift basin evolution. For example, if magmatism does drive strain localization in evolving basins, then changes in fault system dynamics should be accompanied by changes in underlying magma systems and/or zones of magmatic volatile release. The 3 Ma Natron and 7 Ma Magadi basins

are currently in their earliest stages of rifting, and provide an ideal location to test and advance existing models of continental rift initiation and evolution.

4.4 Methods

Field and remote-sensing analyses were used to investigate faults in the Magadi and Natron basins. Fault traces were mapped from 0.5-m-resolution aerial photographs (provided by the Polar Geospatial Center, University of Minnesota). Individual segments were identified by the presence of visible fault tips. Following the method of Vetel et al. (2005), segments were interpreted to form part of a longer, segmented fault if they: (1) exhibited relay zones with small offsets relative to the segment length, (2) had similar dip directions, and (3) displayed regular and systematic changes in throw patterns between segments, indicating that segments are geometrically and kinematically coherent (Peacock and Sanderson, 1991; Walsh and Watterson, 1991; Cartwright et al., 1995; Bohnenstiehl and Kleinrock, 1999; Walsh et al., 2003). Fault throws were measured from 30 m SRTM (Shuttle Radar Topography Mission) data, which has an estimated vertical error of 7.6 m (95% confidence) in the study area (Rodríguez et al., 2005). These remote-sensing analyses were verified with three field investigations in the Magadi and Natron basins from 2013-2015 (Fig.4.3). Throws, and occasionally lengths, were measured on border fault and intra-rift fault segments in the field using a Trimble GPS (3.0 m mean vertical error) (Fig. 4.4). These faults were also examined for evidence of recent rupturing, such as fresh scarp surfaces or open fissures (Rowland et al., 2007) (Fig. 4.3A-D). Throws were converted to displacements and heaves by assuming an optimal 60° dip for normal faults (Fig. 4.5).

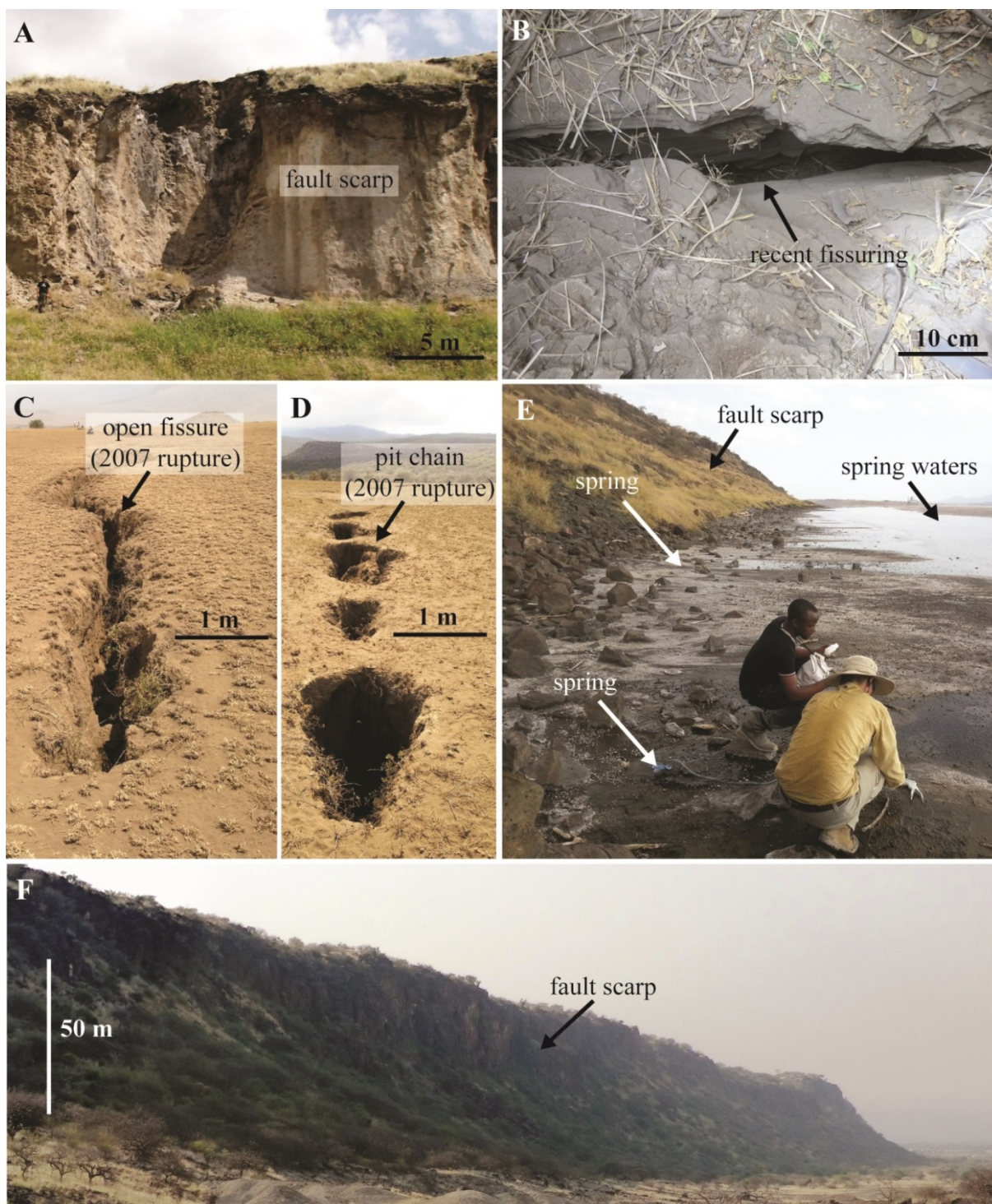


Figure 4.3. Field images from the Natron and Magadi basins. (A) Small border fault segment (<30 m high) in the Natron basin displacing a 200 ± 5 ka tuff and Pleistocene debris avalanche deposits sourced from Oldoinyo Lengai volcano (Sherrod et al., 2013) (photo location: 2.6122°S , 35.8661°E). (B) Recent dilational fissure along the trace of a subsidiary fault segment of the Natron border fault (photo location: 2.6801°S , 35.8821°E). (C) Open fissure related to recent activity along an intra-rift fault in the Natron basin during the 2007 dike-related rifting event (photo location: 2.7272°S , 36.0696°E). (D) Aligned pit chains related to the 2007 earthquake

rupture (photo location: 2.7277°S, 36.0693°E). (E) Fault-parallel springs expelling from the base of an intra-rift fault in the Magadi basin (photo location: 1.8599°S, 36.3064°E). (F) Intra-rift fault scarp (77 m high) dissecting ~0.9 Ma Magadi trachyte lavas in the Magadi basin (photo location: 1.82061°S, 36.2044°E).

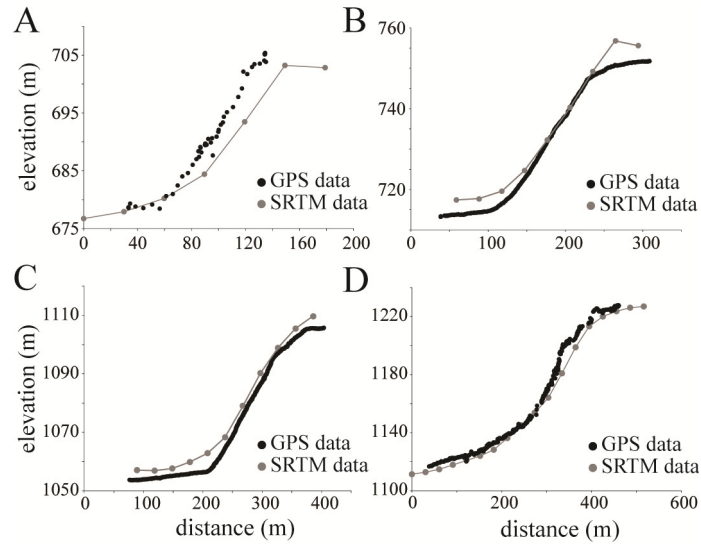


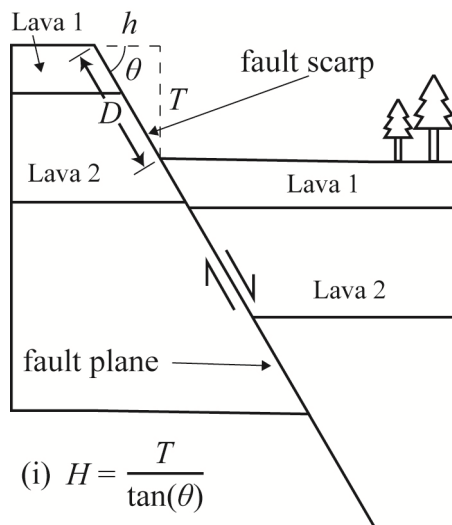
Figure 4.4. Examples of fault profiles in the Natron and Magadi basins measured using a Trimble GPS. SRTM data presented for comparison. (A) Scarp location is 1.8258°S, 36.2083°E. (B) Scarp location is 1.8603°S, 36.2159°E. (C) Scarp location is 1.8388°S, 36.5011°E. (D) Scarp location is 1.50138°S, 36.4965°E.

4.4.1 Strain calculations

Fault-scaling relations in the Magadi and Natron basins were investigated to calculate horizontal normal strain. First, to estimate individual fault displacements within the large fault population (>1000 faults), fault displacement-length ratios were constrained in the Magadi-Natron region. The conventional relationship between maximum displacement, D_{max} , and fault length, L , for continental faults is defined as:

$$D_{max} = \gamma L^n, \quad (\text{eq. 4.1})$$

where γ is the scaling factor or displacement-length coefficient, and n is a power-law



$$(i) H = \frac{T}{\tan(\theta)}$$

$$(ii) D = \frac{T}{\sin(\theta)}$$

$$(iii) \text{ extension rate} = \frac{\Delta h}{\Delta t}$$

$$(iv) \text{ slip rate} = \frac{\Delta D}{\Delta t}$$

Figure 4.5. Simplified cross-sectional depiction of a normal fault (orthogonal to fault strike). Annotated are fault heave (h), throw (T) and dip (θ). By assuming a fault dip (optimally 60° for normal faults), throw can be converted to both (i) heave and (ii) displacement (D). The youngest displaced lava, situated at the top of the fault scarp (lava 1), provides a maximum age for the fault. The age of the fault can be compared against the cumulative heave and displacement to calculate the time-averaged (iii) extension rate and (iv) slip rate, respectively.

exponent that defines the rate of displacement accumulation with increasing fault length (Scholz and Cowie, 1990; Cowie et al., 1993; Dawers et al., 1993; Cartwright et al., 1995; Schultz et al., 2006). Although the value of n for individual fault datasets has been shown to be as high as 2 in some instances (Walsh and Watterson, 1988; Marrett and Allmendinger, 1991; Gillespie et al., 1992), linear elastic fracture mechanics models predict $n = 1$ (Cowie and Scholz, 1992; Bonnet et al., 2001), which is consistent with the full range of global displacement-length datasets (Cowie and Scholz, 1992; Gudmundsson, 1992; Dawers et al.,

1993; Cowie et al., 1993, 1994; Carbotte and MacDonald, 1994; Dawers and Anders, 1995; Cartwright et al., 1995; Schlische et al., 1996; Bohnenstiehl and Kleinrock, 1999, 2000; Schultz et al., 2006, 2010). Therefore, studies quantifying extensional strains in fault populations often assume a linear relationship between fault displacement and length (e.g., Cowie et al., 1993; Carbotte and MacDonald, 1994; Schultz et al., 2010; Nahm and Schultz, 2011). The displacement-length coefficient, however, does vary between fault populations depending on the tectonic setting and mechanical properties of the host rock (Cowie and Scholz, 1992; Bohnenstiehl and Kleinrock, 2000), and therefore must be determined by analyzing displacement-length ratios for each system of interest. On Earth, values of γ typically range from 10^{-1} to 10^{-3} (Schultz et al., 2010). Constraining this relationship within a given fault population (see Section 4.4.2), and assuming a characteristic fault dip at depth, allows an estimate of D_{\max} on any fault within a population from only measurements of L (Cowie et al., 1993, 1994; Carbotte and MacDonald, 1994; Nahm and Schultz, 2011).

Although D_{\max} can be inferred from fault length data, estimates of crustal strain are based on average, rather than maximum, displacements along faults. The displacement profile along the trace of an individual fault tends to be bell-shaped or elliptical (Dawers et al., 1993; Cartwright et al., 1995; Gupta and Scholz, 2000; Kattenhorn and Pollard, 2001), where the displacement remains relatively constant over at least the central third of the fault before reducing to zero at the fault tips (Walsh and Watterson, 1988; Cowie et al., 1993; Willemsse et al., 1996; Peacock, 2002). Therefore, to estimate the average displacement along a given fault, the maximum displacement must be corrected by a value, κ , depending on the shape of the displacement distribution along the fault trace. Fault formation under the assumption of linear

elastic fracture mechanics behavior (Pollard and Fletcher, 2005) is expected to produce an ideal elliptical displacement profile that would result in a κ of 0.7854 (Schultz et al., 2010).

The brittle horizontal normal strain (ε_n) represented by a normal fault population (number of faults = N) may be estimated by summing the extensional strain accommodated along all faults, and is given by the Kostrov relation (Scholz and Cowie, 1990; Nahm and Schultz, 2011):

$$\varepsilon_n = \frac{\sin\delta\cos\delta}{V} \sum_{i=1}^N D_i L_i H_i, \quad (\text{eq. 4.2})$$

where δ is fault dip (assumed to be optimally 60° for normal faults), V is the volume of the faulted region, L is fault length, H is fault depth extent, and D is average displacement ($\kappa \times D_{max}$). Studies investigating fault population strain on Earth's surface (Gupta and Scholz, 2000) and seafloor (Cowie et al., 1993), and other planetary bodies (e.g., Mars; Nahm and Schultz, 2011), make the simplifying assumption that H is equal to L . This assumption is consistent with a downward propagating fault model that has been interpreted by some authors for magmatic rift settings (e.g., Ethiopia and Iceland; Gudmundsson, 1992; Acocella et al., 2003, 2008). Once L and, hence H , is equal to the depth of the brittle crust, faults can only grow by increasing L while H remains constant (Cowie et al., 1993). As a result, horizontal extensional strains may be estimated from two separate equations for small ($L <$ brittle crust thickness) and large ($L >$ brittle crust thickness) faults. For small faults, the brittle horizontal normal strain can be calculated using:

$$\varepsilon_n = \frac{\sin\delta\cos\delta}{V} \sum_{i=1}^N \gamma \kappa (L_i^3), \quad (\text{eq. 4.3})$$

whereas the brittle horizontal normal strain for large faults may be calculated from the equation:

$$\varepsilon_n = \frac{\cos\delta}{A} \sum_{i=1}^N \gamma \kappa (L_i^2), \quad (\text{eq. 4.4})$$

where A is the area of the faulted region.

The equations and scaling relations described above were used to estimate horizontal normal strain within fault populations of the Magadi and Natron basins. Brittle crust thickness estimates are from Albaric et al. (2009) for central Magadi and the N. Natron/S. Magadi border (11 and 19 km, respectively).

4.4.2 Measuring fault lengths, throws, and slip rates from remote sensing and field data

Broad-scale analyses of fault populations from remote-sensing data are prone to both natural and detection biases (Soliva and Schultz, 2008; Schultz et al., 2010). Natural biases are a consequence of processes such as erosion and basin infilling, whereas detection biases relate to the resolution of the data acquisition method (e.g., aerial or satellite photos, SRTM data). These factors lead to truncation biases, which underestimate the size and number of smaller faults in a given population (Schultz et al., 2010). The resolution of aerial photos used to measure fault lengths in this study is 0.5 m/pixel; given the estimated throw-to-length ratio in this study of 0.005 (see Section 4.5.3) and an average $\sim 20^\circ$ slope measured for degraded scarps throughout the field (Fig. 4.4), these images should resolve the hanging wall and footwall cutoffs of faults with lengths >36 m. However, faults with small throws (e.g., <5 m) are also prone to natural bias because they are easily eroded and buried by sediments. For example, faults with lengths <250 m using aerial photography in the Magadi and Natron

basins could not be identified, and only seven faults were identified with lengths between 250 and 500 m (i.e., faults with throws less than ~ 2.5 m). As a result, it is conservatively assumed in this study that faults with throws < 5 m are frequently below the detection limit of the aerial photos due to natural biases, resulting in a fault length truncation bias of 1000 m (Fig. 4.6C). This truncation bias is consistent with that applied by Soliva and Schultz (2008) for faults in the Afar region of the EAR.

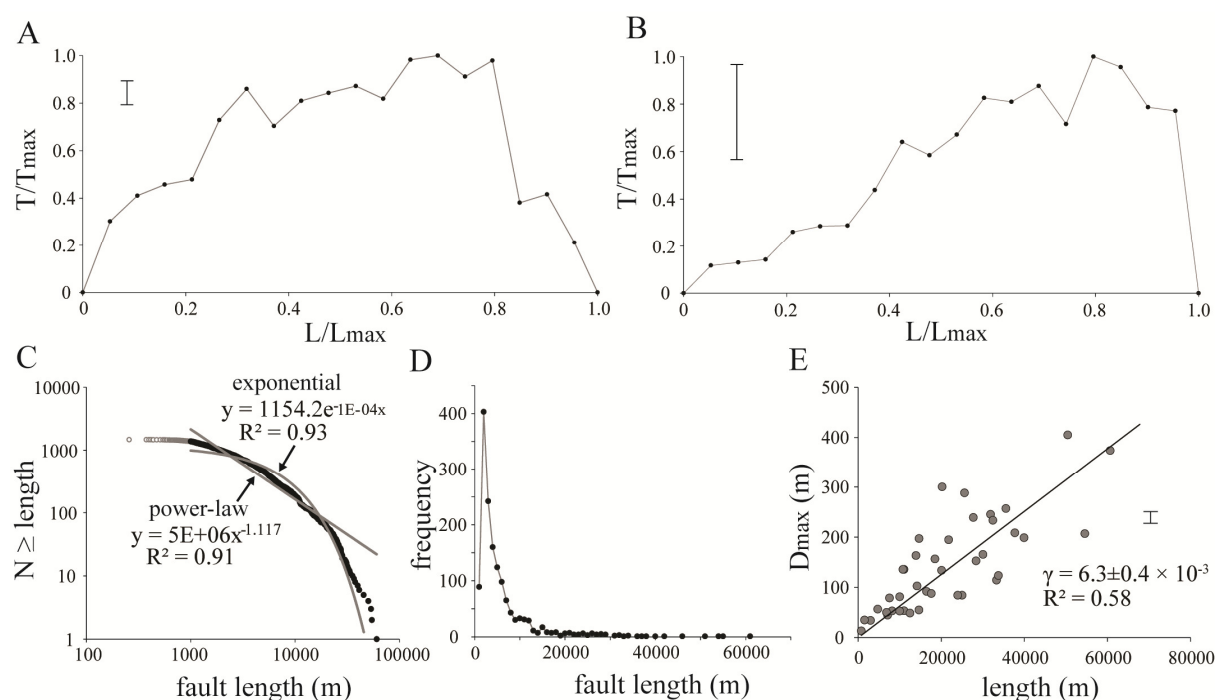


Figure 4.6. Summary plots of remotely-acquired fault data. (A) Example of a throw profile across a fault in the Magadi basin. All length (L) and throw (T) data are normalized to the maximum length (L_{max}) and maximum throw (T_{max}) values, respectively. Error bar (top left) is to 95% confidence. Fault location annotated in Figure 4.7A. (B) Example of an asymmetric throw profile across a fault in the Magadi basin. All length and throw data are normalized as in (A). Error bar (top left) is to 95% confidence. Fault location annotated in Figure 4.7A. (C) Cumulative frequency plot of fault lengths for all intra-rift faults in the Natron and Magadi basins. Gray points represent faults with lengths below the truncation bias limit, whereas black points show fault lengths greater than the truncation bias. Gray lines show exponential (curved line) and power-law (straight line) fits for the data. Comparable R -squared values suggest that length distributions cannot be confidently defined by either negative power-law or negative exponential functions. (D) Incremental length–frequency distribution of all intra-rift faults in the Natron and Magadi basins. (E) Scatter plot of maximum displacement (D_{max}) vs. length for faults in the Natron and Magadi basins (assumed 60° dip). Slope of the best-fit line (black line) represents the displacement–length coefficient (γ). Bar on the right of the graph shows the estimated error of measured fault displacements (95% confidence), whereas length errors are less than the size of the points.

Fault throws could not be measured from aerial photographs – therefore, throw data were remotely acquired from the 30 m SRTM dataset. The accuracy of the throw data depends on the estimated vertical precision of this dataset for the African continent (7.6 m to 95% confidence; Rodríguez et al., 2005). Based on the precision of the SRTM, it is inferred that throws <10 m cannot be confidently measured (i.e., across faults less than ~2000 m in length). Maximum throws were estimated using SRTM data for 40 intra-rift faults in the Natron and Magadi basins by systematically measuring throw along the lengths of faults (e.g., Fig. 4.6A, B). Comparison of fault throws measured in the SRTM with those measured using a Trimble GPS in the field show good agreement (Fig. 4.4). To avoid biases related to erosion and burial by sediments, throws were remotely measured only on well-exposed faults with relatively steep scarps (typically 15-30° dips on the SRTM) that were not surrounded or covered by extensive rift sediments. However, the precision of throw profile analyses will also be affected by sediments that collect against the fault scarp on the downthrown hanging wall (Cartwright et al., 1995). Although the sedimentary cover is expected to be only a few meters thick in arid, extensional basins (e.g., Volcanic Table Lands, Canyonlands, USA; Dawers and Anders, 1995; Moore and Schulz, 1999), the measured throws likely represent minimum values. To avoid detection biases related to the resolution of the SRTM, faults with throws <10 m were not included in comparative throw-length analyses. Throw values were also converted to displacement and heave by assuming an optimal 60° dip for normal faults (Fig. 4.5). Together, fault lengths and throws along 40 intra-rift faults give a best-fit displacement-length coefficient (i.e., γ in eq. 5.1) of $6.3 \pm 0.4 \times 10^{-3}$ (Fig. 4.6E), which is in good agreement with faults dissecting Quaternary lavas in rift zones elsewhere, such as Iceland (Gudmundsson, 1992; Angelier et al., 1997), the Kino Sogo Fault Belt of the Turkana

basin, Kenya (Vetel et al., 2005), and the East Pacific Rise (Cowie et al., 1993, 1994; Carbotte and MacDonald, 1994).

Volcanic rocks at the tops of scarps were sampled for ^{40}Ar - ^{39}Ar age analyses (Table 4.1; refer also to Section 4.9.2), providing constraints on the ages of major lava units and maximum ages of the measured faults. By comparing faulted lava ages with fault throw values, and converting throw to both displacement and heave, these data can be used to estimate maximum slip rates and extension rates, respectively. As shown in Figure 4.5, slip rates refer to changes in displacement over time, whereas extension rates relate to changes in heave over time.

4.5 Results: Fault characteristics, lava chronology, and spring geochemistry of the Natron and Magadi basins

4.5.1 General observations

The 3 Ma Natron basin (Foster et al., 1997) is bounded by a ~600 m-high border fault escarpment (Natron border fault) along its western margin. Rift-normal topographic profiles north of Gelai volcano in the Natron basin (Fig. 4.1D) show the lowest elevations (595 m) in the lake-filled basin adjacent to the currently active Natron border fault, where a number of hydrothermal springs expel water into the lake at the base of the border fault scarp. In addition to the main escarpment (bold black line in Fig. 4.1A), it comprises a number of smaller, subsidiary segments with throws up to 200 m. Incised gullies and ravines within the footwall of the border fault also expose subsidiary faults with measured throws up to 91 m (e.g., sample no. 10, Table 4.1). Locally, the border fault exhibits recent fissures displacing Holocene alluvium (Sherrod et al., 2013) (Fig. 4.3B) and at least one relatively

Table 4.1. $^{40}\text{Ar}/^{39}\text{Ar}$ ages for faulted volcanic rocks in the Magadi and Natron basins. Map of sample locations provided in Fig. 5.7. Also included are the minimum time-averaged slip rates of faults based on acquired dates.

Sample no.	Long. (°E)	Lat. (°S)	Fault throw (m)	Throw error (95%)	Geological unit	$^{40}\text{Ar}/^{39}\text{Ar}$ Ar age (Ma)	Error 1 σ	Minimum time-averaged slip rate (mm yr ⁻¹)*	Error 95% [^]
1	36.1585	-2.4107	59.1	7.3	Gelai lavas	1.158	0.017	0.059	0.005
2	35.8637	-2.6083	125.1	10.2	Sekenge Crater ^b	1.248	0.006	0.116	0.008
3	35.8672	-2.6155	125.1	10.2	Nephelinite ^c	4.057	0.006	N/A ^a	N/A ^a
4	36.1476	-2.7295	59.6	1.9	Gelai lavas	1.053	0.004	0.065	0.002
5	36.1693	-2.6946	68.1	2.6	Gelai lavas	1.190	0.007	0.066	0.002
6	36.1840	-2.6401	57.0	5.7	Gelai lavas	1.167	0.003	0.056	0.005
7	35.8334	-2.5506	151.8	3.4	Sambu basalts	1.968	0.020	0.089	0.000
8	36.2288	-2.4864	75.7	10.2	Gelai lavas	0.961	0.020	0.091	0.008
9	35.8744	-2.5902	N/A ^f	N/A ^f	Tuff ^d	0.095	0.004	N/A	N/A
10	35.8676	-2.5933	90.8	4.3	Natron lavas ^e	1.160	0.027	0.090	0.000
11	35.8787	-2.7814	N/A ^f	N/A ^f	Tuff ^d	0.226	0.006	N/A	N/A
12	35.8818	-2.6795	28.1	1.9	Tuff ^d	0.200	0.005	0.162	0.002
13	36.2184	-1.8617	154.3	5.9	Magadi trachyte	1.367	0.034	0.130	0.001
14	36.2014	-1.8266	76.7	2.3	Magadi trachyte	0.946	0.005	0.094	0.002
15	36.5020	-1.8382	118.1	10.8	Singaraini basalt	1.96	0.09	0.070	0.000
16	36.3634	-1.6091	11.8	2.9	Magadi trachyte	1.152	0.013	0.012	0.003
17	36.2834	-1.9815	73.2	7.2	Magadi trachyte	1.15	0.014	0.073	0.005
18	36.4967	-1.5013	52.9	2.3	Limiru trachyte	2.048	0.021	0.030	0.001
19	36.3693	-1.8108	N/A	N/A	dike intrusion	1.098	0.02	N/A	N/A

*slip rates assume a 60° dip on all faults at depth.

[^]slip rate errors consider both the errors in age and throw presented.

^alavas outcrop below sample no. 2. Most recent slip rate is based on sample no. 2.

^bsampled a basaltic boulder with a breadcrust appearance, suggesting it may be a primary component of the deposit.

^clavas likely sourced from Mosonik volcano.

^dinferred to be from Oldoinyo Lengai based on proximity, but could also be sourced from the Natron-Engaruka field.

^ebasalt occurs as part of Natron escarpment sequence. The source is unknown.

^fdraping over subsidiary scarps with no observable offset.

young fault segment (Fig. 4.3A) offsets tuff (maximum age of 200±5 ka; Table 4.1) and debris avalanche deposits sourced from Oldoinyo Lengai (Kervyn et al., 2008; Sherrod et al., 2013). This fault exhibits up to 28.1±1.9 m of throw, implying recently and probably ongoing border fault activity (0.16 mm yr⁻¹ since the late Pleistocene on this subsidiary segment). Tuff deposits with $^{40}\text{Ar}/^{39}\text{Ar}$ ages ranging from 91±4 to 230±6 ka are observed draping some subsidiary border fault segments with no accompanying fault displacements; this suggests that

not all the observed fault segments along the border fault have produced surface ruptures since 226 ka.

For this study, the intra-rift faults of the Natron basin dissecting Gelai volcano lavas were measured and sampled in the southernmost ~40 km of the basin. Logistical restrictions prevented access to intra-rift faults in Magadi Trachyte lavas between Lenderut volcano and the northern slopes of Gelai (Fig. 4.7A). Faults analyzed in the field on and around Gelai volcano exhibit typical throws of between 50 and 100 m. Age dating of faulted lavas around Gelai reveals that these faults have been active since ~1.2 Ma, and ongoing intra-rift fault activity in the Natron basin is suggested by persistent, shallow (<10 km) tectonic earthquakes below Gelai, with magnitudes ranging from 1.0 to 4.5 (Chapter 3), as well as a 2007 dike-induced surface rupture (Baer et al., 2008; Calais et al., 2008). This surface rupture produced a small dilational fault scarp (up to 65 cm throw; Wauthier, 2011; Fig. 4.3C), which could still be observed ~7 years later as a series of aligned pit chains (up to 5 m long and 2 m wide; Fig. 4.3D). Throws documented by Wauthier (2011) were rapidly removed by erosion of the original small scarp in loose surface materials.

The 7 Ma Magadi basin (Crossley, 1979) comprises a ~1600 m-high border fault escarpment (the Nguruman fault). During fieldwork, there was no identified evidence of recent rupturing, such as recently opened fissures or fault displacements on young <250 ka volcanics or sediments, which stands in contrast to the Natron border fault (Fig. 4.3A and B). Based on field observations, discussions with the local residents, and existing hydrothermal spring maps (e.g., Baker, 1958; Eugster, 1970), no springs are present along the Nguruman border fault escarpment of the Magadi basin. Late Pleistocene lake deposits (e.g., Oloronga Beds; Baker, 1958; Behr and Rohricht, 2000) within ~20 km the Nguruman escarpment

suggest that a paleo-lake was once situated along the western side of the Magadi basin, forming a northern-extension of present-day Lake Natron (Crossley, 1979; refer to Fig. C1 in Appendix C).

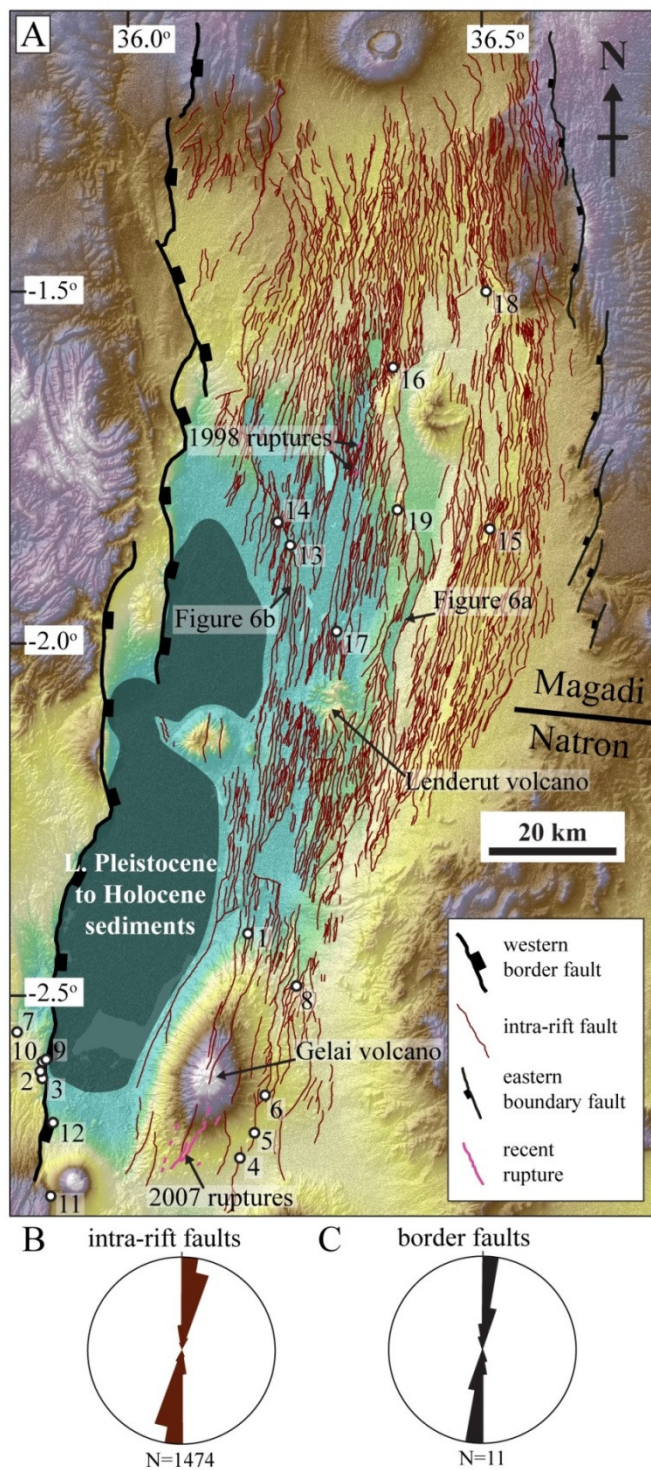


Figure 4.7 (previous page). (A) Distribution of fault traces in the Natron-Magadi region as mapped from 0.5-m-resolution aerial photographs. Thick black lines are rift margin border faults; thin black lines are opposing rift margin boundary faults; thin red lines are intra-rift faults. The western border faults are the major fault structures (throws >1000 m; Baker et al., 1971; Ebinger et al., 1997; Birt et al., 1997) defining the original half-graben basin structure. The eastern boundary fault is an old fault escarpment (2.3-3.3 Ma Ngong-Turoka fault; Baker and Mitchell, 1976) that defines the eastern margin of the basin, but with significantly less throw (~200-500 m) than the border faults. Only the main escarpments along the rift-bounding faults are shown; however, additional minor subsidiary fault segments are also present. Numbers refer to sample locations for $^{40}\text{Ar}/^{39}\text{Ar}$ dating of faulted volcanics (refer to Table 4.1). Recent ruptures from Wauthier (2011) and Ibs-von Seht et al. (2001) were also identified and mapped in the field. The locations of the fault throw profiles shown in Figure 4.6A and B are annotated. Late Pleistocene to Holocene lake sediments (dark shading) likely conceal some faults in the region, particularly below present day Lake Natron (refer to Figure 4.1). (B) Length-weighted rose diagram of the strikes of all intra-fault traces in the Natron-Magadi region. (C) Length-weighted rose diagram of the strikes of border and boundary fault escarpments in the Natron-Magadi region.

Rift-normal elevation profiles show that the deepest part of the Magadi basin occurs away from the border fault in the rift center (603 m elevation compared to 680 m at the base of the Nguruman escarpment), where faults pervasively dissect 0.95-1.37 Ma trachyte lavas (Fig. 4.1C). Recent ESE-WNW extension is indicated by rift-parallel, dilational joint sets in Late Pleistocene and Holocene lake sediments in the intra-rift graben and around Lake Magadi (Atmaoui and Hollnack, 2003). This assertion is further supported by a surface rupturing event during a period of enhanced seismicity in 1998, which produced a small scarp (~10 cm throw; Ibs-von Seht et al., 2001; Atmaoui and Hollnack, 2003) (Fig. 4.7). Within the intra-rift fault system, numerous springs feed water into perennial Lake Magadi. Much like Lake Natron, this shallow lake (only a few meters deep) has little surface drainage input and a high evaporation rate, yet survives due to the influx of CO_2 -rich, saline fluids from below (Eugster, 1970; Roberts et al., 1993; Chapter 3). The combination of CO_2 -rich spring waters, alkali-rich volcanics, saline fluids, and arid conditions create unique environmental conditions necessary to produce economically viable trona and nahcolite deposits in these lakes (Eugster, 1970; Jones et al., 1977; Monnin and Schott, 1984; Jagniecki et al., 2015).

4.5.2 Geochronology of volcanic units and fault slip rates

The timing of fault activity was investigated using new $^{40}\text{Ar}/^{39}\text{Ar}$ dating of volcanic units (Table 4.1) and by reviewing geological maps and previously published K-Ar and $^{40}\text{Ar}/^{39}\text{Ar}$ ages (see Fig. C1 in Appendix C). Volcanic rocks dissected by 17 faults were sampled for $^{40}\text{Ar}/^{39}\text{Ar}$ age analyses in the Magadi and Natron basin, including 13 intra-rift faults (6 from Magadi and 7 from Natron) and 4 fault segments that collectively form part of the Natron border fault escarpment. Sampled rocks include basalt, trachyte, and nephelinite lavas, as well as volcanic tuff. All samples were collected along the footwall cutoffs at the tops of fault scarps and away from fault tips to avoid the reduced fault throw in those regions. Determined ages range from 0.10 to 4.05 Ma.

These data provide new constraints on the timing of volcanic events that were previously dated using K-Ar techniques (Isaacs and Curtis, 1974; Baker and Mitchell, 1976; Crossley, 1979; Baker et al., 1988; Foster et al., 1997). In the Natron basin, nephelinite (sample no. 3, Fig. 4.7A and Table 4.1) sampled on the Natron border fault and the eastern flank of Mosonik volcano (Fig. C1) gives an age of 4.06 Ma, suggesting this volcano began erupting ~0.5 million years earlier than previously estimated (Dawson, 1992; Foster et al., 1997). Basalts from Oldonyo Sambu volcano (Fig. C1), sampled at the top of the footwall of the Sangani fault segment of the Natron border fault (sample no. 7), give an age of 1.97 Ma. Although this date is consistent with previous K-Ar studies, which range from 1.8-3.5 Ma (Isaacs and Curtis, 1974), the date of 1.8 Ma was originally considered anomalous, with the authors favoring an age of 3.1-3.5 Ma for the volcano. This new $^{40}\text{Ar}/^{39}\text{Ar}$ age, however, suggests that Oldonyo Sambu was indeed active until ~1.97 Ma. Sekenge Crater rim pyroclastic deposits were also sampled (Neukirchen et al., 2010; Sherrod et al., 2013) (sample

no. 2, Fig. 4.7A). These deposits are displaced by a subsidiary fault segment in the footwall of the Natron border fault escarpment. They contain rare basaltic breadcrust bombs (up to 30 cm diameter), which give a maximum age of 1.25 Ma. Tuff in close proximity to Oldoinyo Lengai (sample no. 9, 11, and 12) range in age from 0.10-0.23 Ma. Some of these deposits are offset by small segments of the Natron border fault in the hanging wall of the main escarpment. Although these deposits cannot be correlated to Oldoinyo Lengai with complete certainty, the dates are within the range of published ages for the volcano (minimum age of 350 ka; Sherrod et al., 2013). Faulted lavas in the intra-rift portion of the Natron valley were derived from Gelai volcano. The new ages presented here demonstrate a longer duration of activity for Gelai (minimum of 230,000 years), with ages in the range 0.96-1.19 Ma (sample no. 1, 4, 5, 6, and 8), compared to 1.11-1.19 Ma reported previously by Mana et al. (2015).

In the Magadi basin, age data suggest that the Singaraini basalt was emplaced by 1.96 Ma (sample no. 15; Figs. 4.7A and Table 4.1), rather than the 2.31 Ma originally proposed by Baker and Mitchell (1976) based on K-Ar dating. This study also provides the first published $^{40}\text{Ar}/^{39}\text{Ar}$ ages for Magadi trachyte lavas (sample no. 13, 14, 16, 17), a recent and widespread lava unit observed along the center of the Natron and Magadi basins. The new ages of 0.95-1.37 Ma are within previously documented K-Ar ages ranging 0.8-1.4 Ma (Baker and Mitchell, 1976; Baker et al., 1988). However, only the youngest lavas were sampled, exposed at the tops of fault scarps – therefore, these data only reflect the ages of lavas emplaced during the later stages of the Magadi trachyte volcanic event. A new date of 2.05 Ma for Limiru trachyte (sample no. 18) is consistent with the 1.88-2.01 Ma age of Baker and Mitchell (1976).

Age dating of faulted lavas at the tops of fault scarps provides the maximum ages of sampled faults. When combined with measurements of fault throw, the dates also constrain time-averaged minimum slip rates (Fig. 4.5). Minimum slip rates (Table 4.1) for intra-rift faults in the Natron basin range 0.06-0.09 mm yr⁻¹. Subsidiary border fault segments in Natron exhibit higher minimum slip rates, ranging 0.09-0.16 mm yr⁻¹. Time-averaged minimum slip rates estimated for sampled intra-rift faults of the Magadi basin range 0.01-0.13 mm yr⁻¹, but are generally higher than slip rates in equivalent-age lavas in the Natron basin. However, these data (Table 4.1) do not include the largest fault throws (up to 362 m) measured from SRTM data in Magadi trachyte lavas, which would suggest that intra-rift faults have maximum slip rates ranging 0.30-0.45 mm yr⁻¹ in the 0.95 to 1.37 Ma Magadi trachytes.

4.5.3 Fault statistics of intra-rift fault populations

In all, 1,474 intra-rift faults were identified in the Natron and Magadi basins. The mean trend of intra-rift faults (008°) roughly parallels the border fault system (006° mean trend) (Fig. 4.7B, C). Intra-rift fault lengths range over three orders of magnitude, from 0.26 to 60.7 km (Fig. 4.6C, D). Fault throws were measured along 40 well-exposed intra-rift faults. Throw profiles are often bell-shaped and consistent with unrestricted fault growth, where fault tips grow unimpeded during each slip event (Cowie and Scholz, 1992; Cartwright et al., 1995; Nicol et al., 1996) (Fig. 4.6A). Throw profiles along some faults in the Natron and Magadi basins also exhibit varying degrees of asymmetry (Kattenhorn et al., 2013) (Fig. 4.6B). Asymmetric throw profiles are indicative of restricted fault growth, where propagation at one end of the fault is stymied by a mechanical barrier (Nicol et al., 1996; Manighetti et al., 2001). Maximum throws are as high as 362 m within the Magadi trachyte in the Magadi basin (Fig.

4.6E). The displacement-length coefficient of $6.3 \pm 0.4 \times 10^{-3}$ is low compared to normal fault populations in softer (typically sedimentary) rocks (e.g., 10^{-1} to 10^{-2} ; Schultz et al., 2006), but is comparable to faults dissecting Quaternary lavas in the Krafla rift zone, Iceland (Angelier et al., 1997), and Kino Sogo Fault Belt of the Turkana basin, Kenya (Vetel et al., 2005), and the East Pacific Rise (Cowie et al., 1993, 1994; Carbotte and MacDonald, 1994).

4.5.4 Fault-related extensional strain

Faults were subdivided into populations based on the ages of the volcanic units they dissect (Table 4.2; Fig. C1). Ages were determined from the new and existing $^{40}\text{Ar}/^{39}\text{Ar}$ analyses. In instances where no $^{40}\text{Ar}/^{39}\text{Ar}$ dates were available, existing K-Ar ages were applied. Total fault-related strain was then calculated within each lava unit.

Extension rates in lava groups

Fourteen major volcanic units are identified in this study to subdivide the fault population. These units give maximum ages for the faults dissecting them, given that the time interval between lava eruption and subsequent faulting cannot be determined. The ages of faults can then be translated into a time-averaged extension rate since the eruption of each respective unit based on the calculated horizontal extensional strain within the fault population (Fig. 4.5; refer also to Section 4.4).

Extensional strain was calculated in each of the fault populations using the method described in Section 4.4.1. The time-averaged extension rate was then estimated by dividing total extension by the age of the lava unit (Table 4.2). The mean, time-averaged extension rates reach as high as $0.93 \pm 0.28 \text{ mm yr}^{-1}$ (unit 3; Table 4.2) for intra-rift faults in the 7 Ma Magadi basin. Estimated extension rates are lower in intra-rift fault populations in the 3 Ma

Natron basin (up to $0.47 \pm 0.14 \text{ mm yr}^{-1}$), consistent with the generally lower slip rates along intra-rift faults in the Natron basin compared to the Magadi basin. These extension rates are within the modeled range (i.e., less than) of 1.8 to 2.0 mm yr^{-1} for the Natron-Magadi region (Saria et al., 2014; refer to Section 4.8.3). The highest extension rates occur in the center of each intra-rift fault population, decreasing to 0.20-0.30 mm yr^{-1} in the eastern ~20 km of the intra-rift fault population in the Singaraini basalt and Limiru trachyte lavas. In each basin, extension rates are lowest around the extinct Olorgesailie, Eyaseti, Lenderut, and Shompole volcanoes ($< 0.03 \text{ mm yr}^{-1}$). Away from these volcanoes, extension rates are lowest ($< 0.1 \text{ mm yr}^{-1}$) in the western 10-20 km of the intra-rift fault populations. For example, Late Pleistocene lake sediments in southwest Magadi basin are relatively unfaulted, suggesting little to no recent fault activity. In the Natron basin, however, Holocene sediments from ephemeral Lake Natron possibly mask the surface expression of recent faults and thus prohibit a detailed analysis of strain on the western side of the Natron basin (discussed further in Section 4.6.1). Recently observed seismicity implies active normal faulting below the lake (Chapter 3). However, displacements on these faults are too low to produce scarps high enough to rise above the shallow Lake Natron waters (a few meters deep).

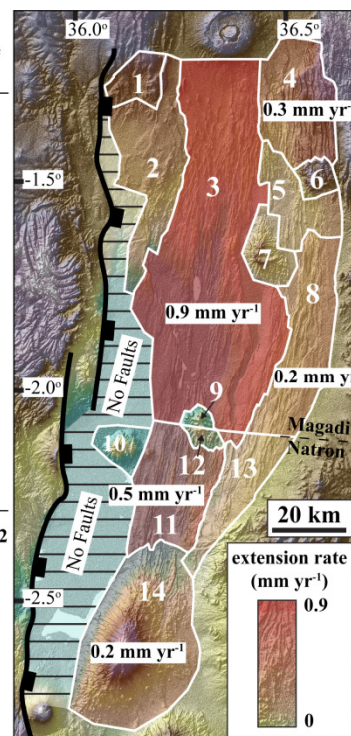
Extension rates across the Magadi and Natron basins

To understand how strain is distributed within intra-rift faults across-rift, fault-related extensional strain was analyzed along two rift-normal transects through the Magadi and Natron basins (Fig. 4.8). Rift-normal extensional strain was calculated in 15 rectangular areas, 4 km wide by 15 km long, with long-axes trending parallel to rift faults. Results of these analyses, presented in Figure 4.8B and 4.8D, show how intra-rift fault-strain is distributed across each basin. Similar to results shown in Table 4.2, analyzed faults in the Magadi basin

accommodate more extensional strain (up to 6.8%) than those in Natron (up to 4.0%). Within the center of the Magadi basin total extension exceeds 3% in 10 of the 15 analyzed areas (Fig. 4.8B). In contrast, only 2 of the 15 analyzed areas in Natron exhibit extension in excess of 3% (Fig. 4.8D).

Table 4.2. Summary of the general distribution of fault-strain calculated in designated lava units in the Magadi and Natron basins. The areal distributions of the lava units are from the geological map in Supplementary Figure C1. Length values correspond to the length of the unit in a N-S direction, whereas mean width is the mean width in an E-W direction. Map shows the distribution of each lava group (1 through 14). Extension rates represent the mean extension rate based on the mean width, total strain, and age of each unit. Errors are based on the range of ages of faulted lavas and the vertical uncertainty of the SRTM. Brittle crustal thicknesses used for strain calculations (from Albaric et al., 2009) are 11 km for areas 1 to 8, and 19 km for areas 9 to 14. Areas not included (southwest Magadi, Lake Natron) contain no faults visible in the aerial photos. Each unit is shaded (red) based on relative extension rate (inset map). Also annotated are the extension rates in lava units with rates ≥ 0.2 mm yr⁻¹.

unit no.	unit name	area (km ²)	length (km)	mean width (km)	strain	extension (km)	age of faulted lavas (Ma)	extension rate (mm yr ⁻¹)	
Magadi	1	Mao	162	15.2	10.6	0.0534±0.0003	0.057±0.004	0.60	0.095±0.006
	2	West Magadi	816	63.8	12.8	0.0123±0.0008	0.158±0.010	1.70-2.30	0.082±0.017
	3	Magadi T.	2542	95.8	26.5	0.0405±0.0026	1.075±0.068	0.95-1.37	0.932±0.277
	4	Limiru	566	34.9	16.2	0.0349±0.0022	0.566±0.036	2.05	0.300±0.035
	5	Ol Tepesi	313	28.3	11.0	0.0189±0.0012	0.208±0.013	1.40-1.65	0.138±0.020
	6	Ol Eyaseti	88	11	8.0	0.0122±0.0008	0.097±0.006	5.60-5.90	0.017±0.002
	7	Ologresailie	186	21.2	8.8	0.0065±0.0004	0.057±0.004	2.20-2.70	0.024±0.004
	8	Singaraini	672	54.7	12.3	0.0322±0.0020	0.396±0.025	1.96	0.202±0.013
	9	Lenderut	38	6.8	5.5	0.0034±0.0002	0.019±0.001	2.50-2.70	0.007±0.001
Natron	10	Shompole	131	13.5	9.723	0.0007±0.00004	0.007±0.0004	2.00	0.003±0.0002
	11	Magadi T.	636	35.7	17.81	0.0306±0.0019	0.545±0.035	0.95-1.37	0.473±0.140
	12	Lenderut	45	7.3	6.146	0.0074±0.0005	0.046±0.003	2.50-2.70	0.018±0.002
	13	Singaraini	362	38.7	9.362	0.0260±0.0016	0.243±0.015	1.96	0.124±0.008
	14	Gelai	1194	50	23.88	0.0099±0.0006	0.235±0.015	0.95-1.17	0.222±0.014



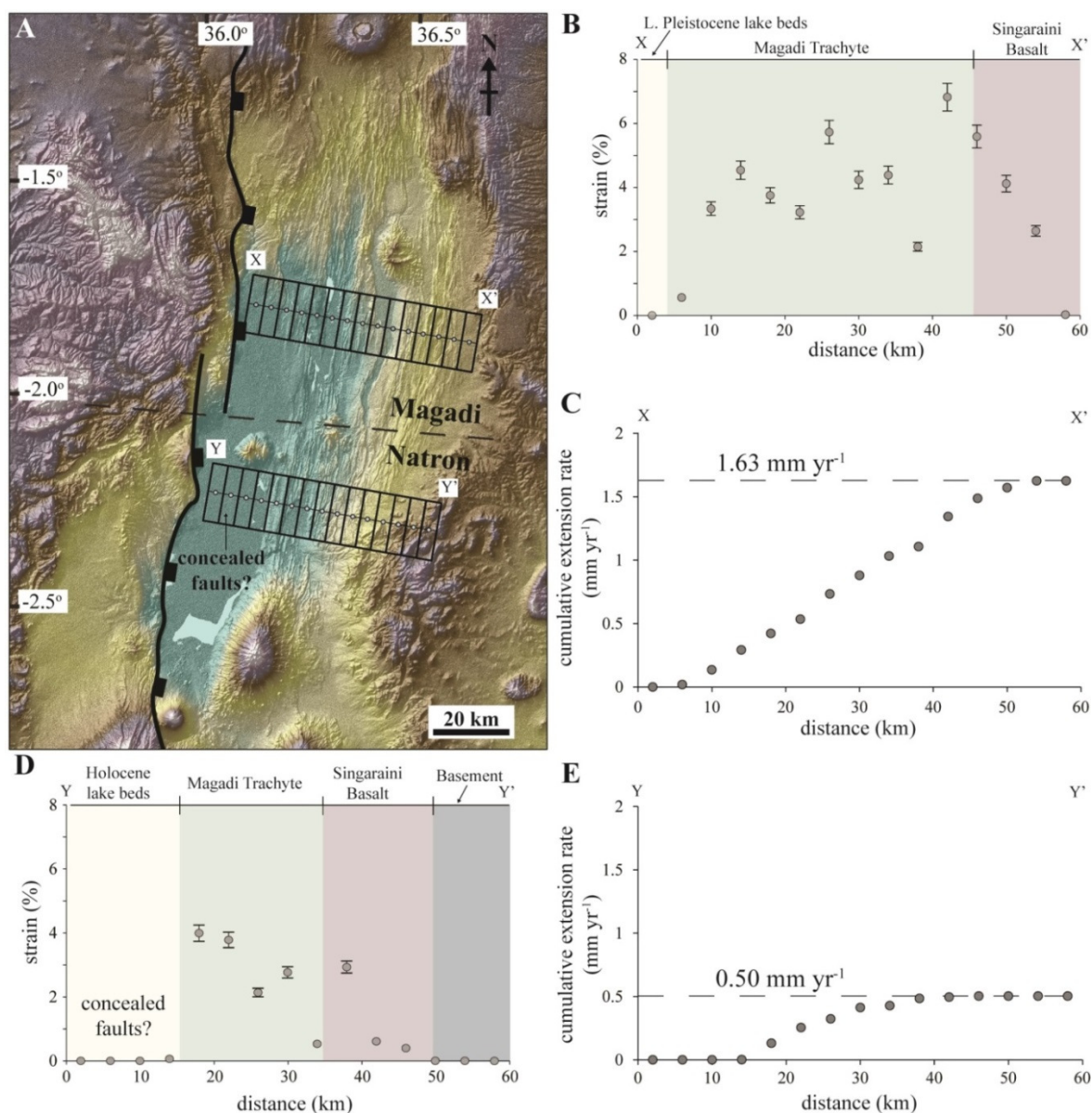


Figure 4.8. Rift-normal distribution of intra-rift fault-related strain across the Magadi and Natron basins. (A) Annotated SRTM image showing the location of each transect and the polygons in which strain was calculated. Gray-filled circles in the center of each box correspond to the locations of data points in B-E. (B) Strain calculated in each polygon along profile X-X' in the Magadi basin. Confidence intervals consider the vertical precision of the SRTM to 95 % certainty. Points without confidence intervals have uncertainties below the resolution of the data point. Faults dissect 0.3 Ma lacustrine sediments (Behr and Rohricht, 2000), 1.15 Ma Magadi trachyte lavas (mean age of sampled lavas), and 1.96 Ma Singaraini basalt lavas (Table 4.2). Colors refer to the geological units dissected by the faults. The ages of these units are used to estimate extension rates in C. (C) Cumulative extension rate in the intra-rift fault population of the Magadi basin. Extension rates in each polygon are summed from west to east, resulting in a total time-averaged extension rate of 1.63 ± 0.10 mm yr⁻¹. (D) Strain calculated in each polygon along profile Y-Y' in the Natron basin. Ephemeral lake waters and Lake Natron sediments (Holocene age) potentially mask faults within ~16 km of the border fault. No rift faults are identified in the basement. (E) Cumulative extension rate in the intra-rift fault population of the Natron basin. Extension rates in each polygon are summed from west to east, resulting in a total time-averaged extension rate of 0.50 ± 0.03 mm yr⁻¹.

Time-averaged extension rates were estimated by dividing the total extension by the age of the lavas displaced by faults (Fig. 4.8). By summing values across each transect from west to east in Figures 4.8C and 4.8E, the total time-averaged extension rates in the intra-rift populations were calculated. Results show that intra-rift faults in the 7 Ma Magadi basin accommodate more extension ($1.63 \pm 0.10 \text{ mm yr}^{-1}$) than those in the younger, 3 Ma Natron basin ($0.50 \pm 0.03 \text{ mm yr}^{-1}$). The remaining extension for each basin is likely focused along border faults (refer to Section 4.6.1).

It is notable that some intra-rift faults in transect Y-Y' across the Natron basin may be concealed by Holocene lake deposits within ~16 km of the Natron border fault (Fig. 4.8A). These complications provide additional uncertainties in the presented extension rate estimates. Given that intra-rift faults in Magadi clearly accommodate more strain than those in Natron (Fig. 4.8B and D), extension rates within 16 km of the Nguruman border fault can perhaps provide an upper limit for intra-rift faults buried by Lake Natron sediments. Analyses show that well-exposed faults in Pleistocene lake sediments and Magadi trachytes within 16 km of the Nguruman border fault in the Magadi basin (transect X-X'; Fig. 4.8) accommodate $0.36 \pm 0.01 \text{ mm yr}^{-1}$. Assuming this is an upper limit for faults below Lake Natron, it is estimated that intra-rift faults in the Natron basin accommodate between 0.47 and 0.90 mm yr^{-1} of extension.

4.5.5 Estimating flexure of the border fault hanging wall

Slip along a planar normal fault in the upper crust can be modeled by assuming that two vertical line-loads are applied in equal and opposite directions to an elastic plate either side of the fault plane (i.e., where $x = 0$ in Figure 4.9) (Vening Meinez, 1950; Turcotte and Schubert, 1982; Stein et al., 1988; Bott, 1996). The footwall and hanging wall of the fault locally respond to this load by bending, with the subsequent deflection profile (i.e., hanging wall flexural profiles in Fig. 4.9) dependent on the rigidity of the plate. Fault slip can thus generate extensional bending stresses that manifest at the near-surface in the flexing hanging wall and, in part, can drive the initiation of intra-rift faults (McClay and Ellis, 1987; Lavier et al., 2000; Imber et al., 2003; Ebinger et al., 2005).

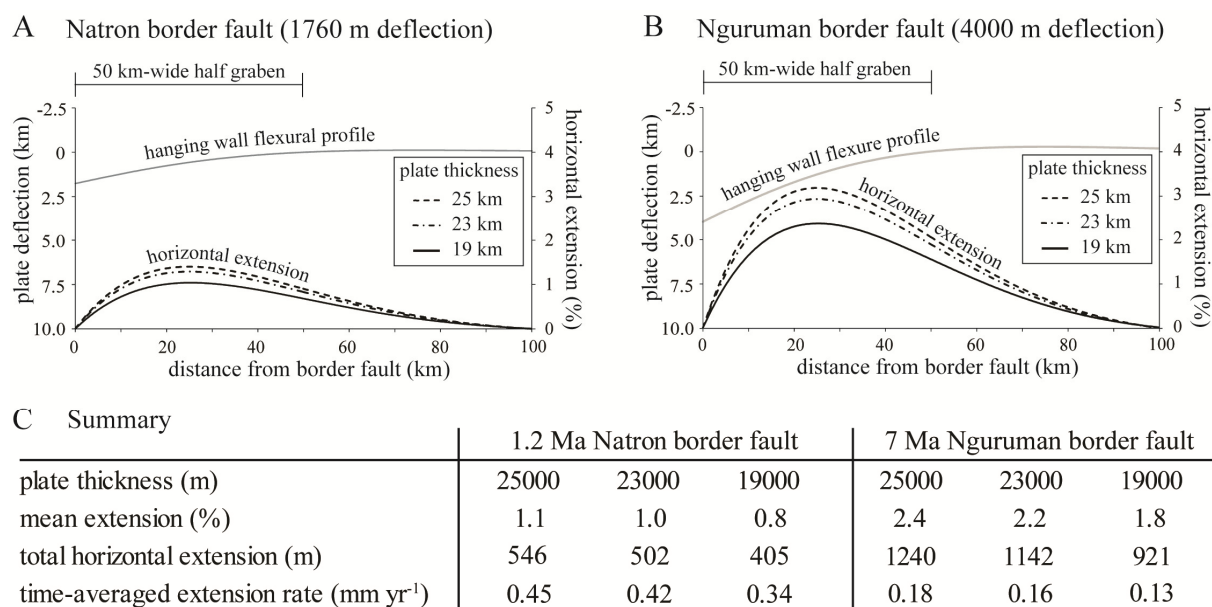


Figure 4.9. Results of modeled broken plate deflections from border faulting and the development of 50-km-wide half-graben basins. Both the flexural profile and horizontal extensional strain were estimated using the methods of Turcotte and Schubert (1982) and Billings and Kattenhorn (2005), and are described further in the Supplementary Materials. (A) Expected flexural profile for a 1.76-km-deep by 50-km-wide half-graben basin in Natron. Maximum deflection (1.76 km) occurs at the left of the graph (distance = 0 km) and approaches zero at 50 km. Also plotted is the horizontal extension that would result across the basin from the deflection of a 19, 23 and 25 km-thick plate. (B) Expected flexural profile for a 4.0 km-deep by 50 km-wide half-graben basin in Magadi. Maximum deflection (4.0 km) occurs at the left of the graph (distance = 0 km) and approaches zero at

50 km. Also plotted is the horizontal extension that would result across the basin from the deflection of a 19, 23 and 25 km-thick plate. (C) Summary of data from the models presented in A and B. Mean extension (%) and total horizontal extension considers the average of all the extensional strain over the 50-km-wide basin. The time-averaged extension is estimated by dividing the total extension by the age of the half-graben basin.

Estimating extensional bending stresses from border fault activity in each basin first requires constraints on subsurface border fault throws, which are provided by both gravity and seismic velocity data in the region (Birt et al., 1997; Ebinger et al., 1997). These studies give estimates of rift basin sediment fill of 3.6 km for Magadi and 1.6 km for Natron. Above the ground surface, the Nguruman and Natron escarpments exhibit throws of ~1.4 km and ~0.6 km, respectively. Summing values of subaerial and subsurface throws for each basin equates to total border fault throws of 2.2 km for Natron, and 5.0 km for Magadi. Assuming a ratio of upthrow to downthrow on the fault of 0.2 (e.g., Stein and Barrientos, 1985; refer to Section 4.8.2), the maximum downward deflection of the hanging wall (i.e., deflection at $x = 0$ in Figure 4.9) is estimated to be 4 km for Magadi and 1.76 km for Natron. These values are within constraints provided by basins depths (Birt et al., 1997; Ebinger et al., 1997), which require minimum hanging wall deflections of 3.6 km and 1.6 km in Magadi and Natron, respectively.

Based on hanging wall deflections for each basin and a mean basin width of 50 km (Foster et al., 1997; Ebinger, 2005), the flexural profile and subsequent horizontal extensional strain can be approximated using the methods of Turcotte and Schubert (1982) and Billings and Kattenhorn (2005) (Fig. 4.9 and Section 4.8.2). Using effective elastic thicknesses ranging 19-25 km for rift basins in North Tanzania, based upon Ebinger et al. (1997), it is estimated that border fault flexure has produced approximately 0.8-1.1% and 1.8-2.4% of extension in the Natron and Magadi basins, respectively. By making the simplifying

assumption that strain was accumulated at a constant rate from border fault activation to the present day, time-averaged extension rates related to hanging wall flexure range 0.34-0.45 mm yr⁻¹ for Natron and 0.13-0.18 mm yr⁻¹ for Magadi. These results have implications for how much regional extension is accommodated via intra-rift faulting in each basin (discussed further in Section 4.6.1).

4.5.6 Distribution of springs and their geochemistry

Hydrothermal springs are observed at the base of some fault scarps in the study region, and are often aligned in fault-parallel clusters (Figs. 4.3E and 4.10A). In Magadi, springs occur in a ~11-km-wide zone (measured rift-normal) in the center of the basin, whereas springs in the Natron basin are present along a ~23-km-wide zone extending rift-normal from the border fault eastward across the hanging wall to an antithetic fault bounding the eastern side of Lake Natron. No springs are documented or observed along the Nguruman border fault of the Magadi basin, nor are any springs present in the center of the intra-rift fault population in Natron.

Spring water samples were collected in the field using Giggenbach bottles, and dissolved gases were analyzed at the Volatiles Laboratory and Center for Stable Isotopes, University of New Mexico (UNM) (refer to Section 4.9.1 for detailed methods). Sampled springs exhibit high pH (8.9-10.2) and warm temperatures from 35.0 to 50.7°C (Table 4.3). The N₂-He-Ar systematics of spring samples were compared with fluids and gases from springs, gas vents, and fumaroles from the Rungwe Province (southern Tanzania) and Oldoinyo Lengai volcano of the EAR (Fischer et al., 2009; de Moor et al., 2013a) (Fig. 4.10B). On a N₂-He- Ar ternary diagram (Fig. 4.10B), fluids derived from the mantle should

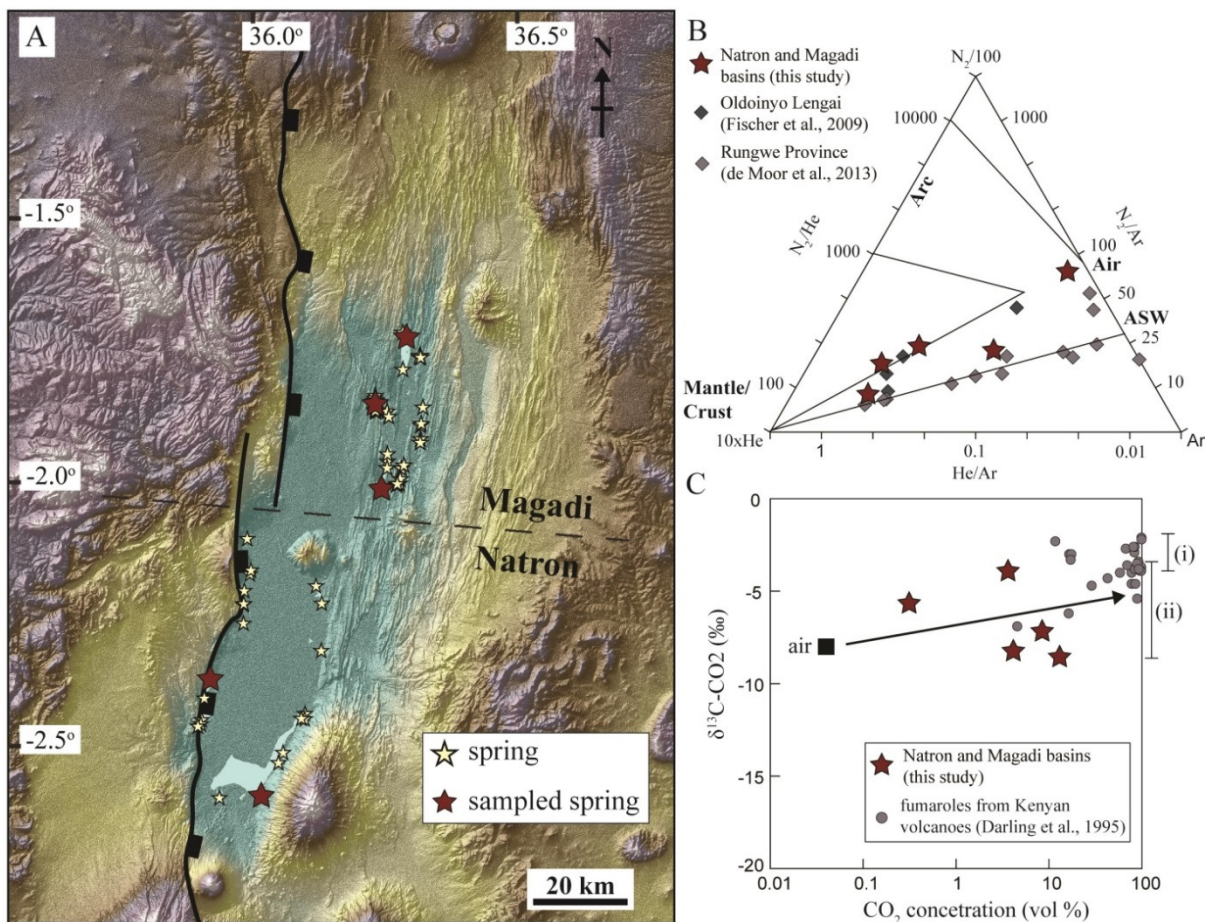


Figure 4.10. (A) Annotated DEM map of the Natron and Magadi basins, showing the distribution of springs (yellow stars) mapped in this study and from Baker (1958) and Eugster (1970). Springs sampled for geochemical analyses are annotated as red stars (see Table 4.3). Border faults are annotated as black lines. (B) Ternary plot of N_2 -He-Ar abundances in the sampled springs (red stars) compared to samples from Rungwe Province (light grey diamonds) and Oldoinyo Lengai (dark grey diamonds) (Fischer et al., 2009; de Moor et al., 2013a). Samples from this study plot on a mixing line between air-saturated water and a mantle end-member. (C) Carbon isotope compositions and concentrations of spring samples in this study (red stars) compared to gases from fumaroles at Kenyan volcanoes (grey circles) from Darling et al. (1995). The $\delta^{13}C-CO_2$ values are presented as per mil (‰) against a standard Pee Dee belemnite (PDB) limestone. Also shown are the range of isotope values for (i) Oldoinyo Lengai fumaroles and (ii) mantle carbon, from Fischer et al. (2009) and Sano and Marty (1995), respectively. Black arrow represents a typical mixing line between mantle carbon and air observed for magmatic volatiles (e.g., Parks et al., 2013; Chapter 3).

Table 4.3. Composition of spring samples from the Natron and Magadi basins (locations shown in Fig. 4.10). Gas compositions are reported as % volume. Gas volumes below the detection limit are reported as “<dl”.

area	ID	lat. °S	long. °E	Temp °C	pH	Ar	He	N ₂	O ₂	CO ₂	H ₂	CH ₄	CO	δ ¹³ C-CO ₂ permil.
Magadi	KN14-S01	1.8574	36.2190	48.4	8.9	0.932	0.199	92.955	1.331	4.130	0.029	0.416	0.008	-8.28±0.04
Magadi	KN14-S06	1.9983	36.2313	44.6	9.9	0.811	0.293	88.703	1.307	8.444	0.018	0.424	<dl	-7.18±0.12
L. Magadi	KN14-S08	1.7276	36.2809	83.5	9.5	0.240	0.084	33.486	0.625	46.195	0.031	19.339	<dl	-7.27±0.05
Natron	TZ14-S01	2.3731	35.9058	50.7	10.3	1.666	0.637	95.140	1.285	0.312	0.020	0.940	<dl	-5.66±0.42
Natron	TZ14-S06	2.5928	36.0160	36.8	9.2	1.403	0.112	74.751	10.720	13.014	<dl	<dl	<dl	-8.57±0.07

plot near the He apex, consistent with He/Ar and N₂/Ar ratios of the upper mantle, which are shown to be ~1 and 80, respectively (Burnard et al., 1997; Marty and Zimmermann, 1999). In contrast, both air and air-saturated water have N₂/Ar ratios of 84 and ~40 (varies slightly depending on temperature), respectively, and low proportions of He relative to Ar (<0.01) (de Moor et al., 2013a). Consistent with magmatic gases and fluids from the Rungwe Province and Oldoinyo Lengai volcano, spring samples from the Natron and Magadi basins fit on a mixing line between air-saturated water and a mantle/crust end-member (Fig. 4.10B). Values of $\delta^{13}\text{C}$ (Table 4.3) from CO₂ gases dissolved in spring samples also overlap with mantle carbon values ($-6.5\pm 2.5\text{‰}$). These data are also consistent with isotope values from diffusely degassing CO₂ in the Magadi and Natron basins, which show a mixing relationship between air and mantle-derived CO₂ released from degassing magmas (Chapter 3). Plots of $\delta^{13}\text{C}$ -CO₂ and CO₂ concentrations of springs in the region also fit on a mixing line between air and magmatic CO₂ (Darling et al. 1995; Sano and Marty, 1995) (Fig. 4.10C).

4.6 Discussion

Data presented in this study are critical for investigating the development of rift basin architecture during continental rifting in the EAR, particularly the magmatic-tectonic processes that influence faulting in the first 10 million years of rift development (Fig. 4.2A and 4.2B). Results from this study provide insights into how and when strain migrates to the rift center prior to the development of magmatic segments, like those observed today in the Main Ethiopian Rift (Keranen et al., 2004; Fig. 4.2C). The evolution of fault systems in early-stage basins is discussed below by comparing the 7 Ma Magadi and 3 Ma Natron basins. Specific topics of interest are:

- 1) the volcanic-tectonic history of the Natron-Magadi region;
- 2) importance of flexure of the border fault hanging wall for intra-rift faulting;
- 3) amount of strain accommodated between border faults and intra-rift faults in each basin;
- 4) evolving fault strain and basin morphology during early-stage rift development; and
- 5) processes assisting the evolution of fault systems (e.g., kinematic, magmatic, hydrothermal).

4.6.1 Fault evolution during early-stage continental rifting

Tectonic-magmatic history of the Magadi and Natron basins

Data presented in this study in context with previous work reveal that rift activity in the Natron and Magadi basins is characterized by persistent faulting and punctuated phases of volcanic activity (Baker and Mitchell, 1976; Crossley, 1979; Le Gall et al., 2008; Guth, 2015) (refer to Figs. 4.7 and C1). The earliest stages of rifting in the Natron-Magadi region were characterized by faulting and volcanism along the Enguruman escarpment of the Magadi basin. Faulting initiated on the rift border at ~7 Ma, prior to the eruption of Lengitoto trachyte lavas (6.9-5.0 Ma) along the western rift edge (Crossley, 1979). Volcanism began on the eastern border of Magadi at ~6.7 Ma with the eruption of Ol Eyaseti volcanics (Baker et al., 1971; Baker and Mitchell, 1976). The next major phase of volcanism involved eruption of Kirikiti lavas along the western side of the basin and the rift center from 5.1 to 2.5 Ma (Baker et al., 1971; Crossley, 1979). During this period, volcanism in the Natron region initiated with the development of Mosinik volcano at 4.05 Ma (Table 4.1), followed by faulting along the now-extinct Oldonyo Ogot border fault escarpment at ~3 Ma (Foster et al., 1997; Le Gall et

al., 2008; Stollhofen and Stanistreet, 2012). The Ngong-Turoka fault, which bounds the eastern side of Magadi basin, was active during this time from 2.3 to 3.3 Ma (Baker and Mitchell, 1976), as well as the Lenderut (2.5-2.7 Ma), Ologesaile (2.2-2.7 Ma), and Ngong (2.5-2.6 Ma) composite volcanoes and related volcanics (Baker et al., 1971; Fairhead et al., 1972; Baker and Mitchell, 1976; Baker et al., 1977). Since 2 Ma, the Magadi and Natron basins have been subject to widespread, basin-filling lava eruptions, including the Limiru trachytes (2.05 Ma) and Singaraini basalts (1.96), with additional volcanism from Oldonyo Sambu (1.8 Ma to, possibly, 3.5 Ma) and Shompole volcanoes (1.96 Ma – present(?)) (Fairhead et al., 1972; Isaacs and Curtis, 1974; Le Gall et al., 2008; Table 4.1). The final phase of tectonic-magmatic activity in the region was marked by a shift in border faulting in Natron from the Oldonyo Ogol escarpment to the Natron border fault between 1.0 and 1.2 Ma (Foster et al., 1997). Changes in the location of border faulting in Natron were both accompanied and preceded by voluminous axial volcanism in the rift center (combined minimum volume = 1263 km³; Guth, 2015), with eruption of Gelai volcanics (0.95-1.23 Ma) and Magadi trachyte lavas (0.95-1.4 Ma) (Baker and Mitchell, 1976; Table 4.1). This volcanic resurfacing event filled the entire rift valley floor, erasing earlier faulted topography (Baker and Mitchell, 1976). Since this time, both rift basins have been characterized by an extended phase (~1 Ma to present) of rift-parallel, intra-rift faulting (Baker, 1958; Crossley, 1979; Le Gall et al., 2008; Fig. 4.7), whereas volcanism has been largely absent (Chapter 2). Intra-rift faults dissecting rift valley-filling lavas provide important information on the upper crustal extensional strain accommodated within the rift center since these final phases of volcanic activity (Fig. 4.8).

Intra-rift faulting in the Natron and Magadi basins: regional extension vs hanging wall flexure

Large-scale fault slip (e.g., >1000 m) along border faults, and subsequent flexure of the down-thrown hanging wall, generates extensional stresses in half-graben basins (Vening Meinesz, 1950; McClay and Ellis, 1987; Lavier et al., 2000; Imber et al., 2003; Cowie et al., 2005) (Fig. 4.9). During early-stage rifting in the Eastern rift, strain was primarily accommodated through slip along border faults (Hayward and Ebinger, 1996), which accumulated displacements on the order of 1000s of meters over the lifetime of rifting. It follows that some intra-rift faults must be activated from flexural stresses in the border fault hanging wall (Ebinger, 2005) (Fig. 4.9). These faults accommodate only localized bending strains, rather than regional extension. Therefore, in order to calculate the amount of regional extension accommodated via intra-rift faulting, extension related to hanging wall flexure must be considered (Table 4.4).

Table 4.4. Summary of strains accommodated by intra-rift and border fault populations in the Magadi-Natron region, based on fault-strain and bending strain analyses. Sources of data are shown in parentheses.

	Basin Age (Ma)	Regional extension rate (mm/yr)	Border fault throw (m)	Flexural strain (% extension) ^a	Flexural extension rate (mm/yr) ^b	Intra-rift extension rate (mm/yr) ^c	Regional extension accommodated via intra-rift faulting (mm/yr) ^d	Border fault extension rates (mm/yr) ^e
Natron	3 (1)	1.8 (3)	2200 (4)	0.8-1.1	0.34-0.45	0.47-0.90	0.02-0.56	1.24-1.78
Magadi	7 (2)	2 (3)	5000 (5)	1.8-2.4	0.13-0.18	1.52-1.73	1.34-1.60	0.40-0.66

^a strains related to flexure of the border fault hanging wall from Figure 9.

^b time-averaged extension rate estimated by dividing total extension related to flexure by the age of the border fault.

^c estimated from rift-normal transects shown in Figure 8.

^d estimated by subtracting the range of flexural extension rates from the range of extension rates for intra-rift faults.

^e estimated by subtracting the range of intra-rift extension rates in d, from the model regional extension rate.

References: (1) Foster et al. (1997); (2) Crossley et al. (1979); (3) Saria et al. (2014); (4) Ebinger et al. (1997); (5) Birt et al. (1997).

Transects X-X' and Y-Y' in Figure 4.8 show the distribution of strain across intra-rift fault populations in the Magadi and Natron basins, as well as the cumulative time-averaged

extension rate. Subtracting extension rates related to hanging wall flexure (Fig. 4.9) from these estimates provides constraints on the amount of regional extension accommodated in the intra-rift fault systems (Table 4.4). Calculations from this study suggest that hanging wall flexure in the Magadi basin has produced 0.13-0.18 mm yr⁻¹ of extension. This hanging wall flexure accounts for only a small fraction (<12%) of extension observed in this fault system (1.52-1.73 mm yr⁻¹). Based on these estimates, it is inferred that intra-rift faults in Magadi accommodate 1.34-1.60 mm yr⁻¹ of regional extension. Hanging wall flexure in the Natron basin, however, can explain a significant portion of observed strain in the intra-rift fault systems (0.34-0.45 mm yr⁻¹), accounting for between 38 and 96% of the 0.47-0.90 mm yr⁻¹ time-averaged extension represented by intra-rift faults (Table 4.4). These results imply that intra-rift faults in the Natron basin accommodate 0.02-0.56 mm yr⁻¹ of regional extension.

Border fault vs intra-rift faulting

Fault system analyses presented in this study do not provide direct constraints on border fault extension rates. However, in early-stage rift basins the extension accommodated by fault systems (border faults and intra-rift faults) should equal the far-field extension rate. Therefore, by assuming that modeled plate motion vectors for the EAR (i.e., Saria et al., 2014) accurately reflect extension rates over the last few million years, and assuming that all upper crustal strain is accommodated along faults observed in the 50 km-wide basins, the maximum border fault extension rates can be estimated by subtracting the plate motion vectors by the calculated time-averaged extension in the intra-rift fault populations (Table 4.4; refer to Section 4.8.3). These results can then be compared with time-averaged extension of border faults from basin depth estimates (refer to Section below).

Subtracting 1.34-1.60 mm yr⁻¹ of regional extension measured across the Magadi intra-rift fault system in this study from the modeled 2.0 mm yr⁻¹ extension rate for the basin, it is estimated here that the Nguruman border fault accommodates 0.40-0.66 mm yr⁻¹ of extension. This is 20 to 33% of the regional extension. Similarly, by subtracting the 0.02-0.56 mm yr⁻¹ of regional extension measured across intra-rift faults of the Natron basin from the modeled 1.8 mm yr⁻¹, the Natron border fault is estimated to accommodate 1.24-1.78 mm yr⁻¹ of extension, which is 69 to 99% of the regional extension. Hence, border fault activity is a far greater contributor to regional extension in the 3 Ma Natron basin than the 7 Ma Magadi basin. This is consistent with field observations of recent activity along subsidiary segments of the Natron border fault (Fig. 4.3A, B).

Border fault slip-rates from subsurface throw

Border fault extension rate estimates presented in Table 4.4 may be further tested by comparing these values with estimated extension rates based on the age, throw, and assumed dip of the rift basin border faults (Table 4.5). Using a range of possible ages for the Natron border fault (1.0-1.2 Ma; Foster et al., 1997) and an assumed fault dip of 50-60°, consistent with focal plane mechanisms in the region and normal faults generally (Foster et al., 1997; Lambert et al., 2014), the 2.2 km of throw accumulated on the Natron border fault corresponds to an extension rate of 1.06-1.85 mm yr⁻¹. This compares well to the 1.24-1.78 mm yr⁻¹ from the fault strain analysis summarized in Tables 4.4 and 4.5. Similarly, a range of reasonable ages for the Nguruman fault (6.9-7.1 Ma; Crossley, 1979) and an assumed fault dip of 50-60° corresponds to an extension rate of 0.41 to 0.61 mm yr⁻¹, which also compares favorably to the 0.4-0.66 mm yr⁻¹ from the fault strain analysis (Tables 4.4 and 4.5). This

simple approach provides comparable results, which lends confidence to the fault-strain analyses in this study (Fig. 4.11; Table 4.4).

Extension rates across the Natron border fault, however, do not match results from age dating and fault throw analyses collected along border fault segments in the field (e.g., Samples 2, 3, and 12 in Table 4.1; Table 4.5). Of note, the border fault segments analyzed in the field in this study are subsidiary structures of the main escarpment (Sherrod et al., 2013). Due to the border fault's size and the substantial basin-fill sediments concealing its vertical dimensions (Ebinger et al., 1997; Sherrod et al., 2013), analyses of extension rates along the primary fault escarpment can only be constrained from subsurface information (Section 4.5.5) or indirect techniques, such as the fault-strain analysis discussed in Section 4.5.4.

Border fault extension rates shown in Table 4.5 correspond to a range of possible slip rates that are consistent with rates along major normal faults on Earth. Slip rates are well constrained for normal faults in extensional terrains such as the Apennines (Italy), Taupo Rift (New Zealand), and Basin and Range (United States). Field studies show that normal fault slip rates are typically on the order of 0.1 to 4 mm yr⁻¹ (Villamor and Berryman, 2001; Hetzel and Hampel, 2005; Kent et al., 2005; Villamor and Berryman, 2006; Hampel et al., 2007; Berryman et al., 2008; Blakeslee and Kattenhorn, 2013; Wilkinson et al., 2015), although they may reach as high as 10s of mm yr⁻¹ during periods of co-volcanic slip associated with caldera-forming, rhyolite volcanism in magmatic rifts (e.g., the Paeroa fault of the Taupo Rift, New Zealand; Rowland et al., 2010; Downs et al., 2014). Compared to normal faults elsewhere, the Natron border fault exhibits a relatively high slip rate, with estimates from this study ranging anywhere from 1.93 to 3.56 mm yr⁻¹. The slip rate of 0.62-1.32 mm yr⁻¹ estimated for the Nguruman fault is typical of normal faults at many extensional settings.

Table 4.5. Comparison of border extension rates and slip rates from analyses of basin depths and ages, time-average extension rates in intra-rift fault systems, and field data collected on subsidiary border fault segments. Border fault ages from Foster et al. (1997) and Crossley (1979).

<u>Natron border fault</u>												
	basin depth (m)	scarp height (m)	throw (m)	heave (m)	min. fault age (Ma)	max. fault age (Ma)	min. extension rate (mm yr ⁻¹)	max. extension rate (mm yr ⁻¹)	min. slip rate (mm yr ⁻¹)	max. slip rate (mm yr ⁻¹)		
<u>60° dip</u>	1600	600	2200	1270	1	1.2	1.06	1.27	2.12	2.54		
							From fault-strain data ^a :		1.24	1.78	2.48	3.56
							From ⁴⁰ Ar/ ³⁹ Ar dates ^b :		0.05	0.08	0.09	0.16
<u>55° dip</u>	1600	600	2200	1541	1	1.2	1.28	1.54	2.24	2.69		
							From fault-strain data ^a :		1.24	1.78	2.16	3.10
							From ⁴⁰ Ar/ ³⁹ Ar dates ^b :		0.06	0.1	0.10	0.17
<u>50° dip</u>	1600	6000	2200	1846	1	1.2	1.54	1.85	2.39	2.87		
							From fault-strain data ^a :		1.24	1.78	1.93	2.77
							From ⁴⁰ Ar/ ³⁹ Ar dates ^b :		0.07	0.12	0.10	0.18

<u>Nguruman border fault</u>												
	basin depth (m)	scarp height (m)	throw (m)	heave (m)	min. fault age (Ma)	max. fault age (Ma)	min. extension rate (mm yr ⁻¹)	max. extension rate (mm yr ⁻¹)	min. slip rate (mm yr ⁻¹)	max. slip rate (mm yr ⁻¹)		
<u>60° dip</u>	3600	1400	5000	2887	6.9	7.1	0.41	0.42	0.81	0.84		
							From fault-strain data ^a :		0.40	0.66	0.80	1.32
							From ⁴⁰ Ar/ ³⁹ Ar dates ^b :		NA	NA	NA	NA
<u>55° dip</u>	3600	1400	5000	3501	6.9	7.1	0.49	0.51	0.86	0.88		
							From fault-strain data ^a :		0.40	0.66	0.70	1.15
							From ⁴⁰ Ar/ ³⁹ Ar dates ^b :		NA	NA	NA	NA
<u>50° dip</u>	3600	1400	5000	4196	6.9	7.1	0.59	0.61	0.92	0.95		
							From fault-strain data ^a :		0.40	0.66	0.62	1.03
							From ⁴⁰ Ar/ ³⁹ Ar dates ^b :		NA	NA	NA	NA

^aborder fault extension rates based on data from Table 4.

^bslip rates on subsidiary border fault segments based on data from Table 1.

By contrast, the highest slip rates on individual intra-rift faults (up to 0.45 mm yr⁻¹) in both the Natron and Magadi basins are lower than the surrounding border faults (cf. Tables 4.1 and 4.5). These low slip rates are, however, consistent with a rift system where extensional strains are spread over a wide area and accommodated on many faults (e.g., >100).

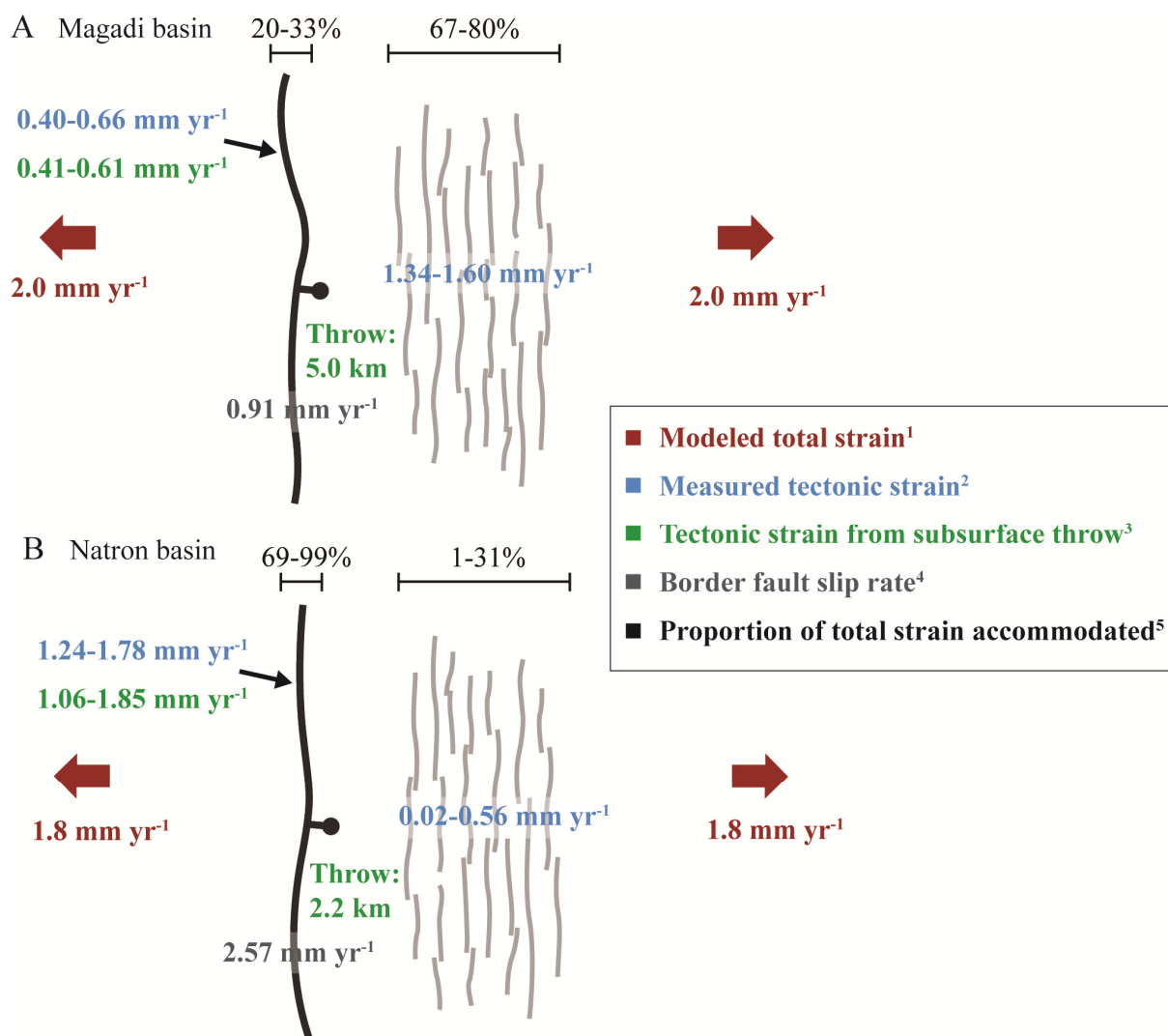


Figure 4.11. Summary of strain data from this study. (A) Distribution of fault strain in the 7 Ma Magadi basin. Black lines and grey lines represent border faults and intra-rift faults, respectively. Based on estimated extension rates, the greatest proportion of regional extension (i.e., modeled total strain) is accommodated in the intra-rift fault system (67-80% of total strain). In all, analyses from this study give a mean border fault slip rate of 0.91 mm yr⁻¹. (B) Distribution of fault strain in the 3 Ma Natron basin. Based on estimated extension rates, the greatest proportion of regional extension (i.e., modeled total strain) is accommodated along the border fault (69-99% of total strain). In all, analyses from this study give a mean border fault slip rate of 2.57 mm yr⁻¹. Numbers in superscript in the key refer to data sources, and include: (1) Saria et al. (2014); (2) Table 4.4 (this study); (3) Ebinger et al. (1997), Birt et al. (1997), Table 4.5 in this study; (4) mean values from Table 4.5 in this study; and (5) Table 4.4 in this study.

Evolution of fault-related strain and structural relief in the Natron-Magadi region

Results presented here provide the first quantitative analysis of the spatial and temporal distribution of fault-related strain over the course of early-stage rift evolution in the Magadi and Natron basins (Fig. 4.11). These data illustrate how fault-related strain is distributed within rift basins after approximately 3 and 7 million years of rifting. Accounting for the various sources of uncertainty, there are clear differences in how strain is distributed between Natron and Magadi. Specifically, in the Natron basin, the majority (>69 %) of regional extension is accommodated along the border fault, whereas in Magadi the greatest strain is primarily accommodated in the rift center in the intra-rift fault population (>67 %). Furthermore, during early-stage rifting in the 3 Ma Natron basin, a significant amount of intra-rift faulting (38-96 %) is driven by hanging wall flexure of the border fault. After 7 million years of rifting, however, flexure of the border fault hanging wall has less influence on the formation of intra-rift faults (refer to Table 4.4). Intra-rift fault populations instead accommodate the majority of regional extension as border faults become less active, as illustrated by the Magadi rift basin.

Evolving fault system dynamics in continental rift basins are accompanied by changes in structural relief that affect water and sediment catchments (Scholz et al., 1990; Gawthorpe and Leeder, 2000; Ebinger and Scholz, 2012). For example, zones of maximum subsidence in half-graben basins in the Malawi and Tanganyika rifts of East Africa occur adjacent to border faults, where more than 4 km of syn-rift sediments have accumulated (Scholz et al., 1990). Similarly, border fault subsidence in the Natron and Magadi region has clearly been a major control on the position of ephemeral lakes (Ebinger and Schultz, 2012). However, the transition to intra-rift faulting in the Magadi basin also appears to have affected the position of

Lake Natron and the development of Lake Magadi (Crane, 1981) (Fig. 4.12). As shown in Figure 4.1C, the lowest relief in the Magadi basin occurs in the rift center, consistent with the focusing of strain into the intra-rift fault system. In the Natron basin, however, the lowest relief is observed adjacent to the border fault escarpment (Fig. 4.1D), where the greatest amount of strain is also accommodated. The occurrence of Pleistocene lake sediments from Lake Natron northward along the base of the Nguruman escarpment indicates that paleo-Lake Natron extended further north into the Magadi basin during the Pleistocene (Crossley, 1979). The transition to intra-rift faulting in the Magadi basin, and subsequent reduction in border activity, may explain the southward retreat of the northern shoreline of Lake Natron, as areas of structural relief evolved in response to changes in fault system dynamics (Fig. 4.12). However, during warmer and wetter climatic periods in the Late Pleistocene, increasing water levels have also occasionally resulted in both Lake Natron and Magadi forming a single, contiguous lake (Roberts et al., 1993). Similar patterns in the distribution of lake systems in the Natron-Magadi region are observed in basins of different ages across south Kenya and north Tanzania (Fig. 4.13). For example, in the 1 Ma Manyara and 3 Ma Natron basins, lakes occur adjacent to border fault escarpments, whereas in more evolved basins (7-15 Ma), Kenya rift lakes are situated along the rift axis. The positions of these lakes likely reflect the locus of upper crustal strain (rift border vs rift axis) within these basins (Ebinger and Scholz, 2012).

4.6.2 Source of spring waters in the Natron and Magadi basins

Diffuse soil CO₂ flux surveys and carbon isotope analyses from the Natron and Magadi basins reveal that rift-wide fault systems in the region act as pathways for the rise of mantle-derived CO₂ (Chapter 3). These CO₂-rich fluids are likely sourced from magma bodies, which have been detected geophysically in the lower crust and/or upper mantle (Birt

et al., 1997; Roecker et al., 2015; Chapter 3). Is the chemical signature of springs in the Natron and Magadi basins also consistent with a magmatic source?

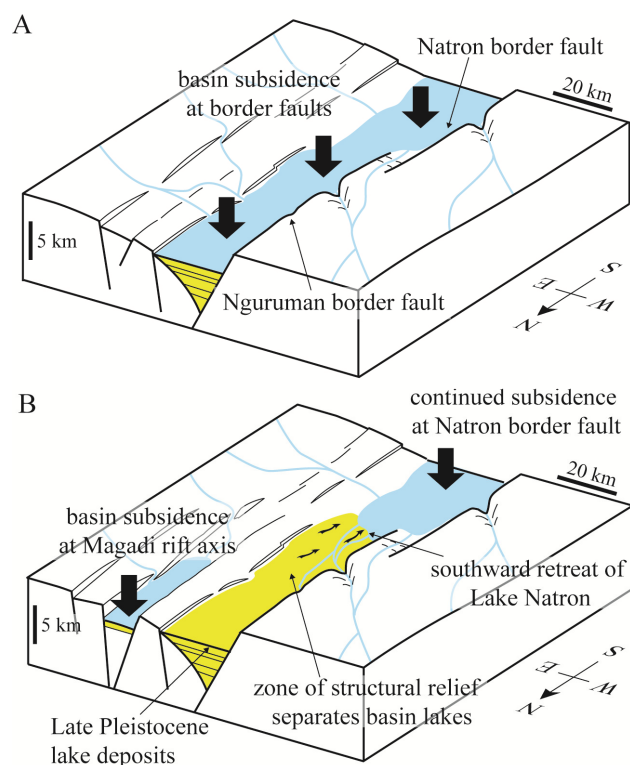


Figure 4.12. Conceptual model of changing structural relief and water/sediment catchments resulting from fault system evolution in the Magadi-Natron region. (A) High activity on the border faults results in the formation of a contiguous lake in response to subsidence along the western side of the basins. (B) Over time, the locus of the strain, and greatest subsidence, in the Magadi basin migrates away from the Nguruman border fault and into the intra-rift fault population. Although the rate of subsidence along the Nguruman escarpment reduces, strain continues to be accommodated along the border fault in Natron, with continued subsidence along the western side of the basin. A zone of structural relief begins to develop at the base of the Nguruman escarpment in response to these evolving fault dynamics. The original border fault lake therefore retreats southward into Natron and a new lake develops in the subsiding center of the Magadi basin.

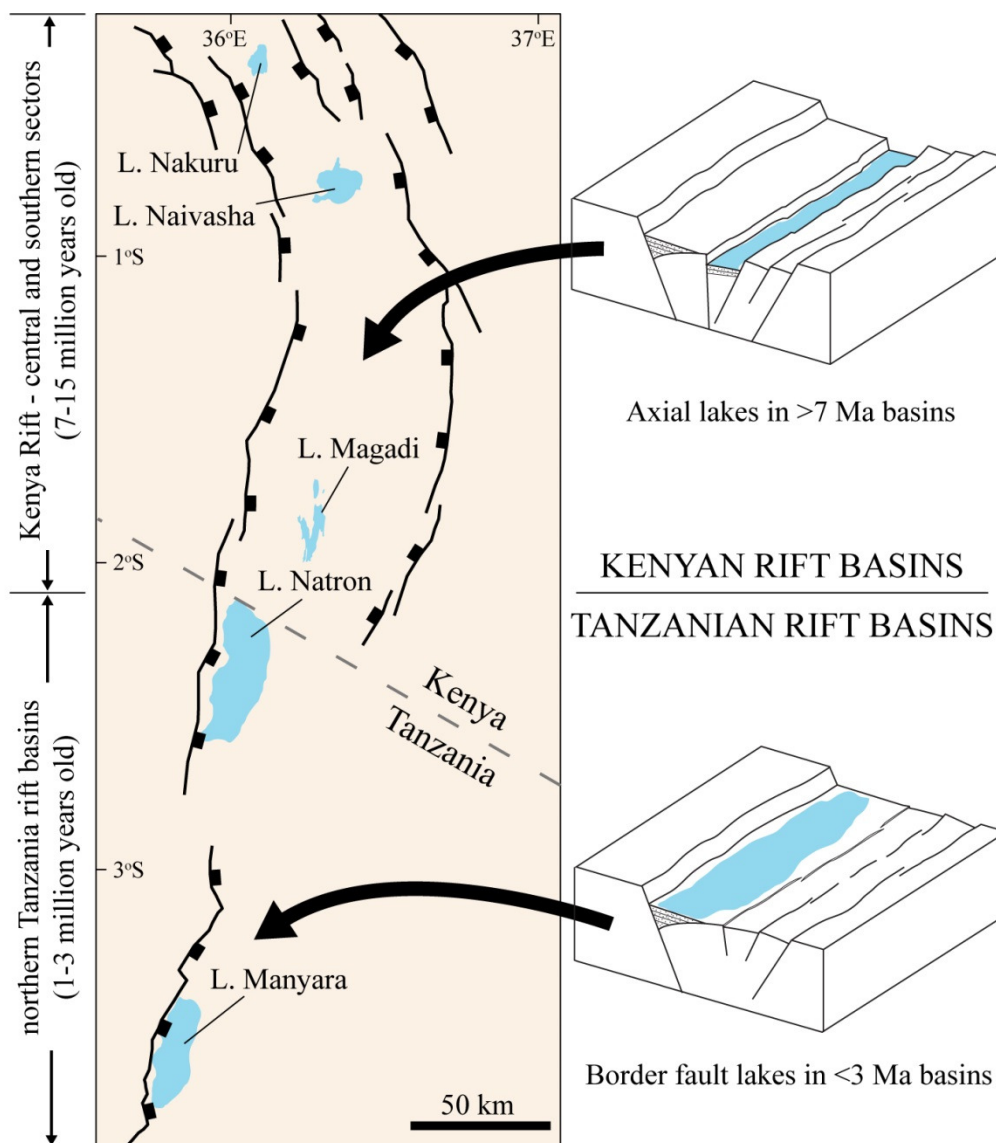


Figure 4.13. Distribution of basin lakes in North Tanzania and the Kenya rift. Major rift-bounding faults are from Smith (1994). Basin lakes in the 1-3 Ma Tanzanian basins (Manyara and Natron) occur adjacent to the border faults. Basin lakes in 7-15 Ma rift basins in the Kenya rift occur along the rift axis.

Spring samples from this study exhibit N_2/Ar ratios (15-67) within the range of, or slightly less than, air-saturated water (Fig. 4.10B). High He contents shown in Figure 4.10B, however, suggest additional inputs from either mantle or crustal sources. Similar N_2 -He-Ar abundances have been observed previously in the EAR for springs in the Rungwe Province

and fumaroles from Oldoinyo Lengai, which were interpreted to be sourced from magma bodies at depth (Fischer et al., 2009; Barry et al., 2013; de Moor et al., 2013a). A magmatic interpretation for the observed N₂-He-Ar abundances is also consistent with $\delta^{13}\text{C-CO}_2$ values in the Natron and Magadi springs (Fig. 4.10C), and isotope investigations of diffusely degassing CO₂ (Chapter 3). In line with this assertion, unpublished helium isotope data from springs in Lake Magadi (reported in McNitt et al., 1989) are consistent with significant contributions (~25-50%) of mantle-derived fluids. These geochemical data, combined with geophysical studies supporting the presence of lower crustal and upper mantle magma bodies in the region (Birt et al., 1997; Roecker et al., 2015), suggest a magmatic, rather than crustal, source for dissolved gas species in Natron and Magadi springs.

4.6.3 Controls on fault system evolution

Fault strain analyses in this study demonstrate that the Magadi and Natron basins are in a transitional stage of continental rift evolution – the locus of strain is actively transitioning from border faults to intra-rift fault populations (e.g., Fig. 4.2A, B). Previous studies in the Main Ethiopian Rift have attributed these transitions to the influence of magmatism, oblique rifting, and crustal inheritance (Chorowicz et al., 1994; Bonini et al., 1997; Kendall et al., 2005; Corti, 2008). Below it is discussed how each of these processes applies to the Natron and Magadi basins, as well as the role of magmatic fluids.

Crustal inheritance

Chorowicz et al. (1994) attributed intra-rift faulting in the Main Ethiopian Rift in the Late Pleistocene to the reactivation of preexisting Pan-African basement structures. This interpretation was challenged in later studies (e.g., Bonini et al., 1997; Corti, 2009) given the

difficulties in explaining why optimally oriented structural fabrics would not be activated immediately during the initial stages of rifting. The influence of crustal inheritance in the Kenya rift is illustrated by orientations of transfer structures between border faults, as well as the broad geometry of central Kenya rift basins, which follow major NW-SE-striking shear zones mapped in Mozambique basement rocks (Smith and Mosley, 1993; Mosley, 1993; Smith, 1994; Katumwehe et al., 2015b; Robertson et al., 2015). These observations support previous assertions that border faulting in the EAR often initiates on preexisting basement fabrics (McConnell, 1972; Daly et al., 1989; Foster et al., 1997; Katumwehe et al., 2015a; Laó-Dávila et al., 2015). However, as basins evolve and favorably oriented faults develop orthogonal to the regional extension direction, the earlier formed, unfavorably oriented and/or located faults are eventually abandoned (Ebinger, 2005). Structural investigations in the Kenya rift show a number of transverse, NW-SE-striking intra-rift faults, which probably initiated on preexisting basement fabrics (Le Turdu et al., 1999; Atmaoui and Hollnack, 2003; Kattenhorn et al., 2013). However, the majority of intra-rift faults in the Natron and Magadi basins, as well as intra-rift faults further north in the Naivasha-Nakuru basin (Chapter 2), trend orthogonal to the ESE-WNW regional extension direction (Fig. 4.7), and oblique to the NW-SE-striking basement structures. These observations suggest that, although some border fault segments and intra-rift faults (e.g., Kordjya fault of the Magadi basin; Le Turdu et al., 1999; Kattenhorn et al., 2013; see Chapter 5) may have initiated along inherited crustal fabrics (e.g., Smith and Mosley, 1993; Foster et al., 1997), the transition to an intra-rift dominated faulting regime in the study area cannot be attributed to the reactivation of basement weaknesses.

Oblique rifting

Strain localization into intra-rift faults in the Main Ethiopian Rift has also been proposed to be the result of oblique extension along the border fault system (rift obliquity up to 45°; Corti, 2008; Agostini et al., 2011b) (discussed in Section 4.2). These assertions are based on the timing and kinematics of faulting observed from analog experiments (Corti, 2008; Agostini et al., 2011b; Corti, 2012), which compare favorably with field and remote-sensing studies in the region (Corti, 2009; Agostini et al., 2011a). Rifting in the Natron and Magadi basins, however, has been inferred to occur primarily under orthogonal extension (Le Gall et al., 2008). Accordingly, intra-rift faults (008° mean trend) and border faults (006° mean trend) trend roughly normal to the 090-110° extension direction inferred from analyses of fault plane solutions, volcanic vent alignments, neotectonic joints, and GPS plate motion vectors (Ibs-von Seht et al., 2001; Atmaoui and Hollnack, 2003; Brazier et al., 2005; Stamps et al., 2008; Saria et al., 2014; Chapter 2). Focal mechanisms for earthquakes in the central parts of the Natron basin (Lambert et al., 2014) show dip-slip motions along NNE-trending normal faults. It is therefore unlikely that the evolution to intra-rift faulting in the study area has been assisted by oblique-style rifting along the border system.

Role of magma

The development of intra-rift fault systems in the Natron and Magadi region has occurred with accompanying magma intrusion (Calais et al., 2008) and magmatic volatile release in the rift basins (Chapter 3). An axial gravity anomaly has been traced along the Kenya rift into the Magadi basin (Baker and Wohlenberg, 1971; Mechie et al., 1997; Ibs-von Seht et al., 2001), and interpreted as lower-crustal intrusions. Ibs-von Seht et al. (2001) attributed high seismic velocities in the center of the Magadi basin to a zone of cooled mid- to

upper-crustal dikes, and Birt et al. (1997) observed a low seismic velocity zone in the upper mantle, which they interpreted as partial melt below the central rift axis. The presence of magma along the rift center is consistent with asthenospheric upwelling and enhanced melt production below the zone of maximum lithospheric extension in the center of the rift (Rooney, 2010) – in other words, where the border fault intersects the lower crust (e.g., Brun et al., 1992; Brun, 1999; Lavier et al., 2000; Ebinger and Casey, 2001; Ebinger, 2005). Furthermore, asthenospheric melts are likely guided (upward) along steep gradients in the lithosphere-asthenosphere boundary produced by thinning and flexing of the lithosphere, resulting in magma migration at depth from the rift margins into the rift center (Rooney et al., 2011, 2014; Keir et al., 2015). Dikes ascending from melt zones at depth can also be guided into the rift center along intra-rift faults (Casey et al., 2006; Le Corvec et al., 2013b), some of which formed from flexure in the border fault hanging wall (Section 4.5.5).

Magma rising into the center of these rift basins is likely to help localize deformation in intra-rift fault populations and drive the transition from border fault to intra-rift fault dominated strain accommodation (Ebinger and Casey, 2001; Keir et al., 2006; Beutel et al., 2010). For example, dikes emplaced at mid- to upper-crustal levels enhance extensional stresses in the area above the dike tip (Rubin and Pollard, 1998). These static stress changes can initiate faulting in the shallow crust, as has been demonstrated during dike-rifting events in Iceland and Ethiopia (Bjornsson et al., 1977; Rowland et al., 2007; Belachew et al., 2013; Wright et al., 2012; Sigmundsson et al., 2015). Similarly, a diking event in south Natron in 2007 was accompanied by slip along several intra-rift faults based on seismicity, focal mechanisms, InSAR displacements and measured surface ruptures (Baer et al., 2008; Calais et al., 2008; Biggs et al., 2009a; Wauthier, 2011). However, this event was confined to a

volcanic field at the southern end of the Natron basin, and may not represent a rift-wide process of upper crustal diking from the center of the Natron basin northward along the length of Magadi (Chapter 2). Despite the presence of underlying magma at the rift center (Birt et al., 1997), there is no evidence (i.e., volcanic cones, lava flows) of significant surface-breaching dike intrusions since the eruption of Magadi trachyte lavas (Chapter 2), suggesting dike arrest at predominantly lower- to mid-crustal depths, with upper crustal strain accommodated almost purely by normal faulting.

Numerical modeling studies show that cooling magma intrusions transfer heat to the surrounding country rock, causing thermally-driven variations in crustal rheology (Daniels et al., 2014). Dike intrusions can therefore locally weaken lithosphere and assist in crustal thinning and strain localization in the basin center (Bialas et al., 2010; Daniels et al., 2014). Extensional stresses are also shown numerically to localize around cooled axial intrusions emplaced within continental crust (Beutel et al. 2010), thereby focusing extensional strain into the rift center even during episodes of low magma flux. In the Magadi basin in particular, geophysical and geochemical observations (e.g., Baker and Wohlenberg, 1971; Birt et al., 1997; Mechie et al., 1997; Ibs-von Seht, 2001; Chapter 3) suggest that the transition to intra-rift faulting shown in this study (Section 4.6.1; Fig. 4.11) has been accompanied by axial magma emplacement in the lower crust and upper mantle. These observations provide support for the potential role of magmatism in assisting the transition to focused intra-rift faulting in the study region.

Role of magmatic fluids

An important factor controlling lithospheric weakening and the localization of rifting of cratonic lithosphere is the presence of CO₂-rich fluids (Geissler et al., 2005; Lindenfeld et al., 2012; Albaric et al., 2014). In continental rift settings exhibiting high fluid flow (e.g., Taupo Volcanic Zone, New Zealand), the magnitude of extensional tectonic stresses required for normal faulting decreases locally in areas exhibiting high pore-fluid pressures (Reyners et al., 2007; Rowland and Simmons, 2012). Similarly, lower crustal earthquakes observed in the EAR may require anomalously high pore-fluid pressures at depth (Seno and Saito, 1994; Lindenfeld et al., 2012), with some of these fluids likely exsolved from lower crustal magma intrusions (Keir et al., 2009a; Chapter 3). The rheology of lithosphere, particularly within fault zones, will vary cyclically depending on the presence or absence of fluids (Yardley et al., 2010). Deeply derived, magmatic fluids (e.g., CO₂, H₂O) are redistributed en masse during earthquake slip events (Sibson, 2000; Brodsky et al., 2003; Shelly et al., 2015). Depending on oxygen fugacity, the presence of these magmatic fluids (i.e., CO₂ and H₂O) may enhance intracrystalline deformation in quartz and other crystalline minerals (Chen et al., 2006; Chernak et al., 2009; Holyoke and Kronenberg, 2013). During periods of seismic quiescence, fluids present in fault zones are gradually consumed during hydration reactions to produce weaker, fine-grained, hydrous minerals (Moore and Rymer, 2007; Yardley et al., 2010).

Geochemical data from spring systems throughout the Natron and Magadi basins (Fig. 4.10) support the release of volatiles into the rift from magma bodies at depth. The high output of magmatic gases (>1 Mt yr⁻¹ of magmatic CO₂; Chapter 3) along rift-wide fault networks in the Magadi-Natron region suggests a significant supply of deeply circulating fluids, which may be able to weaken faults and assist in strain localization. In line with these

assertions, the locations of hot springs in the Magadi-Natron region coincide with areas of high strain (Figs. 4.8 and 4.10; Table 4.2). For example, time-averaged extension rates in the Magadi basin are highest within faults dissecting the Magadi Trachyte lava group (0.93 ± 0.28 mm yr⁻¹) in the center of the rift. Within this area of high strain (unit 3 in Table 4.2), hot springs manifest at the base of intra-rift fault scarps (Fig. 4.3E), whereas no springs were observed along the Nguruman border fault escarpment. In the Natron basin, however, hydrothermal systems are present along the western border fault of the rift and ~20 km outward into the border fault hanging wall. In contrast to Magadi, the border fault accommodates significantly more regional extension (1.24 - 1.78 mm yr⁻¹) than intra-rift faults (0.02 - 0.56 mm yr⁻¹). Therefore, fluids in the Natron basin likely ascend from crustal magma bodies along the border fault, and then possibly outward into nearby faults forming in the flexing border fault hanging wall (Fig. 4.14). The close associations between areas of high strain and volatile release suggest that magmatic volatiles may also play an active role in weakening lithosphere and assisting the transition to focused intra-rift faulting in the study region.

4.6.4 Conceptual model: evolving fault-fluid systems in the Natron and Magadi basins

Comparison of the 3 Ma Natron and 7 Ma Magadi basins provides a revised conceptual model for evolving fault and magmatic volatile systems during early-stage rifting. Results from the Natron basin show that, within the first 3 million years of rifting, border faults accommodate the majority of strain (>69 %) related to regional extension. In Natron specifically, the depth of syn-rift basin fill suggests the border fault system accrued ~2200 m of throw during this period, which caused significant flexure of the hanging wall in the ~50-km-wide half-graben basin. Horizontal extensional strain related to this flexure drove the

formation of intra-rift faults, which acted to both accommodate regional extension as well as localized stresses in the flexing hanging wall. Evidence for diking in south Natron (Calais et al., 2008; Biggs et al., 2013; Chapter 2), lower crustal seismicity (Roecker et al., 2015; Chapter 3), and rift-wide release of magmatic volatiles at the surface (Chapter 3; Fig. 4.10) support the development of intra-rift fault systems coevally with the emplacement of crustal magmas. Fluids released from magmas interact with these fault systems (Chapter 3) (Figs. 4.10 and 4.14), and may explain the presence of lower- to mid-crustal earthquake swarms documented in these basins (Seno and Saito, 1994; Chapter 3). The focusing of magma toward the rift center and concomitant release of magmatic fluids into the flexing hanging wall provides a previously unrecognized mechanism that may help to weaken crust and assist the transition to intra-rift dominated strain accommodation.

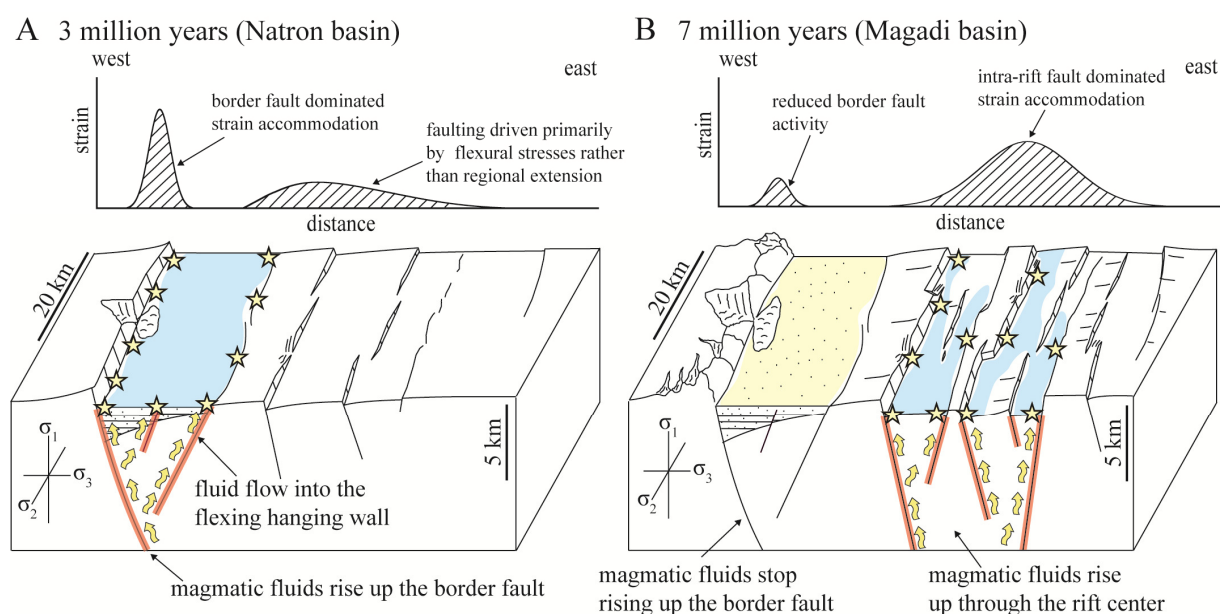


Figure 4.14. Conceptual model of evolving fault-related strain and magmatic fluid systems during early-stage rifting (<7 Ma) in the Natron and Magadi basins. (A) Rift configuration 3 million years after rift initiation in the Natron basin. Strain is primarily accommodated along the border fault. Minor faulting occurs on intra-rift faults in the rift center from stresses generated by flexure of the border fault hanging wall. These intra-rift faults accommodate only a small proportion of regional extension. Magmatic fluids ascend the crust (yellow arrows) along the border fault system and then outward into nearby intra-rift faults in the flexing hanging wall (red lines).

These fluids are observed at the surface as hot springs (yellow stars) that feed water into an ephemeral lake (light blue). (B) Rift configuration 7 million years after rift initiation in the Magadi basin. At this stage of rifting, the locus of strain has migrated from the border fault to the intra-rift fault population. The border fault escarpment becomes progressively more degraded. Magmatic fluids ascend the crust in areas of high strain in the center of the rift, and no longer rise up along the relatively inactive border fault. Paleo-lake deposits on the rift border (light yellow) on the western side of the basin reflect the earlier locus of strain and hydrothermal fluid release. Based on previous studies in the study area, magma bodies sourcing the fluids are likely situated at upper mantle and/or lower crustal depths (Birt et al., 1997; Mechie et al., 1997; Chapter 3).

Findings from the Magadi basin show that, by 7 million years, regional extension was primarily accommodated in the intra-rift fault population. By this stage of rifting, the border fault became relatively less active (accommodating $0.40\text{-}0.66\text{ mm yr}^{-1}$ of extension, compared to $1.24\text{-}1.78\text{ mm yr}^{-1}$ in Natron), and hanging wall flexure played only a minor role in driving intra-rift faulting. The transition to intra-rift faulting was accompanied by widespread magma emplacement below the rift axis (Baker and Wohlenberg, 1971; Birt et al., 1997; Ibs-von Seht, 2001; Chapter 3). Furthermore, the migration of strain away from the border fault into the rift center is followed by a similar migration in the locations of magmatic volatile release. These observations highlight a strong association between strain localization and the release of magmatic fluids in the rift. Magmatic volatiles may therefore help to weaken lithosphere and localize strain in the rift center prior to the establishment of magmatic segments, like those present in the Main Ethiopian Rift further north.

4.7 Conclusions

This study is the first to investigate the evolving distribution of upper crustal deformation in the 3 Ma Natron and 7 Ma Magadi basins from quantitative fault-strain analyses. These data are examined alongside spring geochemistry and new $^{40}\text{Ar}/^{39}\text{Ar}$ ages of rift volcanics to elucidate the timing of volcanic and tectonic activity. New $^{40}\text{Ar}/^{39}\text{Ar}$ ages provide revised constraints on the timing of activity in the Natron basin from Mosonik (as old

as 4.05 Ma), Gelai (0.95-1.23 Ma), and Oldonyo Sambu volcanoes (as young as 1.97 Ma). Results also suggest that the Singaraini basalts in the Magadi basin were emplaced by 1.96 Ma. Intra-rift faults measured and dated in the field in the Natron basin exhibit minimum slip rates that range 0.06-0.09 mm yr⁻¹, whereas analyzed (subsidiary) border fault segments range 0.09-0.16 mm yr⁻¹. Time-averaged minimum slip rates from intra-rift faults measured in the field in Magadi range 0.01-0.13 mm yr⁻¹, but likely reach as high as 0.45 mm yr⁻¹ on the largest faults. Basin-wide strain analyses give estimated slip rates of 1.93-3.56 mm yr⁻¹ for the Natron border fault and 0.62-1.32 mm yr⁻¹ for the Nguruman border fault, which are in good agreement with estimates based on rift basin depths and border fault ages.

Results from the Natron basin in this study show that, within the first 3 million years of rifting, border faults accommodate the majority of strain (>69 %) related to regional extension. Flexure of the border fault hanging wall may have been an important driver of the initial formation of intra-rift faults, which ultimately accommodated both regional extension as well as localized stresses in the flexing plate. Within the 7 Ma Magadi basin, regional extension is primarily accommodated in the intra-rift fault population (67-80%), revealing a transition from border fault to intra-rift fault dominated strain accommodation sometime between 3 and 7 million years after rift initiation. The transition to intra-rift faulting in the Magadi basin also affected the position of Lake Natron and the development of Lake Magadi, where a reduction in activity along the Nguruman border fault resulted in the southward retreat of the northern shoreline of Lake Natron.

The localization of strain into intra-rift faults in the Magadi basin did not require the reactivation of preexisting structures (Chorowicz, et al., 1994) or oblique-style rifting (Corti, 2008), as has been asserted previously for the Main Ethiopian Rift. Instead, the transition to

intra-rift faulting in Magadi has been accompanied by recent magmatism and magmatic volatile release in the rift center. Areas of high strain in each basin also coincide with the presence of hydrothermal spring systems, and geochemical analyses of dissolved gas species support a magmatic source for these fluids. These observations highlight a strong association between strain localization and the introduction of magmatic fluids into the rift. The ascent of magmatic volatiles within rift basins may therefore help to weaken lithosphere and localize strain in the rift center prior to the establishment of magmatic segments, like those present in the Main Ethiopian Rift further north.

4.8 Supporting information

4.8.1 Supplemental Map

Figure C1 of Appendix C provides a supplemental geological map of the Magadi-Natron region. The map shows the broad distribution of major geological units from Baker (1958), Baker (1963), Crossley (1979), Sherrod (2013), and Guth and Wood (2014), with ages and brief descriptions provided in the key. This map provides the basis for defining volcanic units in Table 4.2, which were used for broad strain analyses. Some revised unit ages are provided based on data from this study, and some units of overlapping age have been merged. For more precise units boundaries, please refer to the referenced work, particularly Sherrod (2013), and Guth and Wood (2014).

4.8.2 Modelling extensional strain from hanging wall flexure

The theoretical plate deflection and extensional strains from large-scale border fault displacements were modelled using the method of Turcotte and Schubert (1982), described in Billings and Kattenhorn (2005), where a vertical line-load is applied to the hanging wall side

of the plate at the origin, which occurs at intersection of the fault plane and upper contact of the hanging wall (i.e., where $x = 0$ in Figure 4.9). The fault is assumed to behave as a weak zone that doesn't locally transmit torque to the plate either side of the fault. The deflection profile across the border fault hanging wall from Billings and Kattenhorn (2005) is:

$$\omega = \omega_0 e^{-x/\alpha} \cos (x/\alpha) \quad (\text{eq. 4.5})$$

where ω_0 is the maximum deflection, x defines the position away from the fault along the deflecting plate, and α is defined by:

$$\alpha = [Eh^3/(3\rho_0g (1 - \nu^2))]^{1/4} \quad (\text{eq. 4.6})$$

where E is Young's modulus, ν is Poisson's ratio (0.25), g is acceleration due to gravity, h is the thickness of the plate, and ρ_0 is the density of the underlying layer (quartzo-feldspathic lower crust is $\sim 2,950 \text{ kg m}^{-3}$).

Total border fault throw for each basin is assumed to equal the sum of the observable border fault throw at the surface and the depth of the rift-basin fill estimated from previous studies (Birt et al., 1997; Ebinger et al., 1997). Throw values can be converted to a maximum deflection in the hanging wall by estimating the ratio (r) of upthrow to downthrow on the fault from the equation (Turcotte and Schubert, 1982):

$$r = (\rho_a/\rho_b)^{3/4} \quad (\text{eq. 4.7})$$

where ρ_a is density difference between upper ($2,650 \text{ kg m}^{-3}$) and lower crust ($2,950 \text{ kg m}^{-3}$), and ρ_b is density difference between upper crust and air. From eq. 4.7, an r value of 0.2 is obtained, which is consistent with r values of normal faults observed on earth (e.g., Borah

Peak fault; Stein and Barrientos, 1985) and from modelling studies, which typically range from 0.2 to 0.5 (Rubin and Pollard, 1988; Ebinger et al., 1991; Grant and Kattenhorn, 2004).

The range of the thicknesses for the deflecting plate in the presented models comes from Ebinger et al. (1997), who estimated the elastic thickness of the crust in 1-3 Ma basins in Tanzania sectors of the Easter rift from gravity data. Deflections for plates of different thicknesses (19, 23, and 25 km) were then modeled by adjusting parameters in eq. 4.5 such that the plate deflection produces a 50-km-wide half-graben basin (i.e., $\omega = 0$ at $x = 50,000$) characteristic of the Eastern rift (Foster et al., 1997; Ebinger, 2005). Plate deflections exhibit low sensitivity to changes in ρ_0 and ν compared to changes in h and E , so a range of Young's modulus values were used ($E = 5, 7, 13$ GPa for h values of 25, 23 and 19 km, respectively) to produce each deflection profile. Using this approach, identical flexural profiles were produced for half-grabens with plate thicknesses of 19, 23, and 25 km. From these flexural profiles, the horizontal extensional strain is calculated using the following equation from Billings and Kattenhorn (2005):

$$\varepsilon = -y (d^2\omega/dx^2) \quad (\text{eq. 4.8})$$

where y is the vertical distance from the center of the plate (downward is positive).

4.8.3 Modelled extension rates of the Magadi and Natron basins

To derive the long-term surface motions shown in Figures 4.1 and 4.15, the angular velocity vector is calculated for the Somalian plate (S) relative to the Victoria Block (V) using the recent kinematic block model of Saria et al. (2014) in a Cartesian geocentric coordinate system in an Earth Centered, Earth-Fixed frame (ECEF; deg/Ma):

$${}_{v}\bar{\Omega}_s = \begin{bmatrix} -0.089108 \\ -0.059761 \\ 0.019995 \end{bmatrix}$$

Assuming tectonic motions are well described by rigid plate motions on a sphere (i.e. McKenzie and Parker, 1967), a 3-component velocity vector can be calculated at each position (\bar{P}) using the following:

$$\bar{v} = R \frac{\pi}{180} 10^{-6} ({}_s\bar{\Omega}_v \times \bar{P}) \quad (\text{eq. 4.9})$$

where R is the Earth's radius. From this equation, long-term extension through the center of the Magadi (-1.67°S, 36.302°E) and Natron basins (-2.38°S, 36.171°E) is estimated to be 2.0 mm yr⁻¹ and 1.8 mm yr⁻¹, respectively.

4.9 Supporting methods

4.9.1 Natron and Magadi springs: sampling and analytical methods

Spring samples were collected in the field in pre-evacuated Giggenbach bottles. A tube was inserted deep into the outflow area in the spring. Gas-rich water was then siphoned through silicon tubing into the bottle. For each sample, ~50% of the volume of the Giggenbach bottle was filled with spring water, thereby leaving a headspace into which dissolved inert gases could be partitioned. Gases in these headspaces were analyzed at the Volatiles Laboratory, University of New Mexico (UNM) using a Gow-Mac series G-M 816 Gas Chromatograph (GC) and a Pfeiffer Quadrupole Mass Spectrometer (QMS), which has a mass range from 0 to 120 amu. Gas compositions were measured simultaneously by the combined system of GC and QMS. Relative abundances of CO₂, CH₄, H₂, Ar+O₂, N₂, and CO

in the headspaces were measured on the GC using a He carrier gas. Gas species were separated on the GC using a Hayes Sep pre-column and 5Å molecular sieve columns. A discharge ionization detector was used for CO₂, CH₄, H₂, Ar+O₂, N₂ and CO, respectively (Giggenbach and Goguel 1989). He, Ar, O₂, and N₂ in the headspaces were also analyzed for their relative abundances on the QMS with a secondary electron multiplier detector in dynamic mode. Combining the data from GC and QMS, the relative abundances of CO₂, CH₄, H₂, Ar, O₂, N₂, and CO were acquired. $\delta^{13}\text{C}$ values of CO₂ in the headspaces were measured

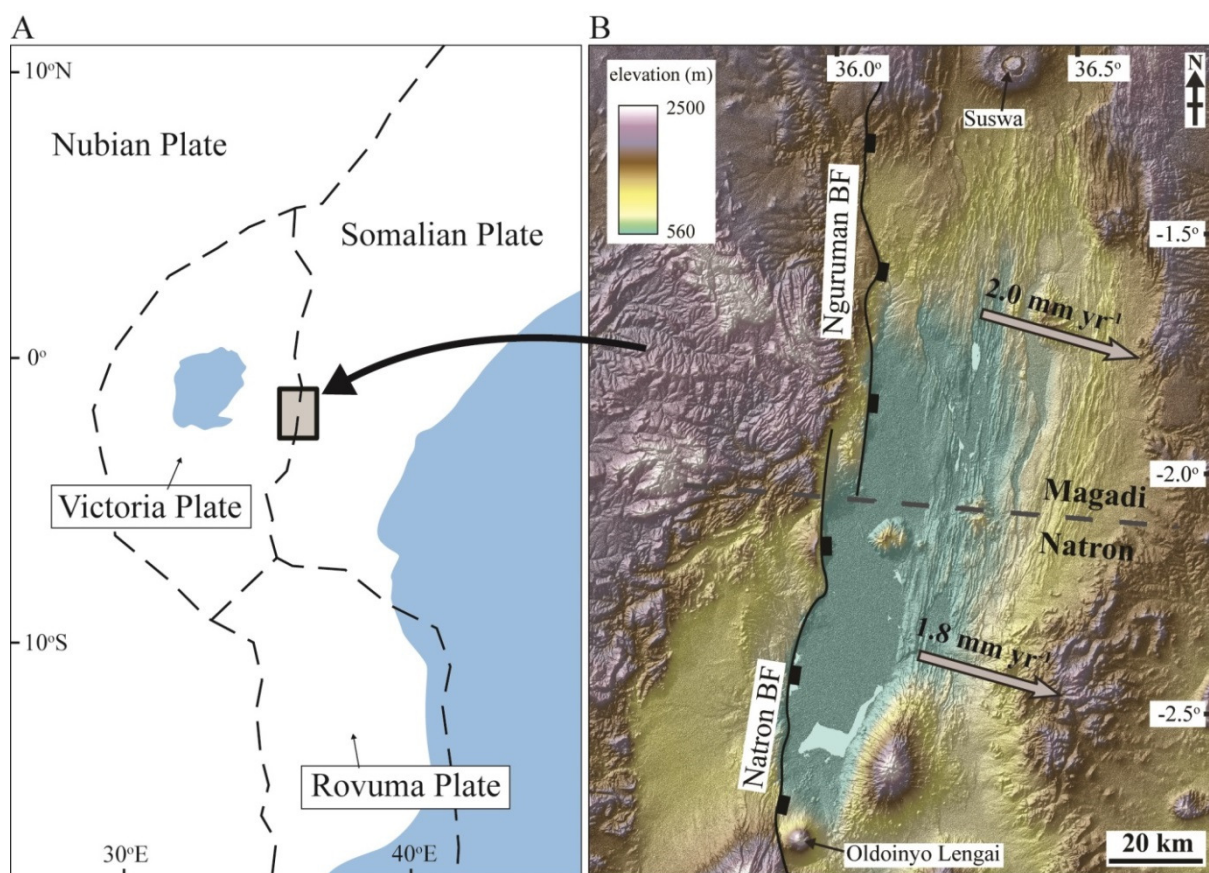


Figure 4.15. A: Distribution of plates and plate boundaries (dashed lines) throughout East Africa including the Nubian and Somalian plates, and the Victoria and Rovuma sub-plates of Saria et al. (2014). B: Velocity vectors (long-term extension rates) for the Natron and Magadi basins based on the movement of the Somalian plate relative to the adjacent Victoria plate from the kinematic model of Saria et al. (2014). BF = border fault.

by an Isotope Ratio Mass Spectrometer (Finnigan Delta XL) with a gas bench at the Center for Stable Isotopes, UNM. The $\delta^{13}\text{C-CO}_2$ values are presented as per mil (‰) against the standard, Pee Dee belemnite (PDB). Using the Oztech isotope ratio reference gas, the standard error of the analyses is $\pm 0.2\text{‰}$ (1σ).

4.9.2 $^{40}\text{Ar}/^{39}\text{Ar}$ dating of Magadi and Natron volcanics

Twelve samples (9 lavas and 3 tuffs) from the Natron basin and 7 samples from Magadi basins (7 lavas) were analyzed using $^{40}\text{Ar}/^{39}\text{Ar}$ laser incremental-heating techniques in the Earth and Planetary Sciences Noble Gas Laboratory at Rutgers University on a MAP-215-50 mass spectrometer (Table C1 in Appendix C). Samples were crushed and then sieved using 30 and 50 mesh size ranges, washed in an ultrasonic bath in distilled water, and dried in an oven at $\sim 80^\circ\text{C}$. Phenocrysts were then hand-picked from the samples under a binocular microscope. In instances where it was not possible to remove all phenocrysts, samples were labeled as “whole rock”, while “matrix” indicates samples in which all phenocrysts were removed from the groundmass (refer to Table C1). Sample 3 was particularly enriched in plagioclase phenocrysts that were dated after separating it using a Frantz Isodynamic Separator. Mica was manually separated from the volcanic tuffs.

Samples were loaded into Al irradiation disks along with multiple splits of a monitor mineral (Fish Canyon Sanidine; 28.201 ± 0.046 Ma; Kuiper et al. 2008) and neutron irradiated at 1000 kW for 0.25 hours using Cd-foil shielding in the central thimble facility of the USGS TRIGA reactor in Denver, Colorado. Corrections for interfering neutron reactions from Ca and K were performed using the following correction constants: $(^{36}\text{Ar}/^{37}\text{Ar})_{\text{Ca}} = (2.64 \pm 0.02) \times 10^{-4}$; $(^{39}\text{Ar}/^{37}\text{Ar})_{\text{Ca}} = (6.73 \pm 0.04) \times 10^{-4}$; $(^{38}\text{Ar}/^{39}\text{Ar})_{\text{K}} = (1.34 \pm 0.02) \times 10^{-2}$ from Dalrymple

and Ryder (1993) and Dalrymple et al. (1981); and $(^{40}\text{Ar}/^{39}\text{Ar})_{\text{K}} = (2.85 \pm 0.5) \times 10^{-4}$, which is determined from measurements of kalsilite glass. Age calculations were made using the current accepted decay constants and isotopic abundances of Steiger and Jäger (1977): $\lambda_{\text{e}} = 5.81 \times 10^{-11} \text{ yr}^{-1}$, $\lambda_{\beta} = 4.962 \times 10^{-10} \text{ yr}^{-1}$, $^{40}\text{K}/\text{K}_{\text{total}} = 1.167 \times 10^{-4}$.

After neutron irradiation, samples were then placed into individual pits in a stainless steel planchet and loaded into an ultra-high vacuum extraction system. The extraction system was then baked overnight at a temperature of 60-80° C.

The $^{40}\text{Ar}/^{39}\text{Ar}$ incremental-heating results include integrated/total-fusion ages (which are similar to conventional K-Ar ages), plateau ages if the necessary criteria are fulfilled (see below), and inverse-isochron ages (Table C1). The plateau ages are defined by at least three contiguous incremental steps representing at least 50% of the total $^{39}\text{Ar}_{\text{K}}$ released from the sample, and with any two adjacent fractions that must be analytically indistinguishable at the 95% confidence level following Fleck et al. (1977). Once all the necessary corrections (e.g., blanks, decay, mass spectrometer mass fractionation) are made, the apparent ages, assuming an atmospheric $^{40}\text{Ar}/^{36}\text{Ar}$ ratio of 298.61 ± 0.09 (average of published results from Lee et al. (2006) and Valkiers et al. (2010)) for the trapped component, are cast on a standard plateau diagram.

Isotopic data are then plotted on an $^{36}\text{Ar}/^{40}\text{Ar}$ versus $^{39}\text{Ar}/^{40}\text{Ar}$ isotope correlation diagram to determine the “measured” $^{40}\text{Ar}/^{36}\text{Ar}$ ratio of the trapped component and age by a linear fit to the data array (see McDougall and Harrison, 1999). The “measured” $^{40}\text{Ar}/^{36}\text{Ar}$ ratio of the trapped component is then used to recalculate the apparent ages, which are then

re-plotted on a standard plateau diagram. These results are listed under the heading as “Corrected for “Trapped” $^{40}\text{Ar}/^{36}\text{Ar}$ ” in Table C1 in Appendix C.

Four of the twenty (20%) measurements have statistically non-atmospheric “trapped” $^{40}\text{Ar}/^{36}\text{Ar}$ ratios and are enriched in ^{36}Ar (see results reported in Table C1). It is believed that the recalculated plateau ages, that take into account the isochron determined $^{40}\text{Ar}/^{36}\text{Ar}$ ratio for the “trapped” component, produce the most accurate age for the simple reason that this interpretation makes fewer assumptions. Ages that are considered the most reliable are reported in bold and highlighted in yellow. For samples that were measured in duplicate, the variance weighted average is the preferred age.

CHAPTER 5: ACTIVATION OF PREEXISTING TRANSVERSE STRUCTURES DURING CONTINENTAL RIFT EVOLUTION

5.1 Abstract

Inherited crustal weaknesses have long been recognized as important factors in strain localization and basin development in the East African Rift (EAR). However, the timing and kinematics (e.g., sense of slip) of transverse (rift-oblique) faults that exploit these weaknesses are debated, and thus the roles of inherited weaknesses at different stages of rift basin evolution are often overlooked. The mechanics of transverse faulting were addressed through an analysis of the Kordjya fault of the Magadi basin (Kenya Rift). Fault kinematics were investigated from field and remote-sensing data collected on fault and joint systems. Results indicate that the transverse Kordjya fault has reactivated earlier developed rift-parallel faults as oblique-normal faults with a component of sinistral shear. In all, these fault motions accommodate dip-slip on an underlying transverse structure that exploits the Aswa basement shear zone. This study shows that transverse faults may be activated through a complex interplay among magma-assisted strain localization, preexisting structures, and local stress rotations. Rather than forming during rift initiation, transverse structures can develop after the establishment of rift-parallel fault systems, and may exhibit dip-slip kinematics when activated from local stress rotations. The Kordjya fault is shown here to form a kinematic linkage that transfers strain to a newly developing center of concentrated magmatism and normal faulting. It is concluded that recently activated transverse faults not only reveal the effects of inherited basement weaknesses on fault development, but also provide important clues regarding developing magmatic and tectonic systems as continental rift basins evolve.

5.2 Introduction

Inherited crustal weaknesses—such as steeply dipping foliation planes, fracture sets and shear zones—are known to play important roles in localizing strain and influencing the architecture of continental rifts (Dixon et al., 1987; Rosendahl, 1987; Daly et al., 1989; Dunbar and Sawyer, 1989; Hetzel, 1994; Bonini et al., 1997). At some rift settings, like the East African Rift, far-field tectonic forces are theoretically too small to rupture the thick continental lithosphere (Buck, 2004, 2006; Stamps et al., 2014). Such rifts are thought to initiate in zones of intense magmatism (Kendall et al., 2005; Beutel et al., 2010; Bialas et al., 2010; Daniels et al., 2014), fluid-driven weakening (i.e., mantle metasomatism; Hui et al., 2015; Leseane et al., 2015; Mana et al., 2015), and along preexisting lithospheric weaknesses (Keranen et al., 2009; Katumwehe et al., 2015a). Early-stage rift basins (< 10 Ma) provide ideal natural laboratories for investigating the effects of these processes on rift initiation and development (Modisi et al., 2000; Calais et al., 2008; Kinabo et al., 2008; Le Gall et al., 2008; Laó-Dávila et al., 2015; see also Chapters 2, 3, and 4).

The earliest states of rifting involve a competition between the formation of new, optimally oriented faults in strong, intact rock, and non-optimally oriented faults that follow and exploit preexisting crustal weaknesses (Youash, 1969; Sibson, 1985; Smith and Mosley, 1993; Morley, 1995; Morley et al., 2004; Agostini et al., 2009; Corti, 2012). Newly developed faults that define the dominant structural fabric of the rift system are expected to trend orthogonal to the regional least compressive stress (σ_3) (Anderson, 1951) and have been previously termed *orthogonal faults* (e.g., Morley et al., 2004). Here, they are referred to as *rift-parallel faults* to avoid mechanical inferences based purely on fault orientation. Faults trending oblique to the dominant rift trend (oblique to the regional σ_3) often initiate along

preexisting weaknesses that cut across the dominant fault fabric (Morley et al., 2004), and are referred to here as *transverse faults* (e.g., Ben-Avraham and Ten Brink, 1989) (Fig. 5.1C).

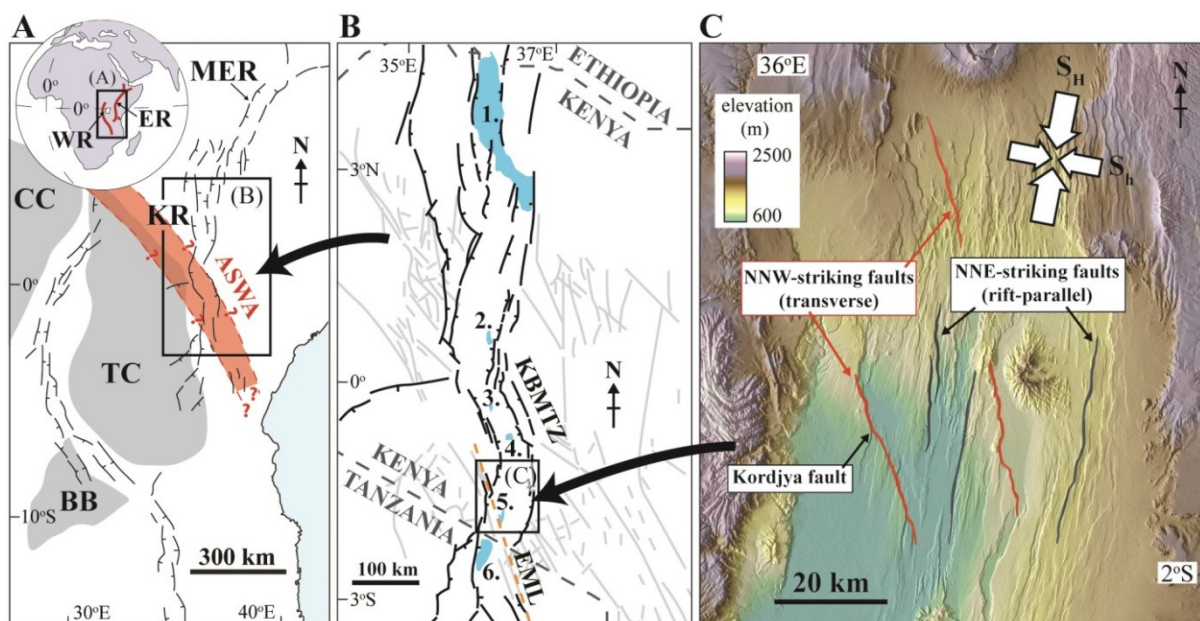


Figure 5.1. A: Distribution of major rift faults (black lines) across East Africa. Grey polygons represent Archean cratons; white fill represents Proterozoic basement rocks (after Corti, 2009 and Morley, 2010). Ocean is colored light blue. Annotated are the Congo Craton (CC), Tanzanian Craton (TC), and Bangweulu Block (BB), as well as the Main Ethiopian Rift (MER) and Kenya Rift (KR). The general location and trend of the Aswa shear zone (ASWA) is illustrated in red, with its distribution based on Smith (1994) and Katumwehe et al. (2015b). Inset (globe) shows the location of the map in A. Annotated on the globe are the Eastern rift (ER) and Western rift (WR) of the East African Rift, shown as red lines. B: Distribution of major rift faults (black lines) and preexisting basement structures (grey lines) in the Kenya Rift (after Smith and Mosley, 1993). Also annotated are the Kerio-Bogoria-Marmanet transfer zone (KBMTZ) and major basin lakes, including (1) Turkana, (2) Baringo, (3) Nakuru, (4) Naivasha, (5) Magadi, and (6) Natron. The Engorika-Magadi-Lembolos (EML) lineament, along which the Kordjya fault lies, is shown as a dashed orange line. C: Annotated Shuttle Radar Topography Mission (SRTM) map of the Magadi basin. Selected examples of transverse (red) and rift-parallel (black) faults are annotated. The orientations of the greatest (S_H) and least (S_h) horizontal compressive stress, based on data from Ibs-von Seht et al. (2001) and Atmaoui and Hollnack (2001), are illustrated by white arrows. Transverse faults trend oblique, whereas rift-parallel faults trend normal, to the regional least compressive stress prevalent throughout the basin. Note how transverse faults in C trend roughly parallel to the dominant NNW-SSE strike of the preexisting basement structures in B.

In the East African Rift (EAR), the effects of preexisting weaknesses on the distribution and nature of faulting are visible on many scales (Morley, 1995) (Fig. 5.1). At the continental scale, rift basins preferentially form within Proterozoic basement rocks and are

located near the margins of Archean cratons (e.g., Tanzanian craton) (Daly et al., 1989; Smith and Mosley, 1993; Ring, 1994; Simiyu and Keller, 2001; Morley, 2010) (Fig. 5.1A). This effect has divided the entire rift system into distinct Eastern and Western rifts (Rosendahl, 1987; Chorowicz, 1992; Koptev et al., 2015). Ductile and brittle shear zones in basement rocks also exhibit a control on rift basin segmentation and orientation. For example, a series of N to NW-trending basement shear zones, with lengths of up to 1000s of km (e.g., Aswa shear zone; Chorowicz, 1989; Katumwehe et al., 2015b), have been documented throughout east and northeast Africa from field, remote-sensing, and geophysical studies (Smith and Mosley, 1993; Hetzel and Strecker, 1994; Birt et al., 1997; Vauchez et al., 2005; Katumwehe et al., 2015b; Roberston et al., 2015) (Fig. 5.1). These shear zones are responsible for abrupt changes in the orientation of the rift, such as the 130-km-long, NNW-trending Kerio-Bogoria-Marmanet transfer zone (Smith and Mosley, 1993), which accommodates an overall left step in the central Kenya Rift between Lake Baringo and Lake Naivasha (Chorowicz, 1989; Hetzel and Strecker, 1994; Le Turdu et al., 1999) (Fig. 5.1B). Preexisting basement shear zones also control the location of transfer zones between major rift-bounding faults (Chorowicz, 1989, 1992; Smith and Mosley, 1993; Ring, 1994). At still smaller scales, inherited weaknesses control the orientations and kinematics of shorter faults (lengths no greater than a few tens of kilometers) within the centers of rift basins (Le Turdu et al., 1999; Le Gall et al., 2000; Manighetti et al., 2001) (Fig. 5.1C).

Many questions exist regarding the state of stress (orientation of σ_3) and kinematics (e.g., sense of slip) of faulting during the reactivation of preexisting structures in the EAR. During rift initiation, some fault systems may initiate on lithospheric weaknesses, often trending oblique to the regional extension direction and dominant NNE-SSW trend of the rift

(Rosendahl, 1987; Versfelt and Rosendahl, 1989; Chorowicz, 1992; Chorowicz and Sorlien, 1992; Kilembe and Rosendahl, 1992; Modisi et al., 2000; Corti, 2008). Transverse faults exploiting these obliquely-oriented weaknesses are therefore expected to fail as either oblique-normal or strike-slip faults (Rosendahl, 1987; Kilembe and Rosendahl, 1992; Le Turdu et al., 1999; Corti, 2008; Agostini et al., 2009).

Although field kinematic indicators often support this view (Chorowicz, 1989, 1992; Chorowicz and Sorlien, 1992; Ring et al., 1992; Wheeler and Karson, 1994), regional syntheses of recent focal mechanisms show that many transverse structures exhibit dip-slip (normal) kinematics (e.g., Koehn et al., 2010; Delvaux and Barth, 2010). Dip-slip faulting along transverse structures requires a rotation of σ_3 away from the *first-order* (regional) extension direction (~E-W to ESE-WNW) imposed by plate boundary forces across the EAR (Lithgow-Bertelloni and Guynn, 2004; Stamps et al., 2008). These rotations can be produced by *second-order* stress fields, with length-scales on the order of 100-1000 km, resulting from processes such as lithospheric flexure and buoyancy forces related to elevated mantle temperatures (Zoback, 1992). Additionally, *third-order* stress fields, typically occurring on scales of <100 km along rift systems, drive stress perturbation locally within and between individual rift segments (Delvaux and Barth, 2010). In the EAR, these third-order stress fields are inferred to result from: (1) mechanical interactions between segmented rift basins (Koehn et al., 2008; Agostini et al., 2009; Koehn et al., 2010; see also Chapter 2); (2) strength anisotropies related to the presence of shear zones (Morley, 2010); (3) volcano topography (Tibaldi et al., 2014); and (4) magma overpressures (Ring et al., 2005; see also Chapter 2). Temporal variations in the regional stress state across the entire EAR (e.g., a rotation from E-W to NW-SE extension in the Late Pleistocene; Bosworth and Strecker, 1997), resulting from

changes in far-field plate boundary forces, have also been inferred from the geological record (Strecker and Bosworth, 1991; Delvaux et al., 1992; Ring, 1992; Bonini et al., 1997; Delvaux, 2001).

Together, these studies suggest that the role of preexisting weaknesses should vary over the course of rift evolution. For example, transverse structures should activate/deactivate in response to changes in far-field plate boundary forces, as well as more localized rotations of σ_3 as segmented basins progressively merge and interact, and new zones of focused magmatism develop (Morley and Nelson, 1990; Schlische, 1993; Modisi et al., 2000; Densmore et al., 2007; Ebinger et al., 2013). Furthermore, long-term rifting should be accompanied by lithospheric strength reductions (due to heating and thinning) and the formation of new, optimally-oriented, rift-parallel faults; therefore, non-optimally oriented, transverse faults should be progressively abandoned as rift basins evolve (Chorowicz and Sorlien, 1992; Ebinger, 2005; Corti, 2008; Agostini et al., 2009). The Kenya Rift of the EAR exhibits numerous transverse faults, which trend subparallel to NW-trending basement structures (Mosley, 1993; Smith and Mosley, 1993; Le Turdu et al., 1999; Robertson et al., 2015) (Fig. 5.1). Here, we test the timing and kinematics of transverse faulting, and its association with evolving rift basin segmentation, through an analysis of the Kordjya fault of the Magadi basin, Kenya.

5.3 Transverse faulting in the Magadi basin of the Kenya Rift

The Kenya Rift is a ~900-km-long sector of the EAR comprising a series of discrete, asymmetric rift basins, ~100 km long and 10s of km wide (Fig. 5.1B). Upper crustal strain in the Kenya Rift is primarily accommodated along two types of fault systems: (1) *border faults*,

which bound the rift and are 100s of kilometers long and accrue 1000s of meters of throw; and (2) *intra-rift faults*, which are smaller than border faults (10s of kilometers long, with 10s to 100s of meters of throw) and form in the central, inner depressions of rift basins. Faulting in the Kenya Rift initiated ~25 Ma in the Turkana depression (Morley et al., 1992; Ebinger et al., 2000). Since then, extension has gradually migrated southward along the Kenya Rift, with rift basins forming in central Kenya (e.g., Naivasha-Nakuru basin at 10-15 Ma; Smith, 1994; Spiegel et al., 2007; Acosta, 2015), and southern Kenya (e.g., the Magadi basin by 7 Ma; Crossley, 1979).

The Magadi basin (Figs. 5.1C and 5.2) consists of pervasively faulted volcanic and sedimentary sequences (23 Ma to present) overlying Mozambique basement rocks (Baker, 1958, 1963; Baker and Mitchell, 1976; Crossley, 1979; Nyamai et al., 2003). It is bounded to the west by the ~7 Ma Nguruman border fault escarpment (Crossley, 1979; Birt et al., 1997; Chapter 4). Numerous intra-rift faults are observed in the center of the basin dissecting <3 Ma volcanics (Baker, 1958; Baker et al., 1976; Atmaoui and Hollnack, 2003). Recent analysis of the distribution of fault strain within the Magadi basin (see Chapter 4) suggests that the locus of faulting recently migrated away from the border fault and into the center of the basin, within the intra-rift fault population. A number of transverse fault structures are observed within this intra-rift fault system. They are thought to have formed during reactivation of NNW-trending basement fabrics (Smith and Mosley, 1993; Le Turdu et al., 1999) (Fig. 5.1B and C).

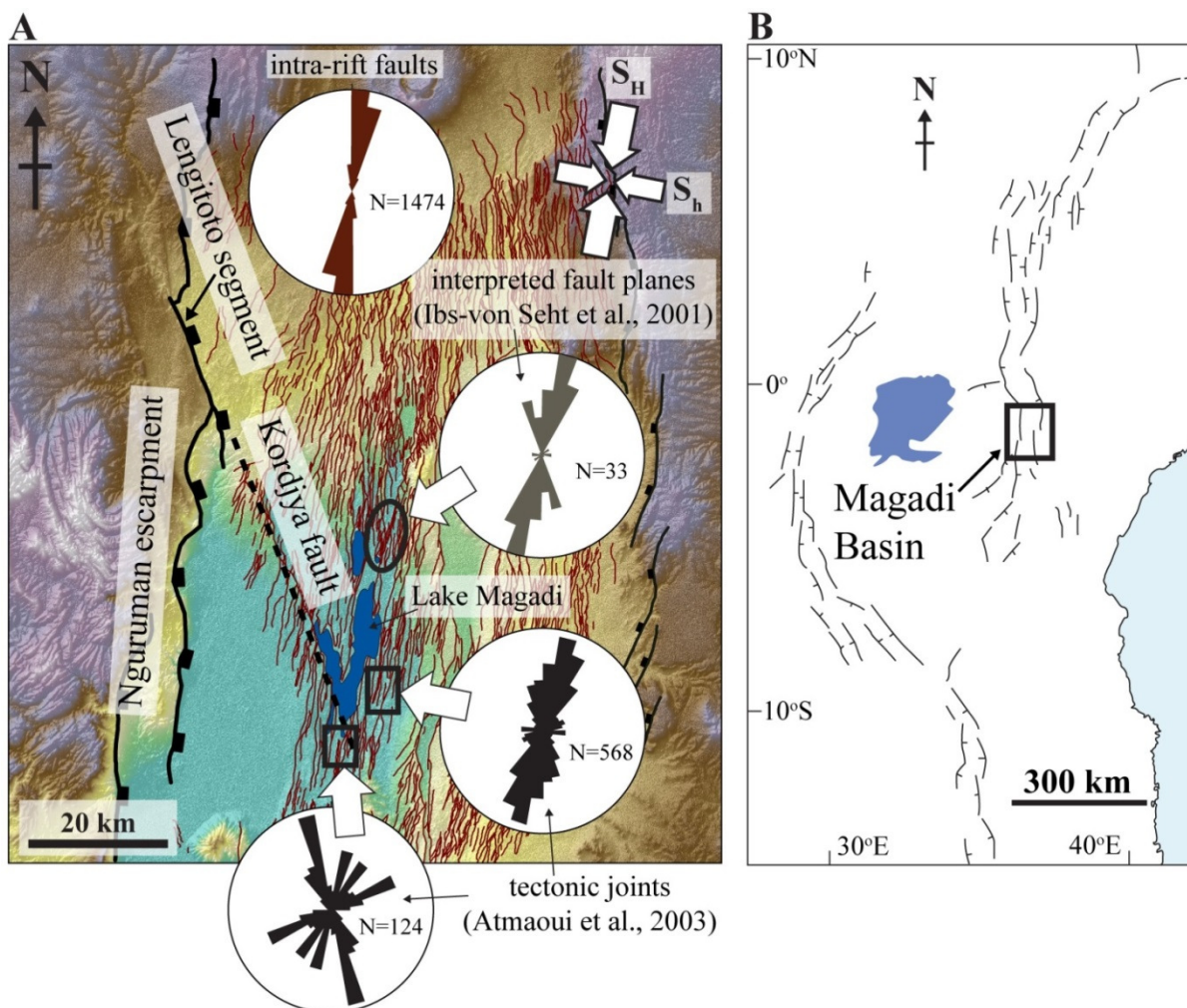


Figure 5.2. A: Existing structural data from the Magadi Basin of the Kenya Rift. Fault traces were mapped from 0.5 m resolution aerial photography (refer to Chapter 4). Thick black lines represent the western border fault, whereas thin black lines show the eastern boundary fault (Ngong-Turoka fault; Baker and Mitchell, 1976). Red lines represent intra-rift fault traces. The orientations of the greatest (S_H) and least (S_h) horizontal compressive stress, based on data from Ibs-von Seht et al. (2001) and Atmaoui and Hollnack (2001), are illustrated with white arrows. Fault planes (primarily dip-slip normal faults) from Ibs-von Seht et al. (2001) were interpreted from 33 focal mechanisms acquired from the 1998 seismic swarm in the center of the Magadi basin. The trace of the Kordjya fault (dashed black line) is from Atmaoui and Hollnack (2003). This fault trace lines up with the Lengitoto border fault segment and forms part of the Engorika-Magadi-Lembolos structural lineament (Fig. 5.1B). Lake Magadi is represented by the dark blue polygon. B: Inset of the East African Rift, showing the distribution of major rift faults (black lines), and location of Magadi Basin shown in A. Lake Victoria represented by the dark blue polygon.

Previous studies investigating the development and kinematics of transverse faults in the Magadi basin focused on the Kordjya fault (Le Turdu et al., 1999; Atmaoui and Hollnack,

2003) (Fig. 5.2). This fault bounds the western shore of Lake Magadi near the center of the basin. Towards the NW and away from the center of the rift basin, the Kordjya fault cuts obliquely across the dominant rift-parallel fault fabric and aligns along-strike with a subsidiary segment of the Nguruman border fault (Lengitoto fault) at its northwestern end. Previous studies (e.g., Smith and Mosley, 1993; Le Turdu et al., 1999) proposed that the Kordjya fault follows a preexisting, basement shear zone (Aswa shear zone), that was reactivated either before or synchronously with the dominant, rift-parallel fault pattern in response to an ESE-WNW directed extension. Accordingly, earthquake focal mechanisms, analyses of neo-tectonic joints (~10 ka to present), and the dominant NNE-trending intra-rift fault pattern, all suggest that σ_3 is oriented ESE-WNW across the Magadi basin (Ibs-von Seht et al., 2001; Atmaoui and Hollnack, 2003) (Fig. 5.2). The assertion has been that the Kordjya fault, and similar NW-trending transverse faults in the Kenya Rift, formed as oblique-normal faults with a dextral component of shear (Smith and Mosley, 1993; Le Turdu et al., 1999; Atmaoui and Hollnack, 2003). In fact, ESE-WNW extension implies roughly equal amounts of normal dip-slip and dextral strike-slip motion along the Kordjya fault.

Current hypotheses regarding the development of the Kordjya fault system are conceptually sound from a fault-mechanical and rift evolution perspective (e.g., Rosendahl, 1987; Chorowicz, 1989; Kilembe and Rosendahl, 1992). However, the orientations of some joint sets measured by Atmaoui and Hollnack (2003) deviated significantly from fractures measured across the rest of the basin (Fig. 5.2). Specifically, a dominant NNW-trending (transverse) joint set was recorded in the vicinity of the transverse Kordjya fault. This is counter-intuitive given that joints theoretically form normal to σ_3 (Anderson, 1951; Pollard and Aydin, 1988), which has been proposed to be oriented WNW-ESE across the basin (Ibs-

von Seht et al., 2001; Stamps et al., 2008). The Magadi basin is also in a “transitional phase” in its development, where the locus of strain (i.e., magmatism and faulting) has recently begun migrating from the rift borders to the rift center (see Chapter 4). Has the Kordjya fault formed in response to this recent change in rift system dynamics? These considerations motivate a revision of the mechanics of transverse faulting in the Magadi basin of the Kenya Rift. Specifically, this study focuses on the timing of the Kordjya fault with respect to the dominant rift-parallel fault fabric. We provide a revised kinematic model for this transverse fault by considering the role of inherited basement weaknesses, magmatism, and magmatic volatile release, and the effects of evolving rift basin architecture on the activation of transverse faulting in the Magadi basin.

5.4 Field observations and remote-sensing analysis of the Kordjya fault system

5.4.1 Methods

Fault segment traces and throws were measured along the Kordjya fault from high-resolution aerial photography (0.5 m/pixel) and Shuttle Radar Topography Mission (SRTM) data (30 m horizontal resolution, 7.6 m vertical precision; Rodríguez et al., 2005). The strikes of joints (lengths >5 m) were measured in the field in Late Pleistocene to Holocene sediments and on faulted lavas within 50 m of fault scarps (Fig. 5.3A to C). Horizontal opening vectors were measured between matching features (e.g., abrupt changes in strike) on opposing margins of dilational joints (Fig. 5.3D). Fault planes and rakes were also measured on (rare) striated fault-gouge sediments (Fig. 5.3E). Fault striations provided the sense of fault slip (Delvaux et al., 1992; Ring, 1992; Ring et al., 2005). Horizontal opening vectors along joints were used to infer the orientation of σ_3 , however, where no opening vectors or other kinematic

indicators (i.e., dilational jogs, tail cracks) were present, the extension direction (i.e., σ_3) was inferred to be perpendicular to joint strike (Pollard and Aydin, 1988).

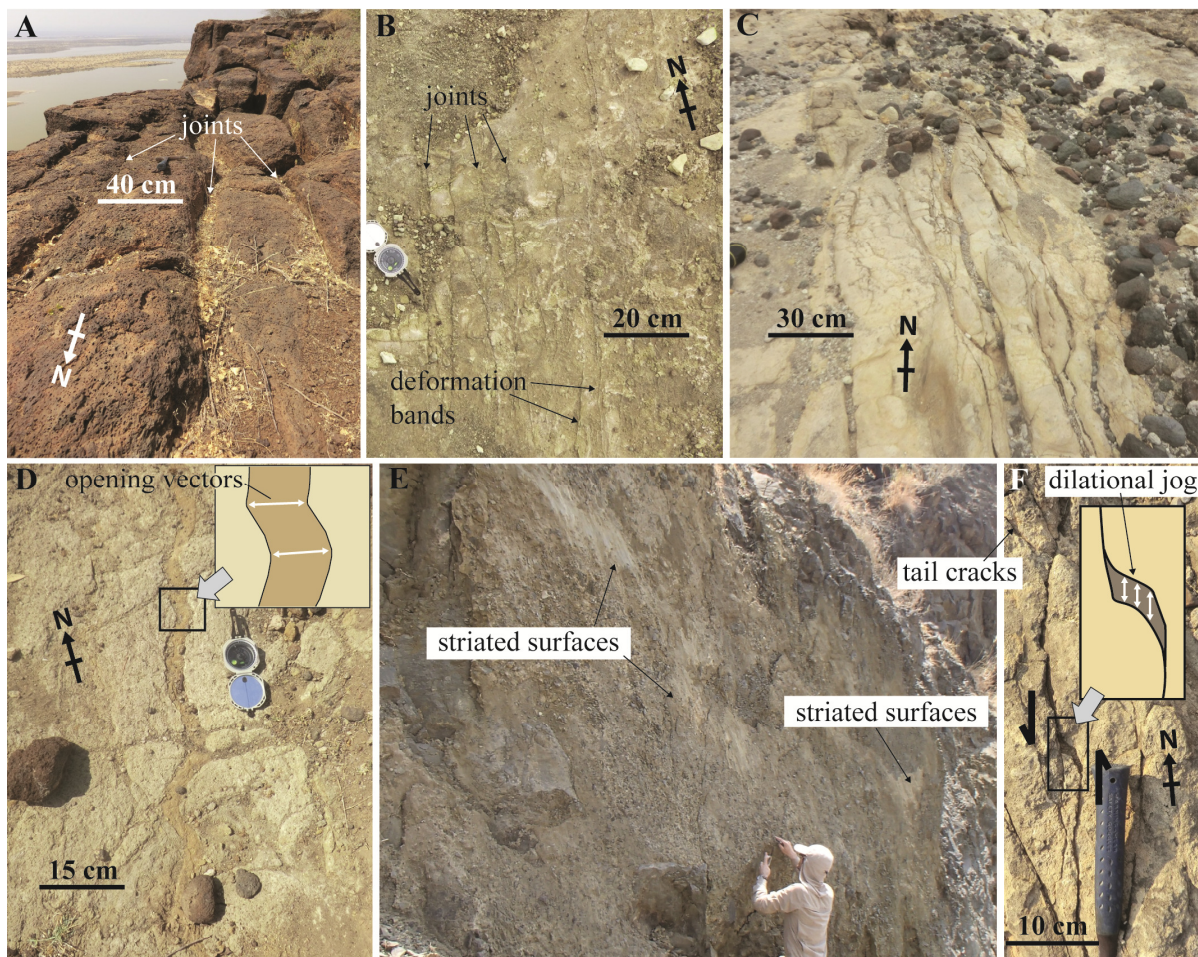


Figure 5.3. Photos of structural features mapped in the field. A: Tectonic joints near the footwall cutoff of the Kordjya fault in Magadi trachyte lavas (photo location: $1^{\circ}51'40.01''\text{S}$, $36^{\circ}13'05.19''\text{E}$). B: Rift-parallel joints and deformation bands in Late Pleistocene sediments (photo location: $2^{\circ}01'05.60''\text{S}$, $36^{\circ}13'56.33''\text{E}$). C: NNW-trending tectonic joints in the hanging wall of the Kordjya fault in Late Pleistocene sediments (photo location: $1^{\circ}49'32.59''\text{S}$, $36^{\circ}12'10.94''\text{E}$). D: Sediment-filled joint (photo location: $1^{\circ}50'06.50''\text{S}$, $36^{\circ}12'06.12''\text{E}$). Inset shows the dilation vector based on piercing points between matching fracture walls. E: Striated fault surface of a rift-parallel fault segment adjacent to the Kordjya fault, showing sinistral oblique-normal motion (rake = 70°N ; photo location: $1^{\circ}51'10.66''\text{S}$, $36^{\circ}12'59.57''\text{E}$). F: Kinematic indicators (dilational jog and tailcracks) on NNE-trending joints near the Kordjya fault, revealing a component of sinistral shear (photo location: $1^{\circ}49'32.92''\text{S}$, $36^{\circ}12'11.25''\text{E}$).

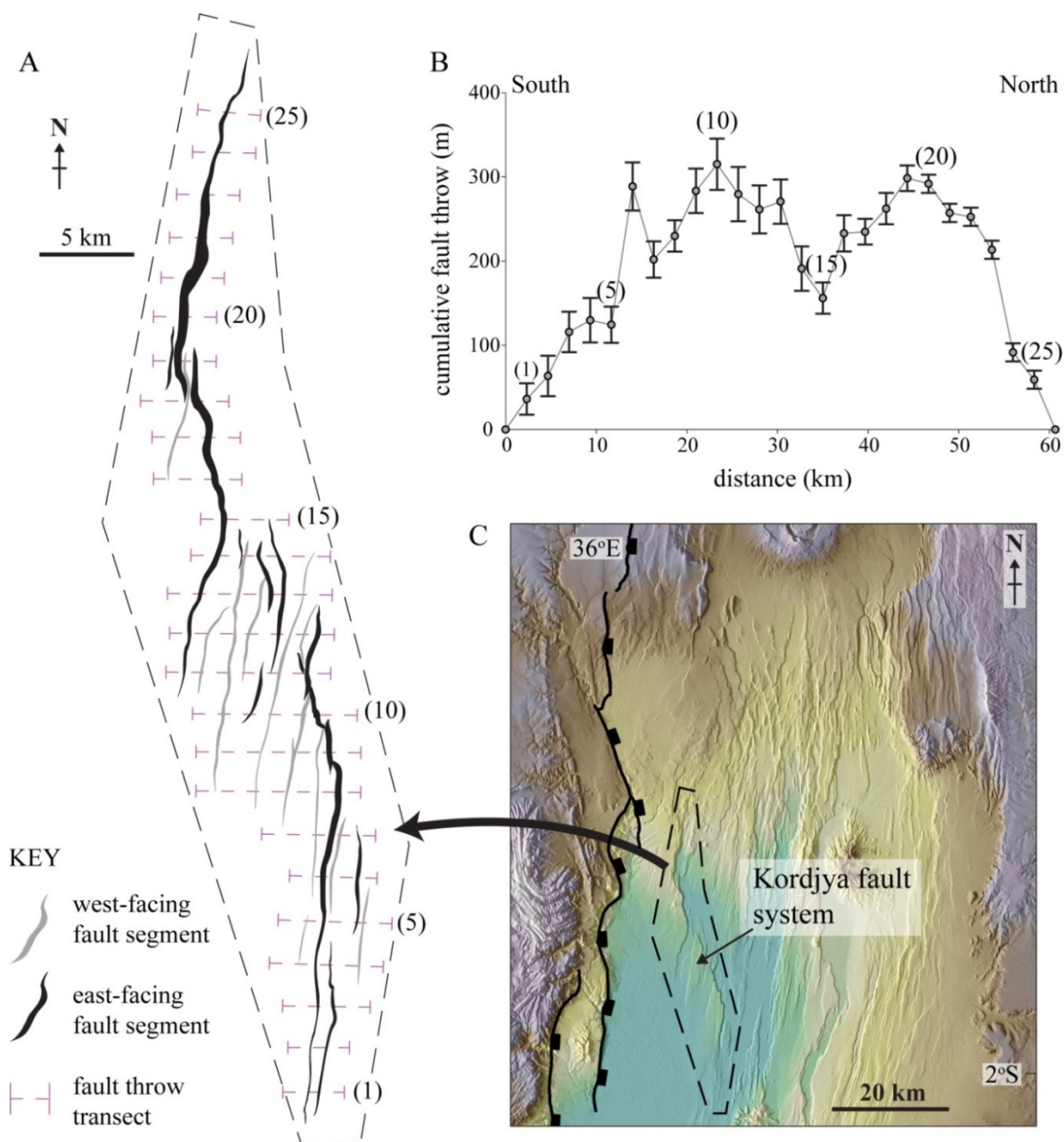


Figure 5.4. A: Fault polygon map of the Kordjya fault system, comprising numerous rift-parallel fault segments aligned in a NNW-trending, en echelon pattern. East- and west-facing segments were mapped from an SRTM hillshade, and polygon thicknesses represent heave components of the fault scarps (i.e., a proxy for throw distribution, although also influenced by scarp degradation). Cumulative fault throws were measured along 25 ~E-W transects, shown as purple dashed lines. Only the major segments, with heaves visible in the 30 m SRTM, are included in this map. Dashed black polygon corresponds to the area demarcated in C. B: Fault throw distribution along the Kordjya fault, showing an elliptical profile consistent with a geometrically coherent system. Each throw value represents the cumulative throw measured along each transect in A. Numbers correspond to numbered transects in A. Error bars are to 95% confidence. C: Annotated SRTM map of the Magadi basin showing the location of the Kordjya fault system. The Nguruman border fault escarpment is annotated as a bold black line.

5.4.2 General structure

The Kordjya fault was previously mapped as a continuous NNW-trending fault (e.g., Atmaoui and Hollnack, 2003). However, this analysis indicates that the Kordjya fault consists of a complex system of predominantly NNE-striking, rift-parallel fault segments that collectively form a NNW-trending array of en echelon faults (Figs. 5.2 and 5.4). To test whether these rift-parallel faults are kinematically coherent (Walsh and Watterson, 1988), the distribution of fault throw was analyzed from cumulative throw data collected along 25 E-W transects throughout the inferred system. As shown Figure 5.4A and B, the throws of faults were summed where they intersect each transect line (purple dashed lines in Fig. 5.4A). This approach reveals an elliptical throw profile typical of geometrically and kinematically coherent fault segment arrangements (Walsh and Watterson, 1988; Dawers et al., 1993; Cartwright et al., 1995; Nicol et al., 1996) (Fig. 5.4B).

In all, the Kordjya fault is made up of 32 segments that form a roughly 60-km-long system. These segments merge into the main fault trace of the NNW-trending Kordjya fault (dashed line in Fig. 5.2A and light red polygon in Fig. 5.5A), hereafter termed the *main Kordjya fault*. Segments can be east- or west-facing (black and grey polygons, respectively, in Figure 5.4A). Although fault segments are primarily rift-parallel, a few shorter (up to ~4 km-long) NNW-striking segments are present along the main Kordjya fault, suggesting the Kordjya fault may be starting to form a through-going structure that could potentially by-pass the original en echelon, rift-parallel segments it currently exploits. Elevation profiles perpendicular to the strike of the Kordjya fault reveal a topographic profile consistent with the footwalls and hanging walls of normal faults observed from field and numerical modelling studies (Ebinger et al., 1991; Bott, 1996; Grant and Kattenhorn, 2004). For example, as shown

in Figure 5.5, the ground surface gently dips away from the Kordjya fault scarp on the footwall side, whereas on the hanging wall side, the ground surface gently dips toward the fault scarp. At the southwestern end of the main Kordjya fault, sets of fault-parallel springs emanate from the base of the fault scarp, and feed water into perennial Lake Magadi on the hanging wall side of the fault (Fig. 5.6; see also Chapter 4).

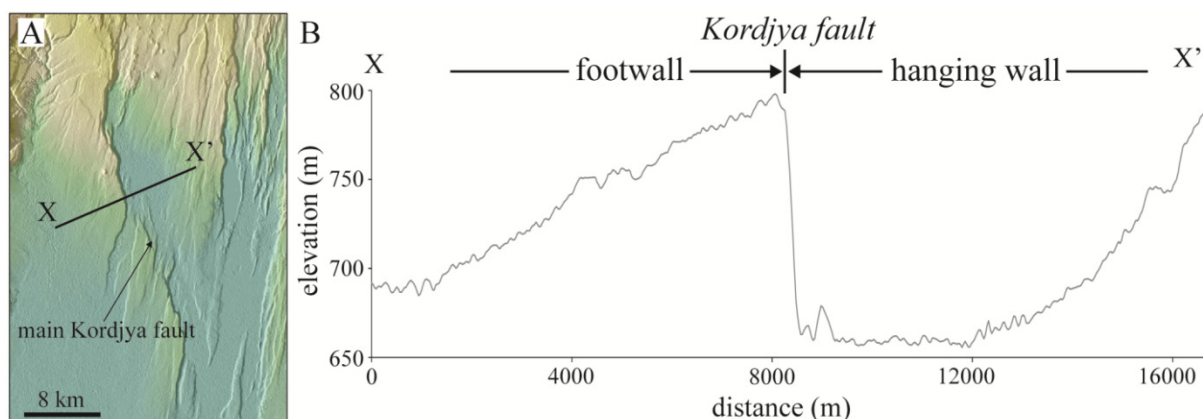


Figure 5.5. A: Annotated SRTM map of the Magadi basin showing the location of the main Kordjya fault. The black line marked X-X' refers to the location of the elevation profile in B. B: Elevation profile perpendicular to the main Kordjya fault (35× vertical exaggeration). The hanging wall and footwall of the fault are annotated above. The elevation profile across the footwall, showing the topography gently dipping away from the fault, is consistent with the footwall profile of a normal fault. Similarly, the elevation profile across the hanging wall, where the topography gently dips towards the fault, is consistent with the hanging wall of normal a fault (e.g., Ebinger et al., 1991; Bott, 1996).

Throw profiles were analyzed along individual rift-parallel fault segments exhibiting throws >25 m (n = 10) (Fig. 5.7). Although the entire Kordjya fault system collectively exhibits an elliptical throw profile (Fig. 5.4B), throw profiles along the individual rift-parallel fault segments that comprise the Kordjya fault are asymmetric (Fig. 5.7B). Maximum fault throws occur near the intersection of these segments with the main Kordjya fault (yellow stars in Fig. 5.7A). Here, the rift-parallel fault segments begin to interact and link with one another, where they exhibit both hard- and soft-linked relay zones (Gibbs, 1984; Childs et al., 1996).

Soft-linked segments show no physical links between one another, yet are kinematically coherent (Walsh and Watterson, 1991) (Fig. 5.4). They exhibit relatively high throw gradients after intersecting the main Kordjya fault – throw quickly decreases from the maximum

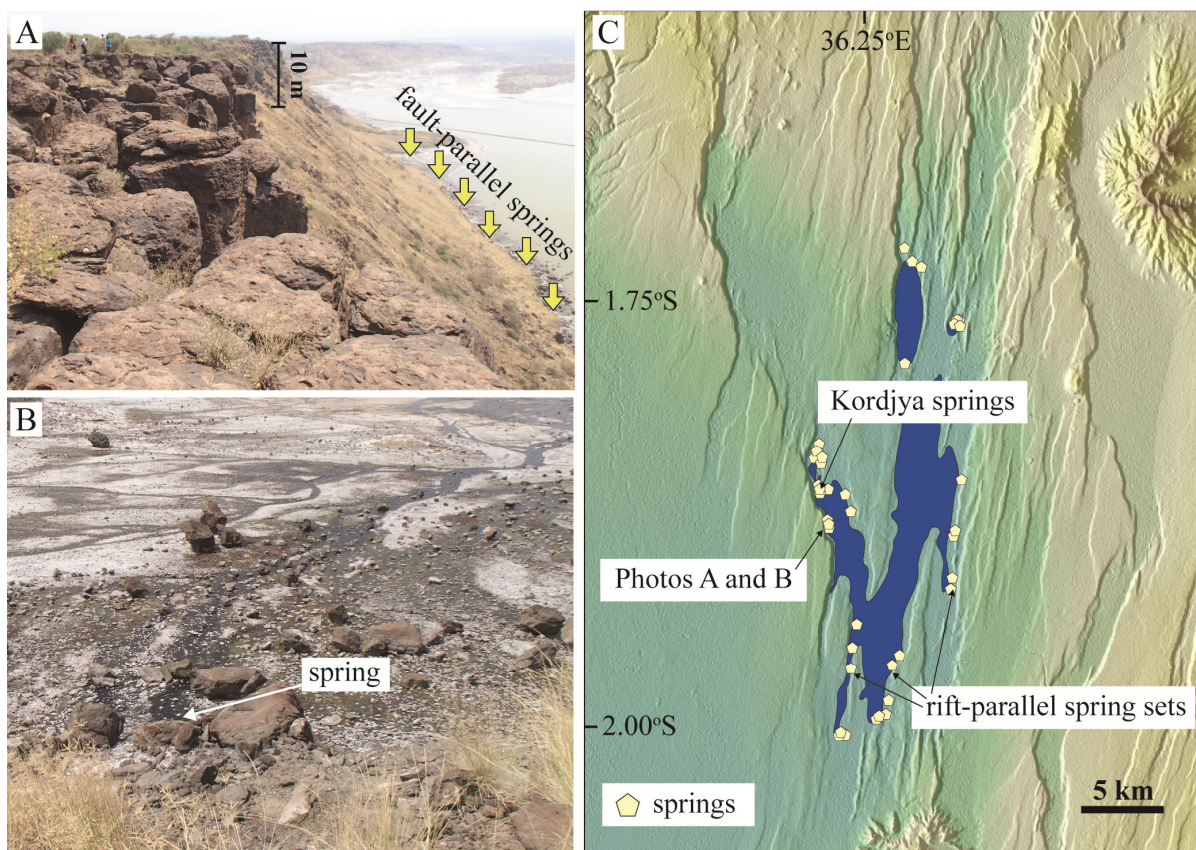


Figure 5.6. Distribution of springs along the Kordjya fault and Lake Magadi. Spring locations are based on observations from this study and data from Baker (1963). A: Photo to the NNW of the Kordjya fault (location annotated in C). The height of the fault scarp here is ~154 m. B: Photo to to NE of a spring at the base of the Kordjya fault. Springs here flow ENE into Lake Magadi. C: Annotated SRTM image of the center of the Magadi basin showing the distribution of springs (yellow pentagons) and lake waters (dark blue polygon). Most springs occur along rift-parallel faults in the axial depression of the Magadi basin, however, sets of springs are also observed along the transverse Kordja fault.

value to zero at fault tips (e.g., the northern ends of Segments 2 and 8 in Figure 5.7). Fault throws for hard-linked segments, however, do not reduce to zero, as they exhibit identifiable connections with adjacent segments across the main Kordjya fault (e.g., northern end of

Segment 1 in Figure 5.7). Some rift-parallel segments also interact with shorter NNW-trending segments that appear to be developing a through-going, transverse fault trace. At rare localities segments do not appear to interact directly with neighboring segments as they cross the main Kordjya fault. For example, segment 10 of Figure 5.7 can be traced across the main Kordjya fault into the hanging wall side. However, its maximum throw still occurs at its intersection with the main Kordjya fault, which is typical of all rift-parallel segments forming the entire fault system. These segments also exhibit a relatively sharp reduction in throw from the location of maximum throw to the tip of the fault, producing the characteristic asymmetric profile.

Many rift-parallel fault segments terminating near the main Kordjya fault exhibit curved ends (in a counter-clockwise sense) reminiscent of tailcracks (Cruikshank et al., 1991; Willemsse et al., 1997; Marshall and Kattenhorn, 2005; Watkinson and Ward, 2006) (Fig. 5.8). Curved ends are not present at fault tips occurring away from the main Kordjya fault (e.g., southern end of Segment 1, Fig. 5.7). Field and modeling studies show that fault tip geometries can be used as kinematic indicators of the sense of slip, specifically to determine if fault motion is characterized by a component of sinistral or dextral shear (Pollard and Aydin, 1988; Cruikshank et al., 1991; Kattenhorn, 2004). Left-curving (counter-clockwise rotation) and right-curving (clockwise rotation) tailcracks indicate a component sinistral shear and dextral shear, respectively. The ends of many rift-parallel faults intersecting the main Kordjya fault exhibit left-curving geometries, which suggest a component of sinistral shear in addition to the predominantly dip-slip motions expected along these oblique-normal faults (Fig. 5.8).

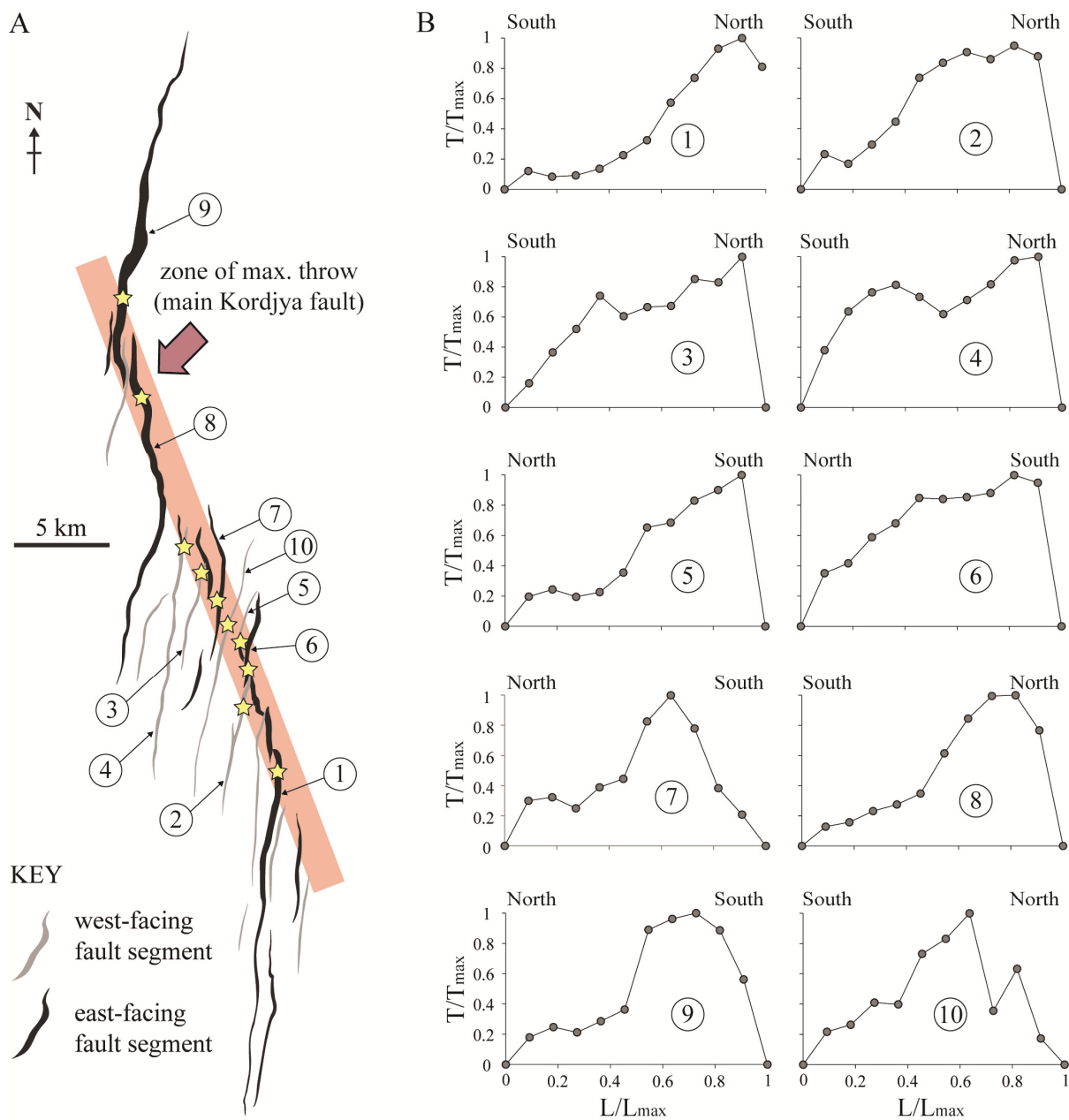


Figure 5.7. Distribution of fault throw along rift-parallel segments that comprise the NNW-trending Kordjya fault system. A: Map view of rift-parallel fault segments (see Fig. 5.4C for location). East- and west-dipping segments were mapped from an SRTM hillshade, and line thickness corresponds to the fault scarp width (i.e., fault heave). Numbers correspond to fault throw profiles shown in B. The location of maximum fault throw for each analyzed segment is shown as a yellow-filled star, and define a NNW-trending zone (light red rectangle) that follows the trace of the main Kordjya fault (see Fig. 5.2A). B: Fault throw data collected along rift-parallel fault segments. Numbers correspond to faults annotated in A. Throw (T) and length (L) data in each plot are normalized by the maximum throw (T_{max}) and length (L_{max}) values, respectively, along each fault. Plots exhibit asymmetric throw profiles with maximum throw values occurring along the trace of the main Kordjya fault. Hard-linked faults exhibit non-zero throw values at fault tips.

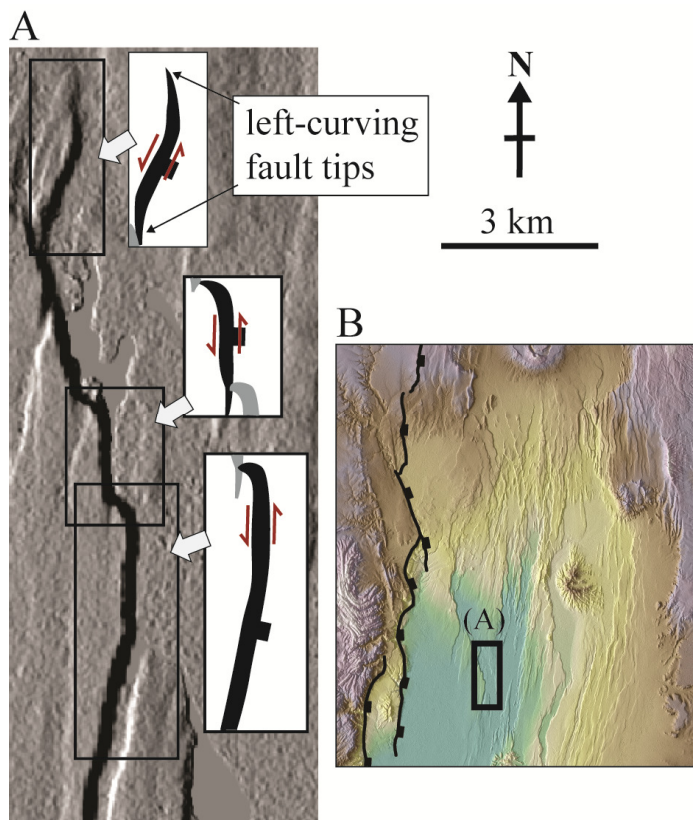


Figure 5.8. A: Annotated SRTM hillshade (lighting from the W) showing east-dipping rift-parallel faults terminating at the main Kordjya fault (scale bar in the top right). N- to NNE-trending fault segments exhibit left-curving tip zones indicative of a component of sinistral shear (red arrows). B: Location of A in the Magadi basin.

The ~60-km-long Kordjya fault has a maximum throw of 315.1 ± 10.7 m and displaces 0.95 to 1.37 Ma Magadi trachyte lavas (ages from Chapter 4). Assuming an optimal fault dip of 60° , these fault throw and age data correspond to a minimum time-averaged slip rate of $0.26\text{--}0.40$ mm yr⁻¹, consistent with slip rates (typically $0.1\text{--}4$ mm yr⁻¹) along major normal faults in extensional systems elsewhere. Examples include the Wasatch, Lake Tahoe, Campo Felice, Rangipo, and Paeroa faults of the Basin and Range (USA; Machette et al., 1991; Zhang et al., 1999; Hetzel and Hampel, 2005; Kent et al., 2005), Taupo Rift (New Zealand; Villamor and Berryman, 2001, 2006; Berryman et al., 2008; Downs et al., 2014), and

Central Apennines (Italy; Galadini and Galli, 2000; Wilkinson et al., 2015). The throw-length ratio of the Kordjya fault system (0.0053) is consistent with ratios produced by normal faults dissecting rift lavas elsewhere (e.g., Iceland; Gudmundsson, 1992; Angelier et al., 1997), as well as regional data from the Natron and Magadi basins, which exhibit a mean throw-length ratio of 0.0059 for all measured faults (see Chapter 4).

5.4.2 Fault kinematic indicators from field observations

Systematic joint sets and rare deformation bands (~1 mm-wide) were analyzed along and around the Kordjya fault system (Figs. 5.3 and 5.9). Occasionally, tectonic joints (<4-cm-wide) are filled with very fine-grained sediment (Fig. 5.3D). Consistent with previous studies on tectonic joints in the region (Atmaoui and Hollnack, 2003), two dominant joint sets and two sets of horizontal opening vectors are observed (Fig. 5.9D). NNE-trending joints (locations v-vii in Figure 5.9A) are observed away from the main Kordjya fault (light red polygon in Figure 5.7), and are consistently present throughout the Magadi basin (Atmaoui and Hollnack, 2003). These tectonic joints trend parallel to rift-parallel faults throughout the Magadi basin (intra-rift faults in Fig. 5.2A) and exhibit a mean opening vector of 115° , which is consistent with previous estimates of the regional extensional direction ($105\text{-}115^\circ$) from investigations of joints and focal plane mechanism (Ibs-von Seht et al., 2001; Atmaoui and Hollnack, 2003) (Fig. 5.2). However, in the vicinity of the main Kordjya fault (light red polygon in Figure 5.7), a second, NNW-trending joint set is present (locations i, iii, and iv in Figure 5.9A). Rare N- to NNE-trending joints observed here exhibit dilational jogs and left-curving tailcracks, consistent with a component of left-lateral shear (Fig. 5.3F). The NNW-trending joints exhibit a mean opening vector of 079° (refer to location iii in Figure 5.9A), which is normal to the mean joint orientation and the main Kordjya fault trace, but oblique to

the regional extension direction. Measured fault surfaces on rift-parallel faults intersecting the main Kordjya fault exhibit strikes and dips ranging $015\text{-}025^\circ$ and $78\text{-}87^\circ$, respectively.

Striations on these surfaces exhibit rakes of 70°N , consistent with a sinistral component of shear along NNE-trending rift-parallel faults in the vicinity of the Kordjya fault (Fig. 5.9).

Overall, joint and fault kinematic data (locations i-iv in Figure 5.9) support ENE-WSW extension in the vicinity of the main Kordjya fault, which would likely produce dip-slip motions on a NNW-trending fault structure.

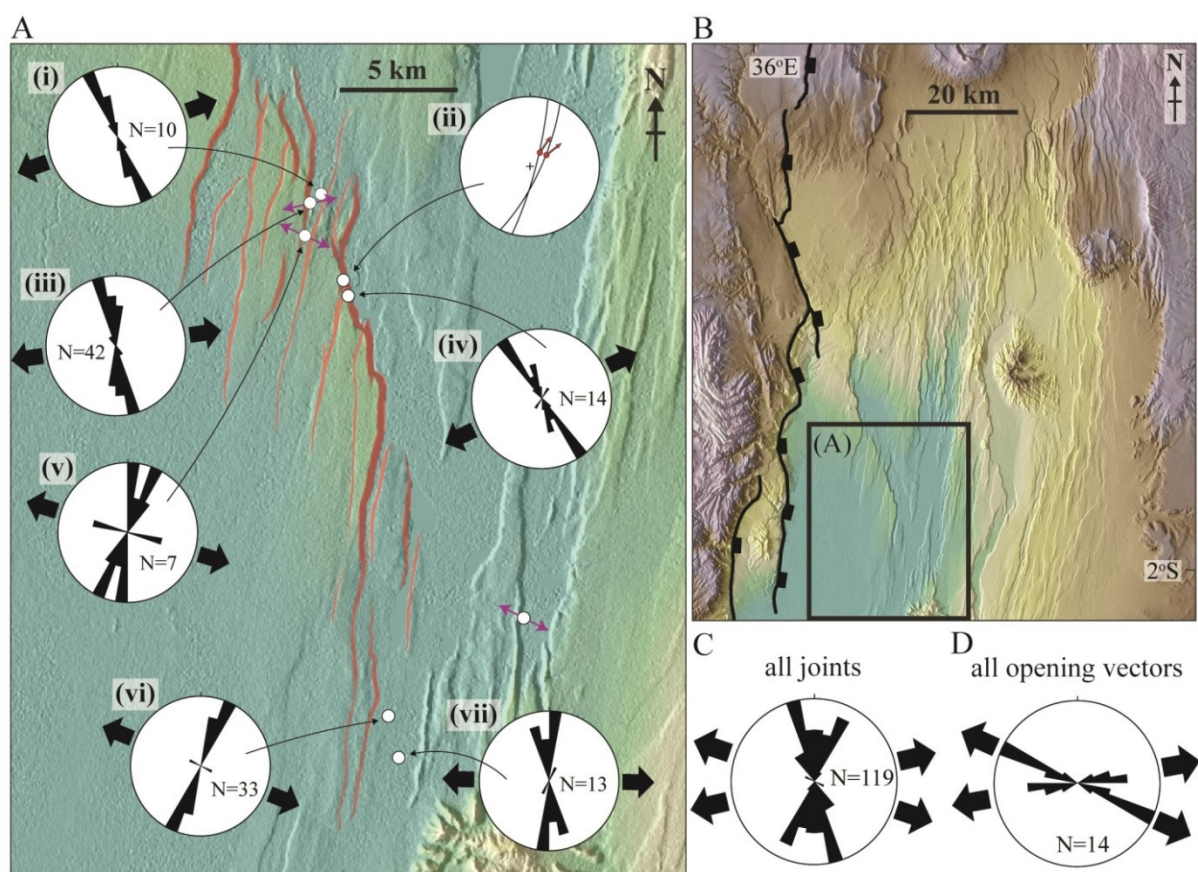


Figure 5.9. A: Tectonic joint measurements around the Kordjya fault system. Sample locations (white circles) are annotated on an SRTM map of the Kordjya fault. Red polygons represent scarps of the Kordjya fault segments shown in Figs. 5.4 and 5.5. Rose plots show joint strikes at the seven locations. Bold black arrows represent the inferred extension directions during original joint development, assumed to be normal to the mean trend of the tectonic joint set. Purple arrows represent the mean dilation vectors at select locations. Also shown is a lower hemisphere stereonet plot of fault plane orientations (great circles) and slip vectors (red arrows) along the main Kordjya fault trace, with the bold black arrows indicating the inferred extension direction. Note the

change in extension directions from ENE-WSW near the main Kordjya fault, to ESE-WNW south and east of the fault. B: Annotated SRTM map of the Magadi basin showing the location of the map in A. Nguruman border fault escarpment annotated as a bold black line. C: Rose plot of the strikes of all measured tectonic joints. Bold black arrows represent the inferred, disparate extension directions, assumed to be normal to the dominant NNW-trending and NNE-trending joint sets. D: Rose plot of all measured dilation vectors observed across joints. Bold black arrows represent the inferred, disparate extension directions.

5.5 Discussion

5.5.1 Kinematics and timing of faulting in the Kordjya system

To create a conceptual kinematic model for the Kordjya fault system, it is important to consider the mechanics of the rift-parallel fault segments (Fig. 5.10). Previous studies in the Magadi area have suggested that NNE-striking rift-parallel faults across the Magadi basin exhibit dip-slip kinematics, whereas NNW-trending transverse structures act as oblique-normal faults with a component of dextral shear (Smith and Mosley, 1993; Le Turdu et al., 1999; Atmaoui and Hollnack, 2003). These assertions are supported by focal mechanisms recorded from earthquakes during the 1998 Magadi seismic swarm, which revealed ENE-WSW extension along the rift center (Ibs-von Seht et al., 2001) (Fig. 5.2). Additionally, the inferred regional extension direction from neo-tectonic joints and GPS modeling data suggest that σ_3 is oriented perpendicular to the rift-parallel fault system (Atmaoui and Hollnack, 2003; Calais et al., 2006; Stamps et al., 2008; Saria et al., 2014), which would result in dip-slip normal faulting along these faults. Joint systems measured away from the main Kordjya fault in this study (locations vi-vii, Fig. 5.9) also support this assertion. For example, analyzed joint sets alongside rift-parallel fault segments south of the main Kordjya fault trace (location v-vii, Fig. 5.9) exhibit a dominant N- to NE-trend, with ESE-WNW oriented dilation vectors. Similarly, joints east of the main Kordjya fault trend NNE-SSW (Atmaoui and Hollnack,

2003) (Fig. 5.9). This extension direction is expected to produce dip-slip kinematics on rift-parallel faults, which is consistent with the kinematic data of Ibs-von Seht et al. (2001).

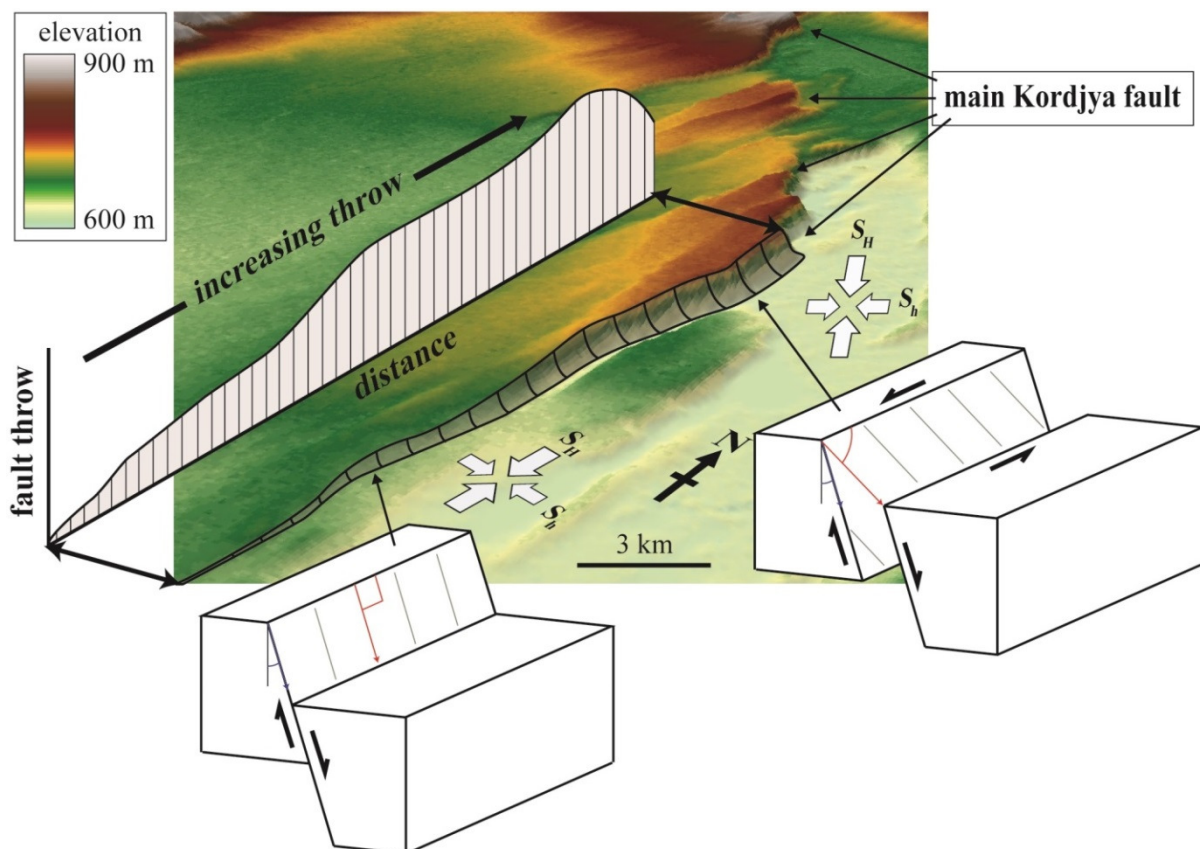


Figure 5.10. Conceptual illustration of the kinematics of rift-parallel faults in the Kordjya fault system, annotated on a SRTM map (oblique-aerial view). The superposed idealized fault throw profile (see Fig. 5.5) shows the maximum fault throw where the rift-parallel fault approaches the main Kordjya fault. The corresponding fault scarp is shaded grey and outlined in black on the SRTM map. The orientations of the greatest (S_H) and least (S_h) horizontal compressive stress are based on joint and fault-slip data in Fig. 5.7. South of the main Kordjya fault, the least compressive stress is parallel to the ESE-WNW regional extension direction, but rotates in the vicinity of the main Kordjya fault, resulting in ENE-WSW extension. Conceptual block diagrams show along-strike changes in the sense of slip along rift-parallel faults based on inferred stress regimes and fault slip data collected in the field. South of the main Kordjya fault, NNE-trending rift-parallel faults exhibit pure dip-slip motions (slip vectors indicated by red arrows), whereas in the vicinity of the main Kordjya fault they exhibit oblique-slip with a component of sinistral shear.

However, the present analysis of rift-parallel faults and joints alongside the main Kordjya fault reveals a more complex kinematic model for some rift-parallel faults in the

Magadi basin (Fig. 5.9). Fault tip zone geometries, slip vectors, and dilational jogs observed on (rare) NNE-striking joints (Figs. 5.3, 5.8 and 5.9) are consistent with a component of left-lateral shear along NNE-striking extensional structures near the main Kordjya fault. Joint sets here dominantly trend NNW, rather than the NNE, and exhibit ENE-trending dilation vectors, which suggests ENE-WSW extension in the vicinity of the main Kordjya fault. This extension direction should theoretically result in a component left-lateral shear along the NNE-striking rift-parallel fault segments (Fig. 5.10).

A change in the kinematic behavior of rift-parallel faults in the vicinity of the main Kordjya fault is further supported by the asymmetric nature of analyzed fault throw profiles (Figs. 5.7 and 5.10). Specifically, the maximum fault throws along these rift-parallel faults all correspond to where they intersect the main Kordjya fault (light red polygon in Figure 5.7), suggesting the Kordjya fault system has locally reactivated these rift-parallel structures. The implication is that these rift-parallel faults formed prior to the development of the Kordjya fault, in response to the regional ESE-WNW extension (Fig. 5.11). Once the rift-parallel fault fabric was established in 0.95-1.37 Ma Magadi trachyte lavas (ages from Chapter 4), the Kordjya fault system initiated, possibly from the reactivation of the NNW-trending Aswa basement shear zone (Smith and Mosley, 1993; Smith, 1994; Le Turdu et al., 1999) (Fig. 5.11D and E). The reactivation of this basement fabric probably occurred in response to a localized shift in the orientation σ_3 from ESE-WNW to ENE-WSW, which optimally oriented NNW-trending basement fabrics with respect to this (local) stress field. The WSW-ENE extension inferred from field data is expected to translate to dip-slip motion along a NNW-trending structure at basement depths (Fig. 5.11E). The earlier formed rift-parallel structures in the vicinity of the Kordjya fault were thus reactivated as oblique-normal faults with

component of left-lateral shear in order to accommodate dip-slip motion along this NNW-trending fault (Fig. 5.12). Fault-slip along these reactivated, rift-parallel faults occurs preferentially within the vicinity of main Kordjya fault, thereby resulting in the observed asymmetric fault throw profiles (Figs. 5.7 and 5.10)

Alternatively, the sinistral oblique motions inferred for the en echelon, rift-parallel faults could result from bookshelf faulting (e.g., Sigmundsson et al., 1995) that accommodates dextral shear along the deep-seated, transverse Kordjya fault. A component of dextral shear along the NNW-trending transverse structure would result from E-W to ESE-WNW extension in the vicinity of the Kordjya fault; however, this extension direction is not consistent with kinematic data presented in this study (Fig. 5.9), nor in previous work (Atmaoui and Hollnack, 2003; Fig. 5.2). Instead, the local orientation of σ_3 (WSW-ENE) and topographic profiles across the footwall and hanging wall of the NNW-trending main Kordjya fault are consistent with normal faulting (Figs. 5.5 and 5.9). Therefore, the most consistent model is that of dip-slip faulting at basement depths resulting from a counterclockwise rotation of σ_3 in the vicinity of the main Kordjya fault (Fig. 5.11E).

5.5.2 An alternative model for transverse faulting and the reactivation of preexisting structures in the Kenya Rift

The revised kinematic model for the Kordjya fault system presented here (Figs. 5.11 and 5.12) contrasts with previous assertions of the timing and kinematics of transverse faulting in the Kenya Rift. Many studies favor the reactivation of preexisting weaknesses during the initiation of rifting (Verfelt and Rosendahl, 1989; Chorowicz, 1992; Chorowicz and Sorlien, 1992; Modisi et al., 2000). In the Kenya Rift specifically, transverse faults are

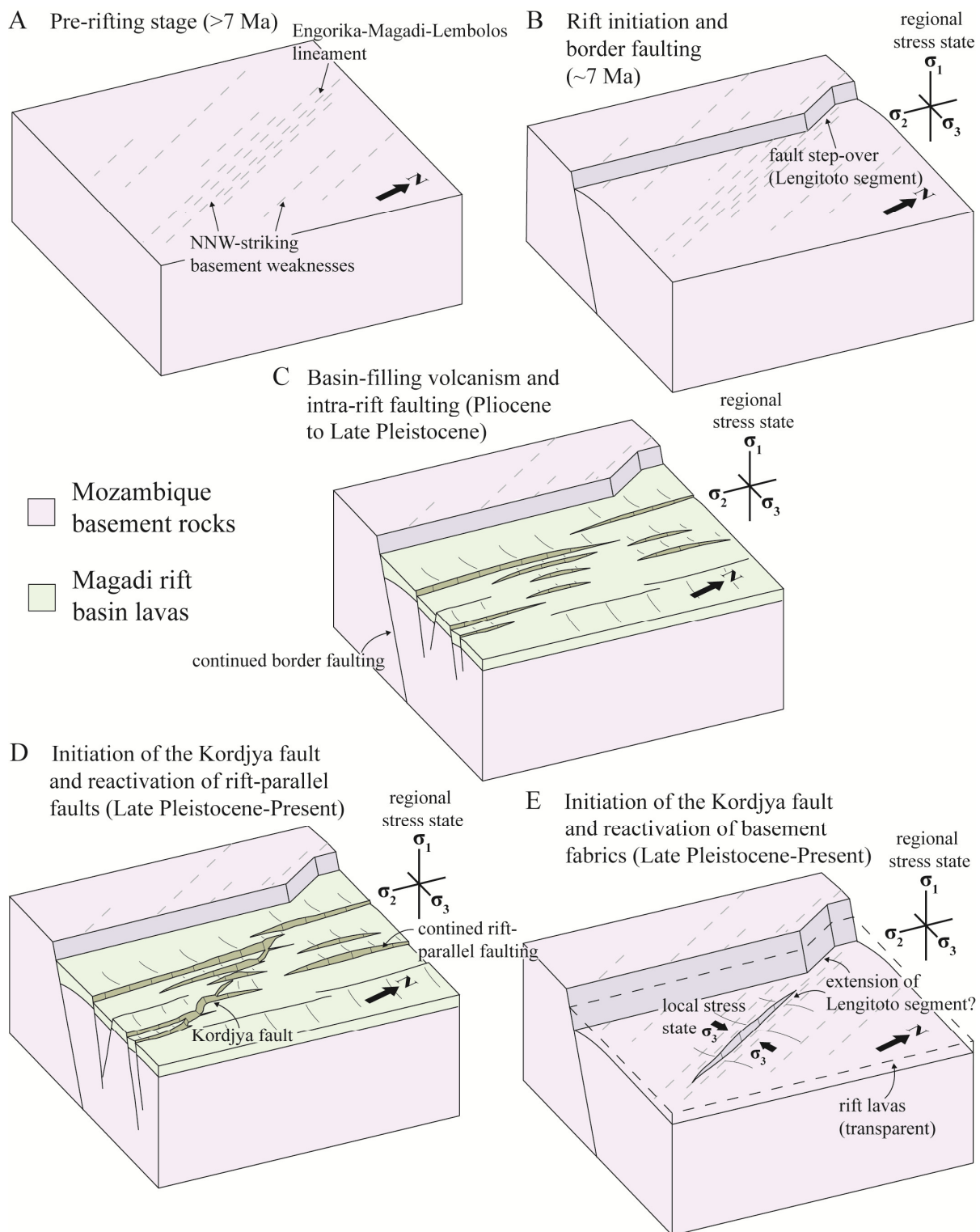


Figure 5.11. Simplified model of the timing of border, rift-parallel and transverse faulting in the Magadi basin. A: Prior to rifting, the area dominantly comprised Mozambique basement rocks with NNW-striking shear fabrics of the Aswa suture zone (Smith and Mosley, 1993). B: Faulting along the Enguruman border fault initiated at ~7 Ma (Crossley, 1979). Segmentation along the border fault, and subsequent development of the Lengitoto

segment, was controlled by NNW-striking, preexisting weaknesses in Mozambique rocks. Specifically, the Lengitoto fault segment localized along the Engorika-Magadi-Lembolos structural lineament (shown in A). C: Following the development of the Nguruman border fault, the Magadi basin went through a phase of basin-filling volcanism and intra-rift faulting. The rift-parallel fault segments comprising the Kordjya fault today formed after the emplacement of Magadi trachyte lavas in the Mid- to Late Pleistocene. D: Initiation of the transverse Kordjya fault. A series of en echelon arranged rift-parallel faults were reactivated as oblique-normal faults, to produce a kinematically coherent, NNW-trending fault system. The Kordjya fault aligns with Lengitoto segment of the border fault and sits along the Engorika-Magadi-Lembolos lineament, suggesting the Kordjya fault may in part relate to the reactivation of a long-lived, influential basement fabric. E: Inferred geometry of the Kordjya fault below syn-rift volcanics of the Magadi basin. The structure forms a through-going, NNW-trending, normal fault at depth, which represents the SW extension of the Lengitoto border fault segment. The local orientation of σ_3 (bold black arrows) is inferred from field data in this study, which would result in dip-slip normal fault motions along a NNW-trending structure at basement depths.

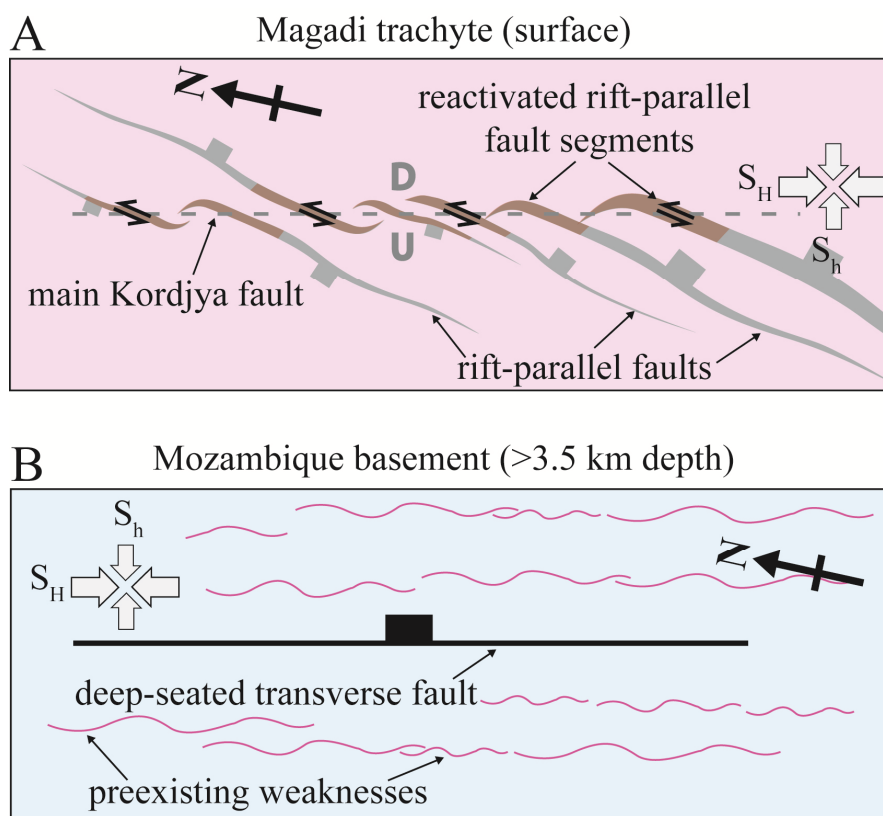


Figure 5.12. Conceptual model of the kinematics of the Kordjya fault system in the near-surface (A) and at basement depths (B). A: Map view illustration of fault mechanics of the Kordjya fault within Magadi trachyte lavas in the near-surface. Rift-parallel faults (gray polygons) trending oblique to the trace of the main Kordjya fault (dashed gray line) are reactivated (light brown fault segments) with a component of sinistral shear in order to accommodate dip-slip motion along a NNW-trending normal fault at basement depths (B). D and U correspond to the down-thrown hanging wall and up-thrown footwall, respectively, of the basement fault. B: Within the Proterozoic basement, the Kordjya fault is interpreted in this study to behave as a pure dip-slip normal fault through the reactivation of a NNW-trending, transverse, preexisting weaknesses of the Aswa shear zone, represented by Engorika-Magadi-Lembolos structural lineament of Smith and Mosley (1993). The depth of basement (>3.5 km) is based on the thickness of rift-basin sediments and volcanics from Birt et al. (1997).

thought to reactivate NNW-trending basement weaknesses (Mosley, 1993), and fail with a component of dextral shear in order to accommodate regional ESE-WNW extension (Smith and Mosley, 1993; Le Turdu et al., 1999; Atmaoui and Hollnack, 2003). Over the course of rift evolution, transverse faults in the EAR should theoretically be abandoned as more favorably oriented rift-parallel faults develop and the lithosphere weakens via heating and stretching (Chorowicz and Sorlien, 1992; Ebinger, 2005; Corti, 2008; Agostini et al., 2009).

By contrast, the reactivation of NNE-trending structures by the Kordjya fault system suggests that these rift-parallel faults, which formed in response to regional ESE-WNW extension, developed prior to the activation of the present day NNW-trending transverse fault (Fig. 5.11C). Field kinematic data favor dip-slip fault kinematics on the Kordjya fault, rather than the previously predicted oblique-slip behavior (Le Turdu et al., 1999). Conversely, rift-parallel faults ultimately developed sinistral oblique-normal slip kinematics, rather than dip-slip, in order to accommodate localized ENE-WSW extension across the Kordjya fault system (Fig. 5.12).

The revised kinematic model supports the assertions of recent studies that many transverse faults across the EAR exhibit dip-slip kinematics (e.g., Modisi et al., 2000; Delvaux and Barth, 2010; Morley, 2010). These studies inferred fault kinematics from focal plane mechanism and aeromagnetic data of displaced subsurface features (dikes), revealing dip-slip normal fault motions along major transverse structures. The reactivation of preexisting structures under these models results from local rotations of σ_3 away from the regional stress state.

Reactivation of pre-existing weaknesses during rift evolution in the Magadi basin

Given the abundance of rift-parallel faults in the Magadi basin that prevailed during early rift evolution (i.e., since ~7 Ma) the recent tendency for dip-slip activity along transverse features like the Kordjya fault suggests a change in rift driving forces. Specifically, the development of the Kordjya fault relates to evolving magma systems and rift basin tectonic architecture, including the interaction between first-order rift basin segments and inherited crustal weaknesses, as well as the temporally changing partitioning of fault strain within the rift basin.

The tectonic-magmatic development of the Magadi basin over the last 7 million years is comparable to existing conceptual models for basin evolution in the Eastern rift (e.g., Hayward and Ebinger, 1996; Ebinger and Casey, 2001; Corti, 2009; see Fig. 4.2, Chapter 4). These studies suggest that strain is initially accommodated along rift border faults before migrating toward the rift center, where regional extension is accommodated by magmatism and intra-rift faulting. Similarly, the initial stages of rifting in Magadi (~7-5 Ma) were characterized by faulting and volcanism along the rift borders (Fig. 5.13A). Faulting initiated on the Nguruman border fault escarpment at ~7 Ma, ultimately developing into a 1.6 km high escarpment and creating an asymmetric basin with a westward-dipping flexure. Border fault development was accompanied by the eruption of Lengitoto trachyte lavas (6.9-5.0 Ma) along the western rift edge (Crossley, 1979). Rift volcanism initiated on the eastern border of Magadi at ~6.7 Ma (Fig. 5.13A) with the eruption of Ol Eyaseti volcanics (Baker et al., 1971; Baker and Mitchell, 1976).

From 5 Ma onwards, volcanic activity was distributed across both the rift borders and the central rift axis (Fig. 5.13B), including the Ngong (2.5-2.6 Ma) composite volcano and related volcanics (Baker and Mitchell, 1976; Saggerson, 1991), as well as widespread lava eruptions of the Kirikiti and Limiru trachytes (5.1-2.5 and 2.05 Ma, respectively) (Baker et al., 1971; Crossley, 1979; see also Chapter 4). The Ngong-Turoka fault escarpment, which bounds the eastern side of the basin, also developed during this period (2.3-3.3 Ma) (Baker and Mitchell, 1976).

Since ~2 Ma, however, volcanism and faulting in the Magadi basin became increasingly focused into the rift center (Fig. 5.13C). This transition was accompanied by emplacement of magmas below the central rift axis (inferred from gravity and seismic tomography data; Baker and Wohlenberg, 1971; Birt et al., 1997; Ibs-von Seht et al., 2001), eruption of voluminous rift lavas (e.g., 295 km³ Magadi trachyte lavas; Guth, 2015), and release magmatic volatiles along fault systems in the rift center (e.g., >1 Mt yr⁻¹ of magmatic CO₂; Chapters 3 and 4). Together, these observations support a magmatic- and fluid-driven model of strain localization into the central rift axis (i.e., Ebinger and Casey, 2001; Keir et al., 2006; Beutel et al., 2010), with some intra-rift faulting also resulting from extensional stresses in a flexing border fault hanging wall (see Chapter 4). The focusing of strain into the intra-rift fault system has resulted in basin subsidence along the central axis of the valley floor, creating the topographically lowest point within the rift valley (Fig. 5.13C), and forming a catchment basin for axial Lake Magadi since the Late Pleistocene (Behr and Röhrlich, 2000; see also Fig. 4.12, Chapter 4).

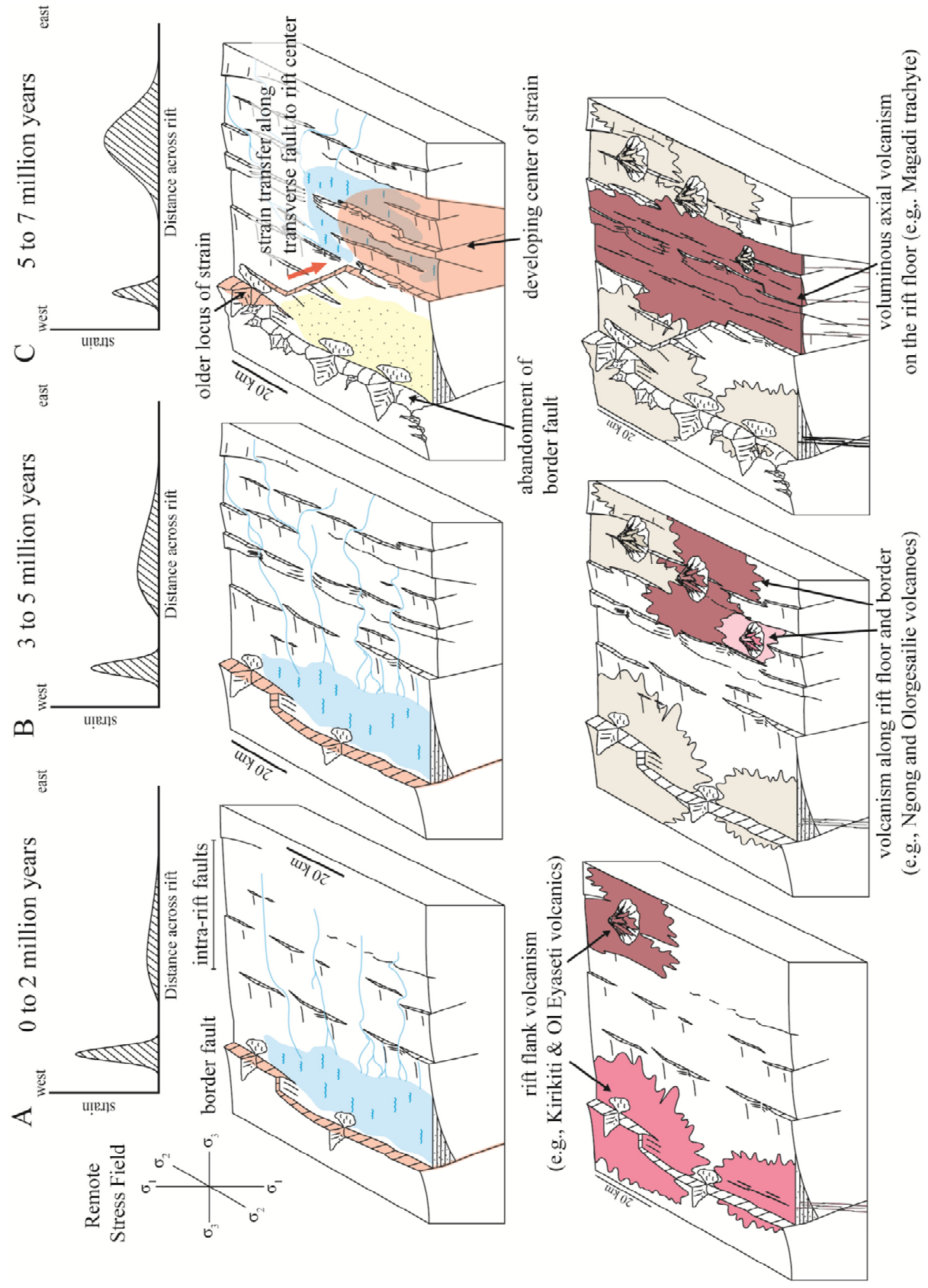


Figure 5.13. (previous page). Conceptual model of the tectonic-magmatic evolution of the Magadi basin and the development of the transverse Kordjya fault. In parts A-C, the top panel shows the distribution of fault strain (idealized graphs) based on existing models of basin evolution in the Eastern rift (e.g., Ebinger, 2005) and fault system analyses from Chapter 4, the middle panel shows the corresponding conceptual rift basin tectonic architecture (areas of high fault strain highlighted light red), and the bottom panel shows the (idealized) distribution of volcanic activity. A: During the earliest stages of rifting (first 2 million years), upper crustal strain is focused on the western border of the basin, and volcanism occurs on the eastern and western boundaries (lavas shown in purple and brown). B: 2-5 million years after rift initiation. Strain is primarily accommodated along the rift borders; however, a system of intra-rift faults begins to develop. Volcanism occurs along both the rift borders and the central rift axis. C: In the past few million years of rifting, fault strain became focused into the center of the Magadi basin below Lake Magadi. The transverse Kordjya fault developed in response to the changing rift basin architecture and kinematically links the center of the basin with older locus of strain along the rift border.

The migration of strain toward the rift center seen in the Magadi basin represents a fundamental change in along-axis segmentation within this section of rift. Developing rift segments in East Africa typically grow and link through along-axis propagation and subsequent interaction of fault and magmatic systems (e.g., Ebinger, 1989; San'kov et al., 2000, 2009; Densmore et al., 2007; Beutel et al., 2010; Allken et al., 2012; Wauthier et al., 2015; see also Chapter 2). Transverse fault zones that create physical and mechanical linkages between rift segments may subsequently develop, re-adjust, or become abandoned in response to rift propagation and evolution (e.g., Chorowicz, 1989; Ebinger, 1989; Morley et al., 1990; Modisi et al., 2000; Densmore et al., 2007; Koehn et al., 2010; Ebinger and Scholz, 2012). Consequently, new transverse faults can potentially reactivate preexisting fabrics during later stages of rifting as first-order rift segments develop and interact. Under this model, the reactivation of non-optimally-oriented, preexisting basement weaknesses may post-date the development of rift-parallel faults, with transverse structures forming at later stages of rift evolution (e.g., the transfer zones between intra-rift fault segments of Corti (2008) and Agostini et al. (2009)). Depending on how σ_3 reorients within interaction zones between newly developing rift segments (Pollard and Aydin, 1984; see also Chapter 2), these transverse faults may also exhibit dip-slip kinematics (e.g., Koehn et al., 2010; Morley, 2010),

rather than forming as the oblique-slip structures predicted during the reactivation of basement fabrics during rift initiation (e.g., Kilembe and Rosendahl, 1992; Ring, 1992; Smith and Mosley, 1993; Le Turdu et al., 1999).

Consistent with the studies described above, a number of lines of evidence suggest that the activation of the Kordjya fault occurred as a response to evolving rift segmentation in the Magadi basin (Fig. 5.13). Firstly, the Kordjya fault system post-dates the formation of the rift-parallel faults in the rift center, which have accommodated a significant proportion of regional tectonic strain (67-80%) within the last ~1 million years (see Chapter 4). The Kordjya fault therefore initiated immediately after, or possibly with, the establishment of this new centralized region of magma- and fault-related strain accommodation within the central rift axis (Fig. 5.13C). Secondly, the SW section of the main Kordjya fault merges into the axial depression (i.e., Lake Magadi) of the Magadi basin. To the NW, the fault cuts across the dominant rift-parallel structural fabric, and can be traced into the Lengitoto segment of the border fault (Atmaoui and Hollnack, 2003; Fig. 5.2). This border fault segment shares the same orientation as the Kordjya fault and likely exploits the same NNW-striking basement weaknesses (Figs. 5.2A and 5.11E). The Kordjya fault is therefore inferred to connect the developing locus of strain in the rift center, with the previous locus of strain along the rift border. Thirdly, the development of the Kordjya system is in part related to a counter-clockwise rotation of the least compressive stress direction locally within the basin. The described counter-clockwise rotation of σ_3 is consistent with a mechanical interaction between offset, left-stepping rift basin segments, as has been inferred for NNW-trending transverse faults and volcanic cone lineaments between the left-stepping Pangani and Natron basins further south (Tanzania) (see Fig. 2.16, Chapter 2).

These observations show that transverse faults exploiting preexisting weaknesses, like the Kordjya fault, may initiate at later stages of rift basin evolution and act as a critical kinematic linkages between developing centers of magmatic and tectonic strain. Although additional NNW-trending transverse faults are present in the Magadi (Fig. 5.1C), the Kordjya fault is unique in that it has accumulated a large amount of throw (>300 m) and has observed links with the Lengitoto border fault segment. These observations suggests that (1) this structure has become a dominant transverse feature within the Magadi basin, and (2) slip along the Kordjya fault has become the preferred mode of strain transfer from the rift border to the rift center. The preference for fault slip along the Kordjya fault, rather than other transverse features, may in part relate to the presence of an influential basement weakness and, potentially, magmatic volatile release in this part of rift. In support of the former, the Kordjya fault has localized along the same NNW-trending, transverse structural zone as the Lengitoto border fault segment. Both these faults line up along the NNW-striking Engorika-Magadi-Lembolos lineament of Smith and Mosley (1993) (Fig. 5.1B), which is a transverse structural fabric that has developed within the Aswa shear zone (Fig. 5.1A). During the initial stages of rifting in Magadi, which were characterized by border fault development, this basement weakness also acted as a locus of strain transfer, accommodating a left-step in the rift bounding fault system (i.e., Smith and Mosley, 1993) (Fig. 5.11B). Observations presented here suggest that this basement weakness continues to play a role in strain transfer in the present day. The Kordjya fault represents an extension of the original Lengitoto fault segment, thereby connecting the newly developed locus strain in the rift center with the older locus of strain along the rift border. By transferring strain to the rift center, the Kordjya fault acts to cut off the Nguruman fault south of the Lengitoto segment (Fig. 5.13C).

The preference for fault slip along the transverse Kordjya fault may have been further assisted by the rise of magmatic fluids within the rift center. Although spring systems situated near Lake Magadi typically rise to the surface along rift-parallel faults, they also emanate from the Kordjya fault along a ~10 km stretch at the southwestern end of the structure (Fig. 5.6). Spring geochemistry, carbon isotope analyses, and diffuse soil CO₂ flux data (Chapters 3 and 4) also support the rise of significant volumes of magmatic volatiles along the NNW-striking Kordjya fault. Fluid infiltration is shown to weaken faults from hydration mineral reactions (Moore and Rymer, 2007) and enhanced pore-fluid pressures (Sibson, 2000), and thus magmatic volatile release could feasibly have assisted in the development of the transverse Kordjya fault in this part of the rift.

Although this study is unable to quantify the extent to which faulting along the Kordjya fault has been assisted by fault-fluid interactions, the idea is consistent with transfer zones in continental rifts elsewhere. For example, transfer faults in the Taupo Rift (New Zealand) produce zones of increased vertical permeability where they intersect rift-parallel faults (Rowland and Simmons, 2012). Factors like this contribute to higher bulk permeabilities in transfer zones compared to rift segments, resulting in enhanced hydrothermal fluid flow (Rowland and Sibson, 2004; Wilson and Rowland, 2016). These zones are prone to fluid-assisted failure, with fault weakening driven by changes in pore-fluid pressure (Rowland and Simmons, 2012). It is therefore possible that the release of magmatic fluids along the Kordjya fault system—in addition to the effects of inherited basement weaknesses—assisted faulting along this part of the Magadi basin, promoting development of a major transfer fault structure.

5.6 Conclusions

This study provides a revised field and remote-sensing analysis of the mechanics of faulting along the transverse Kordjya fault of the Magadi basin. Results demonstrate that the NNW-trending, transverse Kordjya fault is a complex system of NNE-striking, left-stepping, en echelon rift-parallel faults. The structure developed by reactivating rift-parallel faults as oblique-normal faults with a component of sinistral shear. These kinematically coherent oblique-normal faults collectively accommodate dip-slip motion along a reactivated, underlying, NNW-trending basement structure likely related to the Aswa shear zone.

Field analysis of tectonic joint sets and fault slip vectors also show that the least compressive stress in the vicinity of the Kordjya fault rotated to an ENE-WSW direction, in contrast to the ESE-WNW regional extension direction throughout the basin. The tendency for predominantly dip-slip fault activity along transverse features suggests a recent change in rift driving forces in the Magadi basin. These changes are likely the result of an interplay among magma-assisted strain localization at the rift center, inherited crustal fabrics, and a localized counter-clockwise rotation of σ_3 related to interacting segments of the southern Kenya Rift. Since the Mid- to Late Pleistocene, the Kordjya fault has become a dominant transverse feature within the rift basin, and represents a southwestern extension of the original Lengitoto border fault segment. This fault currently acts as a critical kinematic linkage between the newly developed locus strain in the rift center and the older locus of strain along the rift border. The preference for fault slip along the Kordjya fault, rather than other transverse structures, may in part relate to the presence of an influential basement weakness and, potentially, magmatic fluid weakening. By transferring strain to the rift center, the Kordjya fault acts to cut off the Nguruman border fault south of the Lengitoto segment.

Results from this study have implications for the timing and kinematics of fault systems that exploit preexisting basement weaknesses in the EAR. Specifically, field observations and data from this study lead to the following broad conclusions:

- 1) The reactivation of preexisting weaknesses and subsequent formation of transverse faults can postdate the development of widespread rift-parallel fault systems within rift basins.
- 2) Transverse faults throughout the EAR may exhibit predominantly dip-slip kinematics due to local rotations of σ_3 .
- 3) During rift development, preexisting transverse structures can be reactivated in response to evolving magmatic systems and basin tectonic architecture.

It follows that recently activated transverse faults observed throughout the EAR may not only reveal the effects of inherited basement weaknesses on fault system dynamics, but also provide important clues regarding developing magmatic and tectonic strain fields as continental rift basins evolve.

CHAPTER 6: THE ROLE OF SILLS IN FEEDING FLOOD BASALT ERUPTIONS

Chapter based on: Muirhead, J. D., Airoidi, G., White, J.D.L., Rowland, J.V., 2014, Cracking the lid: Sill-fed dikes are the likely feeders of flood basalt eruptions: Earth and Planetary Science Letters, v. 406, p. 187-197, doi:10.1016/j.epsl.2014.08.036.

6.1 Abstract

Although subparallel swarms of dikes are thought to be the primary feeders to voluminous volcanic eruptions, increasing recognition of volumetrically significant sill complexes suggests that they too play an important role in magma ascent through the shallow crust. However, the extent to which sills and interconnected, sill-fed dikes actually transport magma to the earth's surface in many large igneous provinces (LIP) is presently unclear. By analyzing field relationships and dimensions of intrusions of the Ferrar LIP in South Victoria Land, Antarctica, I show that sill-fed dikes were the likely feeders for voluminous flood basalt eruptions. These intrusions are small but numerous, with cumulative dimensions equivalent to a feeder network 308,000 km long and 1.8 m wide. Due to the tremendous aerial extent of this intrusive network, each individual dike-feeder segment would only be required to actively feed magma for 2 to 3 days on average to erupt the 70,000 km³ of flood lavas represented by the Kirkpatrick basalts. The Ferrar intrusions form a broadly-distributed array of small, moderately dipping dikes (<2 km long, 1.8 m wide, 56° mean dip) exhibiting almost any orientation. This sill-fed dike network contrasts with dike swarms conventionally depicted to feed flood basalt provinces, and has the appearance of a variably “cracked lid” atop a sill complex. The cracked lid model may apply to a range of shallow feeder systems (<4 km

depth) intruding sedimentary basins, where the effects of far-field tectonic stresses are negligible and sill intrusions exert the dominant control on dike orientations. This study demonstrates that sill inflation, and resulting deformation of surrounding host rock, plays a critical role in the ascent of magma in shallow volcanic systems that span the full spectrum of eruptive volumes.

6.2 Introduction

Dike intrusion is conventionally considered the dominant process by which magma ascends through cold lithosphere to feed eruptions at the surface (Anderson, 1951; Lister and Kerr, 1991; Rubin, 1995). In particular, giant dike swarms (20-40 m wide, 100s-1000s of km long) are often invoked as the primary feeders to flood basalt eruptions (Ernst et al., 1995; Self et al., 1997; Coffin et al., 2006; Ray et al., 2007; Bryan and Ernst, 2008; Hooper et al., 2010). This key role of regionally extensive, collinear swarms of dikes has been further supported by thermo-mechanical modeling of large-scale intrusions (Fialko and Rubin, 1999) and geochemical links between dike swarms and overlying flood basalt lavas (Hanghøj et al., 2003).

Recent field observations, however, point to limitations in this model. Although most observations of giant dikes occur in Precambrian shields, where they are inferred to have intruded at paleodepths of 6-15 km (e.g. Proterozoic dikes of the Canadian shield: Ernst et al., 1995), sills are volumetrically dominant at shallower paleodepths (<4 km) in many flood basalt provinces. Examples include the 250 Ma Siberian Traps (Hawkesworth et al., 1995), 1.1 Ga Mid-Continental Rift, Canada (Hollings et al., 2010), and 183 Ma western Karoo igneous province, South Africa (Marsh et al., 1997; Chevallier and Woodford, 1999; Hastie et

al., 2014). Seismic reflection studies by Cartwright and Hansen (2006) have also revealed interconnected sills over vertical distances of 8-12 km in the Møre and Vøring Basins, offshore Norway. These results imply that sill complexes may play a more important role in shallow magma ascent than generally considered.

However, the extent to which sills and sill-fed dikes are able to feed voluminous lava eruptions at the Earth's surface remains unclear (Larsen and Marcussen, 1992; Hald and Tegner, 2000; Cartwright and Hansen, 2006). For many LIPs, the sub-vertical conduits (dikes) connecting flood lavas to underlying sills have not been recognized (e.g., the 1270 Ma Mackenzie and 723 Ma Franklin LIPs: Ernst and Baragar, 1992; Bedard et al., 2012). This owes in part to a lack of preservation at relevant stratigraphic levels. Consequently, the processes controlling the upward transport of magma and the geometric relationships between sills, dikes and lavas are poorly constrained for many sill-dominated LIPs. For example, the 250 Ma Siberian LIP comprises a shallow (<5 km paleodepth) intrusive system dominated by sills (Czamanske et al., 1995; Arndt et al., 1998; Li et al., 2009). Although the intrusive and extrusive components of the system are geochemically linked (Fedorenko and Czamanske, 1997), little has been published about their physical connections. Geochemical studies demonstrate that sills formed the lateral component of the conduit system for the Siberian traps lavas (Naldrett et al., 1995). However, questions remain regarding: (1) the geometrical relationships between sills, dikes and lavas, (2) the processes driving the formation of dikes, and (3) the eruption feeding capacity of the sill-fed dike network that possibly fed the Siberian lavas.

Additional challenges in studies of sill-fed dike networks arise from the limitations of seismic reflection methods, which are key tools for visualizing the 3-D geometry of sill

complexes in LIPs (e.g., Malthe-Sørensen et al., 2004; Thomson and Hutton, 2004; Hansen and Cartwright, 2006a; Schofield et al., 2012a; Magee et al., 2013a). For example, seismic reflection cannot discern thin (<10 m), sub-vertical structures such as dikes, which may be instrumental for transporting magma between sills and the Earth's surface in these systems. Despite these limitations, seismic reflection surveys have successfully detected volcanic constructs a few hundred meters above the lateral terminations of sills in the Ceduna basin, offshore Australia (Magee et al., 2013a), and the Faeroe-Shetland basin, offshore UK (Davies et al., 2002). Geophysical studies such as these support the role of sills and sill-fed dikes in feeding eruptions, with the Ceduna examples having relatively small eruptive volumes (typically <10 km³: Magee et al., 2013a).

This study takes a novel approach to investigate the eruption-feeding capacity of sill complexes using observations from shallow (<4 km paleodepth), sill-fed intrusions of the 183 Ma Ferrar LIP, Antarctica (Encarnación et al., 1996). Previous models did not consider the role these intrusions played in feeding the overlying flood lavas (Elliot and Fleming, 2004). It is instead inferred that >100 m-thick megadikes or subparallel dike swarms transported magma upward through the shallow crust to eruption. However, to date, neither have been discovered (Elliot and Fleming, 2004, 2008). To re-examine the necessity of such regionally-extensive, subparallel dike swarms, this study addresses the following question: might the observed network of sill-fed dikes be responsible for bringing magma to the surface from shallow depths?

6.3 Review of intrusion dynamics of the Ferrar LIP

The Ferrar LIP is exposed for 3,500 km along the Transantarctic Mountains (Elliot and Fleming, 2004). Post-Ferrar uplift has produced a series of tilted fault blocks, and exhumation of the Ferrar intrusions with relatively little deformation (Gleadow and Fitzgerald, 1987; Marsh, 2004). Volume estimates of the Ferrar LIP yield $\sim 300,000 \text{ km}^3$ of magma (Ross et al., 2005), with dikes comprising $<1\%$ (Fig. 6.1). The greatest proportion of magma was emplaced as sills ($170,000 \text{ km}^3$), while the Dufek layered mafic intrusion and Kirkpatrick flood basalts represent approximately $60,000 \text{ km}^3$ and $70,000 \text{ km}^3$ of magma, respectively (Ross et al., 2005, and references therein).

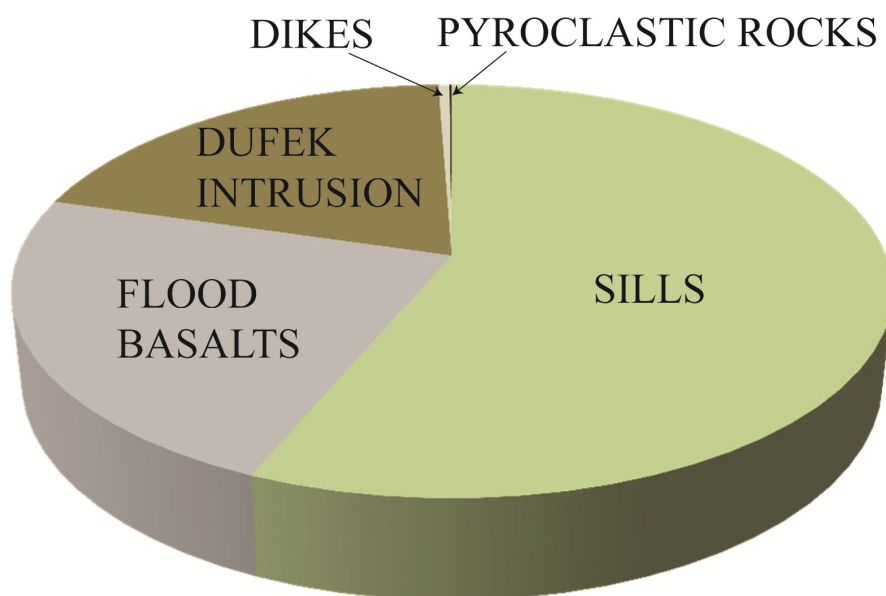


Figure 6.1. Pie chart illustrating the relative volumes of the various components of the Ferrar LIP. Volume estimates from Ross et al. (2005). The inferred volume of dikes is calculated from this study.

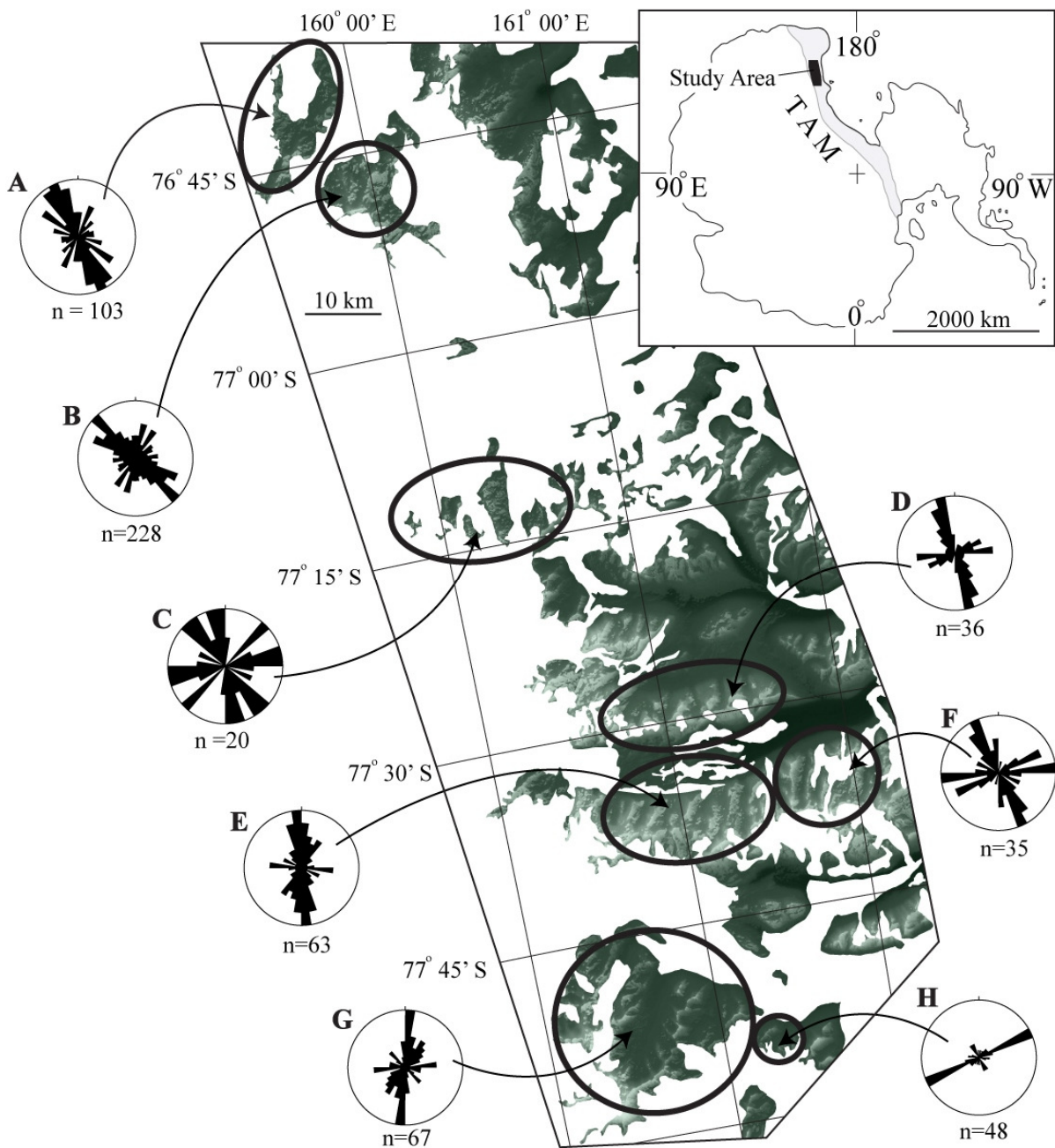


Figure 6.2. DEM image of areas of South Victoria Land examined in this study. Areas of persistent ice cover are annotated white. Dikes were only examined at locations where Beacon Supergroup and/or Mawson Formation rocks are present. Rose diagrams are of dike strikes. Only areas where >20 dikes were measured are presented here, and include Allan Hills (A), Coombs Hills (B), Head Mountains (C), Olympus range (D), Asgard Range (E), Fenrir Valley (F), Beacon Heights (G), and Terra Cotta Mountain-Mt Kuipers (H). Inset (top right) shows the location of the study area in Antarctica. TAM = Transantarctic Mountains.

South Victoria Land, Antarctica, provides superb exposures of the shallow (<4 km paleodepth) plumbing system of the Ferrar LIP (see Muirhead et al. (2012) for a detailed review) (Figs. 6.2 and 6.3). Up to 2000 m-high vertical exposures of interconnected dikes and sills are present over a ~10,000 km² area, and some sills can be traced laterally >50 km along their lengths (Marsh and Zeig, 1997; Marsh, 2004). Key areas along the Transantarctic Mountains (i.e., North Victoria Land and Central Transantarctic Mountains) exhibit similar intrusive networks, suggesting that the Ferrar LIP forms an interconnected sill network within the Beacon Supergroup along its entire length (Elliot and Fleming, 2004; Leat, 2008; Muirhead et al., 2012). In South Victoria Land, Ferrar dike intrusions are hosted by a ~2.5 km-thick sequence of sedimentary rocks (Beacon Supergroup) and volcanoclastics (Mawson Formation), and are rarely observed dissecting the underlying basement granitoids (Table 6.1). The Beacon Supergroup dips shallowly, 1-2° to the west (Gleadow and Fitzgerald, 1987), although significant local variations exist where strata have been buckled and tilted from the forceful intrusion of Ferrar sills (Grapes et al., 1974; Korsch, 1984; Pyne, 1984; Airoidi et al., 2011). While no regionally distributed, sub-parallel dike swarms are known (Elliot and Fleming, 2004, 2008), swarms of moderately dipping, sill-fed dikes extend from sills at a number of locations, including Coombs Hills, Mt Gran, Terra Cotta Mountain, Allan Hills, and Pearse Valley (Elliot and Fleming, 2004; 2008; White et al., 2009; Muirhead et al., 2012: Figs. 6.3 and 6.4).

Early work on intrusion mechanics of the Ferrar LIP highlighted the governing role of sills (Grapes et al., 1974; Korsch, 1984; Pyne, 1984). A later study by Wilson (1993), however, suggested that dike orientations in South Victoria Land were controlled by a far-field transtensional environment. Recent work has tested both models by combining structural

analyses (White et al., 2009; Airoidi et al., 2011; Muirhead et al., 2012) and anisotropy of magnetic susceptibility (AMS) analysis of magma flow directions (Guegan, 2006; Airoidi et al., 2012). These studies point to a sill-driven model for Ferrar dike emplacement, and suggest that evidence for a far-field extensional, or trans-tensional, tectonic regime during Ferrar dike emplacement is lacking.

Table 6.1. Simplified stratigraphy of South Victoria Land, Antarctica. Table modified from McClintock (2001) and Airoidi et al. (2011).

		Stratigraphic Unit	Description	Max. Thickness
Jurassic	Ferrar Group	Kirkpatrick Basalt	Basalt lava flows and pillow-palagonite breccias, with intercalated Mawson Formation and Beacon Supergroup deposits	380
		Ferrar Dolerite	Tholeiitic sills, dikes and localized sheet swarms	
		Mawson Formation	Heterolithic, poorly - to unbedded basaltic tuff-breccia and lapilli-tuff, minor bedded lapilli-tuff and tuff. Widespread peperite, hyaloclastite and swirly dikes	400+
Triassic	Victoria Group	Lashly Formation	Arkosic and volcanoclastic sandstone, greenish grey and grey siltstone. Roots and stems are common in the lower part	520+
		Feather Conglomerate	Quartz pebble conglomerate, quartzose and arkose sandstone, siltstone and grit	220
Permian	Victoria Group	Weller Coal Measures	Quartzose and minor arkosic sandstone and minor carbonaceous siltstone. Pebbles and boulders appear scattered and in lenses. Coal, logs and stems in the upper part	250
		Meschel Tillite	Tillite, conglomerate, sandstone and siltstone. Locally slump-folded	70
Devonian	BEACON SUPERGROUP Taylor Group	Aztec Siltstone	Siltstone and sandstone. Fish fossils, plant roots, mudcracks and ripplemarks are common	220
		Beacon Heights Orthoquartzite	Indurated quartz and arenites with occasional quartz grit lenses. Rare lycopod stems	340
		Arena Sandstone	Quartz arenites and siltstone, ferruginous layers, burrows and trails	360
		Altar Mountain Formation	Sandstone, siltstone and subarkose. Burrows and trails	240
		New Mountain Sandstone	Quartzose sandstone with minor siltstone, breccia, conglomerate and fossils	270
		Terra Cotta Siltstone	Siltstone with interbedded sandstone layers	60
		Windy Gully Sandstone	Pebbly quartzose sandstone	50
Cambrian-Ordovician	Basement	Granite Harbour Intrusives	Undifferentiated granitoids	
		Skelton Group	Upper amphibolite facies metasediments	

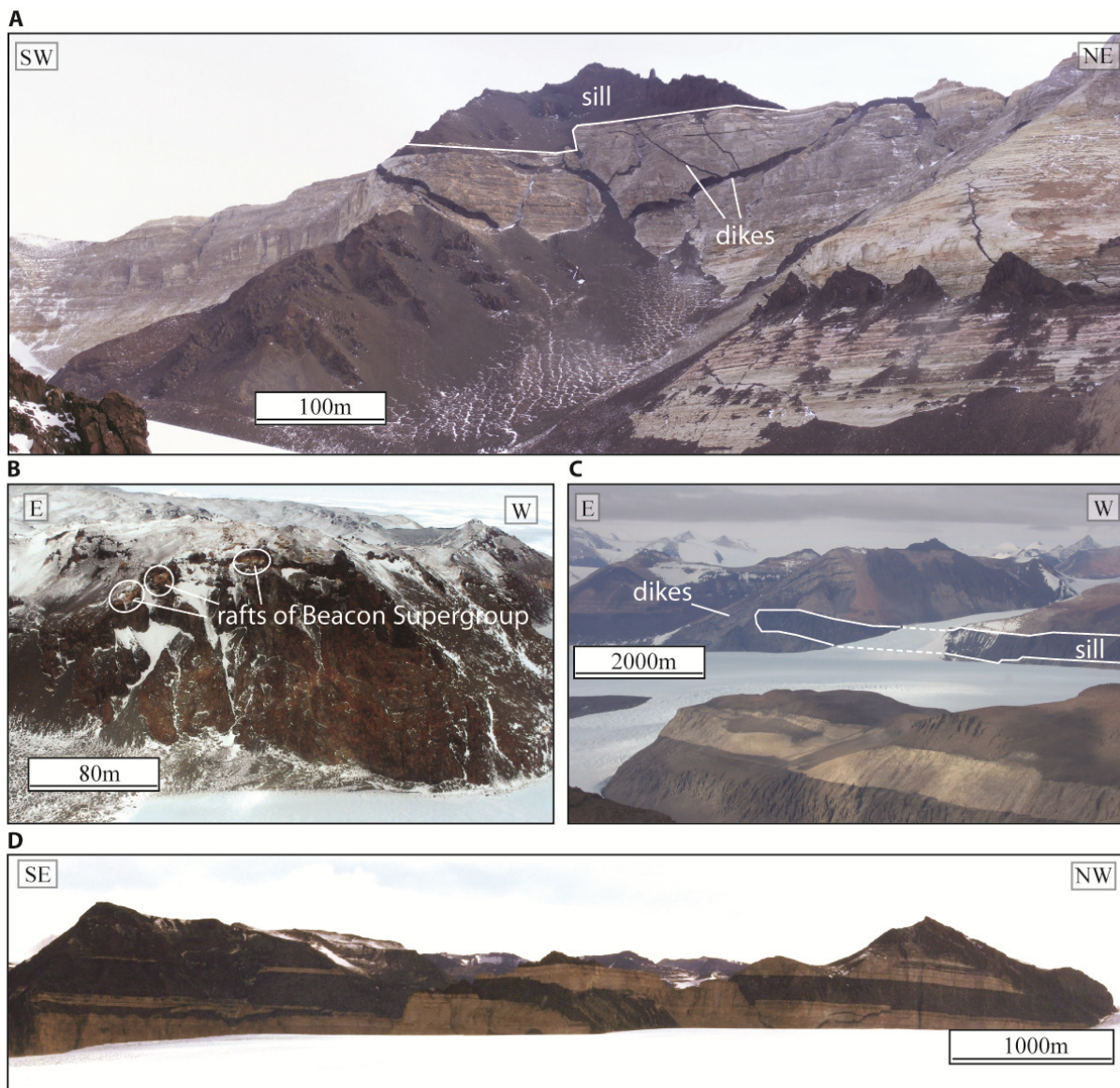


Figure 6.3. Photos illustrating the shallow (<4 km paleodepth) plumbing system of the Ferrar LIP in South Victoria Land. A: Dikes at Terra Cotta Mountain ascend the stratigraphy and connect to an overlying sill. B: Exposure of a thick sill at Coombs Hills with country rock rafts near the upper contact. C: Exposures of extensive sills and dike swarms near Taylor Glacier. D: Sills intruding Beacon Supergroup rocks in the Beacon Heights region.

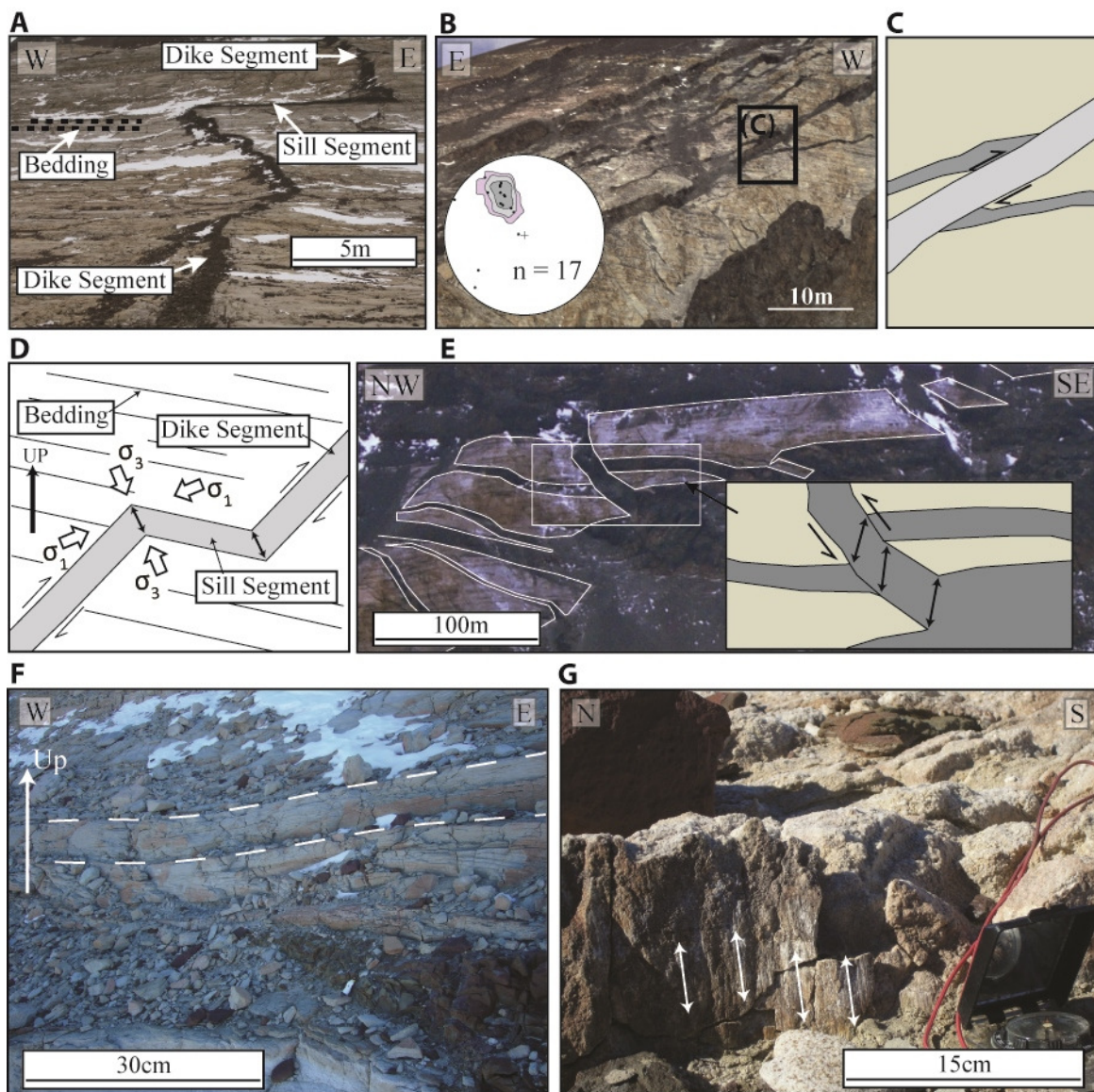


Figure 6.4. A: Stepped dike-sill geometry at Allan Hills. B: Moderately inclined dikes on the northern slopes of Terra Cotta Mountain. Contour plot of poles to dike planes from Muirhead et al. (2012). C: Schematic of cross-cutting dikes highlighted in B. Half arrows indicate the inferred sense of shear given the offset accrued on the early intruded dike (dark grey). D: Simplified kinematic model after Muirhead et al. (2012) for stepped dike-sill intrusions. Opening normal to both the sill and dike results in a dilation vector (double sided arrow) oblique to both the dike and sill plane, and a component of reverse shear along the dike plane (half arrows). Bold white arrows show the inferred local orientations the least (σ_3) and greatest (σ_1) compressive stresses. E: Photo of intrusions seen from Pearse Valley. Moderately inclined dikes extend from a sill periphery into an overlying sill. Inset illustrates dike kinematics inferred from cross-cutting relationships between dikes. F: Folded strata at the lateral termination of a sill segment. G: Mineral striations on a dike selvage at Allan Hills. Double sided arrows indicate the orientation of the striations.

The current line of thinking is that dike intrusions in the upper 4 km of the plumbing system represent the response of the country rock to forceful intrusion of sills (Muirhead et al., 2012). Ferrar dikes are typically sandwiched between larger sills, producing stepped, dike-sill geometries (Fig. 6.4a). Field observations show that country rock at the lateral ends of sill segments was buckled upward (Grapes et al., 1974; Korsch, 1984; Airoidi et al., 2011: Fig. 6.4f), generating local extensional stresses (Johnson and Pollard, 1973; Gouly and Schofield, 2008). These stresses led to the formation of fractures that could be exploited by magma that ascended the stratigraphy before deflecting back into sills at higher stratigraphic levels (Thompson and Schofield, 2008; Airoidi et al., 2011; Muirhead et al., 2012: Fig. 6.4a and e). AMS studies support these assertions, demonstrating that magma was “passively” drawn into localized zones of high stress generated from underlying sills, rather than actively forming fractures ahead of the dike tip (Airoidi et al., 2012). In these instances, advancement of the crack in front of the dike did not depend solely on magma pressures in the inflating dike tip, and subsequent widening of dike segments was enhanced by jacking-up of the crust above underlying sills (Fig. 6.4a and d). The proposed process of intrusion is consistent with dike and sheet formation in sill complexes elsewhere, based on field observations (Johnson and Pollard, 1973; Polteau et al., 2008), numerical simulations (Malthe-Sørensen et al., 2004), laboratory experiments (Galland et al., 2009), and seismic reflection studies (Thomson and Hutton, 2004; Hansen and Cartwright, 2006a; Thompson and Schofield, 2008; Magee et al., 2014).

In line with analogue modelling of sill-fed dike intrusions (Galland et al., 2009), Ferrar dikes exhibit a component of reverse shear along the dike plane (Muirhead et al., 2012). For example, exposures of dikes at Terra Cotta Mountain and Pearse Valley show that

dikes dissected by later intrusions were uplifted on the hangingwall side (Morrison, 1989: Fig. 6.4e). Striated surfaces along dike margins further support a component of shear during the intrusion process (Fig. 6.4g), although the timing of these shearing events relative to dike emplacement is difficult to constrain (Muirhead et al., 2012). Similar kinematic models have been invoked for cone sheet intrusions on the Canary Islands (Schirnack et al., 1999), and laterally-emplaced regional dikes deflected into inclined sheets at Ardnamurchan, Scotland (Magee et al., 2012). In all, these recent insights add to a growing body of evidence that the shallowly intruded dikes of the Ferrar LIP formed under a dominantly sill-driven process.

6.4 Methods

To establish a regional picture of the orientations and dimensions of intrusions in South Victoria Land, 644 sill-fed dikes were analyzed, comprising a number of irregular or *en echelon* stepping segments (Appendix D). Dike lengths, widths and strikes were collected from a combination of published maps and datasets (Korsch, 1984; Pyne, 1984; Guegan, 2006; Airoidi et al., 2011; Muirhead et al., 2012; Cox et al., 2012) and DigitalGlobe satellite imagery (1 to 2 m-horizontal resolution) courtesy of Google Earth (Fig. 6.5).

As a result of the data-mining method and the nature of the exposures, certain limitations exist in the dataset. Scree and ice cover limited traceability of ~75% of dikes, so the reported lengths are minimum values. However, since no dikes can be traced across glaciers into neighboring nunataks, it is unlikely that many intrusions exceed lengths of a few km. Dike segment widths were acquired from four previous field studies (Appendix D), and in many instances are not matched with length data, so aspect ratios could not be examined for most intrusions. The segment width data presented here (n = 401) is not as complete as the

length and strike data, as true dike widths must be collected in the field. Nonetheless, the calculated 1.8 m mean width from 401 dike segments is in agreement with assertions of previous authors, estimating Ferrar dikes to be between 1 and 2 m wide (Pyne, 1984; Wilson, 1993; Ross et al., 2008).

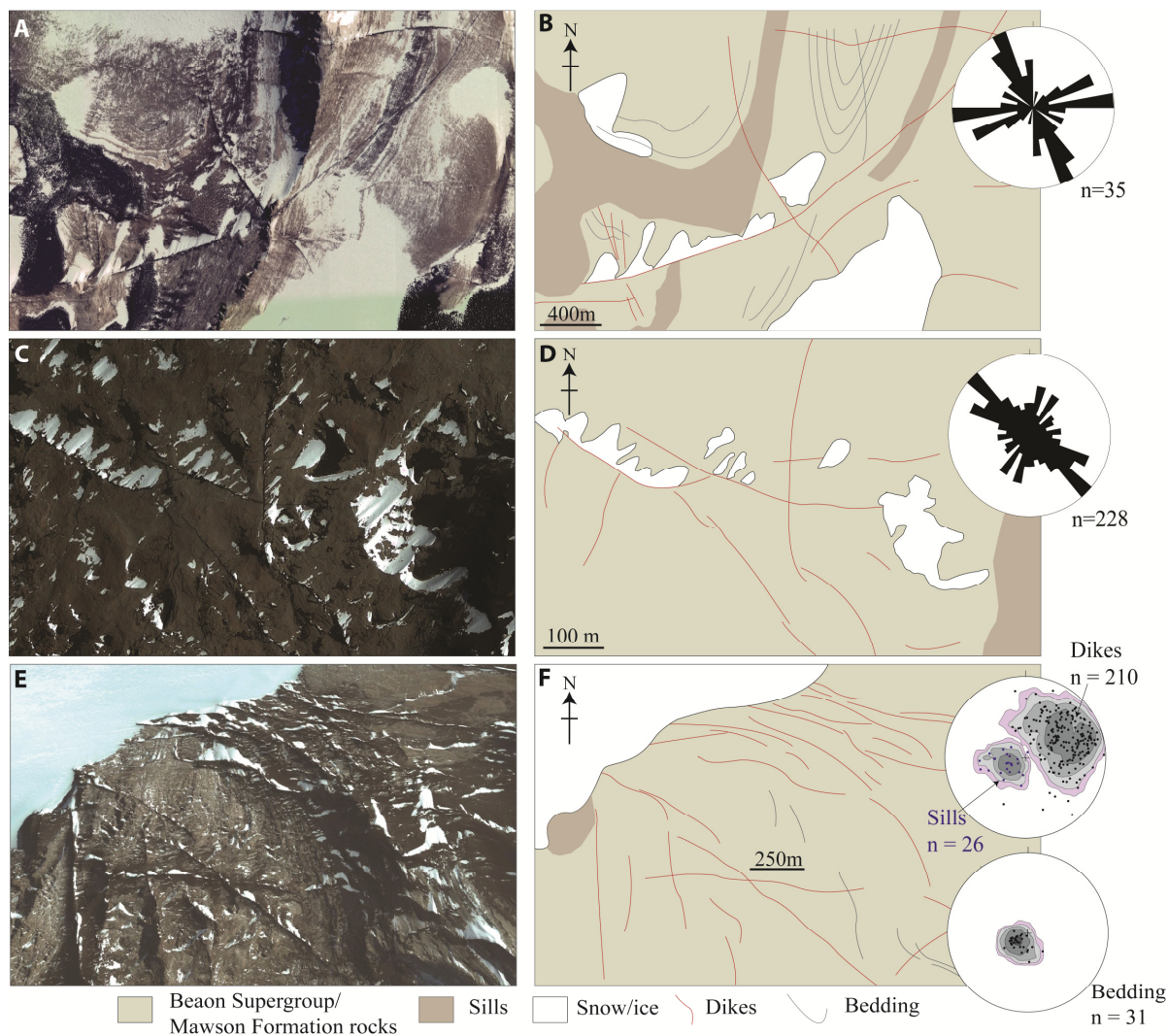


Figure 6.5. Google Earth images of Ferrar dikes intruding Beaon Supergroup and Mawson Formation rocks in South Victoria Land. A: Plan-view image of dikes in the Fenrir Valley. B: Simplified schematic of A. Rose diagram is of measured dike strikes in the Fenrir Valley from this study. C: Plan-view image of dikes at Coombs Hills. D: Simplified schematic of C. Rose diagram is of measured dike strikes at Coombs Hills from this study. E: Oblique aerial view of a sub-parallel swarm of moderately dipping dikes at Allan Hills. F: Simplified schematic of E. Contour plots are of poles to dike, sill, and bedding planes collected in the field by Muirhead et al. (2012). Note the moderate dip of the dikes as well as the common dip direction.

6.5 Results

Dikes mapped in this study are exposed in the Beacon Supergroup and Mawson Formation over an area of 458 km². The dikes are broadly distributed, with mean lengths and widths of 550 m and 1.8 m, respectively (Fig. 6.6). Field analyses at Allan Hills and Terra Cotta Mountain (Airoidi et al., 2011; Muirhead et al., 2012) show that dikes are moderately dipping (56° mean; Fig. 6.6c). Where dikes form local, subparallel arrays (e.g., Allan Hills and Terra Cotta Mountain), they also exhibit common dip directions (Figs. 6.4b and 6.5f), consistent with intrusion under local, magma-induced stresses (Klausen, 2004; Muirhead et al., 2012). The complete catalogue of dike strikes shows that all orientations are well represented and, similarly, length-weighted histograms of dike strikes show a wide range of orientations (Fig. 6.7). A weak NNW-SSE alignment is, however, observed in the length-weighted strike data, the implications of which are discussed further in Section 6.6.3.

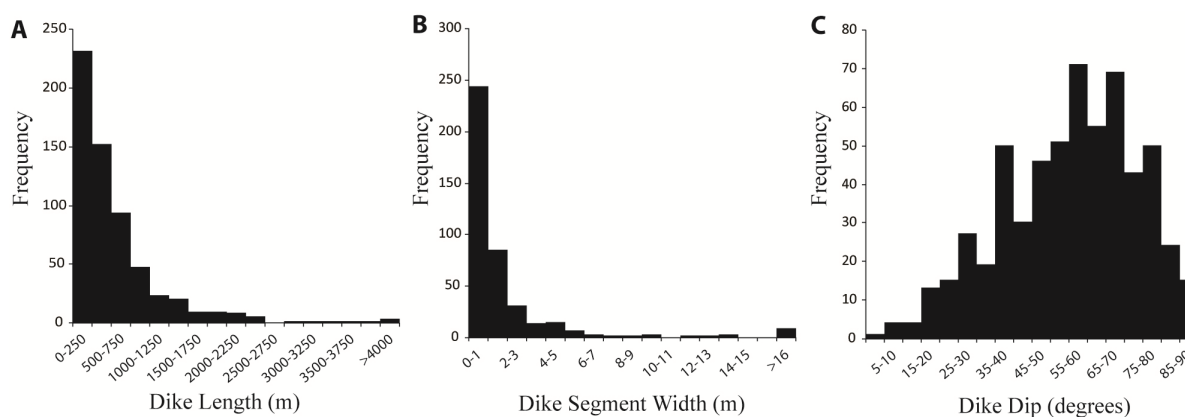


Figure 6.6. A: Frequency histogram of dike lengths measure in this study. B: Frequency histogram of measured dike segment widths. C: Frequency histogram of observed dike dips.

The aerial extent and volume of Ferrar dikes was calculated by first considering the ratio of dikes to country rock in the study area. The 595 dikes mapped in plan view represent

a combined aerial extent of 0.56 km^2 . This gives an average dike to country rock ratio of 1:815. Applying the same ratio over the full extent of the Ferrar province ($3,000 \times 150 \text{ km}$: Ross et al. 2005), Ferrar dikes can be inferred to have covered a total area of 550 km^2 , corresponding to a volume of $1,380 \text{ km}^3$ within the 2.5 km-thick Beacon Supergroup and Mawson Formation host rocks. For comparison, a single fissure of equivalent size would be 3,000 km long \times 184 m wide, or, using the mean width of 1.8 m, a cumulative dike network totalling 308,000 km in length.

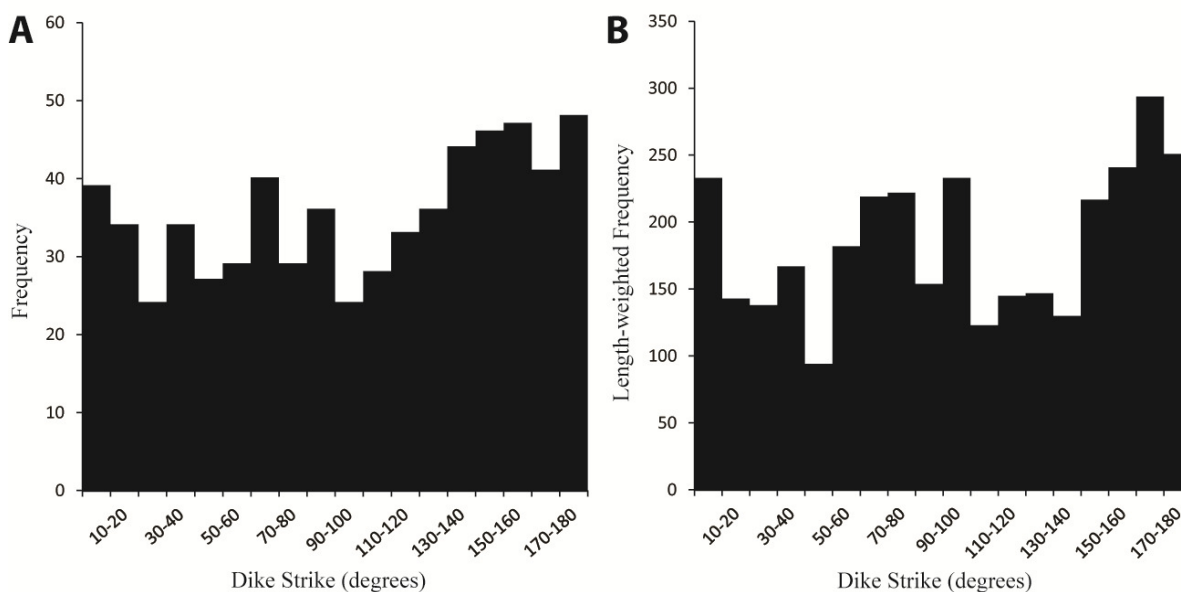


Figure 6.7. A: Frequency histogram of dike strikes measure in this study. B: Length-weighted frequency histogram of dike strike.

6.6 Discussion

6.6.1 Did the inferred Ferrar dike-fissure network feed the flood basalts?

Two basic conditions must be met to conclude that sill-fed dikes of the Ferrar large igneous province fed flood basalt lavas: (1) the intrusions must have extended all the way to

the surface; and (2) the size of the network must be sufficient to erupt the 70,000 km³ of flood lavas on a reasonable timescale. Tracing subsurface dikes vertically to the surface is challenging in the Ferrar, due to rare exposure of the basal contact of the Kirkpatrick lavas. However, a close kinship is observed between Ferrar dikes and volcanic rocks of the Mawson Formation (McClintock and White, 2006). Shallowly intruded sills and sill-fed dikes at Coombs Hills and Shapeless Mountain transition at their lateral ends into intrusive tuff breccias (Korsch, 1984; Elliot and Grimes, 2011), indicating that these sill-fed dikes did indeed feed surface eruptions (Gunn and Warren, 1962; McClintock and White, 2006; Airoidi et al., 2011; Elliot and Grimes, 2011). Furthermore, this study reveals that the dike to country rock ratio remained constant as intrusions ascended toward the surface. This is shown in the Coombs-Allan Hills region (~800-0 m paleodepth: Ross et al., 2008), where the dike to country rock ratio of 1:880 is comparable with the mean value of 1:815. It would therefore be unreasonable to assume that the sill-fed dike network terminated abruptly only a few tens of meters below the paleosurface. Lastly, in areas exhibiting evidence for extensive volcanism, such as nested diatremes, mafic pyroclastic density currents, fall deposits, and basalt lavas (e.g. Coombs Hills and Allan Hills: White and McClintock, 2001; Ross and White, 2005; McClintock and White, 2006; Ross et al., 2008), the shallow plumbing system is dominated by sill-fed dikes; no other potential feeders are recognized. Until competing shallow dike-feeders are discovered throughout the Ferrar LIP, it is fair to assume that the sill-fed dike network locally extended all the way to the surface.

A relatively simple approach may be taken to address criterion (2), the feeding capacity of the sill-fed dike network. A reasonable lava effusion rate was applied to the cumulative dike network (308,000 km long) to establish the time required to produce the

70,000 km³ Kirkpatrick flood basalts. This method has been similarly used to analyze dike-feeder systems of the Deccan province (Ray et al., 2007). Lava effusion rates are taken from the 1873-74 eruption of Laki, Iceland, which produced 14.7 ± 1.0 km³ of lava, representing the most voluminous basaltic lava eruption of historic time. During this eruption, which lasted 8 months, lava erupted during discrete events on individual dike-fissure segments that were active for weeks to months at a time (Thordarson et al., 1996), with maximum effusion rates of ~ 2 m³ s⁻¹ per meter length of fissure (Self et al., 1997). After a few days to weeks of activity, lava effusion on each individual segment reduced and focused on a few point sources (central magma conduits) along the fissures. In some respects, flood basalt eruptions represent scaled-up versions of these basaltic fissure eruptions (Bryan and Ferrari, 2013). Individual flood basalt lavas erupt for years to decades at a time (Self et al., 1997), providing constraints on the timescales over which lavas may be fed from individual feeder dikes. Activity across the entire fissure network occurs over 10^5 - 10^6 years (Ray et al., 2007; Bryan and Ferrari, 2013), with decades-long eruptions alternating with tens to hundreds of millenia of inactivity. Assigning a conservative lava effusion rate of 1 m³ s⁻¹ per meter of dike-feeder length in the Ferrar LIP (i.e., mean effusion rates for Kilauea: Self et al., 1997), each individual segment (10^2 - 10^3 m long) of the 308,000 km-long, dike-feeder system requires an average of only 2 to 3 days of activity to cumulatively produce the volume of the Kirkpatrick basalts over the timescale of Ferrar LIP emplacement ($\sim 10^6$ years: Heimann et al., 1994). Given that individual fissure segments in large-scale basaltic eruptions are observed and theoretically demonstrated to have eruptive durations of 2-3 weeks (Thordarson et al., 1996; Thordarson and Self, 1998), it is reasonable to conclude that the Ferrar dike network transported magma

upward to eruption throughout the area of its shallow plumbing system to feed the Kirkpatrick flood lavas.

6.6.2 Additional ascent through conduits and roof collapse

In addition to the dike network, volcanic plugs observed at Coombs Hills, Allan Hills, and Shapeless Mountain have been highlighted as potential feeders to the flood basalts (Korsch, 1984; Reubi et al., 2005; Ross et al., 2008). These plugs likely represent complex conduit structures that could have contributed to upward magma transport at shallow depths. They are probably sites where magma flow in dikes localized into point sources (e.g. Delaney and Pollard, 1982; refer also to the “pyroclastic massifs” of Chapter 7), which were enhanced at dike intersections (cf. Appendix 1 of Korsch, 1984). Furthermore, large tilted blocks (up to 500 m in diameter), interpreted by White et al. (2009) as fragmented sill roofs, have been observed “floating” in shallow sills that intruded a few hundred meters from the paleosurface (Fig. 6.3b). Based on these observations, White et al. (2009) suggest that wholesale breakup of country rock occurred at some localities above shallowly intruded sills. The model presented here (Fig. 6.8) is complementary to this hypothesis, as a variably oriented, crosscutting network of dikes extending vertically from a shallow sill to the surface, or an overlying partially molten sill, is expected to isolate domains of country rock, which can then be engulfed in magma. The domains of country rock described by White et al. (2009) may, however, represent “bridges” that became isolated as adjacent sill segments coalesced (Hutton et al., 2009; Scholfied et al., 2012a). The isolated blocks observed in Ferrar sills, up to 500 m in diameter, are an order of magnitude larger than broken bridges observed in shallow sills elsewhere (e.g. Theron Mountains, Antarctica: Hutton, 2009).

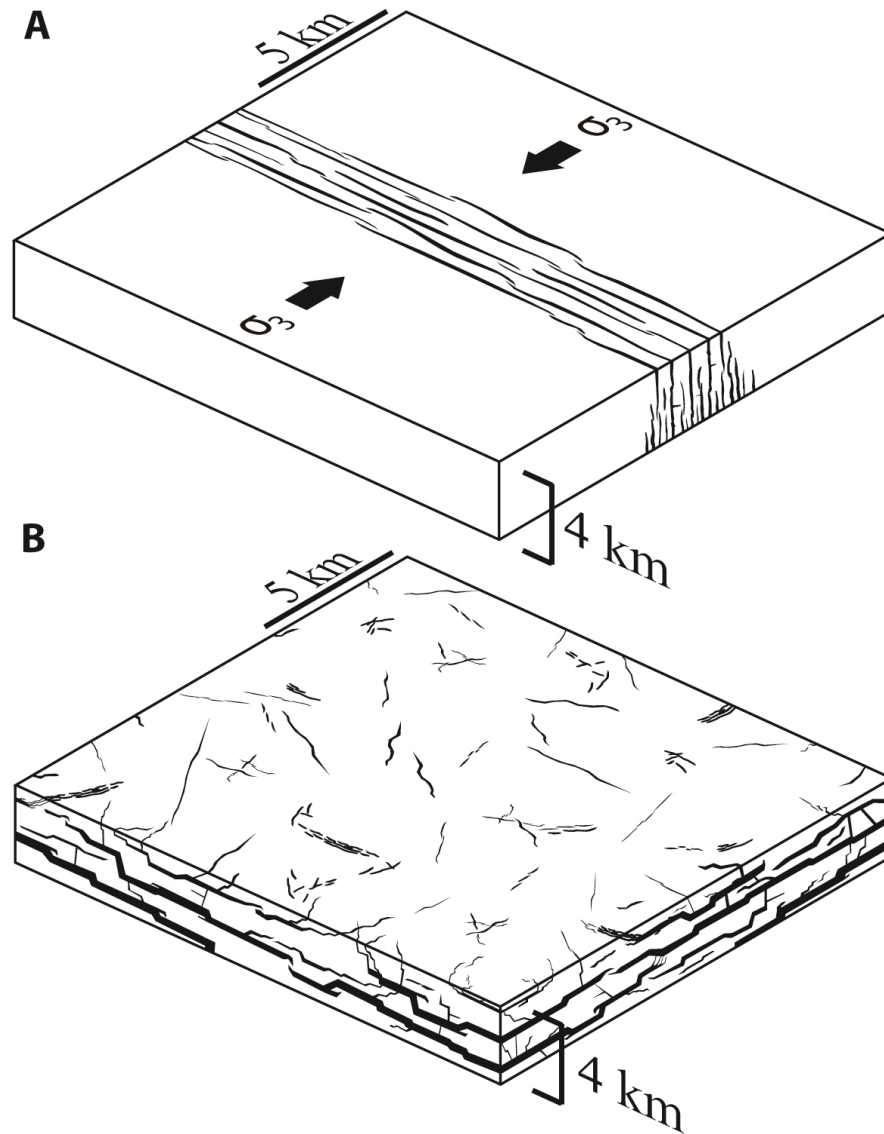


Figure 6.8. Schematic illustration of end-member, shallow (< 4 km depth) feeder systems for flood basalt provinces. A: Long, subparallel aligned dikes oriented perpendicular to a far-field least principal stress direction. Note that on the scale of a craton (i.e. 1000s of km), swarms like these can also form a radial pattern (Ernst et al., 1995). B: The cracked lid model. Short dikes of almost any orientation overlie a network of sills.

6.6.3 The cracked lid: an end-member feeder style for flood basalt volcanism

The observed dike network of the Ferrar is at odds with the traditional model of shallow magma ascent invoked for many LIPs, which involve subparallel swarms of large,

steep dikes (>100 km long, 20-40 m wide, >75° dip) (Ernst et al., 1995; Ray et al., 2007; Bryan and Ernst, 2008). In contrast, the Ferrar's sill-fed dikes form a broadly-distributed array of smaller, moderately dipping intrusions (<2 km long, 1.8 m wide, 56° mean dip) of any orientation. Although a very weak NNW-SSE trend is present in the length-weighted strike data (Fig. 6.7), it is significantly weaker than those produced by dikes forming in extensional tectonic regimes in magmatic rifts (e.g., Tertiary rifts of Iceland: Gudmundsson, 1995a; 2002) or giant dike systems (e.g., Okavango and Lembobobo dike swarms; Aubourg et al., 2008; Klausen, 2009). Rather, Ferrar dike orientations have similarities to dike networks that intruded into isotropic stress regimes, such as the Nasi-Pune swarm of the 66 Ma Deccan Province, India (Hooper, 1990; Vanderklusen et al., 2011), and dikes of the Navajo volcanic field, USA (Laughlin et al., 1986). These observations imply that a regional extensional stress regime did not influence the orientations of Ferrar dikes at shallow paleodepths (<4 km).

This conclusion is in line with recent studies addressing the controls on Ferrar dike formation (White et al., 2009; Airoidi et al., 2011, 2012; Muirhead et al., 2012). These studies have dismissed shallow dike emplacement as part of a far-field extensional stress regime based on (1) the predominance of Ferrar sills and sill-fed dikes, (2) the moderate dips (~50° mean) exhibited by dikes, and (3) the lack of steeply dipping, subparallel dike swarms. Instead, dikes at Allan Hills, Coombs Hills and Terra Cotta Mountain appear to have been emplaced into a local magmatic stress regime, with dikes forming at the propagation fronts of sills. It is therefore possible that the weak NNW-SSE trend in Ferrar dike orientations represents a common process related to sill formation, such as a preferred propagation direction (White et al., 2005).

This sill-driven, dike feeder system creates a remarkable scene in plan view, resembling a variably “cracked lid” overlying a sill network (Fig. 6.8). This cracked lid model represents an end-member example of a flood basalt feeder system, where the effects of far-field tectonic stresses are negligible and sill intrusions exert the dominant control on dike orientations.

6.6.4 When does the cracked lid arise?

The cracked lid may be the archetypal model for shallow feeder systems of LIPs that intruded sedimentary basins where the influence of any far-field extensional tectonics is negligible. Seismically observed, sill-dominated LIPs intrude sedimentary basins in offshore Australia (Magee et al., 2013a; Rohrman, 2013), Norway (Thomson and Hutton, 2004; Cartwright and Hansen, 2006; Thomson and Schofield, 2008) and Senegal (Hansen et al., 2008). The processes governing dike formation in these provinces are strikingly similar to those inferred for the Ferrar sill-fed dikes. For example, shallowly dipping, concentric dikes of any orientation extend from the peripheries of sills and form in response to sill-roof uplift (Thomson and Hutton, 2004). Observations of sill-fed dikes in seismically observed LIPs are, however, restricted to thicker (>10 m), shallowly dipping ($<40^\circ$) intrusions. Thus, the distribution and geometry of thinner dikes (<10 m) comprising the vertical component of these feeder systems cannot be easily resolved. Nonetheless, the similarity in dike formation processes combined with the abundance of sills in seismically observed LIPs suggests that a cracked lid feeder system may be present in many of these provinces.

Despite the geometric similarities between the Ferrar plumbing system and sill complexes generally, many seismic reflection studies reveal the presence of “intrusive LIPs”

that are not demonstrated to have fed voluminous outpourings of flood lavas (Rohrman, 2013). Further, it is common for seismically imaged sill complexes to be coupled with extrusive components that have small eruptive volumes, such as the Ceduna Sub-basin, offshore Australia, where edifice volumes are typically $<10 \text{ km}^3$ (Magee et al., 2013a).

Given that many sill complexes do not erupt significant lava volumes, why did sills and sill-fed dikes of the Ferrar LIP lead to eruption of a flood basalt province? Rohrman (2013) demonstrates that, as magma ascends sedimentary basins, decreasing sediment densities produce a corresponding decrease in magma overpressure gradients. Consequently, if a sedimentary sequence is sufficiently thick magma ascent will terminate. Compared to intrusive LIPs observed in seismic reflection surveys (e.g., Rockall Basin, offshore United Kingdom: Thomson and Hutton, 2004), which are known to have been emplaced in basinal sedimentary successions as thick as 12 km (Cartwright and Hansen, 2006), intrusions of the Ferrar LIP traversed only a relatively thin sequence of sedimentary rocks (~2.5 km) and, as a consequence, breached the surface to feed flood basalt eruptions. This basic observation supports the assertion of Rohrman (2013) that sedimentary basin thickness has a first-order control on the eruptive capacity of a sill complex. In addition to basin thickness, the vertical ascent of magma within sill complexes will also be affected by magma buoyancy, source pressure and solidification, and by the physical properties of the host rock, such as density, rigidity contrasts, pre-existing structures, fluid pressure, and rheology (Kavanagh et al., 2006; Thomson, 2007; Schofield et al., 2012b; Le Corvec et al., 2013b; Chanceaux and Menand, 2014; Kavanagh and Pavier, 2014; Krumbholz et al., 2014).

An ideal field location to compare and contrast the controls on magma ascent in the Ferrar LIP is the contemporaneously emplaced dikes and sills of the western Karoo basin

(Encarnación et al., 1996; Marsh et al., 1997; Chevallier and Woodford, 1999; Schofield et al., 2010). The intrusive pattern in the western Karoo basin is similar to that observed in the Ferrar LIP, exhibiting widespread sills and an arrangement of dikes that to some degree mimic the cracked lid pattern described in this study (Marsh et al., 1997; Chevallier and Woodford, 1999; Fig. 6.8). However, compared to the Ferrar LIP, the Karoo Province records a protracted magmatic/tectonic history (~183-174 Ma) and the geometry of the shallow plumbing exhibits greater structural complexity (Hastie et al., 2014). Although dikes are observed extending from sill peripheries in the western Karoo basin, imposed on this dike-sill network are broadly distributed (200 to > 400 km wide) NW-SE striking dikes, indicating a zone of right-lateral shear (Chevallier and Woodford, 1999). Additionally, long, collinear dike swarms extend along the northern and eastern boundary of the Kaapvaal Craton and appear to form a triple junction (Aubourg et al., 2008; Klausen, 2009; Hastie et al., 2014). Consequently, linking specific dike-feeder systems with Karoo flood basalts is challenging. Geochemical analyses by Galerne et al. (2008) demonstrate a close kinship between the saucer-shaped, Golden Valley Sill and the earliest erupted Lesotho lavas. However, it is yet to be determined whether or not flood lavas of the Karoo LIP were primarily fed by a sill-fed dike system exhibiting a cracked lid pattern, rather than regionally extensive, collinear dike swarms.

6.6.5 Applications to active volcanic systems

Although larger in scale than any of today's active mafic volcanic systems, intrusions of the Ferrar LIP highlight the influence of sills on upward magma transport, with potential implications for hazard forecasting. Models of shallow, sill-assisted dike intrusion (Johnson and Pollard, 1973; Polteau et al., 2008) diverge from classic depictions of ascending magma

(Anderson, 1951), where upward (or lateral) propagation of a dike requires that magma pressure in the dike exceeds the regional least compressive stress. In a shallow, interconnected sill-dike network, sill inflation may promote the ascent of magma in dikes, by creating localized zones of extension at the sill periphery and assisting opening of the dike walls as the sill inflates (Johnson and Pollard, 1973; Gouly and Schofield, 2008; Galland et al., 2009). In these systems, the timing and location of volcanic eruptions may be related to sill inflation/deflation events. Field observations from the Ferrar LIP reveal a shallow magma system composed of complex, interconnected dike-sill geometries, one in which dikes often emanate from the lateral ends of sills (Muirhead et al., 2012; Fig. 6.4). Given these basic geometric relations it is likely that, during Ferrar magmatism, ground deformation related to sill inflation may have been laterally offset from eruption sites. These interpretations are in line with InSAR deformation studies of recent eruptions (e.g., 2004 Asama eruption (Japan), 2005 Fernandina eruption (Galapagos): Chadwick et al., 2011; Aoki et al., 2013), experimental modelling of magmatic intrusions (Galland, 2009, 2012), seismic reflection observations of sills in the Ceduna basin, offshore Australia (Magee et al., 2013a), and field observations in monogenetic basaltic fields (Bakony-Balaton Highland Volcanic Field, Hungary: Nemeth and Martin, 2007), where eruption sites occur above the lateral terminations of sills rather than above the sill center.

6.7 Conclusions

This study is the first to catalogue the dimensions and distribution of regionally exposed sill-fed dike intrusions of the Ferrar LIP in South Victoria Land, Antarctica. Dikes of the Ferrar LIP formed an aerially extensive dike network, with a cumulative length of 308,000 km. Applying reasonable effusion rates to this shallow dike system reveals that each

individual segment of this feeder array could have been active for as little as 2 to 3 days to produce the volume of the Kirkpatrick flood lavas. The observed sill-fed dike network of the Ferrar LIP is at odds with the traditional model of magma ascent invoked for many LIPs, and resembles a variably “cracked lid” atop a sill network. The cracked lid may be the archetypal model for shallow feeder systems of LIPs that intruded sedimentary basins where the influence of far-field extensional tectonics is negligible. This study reveals that shallow magma systems composed dominantly of sills are capable of feeding voluminous outpourings of lava, and highlights the important role sills likely play in feeding active volcanic systems.

CHAPTER 7: SHALLOW FEEDER SYSTEMS TO MONOGENETIC ERUPTIONS

Chapter based on: Muirhead, J.D., Van Eaton, A.R., Re, G., White, J.D.L., Ort, M.H., 2016, Monogenetic volcanoes fed by interconnected dikes and sills in the Hopi Buttes volcanic field, Navajo Nation, USA: *Bulletin of Volcanology*, v. 78, p. 1-16, doi: 10.1007/s00445-016-1005-8.

7.1 Abstract

Although monogenetic volcanic fields pose hazards to major cities worldwide, their shallow magma feeders (<500 m depth) are rarely exposed and, therefore, poorly understood. This study investigates exposures of dikes and sills in the Hopi Buttes volcanic field, Arizona, to shed light on the nature of its magma feeder system. Shallow exposures reveal a transition zone between intrusion and eruption within 350 m of the syn-eruptive surface. Using a combination of field- and satellite-based observations, three types of shallow magma systems have been identified: (1) dike-dominated, (2) sill-dominated, and (3) interconnected dike-sill networks. Analysis of vent alignments using pyroclastic massifs and other eruptive centers (e.g., maar-diatremes) shows a NW-SE trend, parallel to that of dikes in the region. It is therefore inferred that dikes fed many of the eruptions. Dikes are also observed in places transforming to transgressive (ramping) sills. Estimates of the observable volume of dikes (maximum volume of $1.90 \times 10^6 \text{ m}^3$) and sills (minimum volume of $8.47 \times 10^5 \text{ m}^3$) in this study, reveal that sills at Hopi Buttes make up at least 30% of the shallow intruded volume ($\sim 2.75 \times 10^6 \text{ m}^3$ total) within 350 m of the paleosurface. Also identified are saucer-shaped sills, which are not traditionally associated with monogenetic volcanic fields. This study

demonstrates that shallow feeders in monogenetic fields can form geometrically complex networks, particularly those intruding poorly-consolidated sedimentary rocks. It is concluded that the Hopi Buttes eruptions were primarily fed by NW-SE-striking dikes. However, saucer-shaped sills also played an important role in modulating eruptions by transporting magma toward and away from eruptive conduits. Sill development could have been accompanied by surface uplifts on the order of decimeters. It is inferred that the characteristic feeder systems described here for the Hopi Buttes may underlie monogenetic fields elsewhere, particularly where magma intersects shallow, and often weak, sedimentary rocks. Results from this study support growing evidence of the important role of shallow sills in active monogenetic fields.

7.2 Introduction

A number of major cities are built on active volcanic fields (e.g., Auckland, New Zealand, and Mexico City, Mexico), hosting tens to hundreds of cinder cones and explosive maar-diatremes. These volcanoes typically arise from small, episodic eruptions $<1 \text{ km}^3$ in volume (Kereszturi and Nemeth 2012; Le Corvec et al. 2013a), and exhibit shifts between effusive and explosive activity (Houghton et al., 1999; Ort and Carrasco-Núñez, 2009; McGee et al., 2012; Valentine and Cortés, 2013). Thus, volcanic hazards in monogenetic fields may change in style and scale over the course of a single, ongoing eruption.

Previous studies have shown that eruption style, duration and location are linked to changes in and around the underlying magma system, such as the regional and local stress fields (Buck et al., 2006; Wadge and Burt, 2011), magma supply rate (Houghton et al., 1999; Mastin et al., 2004; Valentine and Cortés, 2013; Lefebvre et al., 2016), magma composition (McGee et al., 2012), volatile exsolution (Sparks, 1978; Rotella et al., 2014; Harp and

Valentine, 2015) and magma-water interaction (White, 1991; Ort and Carrasco-Núñez, 2009; Ross and White, 2012). Changes in intrusion geometry (e.g., transitions from dikes to sills) and magma flow within shallow feeder systems also play a role in modulating eruption location and behavior (Lefebvre et al., 2012; Kavanagh et al., 2015; Richardson et al., 2015; Lefebvre et al., 2016), as well as the warning signs of impending activity (Sparks et al., 2012; Segall, 2013; Rivalta et al., 2015). For example, the 1943-1952 eruption of Parícutin, Mexico, was preceded by meter-scale surface uplifts (Foshag and Gonzalez-Reyna, 1956), which are often related to the emplacement of dikes and/or sills (Chadwick et al., 2011; Bonaccorso et al., 2013). GPS and InSAR studies of more recent volcanic crises have also shown both inflation/deflation and lateral ground surface movements over the course of an eruption, linked to deflation or replenishment of shallow magma bodies and propagation of dikes and sills (Wright et al., 2012; Biggs et al., 2013; Aoki et al., 2013; Sigmundsson et al., 2015). However, eruptions in monogenetic fields have rarely been observed with the modern tools (e.g., InSAR, GPS) required to detect magma movement and constrain the geometry and interconnectivity of subsurface intrusive feeders (c.f., Chadwick et al., 2011; Albert et al., 2016). Furthermore, extinct fields typically lack adequate geological exposures of the shallow intrusions (<500 m depth) that feed monogenetic volcanoes. Therefore, the nature and evolution of shallow intrusive networks in many monogenetic fields remain unclear.

Models of shallow magma transport in monogenetic volcanic fields have largely focused on dikes, which have steep dips and cut across stratigraphy (Anderson 1951; Delaney and Gartner, 1997; Brown and Valentine, 2013; Rivalta et al., 2015). Sills are typically ignored or assumed to be of second-order importance. However, recent studies have found that sills may be substantially more common than previously assumed at a range of volcanic

settings, particularly where magma intrudes shallow sedimentary successions (Cartwright and Hansen, 2006; Nemeth and Martin, 2007; Muirhead et al., 2012; Magee et al., 2013b; Richardson et al., 2015). For example, seismic reflection studies from offshore UK and Australia show that basaltic magmas intruded sediments to form complex networks of dikes, sills and sheets (Thomson and Hutton 2004; Cartwright and Hansen 2006; Magee et al. 2013a, 2014). Similar findings have emerged from field-based mapping in the Ferrar-Karoo large igneous province of southern Africa (Polteau et al. 2008) and Antarctica (Airoldi et al. 2011, 2012; Muirhead et al. 2012). The compelling suggestion is that sills can and do provide critical pathways to feed eruptions (Magee et al., 2013a; Muirhead et al. 2014). However, it is largely unknown if geometrically complex intrusive networks underpin monogenetic feeder systems, despite the important implications for how eruptions are fed and modulated. For example, what are the relative volumes of sills compared to dikes in monogenetic volcanic fields? What are the geometric relations between dikes, sills and other eruptive conduits, and how does magma flow within and between these intrusive structures? These questions are addressed in this study within the well-exposed plumbing system of the late Miocene Hopi Buttes volcanic field. This field area provides rare, high-quality exposures of feeder systems that illuminate the geometry and interconnectivity of shallow intrusions and eruptive conduits within 350 m of the pre-eruptive surface.

7.3 Background on the Hopi Buttes volcanic field, Navajo Nation, Arizona

Eruptions of the Hopi Buttes volcanic field were fed by conduits that passed through flat-lying, wet sediments of the southern Colorado Plateau at ~7 Ma (White 1990, 1992; Billingsley et al. 2013) (Figs. 7.1 and 7.2). The field bears similarities to a number of currently-active examples in terms of the poorly consolidated sedimentary host rock, narrow

range of small volcano types (scoria cones with lavas to deeply-cut maars), and number and density of volcanic centers (~ 300 and $1.3 \times 10^{-7}/\text{m}^2$, respectively). Broadly similar fields include the Chichinautzín (Mexico), Auckland (New Zealand), Eifel (Germany) and

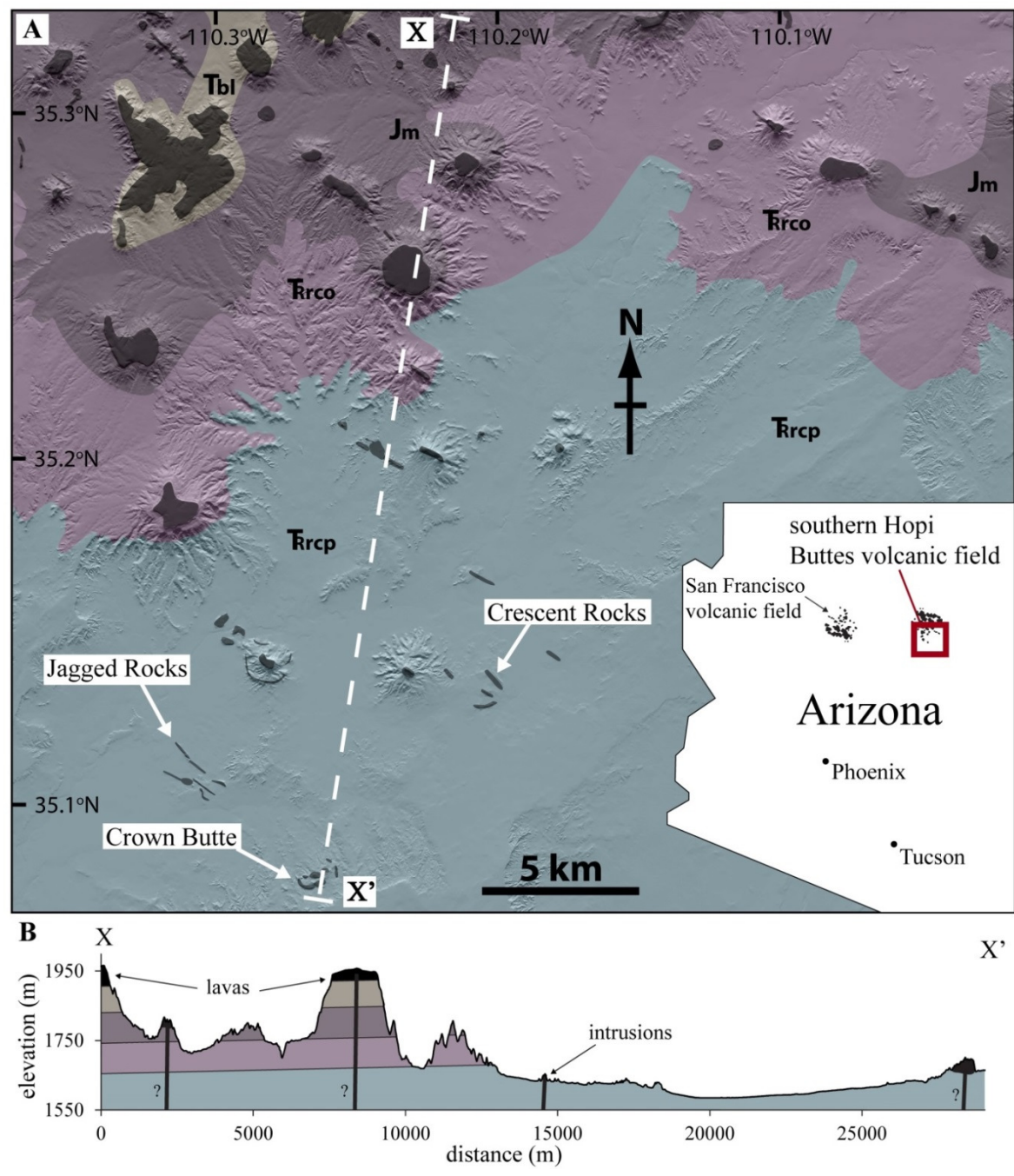


Figure 7.1. A: Simplified geological map of the southern Hopi Buttes volcanic field, modified from Billingsley et al. (2013) and Lefebvre (2013). The map is draped on a 10 m-resolution hill shade. Stratigraphic units are

defined in Table 1. Igneous rocks in the Hopi Buttes volcanic field are shown in black. The locations of the intrusive complexes in this study are annotated. B: Geological cross-section (X-X') oriented approximately north-south across southern Hopi Buttes. The stratigraphy has an assumed dip of $\sim 1^\circ$ to the northwest (Billingsley et al., 2013).

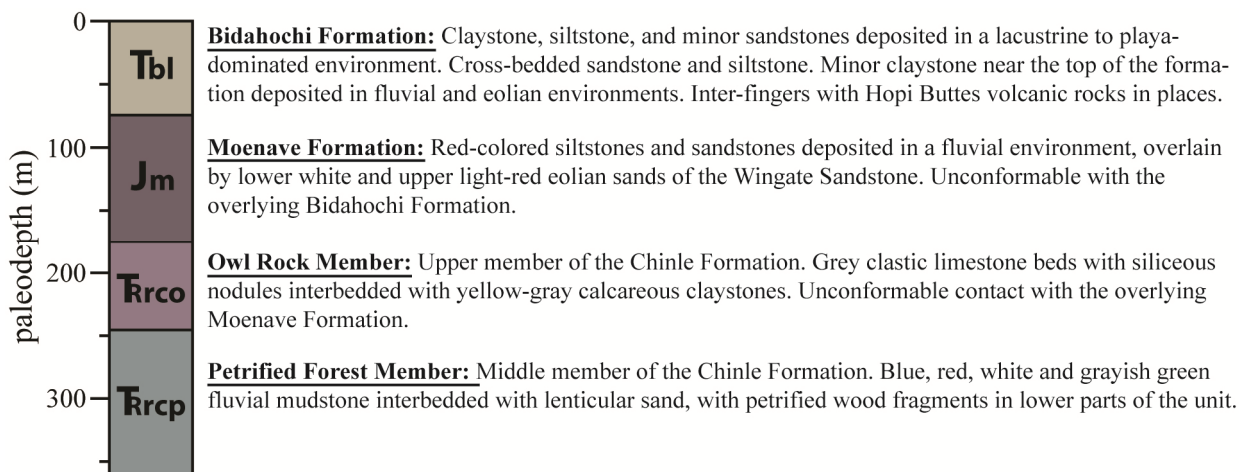


Figure 7.2. Simplified stratigraphy of the Hopi Buttes region.

San Francisco (Arizona, USA) volcanic fields (Le Corvec et al. 2013a, and references therein). Volcanoes of the Hopi Buttes are exposed at different stratigraphic levels, from subaerial volcanic deposits to hundreds of meters below the paleosurface. This provides a superb cross-section of the system from intrusion to eruption. In general, the erosion surface deepens from north to south, exposing lavas and maar-diatremes in the northeast and igneous intrusions to the south (Fig. 7.1). This study focuses on the structure and volcanology of the intrusive-eruptive transition within ~ 350 m of the paleosurface in southern Hopi Buttes.

7.4 Methods

7.4.1 Terminology

Table 7.1 provides a summary of terms used in this study. Coherent intrusions are classified as *dikes* (mean dip $\geq 60^\circ$), *sills* ($\leq 10^\circ$), and *inclined sheets*, which have an intermediate dip from 10 - 60° (Annels, 1967; Klausen., 2004; Pasquaré and Tibaldi, 2007; Airoidi et al., 2011). In practice, the sills and inclined sheets are closely interrelated, producing ramped step-and-stairs or transgressive geometries, as shown in Figure 7.3C (Francis, 1982; Airoidi et al., 2011; Re et al., 2015). Therefore, sills and inclined sheets are collectively referred to as *transgressive sills* in this study. *Pyroclastic massif* is used to refer to the prominent, sub-cylindrical to tabular breccia bodies exposed throughout Hopi Buttes (Figs. 7.3A, B and 7.4) after Re et al. (2015). Previous studies have used the terms *volcanic conduits* or *plugs*, inferring that they represent zones where magma focused to feed eruptions (Delaney and Pollard, 1981; Keating et al., 2008; Kiyosugi et al., 2012; Friese et al., 2013; Harp and Valentine, 2015). In this paper, the term *pyroclastic massif* is preferred to avoid a genetic association, and to be consistent with recent work in the Hopi Buttes (Re et al., 2015; Lefebvre et al., 2016). *Maar* is used for explosion craters cut into the ground, surrounded by volcanic ejecta, and *diatrema* for infill of the subsurface continuation of the maar structure (White and Ross, 2011; Fig. 7.3E, F).

Table 7.1. Definition of terms applied in this study (references in superscript).

	term	description
intrusion type	dike ^{1,2}	planar intrusion dipping >60° and discordant to bedding
	sill ²	planar intrusion dipping <10° and often bedding concordant
	sheet ³	planar intrusion dipping 10-60° and discordant to bedding
	transgressive sill ⁴	composite intrusion comprising alternating sheet and sill segments, dipping <60°
	saucer-shaped sill ^{5,6}	composite intrusion comprising an inclined outer rim transgressing upward from the edge of an inner sill forming a concave-upward geometry
	cusate sill ⁷	convex upward intrusion with an outer transgressive sill fed by an inner dike intrusion
	peperite ⁸	intrusive rock resulting from the mingling between viscous magma and viscous host; commonly extends from the margins of intrusions and lacking a systematic planar structure; exhibits either fluidal or blocky shapes
intrusive features	segment, lobe ^{9,10}	single, planar intrusive element; sets of sub-parallel, closely spaced segments, offset from one another, form a single intrusive body (dike or sill); segment often merge with continued dilation and growth
	segment tip ¹¹	lateral (or vertical) termination of a segment; segment tips either gradually taper or show no gradual decrease in thickness, forming a blunt termination
	offset, step ¹⁰	area along an intrusion where closely spaced, sub-parallel segments become disconnected, typically exhibiting minor overlap (10-100 cm) between the segment tips; the host rock contained within a step, situated between the offset segment ends, is termed a bridge
	horn ¹⁰	Thin (typically a few cms), wedge-shaped apophysis extending from a blunt segment tip
eruptive centers	maar ¹²	volcano with little to no relief comprising a central crater (typically 500-1000 m diameter) cut into the ground with a surrounding ejecta ring; commonly interpreted to be underlain by a diatreme
	diatreme ¹²	steep-sided, typically cone-shaped structure comprising volcanoclastic and fragmented country rock; entire structure enclosed by country rocks; extends from crater floor downward to a feeder dike at depth
	scoria cone ¹³	small (10s to 100s m high) cone-shaped volcanic landform dominantly composed of vesicular, basaltic volcanic clasts a few mm to 10s of cm in diameter
	pyroclastic massif ^{14,15,16,17}	sub-cylindrical, brecciated intrusive body typically >5 m wide and comprising coherent intrusive rock, country rock, juvenile fragments (typically variably welded spatter and scoria), and mixed fluidal and blocky peperite; considered the root zone or conduit to a diatreme or scoria cone; also termed a plug, conduit, and spatter dike

References: (1) Rubin (1995); (2) Anderson (1951); (3) Annels (1967); (4) Airoidi et al. (2011); (5) Chevallier and Woodford (1999); (6) Magee et al. (2014); (7) Mathieu et al. (2008); (8) Skilling et al. (2002); (9) Pollard et al. (1975); (10) Hoek (1991); (11) Kattenhorn and Watkeys (1995); (12) White and Ross (2011); (13) Wood (1980); (14) Lefebvre et al. (2012); (15) Re et al. (2015); (16) Delaney and Pollard (1981); (17) Kiyosugi et al. (2012)

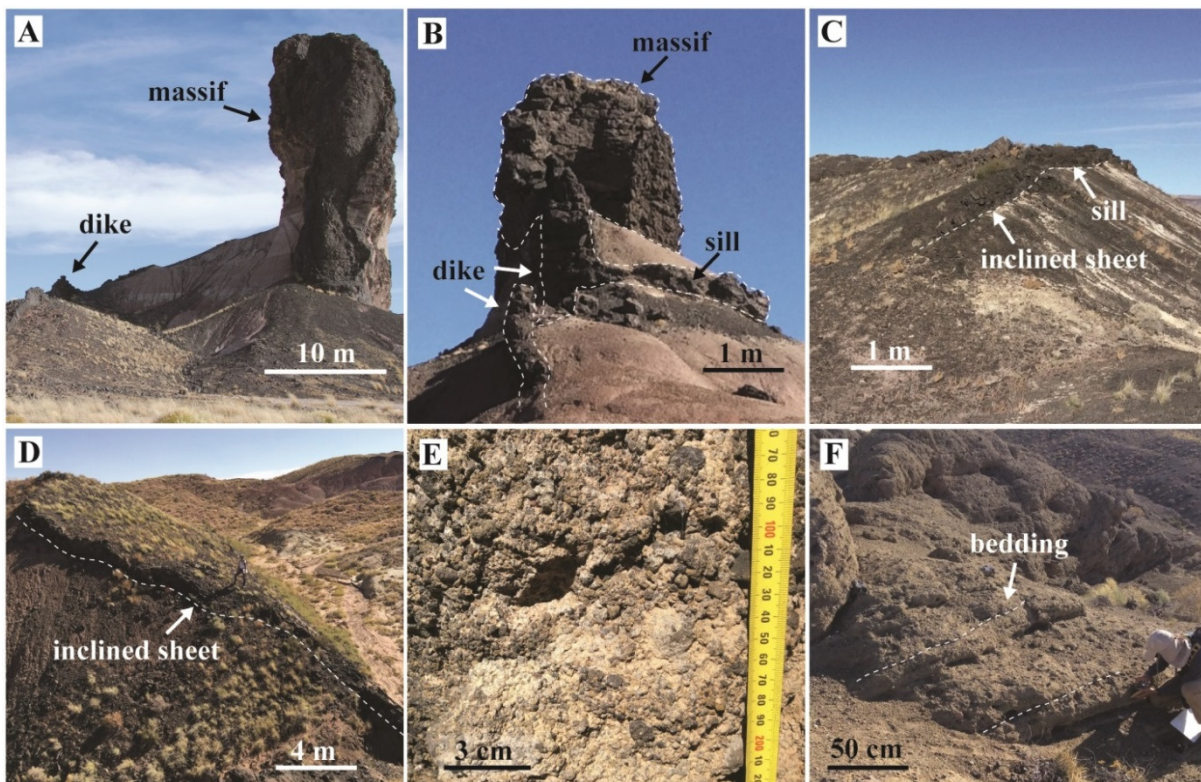


Figure 7.3. A: Dike in close proximity to a 40 m-high massif structure at Jagged Rocks (lat: 35.11318°N, long: 110.31209°W). B: Dike transitioning vertically into a massif and connecting to a sill intrusion. No cross-cutting relations are observed between the dike, sill, and conduit (lat: 35.10406°N, long: 110.30943°W). Intrusive margins indicated by dashed white lines. C: Inclined sheet transitioning up section into a sill, forming a transgressive sill (lat: 35.13318°N, long: 110.19773°W). Lower margin indicated by dashed white line. D: Moderately dipping (~50°) inclined sheet in the Crown Butte complex (lat: 35.08122°N, long: 110.26406°W). Lower margin indicated by dashed white line. E: Diatreme bed comprising juvenile volcaniclasts and country rock fragments (typically 1-10 mm diameter) (lat: 35.07679°N, long: 110.26557°W). F: Weakly bedded (upper) diatreme units. Dashed white lines show select bedding contacts (lat: 35.07858°N, long: 110.26279°W).

7.4.2 Field measurements and remote sensing

Field measurements and remote-sensing analysis were used to characterize the nature and geometry of the shallow intrusive system in southern Hopi Buttes. First, the broad-scale spatial distribution and orientation of 258 dikes, 73 pyroclastic massifs and 24 maar-diatremes were measured using Google Earth satellite imagery (~25-50 cm pixel resolution), alongside the geological map of Billingsley et al. (2013) (Appendix E). These satellite-based

observations were refined during fieldwork, which involved measuring the thickness, strike and dip of more than 300 intrusive segments, and documenting textural and field relations. Intrusion segments were defined in the field where offsets exceeded 0.5 m. Individual segments were identified in satellite imagery where intrusions were visibly disconnected.

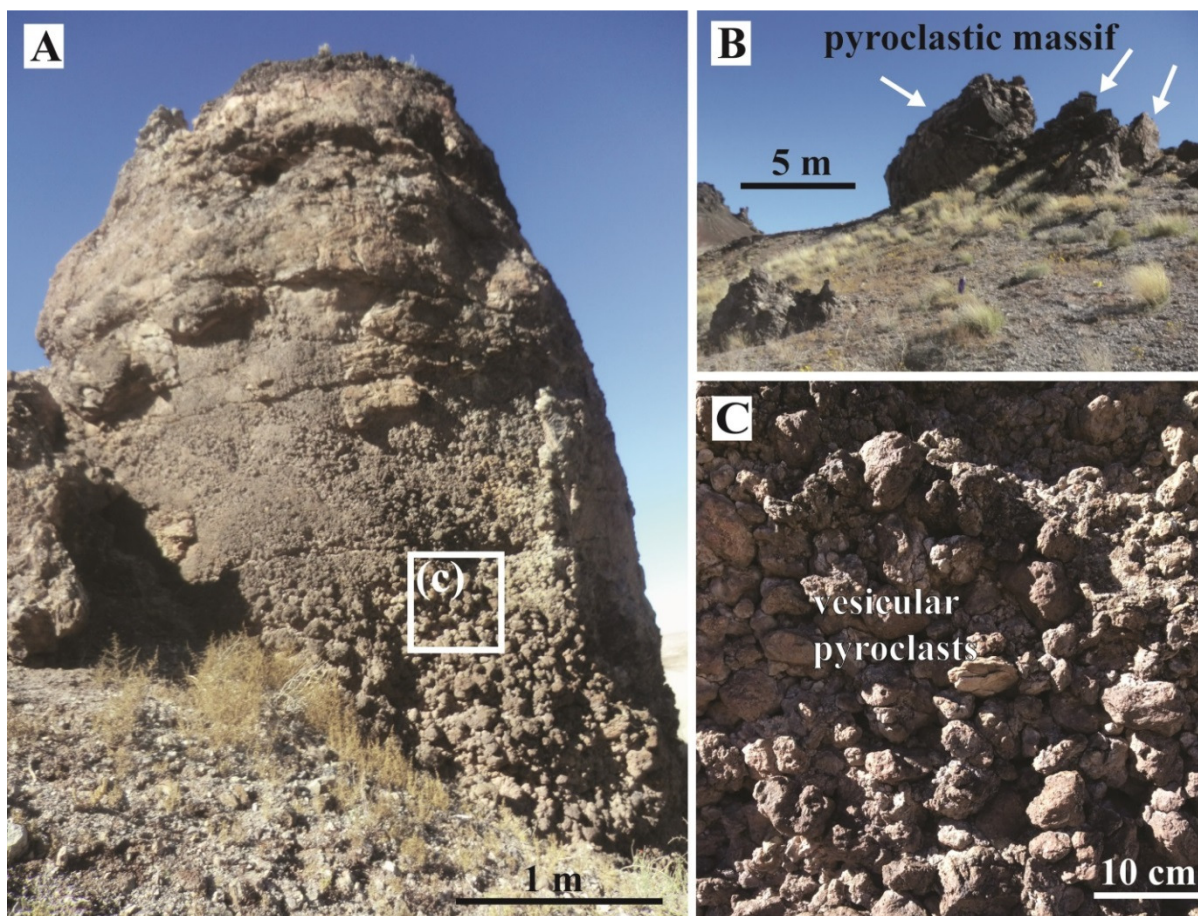


Figure 7.4. Example of a pyroclastic massif deposit (lat: 35.07586°N, long: 110.27075°W). A: Pyroclastic massif structure (8-10 m-high) in the Crown Butte area, containing weakly bedded, normally-graded pyroclasts. B: Silhouette of the massif on the horizon. C: Close-up of weakly bedded, vesicular pyroclasts in b. Note the well sorted, clast-supported framework of the juvenile clasts.

Remote-sensing data of dike lengths and sill areas, combined with field measurements of thickness, were used to estimate the volume of the observed intrusions in the upper ~350 m of the plumbing system. These estimates provide constraints on the minimum volume of

transgressive sills relative to dikes. The maximum volume of dikes can be reasonably estimated by assuming that all the dikes observed in south Hopi Buttes extended to the paleo-surface (Richardson et al., 2015), and were thus approximately 350 m high. We assume a constant mean thickness of 0.45 m, consistent with the mean value from hundreds of field measurements along the lengths of dikes. The true areal extents of transgressive sills are more difficult to constrain. However, by considering only the observable areas of transgressive sill segments (rather than assuming a maximum lateral extent) and their field-derived, mean thickness (0.85 m), a conservative minimum volume for the sills may be determined. Their actual volume therefore is clearly larger than the presented values, as shown in eroded fields elsewhere, such as the San Rafael volcanic field, Utah (Delaney and Gartner, 1997; Richardson et al., 2015). However, this simple approach allows an examination of their minimum volumetric importance within the shallow plumbing system.

Using spatial data from the satellite analysis of the field area (Fig. 7.1; Table E1 of Appendix E), we investigated the alignments of variably eroded eruptive centers (pyroclastic massifs and maar-diatreme deposits) using the method of Le Corvec et al. (2013a). As summarized in Figure 7.5, the linear regression algorithm calculates best-fit lines between nearest-neighbor triplets (i.e., 3-point alignments between eruptive centers). Each lineament must satisfy length and width tolerances to be included. A length tolerance of 3,878 m was used based on the method of Le Corvec et al. (2013a), which finds the optimal length for minimizing artifacts (<10%) using the density of volcanic centers (refer also to Section 7.9.1). A conservative width tolerance of 10 m was applied, which is well within the range of ‘A-grade’ lineaments (<125 m) defined by Paulsen and Wilson (2010), and has been used in previous alignment studies in monogenetic fields (Le Corvec et al., 2013a).

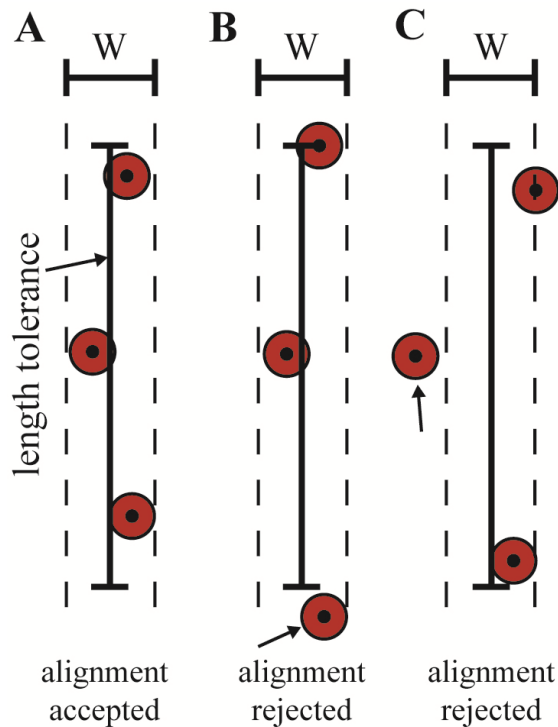


Figure 7.5. Criteria for detecting alignments slightly modified from Le Corvec et al. (2013a). An alignment consists of three points (i.e., eruptive centers). A: Example of an acceptable alignment where all the three points are within predetermined length and the width (W) tolerances. B: Example of a rejected alignment where one point lies outside of the predetermined length tolerance (reject point indicated by arrow). C: Example of a rejected alignment where one point lies outside of the predetermined width tolerance (rejected point indicated by arrow).

7.5 Results

7.5.1 Broad-scale arrangement of dikes, transgressive sills, and pyroclastic massifs

Dike segments analyzed in Google Earth imagery exhibit a mean strike of 126° , which is sub-parallel to the mean trend (139°) of eruptive center alignments in the southern Hopi Buttes (Figs. 7.6A, B). Field measurements of dike segments and systematic joint-sets are in agreement with this overall NW-SE trend, striking 129° and 131° , respectively (Figs. 7.6C, D). The mean dike width, calculated from field measurements of hundreds of segments along the lengths of dikes throughout the field, is 0.45 m, and dikes have an observed cumulative

length of ~12 km estimated from satellite imagery. These estimates give a total exposed areal extent of $5.44 \times 10^3 \text{ m}^2$. Assuming that all dikes extended from the current exposure level to the surface, the maximum volume of observed dikes in the upper 350 m of the plumbing system is $\sim 1.90 \times 10^6 \text{ m}^3$. This suggests that dikes comprise a maximum of 69% of the solidified plumbing system at this level, with the rest represented by transgressive sills (Table 7.2).

Dikes are observed in places connected to transgressive sills (Fig. 7.3B). Transgressive sills form the dominant component of some complexes in the southern Hopi Buttes. These intrusions ascend the stratigraphy step-wise, transitioning between shallow-dipping sill segments and moderately-dipping inclined sheets. Sills may directly intrude bedding in layered sedimentary rocks (Fig. 7.7), but also occur in massive mudstones with no observable bedding. Sills typically have sharp contacts with the surrounding country rock. In places, though, they exhibit margins of fluidal peperite within a brecciated host consisting of a mixture of intrusive and country rock fragments (Fig. 7.8). Transgressive sill segments have mean dips and thicknesses of 21° and 0.85 m, respectively, and a total exposed areal extent of $9.97 \times 10^5 \text{ m}^2$. Together, the mean width and measured area of sills equates to an observable volume of $8.47 \times 10^5 \text{ m}^3$, suggesting that transgressive sills comprise a minimum of 31% of the total intrusive volume of the shallow plumbing system at southern Hopi Buttes, which is estimated to be $\sim 2.75 \times 10^6 \text{ m}^3$ (Table 7.2).

Pyroclastic massifs are prominent structures made up of chaotic domains of coherent to swirly intrusions, vesicular pyroclasts (scoria), and blocky to fluidal sedimentary host rock, all of which were emplaced below the contemporary ground surface (Lefebvre et al., 2012). In

map view, the massifs have subequant to elongate outlines, with long axes often trending subparallel to the overall NW-SE trend from dike alignments (Fig. 7.9).

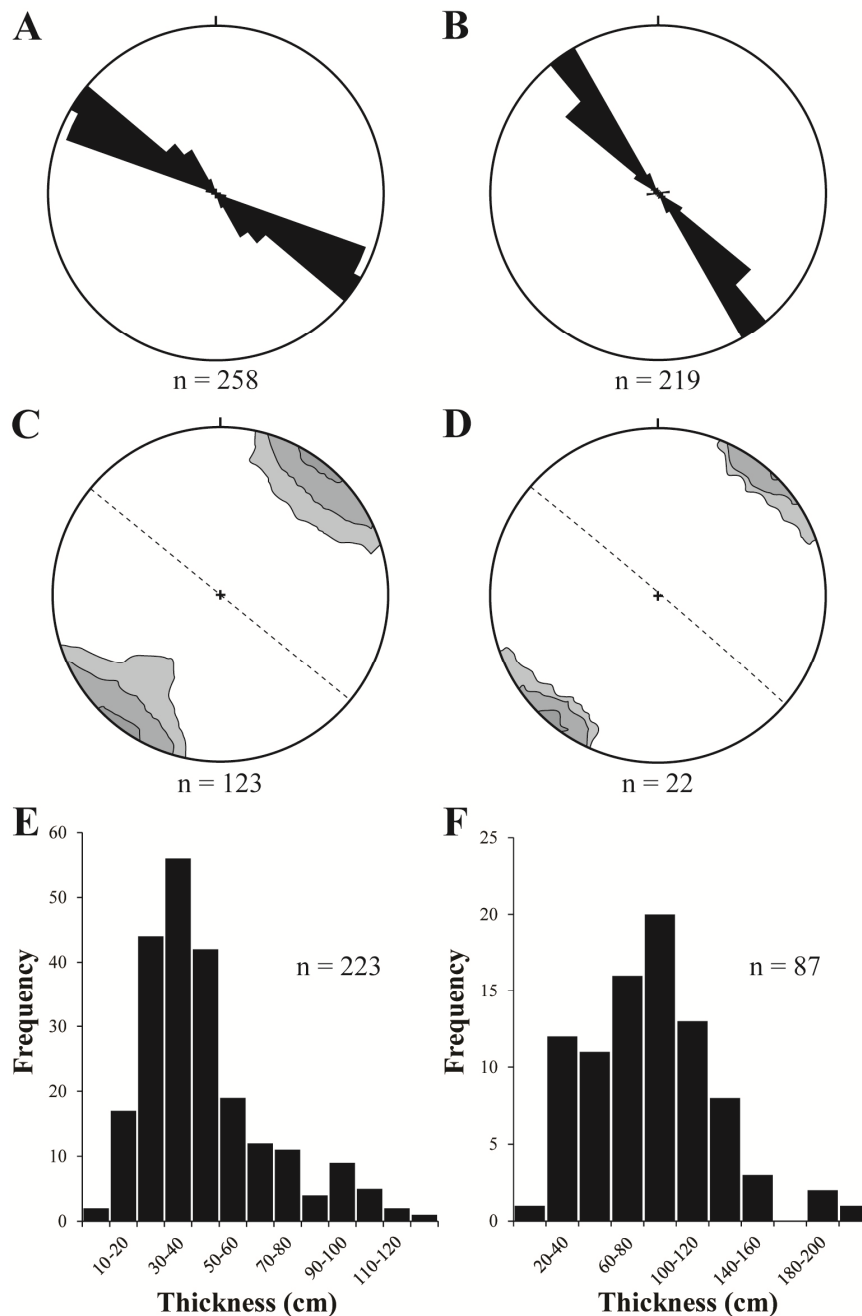


Figure 7.6. Structural data in the southern Hopi Buttes region collected from both the field and Google Earth imagery. A: Rose plot of dike segment trends as observed in Google Earth. B: Rose plot of eruptive centers alignments. C: Contour plot of poles to planes of dike segment strikes. Great circle (dashed black line) represents the mean dike orientation. D: Contour plot of poles to planes of joint strikes measured in sandstones. Great circle

(dashed black line) represents the mean dike orientation. E: Histogram of dike segment thicknesses measured in the field. F: Histogram of transgressive sill segment thicknesses measured in the field.

Table 7.2. Summary of dike and transgressive sill dimensions in the southern Hopi Buttes.

intrusion type	cumulative length (m)	mean width (m)	area (m ²)	volume (m ³)	percentage
dikes	12,091 ^a	0.45 ^b	5,441 ^c	1,904,350 ^e	69% (max.)
transgressive sills	N/A	0.85 ^b	996,650 ^d	847,152 ^f	31% (min.)

^a cumulative dike length calculated by summing the length of all dike segments mapped in Google Earth imagery

^b dike and sill mean width measured in the field from >300 intrusive segments

^c dike area estimated by multiplying mean width and cumulative length

^d transgressive sill area calculated from the cumulative area of all transgressive sills mapped in Google Earth

^e calculated by multiplying dike area by an assumed height of 350 m, providing a maximum estimate for the upper 350 m of the system

^f sill volume calculated by multiplying mean width by total area, providing a minimum observable volume in the upper 350 m of the system

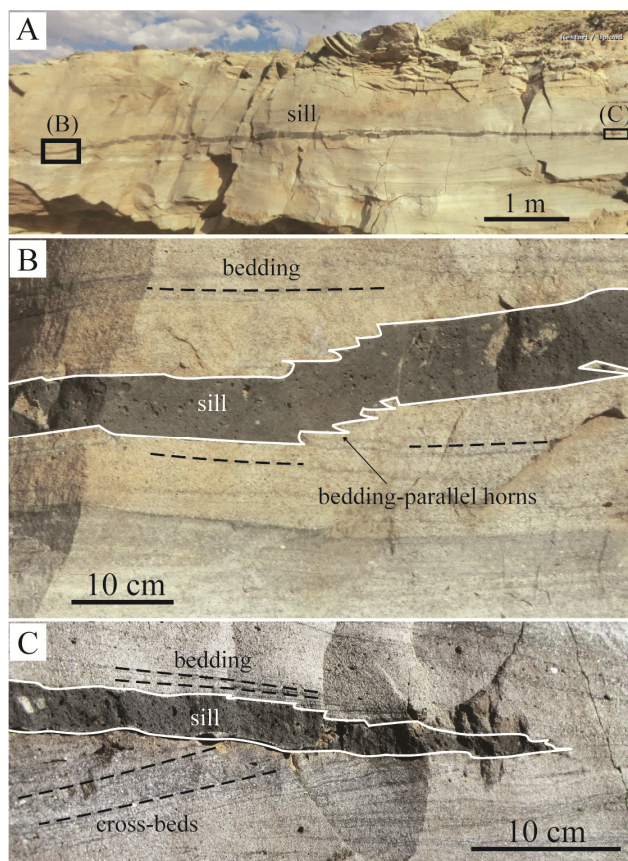


Figure 7.7. Thin (~10 cm thick) sill intrusion (A) in fine to medium grained sandstones of the Chinle Formation (lat: 35.07701°N, long: 110.27102°W). Sill margins commonly following bedding planes, and thin, bedding-parallel horns are seen extending from sill segments (B and C).

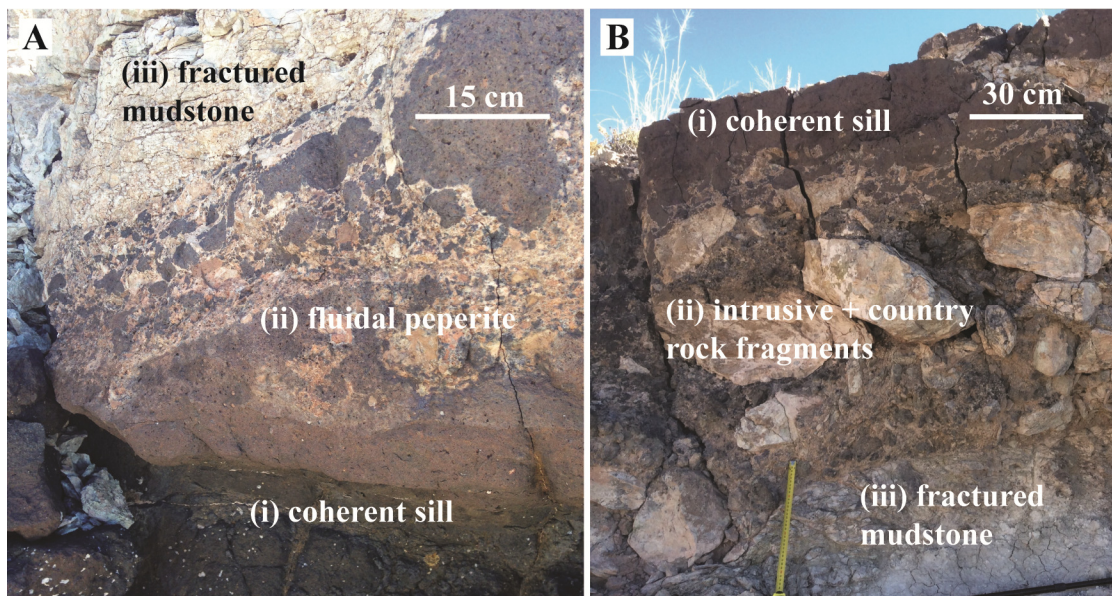


Figure 7.8. A: Upper margin of a sill at Crown Butte (lat: 35.07563°N, long: 110.27027°W). The intrusion changes vertically from (i) coherent intrusive rock, to (ii) fluidal peperite margin, to (iii) mixed, angular, intrusive and country rock fragments with variable peperite, to (iv) fractured country rock (mudstone). B: Lower margin of a sill at Crown Butte showing a downward transition from (i) coherent intrusive rock, to (ii) mixed, angular, intrusive and country rock fragments with variable peperite, to (iii) fractured mudstone.

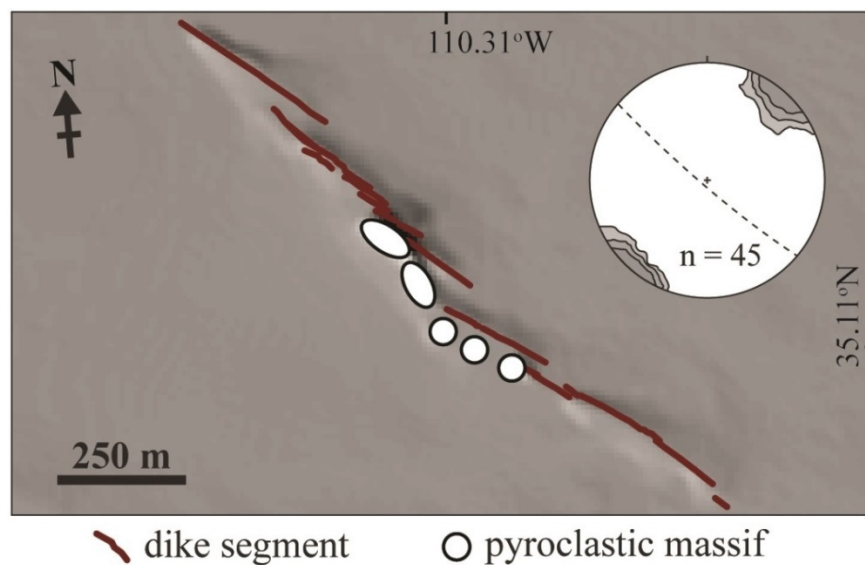


Figure 7.9. Simplified map of northwest Jagged Rocks on a 10 m-resolution hillshade. Location of the complex annotated in Figure 7.1. The stereonet is a lower hemisphere projection of contours of poles to dike planes. Great circle (dashed line) represents the mean dike orientation.

7.5.2 Field observations of intrusive complexes

Intrusive complexes in the southern Hopi Buttes may be broadly categorized into three kinds of feeder systems: (1) dike-dominated; (2) sill-dominated; and (3) interconnected dike-sill networks. The following sections provide field examples, all of which intruded the Petrified Forest Member sedimentary rocks (Fig. 7.2) at depths of ~250-350 m below the syn-eruptive surface (Billingsley et al., 2013; Re et al., 2015).

Dike-dominated feeder system: Jagged Rocks complex

The northwest portion of the Jagged Rocks complex exemplifies the classic model of a dike-dominated volcanic feeder system (e.g., Mono-Inyo Craters; Reches and Fink, 1988). It contains a 50 cm-wide, NW-SE-trending dike with a right-stepping *en echelon* pattern (Re et al., 2015; Fig. 9). Five pyroclastic massifs are located in the center of the dike, in a NW-SE alignment that is consistent with both the strike of the dike and the broader regional trend of Hopi Buttes volcanic field. Relations between the dikes and massifs are complex (Figs. 7.3B and 7.10). At many localities, dikes are cross-cut by massifs and vice-versa; at others they seamlessly merge into one another, suggesting synchronous or overlapping periods of activity.

Sill-dominated feeder system: Crown Butte complex

The Crown Butte complex contains four massifs, two diatremes, and numerous transgressive sill segments, but lacks exposed dikes (Fig. 7.11). The transgressive sill segments dip into the center of the complex, resulting in a saucer shape (long axis ~1.3 km across, trending roughly E-W). The overall geometry mimics saucer-shaped sills in the Karoo and the North Atlantic igneous provinces (Thomson and Hutton, 2004; Galland et al., 2009;

Scholfield et al., 2010; Hansen et al., 2011). Typical of those field areas, the arrangement of intrusive segments, or lobes, and the gradual tapering and termination of sills at the outer edges of the system are consistent with a primary magma flow direction radially away from the center of the complex (Hansen and Cartwright, 2006b; Schofield et al., 2010; Schofield et al., 2012a) (Fig. 7.12).

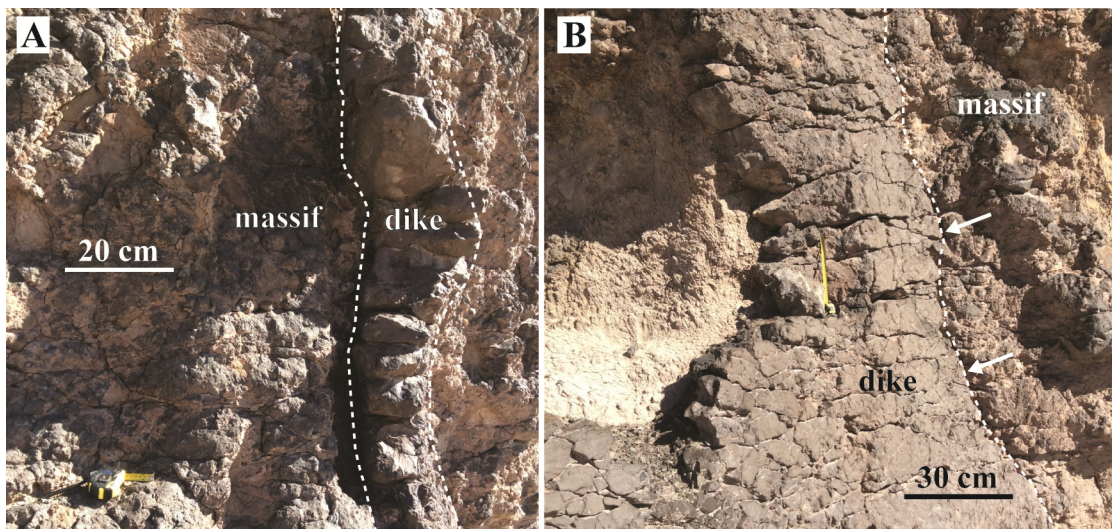


Figure 7.10. A: Dike intruding a pyroclastic massif structure indicating the dike post-dates this part of the massif (lat: 35.11176°N, long: 110.31104°W). Dike margins indicated by white dashed lines. B: Same dike as in A, but here it is cut by the pyroclastic massif (indicated by white arrows), suggesting the massif here post-dates the dike.

The two diatremes, located in the center of the sill Crown Butte complex, contain bedded, upper-diatreme facies deposits that dip toward the center of the diatreme (White and Ross, 2011). The deposits are crudely bedded on a cm- to m-scale, consisting of lithic-rich and poorly-sorted, mafic scoria, greenschist, chert and mudstone in a slightly greenish (palagonitized) matrix (Fig. 7.3E, F). The four pyroclastic massifs are located on the eastern edge of the complex. A direct contact between the massifs and transgressive sills has not been identified, but they occur within a few tens of meters of one another. No NW-striking dikes

are observed in the vicinity of massifs or the complex generally. Furthermore, alignments between massifs and diatremes trend ~E-W, which is subparallel to the long axis of the saucer-shaped intrusion, yet oblique to the broad-scale NE-SW structural trend in Hopi Buttes (Fig. 7.11). The underlying feeder to the Crown Butte complex is not exposed, and is inferred to be either a dike or transgressive sill below the current exposure level.

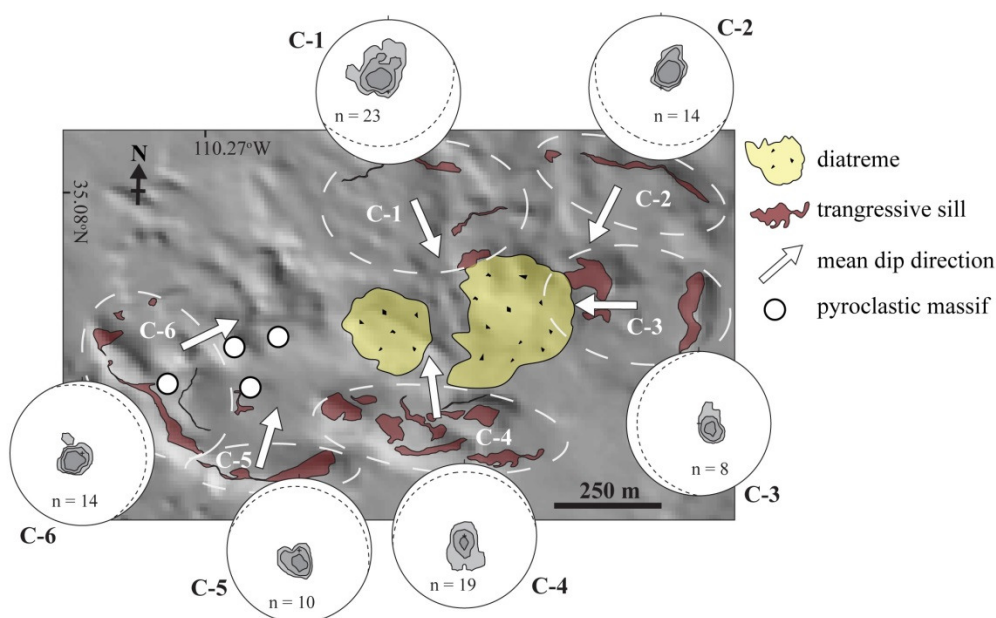


Figure 7.11. Simplified map of Crown Butte on a 10 m-resolution hillshade. Location of the complex annotated in Figure 7.1. Stereonets are lower hemisphere projections of contours of poles to intrusion planes for each labelled area represented by a dashed ellipse. Great circles (dashed line) represent the mean intrusion orientation for each area.

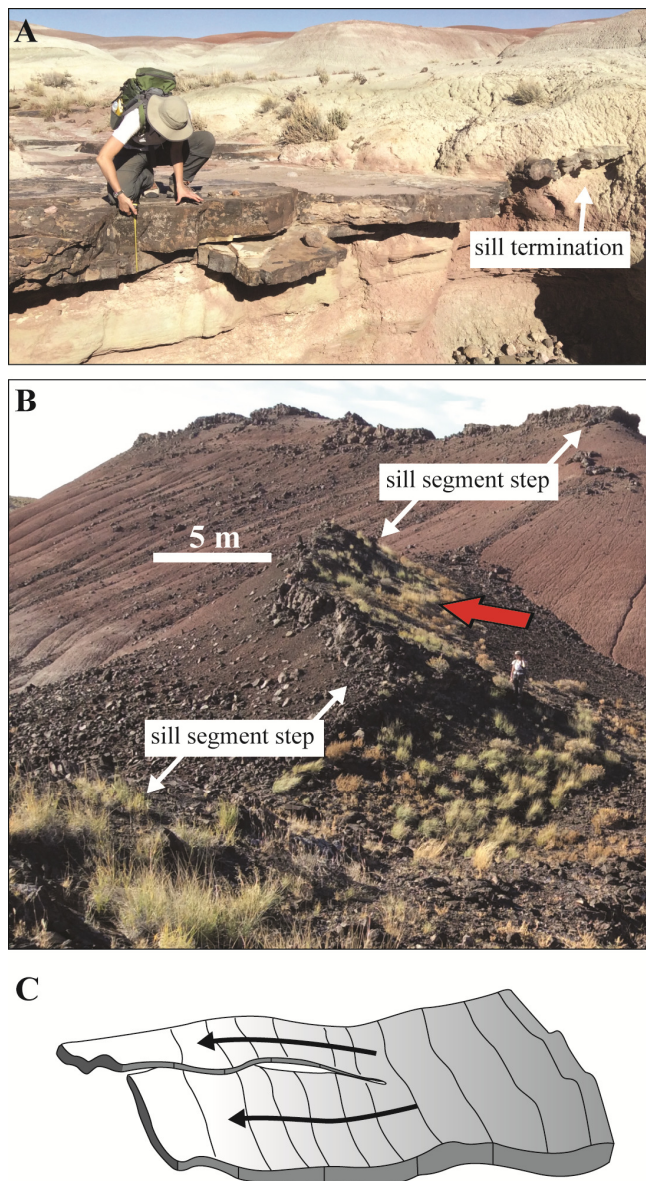


Figure 7.12. Transgressive sills at Crown Butte. A: Distal termination of a sill segment at the southern edge of the complex (lat: 35.07427°N, long: 110.26146°W). B: Steps between segmented sill lobes with ~5-10 m vertical offsets (lat: 35.07395°N, long: 110.26263°W). Red arrow indicates the inferred direction propagation based on the nature of the segmentation and long-axis of the country-rock bridge between segments (Schofield et al., 2012a) (refer to Table 2). C: Conceptual illustration of the growth of segment lobes from a single parent intrusion modified from Scholfield et al. (2012a). Arrows represent propagation direction, which is aligned to the long-axis of the segment and the long-axis of the bridge between segments.

Interconnected dike-sill network: Crescent Rocks complex

The Crescent Rocks complex consists of two sub-parallel dikes and two pyroclastic massifs surrounded by transgressive sills (Fig. 7.13). As with Jagged Rocks, the cross-cutting relations between dikes and massifs are complex, and in places dikes merge seamlessly into the walls of the massifs. Dikes and massifs exhibit NW-SE trends, subparallel to the broad-scale, basement-controlled structural trend in Hopi Buttes (Marshak et al., 2000; Re et al., 2015). Transgressive sill segments are primarily exposed in the eastern half of the complex, although small, discontinuous outcrops (areas of 10-100 m²) are present in the west. These transgressive sills all dip into the center of the complex, forming a semi-saucer shape (Fig. 7.13). The western half of the saucer is not exposed, or possibly never formed. The arrangement of intrusive segments (or lobes) is consistent with a primary magma flow direction away from the dikes and massifs in the center of the complex (Schofield et al., 2012a) (Fig. 7.14). A similar saucer-shaped intrusion is also present in the southwestern portion of the Jagged Rocks complex (Re et al., 2015).

7.6 Discussion

7.6.1 The intrusive-eruptive transition at southern Hopi Buttes

The dikes and transgressive sills of south Hopi Buttes represent the shallowest portions (<350 m) of an extinct monogenetic volcanic field. Intrusions here are exposed in the zone of intrusive-eruptive transition, and thus in some ways were on the “verge of eruption”, as illustrated by the fragmented, brecciated intrusions (massifs), and close spatial association (and transitions) among maar-diatremes, dikes and sills (Re et al., 2015; Lefebvre et al., 2016). Scoria clasts within pyroclastic massifs provide evidence for magma vesiculation,

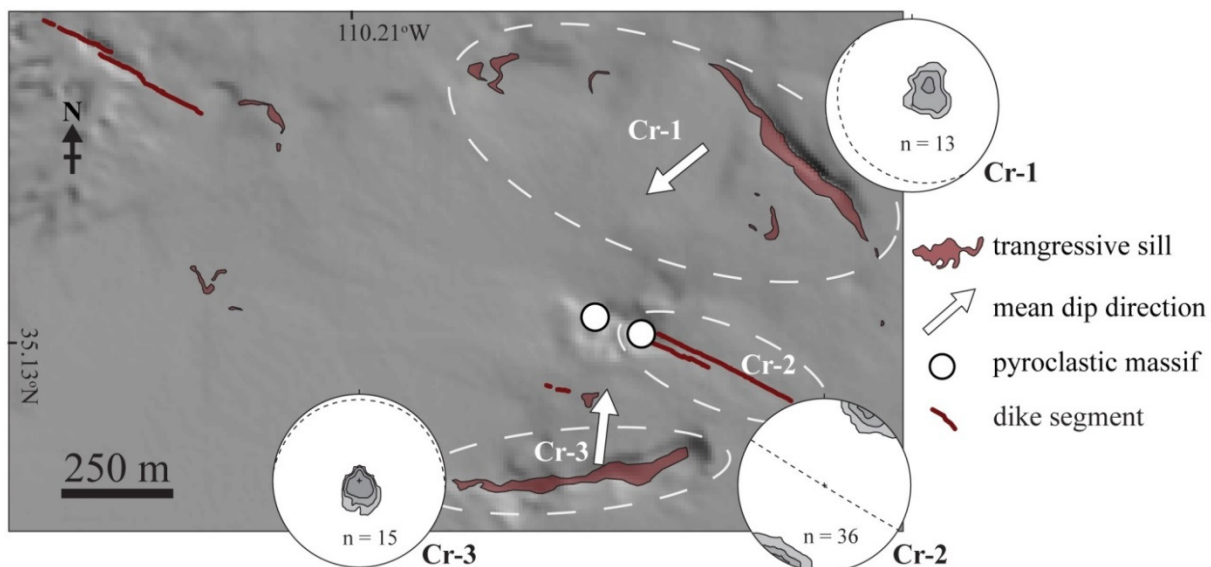


Figure 7.13. Simplified map of Crescent Rocks on a 10 m resolution hillshade. Location of the complex annotated in Figure 7.1. Stereonets are lower hemisphere projections of contours of poles to intrusion planes for each labelled area represented by a dashed ellipse. Great circles (dashed line) represent the mean intrusion orientation for each area.

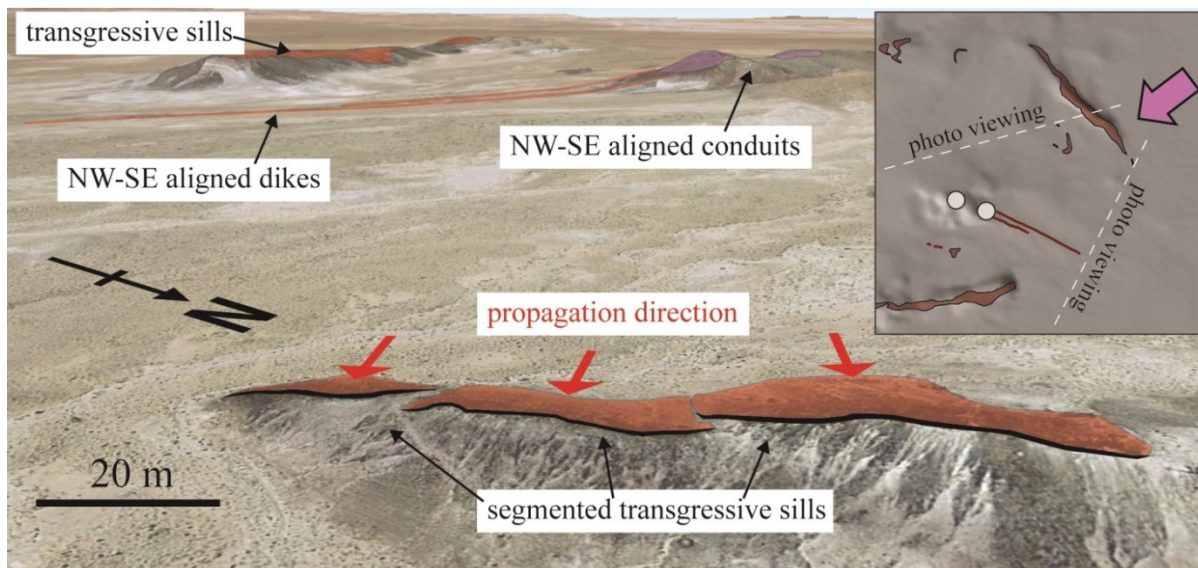


Figure 7.14. Oblique view of a Google Earth image of Crescent Rocks. Inset (top right) shows the viewing direction of the image within the complex (refer also to Fig. 7.10). Segmented transgressive sills are annotated in transparent red. Red arrows signify the inferred propagation direction based on the nature of the segmentation and the long-axis of the country rock bridge between segments (Schofield et al., 2012a) (refer to Table 7.1).

fragmentation and ballistic or column/current particle transport (e.g., debris jets; Ross and White, 2006; Andrews et al., 2014). Yet, the juvenile pyroclasts are also mingled chaotically with non-erupted, coherent magma (Lefebvre et al., 2012). It is inferred that these structures represent the “roots” of subaerial eruptions (Hooten and Ort, 2002; Keating et al., 2008; Lefebvre et al., 2012; Re et al., 2015). As shown in Figure 7.4, beds of juvenile scoria occasionally form normally-graded layers within the pyroclastic massifs, providing compelling evidence that these structures were once open to the atmosphere, feeding eruptions. This is consistent with the interpretation of Re et al. (2015) that massifs in the northwestern and southern sectors of Jagged Rocks represent conduits to multiple volcanoes. Similar structures in the San Rafael and Navajo volcanic fields, USA, and Rauðhólar volcanic chain, Iceland, have also been interpreted as volcanic feeders (Delaney and Pollard, 1981; Kiyosugi et al., 2012; Friese et al., 2013).

7.6.2 Transporting magma to eruption: the role of dikes vs. sills

Ambiguous cross-cutting relations between dikes and massifs suggest near-synchronous formation, and it is likely that dikes developed into the larger, pyroclastic feeders (massifs) through gradual removal and ingestion of country rock (Hooten and Ort, 2002; Keating et al., 2008; Lefebvre et al., 2012; Harp and Valentine, 2015). Structural alignments between massifs and other eruptive centers in the Hopi Buttes region are sub-parallel to the broad-scale dike trends throughout the volcanic field. For example, 84% of eruptive center alignments are within 20° of the mean dike trend (129°). By inference, it is suggested in this study that the majority of volcanoes in the Hopi Buttes were fed by the NW-SE-striking dikes.

Although NW-SE-striking dikes and their related pyroclastic massifs were the primary pathways through which magma was transported to eruption, the abundance of sills throughout the Hopi Buttes suggests that they too played an important role. A good example is the Crown Butte complex, which contains sills and eruptive centers (maar-diatremes, pyroclastic massifs), in the absence of observable dikes. At Crown Butte, the diatremes are positioned in the center of a saucer-shaped sill (Fig. 7.11). Pyroclastic massifs occur near the peripheries of the sill complex and are often surrounded by transgressive sills (Fig. 7.11), which is not the case in the Jagged Rocks or Crescent Rocks field areas (Figs. 7.9, 7.13). Further field investigation is required to constrain the precise timing of sill, diatreme, and massif formation. However, it is clear that the pyroclastic massifs are aligned sub-parallel to the long-axis of the saucer-shaped sill, and at a high angle to the NW-SE regional dike trend. These observations suggest that eruptive centers at Crown Butte may have been sourced directly from transgressive sills rather than NW-SE-trending dikes.

This observation stands in contrast to the Crescent Rocks field area, where massifs are located in the center of the complex and have direct contacts with NW-SE-trending dikes. Similar to Crown Butte, transgressive sills are located at the peripheries of the complex, but no pyroclastic massifs are observed near these intrusions. Although there is little evidence to suggest that transgressive sills at Crescent Rocks transported magma to eruption, it is likely that they were involved in lateral migration of magma away from the central feeding system, as suggested by propagation directions inferred from the arrangement of sill segments (Fig. 7.14).

7.6.3 Transgressive sills in monogenetic fields

Saucer-shaped sills (thicknesses >10 m) are commonly imaged from seismic reflection surveys of large igneous provinces and magmatic rifted margins (Thomson and Hutton, 2004; Cartwright and Hansen, 2006; Magee et al., 2014). Direct field observations are restricted to the Karoo large igneous province of southern Africa (Chevallier and Woodford, 1999) and the Faroe Islands, UK (Hansen et al., 2011). Consistent with interpretations of sill intrusions at Jagged Rocks by Re et al. (2015), the arrangements and orientations of transgressive sills at Hopi Buttes are typical of the outer rim of saucer-shaped intrusions observed in seismic, experimental, and field studies (Galland et al., 2009; Hansen et al., 2011; Magee et al., 2014), where all segments dip toward a common area in the center of the complex (Fig. 7.15). The flat, inner sill of the saucer-shaped structure may be inferred to lie below the current level of exposure (Fig. 7.15D).

To develop a saucer-shaped intrusion, rising magma transforms into a flat-lying sill, which ultimately forms the base of the saucer-shaped structure (Fig. 7.15). The transformation of a dike to a sill may occur due to: (1) changes in magma buoyancy (Francis, 1982), (2) stress rotations (Valentine and Krogh, 2006), and/or (3) ascent through sedimentary layers with alternating mechanical properties (Burchardt, 2008; Thomson and Schofield, 2008; Galland et al., 2009; Magee et al., 2013b). For example, dikes are shown experimentally to transition into sills when they encounter the contact between layers of contrasting rigidity (Kavanagh et al., 2006, 2015). Consistent with this interpretation, numerical modeling studies reveal local stress rotations ahead of vertically propagating dike tips near the contacts between more- and less-rigid layers. In these instances, the least compressive stress becomes vertical (Gudmundsson and Brenner, 2004; Burchardt, 2008),

thereby promoting sill propagation. Alternatively, if a dike intersects a weak layer prone to viscous deformation, such as shale, coal or weakly consolidated sandstone (Schofield et al., 2012b), fracture propagation may be inhibited above the dike tip (Thomson, 2007). When vertical crack propagation ceases, magma may intrude laterally along bedding horizons. Magma intrusion in contact with viscously deforming country rock is commonly marked by the presence of domains of peperite along intrusion margins (Airoldi et al., 2011), like those observed along some sill intrusions at Crown Butte (Fig. 7.8). Field, seismic reflection, numerical modeling, and analog modeling studies show that sill growth at shallow depths is often accommodated by lifting the overburden above the sill roof (Fig. 7.15B) (Johnson and Pollard, 1973; Malthe-Sørensen et al., 2004; Hansen and Cartwright, 2006a; Galland et al., 2009). Stress concentrations at sill peripheries result in both tensile and extensional-shear fracturing and the development of transgressive intrusive sheets (Fig. 7.15B). Magma ascends the stratigraphy radially away from the central sill in these transgressive intrusions, forming an overall saucer shape (Fig. 7.15C). Dynamic stresses changes at sheet tips, host-rock strength variations, and preexisting bedding weaknesses act to alter the path of magma propagation and fracture growth, and thus the transgressive sills exhibit a step-and-stairs geometry (Gudmundsson and Brenner, 2004; Malthe-Sørensen et al., 2004; Airoldi et al., 2011; Mathieu et al., 2015; Walker, 2016) (Fig. 7.3C, D).

Another possibility is that, rather than originating from a central sill, the shallow-dipping ($\sim 20^\circ$), transgressive sill segments extend directly from an (unexposed) dike, resulting in a structural arrangement consistent with a cusped geometry (Mathieu et al., 2008). Morphologically both cusped and saucer-shaped intrusion are quite similar, however, cusped intrusions form experimentally as a result of high shear stresses generated in low-

cohesion sediments ahead of a propagating dike (Mathieu et al., 2008; Abdelmalak et al., 2012; Mourgues et al., 2012). Indeed, dike-tip propagation in shallow, weakly consolidated sediments at Hopi Buttes (Re et al., 2015, and references therein) may have promoted shearing rather than the opening-mode, tensile fracturing expected in competent, brittle rocks (Anderson, 1951; Rubin, 1995). Similar v-shaped transgressive sheets were produced experimentally by Galland et al. (2014), and were shown to form when viscous stresses in the flowing magma (related to magma flux and magma viscosity) were high compared to host rock strength.

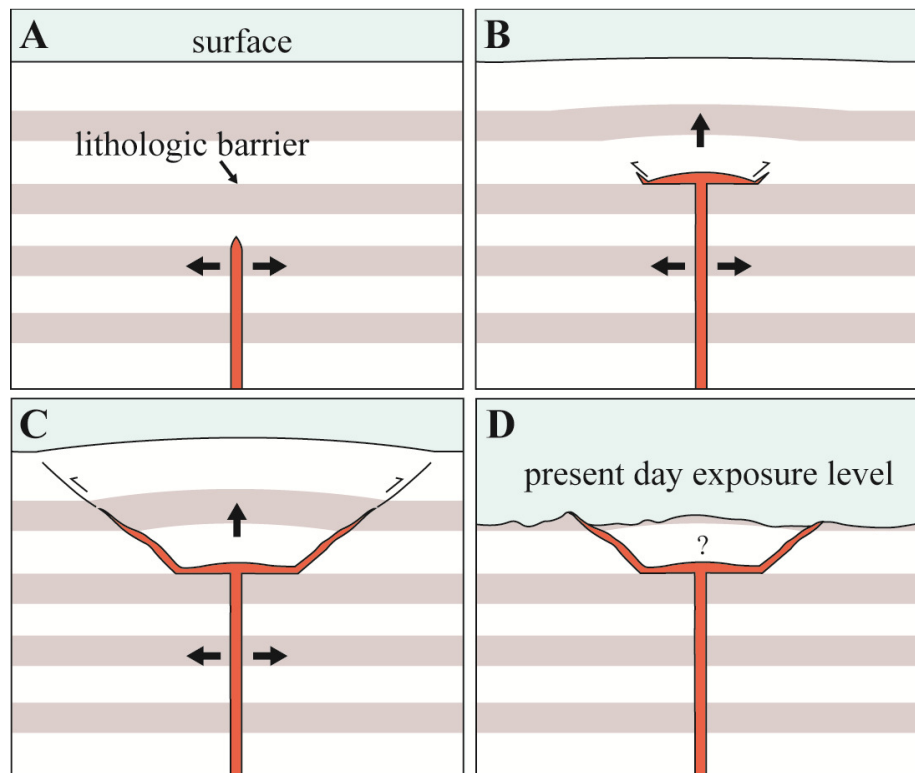


Figure 7.15. Formation of a saucer-shaped sill modified from Galland et al. (2009). The figure illustrates a two-dimensional cross-section through the intrusion, normal to the strike of the initial dike. Note that if the saucer-shaped sill is fed from a linear source (i.e., a dike), it may be elongate with a long-axis parallel to the strike of the dike-feeder. A: A dike propagates vertically until intersecting a lithologic barrier (Thomson, 2007). B: Magma propagates horizontally as a sill until generating extensional-shear fractures at the sill periphery (Galland et al., 2009) that magma can exploit. C: Magma then ascends radially away from the central sill as an inclined sheet (or transgressive sill). D: At Crown Butte and Crescent Rocks the central sill is not exposed at the present day exposure level. However, a saucer-shaped geometry is favored at these localities as the arrangement of

transgressive sill segments is consistent with the outer rim of a saucer, and these types of intrusions are frequently observed in nature from both field and seismic reflection surveys (Chevalier and Woodford, 1999; Cartwright and Hansen, 2006; Thomson, 2007; Hansen et al., 2011).

Lastly, transgressive sills could form in response to subaerial and/or subsurface volcanic activity. As suggested by Re et al. (2015) for sills at southwest Jagged Rocks, the presence of a volcanic load (e.g., a scoria cone) would produce local stress rotations immediately below the volcano, which could lead to sill formation. However, it is unknown whether a scoria cone was present during emplacement of the Jagged Rocks intrusions described by Re et al. (2015). The effect of pyroclastic massif development (i.e., Lefebvre et al., 2012) on vertical dike propagation has never been considered for the Hopi Buttes region. It should be noted that, at the time of formation, the pyroclastic massifs consisted of poorly-consolidated pyroclastics and country rock (Lefebvre et al., 2012; Fig. 7.4C) that could inhibit opening-mode tensile fracturing and, consequently, vertical dike ascent (Thomson, 2007; Mathieu et al., 2008). If vertical dike propagation were temporarily blocked in the central feeding region, magma could have been diverted laterally as transgressive sills. Indeed, transgressive sills in southern Hopi Buttes appear to have propagated away from central massifs (Fig. 7.14), and some sills extend outward from dikes immediately below massif structures (Fig. 7.3B). Regardless of the dynamics of emplacement, these observations demonstrate that shallow intrusive networks in the Hopi Buttes would have been characterized by geometrically complex magma flow.

7.6.4 Implications for other volcanic fields

The strong correlation between eruptive center alignments and dike trends at Hopi Buttes suggests that statistical alignment studies in monogenetic volcanic fields provide

reliable, first-order estimates of the orientations of dike feeder systems (Paulsen and Wilson, 2010; Le Corvec et al., 2013a; Muirhead et al., 2015). However, alignment analyses are unable to resolve the distribution of geometrically complex intrusions, such as transgressive sills. This study shows that monogenetic volcanoes intruding sedimentary sequences can be underlain by complex feeder systems. Estimates of the observable volume of dikes (maximum volume of $1.90 \times 10^6 \text{ m}^3$) and sills (minimum volume of $8.47 \times 10^5 \text{ m}^3$) in this study, reveal that sills at Hopi Buttes make up at least 30% of the shallow (<350 m paleodepth) intruded volume ($\sim 2.75 \times 10^6 \text{ m}^3$ total) (Table 7.2). These sills are essential components of the observed feeder systems (e.g., Crescent Rocks), connecting with both dikes and pyroclastic massifs (Fig. 7.3B). Furthermore, observations presented here reveal that saucer-shaped intrusions are not restricted to major intrusions of large igneous provinces and magmatic rifted margins, but may be common features, at much smaller scales, in monogenetic fields erupting through sedimentary sequences. Sills at Hopi Buttes are thinner than those observed in seismic reflection surveys (which are >10 m). However, they exhibit similar scaling relations to saucer-shaped sills from seismic reflection and numerical modelling studies (e.g., Malthe-Sørensen et al., 2004; Hansen and Cartwright, 2006b), where the diameter of the sill (commonly $\sim 1000 \text{ m}$ at Hopi Buttes) is between 1.5 and 4 times the depth of the overburden (300-350 m at Hopi Buttes). We suggest that the characteristic feeder systems described here may be present beneath monogenetic fields elsewhere, particularly in fields where magma intersects shallow, and often weak, sedimentary rocks (e.g., Auckland and San Francisco volcanic fields), thereby promoting sill formation in the subsurface.

Data presented in this study support a growing body of evidence that sills are important components of monogenetic feeder systems. Nemeth and Martin (2007) found that

sills form a significant portion of the shallow (~200 m paleodepth) intrusive system of the Bakony–Balaton Highland Volcanic Field, Hungary. These sills form part of an interconnected dike-sill network that fed magma to maar-diatreme complexes and other surface eruptions. Sills also constitute the primary intrusive component of the shallow plumbing system of the San Rafael volcanic field, USA (Delaney and Gartner, 1997; Kiyosugi et al., 2012). Recent volume estimates based on ground-based LiDAR surveys and field mapping in the San Rafael volcanic field show that sill intrusions comprised >90% of the intruded volume at ~300-800 m depth (Richardson et al., 2015). Some sills appear to have transported magma directly to and from sub-cylindrical massifs, to both feed and modulate eruptions at the surface. Furthermore, saucer-shaped intrusions observed at Hopi Buttes in the current study and described in southwest Jagged Rocks by Re et al. (2015) represent a previously unrecognized feeder geometry within monogenetic volcanic fields.

These observations suggest that the broad-scale feeder systems of monogenetic volcanoes may include interconnected dike and sill networks, the dynamics of which influence the location and style of eruptive activity. Field observations of diatreme and massif deposits at Hopi Buttes reveal that both vent longevity and eruption style (explosive vs effusive) at many volcanoes were controlled by magma flow within, and development of, underlying intrusions (Lefebvre et al., 2012, 2016). The transition from a dike- to a sill-dominated feeder system shown in this study (Figs. 7.11 and 7.13) thus represents a fundamental change in the dynamics of the intrusive system, which in turn should act to modulate eruptive activity at the surface. For example, it is inferred here that development of transgressive sills may have diverted magma away from a central conduit system (e.g. at Crescent Rocks; Figs. 7.13 and 7.14), potentially resulting in: (1) cessation of eruptive

activity, or (2) decreased magma flux into the conduit-feeder system, resulting in increased water-magma ratios and explosive, maar-forming volcanic activity (Lefebvre et al., 2012; Valentine and Cortés, 2013; Lefebvre et al., 2016). Recent experimental studies also show that the transition from a dike to a sill is characterized by significant pressure drops in the shallow magmatic system (Kavanagh et al., 2015). These authors suggest these pressure reductions would result in decreased volatile solubility in magma and hence volatile exsolution. Depending on the magnitude of the pressure drop, the magma system may become destabilized, triggering additional diking and/or the development of transgressive sills that initiate volcanic eruptions at the surface (Kavanagh et al., 2015). During an eruptive event, these evolving dynamics (i.e., dike to sill transition) would likely be signaled by inflation/deflation of the ground surface associated with sill intrusion (Chadwick et al., 2011; Galland, 2012; Galland and Scheibert, 2013; Kavanagh et al., 2015; Fig 15). This was certainly the case during the monogenetic eruption of Parícutin from 1943-1952 (Foshag and Gonzalez-Reyna, 1956), which exhibited surface uplifts prior to initial eruptions, although it is unknown whether surface inflation was the result of dike and/or sill emplacement. Assuming that sill intrusions at Hopi Buttes were accommodated elastically via sill-roof uplift, an 80 cm-thick, 1,000 m-diameter sill intruding 200 to 350 m below the ground surface would produce 10 to 60 cm of uplift, based on the scaling arguments of Goultly and Schofield (2008) (refer to Section 7.8.1).

7.7 Conclusions

Although volcanic fields pose hazards to major cities worldwide, their shallow (<500 m depth) subsurface feeders are rarely exposed and poorly understood. Exposures of dikes, sills and pyroclastic massifs in southern Hopi Buttes therefore provide a unique window into

the shallow feeder system of a monogenetic volcanic field. Results from this study show that the feeder systems to monogenetic volcanoes may be more complex than conventional depictions of simple dike-fed systems, particularly in fields where magma intersects poorly consolidated sedimentary rocks. Furthermore, some monogenetic fields may be characterized by the presence of thin saucer-shaped sills at shallow levels. From this investigation of the broad distribution and geometries of feeder systems at Hopi Buttes, the following conclusions are drawn:

- 1) The agreement between the trends of eruptive center alignments and dikes suggests that volcanic eruptions were primarily fed by NW-SE-striking dikes.
- 2) Sills, which often exhibit saucer shapes, comprise a significant proportion of the shallow plumbing system (minimum of 31% of the intruded volume).
- 3) Sills were responsible for transporting magma to eruption and/or away from central conduit systems (pyroclastic massifs), thereby playing a critical role in modulating eruption dynamics.
- 4) Intrusion of sills at Hopi Buttes was probably accompanied by surface inflation on the order of decimeters.

The characteristic feeder systems of the Hopi Buttes may underlie monogenetic fields elsewhere, particularly where magma intersects shallow, and often weak, sedimentary rocks. Further field, laboratory and numerical modeling studies are required to improve our understanding of the geometry and subsurface development of intrusive networks like those exposed at Hopi Buttes, with the aim of informing hazard forecasting and prediction in active volcanic fields.

7.8 Supporting information

7.8.1 Estimating surface uplift from shallow sill intrusion at Hopi Buttes

A simple flexure model (e.g., Pollard and Johnson, 1973; Turcotte and Schubert, 1982; Gouly and Schofield, 2008) was applied to estimate the elastic deformation of the overburden above a shallowly intruded sill (Fig. 7.16A). This approach has been used in previous studies (e.g., Gouly and Schofield, 2008) and requires various simplifying assumptions. Firstly, it is assumed that the overlying sill-roof is homogeneous and behaves as a thin elastic plate. The boundary conditions applied are as follows: (1) the top of the model acts as free surface; (2) uplift of the sill roof reduces to zero at and above the periphery of the sill; and (3) a normal stress acts on the base of the sill equal to the excess magma pressure within the sill. Lastly, the sill is assumed to grow quasi-statically, and the uplift of the sill-roof is invariant with depth.

The opening of any magma-filled crack (i.e. dike or sill) at depth (z) requires that magma pressure (p) within the crack exceeds the least compressive stress, which in an isotropic stress environment will be equal to the lithostatic stress. At the time of intrusion a dike or sill will thus have an excess magma pressure, defined as:

$$\Delta p = p - \rho g z \quad (\text{Eq. 7.1})$$

where g is acceleration due to gravity and ρ is the density of the surrounding country rock. Following Pollard and Johnson (1973), Gouly and Schofield (2008) calculated the vertical deflection of an elastic plate (i.e., displacement in the positive z -direction; Fig. 7.16A) above a circular sill with a constant value of excess magma pressure from the following equation:

$$u(r) = \frac{\Delta p}{64D} (R^2 - r^2)^2, \quad r \leq R, \quad (\text{Eq. 7.2})$$

where R is the radius of the sill (half-length), r is the radial position on along the sill, and D is flexural rigidity of the sill-roof defined by:

$$D = \frac{Eh^3}{12(1-\nu^2)} \quad (\text{Eq. 7.3})$$

where E is Young's modulus, h is the thickness of the sill roof, and ν is Poisson's ratio. The excess magma pressure of a fluid-filled crack (e.g., dike or sill) may be estimated from its maximum thickness (t_{max}) from the following equation (Sneddon and Lowengrub, 1969):

$$\Delta p = \frac{(t_{max}E)}{2l(1-\nu^2)} \quad (\text{Eq. 7.4})$$

where l is the intrusion length. By substituting Δp in eq. 7.2 with eq. 7.4 the surface uplift or vertical deflection of the sill roof (u) may be calculated from the following equation:

$$u(r) = \left(\frac{3t_{max}}{32lh^3} \right) (R^2 - r^2)^2, \quad r \leq R, \quad (\text{Eq. 7.5})$$

From eq. (7.5) a range of possible surface uplifts are calculated for sill intrusions at 50 m depth-intervals in the Owl Rock and Petrified Forrest members (~200 – 350 m paleodepth) (Fig. 7.16B). A sill thickness equal to the mean value measured in the field (0.8 m) is applied, as well as a sill radius (500 m) similar to that observed at Crowne Butte, Crescent Rocks and southwest Jagged Rocks (Re et al., 2015). Results show that shallow sill intrusions in the Hopi Buttes volcanic field may have produced surface uplifts between 10 and 60 cm (Fig. 7.16B).

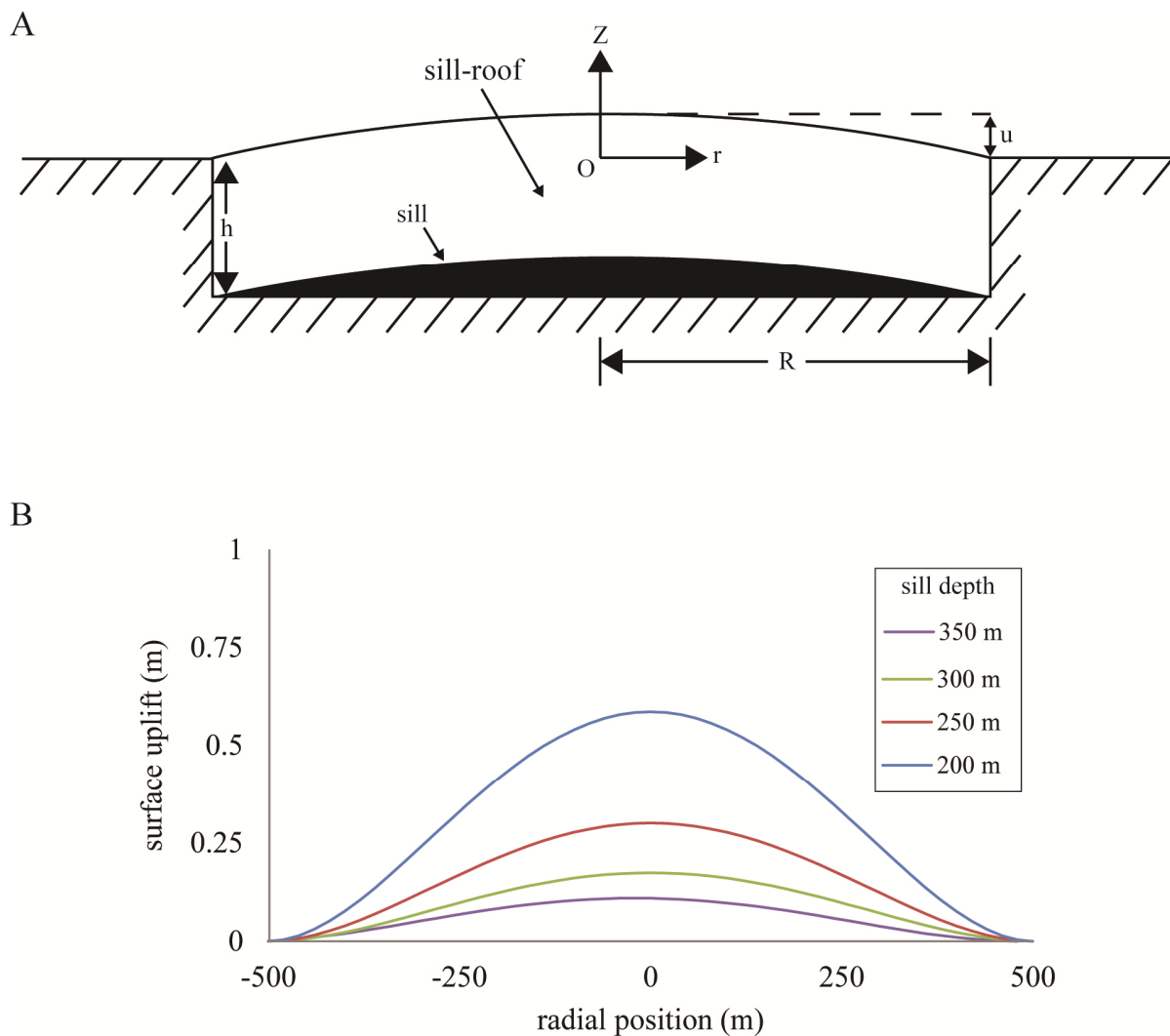


Figure 7.16. A: Schematic illustration of a cross-section through a circular sill and the resulting flexural uplift of the sill-roof. Modified from Gouly and Schofield (2008). B: Plot of vertical displacements (surface uplift) for different radial positions (r) above a circular sill with a maximum thickness of 0.8 m and radius of 500 m. Each line color corresponds to a sill intruded at a different depth (h).

7.9 Supporting methods

7.9.1 Length tolerance for eruptive center alignments

Structural alignment analyses of eruptive centers in this study follow the method of Le Corvec et al. (2013a). Regression lines were calculated for any three separate eruptive centers

(i.e., massifs and diatremes). Alignments were then accepted or rejected based on length and width criteria (Fig. 7.5). In accordance with Le Corvec et al (2013a), a width tolerance of 10 m was used, whereas the length tolerance depended on the eruptive center density within the field (Fig. 7.17A). Eruptive center density was calculated by dividing the number of eruptive centers by the area of the volcanic field estimated using a convex hull, which is a polygon encompassing the entire field area and generated by connecting the least amount of outermost points of the eruptive center population (Hamilton et al., 2010) (Fig. 7.17B). By comparing 3-point alignment data calculated using various length tolerances with morphometric volcanic lineaments (e.g., elongate cones; Tibaldi, 1995) in well-exposed volcanic fields, Le Corvec et al (2013a) created a procedure for minimizing artifacts from alignment analyses. Specifically, the length tolerance (L) for any field can be determined from the density of volcanic centers (d), using the equation:

$$L(d) = -2530\ln(d)-36905 \quad (\text{eq. 7.6})$$

Base on this equation, a length tolerance for Hopi Buttes alignments of 3878 m was applied in this study (Fig. 7.17A).

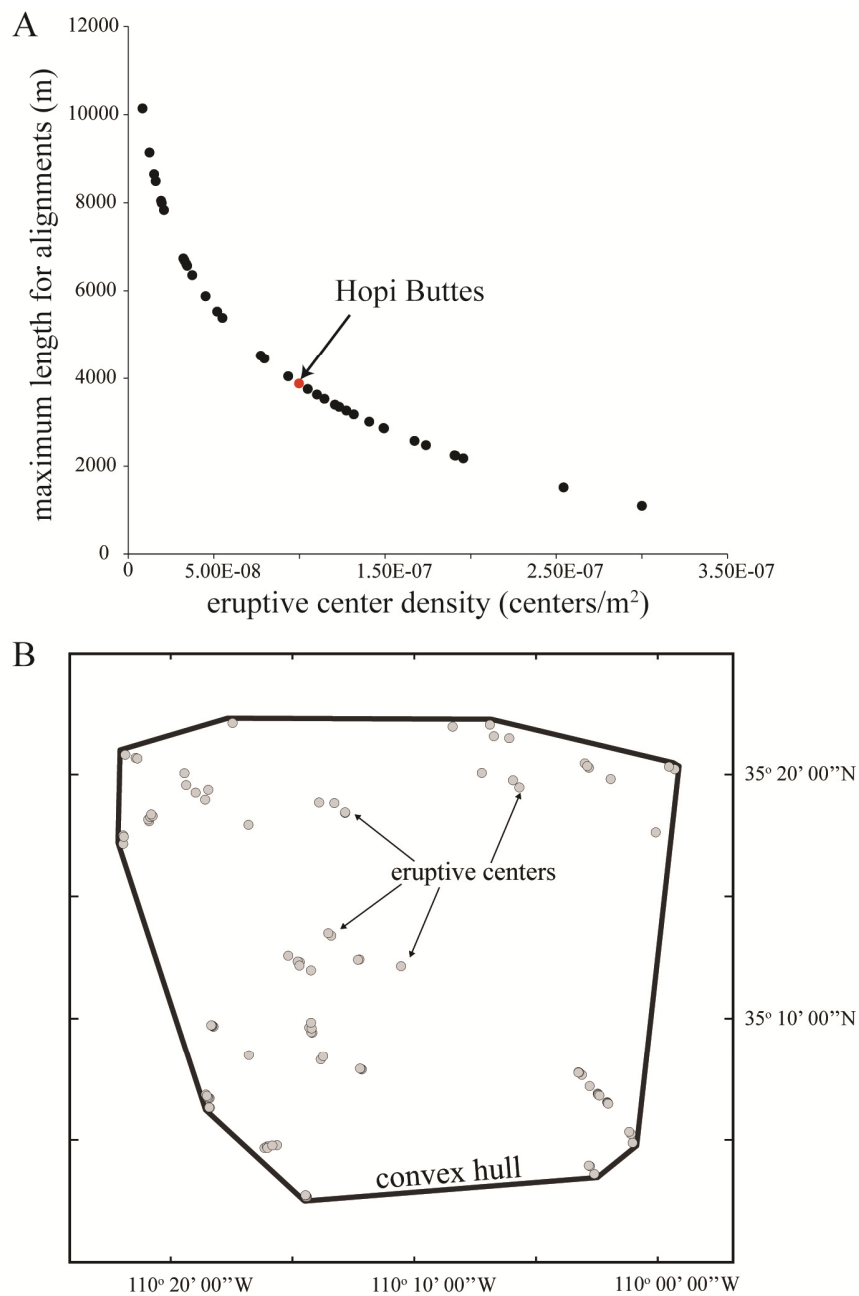


Figure 7.17. A: Plot of eruptive center density vs maximum length tolerance for alignments in the Hopi Buttes volcanic field (red point, this study) and a catalogue of monogenetic volcanic fields worldwide (data from Le Corvec et al., 2013a). B: Distribution of eruptive centers (diatremes and massifs) in southern Hopi Buttes from this study. The convex hull (black polygon) is used to calculate the area of the field.

CHAPTER 8: SYNTHESIS

8.1 Summary of key findings

By integrating structural measurements and field observations with geochronology, geochemistry, and seismicity data, this dissertation has investigated the ways in which tectonic and magmatic processes control faulting, magmatic strain accommodation, fluid transport, and volcanic eruptions. Overall, my work has focused on the role of magmatism, inherited crustal weaknesses, and volatile release in continental rift evolution in the East African Rift (EAR), with implications for magma-rich continental rifts in general (Chapters 2-5). I have also examined the eruption-feeding capacity of interconnected sill complexes over a range of volcanic systems, from small monogenetic fields to large igneous provinces (Chapters 6-7). Below, I revisit each of the five key motivating questions outlined in Chapter 1 in light of new insights developed during my dissertation.

Question 1: How do the orientations and spatial occurrences of upper crustal dike networks vary over the course of continental rift evolution?

Cone lineament data presented in Chapter 2 represent the first regional analysis of along-axis variability in dike intrusions across the East African Rift. Results show that over the past ~1 million years, dikes have rarely reached the surface along the central axis of early-stage rift basins (<10 Ma) in the Eastern rift (e.g., Natron and Magadi basin). Instead, upper crustal diking in these basins is confined to transfer zones, where the dikes have complex geometries, including extension-normal, extension-oblique, and radial patterns. The observed dike arrangements are likely the result of interactions among the regional stress field, local magma-induced stresses, and stress rotations related to mechanical interactions between rift

segments. In contrast, results show that evolved rift basins (>10 Ma) in the Eastern rift are heavily intruded by rift-parallel dikes that accommodate upper crustal extension along the full length of the basin.

These observations provide new understanding of the importance of magmatic processes during rift initiation and evolution, by addressing whether upper crustal dikes play a key role in accommodating regional extension during early-stage rifting. Recently, Calais et al. (2008) suggested that a significant portion of regional extension in early-stage basins in the Eastern rift is accommodated through emplacement of dikes. However, these assertions were based on a single observation of a <10 km-long dike at the southern end of the Natron basin (South Natron field of Chapter 2), inferred from InSAR and seismicity. Analyses presented in this dissertation provide an opportunity to reinterpret the 2007 diking event within the overall structural context of the rift. My work demonstrates that dike intrusions in the South Natron field are restricted to particular structural zones, in this case transfer zones. For this reason, diking events in southern Natron do not represent a basin-wide mode of upper crustal strain accommodation, and more often relate to local perturbations in the tectonic-magmatic stress regime (e.g., pressurized magma chambers). The inferred scarcity of upper crustal dikes along the length of the Natron-Magadi basin instead suggests that normal faulting acts as the primary mode of upper crustal strain accommodation in this part of the rift. As rift basins in the Eastern rift evolve, however, upper crustal diking becomes more prevalent, and rift-parallel swarms begin to accommodate extension along the full length of basins.

Question 2: What is the volume of fault-controlled magmatic CO₂ released along the East African Rift, and the role of magmatic volatiles in driving rift basin development?

This dissertation presents the first diffuse CO₂ flux study investigating degassing away from active volcanic centers in the East African Rift. Analyses in Chapter 3 show that tectonic degassing of CO₂ across rift-wide fault systems in East Africa can release volumes of mantle-derived (i.e., magmatic) CO₂ rivaling those released from active volcanoes. Extrapolating results across the Eastern rift suggests that the EAR releases on the order of 71 ± 33 Mt yr⁻¹ of CO₂ through its fault systems. These results highlight continental rifts as important contributors to Earth's natural CO₂ budget, suggesting they may play an important role in modulating greenhouse conditions, particularly during periods of super-continent breakup.

The high amounts of magmatic CO₂ released in the Natron and Magadi region has wider implications for the role of magmatism in early-stage continental rifting. Although the Natron and Magadi basins have been largely “avolcanic” over the last ~1 million years, significant volumes of intruded magma are required at depth to sustain these high CO₂ fluxes. In support of this assertion, recently acquired seismic tomography data by Roecker et al. (2015) reveal an axial low velocity zone between ~15 and 35 km depth along the Natron-Magadi region.

Although upper crustal diking may not play a critical role in rifting in the Natron and Magadi basins, the emplacement of magma at deeper levels (i.e., upper mantle and/or lower crust) may have had an indirect, yet important, effect. Fault strain analyses presented in Chapter 4 show that areas of high upper crustal strain coincide with hydrothermal spring systems exhibiting a magmatic signature. The focusing of magma toward the rift center and

concomitant release of magmatic fluids may help to weaken lithosphere and assist the transition to intra-rift dominated strain accommodation. Magmatic fluid-driven weakening of lithosphere provides a previously unrecognized mechanism for focusing strain during rift basins evolution (c.f., Ebinger and Casey, 2001; Cort, 2009) prior to the development of magmatic centers and the initiation of nascent sea-floor spreading, like that observed in Ethiopia today (Keranen et al., 2004; Keir et al., 2011a; Wright et al., 2012).

Question 3: How do preexisting structures affect faulting and strain localization during rift initiation and evolution?

Chapter 5 provides a revision of the timing and kinematics of transverse faults that exploit preexisting weaknesses in the Kenya Rift, by analyzing the Kordjya fault of the Magadi basin. Previous studies in East Africa have highlighted the importance of preexisting structures during rift initiation (e.g., Chorowicz, 1992), but this study demonstrates that the activation of preexisting weaknesses is important at all stages of rift evolution. Furthermore, the detailed analysis of the Kordjya fault reveals contrasts with classical depictions of transverse faults (e.g., Chorowicz, 1992; Chorowicz and Sorlien, 1992; Le Turdu et al., 1999; Ebinger, 2005). First, the Kordjya fault post-dates, and even exploits, the rift-parallel fault systems. Second, it exhibits dip slip kinematics rather than a component of dextral or sinistral shear.

These findings are significant because the recent tendency for dip-slip activity along the Kordjya fault, rather than rift-parallel faults, suggests a change in rift driving forces. The relative timing between the development of the Kordjya fault and the rift-parallel segments suggests that the Kordjya fault has activated in response to concentrated magmatism and

normal faulting along the central rift axis. The fault is inferred to act as a critical kinematic linkage transferring strain between the rift border and central rift axis. Results from this study have implications for other transverse fault systems throughout Kenya – namely, they reflect not only the effects of inherited crustal fabrics on fault dynamics, but may also provide important clues regarding evolving magmatic and tectonic strain fields within the Kenya Rift.

Question 4: What is the typical geometrical arrangement of LIP feeder systems and are sill networks capable of feeding voluminous lava eruptions?

Chapter 6 involved the first regional analysis of sill-fed dike intrusions of the Ferrar large igneous province (LIP), Antarctica, and has highlighted a previously unrecognized feeder system to LIP eruptions. The Ferrar intrusions form a broadly-distributed array of relatively small, sill-fed dikes (<2 km long, 1.8 m wide) exhibiting almost any orientation. This sill-fed dike network contrasts with the long (100s to 1000s of km) sub-parallel dike swarms often depicted as the feeders of flood basalt provinces, and has the appearance of a “cracked lid” atop a sill complex. This study demonstrates that shallow magma systems composed dominantly of sills are capable of feeding voluminous outpourings of lava, and highlights the important role that sills play in feeding active volcanic system that span the full spectrum of eruptive volumes.

The conditions that determine whether flood basalt lavas of LIPs will be fed by sub-parallel aligned dike swarms (e.g., Columbia River Flood Basalts; Self et al., 1997) or a cracked lid system (e.g., Ferrar LIP; this study) require further consideration, but are inferred here to relate to both the regional tectonic environment and host rock lithology. The cracked

lid may be the archetypal model for shallow feeder systems of LIPs that intruded sedimentary basins where the influence of far-field extensional tectonics is negligible.

Question 5: What processes govern the intrusive architecture of monogenetic fields, and how does their development affect eruptive style and vent location?

Field- and satellite-based observations of the 7 Ma Hopi Buttes volcanic field presented in Chapter 6 have elucidated three types of shallow magma systems (<500 m depth) in monogenetic volcanic fields: (1) dike-dominated, (2) sill-dominated, and (3) interconnected dike-sill networks. These results show that feeder systems to monogenetic volcanoes may be more complex than conventional depictions of simple dike-fed systems. Furthermore, some monogenetic fields may be characterized by the presence of thin saucer-shaped sills at shallow levels. The likelihood that an intrusion will transition from a dike to a sill is probably controlled by host rock layering. At Hopi Buttes, rigidity contrast between stronger (e.g., consolidated sandstone) and weaker layers (e.g., mudstone) may have produced local stress rotations. Alternatively, viscously deforming, weak country rock could have prevented vertical dike ascent, with magma instead intruding laterally between bedding horizons.

Agreement between the trends of eruptive center alignments and NW-SE-striking dikes suggests that volcanic eruptions in the Hopi Buttes were primarily fed by dikes. However, sills too were responsible for transporting magma to eruption and/or away from eruptive conduits, thereby playing a critical role in modulating eruption dynamics. Dike-sill transitions observed at Hopi Buttes also provide a previously unrecognized mechanism for lateral vent migration during monogenetic eruptions. Changes in eruptive sites are often viewed as a consequence of lateral dike propagation (e.g., Standing Rocks (Arizona),

Tecuitlapa Maar (Mexico); Ort and Carrasco-Núñez, 2009; Lefebvre et al., 2012). This study shows the lateral magma diversions in monogenetic fields can also occur through the formation of sills (often saucer-shaped), which can lead to new eruptive sites 100s meters away from active vents. If these sill-related magma diversions do not ultimately feed eruptions, the migration of magma away from the central feeding region may change magma-water ratios, possibly leading to explosive phreatomagmatic volcanism.

8.2 Future perspectives

Findings presented in this dissertation highlight new avenues of research that will advance our understanding of the dynamics of magmatic-tectonic systems and continental rift processes. Firstly, this work highlights a fundamental question related to how we view subsurface intrusive networks in the East African Rift. To what extent are we biased towards the identification of dike intrusions? The current scientific consensus is that Quaternary magmatism in East Africa is almost entirely dominated by the emplacement of dikes (e.g., Kendall et al., 2005; Mazzarini et al., 2007; Rooney et al., 2011; Calais et al., 2008; Keir et al., 2011a; Wright et al., 2012). However, continental rifting and break-up, like that seen today in East Africa, is commonly associated with the formation of sedimentary basins and generation of significant mafic melt volumes. Chapters 6 and 7 show that magma ascent through sedimentary sequences may often occur through sill networks. In line with this assertion, volcanic rifted margins are shown to host laterally and vertically extensive sill complexes (Cartwright and Hansen, 2006; Magee et al., 2016). Very few studies in areas of active continental break-up consider the potential role of sills within volcanic plumbing systems. Nonetheless, recent InSAR studies have recorded emplacement of sill-like intrusions in rift basins in Ethiopia, Kenya, and Tanzania (Biggs et al., 2009b; Biggs et al., 2011; Pagli

et al., 2012, Biggs et al., 2013), which is further supported by recent observations of sub-horizontally oriented seismic swarms interpreted to reflect sill intrusion between Oldoinyo Lengai and Gelai volcanoes, Tanzania (Weinstein et al., 2015). Together, these observations imply that magma migration in the East African Rift may be facilitated by sill-complex intrusion, in addition to dike emplacement. However, the role that sills play in magma transport in East Africa is poorly constrained and upper crustal sills are not incorporated into calculations of total magma volumes (Ferguson et al., 2010). Furthermore, sill complex formation and subsequent thermal weakening of the crust during rift development represents a currently unexplored mechanism for driving strain localization and continental rift evolution.

Second, rates of magma production during continental rifting in East Africa are poorly constrained, despite having important implications for how rifting initiates and contributes to the growth of continental lithosphere. The flux of magmatic volatiles at the surface is expected to relate to the volume (and rate) of magma emplaced in the subsurface. However, volatile flux measurements in the EAR have never been used to infer magma emplacement rates at depth. Future work should aim to constrain the relationship between geophysically imaged magma systems and magmatic CO₂ flux at the surface. These observations could be integrated with numerical models that account for extensional and thermal-petrographic processes in rift settings (e.g., Karakas and Dufek, 2015) to provide a range of magma supply and accretion rates for rift basins in the EAR.

Third, the effects of H₂O infiltration on deformation processes (e.g., dislocation creep) has long been a focus for rock mechanical studies (Griggs and Blacic, 1965; Tullis and Yund, 1989; Post and Tullis, 1998; Stipp et al., 2006), due in part to the well-known effect of water release on subduction zone processes (Saffer and Tobin, 2011, and references therein).

Results from this dissertation (Chapters 3-5), as well as recent work in the EAR (Lindfeld et al., 2012; Albaric et al., 2014; Mana et al., 2015), suggest CO₂-rich fluids have a fundamental effect on the evolution of divergent plate boundaries, where the release of magmatic CO₂ may weaken rock through mantle metasomatism and increases in pore-fluid pressure.

Consequently, future rock mechanical studies should focus on the effects of carbonic fluids on rock strength (e.g., Chernack et al., 2009) in extensional environments.

Finally, how does dikeing in transfer zones affect extensional processes across the rift? Although upper crustal dikes at some rift settings are confined to transfer zones, they clearly intrude laterally into the distal ends of rift basins (Wauthier et al., 2015; Chapter 2). These intrusions are therefore expected to affect the extensional stress state within adjacent rifts. For example, the 2002 dike intrusion in the Virunga Province (refer to Fig. 2.10, Chapter 2) was shown by Wauthier et al. (2015) to produce static stress changes in the center of the Kivu basin, which in turn initiated fault slip along the rift border. However, numerical and analog modeling studies investigating the mechanical effects of dike intrusion focus on dikeing along the central rift axis rather than transfer zones. Future studies should consider how the locus of dikeing shifts laterally through time (transfer vs central rift axis), and test the mechanical interactions and feedbacks between magmatic and amagmatic portions of rift basins.

REFERENCES

- Abdelmalak, M. M., Mourgues, R., Galland, O., and Bureau, D., 2012, Fracture mode analysis and related surface deformation during dyke intrusion: Results from 2D experimental modelling: *Earth and Planetary Science Letters*, v. 359, p. 93-105, doi: 10.1016/j.epsl.2012.10.008.
- Abebe, B., Acocella, V., Korme, T., and Ayalew, D., 2007, Quaternary faulting and volcanism in the main Ethiopian Rift: *Journal of African Earth Sciences*, v. 48, p. 115-124, doi: 10.1016/j.jafrearsci.2006.10.005.
- Abebe, T., Balestrieri, M. L., and Bigazzi, G., 2010, The Central Main Ethiopian Rift is younger than 8 Ma: confirmation through apatite fission-track thermochronology: *Terra Nova*, v. 22, p. 470-476, doi: 10.1111/j.1365-3121.2010.00968.x.
- Acocella, V., Korme, T., and Salvini, F., 2003, Formation of normal faults along the axial zone of the Ethiopian Rift: *Journal of Structural Geology*, v. 25, p. 503-513, doi: 10.1016/s0191-8141(02)00047-0.
- Acocella, V., Abebe, B., Korme, T., and Barberi, F., 2008, Structure of Tendaho Graben and Manda Hararo Rift: Implications for the evolution of the southern Red Sea propagator in Central Afar: *Tectonics*, v. 27, doi: 10.1029/2007tc002236.
- Acosta, V. T., Bande, A., Sobel, E. R., Parra, M., Schildgen, T. F., Stuart, F., and Strecker, M. R., 2015, Cenozoic extension in the Kenya Rift from low-temperature thermochronology: Links to diachronous spatiotemporal evolution of rifting in East Africa: *Tectonics*, v. 34, p. 2367-2386, doi: 10.1002/2015tc003949.
- Agostini, A., Corti, G., Zeoli, A., and Mulugeta, G., 2009, Evolution, pattern, and partitioning of deformation during oblique continental rifting: Inferences from lithospheric-scale centrifuge models: *Geochemistry, Geophysics, Geosystems*, v. 10, p. Q11015, doi: 10.1029/2009gc002676.
- Agostini, A., Bonini, M., Corti, G., Sani, F., and Manetti, P., 2011a, Distribution of Quaternary deformation in the central Main Ethiopian Rift, East Africa: *Tectonics*, v. 30, p. TC4010, doi: 10.1029/2010tc002833.
- Agostini, A., Bonini, M., Corti, G., Sani, F., and Mazzarini, F., 2011b, Fault architecture in the Main Ethiopian Rift and comparison with experimental models: Implications for rift evolution and Nubia-Somalia kinematics: *Earth and Planetary Science Letters*, v. 301, p. 479-492, doi: 10.1016/j.epsl.2010.11.024.
- Airoldi, G. M., 2011, Magma injection dynamics in the shallow Ferrar LIP (South Victoria Land) [Ph.D. thesis]: Duneidin, University of Otago, 174 p.
- Airoldi, G., Muirhead, J. D., White, J. D. L., and Rowland, J., 2011, Emplacement of magma at shallow depth: insights from field relationships at Allan Hills, south Victoria Land, East Antarctica: *Antarctic Science*, v. 23, p. 281-296, doi: 10.1017/s0954102011000095.
- Airoldi, G., Muirhead, J. D., Zanella, E., and White, J. D. L., 2012, Emplacement process of Ferrar Dolerite sheets at Allan Hills (South Victoria Land, Antarctica) inferred from magnetic fabric: *Geophysical Journal International*, v. 188, p. 1046-1060, doi: 10.1111/j.1365-246X.2011.05334.x.
- Albaric, J., Deverchere, J., Petit, C., Perrot, J., and Le Gall, B., 2009, Crustal rheology and depth distribution of earthquakes: Insights from the central and southern East African Rift System: *Tectonophysics*, v. 468, p. 28-41, doi: 10.1016/j.tecto.2008.05.021.

- Albaric, J., Perrot, J., Deverchère, J., Deschamps, A., Le Gall, B., Ferdinand, R. W., Petit, C., Tiberi, C., Sue, C., and Songo, M., 2010, Contrasted seismogenic and rheological behaviours from shallow and deep earthquake sequences in the North Tanzanian Divergence, East Africa: *Journal of African Earth Sciences*, v. 58, p. 799-811, doi: 10.1016/j.jafrearsci.2009.09.005.
- Albaric, J., Déverchère, J., Perrot, J., Jakovlev, A., and Deschamps, A., 2014, Deep crustal earthquakes in North Tanzania, East Africa: Interplay between tectonic and magmatic processes in an incipient rift: *Geochemistry, Geophysics, Geosystems*, v. 15, p. 374-394, doi: 10.1002/2013gc005027.
- Albert, H., Costa, F., and Marti, J., 2016, Years to weeks of seismic unrest and magmatic intrusions precede monogenetic eruptions: *Geology*, v. 44, p. 211-214, doi: 10.1130/g37239.1.
- Allan, A. S. R., Wilson, C. J. N., Millet, M. A., and Wysoczanski, R. J., 2012, The invisible hand: Tectonic triggering and modulation of a rhyolitic supereruption: *Geology*, v. 40, p. 563-566, doi: 10.1130/g32969.1.
- Allen, S. R., and Smith, I. E. M., 1994, Eruption styles and volcanic hazards in the Auckland volcanic field, New Zealand: *Geoscience Reports of Shizuoka University*, v. 20, p. 5-14.
- Allibone, A. H., Forsyth, P. J., Sewell, R. J., Turnbull, I. M., and Bradshaw, M. A., 1991, *Geology of the Thundergut area, southern Victoria Land, Antarctica*: Wellington Department of Scientific Industrial Research New Zealand Geological Survey miscellaneous series map 21, scale 1:50,000, 1 sheet.
- Allken, V., Huismans, R. S., and Thieulot, C., 2011, Three-dimensional numerical modeling of upper crustal extensional systems: *Journal of Geophysical Research*, v. 116, p. B10409, doi: 10.1029/2011jb008319.
- Ancochea, E., Brandle, J. L., Huertas, M. J., Hernan, F., and Herrera, R., 2008, Dike-swarms, key to the reconstruction of major volcanic edifices: The basic dikes of La Gomera (Canary Islands): *Journal of Volcanology and Geothermal Research*, v. 173, p. 207-216, doi: 10.1016/j.jvolgeores.2008.01.020.
- Anderson, E. M., 1951, *The dynamics of faulting and dyke formation with applications to Britain*: Edinburgh, Oliver and Boyd, 206 p.
- Andrews, R. G., White, J. D. L., Durig, T., and Zimanowski, B., 2014, Discrete blasts in granular material yield two-stage process of cavitation and granular fountaining: *Geophysical Research Letters*, v. 41, p. 422-428, doi: 10.1002/2013gl058526.
- Angelier, J., Bergerat, F., Dauteuil, O., and Villemin, T., 1997, Effective tension-shear relationships in extensional fissure swarms, axial rift zone of northeastern Iceland: *Journal of Structural Geology*, v. 19, p. 673-685, doi: 10.1016/s0191-8141(96)00106-x.
- Annels, A., 1967, *The geology of the Hornafjordur Region* [Ph.D. thesis]: London, University of London, 278 p.
- Aoki, Y., Takeo, M., Ohminato, T., Nagaoka, Y., and Nishida, K., 2013, Magma pathway and its structural controls of Asama Volcano, Japan: *Geological Society of London Special Publications*, v. 380, p. 67-84, doi: 10.1144/SP380.6.
- Arndt, N., Chauvel, C., Czamanske, G., and Fedorenko, V., 1998, Two mantle sources, two plumbing systems: tholeiitic and alkaline magmatism of the Maymecha River basin,

- Siberian flood volcanic province: *Contributions to Mineralogy and Petrology*, v. 133, p. 297-313, doi: 10.1007/s004100050453.
- Aspler, L. B., Cousens, B. L., and Chiarenzelli, J. R., 2002, Griffin gabbro sills (2.11 Ga), Hurwitz Basin, Nunavut, Canada: long-distance lateral transport of magmas in western Churchill Province crust: *Precambrian Research*, v. 117, p. 269-294, doi: 10.1016/s0301-9268(02)00090-6.
- Atmaoui, N., and Hollnack, D., 2003, Neotectonics and extension direction of the southern Kenya Rift, Lake Magadi area: *Tectonophysics*, v. 364, p. 71-83, doi: 10.1016/s0040-1951(03)00051-9.
- Aubourg, C., Tshoso, G., Le Gall, B., Bertrand, H., Tiercelin, J. J., Kampunzu, A. B., Dymont, J., and Modisi, M., 2008, Magma flow revealed by magnetic fabric in the Okavango giant dyke swarm, Karoo igneous province, northern Botswana: *Journal of Volcanology and Geothermal Research*, v. 170, p. 247-261, doi: 10.1016/j.jvolgeores.2007.10.013.
- Ayele, A., Keir, D., Ebinger, C., Wright, T. J., Stuart, G. W., Buck, W. R., Jacques, E., Ogubazghi, G., and Sholan, J., 2009, September 2005 mega-dike emplacement in the Manda-Harraro nascent oceanic rift (Afar depression): *Geophysical Research Letters*, v. 36, p. L20306, doi: 10.1029/2009gl039605.
- Baer, G., and Reches, Z., 1991, Mechanics of emplacement and tectonic implications of the Ramon dike systems, Israel: *Journal of Geophysical Research*, v. 96, p. 11895-11910, doi: 10.1029/91jb00371.
- Baer, G., Hamiel, Y., Shamir, G., and Nof, R., 2008, Evolution of a magma-driven earthquake swarm and triggering of the nearby Oldoinyo Lengai eruption, as resolved by InSAR, ground observations and elastic modeling, East African Rift, 2007: *Earth and Planetary Science Letters*, v. 272, p. 339-352, doi: 10.1016/j.epsl.2008.04.052.
- Baker, B. H., 1958, *Geology of the Magadi area: Geological Survey of Kenya Report 42*, 81 p.
- Baker, B. H., 1963, *Geology of the area of south of Magadi: Geological Survey of Kenya Report 61*, 27 p.
- Baker, B. H., 1986, Tectonics and volcanism of the southern Kenya Rift Valley and its influence on rift sedimentation: *Journal of the Geological Society of London Special Publications*, v. 25, p. 45-57.
- Baker, B. H., and Wohlenberg, J., 1971, Structure and evolution of Kenya Rift Valley: *Nature*, v. 229, p. 538-542, doi: 10.1038/229538a0.
- Baker, B. H., and Mitchell, J. G., 1976, Volcanic stratigraphy and geochronology of the Kedong-Olorgesale area and the evolution of the south Kenya rift valley *Journal of the Geological Society of London*, v. 132, p. 467-484.
- Baker, B. H., Williams, L. A., Miller, J. A., and Fitch, F. J., 1971, Sequence and geochronology of Kenya Rift volcanics: *Tectonophysics*, v. 11, p. 191-215, doi: 10.1016/0040-1951(71)90030-8.
- Baker, B. H., Goles, G. G., Leeman, W. P., and Lindstrom, M. M., 1977, Geochemistry and petrogenesis of a basalt-benmoreite-trachyte suite from the southern part of the Gregory Rift, Kenya: *Contributions to Mineralogy and Petrology*, v. 64, p. 303-332.
- Baker, B. H., Mitchell, J. G., and Williams, L. A. J., 1988, Stratigraphy, geochronology and volcano-tectonic evolution of the Kedong-Naivasha-Kinangop region, Gregory Rift Valley, Kenya: *Journal of the Geological Society of London*, v. 145, p. 107-116.

- Baker, J., Snee, L., and Menzies, M., 1996, A brief Oligocene period of flood volcanism in Yemen: Implications for the duration and rate of continental flood volcanism at the Afro-Arabian triple junction: *Earth and Planetary Science Letters*, v. 138, p. 39-55, doi: 10.1016/0012-821x(95)00229-6.
- Baragar, W. R. A., Ernst, R. E., Hulbert, L., and Peterson, T., 1996, Longitudinal petrochemical variation in the Mackenzie dyke swam, northwestern Canadian shield: *Journal of Petrology*, v. 37, p. 317-359.
- Barker, S. J., Wilson, C. J. N., Morgan, D. J., and Rowland, J. V., 2016, Rapid priming, accumulation, and recharge of magma driving recent eruptions at a hyperactive caldera volcano: *Geology*, v. 44, p. 323-326.
- Barry, P. H., Hilton, D. R., Fischer, T. P., de Moor, J. M., Mangasini, F., and Ramirez, C., 2013, Helium and carbon isotope systematics of cold “mazuku” CO₂ vents and hydrothermal gases and fluids from Rungwe Volcanic Province, southern Tanzania: *Chemical Geology*, v. 339, p. 141-156, doi: 10.1016/j.chemgeo.2012.07.003.
- Bastow, I. D., Pilidou, S., Kendall, J. M., and Stuart, G. W., 2010, Melt-induced seismic anisotropy and magma assisted rifting in Ethiopia: Evidence from surface waves: *Geochemistry, Geophysics, Geosystems*, v. 11, doi: 10.1029/2010gc003036.
- Bedard, J. H., Naslund, H. R., Nabelek, P., Winpenny, A., Hryciuk, M., Macdonald, W., Hayes, B., Steigerwaldt, K., Hadlari, T., Rainbird, R., Dewing, K., and Girard, E., 2012, Fault-mediated melt ascent in a Neoproterozoic continental flood basalt province, the Franklin sills, Victoria Island, Canada: *Geological Society of America Bulletin*, v. 124, p. 723-736, doi: 10.1130/b30450.1.
- Behn, M. D., and Ito, G., 2008, Magmatic and tectonic extension at mid-ocean ridges: 1. Controls on fault characteristics: *Geochemistry, Geophysics, Geosystems*, v. 9, p. Q08O10, doi: 10.1029/2008gc001965.
- Behn, M. D., Buck, W. R., and Sacks, I. S., 2006, Topographic controls on dike injection in volcanic rift zones: *Earth and Planetary Science Letters*, v. 246, p. 188-196, doi: 10.1016/j.epsl.2006.04.005.
- Behr, H.-J., 2002, Magadiite and Magadi chert; a critical analysis of the silica sediments in the Lake Magadi Basin, Kenya: *Society for Sedimentary Geology Special Publications*, v. 73, p. 257-273.
- Behr, H. J., and Rohricht, C., 2000, Record of seismotectonic events in siliceous cyanobacterial sediments (Magadi cherts), Lake Magadi, Kenya: *International Journal of Earth Sciences*, v. 89, p. 268-283, doi: 10.1007/s005319900070.
- Belachew, M., Ebinger, C., Coté, D., Keir, D., Rowland, J. V., Hammond, J. O. S., and Ayele, A., 2011, Comparison of dike intrusions in an incipient seafloor-spreading segment in Afar, Ethiopia: Seismicity perspectives: *Journal of Geophysical Research*, v. 116, p. B06405, doi: 10.1029/2010jb007908.
- Belachew, M., Ebinger, C., and Cote, D., 2013, Source mechanisms of dike-induced earthquakes in the Dabbahu-Manda Hararo rift segment in Afar, Ethiopia: implications for faulting above dikes: *Geophysical Journal International*, v. 192, p. 907-917, doi: 10.1093/gji/ggs076.
- Ben-Avraham, Z., and Ten Brink, U., 1989, Transverse faults and segmentation of basins within the Dead Sea Rift: *Journal of African Earth Sciences*, v. 8, p. 603-616, doi: 10.1016/s0899-5362(89)80047-8.

- Berryman, K., Villamor, P., Nairn, I., van Dissen, R., Begg, J., and Lee, J., 2008, Late Pleistocene surface rupture history of the Paeroa Fault, Taupo Rift, New Zealand: *New Zealand Journal of Geology and Geophysics*, v. 51, p. 135-158, doi: 10.1080/00288300809509855.
- Beutel, E., van Wijk, J., Ebinger, C., Keir, D., and Agostini, A., 2010, Formation and stability of magmatic segments in the Main Ethiopian and Afar rifts: *Earth and Planetary Science Letters*, v. 293, p. 225-235, doi: 10.1016/j.epsl.2010.02.006.
- Bialas, R. W., Buck, W. R., and Qin, R., 2010, How much magma is required to rift a continent?: *Earth and Planetary Science Letters*, v. 292, p. 68-78, doi: 10.1016/j.epsl.2010.01.021.
- Biggs, J., Amelung, F., Gourmelen, N., Dixon, T. H., and Kim, S.-W., 2009a, InSAR observations of 2007 Tanzania rifting episode reveal mixed fault and dyke extension in an immature continental rift: *Geophysical Journal International*, v. 179, p. 549-558, doi: 10.1111/j.1365-246X.2009.04262.x.
- Biggs, J., Anthony, E. Y., and Ebinger, C. J., 2009b, Multiple inflation and deflation events at Kenyan volcanoes, East African Rift: *Geology*, v. 37, p. 979-982, doi: 10.1130/g30133a.1.
- Biggs, J., Bastow, I. D., Keir, D., and Lewi, E., 2011, Pulses of deformation reveal frequently recurring shallow magmatic activity beneath the Main Ethiopian Rift: *Geochemistry, Geophysics, Geosystems*, v. 12, p. Q0AB10, doi: 10.1029/2011gc003662.
- Biggs, J., Chivers, M., and Hutchinson, M. C., 2013, Surface deformation and stress interactions during the 2007-2010 sequence of earthquake, dyke intrusion and eruption in northern Tanzania: *Geophysical Journal International*, v. 195, p. 16-26, doi: 10.1093/gji/ggt226.
- Biggs, J., Robertson, E., and Cashman, K., 2016, The lateral extent of volcanic interactions during unrest and eruption: *Nature Geoscience*, v. 9, doi: 10.1038/ngeo2658.
- Billings, S. E., and Kattenhorn, S. A., 2005, The great thickness debate: Ice shell thickness models for Europa and comparisons with estimates based on flexure at ridges: *Icarus*, v. 177, p. 397-412, doi: 10.1016/j.icarus.2005.03.013.
- Billingsley, G. H., Block, D., and Redsteer, M. H., 2013, Geologic map of the Winslow 30' × 60' quadrangle, Coconino and Navajo counties, Northern Arizona: US Geological Survey Scientific Investigations Map 3247, scale 1:50,000, 25 p.
- Bird, P., Liu, Z., and Rucker, W. K., 2008, Stresses that drive the plates from below: Definitions, computational path, model optimization, and error analysis: *Journal of Geophysical Research*, v. 113, p. B11406, doi: 10.1029/2007jb005460.
- Birt, C. S., Maguire, P. K. H., Khan, M. A., Thybo, H., Keller, G. R., and Patel, J., 1997, The influence of pre-existing structures on the evolution of the southern Kenya Rift Valley - evidence from seismic and gravity studies: *Tectonophysics*, v. 278, p. 211-242, doi: 10.1016/s0040-1951(97)00105-4.
- Bistacchi, A., Tibaldi, A., Pasquare, F. A., and Rust, D., 2012, The association of cone-sheets and radial dykes: Data from the Isle of Skye (UK), numerical modelling, and implications for shallow magma chambers: *Earth and Planetary Science Letters*, v. 339, p. 46-56, doi: 10.1016/j.epsl.2012.05.020.
- Bjornsson, A., Saemundsson, K., Einarsson, P., Tryggvason, E., and Gronvold, K., 1977, Current rifting episode in north Iceland: *Nature*, v. 266, p. 318-323, doi: 10.1038/266318a0.

- Blakeslee, M. W., and Kattenhorn, S. A., 2013, Revised earthquake hazard of the Hat Creek fault, northern California: A case example of a normal fault dissecting variable-age basaltic lavas: *Geosphere*, v. 9, p. 1397-1409, doi: 10.1130/ges00910.1.
- Boccaletti, M., Bonini, M., Mazzuoli, R., Abebe, B., Piccardi, L., and Tortorici, L., 1998, Quaternary oblique extensional tectonics in the Ethiopian Rift (Horn of Africa): *Tectonophysics*, v. 287, p. 97-116, doi: 10.1016/s0040-1951(98)80063-2.
- Bohnenstiehl, D. R. R., and Kleinrock, M. C., 1999, Faulting and fault scaling on the median valley floor of the trans-Atlantic geotraverse (TAG) segment, similar to 26 degrees N on the Mid-Atlantic Ridge: *Journal of Geophysical Research*, v. 104, p. 29351-29364, doi: 10.1029/1999jb900256.
- Bohnenstiehl, D. R., and Kleinrock, M. C., 2000, Evidence for spreading-rate dependence in the displacement-length ratios of abyssal hill faults at mid-ocean ridges: *Geology*, v. 28, p. 395-398.
- Bonaccorso, A., Currenti, G., and Del Negro, C., 2013, Interaction of volcano-tectonic fault with magma storage, intrusion and flank instability: A thirty years study at Mt. Etna volcano: *Journal of Volcanology and Geothermal Research*, v. 251, p. 127-136, doi: 10.1016/j.jvolgeores.2012.06.002.
- Bonali, F. L., Corazzato, C., and Tibaldi, A., 2011, Identifying rift zones on volcanoes: an example from La Reunion island, Indian Ocean: *Bulletin of Volcanology*, v. 73, p. 347-366, doi: 10.1007/s00445-010-0416-1.
- Bonini, M., Souriot, T., Boccaletti, M., and Brun, J. P., 1997, Successive orthogonal and oblique extension episodes in a rift zone: Laboratory experiments with application to the Ethiopian Rift: *Tectonics*, v. 16, p. 347-362, doi: 10.1029/96tc03935.
- Bonini, M., Corti, G., Innocenti, F., Manetti, P., Mazzarini, F., Abebe, T., and Pecskey, Z., 2005, Evolution of the Main Ethiopian Rift in the frame of Afar and Kenya rifts propagation: *Tectonics*, v. 24, doi: 10.1029/2004tc00168.
- Bonnet, E., Bour, O., Odling, N. E., Davy, P., Main, I., Cowie, P., and Berkowitz, B., 2001, Scaling of fracture systems in geological media: *Reviews of Geophysics*, v. 39, p. 347-383, doi: 10.1029/1999rg000074.
- Bosworth, W., 1985, Geometry of propagating rifts: *Nature*, v. 316, p. 625-627.
- Bosworth, W., and Strecker, M. R., 1997, Stress field changes in the Afro-Arabian rift system during the Miocene to Recent period: *Tectonophysics*, v. 278, p. 47-62, doi: 10.1016/s0040-1951(97)00094-2.
- Bott, M. H. P., 1996, Flexure associated with planar faulting: *Geophysical Journal International*, v. 126, p. F21-F24, doi: 10.1111/j.1365-246X.1996.tb04692.x.
- Brändle, J. L., Ancochea, E., Cubas, C. R., and Hernán, F., 1991, Análisis de enjambres de diques radiales utilizando un método matemático: *Geogaceta*, v. 10, p. 97-100.
- Brantley, S. L., and Koepenick, K. W., 1995, Measured carbon-dioxide emissions from Oldoinyo Lengai and the skewed distribution of passive volcanic fluxes: *Geology*, v. 23, p. 933-936.
- Brazier, R. A., Nyblade, A. A., and Florentin, J., 2005, Focal mechanisms and the stress regime in NE and SW Tanzania, East Africa: *Geophysical Research Letters*, v. 32, p. L14315, doi: 10.1029/2005gl023156.
- Brodsky, E. E., Roeloffs, E., Woodcock, D., Gall, I., and Manga, M., 2003, A mechanism for sustained groundwater pressure changes induced by distant earthquakes: *Journal of Geophysical Research*, v. 108, p. B2390, doi: 10.1029/2002jb002321.

- Brooks, A. S., Behrensmeyer, A. K., Yellen, J. E., Deino, A., Sharp, W., and Potts, R., 2007, After the Acheulean: stratigraphy, dating, and archeology of two new formations in the Olorgesailie basin, southern Kenya Rift: *Paleoanthropology*, Internet Journal of the Paleoanthropology Society, p. A15.
- Brown, R. J., and Valentine, G. A., 2013, Physical characteristics of kimberlite and basaltic intraplate volcanism and implications of a biased kimberlite record: *Geological Society of America Bulletin*, v. 125, p. 1224-1238, doi: 10.1130/b30749.1.
- Brun, J. P., 1999, Narrow rifts versus wide rifts: inferences for the mechanics of rifting from laboratory experiments: *Philosophical Transactions of the Royal Society A*, v. 357, p. 695-710, doi: 10.1098/rsta.1999.0349.
- Brun, J. P., Gutscher, M. A., Blum, R., Bois, C., Burg, J. P., Colletta, B., Durbaum, H., Damotte, B., Durst, H., Fuchs, K., Grohmann, N., Hubner, M., Karcher, T., Kessler, G., Klockner, M., Lucazeau, F., Luschen, E., Marthelot, J. M., Meier, L., Ravat, M., Reichert, C., Vernassa, S., Villemin, T., Wenzel, F., and Wittlinger, G., 1992, Deep crustal structure of the Rhine Graben from DEKORP-ECORS seismic reflection data: a summary: *Tectonophysics*, v. 208, p. 139-147, doi: 10.1016/0040-1951(92)90340-c.
- Bryan, S. E., and Ernst, R. E., 2008, Revised definition of large igneous provinces (LIPs): *Earth-Science Reviews*, v. 86, p. 175-202, doi: 10.1016/j.earscirev.2007.08.008.
- Bryan, S. E., and Ferrari, L., 2013, Large igneous provinces and silicic large igneous provinces: Progress in our understanding over the last 25 years: *Geological Society of America Bulletin*, v. 125, p. 1053-1078, doi: 10.1130/b30820.1.
- Buck, W. R., 1991, Modes of continental lithospheric extension: *Journal of Geophysical Research*, v. 96, p. 20161-20178, doi: 10.1029/91jb01485.
- Buck, W. R., 2004, Consequences of asthenospheric variability on continental rifting, *in* Karner, G.D., et al., eds., *Rheology and deformation of the lithosphere at continental margins*: New York, Columbia University Press, p. 1-30
- Buck, W. R., 2006, The role of magma in the development of the Afro-Arabian Rift System: Afar Volcanic Province within the East African Rift System: *Geological Society of London Special Publications*, v. 259, p. 43-54, doi: 10.1144/gsl.sp.2006.259.01.05.
- Buck, W. R., Lavier, L. L., and Poliakov, A. N. B., 2005, Modes of faulting at mid-ocean ridges: *Nature*, v. 434, p. 719-723, doi: 10.1038/nature03358.
- Buck, W. R., Einarsson, P., and Brandsdottir, B., 2006, Tectonic stress and magma chamber size as controls on dike propagation: Constraints from the 1975-1984 Krafla rifting episode: *Journal of Geophysical Research*, v. 111, p. B12404, doi: 10.1029/2005jb003879.
- Burchardt, S., 2008, New insights into the mechanics of sill emplacement provided by field observations of the Njardvik Sill, Northeast Iceland: *Journal of Volcanology and Geothermal Research*, v. 173, p. 280-288, doi: 10.1016/j.jvolgeores.2008.02.009.
- Burnard, P., Graham, D., and Turner, G., 1997, Vesicle-specific noble gas analyses of "popping rock": Implications for primordial noble gases in earth: *Science*, v. 276, p. 568-571, doi: 10.1126/science.276.5312.568.
- Burton, M. R., Sawyer, G. M., and Granieri, D., 2013, Deep Carbon Emissions from Volcanoes: *Carbon in Earth*, v. 75, p. 323-354, doi: 10.2138/rmg.2013.75.11.
- Calais, E., Ebinger, C., Hartnady, C., and Nocquet, J. M., 2006, Kinematics of the East African Rift from GPS and earthquake slip vector data: Afar Volcanic Province within the East African Rift System, v. 259, p. 9-22, doi: 10.1144/gsl.sp.2006.259.01.03.

- Calais, E., d'Oreye, N., Albaric, J., Deschamps, A., Delvaux, D., Deverchere, J., Ebinger, C., Ferdinand, R. W., Kervyn, F., Macheyeke, A. S., Oyen, A., Perrot, J., Saria, E., Smets, B., Stamps, D. S., and Wauthier, C., 2008, Strain accommodation by slow slip and dyking in a youthful continental rift, East Africa: *Nature*, v. 456, p. 783-788, doi: 10.1038/nature07478.
- Campbell, I. H., 2005, Large igneous provinces and the mantle plume hypothesis: *Elements*, v. 1, p. 265-269.
- Canon-Tapia, E., 2016, Reappraisal of the significance of volcanic fields: *Journal of Volcanology and Geothermal Research*, v. 310, p. 26-38, doi: 10.1016/j.jvolgeores.2015.11.010.
- Carbotte, S. M., and Macdonald, K. C., 1994, Comparison of seafloor tectonic fabric at intermediate, fast, and super fast spreading ridges: influence of spreading rate, plate motions, and ridge segmentation of fault patterns: *Journal of Geophysical Research*, v. 99, p. 13609-13631, doi: 10.1029/93jb02971.
- Carey, S., and Sigurdsson, H., 1987, Temporal variations in column height and magma discharge rate during the 79 AD eruption of Vesuvius: *Geological Society of America Bulletin*, v. 99, p. 303-314.
- Cartwright, J., and Hansen, D. M., 2006, Magma transport through the crust via interconnected sill complexes: *Geology*, v. 34, p. 929-932, doi: 10.1130/g22758a.1.
- Cartwright, J. A., Trudgill, B. D., and Mansfield, C. S., 1995, Fault growth by segment linkage - an explanation for scatter in maximum displacement and trace length data from the Canyonlands grabens of SE Utah: *Journal of Structural Geology*, v. 17, p. 1319-1326, doi: 10.1016/0191-8141(95)00033-a.
- Casey, M., Ebinger, C., Keir, D., Gloaguen, R., and Mohamed, F., 2006, Strain accommodation in transitional rifts: extension by magma intrusion and faulting in Ethiopian rift magmatic segments: *Geological Society of London Special Publications*, v. 259, p. 143-163.
- Chadwick, W. W., and Howard, K. A., 1991, The pattern of circumferential and radial eruptive fissures on the volcanoes of Fernandina and Isabela Islands, Galapagos: *Bulletin of Volcanology*, v. 53, p. 259-275, doi: 10.1007/bf00414523.
- Chadwick, W. W., Jonsson, S., Geist, D. J., Poland, M., Johnson, D. J., Batt, S., Harpp, K. S., and Ruiz, A., 2011, The May 2005 eruption of Fernandina volcano, Galapagos: The first circumferential dike intrusion observed by GPS and InSAR: *Bulletin of Volcanology*, v. 73, p. 679-697, doi: 10.1007/s00445-010-0433-0.
- Chanceaux, L., and Menand, T., 2014, Solidification effects on sill formation: An experimental approach: *Earth and Planetary Science Letters*, v. 403, p. 79-88.
- Chapman, G. R., and Brook, M., 1978, Chronostratigraphy of the Baringo Basin, Kenya, in Bishop, W. W., ed., *Geological Background to Fossil Man*: Edinburgh, Scottish Academic Press, p. 207-233.
- Chen, S., Hiraga, T., and Kohlstedt, D. L., 2006, Water weakening of clinopyroxene in the dislocation creep regime: *Journal of Geophysical Research*, v. 111, p. B08203, doi: 10.1029/2005jb003885.
- Chernak, L. J., Hirth, G., Selverstone, J., and Tullis, J., 2009, Effect of aqueous and carbonic fluids on the dislocation creep strength of quartz: *Journal of Geophysical Research*, v. 114, p. B04201, doi: 10.1029/2008jb005884.

- Chesley, J. T., Rudnick, R. L., and Lee, C. T., 1999, Re-Os systematics of mantle xenoliths from the East African Rift: Age, structure, and history of the Tanzanian craton: *Geochimica Et Cosmochimica Acta*, v. 63, p. 1203-1217, doi: 10.1016/s0016-7037(99)00004-6.
- Chevallier, L., and Woodford, A., 1999, Morpho-tectonics and mechanisms of emplacement of the dolerite rings and sills of the western Karoo, South Africa: *South African Journal of Geology*, v. 102, p. 43-54.
- Childs, C., Nicol, A., Walsh, J. J., and Watterson, J., 1996, Growth of vertically segmented normal faults: *Journal of Structural Geology*, v. 18, p. 1389-1397, doi: 10.1016/s0191-8141(96)00060-0.
- Chiodini, G., Cioni, R., Guidi, M., Raco, B., and Marini, L., 1998, Soil CO₂ flux measurements in volcanic and geothermal areas: *Applied Geochemistry*, v. 13, p. 543-552, doi: 10.1016/s0883-2927(97)00076-0.
- Chiodini, G., Cardellini, C., Amato, A., Boschi, E., Caliro, S., Frondini, F., and Ventura, G., 2004, Carbon dioxide Earth degassing and seismogenesis in central and southern Italy: *Geophysical Research Letters*, v. 31, p. L07615, doi: 10.1029/2004gl019480.
- Chiodini, G., Caliro, S., Cardellini, C., Avino, R., Granieri, D., and Schmidt, A., 2008, Carbon isotopic composition of soil CO₂ efflux, a powerful method to discriminate different sources feeding soil CO₂ degassing in volcanic-hydrothermal areas: *Earth and Planetary Science Letters*, v. 274, p. 372-379, doi: 10.1016/j.epsl.2008.07.051.
- Chorowicz, J., 1989, Transfer and transform fault zones in continental rifts: examples in the Afro-Arabian Rift System. Implications of crust breaking: *Journal of African Earth Sciences*, v. 8, p. 203-214, doi: 10.1016/s0899-5362(89)80025-9.
- Chorowicz, J., 1992, The role of ancient structures in the genesis and evolution of the East African Rift: *Bulletin De La Societe Geologique De France*, v. 163, p. 217-227.
- Chorowicz, J., 2005, The East African rift system: *Journal of African Earth Sciences*, v. 43, p. 379-410, doi: 10.1016/j.jafrearsci.2005.07.019.
- Chorowicz, J., and Sorlien, C., 1992, Oblique extensional tectonics in the Malawi Rift, Africa: *Geological Society of America Bulletin*, v. 104, p. 1015-1023.
- Chorowicz, J., Collet, B., Bonavia, F. F., and Korme, T., 1994, Northwest to north-northwest extension direction in the Ethiopian Rift deduced from the orientation of extension structures and fault-slip analysis: *Geological Society of America Bulletin*, v. 106, p. 1560-1570.
- Chu, D. H., and Gordon, R. G., 1999, Evidence for motion between Nubia and Somalia along the southwest Indian ridge: *Nature*, v. 398, p. 64-67.
- Clifton, A. E., and Schlische, R. W., 2001, Nucleation, growth, and linkage of faults in oblique rift zones: Results from experimental clay models and implications for maximum fault size: *Geology*, v. 29, p. 455-458.
- Clifton, A. E., Schlische, R. W., Withjack, M. O., and Ackermann, R. V., 2000, Influence of rift obliquity on fault-population systematics: results of experimental clay models: *Journal of Structural Geology*, v. 22, p. 1491-1509, doi: 10.1016/s0191-8141(00)00043-2.
- Coblentz, D. D., and Sandiford, M., 1994, Tectonic stresses in the African plate: constraints on the ambient lithospheric stress state: *Geology*, v. 22, p. 831-834.

- Coffin, M. F., and Eldholm, O., 1994, Large igneous provinces: crustal structure, dimensions, and external consequences: *Reviews of Geophysics*, v. 32, p. 1-36, doi: 10.1029/93rg02508.
- Coffin, M. F., Duncan, R. A., Eldholm, O., Fitton, J. G., Frey, F. A., Larson, H. C., Mahoney, J. J., Saunders, A. D., Schlich, R., and Wallace, P. J., 2006, Large igneous provinces and scientific ocean drilling: *Oceanography*, v. 19, p. 150-160.
- Condit, C. D., and Connor, C. B., 1996, Recurrence rates of volcanism in basaltic volcanic fields: An example from the Springerville volcanic field, Arizona: *Geological Society of America Bulletin*, v. 108, p. 1225-1241.
- Connor, C. B., and Connor, L. J., 2009, Estimating spatial density with kernel methods, *in* Connor, C. B., Chapman, N. A., and Connor, L. J., eds., *Volcanic and tectonic hazard assessment for nuclear facilities*: Cambridge, Cambridge University Press, p. 387-412.
- Connor, C. B., and Conway, F. M., 2000, Basaltic volcanic fields, *in* Sigurdsson, H., ed., *Encyclopedia of Volcanoes*: San Diego, Academic Press, p. 331-343.
- Cooper, G. F., Wilson, C. J. N., Millet, M. A., Baker, J. A., and Smith, E. G. C., 2012, Systematic tapping of independent magma chambers during the 1 Ma Kidnappers supereruption: *Earth and Planetary Science Letters*, v. 313, p. 23-33, doi: 10.1016/j.epsl.2011.11.006.
- Corti, G., 2008, Control of rift obliquity on the evolution and segmentation of the main Ethiopian rift: *Nature Geoscience*, v. 1, p. 258-262, doi: 10.1038/ngeo160.
- Corti, G., 2009, Continental rift evolution: From rift initiation to incipient break-up in the Main Ethiopian Rift, East Africa: *Earth-Science Reviews*, v. 96, p. 1-53, doi: 10.1016/j.earscirev.2009.06.005.
- Corti, G., 2012, Evolution and characteristics of continental rifting: Analog modeling-inspired view and comparison with examples from the East African Rift System: *Tectonophysics*, v. 522, p. 1-33, doi: 10.1016/j.tecto.2011.06.010.
- Corti, G., Bonini, M., Mazzarini, F., Boccaletti, M., Innocenti, F., Manetti, P., Mulugeta, G., and Sokoutis, D., 2002a, Magma-induced strain localization in centrifuge models of transfer zones: *Tectonophysics*, v. 348, p. 205-218, doi: 10.1016/s0040-1951(02)00063-x.
- Corti, G., Bonini, M., Innocenti, F., Manetti, P., Genene, M., Sokoutis, D., and Cloetingh, S., 2002b, Rift-parallel magma migration and localisation of magmatic activity in transfer zones: *Acta Vulcanologica*, v. 14, p. 17-26.
- Corti, G., Bonini, M., Conticelli, S., Innocenti, F., Manetti, P., and Sokoutis, D., 2003, Analogue modelling of continental extension: a review focused on the relations between the patterns of deformation and the presence of magma: *Earth-Science Reviews*, v. 63, p. 169-247, doi: 10.1016/s0012-8252(03)00035-7.
- Corti, G., Bonini, M., Sokoutis, D., Innocenti, F., Manetti, P., Cloetingh, S., and Mulugeta, G., 2004, Continental rift architecture and patterns of magma migration: A dynamic analysis based on centrifuge models: *Tectonics*, v. 23, doi: 10.1029/2003tc001561.
- Corti, G., Sani, F., Philippon, M., Sokoutis, D., Willingshofer, E., and Molin, P., 2013, Quaternary volcano-tectonic activity in the Soddo region, western margin of the Southern Main Ethiopian Rift: *Tectonics*, v. 32, p. 861-879, doi: 10.1002/tect.20052.
- Corti, G., Agostini, A., Keir, D., Van Wijk, J., Bastow, I. D., and Ranalli, G., 2015, Magma-induced axial subsidence during final-stage rifting: Implications for the development of seaward-dipping reflectors: *Geosphere*, v. 11, p. 563-571, doi: 10.1130/ges01076.1.

- Courtilot, V., Jaupart, C., Manighetti, I., Tapponnier, P., and Besse, J., 1999, On causal links between flood basalts and continental breakup: *Earth and Planetary Science Letters*, v. 166, p. 177-195.
- Cowie, P. A., and Scholz, C. H., 1992, Physical explanation for the displacement-length relationship of faults using a post-yield fracture mechanics model: *Journal of Structural Geology*, v. 14, p. 1133-1148, doi: 10.1016/0191-8141(92)90065-5.
- Cowie, P. A., Scholz, C. H., Edwards, M., and Malinverno, A., 1993, Fault strain and seismic coupling on mid-ocean ridges: *Journal of Geophysical Research*, v. 98, p. 17911-17920, doi: 10.1029/93jb01567.
- Cowie, P. A., Malinverno, A., Ryan, W. B. F., and Edwards, M. H., 1994, Quantitative fault studies on the East Pacific Rise: a comparison of sonar imaging techniques: *Journal of Geophysical Research*, v. 99, p. 15205-15218, doi: 10.1029/94jb00041.
- Cowie, P. A., Underhill, J. R., Behn, M. D., Lin, J., and Gill, C. E., 2005, Spatio-temporal evolution of strain accumulation derived from multi-scale observations of Late Jurassic rifting in the northern North Sea: A critical test of models for lithospheric extension: *Earth and Planetary Science Letters*, v. 234, p. 401-419, doi: 10.1016/j.epsl.2005.01.039.
- Cox, S. C., Turnbull, I. M., Isaac, M. J., Townsend, D. B., and B., S. L., 2012, *Geology of southern Victoria Land, Antarctica: Institute of Geological & Nuclear Sciences geological map 22, scale 1:250 000, 1 sheet.*
- Crane, K., 1981, Thermal variations in the Gregory Rift of southern Kenya: *Tectonophysics*, v. 74, p. 239-262, doi: 10.1016/0040-1951(81)90192-x.
- Crider, J. G., and Pollard, D. D., 1998, Fault Linkage: Three-dimensional mechanical interaction between echelon normal faults: *Journal of Geophysical Research*, v. 103, p. 24373-24391, doi: 10.1029/98jb01353.
- Crossley, R., 1979, The Cenozoic stratigraphy and structure of the western part of the Rift Valley in southern Kenya: *Journal of the Geological Society of London*, v. 136, p. 393-405.
- Crossley, R., and Knight, R. M., 1981, Volcanism in the western part of the Rift Valley in southern Kenya: *Bulletin Volcanologique*, v. 44, p. 117-128.
- Cruikshank, K. M., Zhao, G. H., and Johnson, A. M., 1991, Analysis of minor fractures associated with joints and faulted joints: *Journal of Structural Geology*, v. 13, p. 865-886, doi: 10.1016/0191-8141(91)90083-u.
- Czamanske, G. K., Zen'ko, T. E., Fedorenko, V. A., Calk, L. C., Budahn, J. R., Bullock, J. H., Jr., Fries, T. L., King, B. S., and Siems, D. F., 1995, Petrography and geochemical characterization of ore-bearing intrusions of the Noril'sk type, Siberia; with discussion of their origin: *Resource Geology (Special Issue)*, v. 18, p. 1-48.
- Dalrymple, G. B., and Ryder, G., 1993, $^{40}\text{Ar}/^{39}\text{Ar}$ age spectra of Apollo 15 impact melt rocks by laser heating and their bearing on the history of lunar basin formation: *Journal of Geophysical Research*, v. 98, p. 13085-13095, doi: 10.1029/93je01222.
- Dalrymple, G. B., Alexander, E. C. J., Lannsphere, M. A., and Kraker, G. P., 1981, Irradiation of samples for $^{40}\text{Ar}/^{39}\text{Ar}$ dating using the Geological Survey TRIGA reactor: *United States Geological Survey Professional Paper 1176*, p. 55.
- Daly, M. C., Chorowicz, J., and Fairhead, J. D., 1989, Rift basin evolution in Africa: the influence of steep basement shear zones: *Geological Society of London Special Publications*, v. 44, p. 309-334.

- Daniels, K. A., Bastow, I. D., Keir, D., Sparks, R. S. J., and Menand, T., 2014, Thermal models of dyke intrusion during development of continent-ocean transition: *Earth and Planetary Science Letters*, v. 385, p. 145-153, doi: 10.1016/j.epsl.2013.09.018.
- Darling, W. G., Griesshaber, E., Andrews, J. N., Armannsson, H., and Onions, R. K., 1995, The origin of hydrothermal and other gases in the Kenya Rift valley: *Geochimica Et Cosmochimica Acta*, v. 59, p. 2501-2512, doi: 10.1016/0016-7037(95)00145-x.
- Davies, R., Bell, B. R., Cartwright, J. A., and Shoulders, S., 2002, Three-dimensional seismic imaging of Paleogene dike-fed submarine volcanoes from the northeast Atlantic margin: *Geology*, v. 30, p. 223-226.
- Dawers, N. H., and Anders, M. H., 1995, Displacement-length scaling and fault linkage: *Journal of Structural Geology*, v. 17, doi: 10.1016/0191-8141(94)00091-d.
- Dawers, N. H., Anders, M. H., and Scholz, C. H., 1993, Growths of normal faults - displacement-length scaling: *Geology*, v. 21, p. 1107-1110.
- Dawson, J. B., 1992, Neogene tectonics and volcanicity in the north Tanzania sector of the Gregory Rift Valley - contrasts with the Kenya sector: *Tectonophysics*, v. 204, p. 81-92, doi: 10.1016/0040-1951(92)90271-7.
- Dawson, J. B., 2008, The Gregory Rift Valley and Neogene-Recent Volcanoes of Northern Tanzania: Geological Society, London, Memoir, v. 33, p. 1-98, doi: 10.1144/m33.1.
- de Moor, J. M., Fischer, T. P., Sharp, Z. D., Hilton, D. R., Barry, P. H., Mangasini, F., and Ramirez, C., 2013a, Gas chemistry and nitrogen isotope compositions of cold mantle gases from Rungwe Volcanic Province, southern Tanzania: *Chemical Geology*, v. 339, p. 30-42, doi: 10.1016/j.chemgeo.2012.08.004.
- de Moor, J. M., Fischer, T. P., King, P. L., Botcharnikov, R. E., Hervig, R. L., Hilton, D. R., Barry, P. H., Mangasini, F., and Ramirez, C., 2013b, Volatile-rich silicate melts from Oldoinyo Lengai volcano (Tanzania): Implications for carbonatite genesis and eruptive behavior: *Earth and Planetary Science Letters*, v. 361, p. 379-390, doi: 10.1016/j.epsl.2012.11.006.
- Delaney, P. T., and Pollard, D. D., 1981, Deformation of host rocks and flow of magma during growth of minette dikes and breccia-bearing intrusions near Ship Rock, New Mexico: United States Geological Survey Professional Paper, v. 1202, 61p.
- Delaney, P. T., and Pollard, D. D., 1982, Solidification of basaltic magma during flow in a dike: *American Journal of Science*, v. 282, p. 856-885.
- Delaney, P. T., and Gartner, A. E., 1997, Physical processes of shallow mafic dike emplacement near the San Rafael Swell, Utah: *Geological Society of America Bulletin*, v. 109, p. 1177-1192.
- Delaney, P. T., Pollard, D. D., Ziony, J. I., and McKee, E. H., 1986, Field relations between dykes and joints: Emplacement processes and paleostress analysis: *Journal of Geophysical Research*, v. 91, p. 4920-4938.
- Delvaux, D., 2001, Tectonic and palaeostress evolution of the Tanganyika-Rukwa-Malawi rift segment, East African Rift System: *Peri-Tethys Memoir*, v. 6, p. 545-567.
- Delvaux, D., and Barth, A., 2010, African stress pattern from formal inversion of focal mechanism data: *Tectonophysics*, v. 482, p. 105-128, doi: 10.1016/j.tecto.2009.05.009.
- Delvaux, D., Levi, K., Kajara, R., and Sarota, J., 1992, Cenozoic paleostress and kinematic evolution of the Rukwa: north Malawi rift valley (East African Rift System): *Bulletin Des Centres De Recherches Exploration-Production Elf Aquitaine*, v. 16, p. 383-406.

- Densmore, A. L., Gupta, S., Allen, P. A., and Dawers, N. H., 2007, Transient landscapes at fault tips: *Journal of Geophysical Research*, v. 112, doi: 10.1029/2006jf000560.
- Deutsch, C. V., and Journel, A. G., 1998, *GSLIB: Geostatistical software library and users guide*: New York, Oxford University Press, 369 p.
- Dixon, T. H., Stern, R. J., and Hussein, I. M., 1987, Control of Red Sea Rift geometry by Precambrian structures: *Tectonics*, v. 6, p. 551-571, doi: 10.1029/TC006i005p00551.
- Downs, D. T., Rowland, J. V., Wilson, C. J. N., Rosenberg, M. D., Leonard, G. S., and Calvert, A. T., 2014, Evolution of the intra-arc Taupo-Reporoa Basin within the Taupo Volcanic Zone of New Zealand: *Geosphere*, v. 10, p. 185-206, doi: 10.1130/ges00965.1.
- Dunbar, J. A., and Sawyer, D. S., 1989, How preexisting weaknesses control the style of continental breakup: *Journal of Geophysical Research*, v. 94, p. 7278, doi: 10.1029/JB094iB06p07278.
- Ebbing, J., Lundin, E., Olesen, O., and Hansen, E. K., 2006, The mid-Norwegian margin: a discussion of crustal lineaments, mafic intrusions, and remnants of the Caledonian root by 3D density modelling and structural interpretation: *Journal of the Geological Society of London*, v. 163, p. 47-59, doi: 10.1144/0016-764905-029.
- Ebinger, C. J., 1989, Geometric and kinematic development of border faults and accommodation zones, Kivu-Rusizi Rift, Africa: *Tectonics*, v. 8, p. 117-133, doi: 10.1029/TC008i001p00117.
- Ebinger, C., 2005, Continental break-up: The East African perspective: *Astronomy & Geophysics*, v. 46, p. 16-21.
- Ebinger, C. J., and Sleep, N. H., 1998, Cenozoic magmatism throughout east Africa resulting from impact of a single plume: *Nature*, v. 395, p. 788-791, doi: 10.1038/27417.
- Ebinger, C. J., and Casey, M., 2001, Continental breakup in magmatic provinces: An Ethiopian example: *Geology*, v. 29, p. 527-530.
- Ebinger, C., and Furman, T., 2003, Geodynamical setting of the Virunga volcanic province, East Africa: *Acta Vulcanologica*, v. 15, p. 9-16.
- Ebinger, C., and Scholz, C. A., 2012, Continental rift basins: the East African perspective, *in* Azor Pérez, A., Busby, C., eds., *Tectonics of Sedimentary Basins: Recent Advances*: Blackwell Publishing Ltd., p. 185-208.
- Ebinger, C. J., Deino, A. L., Drake, R. E., and Tesha, A. L., 1989, Chronology of volcanism and rift basin propagation: Rungwe Volcanic Province, East Africa: *Journal of Geophysical Research*, v. 94, p. 15785-15803, doi: 10.1029/JB094iB11p15785.
- Ebinger, C. J., Karner, G. D., and Weissel, J. K., 1991, Mechanical strength of extended continental lithosphere: constraints from the Western rift system, East Africa: *Tectonics*, v. 10, p. 1239-1256, doi: 10.1029/91tc00579.
- Ebinger, C., Djomani, Y. P., Mbede, E., Foster, A., and Dawson, J. B., 1997, Rifting Archaean lithosphere: the Eyasi-Manyara-Natron rifts, East Africa: *Journal of the Geological Society of London*, v. 154, p. 947-960, doi: 10.1144/gsjgs.154.6.0947.
- Ebinger, C. J., Yemane, T., Harding, D. J., Tesfaye, S., Kelley, S., and Rex, D. C., 2000, Rift deflection, migration, and propagation: Linkage of the Ethiopian and Eastern rifts, Africa: *Geological Society of America Bulletin*, v. 112, p. 163-176.
- Ebinger, C., Ayele, A., Keir, D., Rowland, J., Yirgu, G., Wright, T., Belachew, M., and Hamling, I., 2010, Length and Timescales of Rift Faulting and Magma Intrusion: The

- Afar Rifting Cycle from 2005 to Present, *Annual Review of Earth and Planetary Sciences*, v. 38, p. 439-466.
- Ebinger, C. J., van Wijk, J., and Keir, D., 2013, The time scales of continental rifting: Implications for global processes, *in* Bickford, M. E., ed., *The Web of Geological Sciences: Advances, Impacts, and Interactions*, Geological Society of America Special Paper 500, p. 1-26.
- Einarsson, P., 1991, Earthquakes and present-day tectonism in Iceland: *Tectonophysics*, v. 189, p. 261-279, doi: 10.1016/0040-1951(91)90501-i.
- Eldholm, E., Gladchenko, T. P., Skogseid, J., and Planke, S., 2000, Atlantic volcanic margins: a comparative study: *Journal of the Geological Society of London Special Publications*, v. 167, p. 411-428.
- Elliot, D. H., and Fleming, T. H., 2004, Occurrence and dispersal of magmas in the Jurassic Ferrar Large Igneous Province, Antarctica: *Gondwana Research*, v. 7, p. 223-237.
- Elliot, D. H., and Fleming, T. H., 2008, Physical volcanology and geological relationships of the Jurassic Ferrar Large Igneous Province, Antarctica: *Journal of Volcanology and Geothermal Research*, v. 172, p. 20-37, doi: 10.1016/j.jvolgeores.2006.02.016.
- Elliot, D. H., and Grimes, C. G., 2011, Triassic and Jurassic strata at Coombs Hills, south Victoria Land: stratigraphy, petrology and cross-cutting breccia pipes: *Antarctic Science*, v. 23, p. 268-280, doi: 10.1017/s0954102010000994.
- Encarnación, J., Fleming, T. H., Elliot, D. H., and Eales, H. V., 1996, Synchronous emplacement of Ferrar and Karoo dolerites and the early break-up of Gondwana: *Geology*, v. 24, p. 535-538.
- Ernst, R. E., 2014, *Large igneous provinces*: Cambridge University Press, 666 p.
- Ernst, R. E., and Baragar, W. R. A., 1992, Evidence from magnetic fabric for the flow pattern of magma in the Mackenzie giant radiating dyke swarm: *Nature*, v. 356, p. 511-513, doi: 10.1038/356511a0.
- Ernst, R. E., Head, J. W., Parfitt, E., Grosfils, E., and Wilson, L., 1995, Giant Radiating Dyke Swarms on Earth and Venus: *Earth-Science Reviews*, v. 39, p. 1-58, doi: 10.1016/0012-8252(95)00017-5.
- Ernst, R. E., Grosfils, E. B., and Mege, D., 2001, Giant dike swarms: Earth, Venus, and Mars: *Annual Review of Earth and Planetary Sciences*, v. 29, p. 489-534.
- Ernst, R. E., Buchan, K. L., and Campbell, I. H., 2005, Frontiers in Large Igneous Province research: *Lithos*, v. 79, p. 271-297, doi: 10.1016/j.lithos.2004.09.004.
- Eugster, H. P., 1970, Chemistry and origin of the brines of Lake Magadi, Kenya: *Mineralogical Society of America Special Papers*, v. 3, p. 213-235.
- Fairhead, J. D., Mitchell, J. G., and Williams, L. A. J., 1972, New K/Ar determinations on rift volcanics of S. Kenya and their bearing on age of rift faulting: *Science*, v. 238, p. 66-69.
- Falvey, D. A., and Mutter, J. C., 1981, Regional plate tectonics and the evolution of the Australia's passive continental margins: *Journal of Australian Geology and Geophysics*, v. 6, p. 1-29.
- Fedorenko, V. A., and Czamanske, G. K., 1997, Results of new field and geochemical studies of the volcanic and intrusive rocks of the Maymecha-Kotuy area, Siberian Flood-Basalt Province, Russia: *International Geology Review*, v. 39, p. 479-531.

- Ferguson, D. J., Barnie, T. D., Pyle, D. M., Oppenheimer, C., Yirgu, G., Lewi, E., Kidane, T., Carn, S., and Hamling, I., 2010, Recent rift-related volcanism in Afar, Ethiopia: *Earth and Planetary Science Letters*, v. 292, p. 409-418, doi: 10.1016/j.epsl.2010.02.010.
- Fialko, Y. A., and Rubin, A. M., 1999, Thermal and mechanical aspects of magma emplacement in giant dyke swarms: *Journal of Geophysical Research*, v. 104, p. 23033-23049.
- Fischer, T. P., Burnard, P., Marty, B., Hilton, D. R., Furi, E., Palhol, F., Sharp, Z. D., and Mangasini, F., 2009, Upper-mantle volatile chemistry at Oldoinyo Lengai volcano and the origin of carbonatites: *Nature*, v. 459, p. 77-80, doi: 10.1038/nature07977.
- Fleck, R. J., Sutter, J. F., and Elliot, D. H., 1977, Interpretation of discordant $^{40}\text{Ar}/^{39}\text{Ar}$ age-spectra of Mesozoic tholeiites from Antarctica: *Geochimica Et Cosmochimica Acta*, v. 41, p. 15-32, doi: 10.1016/0016-7037(77)90184-3.
- Fleck, R. J., Hagstrum, J. T., Calvert, A. T., Evarts, R. C., and Conrey, R. M., 2014, $^{40}\text{Ar}/^{39}\text{Ar}$ geochronology, paleomagnetism, and evolution of the Boring volcanic field, Oregon and Washington, USA: *Geosphere*, v. 10, p. 1283-1314, doi: 10.1130/ges00985.1.
- Foshag, W. F., and Gonzalez-Reyna, J., 1956, Birth and development of Paricutin volcano: *US Geological Survey Bulletin*, v. 965-D, p. 355-489.
- Foster, A., Ebinger, C., Mbede, E., and Rex, D., 1997, Tectonic development of the northern Tanzanian sector of the east African rift system: *Journal of the Geological Society of London*, v. 154, p. 689-700, doi: 10.1144/gsjgs.154.4.0689.
- Francis, E. H., 1982, Magma and sediment - I. Emplacement mechanism of late Carboniferous tholeiite sills in northern Britain: *Journal of the Geological Society of London*, v. 139, p. 1-20.
- Franke, D., 2013, Rifting, lithosphere breakup and volcanism: Comparison of magma-poor and volcanic rifted margins: *Marine and Petroleum Geology*, v. 43, p. 63-87, doi: 10.1016/j.marpetgeo.2012.11.003.
- Friese, N., Bense, F. A., Tanner, D. C., Gustafsson, L. E., and Siegesmund, S., 2013, From feeder dykes to scoria cones: the tectonically controlled plumbing system of the Rauoholar volcanic chain, Northern Volcanic Zone, Iceland: *Bulletin of Volcanology*, v. 75, doi: 10.1007/s00445-013-0717-2.
- Gaffney, E. S., and Damjanac, B., 2006, Localization of volcanic activity: Topographic effects on dike propagation, eruption and conduit formation: *Geophysical Research Letters*, v. 33, p. L14313, doi: 10.1029/2006gl026852.
- Galadini, F., and Galli, P., 2000, Active tectonics in the central Apennines (Italy) - Input data for seismic hazard assessment: *Natural Hazards*, v. 22, p. 225-270, doi: 10.1023/a:1008149531980.
- Galerne, C. Y., Neumann, E. R., and Planke, S., 2008, Emplacement mechanisms of sill complexes: Information from the geochemical architecture of the Golden Valley Sill Complex, South Africa: *Journal of Volcanology and Geothermal Research*, v. 177, p. 425-440, doi: 10.1016/j.jvolgeores.2008.06.004.
- Galland, O., 2012, Experimental modelling of ground deformation associated with shallow magma intrusions: *Earth and Planetary Science Letters*, v. 317, p. 145-156, doi: 10.1016/j.epsl.2011.10.017.
- Galland, O., and Scheibert, J., 2013, Analytical model of surface uplift above axisymmetric flat-lying magma intrusions: Implications for sill emplacement and geodesy: *Journal*

- of *Volcanology and Geothermal Research*, v. 253, p. 114-130, doi: 10.1016/j.jvolgeores.2012.12.006.
- Galland, O., Planke, S., Neumann, E. R., and Malthe-Sorensen, A., 2009, Experimental modelling of shallow magma emplacement: Application to saucer-shaped intrusions: *Earth and Planetary Science Letters*, v. 277, p. 373-383, doi: 10.1016/j.epsl.2008.11.003.
- Galland, O., Burchardt, S., Hallot, E., Mourgues, R., and Bulois, C., 2014, Dynamics of dikes versus cone sheets in volcanic systems: *Journal of Geophysical Research*, v. 119, p. 6178-6192, doi: 10.1002/2014jb011059.
- Gawthorpe, R. L., and Leeder, M. R., 2000, Tectono-sedimentary evolution of active extensional basins: *Basin Research*, v. 12, p. 195-218, doi: 10.1046/j.1365-2117.2000.00121.x.
- Geissler, W. H., Kampf, H., Kind, R., Brauer, K., Klinge, K., Plenefisch, T., Horalek, J., Zednik, J., and Nehybka, V., 2005, Seismic structure and location of a CO₂ source in the upper mantle of the western Eger (Ohre) Rift, central Europe: *Tectonics*, v. 24, doi: 10.1029/2004tc001672.
- George, R., Rogers, N., and Kelley, S., 1998, Earliest magmatism in Ethiopia: Evidence for two mantle plumes in one flood basalt province: *Geology*, v. 26, p. 923-926.
- Gerlach, T. M., 1989, Degassing of carbon-dioxide from basaltic magma at spreading centers: 1. Afar transitional basalts: *Journal of Volcanology and Geothermal Research*, v. 39, p. 211-219, doi: 10.1016/0377-0273(89)90060-7.
- Germa, A., Connor, L. J., Canon-Tapia, E., and Le Corvec, N., 2013, Tectonic and magmatic controls on the location of post-subduction monogenetic volcanoes in Baja California, Mexico, revealed through spatial analysis of eruptive vents: *Bulletin of Volcanology*, v. 75, doi: 10.1007/s00445-013-0782-6.
- Gibbs, A. D., 1984, Structural evolution of extensional basin margins: *Journal of the Geological Society of London*, v. 141, p. 609-620, doi: 10.1144/gsjgs.141.4.0609.
- Gibson, I. L., 1969, Structure and volcanic geology of an axial portion of the Main Ethiopian Rift: *Tectonophysics*, v. 8, p. 561-565, doi: 10.1016/0040-1951(69)90054-7.
- Giggenbach, W. F., and Goguel, R. L., 1989, Methods for the collection and analysis of geothermal and volcanic water and gas samples: Department of Scientific and Industrial Research Report CD 2387.
- Gillespie, P. A., Walsh, J. J., and Watterson, J., 1992, Limitations of dimension and displacement data from single faults and the consequences for data analysis and interpretation: *Journal of Structural Geology*, v. 14, p. 1157-1172, doi: 10.1016/0191-8141(92)90067-7.
- Gleadow, A. J. W., and Fitzgerald, P. G., 1987, Uplift history and structure of the Transantarctic Mountains - new evidence from fission-track dating of basement apatites in the Dry Valleys area, southern Victoria Land: *Earth and Planetary Science Letters*, v. 82, p. 1-14.
- Gouly, N. R., and Schofield, N., 2008, Implications of simple flexure theory for the formation of saucer-shaped sills: *Journal of Structural Geology*, v. 30, p. 812-817, doi: 10.1016/j.jsg.2008.04.002.
- Grandin, R., Socquet, A., Jacques, E., Mazzoni, N., de Chaballier, J. B., and King, G. C. P., 2010, Sequence of rifting in Afar, Manda-Hararo rift, Ethiopia, 2005-2009: Time-space evolution and interactions between dikes from interferometric synthetic aperture

- radar and static stress change modeling: *Journal of Geophysical Research*, v. 115, p. B10413, doi: 10.1029/2009jb000815.
- Grant, J. V., and Kattenhorn, S. A., 2004, Evolution of vertical faults at an extensional plate boundary, southwest Iceland: *Journal of Structural Geology*, v. 26, p. 537-557, doi: 10.1016/j.jsg.2003.07.003.
- Grapes, R. H., Reid, D. L., and McPherson, J. G., 1974, Shallow dolerite intrusion and phreatic eruptions in the Allan Hills region, Antarctica: *New Zealand Journal of Geology and Geophysics*, v. 17, p. 563-577.
- Griggs, D. T., and Blacic, J. D., 1965, Quartz: anomalous weakness of synthetic crystals: *Science*, v. 147, p. 292-&, doi: 10.1126/science.147.3655.292.
- Gudmundsson, A., 1992, Formation and growth of normal faults at the divergent plate boundary in Iceland: *Terra Nova*, v. 4, p. 464-471, doi: 10.1111/j.1365-3121.1992.tb00582.x.
- Gudmundsson, A., 1995a, Infrastructure and mechanics of volcanic systems in Iceland: *Journal of Volcanology and Geothermal Research*, v. 64, p. 1-22.
- Gudmundsson, A., 1995b, Stress fields associated with oceanic transform faults: *Earth and Planetary Science Letters*, v. 136, p. 603-614.
- Gudmundsson, A., 1998, Magma chambers modelled as cavities explain the formation of rift zone central volcanoes and their eruption and intrusion statistics: *Journal of Geophysical Research*, v. 103, p. 7401-7412.
- Gudmundsson, A., 2002, Emplacement and arrest of sheets and dykes in central volcanoes: *Journal of Volcanology and Geothermal Research*, v. 116, p. 279-298.
- Gudmundsson, A., and Brenner, S. L., 2004, How mechanical layering affects local stresses, unrests, and eruptions of volcanoes: *Geophysical Research Letters*, v. 31, p. L16606, doi: 10.1029/2004gl020083.
- Guegan, E. B. M., 2006, Shallow intrusion conditions in a flood-basalt province; the story from dykes and a sill offshoot along the contact between a vent complex and country rock [M.Sc. thesis]: Dunedin, University of Otago, 187 p.
- Guest, N. J., and Pickering, R., 1966, Kibangaini geological map: Mineral Resources Division, Tanzania, Quarter degree sheet 28, 1:125,000, 1 sheet.
- Gunn, B. M., and Warren, G., 1962, Geology of Victoria Land between the Mawson and Mulock Glaciers, Antarctica: *New Zealand Geological Survey bulletin*, v. 71, p. 1-157.
- Gupta, A., and Scholz, C. H., 2000, Brittle strain regime transition in the Afar depression: Implications for fault growth and seafloor spreading: *Geology*, v. 28, p. 1087-1090.
- Guth, A. L., 2007, Evolution of the Southern Kenya Rift from Miocene to Present with a Focus on the Magadi Area [M.Sc. thesis]: Houghton, Michigan Technological University, 84 p.
- Guth, A. L., 2015, Volcanic volumes associated with the Kenya Rift: recognition and correlation of preservation biases: *Geological Society of London Special Publications*, v. 420, doi: 10.1144/sp420.3.
- Guth, A.L., and Wood, J., 2014, Geological map of the southern Kenya Rift: *Geological Society of America Digital Map and Chart 16*, 1:100,000, 6 sheets.
- Hald, N., and Tegner, C., 2000, Composition and age of tertiary sills and dykes, Jameson Land Basin, East Greenland: relation to regional flood volcanism: *Lithos*, v. 54, p. 207-233, doi: 10.1016/s0024-4937(00)00032-3.

- Halldorsson, S. A., Hilton, D. R., Scarsi, P., Abebe, T., and Hopp, J., 2014, A common mantle plume source beneath the entire East African Rift System revealed by coupled helium-neon systematics: *Geophysical Research Letters*, v. 41, p. 2304-2311, doi: 10.1002/2014gl059424.
- Hamilton, C. W., Fagents, S. A., and Thordarson, T., 2010, Explosive lava-water interactions II: self-organization processes among volcanic rootless eruption sites in the 1783-1784 Laki lava flow, Iceland: *Bulletin of Volcanology*, v. 72, p. 469-485, doi: 10.1007/s00445-009-0331-5.
- Hampel, A., Hetzel, R., and Densmore, A. L., 2007, Postglacial slip-rate increase on the Teton normal fault, northern Basin and Range Province, caused by melting of the Yellowstone ice cap and deglaciation of the Teton Range?: *Geology*, v. 35, p. 1107, doi: 10.1130/g24093a.1.
- Hanghøj, K., Storey, M., and Stecher, O., 2003, An isotope and trace element study of the East Greenland dyke swarm: *Journal of Petrology*, v. 44, p. 2081–2112.
- Hansen, D. M., and Cartwright, J., 2006a, The three-dimensional geometry and growth of forced folds above saucer-shaped igneous sills: *Journal of Structural Geology*, v. 28, p. 1520-1535, doi: 10.1016/j.jsg.2006.04.004.
- Hansen, D. M., and Cartwright, J., 2006b, Saucer-shaped sill with lobate morphology revealed by 3D seismic data: implications for resolving a shallow-level sill emplacement mechanism: *Journal of the Geological Society of London*, v. 163, p. 509-523.
- Hansen, D. M., Redfern, J., Federici, F., Di Biase, D., and Bertozzi, G., 2008, Miocene igneous activity in the Northern Subbasin, offshore Senegal, NW Africa: *Marine and Petroleum Geology*, v. 25, p. 1-15, doi: 10.1016/j.marpetgeo.2007.04.007.
- Hansen, J., Jerram, D. A., McCaffrey, K., and Passey, S. R., 2011, Early Cenozoic saucer-shaped sills of the Faroe Islands: an example of intrusive styles in basaltic lava piles: *Journal of the Geological Society of London*, v. 168, p. 159-178.
- Harp, A. G., and Valentine, G. A., 2015, Shallow plumbing and eruptive processes of a scoria cone built on steep terrain: *Journal of Volcanology and Geothermal Research*, v. 294, p. 37-55, doi: 10.1016/j.jvolgeores.2015.02.008.
- Harte, B., 1983, Mantle peridotite and processes - the kimberlite sample, *in* Hawkesworth, C. J., and Norry, M. J., eds., *Continental Basalts and Mantle Xenoliths*: Nantwich, Cheshire, Shiva Publishing, p. 46-91.
- Hastie, W. W., Watkeys, M. K., and Aurbourg, C., 2014, Magma flow in dyke swarms of the Karoo LIP: Implications for the mantle plume hypothesis *Gondwana Research*, v. 25, p. 736-755.
- Haug, G. H., and Strecker, M. R., 1995, Volcano-tectonic evolution of the Chyulu Hills and implications for the regional stress field in Kenya: *Geology*, v. 23, p. 165-168.
- Havlin, C., Parmentier, E. M., and Hirth, G., 2013, Dike propagation driven by melt accumulation at the lithosphere–asthenosphere boundary: *Earth and Planetary Science Letters*, v. 367, p. 20-28.
- Hawkesworth, C. J., Lightfoot, P. C., Fedorenko, V. A., Blake, S., Naldrett, A. J., Doherty, W., and Gorbachev, N. S., 1995, Magma differentiation and mineralisation in the Siberian continental flood basalts: *Lithos*, v. 34, p. 61-88.
- Hayward, N. J., and Ebinger, C. J., 1996, Variations in the along-axis segmentation of the Afar Rift system: *Tectonics*, v. 15, p. 244-257, doi: 10.1029/95tc02292.

- Heimann, A., Fleming, T. H., Elliot, D. H., and Foland, K. A., 1994, A short interval of Jurassic continental flood basalt volcanism in Antarctica as demonstrated by $^{40}\text{Ar}/^{39}\text{Ar}$ geochronology: *Earth and Planetary Science Letters*, v. 121, p. 19-41.
- Hetzl, R., and Strecker, M. R., 1994, Late Mozambique Belt structures in western Kenya and their influence on the evolution of the Cenozoic Kenya Rift: *Journal of Structural Geology*, v. 16, p. 189-201, doi: 10.1016/0191-8141(94)90104-x.
- Hetzl, R., and Hampel, A., 2005, Slip rate variations on normal faults during glacial-interglacial changes in surface loads: *Nature*, v. 435, p. 81-84, doi: 10.1038/nature03562.
- Hillaire-Marcel, C., Carro, O., and Casanova, J., 1986, ^{14}C and Th/U dating of Pleistocene and Holocene stromatolites from East African paleolakes: *Quaternary Research*, v. 25, p. 312-329, doi: 10.1016/0033-5894(86)90004-9.
- Hilton, D. R., Halldorsson, S. A., Barry, P. H., Fischer, T. P., de Moor, J. M., Ramirez, C. J., Mangasini, F., and Scarsi, P., 2011, Helium isotopes at Rungwe Volcanic Province, Tanzania, and the origin of East African Plateaux: *Geophysical Research Letters*, v. 38, p. L21304, doi: 10.1029/2011gl049589.
- Hoek, J. D., 1991, A classification of dyke-fracture geometry with examples from Precambrian dyke swarms in the Vestfold Hills, Antarctica: *Geologische Rundschau*, v. 80, p. 233-248.
- Hofmann, C., Courtillot, V., Feraud, G., Rochette, P., Yirgu, G., Ketefo, E., and Pik, R., 1997, Timing of the Ethiopian flood basalt event and implications for plume birth and global change: *Nature*, v. 389, p. 838-841.
- Hollings, P., Smyk, M., Heaman, L. M., and Halls, H., 2010, The geochemistry, geochronology and paleomagnetism of dikes and sills associated with the Mesoproterozoic Midcontinent Rift near Thunder Bay, Ontario, Canada: *Precambrian Research*, v. 183, p. 553-571, doi: 10.1016/j.precamres.2010.01.012.
- Hollnack, D., and Stangl, R., 1998, The seismicity related to the southern part of the Kenya Rift: *Journal of African Earth Sciences*, v. 26, p. 477-495, doi: 10.1016/s0899-5362(98)00027-x.
- Holyoke, C. W., and Kronenberg, A. K., 2013, Reversible water weakening of quartz: *Earth and Planetary Science Letters*, v. 374, p. 185-190, doi: 10.1016/j.epsl.2013.05.039.
- Hooper, P. R., 1990, The timing of crustal extension and the eruption of continental flood basalts: *Nature*, v. 345, p. 246-249, doi: 10.1038/345246a0.
- Hooper, P., Widdowson, M., and Kelley, S., 2010, Tectonic setting and timing of the final Deccan flood basalt eruptions: *Geology*, v. 38, p. 839-842, doi: 10.1130/g31072.1.
- Hooten, J. A., and Ort, M. H., 2002, Peperite as a record of early-stage phreatomagmatic fragmentation processes: an example from the Hopi Buttes volcanic field, Navajo Nation, Arizona, USA: *Journal of Volcanology and Geothermal Research*, v. 114, p. 95-106, doi: 10.1016/s0377-0273(01)00282-7.
- Horner-Johnson, B. C., Gordon, R. G., Cowles, S. M., and Argus, D. F., 2005, The angular velocity of Nubia relative to Somalia and the location of the Nubia-Somalia-Antarctica triple junction: *Geophysical Journal International*, v. 162, p. 221-238, doi: 10.1111/j.1365-246X.2005.02608.x.
- Houghton, B. F., Wilson, C. J. N., and Smith, I. E. M., 1999, Shallow-seated controls on styles of explosive basaltic volcanism: a case study from New Zealand: *Journal of*

- Volcanology and Geothermal Research, v. 91, p. 97-120, doi: 10.1016/s0377-0273(99)00058-x.
- Hughes, G. W., Varol, O., and Beydoun, Z. R., 1991, Evidence for middle Oligocene rifting of the Gulf of Aden and for late Oligocene rifting of the southern Red Sea: *Marine and Petroleum Geology*, v. 8, p. 354-358, doi: 10.1016/0264-8172(91)90088-i.
- Hui, H., Peslier, A. H., Rudnick, R. L., Simonetti, A., and Neal, C. R., 2015, Plume-cratonic lithosphere interaction recorded by water and other trace elements in peridotite xenoliths from the Labait volcano, Tanzania: *Geochemistry, Geophysics, Geosystems*, v. 16, p. 1687–1710, doi: 10.1002/2015gc005779.
- Hurwitz, D. M., Long, S. M., and Grosfils, E. B., 2009, The characteristics of magma reservoir failure beneath a volcanic edifice: *Journal of Volcanology and Geothermal Research*, v. 188, p. 379-394, doi: 10.1016/j.jvolgeores.2009.10.004.
- Hutchison, W., Mather, T. A., Pyle, D. M., Biggs, J., and Yirgu, G., 2015, Structural controls on fluid pathways in an active rift system: A case study of the Aluto volcanic complex: *Geosphere*, v. 11, p. 542-562, doi: 10.1130/ges01119.1.
- Hutton, D. H. W., 2009, Insights into magmatism in volcanic margins: bridge structures and a new mechanism of basic sill emplacement - Theron Mountains, Antarctica: *Petroleum Geoscience*, v. 15, p. 269-278, doi: 10.1144/1354-079309-841.
- Ibs-von Seht, M., Blumenstein, S., Wagner, R., Hollnack, D., and Wohlenberg, J., 2001, Seismicity, seismotectonics and crustal structure of the southern Kenya Rift - new data from the Lake Magadi area: *Geophysical Journal International*, v. 146, p. 439-453, doi: 10.1046/j.0956-540x.2001.01464.x.
- Imber, J., Childs, C., Nell, P. A. R., Walsh, J. J., Hodgetts, D., and Flint, S., 2003, Hanging wall fault kinematics and footwall collapse in listric growth fault systems: *Journal of Structural Geology*, v. 25, p. 197-208, doi: 10.1016/s0191-8141(02)00034-2.
- Isaac, M. J., Chinn, T. J., Edbrooke, S. W., and Forsyth, P. J., 1996, Geology of the Olympus Range area south Victoria Land, Antarctica: Institute of Geological & Nuclear Sciences geological map 20, scale 1:50 000, 1 sheet.
- Isaacs, G. L., and Curtis, G. H., 1974, Age of early Acheulian industries from Peninj Group, Tanzania: *Nature*, v. 249, p. 624-627, doi: 10.1038/249624a0.
- Isola, I., Mazzarini, F., Bonini, M., and Corti, G., 2014, Spatial variability of volcanic features in early-stage rift settings: the case of the Tanzania Divergence, East African rift system: *Terra Nova*, v. 26, p. 461-468, doi: 10.1111/ter.12121.
- Jagniecki, E. A., Lowenstein, T. K., Jenkins, D. M., and Demicco, R. V., 2015, Eocene atmospheric CO₂ from the nahcolite proxy: *Geology*, p. 1075-1078, doi: 10.1130/g36886.1.
- Jenness, M. H., and Clifton, A. E., 2009, Controls on the geometry of a Holocene crater row: a field study from southwest Iceland: *Bulletin of Volcanology*, v. 71, p. 715-728, doi: 10.1007/s00445-009-0267-9.
- Johnson, A. M., and Pollard, D. D., 1973, Mechanics of growth of some laccolith intrusions in Henry Mountains, Utah 1: Field observations, Gilbert's model, physical properties and flow of magma: *Tectonophysics*, v. 18, p. 261-309.
- Johnson, E. R., Wallace, P. J., Cashman, K. V., Granados, H. D., and Kent, A. J. R., 2008, Magmatic volatile contents and degassing-induced crystallization at Volcan Jorullo, Mexico: Implications for melt evolution and the plumbing systems of monogenetic

- volcanoes: *Earth and Planetary Science Letters*, v. 269, p. 477-486, doi: 10.1016/j.epsl.2008.03.004.
- Jolie, E., Klinkrueller, M., and Moeck, I., 2015, Diffuse surface emanations as indicator of structural permeability in fault-controlled geothermal systems: *Journal of Volcanology and Geothermal Research*, v. 290, p. 97-113, doi: 10.1016/j.jvolgeores.2014.11.003.
- Jolly, R. J. H., and Sanderson, D. J., 1997, A Mohr circle construction for the opening of a pre-existing fracture: *Journal of Structural Geology*, v. 19, p. 887-892, doi: 10.1016/s0191-8141(97)00014-x.
- Jones, B. F., Eugster, H. P., and Rettig, S. L., 1977, Hydrochemistry of Lake Magadi basin, Kenya: *Geochimica Et Cosmochimica Acta*, v. 41, p. 53-72, doi: 10.1016/0016-7037(77)90186-7.
- Kagoshima, T., Sano, Y., Takahata, N., Maruoka, T., Fischer, T. P., and Hattori, K., 2015, Sulphur geodynamic cycle: *Scientific Reports*, v. 5, doi: 10.1038/srep08330.
- Kamunzu, A. B., Bonhomme, M. G., and Kanika, M., 1998, Geochronology of volcanic rocks and evolution of the Cenozoic Western Branch of the East African Rift System: *Journal of African Earth Sciences*, v. 26, p. 441-461, doi: 10.1016/s0899-5362(98)00025-6.
- Karakas, O., and Dufek, J., 2015, Melt evolution and residence in extending crust: Thermal modeling of the crust and crustal magmas: *Earth and Planetary Science Letters*, v. 425, p. 131-144, doi: 10.1016/j.epsl.2015.06.001.
- Kattenhorn, S. A., 2004, Strike-slip fault evolution on Europa: evidence from tailcrack geometries: *Icarus*, v. 172, p. 582-602, doi: 10.1016/j.icarus.2004.07.005.
- Kattenhorn, S. A., and Watkeys, M. K., 1995, Blunt-ended dyke segments: *Journal of Structural Geology*, v. 17, p. 1532-1542.
- Kattenhorn, S. A., and Pollard, D. D., 2001, Integrating 3-D seismic data, field analogs, and mechanical models in the analysis of segmented normal faults in the Wytch Farm oil field, southern England, United Kingdom: *AAPG Bulletin*, v. 85, p. 1183-1210.
- Kattenhorn, S. A., Muirhead, J. D., Dindi, E., Fischer, T. P., Lee, H., and Ebinger, C. J., 2013, Contribution of Transverse Structures, Magma, and Crustal Fluids to Continental Rift Evolution: The East African Rift in Southern Kenya: Abstract T12B-02 presented at 2013 Fall Meeting, AGU, San Francisco, California, 9–13 December.
- Katumwehe, A. B., Abdelsalam, M. G., and Atekwana, E. A., 2015a, The role of pre-existing Precambrian structures in rift evolution: The Albertine and Rhino grabens, Uganda: *Tectonophysics*, v. 646, p. 117-129, doi: 10.1016/j.tecto.2015.01.022.
- Katumwehe, A. B., Abdelsalam, M. G., Atekwana, E. A., and Laó-Dávila, D. A., 2015b, Extent, kinematics and tectonic origin of the Precambrian Aswa Shear Zone in eastern Africa: *Gondwana Research*, doi: 10.1016/j.gr.2015.03.007.
- Kavanagh, J. L., and Pavier, M. J., 2014, Rock interface strength influences fluid-filled fracture propagation pathways in the crust: *Journal of Structural Geology*, v. 63, p. 68-75, doi: 10.1016/j.jsg.2014.03.001.
- Kavanagh, J. L., Menand, T., and Sparks, R. S. J., 2006, An experimental investigation of sill formation and propagation in layered elastic media: *Earth and Planetary Science Letters*, v. 245, p. 799-813, doi: 10.1016/j.epsl.2006.03.025.
- Kavanagh, J. L., Boutelier, D., and Cruden, A. R., 2015, The mechanics of sill inception, propagation and growth: Experimental evidence for rapid reduction in magmatic

- overpressure: *Earth and Planetary Science Letters*, v. 421, p. 117-128, doi: 10.1016/j.epsl.2015.03.038.
- Keating, G. N., Valentine, G. A., Krier, D. J., and Perry, F. V., 2008, Shallow plumbing systems for small-volume basaltic volcanoes: *Bulletin of Volcanology*, v. 70, p. 563-582, doi: 10.1007/s00445-007-0154-1.
- Keir, D., Kendall, J. M., Ebinger, C. J., and Stuart, G. W., 2005, Variations in late syn-rift melt alignment inferred from shear-wave splitting in crustal earthquakes beneath the Ethiopian rift: *Geophysical Research Letters*, v. 32, p. L23308, doi: 10.1029/2005gl024150.
- Keir, D., Ebinger, C. J., Stuart, G. W., Daly, E., and Ayele, A., 2006, Strain accommodation by magmatism and faulting as rifting proceeds to breakup: Seismicity of the northern Ethiopian rift: *Journal of Geophysical Research*, v. 111, p. B05314, doi: 10.1029/2005jb003748.
- Keir, D., Bastow, I. D., Whaler, K. A., Daly, E., Cornwell, D. G., and Hautot, S., 2009a, Lower crustal earthquakes near the Ethiopian rift induced by magmatic processes: *Geochemistry, Geophysics, Geosystems*, v. 10, p. Q0AB02, doi: 10.1029/2009gc002382.
- Keir, D., Hamling, I. J., Ayele, A., Calais, E., Ebinger, C., Wright, T. J., Jacques, E., Mohamed, K., Hammond, J. O. S., Belachew, M., Baker, E., Rowland, J. V., Lewi, E., and Bennati, L., 2009b, Evidence for focused magmatic accretion at segment centers from lateral dike injections captured beneath the Red Sea rift in Afar: *Geology*, v. 37, p. 59-62, doi: 10.1130/g25147a.1.
- Keir, D., Belachew, M., Ebinger, C. J., Kendall, J. M., Hammond, J. O. S., Stuart, G. W., Ayele, A., and Rowland, J. V., 2011, Mapping the evolving strain field during continental breakup from crustal anisotropy in the Afar Depression: *Nature Communications*, v. 2, doi: 10.1038/ncomms1287.
- Keir, D., Belachew, M., Ebinger, C. J., Kendall, J. M., Hammond, J. O. S., Stuart, G. W., Ayele, A., and Rowland, J. V., 2011, Mapping the evolving strain field during continental breakup from crustal anisotropy in the Afar Depression: *Nature Communications*, v. 2, doi: 10.1038/ncomms1287.
- Keir, D., C. Pagli, I. D. Bastow, and A. Ayele, 2011b, The magma-assisted removal of Arabia in Afar: Evidence from dike injection in the Ethiopian rift captured using InSAR and seismicity: *Tectonics*, v. 30, p. TC2008, doi:10.1029/2010TC002785.
- Keir, D., Bastow, I. D., Corti, G., Mazzarini, F., and Rooney, T. O., 2015, The origin of along-rift variations in faulting and magmatism in the Ethiopian Rift: *Tectonics*, v. 34, p. 464-477, doi: 10.1002/2014tc003698.
- Keller, G. R., Mechie, J., Braile, L. W., Mooney, W. D., and Prodehl, C., 1994, Seismic structure of the uppermost mantle beneath the Kenya Rift: *Tectonophysics*, v. 236, p. 201-216, doi: 10.1016/0040-1951(94)90177-5.
- Keller, J., Zaitsev, A. N., and Wiedenmann, D., 2006, Primary magmas at Oldoinyo Lengai: The role of olivine melilitites: *Lithos*, v. 91, p. 150-172, doi: 10.1016/j.lithos.2006.03.014.
- Kendall, J. M., Stuart, G. W., Ebinger, C. J., Bastow, I. D., and Keir, D., 2005, Magma-assisted rifting in Ethiopia: *Nature*, v. 433, p. 146-148, doi: 10.1038/nature03161.

- Kennedy, B. M., Kharaka, Y. K., Evans, W. C., Ellwood, A., DePaolo, D. J., Thordsen, J., Ambats, G., and Mariner, R. H., 1997, Mantle fluids in the San Andreas fault system, California: *Science*, v. 278, p. 1278-1281, doi: 10.1126/science.278.5341.1278.
- Kent, G. M., Babcock, J. M., Driscoll, N. W., Harding, A. J., Dingler, J. A., Seitz, G. G., Gardner, J. V., Mayer, L. A., Goldman, C. R., Heyvaert, A. C., Richards, R. C., Karlin, R., Morgan, C. W., Gayes, P. T., and Owen, L. A., 2005, 60 k.y. record of extension across the western boundary of the Basin and Range province: Estimate of slip rates from offset shoreline terraces and a catastrophic slide beneath Lake Tahoe: *Geology*, v. 33, p. 365, doi: 10.1130/g21230.1.
- Keranen, K., Klemper, S. L., Gloaguen, R., and EAGLE Working Group, 2004, Three-dimensional seismic imaging of a protoridge axis in the Main Ethiopian rift: *Geology*, v. 32, p. 949-952, doi: 10.1130/g20737.1.
- Keranen, K. M., Klemperer, S. L., Julia, J., Lawrence, J. F., and Nyblade, A. A., 2009, Low lower crustal velocity across Ethiopia: Is the Main Ethiopian Rift a narrow rift in a hot craton?: *Geochemistry, Geophysics, Geosystems*, v. 10, p. Q0AB01, doi: 10.1029/2008gc002293.
- Kereszturi, G., and Németh, K., 2012, Monogenetic Basaltic Volcanoes: Genetic Classification, Growth, Geomorphology and Degradation, *in* Németh, K., ed., *Updates in Volcanology — New Advances in Understanding Volcanic Systems*: Rijeka, Croatia, InTech, p. 3-89.
- Kervyn, M., Ernst, G. G. J., Harris, A. J. L., Belton, F., Mbede, E., and Jacobs, P., 2008, Thermal remote sensing of the low-intensity carbonatite volcanism of Oldoinyo Lengai, Tanzania: *International Journal of Remote Sensing*, v. 29, p. 6467-6499, doi: 10.1080/01431160802167105.
- Kervyn, M., Ernst, G. G. J., de Vries, B. V., Mathieu, L., and Jacobs, P., 2009, Volcano load control on dyke propagation and vent distribution: Insights from analogue modeling: *Journal of Geophysical Research*, v. 114, p. B03401, doi: 10.1029/2008jb005653.
- Kidder, D. L., and Worsley, T. R., 2010, Phanerozoic Large Igneous Provinces (LIPs), HEATT (Haline Euxinic Acidic Thermal Transgression) episodes, and mass extinctions: *Palaeogeography, Palaeoclimatology, Palaeoecology*, v. 295, p. 162-191, doi: 10.1016/j.palaeo.2010.05.036.
- Kilembe, E. A., and Rosendahl, B. R., 1992, Structure and stratigraphy of the Rukwa Rift: *Tectonophysics*, v. 209, p. 143-158, doi: 10.1016/0040-1951(92)90016-y.
- Kinabo, B. D., Hogan, J. P., Atekwana, E. A., Abdelsalam, M. G., and Modisi, M. P., 2008, Fault growth and propagation during incipient continental rifting: Insights from a combined aeromagnetic and Shuttle Radar Topography Mission digital elevation model investigation of the Okavango Rift Zone, northwest Botswana: *Tectonics*, v. 27, doi: 10.1029/2007tc002154.
- Kiyosugi, K., Connor, C. B., Wetmore, P. H., Ferwerda, B. P., Germa, A. M., Connor, L. J., and Hintz, A. R., 2012, Relationship between dike and volcanic conduit distribution in a highly eroded monogenetic volcanic field: San Rafael, Utah, USA: *Geology*, v. 40, p. 695-698, doi: 10.1130/g33074.1.
- Klausen, M. B., 2004, Geometry and mode of emplacement of the Thverartindur cone sheet swarm, SE Iceland: *Journal of Volcanology and Geothermal Research*, v. 138, p. 185-204, doi: 10.1016/j.jvolgeores.2004.05.022.

- Klausen, M. B., 2004, Geometry and mode of emplacement of the Thverartindur cone sheet swarm, SE Iceland: *Journal of Volcanology and Geothermal Research*, v. 138, p. 185-204, doi: 10.1016/j.jvolres.2004.08.009, The Lebombo monocline and associated feeder dyke swarm: Diagnostic of a successful and highly volcanic rifted margin?: *Tectonophysics*, v. 468, p. 42-62, doi: 10.1016/j.tecto.2008.10.012.
- Klein, F. W., 1978, Hypocenter location program HYPOINVERSE, part 1; Users guide to versions 1, 2, 3 and 4; part 2; Source listings and notes: US Geological Survey Open File Report 78-694, 114 p.
- Koehn, D., Aanyu, K., Haines, S., and Sachau, T., 2008, Rift nucleation, rift propagation and the creation of basement micro-plates within active rifts: *Tectonophysics*, v. 458, p. 105-116, doi: 10.1016/j.tecto.2007.10.003.
- Koehn, D., Lindenfeld, M., Rumpker, G., Aanyu, K., Haines, S., Passchier, C. W., and Sachau, T., 2010, Active transection faults in rift transfer zones: evidence for complex stress fields and implications for crustal fragmentation processes in the western branch of the East African Rift: *International Journal of Earth Sciences*, v. 99, p. 1633-1642, doi: 10.1007/s00531-010-0525-2.
- Koenig, E., and Pollard, D. D., 1998, Mapping and modeling of radial fracture patterns on Venus: *Journal of Geophysical Research*, v. 103, p. 15183-15202, doi: 10.1029/98jb00577.
- Koptev, A., Calais, E., Burov, E., Leroy, S., and Gerya, T., 2015, Dual continental rift systems generated by plume–lithosphere interaction: *Nature Geoscience*, v. 8, p. 388-392, doi: 10.1038/ngeo2401.
- Korme, T., Chorowicz, J., Collet, B., and Bonavia, F. F., 1997, Volcanic vents rooted on extension fractures and their geodynamic implications in the Ethiopian Rift: *Journal of Volcanology and Geothermal Research*, v. 79, p. 205-222, doi: 10.1016/s0377-0273(97)00034-6.
- Korsch, R. J., 1984, The structure of Shapeless Mountain, Antarctica, and its relation to Jurassic igneous activity: *New Zealand Journal of Geology and Geophysics*, v. 27, p. 487-504.
- Kronberg, P., 1991, Geometries of extensional fault systems, observed and mapped on aerial and satellite photographs of Central Afar (Ethiopia/Djibouti): *Geologie en Mijnbouw*, v. 70, p. 145-161.
- Krumbholz, M., Hieronymus, C. F., Burchardt, S., Troll, V. R., Tanner, D. C., and Friese, N., 2014, Weibull-distributed dyke thickness reflects probabilistic character of host-rock strength: *Nature Communications*, v. 5, doi: 10.1038/ncomms4272.
- Kuiper, K. F., Deino, A., Hilgen, F. J., Krijgsman, W., Renne, P. R., and Wijbrans, J. R., 2008, Synchronizing rock clocks of Earth history: *Science*, v. 320, p. 500-504, doi: 10.1126/science.1154339.
- Lambert, C., Muirhead, J. D., Ebinger, C. J., Tiberi, C., Roecker, S., Ferdinand-Wambura, R., Kianji, G., and Mulibo, G., 2014, Lower crustal seismicity, volatiles, and evolving strain fields during the initial stages of cratonic rifting, Abstract T53B-4678 presented at 2014 Fall Meeting, AGU, San Francisco, California, 14–18 December.
- Lao-Davila, D. A., Al-Salmi, H. S., Abdelsalam, M. G., and Atekwana, E. A., 2015, Hierarchical segmentation of the Malawi Rift: The influence of inherited lithospheric heterogeneity and kinematics in the evolution of continental rifts: *Tectonics*, v. 34, p. 2399-2417, doi: 10.1002/2015tc003953.

- Larsen, H. C., and Marcussen, C., 1992, Sill intrusion, flood basalt emplacement and deep crustal structure of the Scoresby Sund region, East Greenland, *in* Storey, B. C., Alabaster, T., and Pankhurst, R. J., eds., *Magmatism and the causes of continental break-up*, Geological Society of London Special Publications, v. 68, p. 365–386.
- Laughlin, A. W., Aldrich, M. J., Shafiqullah, M., and Husler, J., 1986, Tectonic implications of the age, composition, and orientation of lamprophyre dikes, Navajo volcanic field, Arizona: *Earth and Planetary Science Letters*, v. 76, p. 361-374, doi: 10.1016/0012-821x(86)90087-7.
- Lavier, L. L., Buck, W. R., and Poliakov, A. N. B., 2000, Factors controlling normal fault offset in an ideal brittle layer: *Journal of Geophysical Research*, v. 105, p. 23431-23442, doi: 10.1029/2000jb900108.
- Le Corvec, N., Spörli, K. B., Rowland, J., and Lindsay, J., 2013a, Spatial distribution and alignments of volcanic centers: Clues to the formation of monogenetic volcanic fields: *Earth-Science Reviews*, v. 124, p. 96-114, doi: 10.1016/j.earscirev.2013.05.005.
- Le Corvec, N., Menand, T., and Lindsay, J., 2013b, Interaction of ascending magma with pre-existing crustal fractures in monogenetic basaltic volcanism: an experimental approach: *Journal of Geophysical Research*, v. 118, p. 968-984, doi: 10.1002/jgrb.50142.
- Le Corvec, N., McGovern, P. J., Grosfils, E. B., and Galgana, G., 2015, Effects of crustal-scale mechanical layering on magma chamber failure and magma propagation within the Venusian lithosphere: *Journal of Geophysical Research*, v. 120, p. 1279-1297, doi: 10.1002/2015je004814.
- Le Gall, B., Tiercelin, J. J., Richert, J. P., Gente, P., Sturchio, N. C., Stead, D., and Le Turdu, C., 2000, A morphotectonic study of an extensional fault zone in a magma-rich rift: the Baringo Trachyte Fault System, central Kenya Rift: *Tectonophysics*, v. 320, p. 87-106, doi: 10.1016/s0040-1951(00)00069-x.
- Le Gall, B., Nonnotte, P., Rolet, J., Benoit, M., Guillou, H., Mousseau-Nonnotte, M., Albaric, J., and Deverchere, J., 2008, Rift propagation at craton margin. Distribution of faulting and volcanism in the North Tanzanian Divergence (East Africa) during Neogene times: *Tectonophysics*, v. 448, p. 1-19, doi: 10.1016/j.tecto.2007.11.005.
- Le Gall, B., Daoud, M. A., Rolet, J., and Egueh, N. M., 2011, Large-scale flexuring and antithetic extensional faulting along a nascent plate boundary in the SE Afar rift: *Terra Nova*, v. 23, p. 416-420, doi: 10.1111/j.1365-3121.2011.01029.x.
- Le Turdu, C., Richert, J. P., Xavier, J.-P., Renaut, R. W., Tiercelin, J.-J., Rolet, J., Lezzar, K. E., and Coussement, C., 1999, Influence of preexisting oblique discontinuities on the geometry and evolution of extensional fault patterns: evidence from the Kenya Rift using SPOT imagery *in* Morley, C. K., ed., *Geoscience of Rift Systems – Evolution of East Africa*: Tulsa, American Association of Petroleum Geologists, v. 44, p. 173–191.
- Leat, P. T., 2008, On the long-distance transport of Ferrar magmas, *in* Thomson, K., and Petford, N., eds., *Structure and Emplacement of High-Level Magmatic Systems*, Geological Society of London Special Publications, v. 302, p. 45-61.
- Lee, C. T. A., Shen, B., Slotnick, B. S., Liao, K., Dickens, G. R., Yokoyama, Y., Lenardic, A., Dasgupta, R., Jellinek, M., Lackey, J. S., Schneider, T., and Tice, M. M., 2013, Continental arc-island arc fluctuations, growth of crustal carbonates, and long-term climate change: *Geosphere*, v. 9, p. 21-36, doi: 10.1130/ges00822.1.

- Lee, H., Muirhead, J. D., Fischer, T. P., Ebinger, C. J., Kattenhorn, S. A., Sharp, Z. D., and Kianji, G., 2016, Massive and prolonged deep carbon emissions associated with continental rifting: *Nature Geoscience*, v. 9, doi: 10.1038/NGEO2622.
- Lee, J. Y., Marti, K., Severinghaus, J. P., Kawamura, K., Yoo, H. S., Lee, J. B., and Kim, J. S., 2006, A redetermination of the isotopic abundances of atmospheric Ar: *Geochimica Et Cosmochimica Acta*, v. 70, p. 4507-4512, doi: 10.1016/j.gca.2006.06.1563.
- Lefebvre, N. S., 2013, Volcanology of maar-diatreme volcanic vent complexes, Hopi Buttes Volcanic Field, Navajo Nation, Arizona, USA [Ph.D. thesis]: Dunedin, University of Otago, 269 p.
- Lefebvre, N. S., White, J. D. L., and Kjarsgaard, B. A., 2012, Spatter-dike reveals subterranean magma diversions: Consequences for small multivalent basaltic eruptions: *Geology*, v. 40, p. 423-426, doi: 10.1130/g32794.1.
- Lefebvre, N. S., White, J. D. L., and Kjarsgaard, B. A., 2016, Arrested diatreme development: Standing Rocks East, Hopi Buttes, Navajo Nation, USA: *Journal of Volcanology and Geothermal Research*, v. 310, p. 186-208, doi: 10.1016/j.jvolgeores.2015.12.007.
- Leseane, K., Atekwana, E. A., Mickus, K. L., Abdelsalam, M. G., Shemang, E. M., and Atekwana, E. A., 2015, Thermal perturbations beneath the incipient Okavango Rift Zone, northwest Botswana: *Journal of Geophysical Research*, v. 120, p. 1210-1228, doi: 10.1002/2014jb011029.
- Lewicki, J. L., and Brantley, S. L., 2000, CO₂ degassing along the San Andreas fault, Parkfield, California: *Geophysical Research Letters*, v. 27, p. 5-8, doi: 10.1029/1999gl008380.
- Li, C. S., Ripley, E. M., and Naldrett, A. J., 2009, A new generic model of the giant Ni-Cu-PGE sulfide deposits associated with the Siberian Flood Basalts: *Economic Geology*, v. 104, p. 291-301.
- Lindenfeld, M., Rumpker, G., Link, K., Koehn, D., and Batte, A., 2012, Fluid-triggered earthquake swarms in the Rwenzori region, East African Rift—Evidence for rift initiation: *Tectonophysics*, v. 566-567, p. 95-104, doi: 10.1016/j.tecto.2012.07.010.
- Lister, J. R., and Kerr, R. C., 1991, Fluid-mechanical models of crack propagation and their application to magma transport in dykes: *Journal of Geophysical Research*, v. 96, p. 10,049-10,077.
- Lithgow-Bertelloni, C., and Gynn, J. H., 2004, Origin of the lithospheric stress field: *Journal of Geophysical Research*, v. 109, p. B01408, doi: 10.1029/2003jb002467.
- Lundin, E. R., and Dore, A. G., 2011, Hyperextension, serpentinitization, and weakening: A new paradigm for rifted margin compressional deformation: *Geology*, v. 39, p. 347-350, doi: 10.1130/g31499.1.
- Macdonald, R., and Baginsk, B., 2009, The central Kenya peralkaline province: a unique assemblage of magmatic systems: *Mineralogical Magazine*, v. 73, p. 1-16, doi: 10.1180/minmag.2009.073.1.1.
- Macdonald, R., Belkin, H. E., Fitton, J. G., Rogers, N. W., Nejbort, K., Tindle, A. G., and Marshall, A. S., 2008, The roles of fractional crystallization, magma mixing, crystal mush remobilization and volatile-melt interactions in the genesis of a young basalt-peralkaline rhyolite suite, the Greater Olkaria Volcanic Complex, Kenya rift valley: *Journal of Petrology*, v. 49, p. 1515-1547, doi: 10.1093/petrology/egn036.

- Machette, M. N., Personius, S. F., and Nelson, A. R., 1991, The Wasatch fault zone, Utah - segmentation and history of Holocene earthquakes: *Journal of Structural Geology*, v. 13, p. 137-149.
- MacIntyre, R. M., Mitchell, J. G., and Dawson, J. B., 1974, Age of fault movements in the Tanzanian sector of the East African Rift System: *Nature*, v. 247, p. 354-356, doi: 10.1038/247354a0.
- Magee, C., Stevenson, C., O'Driscoll, B., Schofield, N., and McDermott, K., 2012, An alternative emplacement model for the classic Ardnamurchan cone sheet swarm, NW Scotland, involving lateral magma supply via regional dykes: *Journal of Structural Geology*, v. 43, p. 73-91, doi: 10.1016/j.jsg.2012.08.004.
- Magee, C., Hunt-Stewart, E., and Jackson, C. A. L., 2013a, Volcano growth mechanisms and the role of sub-volcanic intrusions: Insights from 2D seismic reflection data: *Earth and Planetary Science Letters*, v. 373, p. 41-53, doi: 10.1016/j.epsl.2013.04.041.
- Magee, C., Briggs, F., and Jackson, C. A. L., 2013b, Lithological controls on igneous intrusion-induced ground deformation: *Journal of the Geological Society of London*, v. 170, p. 853-856, doi: 10.1144/jgs2013-029.
- Magee, C., Jackson, C. A.-L., and Schofield, N., 2014, Diachronous sub-volcanic intrusion along deepwater margins: insights from the Irish Rockall Basin: *Basin Research*, v. 26, p. 85-105.
- Magee, C., Muirhead, J. D., Karvelas, A., Holford, S. P., Jackson, C. A. L., Bastow, I. D., Schofield, N., Stevenson, C. T. E., McLean, C., McCarthey, W., and Shtukert, O., 2016, Lateral magma flow in mafic sill-complexes: *Geosphere*, v. 12, doi: 10.1130/ges01256.1.
- Malthe-Sørensen, A., Planke, S., Svensen, H., and Jamtveit, B., 2004, Formation of saucer-shaped sills: *Geological Society of London Special Publications*, v. 234, p. 215-227.
- Mana, S., Furman, T., Turrin, B. D., Feigenson, M. D., and Swisher, C. C., 2015a, Magmatic activity across the East African North Tanzanian Divergence Zone: *Journal of the Geological Society of London*, v. 172, p. 368-389, doi: 10.1144/jgs2014-072.
- Manatschal, G., 2004, New models for evolution of magma-poor rifted margins based on a review of data and concepts from West Iberia and the Alps: *International Journal of Earth Sciences*, v. 93, p. 432-466, doi: 10.1007/s00531-004-0394-7.
- Manega, P. C., 1993, *Geochronology, Geochemistry and Isotopic Study of the Plio-Pleistocene Hominid Sites and the Ngorongoro Volcanic Highlands in Northern Tanzania* [Ph.D. thesis]: Boulder, University of Colorado.
- Manighetti, I., King, G. C. P., Gaudemer, Y., Scholz, C. H., and Doubre, C., 2001, Slip accumulation and lateral propagation of active normal faults in Afar: *Journal of Geophysical Research*, v. 106, p. 13667-13696, doi: 10.1029/2000jb900471.
- Marrett, R., and Allmendinger, R. W., 1991, Estimates of strain due to brittle faulting: sampling of fault populations: *Journal of Structural Geology*, v. 13, p. 735-738, doi: 10.1016/0191-8141(91)90034-g.
- Marsh, B. D., 2004, A magmatic mush column Rosetta Stone: the McMurdo Dry Valleys of Antarctica: *Eos, Transactions, American Geophysical Union*, v. 85, p. 497-502.
- Marsh, B. D., and Zeig, M. J., 1997, The Dias layered intrusion: A new discovery in the Basement Sill of the McMurdo Dry Valleys: *Antarctic Journal of the United States*, v. 16, p. 54-55.

- Marsh, J. S., Hooper, P. R., Rehacek, J., Duncan, R. A., and A.R., D., 1997, Stratigraphy and age of Karoo basalts of Lesotho and implications for correlations within the Karoo Igneous Province, *in* Mahoney, J. J., and Coffin, M. F., eds., Large Igneous Provinces: Continental, Oceanic, and Planetary Flood Volcanism: Washington D.C., American Geophysical Union, Geophysical Monograph Series 100, p. 247-272.
- Marshak, S., Karlstrom, K., and Timmons, J. M., 2000, Inversion of Proterozoic extensional faults: An explanation for the pattern of Laramide and Ancestral Rockies intracratonic deformation, United States: *Geology*, v. 28, p. 735-738.
- Marshall, S. T., and Kattenhorn, S. A., 2005, A revised model for cycloid growth mechanics on Europa: Evidence from surface morphologies and geometries: *Icarus*, v. 177, p. 341-366, doi: 10.1016/j.icarus.2005.02.022.
- Marty, B., and Tolstikhin, I. N., 1998, CO₂ fluxes from mid-ocean ridges, arcs and plumes: *Chemical Geology*, v. 145, p. 233-248, doi: 10.1016/s0009-2541(97)00145-9.
- Marty, B., and Zimmermann, L., 1999, Volatiles (He, C, N, Ar) in mid-ocean ridge basalts: Assessment of shallow-level fractionation and characterization of source composition: *Geochimica Et Cosmochimica Acta*, v. 63, p. 3619-3633, doi: 10.1016/s0016-7037(99)00169-6.
- Masini, E., Manatschal, G., Mohn, G., Ghienne, J. F., and Lafont, F., 2011, The tectono-sedimentary evolution of a supra-detachment rift basin at a deep-water magma-poor rifted margin: the example of the Samedan Basin preserved in the Err nappe in SE Switzerland: *Basin Research*, v. 23, p. 652-677, doi: 10.1111/j.1365-2117.2011.00509.x.
- Mastin, L. G., Christiansen, R. L., Thornber, C., Lowenstern, J., and Beeson, M., 2004, What makes hydromagmatic eruptions violent? Some insights from the Keanakako'i Ash, Kilauea Volcano, Hawai'i: *Journal of Volcanology and Geothermal Research*, v. 137, p. 15-31, doi: 10.1016/j.jvolgeores.2004.05.015.
- Matheson, F. J., 1966, Geology of the Kajiado area: Geological Survey of Kenya Report 70, 51 p.
- Mathieu, L., de Vries, B. V., Holohan, E. P., and Troll, V. R., 2008, Dykes, cups, saucers and sills: Analogue experiments on magma intrusion into brittle rocks: *Earth and Planetary Science Letters*, v. 271, p. 1-13, doi: 10.1016/j.epsl.2008.02.020.
- Mathieu, L., Burchardt, S., Troll, V. R., Krumbholz, M., and Delcamp, A., 2015, Geological constraints on the dynamic emplacement of cone-sheets - The Ardnamurchan cone-sheet swarm, NW Scotland: *Journal of Structural Geology*, v. 80, p. 133-141, doi: 10.1016/j.jsg.2015.08.012.
- Mattsson, H. B., 2012, Rapid magma ascent and short eruption durations in the Lake Natron-Engaruka monogenetic volcanic field (Tanzania): A case study of the olivine melilititic Pello Hill scoria cone: *Journal of Volcanology and Geothermal Research*, v. 247, p. 16-25, doi: 10.1016/j.jvolgeores.2012.07.009.
- Mattsson, H. B., and Tripoli, B. A., 2011, Depositional characteristics and volcanic landforms in the Lake Natron-Engaruka monogenetic field, northern Tanzania: *Journal of Volcanology and Geothermal Research*, v. 203, p. 23-34, doi: 10.1016/j.jvolgeores.2011.04.010.
- Mattsson, H. B., Nandedkar, R. H., and Ulmer, P., 2013, Petrogenesis of the melilititic and nephelinitic rock suites in the Lake Natron-Engaruka monogenetic volcanic field, northern Tanzania: *Lithos*, v. 179, p. 175-192, doi: 10.1016/j.lithos.2013.07.012.

- Mazzarini, F., 2004, Volcanic vent self-similar clustering and crustal thickness in the northern Main Ethiopian Rift: *Geophysical Research Letters*, v. 31, p. L04604, doi:10.1029/2003GL018574.
- Mazzarini, F., 2007, Vent distribution and crustal thickness in stretched continental crust: The case of the Afar Depression (Ethiopia): *Geosphere*, v. 3, p. 152-162, doi: 10.1130/ges00070.1.
- Mazzarini, F., Corti, G., Manetti, P., and Innocenti, F., 2004, Strain rate and bimodal volcanism in the continental rift: Debre Zeyt volcanic field, northern MER, Ethiopia: *Journal of African Earth Sciences*, v. 39, p. 415-420, doi: 10.1016/j.jafrearsci.2004.07.025.
- Mazzarini, F., Keir, D., and Isola, I., 2013a, Spatial relationship between earthquakes and volcanic vents in the central-northern Main Ethiopian Rift: *Journal of Volcanology and Geothermal Research*, v. 262, p. 123-133, doi: 10.1016/j.jvolgeores.2013.05.007.
- Mazzarini, F., Rooney, T. O., and Isola, I., 2013b, The intimate relationship between strain and magmatism: A numerical treatment of clustered monogenetic fields in the Main Ethiopian Rift: *Tectonics*, v. 32, p. 49-64, doi: 10.1029/2012tc003146.
- Mazzarini, F., Le Corvec, N., Isola, I., and Favalli, M., 2016, Volcanic field elongation, vent distribution and tectonic evolution of a continental rift: the Main Ethiopian Rift example: *Geosphere*, doi:10.1130/GES01193.1.
- McClay, K. R., and Ellis, P. G., 1987, Geometries of extensional fault systems developed in model experiments: *Geology*, v. 15, p. 341-344.
- McClintock, M. K., 2001, Phreatomagmatism at Coombs Hills, Antarctica: Magma-water super-volcanism in a wet, failed rift [M.Sc. Thesis]: Dunedin, University of Otago, 174 p.
- McClintock, M., and White, J. D. L., 2006, Large phreatomagmatic vent complex at Coombs Hills, Antarctica: Wet, explosive initiation of flood basalt volcanism in the Ferrar-Karoo LIP: *Bulletin of Volcanology*, v. 68, p. 215-239, doi: 10.1007/s00445-005-0001-1.
- McConnell, R. B., 1972, Geological development of the rift system of eastern Africa: *Geological Society of America Bulletin*, v. 83, p. 2549-2572.
- McDougall, I., and Harrison, T. M., 1999, *Geochronology and thermochronology by the $^{40}\text{Ar}/^{39}\text{Ar}$ methods*: New York, Oxford University Press, 212 p.
- McElroy, C. T., and Rose, G., 1987, *Geology of the Beacon Heights area, southern Victoria Land, Antarctica*: Wellington Department of Scientific and Industrial Research Geological Survey miscellaneous series map 15, scale 1:50 000, 1 sheet.
- McGee, L. E., Millet, M. A., Smith, I. E. M., Nemeth, K., and Lindsay, J. M., 2012, The inception and progression of melting in a monogenetic eruption: Motukorea Volcano, the Auckland Volcanic Field, New Zealand: *Lithos*, v. 155, p. 360-374, doi: 10.1016/j.lithos.2012.09.012.
- McKenzie, D. P., and Parker, R. L., 1967, North Pacific: an example of tectonics on a sphere: *Nature*, v. 216, doi: 10.1038/2161276a0.
- McKenzie, D., and Bickle, M. J., 1988, The volume and composition of melt generated by extension of the lithosphere: *Journal of Petrology*, v. 29, p. 625-679.
- McNitt, J. R., Klein, C. W., and Koenig, J. B., 1989, Probable subsurface temperature at Lake Magadi, Kenya, as indicated by hot spring geochemistry and the potential for

- development of geothermal electric power: US Department of Energy Report DOE/ID/12850-T1, 29 p.
- Mechie, J., Keller, G. R., Prodehl, C., Khan, M. A., and Gaciri, S. J., 1997, A model for the structure, composition and evolution of the Kenya rift: *Tectonophysics*, v. 278, p. 95-119, doi: 10.1016/s0040-1951(97)00097-8.
- Menzies, M., 1983, Mantle ultramafic xenoliths in alkaline magmas: evidence for mantle heterogeneity modified by magma activity, *in* Hawkesworth, C. J., and Norry, M. J., eds., *Continental Basalts and Mantle Xenoliths*: Nantwich, Cheshire, Shiva Publishing, p. 92-110.
- Modisi, M. P., Atekwana, E. A., Kampunzu, A. B., and Ngwisanyi, T. H., 2000, Rift kinematics during the incipient stages of continental extension: Evidence from the nascent Okavango rift basin, northwest Botswana: *Geology*, v. 28, p. 939-942.
- Mollel, G. F., Swisher, C. C., Feigenson, M. D., and Carr, M. J., 2008, Geochemical evolution of Ngorongoro Caldera, Northern Tanzania: Implications for crust-magma interaction: *Earth and Planetary Science Letters*, v. 271, p. 337-347, doi: 10.1016/j.epsl.2008.04.014.
- Monnin, C., and Schott, J., 1984, Determination of the solubility products of sodium carbonate minerals and an application to trona deposition in Lake Magadi (Kenya): *Geochimica Et Cosmochimica Acta*, v. 48, p. 571-581, doi: 10.1016/0016-7037(84)90285-0.
- Moore, D. E., and Rymer, M. J., 2007, Talc-bearing serpentinite and the creeping section of the San Andreas fault: *Nature*, v. 448, p. 795-797, doi: 10.1038/nature06064.
- Moore, J. M., and Schultz, R. A., 1999, Processes of faulting in jointed rocks of Canyonlands National Park, Utah: *Geological Society of America Bulletin*, v. 111, p. 808-822.
- Morewood, N. C., and Roberts, G. P., 1997, Geometry, kinematics and rates of deformation in a normal fault segment boundary, central Greece: *Geophysical Research Letters*, v. 24, p. 3081-3084.
- Morley, C. K., 1995, Developments in the structural geology of rifts over the last decade and their impact on hydrocarbon exploration: *Geological Society of London Special Publication*, v. 80, p. 1-32.
- Morley, C. K., 1999, Patterns of displacement along large normal faults: Implications for basin evolution and fault propagation, based on examples from east Africa: *AAPG Bulletin*, v. 83, p. 613-634.
- Morley, C. K., 2010, Stress re-orientation along zones of weak fabrics in rifts: An explanation for pure extension in 'oblique' rift segments?: *Earth and Planetary Science Letters*, v. 297, p. 667-673, doi: 10.1016/j.epsl.2010.07.022.
- Morley, C. K., Nelson, R. A., Patton, T. L., and Munn, S. G., 1990, Transfer zones in the East African Rift System and their relevance to hydrocarbon exploration in rifts: *AAPG Bulletin*, v. 74, p. 1234-1253, doi.
- Morley, C. K., Wescott, W. A., Stone, D. M., Harper, R. M., Wigger, S. T., and Karanja, F. M., 1992, Tectonic evolution of the northern Kenya Rift: *Journal of the Geological Society of London*, v. 149, p. 333-348, doi: 10.1144/gsjgs.149.3.0333.
- Morley, C. K., Haranya, C., Phoosongsee, W., Pongwapee, S., Kornsawan, A., and Wonganan, N., 2004, Activation of rift oblique and rift parallel pre-existing fabrics during extension and their effect on deformation style: examples from the rifts of

- Thailand: *Journal of Structural Geology*, v. 26, p. 1803-1829, doi: 10.1016/j.jsg.2004.02.014.
- Morner, N. A., and Etiope, G., 2002, Carbon degassing from the lithosphere: Global and Planetary Change, v. 33, p. 185-203, doi: 10.1016/s0921-8181(02)00070-x.
- Morrison, A. D., 1989, Ferrar Dolerite intrusions at Terra Cotta Mountain, southern Victoria Land, Antarctica [M.Sc. thesis]: Dunedin, University of Otago, 165 p.
- Mosley, P. N., 1993, Geological evolution of the late Proterozoic Mozambique Belt of Kenya: *Tectonophysics*, v. 221, p. 223-250, doi: 10.1016/0040-1951(93)90334-g.
- Mourgues, R., Bureau, D., Bodet, L., Gay, A., and Gressier, J. B., 2012, Formation of conical fractures in sedimentary basins: Experiments involving pore fluids and implications for sandstone intrusion mechanisms: *Earth and Planetary Science Letters*, v. 313, p. 67-78, doi: 10.1016/j.epsl.2011.10.029.
- Muirhead, J. D., Airoidi, G., Rowland, J. V., and White, J. D. L., 2012, Interconnected sills and inclined sheet intrusions control shallow magma transport in the Ferrar large igneous province, Antarctica: *Geological Society of America Bulletin*, v. 124, p. 162-180, doi: 10.1130/b30455.1.
- Muirhead, J. D., Airoidi, G., White, J. D. L., and Rowland, J. V., 2014, Cracking the lid: Sill-fed dikes are the likely feeders of flood basalt eruptions: *Earth and Planetary Science Letters*, v. 406, p. 187-197, doi: 10.1016/j.epsl.2014.08.036.
- Muirhead, J. D., Kattenhorn, S. A., and Le Corvec, N., 2015, Varying styles of magmatic strain accommodation in the East African Rift: *Geochemistry, Geophysics, Geosystems*, v. 16, p. 2775-2795, doi: 10.1002/2015gc005918.
- Muirhead, J. D., Van Eaton, A. R., Re, G., White, J. D. L., and Ort, M. H., 2016, Monogenetic volcanoes fed by interconnected dikes and sills in the Hopi Buttes volcanic field, Navajo Nation, USA: *Bulletin of Volcanology*, v. 78, p. 1-16, doi: 10.1007/s00445-016-1005-8.
- Mulibo, G. D., and Nyblade, A. A., 2009, The 1994-1995 Manyara and Kwamtoro earthquake swarms: variation in the depth extent of seismicity in Northern Tanzania: *South African Journal of Geology*, v. 112, p. 387-404, doi: 10.2113/gssajg.112.3-4.387.
- Mulibo, G. D., and Nyblade, A. A., 2013a, Mantle transition zone thinning beneath eastern Africa: Evidence for a whole-mantle superplume structure: *Geophysical Research Letters*, v. 40, p. 3562-3566, doi: 10.1002/grl.50694.
- Mulibo, G. D., and Nyblade, A. A., 2013b, The P and S wave velocity structure of the mantle beneath eastern Africa and the African superplume anomaly: *Geochemistry, Geophysics, Geosystems*, v. 14, p. 2696-2715, doi: 10.1002/ggge.20150.
- Muller, O. H., and Pollard, D. D., 1977, The stress state near Spanish Peaks, Colorado determined from a dike pattern: *Pure and Applied Geophysics*, v. 115, p. 69-86.
- Nahm, A. L., and Schultz, R. A., 2011, Magnitude of global contraction on Mars from analysis of surface faults: Implications for martian thermal history: *Icarus*, v. 211, p. 389-400, doi: 10.1016/j.icarus.2010.11.003.
- Naldrett, A. J., Fedorenko, V. A., Lightfoot, P. C., Kunilov, V. I., Gorbachev, N. S., Doherty, W., and Johan, Z., 1995, Ni-Cu-PGE deposits of the Noril'sk region, Siberia - their formation in conduits for flood-basalt volcanism: *Transactions of the Institution of Mining and Metallurgy*, v. 104, p. B18-B36.
- Negrete-Aranda, R., Canon-Tapia, E., Brandle, J. L., Ortega-Rivera, M. A., Lee, J. K. W., Spelz, R. M., and Hinojosa-Corona, A., 2010, Regional orientation of tectonic stress

- and the stress expressed by post-subduction high-magnesium volcanism in northern Baja California, Mexico: Tectonics and volcanism of San Borja volcanic field: *Journal of Volcanology and Geothermal Research*, v. 192, p. 97-115, doi: 10.1016/j.jvolgeores.2010.02.014.
- Nemeth, K., and Martin, U., 2007, Shallow sill and dyke complex in western Hungary as a possible feeding system of phreatomagmatic volcanoes in "soft-rock" environment: *Journal of Volcanology and Geothermal Research*, v. 159, p. 138-152, doi: 10.1016/j.jvolgeores.2006.06.014.
- Neukirchen, F., Finkenbein, T., and Keller, J., 2010, The Lava sequence of the East African Rift escarpment in the Oldoinyo Lengai – Lake Natron sector, Tanzania: *Journal of African Earth Sciences*, v. 58, p. 734-751, doi: 10.1016/j.jafrearsci.2010.06.002.
- Nicol, A., Watterson, J., Walsh, J. J., and Childs, C., 1996, The shapes, major axis orientations and displacement patterns of fault surfaces: *Journal of Structural Geology*, v. 18, p. 235-248, doi: 10.1016/s0191-8141(96)80047-2.
- Nixon, C. W., Bull, J. M., and Sanderson, D. J., 2014, Localized vs distributed deformation associated with the linkage history of an active normal fault, Whakatane Graben, New Zealand: *Journal of Structural Geology*, v. 69, p. 266-280, doi: 10.1016/j.jsg.2014.06.005.
- Nonnotte, P., Guillou, H., Le Gall, B., Benoit, M., Cotten, J., and Scaillet, S., 2008, New K-Ar age determinations of Kilimanjaro volcano in the North Tanzanian diverging rift, East Africa: *Journal of Volcanology and Geothermal Research*, v. 173, p. 99-112, doi: 10.1016/j.jvolgeores.2007.12.042.
- Nyamai, C. M., Mathu, E. M., Opiyo-Akech, N., and Wallbrecher, E., 2003, A reappraisal of the geology, geochemistry, structures and tectonics of the Mozambique Belt in Kenya, east of the rift system: *African Journal of Science and Technology*, v. 4, p. 51-71.
- Nyblade, A. A., and Brazier, R. A., 2002, Precambrian lithospheric controls on the development of the East African rift system: *Geology*, v. 30, p. 755-758, doi: 10.1130/0091-7613(2002)030<0755:plcotd>2.0.co;2.
- Nyblade, A. A., Birt, C., Langston, C. A., Owens, T. J., and Last, R. J., 1996, Seismic experiment reveals rifting of craton in Tanzania: *Eos, Transactions, American Geophysical Union*, v. 77, p. 517-521.
- O'Reilly, B. M., Hauser, F., Jacob, A. W. B., and Shannon, P. M., 1996, The lithosphere below the Rockall Trough: Wide-angle seismic evidence for extensive serpentinisation: *Tectonophysics*, v. 255, p. 1-23, doi: 10.1016/0040-1951(95)00149-2.
- Olson, J., and Pollard, D. D., 1989, Inferring paleostress from natural fracture patterns: a new method: *Geology*, v. 17, p. 345-348.
- Olson, J., and Pollard, D. D., 1991, The initiation and growth of en echelon veins: *Journal of Structural Geology*, v. 13, p. 595-608.
- Ort, M. H., and Carrasco-Nunez, G., 2009, Lateral vent migration during phreatomagmatic and magmatic eruptions at Tecuítlapa Maar, east-central Mexico: *Journal of Volcanology and Geothermal Research*, v. 181, p. 67-77, doi: 10.1016/j.jvolgeores.2009.01.003.
- Pagli, C., Wright, T. J., Ebinger, C. J., Yun, S.-H., Cann, J. R., Barnie, T., and Ayele, A., 2012, Shallow axial magma chamber at the slow-spreading Erta Ale Ridge: *Nature Geoscience*, v. 5, p. 284-288, doi: 10.1038/ngeo1414.

- Pallister, J. S., McCausland, W. A., Jonsson, S., Lu, Z., Zahran, H. M., El Hadidy, S., Aburukbah, A., Stewart, I. C. F., Lundgren, P. R., White, R. A., and Moufti, M. R. H., 2010, Broad accommodation of rift-related extension recorded by dyke intrusion in Saudi Arabia: *Nature Geoscience*, v. 3, p. 705-712, doi: 10.1038/ngeo966.
- Paquet, F., Dauteuil, O., Hallot, E., and Moreau, F., 2007, Tectonics and magma dynamics coupling in a dyke swarm of Iceland: *Journal of Structural Geology*, v. 29, p. 1477-1493, doi: 10.1016/j.jsg.2007.06.001.
- Parks, M. M., Caliro, S., Chiodini, G., Pyle, D. M., Mather, T. A., Berlo, K., Edmonds, M., Biggs, J., Nomikou, P., and Raptakis, C., 2013, Distinguishing contributions to diffuse CO₂ emissions in volcanic areas from magmatic degassing and thermal decarbonation using soil gas Rn-222-delta C-13 systematics: Application to Santorini volcano, Greece: *Earth and Planetary Science Letters*, v. 377, p. 180-190, doi: 10.1016/j.epsl.2013.06.046.
- Parsons, T., and Thompson, G. A., 1991, The role of magma overpressure in suppressing earthquakes and topography: Worldwide examples: *Science*, v. 253, p. 1399-1402.
- Pasche, N., Schmid, M., Vazquez, F., Schubert, C. J., Wuest, A., Kessler, J. D., Pack, M. A., Reeburgh, W. S., and Burgmann, H., 2011, Methane sources and sinks in Lake Kivu: *Journal of Geophysical Research*, v. 116, p. G03006, doi: 10.1029/2011jg001690.
- Pasquarè, F., and Tibaldi, A., 2007, Structure of a sheet-laccolith system revealing the interplay between tectonic and magma stresses at Stardalur Volcano, Iceland: *Journal of Volcanology and Geothermal Research*, v. 161, p. 131-150, doi: 10.1016/j.jvolgeores.2006.11.009.
- Paulsen, T. S., and Wilson, T. J., 2010, New criteria for systematic mapping and reliability assessment of monogenetic volcanic vent alignments and elongate volcanic vents for crustal stress analyses: *Tectonophysics*, v. 482, p. 16-28, doi: 10.1016/j.tecto.2009.08.025.
- Peacock, D. C. P., 2002, Propagation, interaction and linkage in normal fault systems: *Earth-Science Reviews*, v. 58, p. 121-142, doi: 10.1016/s0012-8252(01)00085-x.
- Peacock, D. C. P., and Sanderson, D. J., 1991, Displacements, segment linkage and relay ramps in normal fault zones: *Journal of Structural Geology*, v. 13, p. 721-733, doi: 10.1016/0191-8141(91)90033-f.
- Perez, N. M., Hernandez, P. A., Padilla, G., Nolasco, D., Barrancos, J., Melian, G., Padron, E., Dionis, S., Calvo, D., Rodriguez, F., Notsu, K., Mori, T., Kusakabe, M., Arpa, M. C., Reniva, P., and Ibarra, M., 2011, Global CO₂ emission from volcanic lakes: *Geology*, v. 39, p. 235-238, doi: 10.1130/g31586.1.
- Petibon, C. M., Kjarsgaard, B. A., Jenner, G. A., and Jackson, S. E., 1998, Phase relationships of a silicate-bearing natrocarbonatite from Oldoinyo Lengai at 20 and 100 MPa: *Journal of Petrology*, v. 39, p. 2137-2151, doi: 10.1093/petrology/39.11.2137.
- Pik, R., Marty, B., and Hilton, D. R., 2006, How many mantle plumes in Africa? The geochemical point of view: *Chemical Geology*, v. 226, p. 100-114, doi: 10.1016/j.chemgeo.2005.09.016.
- Pinel, V., and Jaupart, C., 2003, Magma chamber behavior beneath a volcanic edifice: *Journal of Geophysical Research*, v. 108, p. B2072 doi: 10.1029/2002jb001751.
- Pinel, V., and Jaupart, C., 2004, Magma storage and horizontal dyke injection beneath a volcanic edifice: *Earth and Planetary Science Letters*, v. 221, p. 245-262, doi: 10.1016/s0012-821x(04)00076-7.

- Pinzuti, P., Mignan, A., and King, G. C. P., 2010, Surface morphology of active normal faults in hard rock: Implications for the mechanics of the Asal Rift, Djibouti: *Earth and Planetary Science Letters*, v. 299, p. 169-179, doi: 10.1016/j.epsl.2010.08.032.
- Pocknall, D. T., Chinn, T. J., Sykes, R. O., and Skinner, D. N. B., 1992, *Geology of the Convoy Range area, southern Victoria Land, Antarctica*: Wellington Department of Scientific and Industrial Research New Zealand Geological Survey miscellaneous series map 19, 1:50 000, 1 sheet.
- Pollard, D. D., and Johnson, A. M., 1973, Mechanics of growth of some laccolithic intrusions in Henry Mountains, Utah 2: Bending and failure of overburden layers and sill formation: *Tectonophysics*, v. 18, p. 311-354.
- Pollard, D. D., and Aydin, A., 1984, Propagation and linkage of ocean ridge segments: *Journal of Geophysical Research*, v. 89, p. 17-28, doi: 10.1029/JB089iB12p10017.
- Pollard, D. D., and Aydin, A., 1988, Progress in understanding jointing over the past century: *Geological Society of America Bulletin*, v. 100, p. 1181-1204, doi: 10.1130/0016-7606(1988)100<1181:piujot>2.3.co;2.
- Pollard, D. D., and Fletcher, R. C., 2005, *Fundamentals of structural geology*: Cambridge, University Press, 496 p.
- Pollard, D. D., Muller, O. H., and Dockstader, D. R., 1975, The form and growth of fingered sheet intrusions: *Geological Society of America Bulletin*, v. 86, p. 351-363.
- Pollard, D. D., Segall, P., and Delaney, P. T., 1982, Formation and interpretation of dilatant echelon cracks: *Geological Society of America Bulletin*, v. 93, p. 1291-1303.
- Polteau, S., Ferre, E. C., Planke, S., Neumann, E. R., and Chevallier, L., 2008, How are saucer-shaped sills emplaced? Constraints from the Golden Valley Sill, South Africa: *Journal of Geophysical Research*, v. 113, p. B12104, doi: 10.1029/2008jb005620.
- Post, A., and Tullis, J., 1998, The rate of water penetration in experimentally deformed quartzite, implications for hydrolytic weakening: *Tectonophysics*, v. 295, p. 117-137, doi: 10.1016/s0040-1951(98)00145-0.
- Potts, R., and Deino, A., 1995, Mid-Pleistocene change in large mammal faunas of East Africa: *Quaternary Research*, v. 43, p. 106-113, doi: 10.1006/qres.1995.1010.
- Potts, R., Shipman, P., and Ingall, E., 1988, Taphonomy, paleoecology, and hominids of Lainyamok, Kenya: *Journal of Human Evolution*, v. 17, p. 597-614, doi: 10.1016/0047-2484(88)90087-5.
- Priest, G. R., 1990, Volcanic and tectonic evolution of the Cascade volcanic arc, central Oregon: *Journal of Geophysical Research*, v. 95, p. 19583-19599, doi: 10.1029/JB095iB12p19583.
- Pyne, A. R., 1984, *Geology of the Mt Fleming area, South Victoria Land, Antarctica*: New Zealand Journal of Geology and Geophysics, v. 27, p. 505-512.
- Ray, R., Sheth, H. C., and Mallik, J., 2007, Structure and emplacement of the Nandurbar-Dhule mafic dyke swarm, Deccan Traps, and the tectonomagmatic evolution of flood basalts: *Bulletin of Volcanology*, v. 69, p. 537-551, doi: 10.1007/s00445-006-0089-y.
- Re, G., White, J. D. L., and Ort, M. H., 2015, Dikes, sills, and stress-regime evolution during emplacement of the Jagged Rocks Complex, Hopi Buttes Volcanic Field, Navajo Nation, USA: *Journal of Volcanology and Geothermal Research*, v. 295, p. 65-79, doi: 10.1016/j.jvolgeores.2015.01.009.

- Reches, Z., and Fink, J., 1988, The mechanisms of intrusion of the Inyo Dike, Long Valley Caldera, California: *Journal of Geophysical Research*, v. 93, p. 4321-4334, doi: 10.1029/JB093iB05p04321.
- Renne, P. R., and Basu, A. R., 1991, Rapid eruption of the Siberian Traps flood basalts at the Permo-Triassic boundary: *Science*, v. 253, p. 176-179, doi: 10.1126/science.253.5016.176.
- Reubi, O., Ross, P. S., and White, J. D. L., 2005, Debris avalanche deposits associated with large igneous province volcanism: An example from the Mawson Formation, central Allan Hills, Antarctica: *Geological Society of America Bulletin*, v. 117, p. 1615-1628, doi: 10.1130/b25766.1.
- Reyners, M., Eberhart-Phillips, D., and Stuart, G., 2007, The role of fluids in lower-crustal earthquakes near continental rifts: *Nature*, v. 446, p. 1075-1078, doi: 10.1038/nature05743.
- Richardson, J. A., Connor, C. B., Wetmore, P. H., Connor, L. J., and Gallant, E. A., 2015, Role of sills in the development of volcanic fields: Insights from lidar mapping surveys of the San Rafael Swell, Utah: *Geology*, v. 43, p. 1023-1026, doi: 10.1130/G37094.1.
- Ring, U., 1994, The influence of preexisting structure on the evolution of the Cenozoic Malawi Rift (East African Rift System): *Tectonics*, v. 13, p. 313-326, doi: 10.1029/93tc03188.
- Ring, U., Betzler, C., and Delvaux, D., 1992, Normal vs strike-slip faulting during development in East Africa: the Malawi Rift: *Geology*, v. 20, p. 1015-1018.
- Ring, U., Schwartz, H. L., Bromage, T. G., and Sanaane, C., 2005, Kinematic and sedimentological evolution of the Manyara Rift in northern Tanzania, East Africa: *Geological Magazine*, v. 142, p. 355-368, doi: 10.1017/s0016756805000841.
- Ritsema, J., Nyblade, A. A., Owens, T. J., Langston, C. A., and VanDecar, J. C., 1998, Upper mantle seismic velocity structure beneath Tanzania, east Africa: Implications for the stability of cratonic lithosphere: *Journal of Geophysical Research*, v. 103, p. 21201-21213, doi: 10.1029/98jb01274.
- Rivalta, E., Taisne, B., Bungler, A. P., and Katz, R. F., 2015, A review of mechanical models of dike propagation: Schools of thought, results and future directions: *Tectonophysics*, v. 638, p. 1-42, doi: 10.1016/j.tecto.2014.10.003.
- Roberts, M. A., 2002, The geochemical and volcanological evolution of the Mt. Meru region, northern Tanzania [Ph.D. thesis]: University of Cambridge, 264 p.
- Roberts, N., Taieb, M., Barker, P., Damnati, B., Icole, M., and Williamson, D., 1993, Timing of the Younger Dryas event in East Africa from lake level changes: *Nature*, v. 366, p. 146-148, doi: 10.1038/366146a0.
- Robertson, E. A. M., Biggs, J., Cashman, K. V., Floyd, M. A., and Vye-Brown, C., 2015, Influence of regional tectonics and pre-existing structures on the formation of elliptical calderas in the Kenyan Rift: *Geological Society of London Special Publications*, v. 420, doi: 10.1144/sp420.12.
- Rodriguez, E., Morris, C. S., Belz, J. E., Chapin, E. C., Martin, J. M., Daffer, W., and Hensley, S., 2005, An assessment of the SRTM topographic products: Jet Propulsion Laboratory Technical Report D-31639, 125 p.
- Roecker, S. W., Ebinger, C. J., Tiberi, C., Mulibo, G. D., Ferdinand, R. W., Muzuka, A., Khalfan, M., Kianji, G., Gautier, S., Albaric, J., and Peyrat, S., 2015, Images of the

- East Africa Rift System from the joint inversion of body waves, surface waves, and gravity: investigating the role of magma in early-stage continental rifting, Abstract T51G-3013 presented at 2013 Fall Meeting, AGU, San Francisco, California, 14–18 December.
- Rogers, N. W., James, D., Kelley, S. P., and De Mulder, M., 1998, The generation of potassic lavas from the eastern Virunga province, Rwanda: *Journal of Petrology*, v. 39, p. 1223-1247, doi.
- Rohrman, M., 2013a, Intrusive large igneous provinces below sedimentary basins: An example from the Exmouth Plateau (NW Australia): *Journal of Geophysical Research*, v. 118, p. 4477-4487, doi: 10.1002/jgrb.50298.
- Roman, A., and Jaupart, C., 2014, The impact of a volcanic edifice on intrusive and eruptive activity: *Earth and Planetary Science Letters*, v. 408, p. 1-8, doi: 10.1016/j.epsl.2014.09.016.
- Rooney, T. O., 2010, Geochemical evidence of lithospheric thinning in the southern Main Ethiopian Rift: *Lithos*, v. 117, p. 33-48, doi: 10.1016/j.lithos.2010.02.002.
- Rooney, T., Furman, T., Bastow, I., Ayalew, D., and Yirgu, G., 2007, Lithospheric modification during crustal extension in the Main Ethiopian Rift: *Journal of Geophysical Research*, v. 112, p. B10201, doi: 10.1029/2006jb004916.
- Rooney, T. O., Bastow, I. D., and Keir, D., 2011, Insights into extensional processes during magma assisted rifting: Evidence from aligned scoria cones: *Journal of Volcanology and Geothermal Research*, v. 201, p. 83-96, doi: 10.1016/j.jvolgeores.2010.07.019.
- Rooney, T. O., Herzberg, C., and Bastow, I. D., 2012, Elevated mantle temperature beneath East Africa: *Geology*, v. 40, p. 27-30, doi: 10.1130/g32382.1.
- Rooney, T. O., Bastow, I. D., Keir, D., Mazzarini, F., Movsesian, E., Grosfils, E. B., Zimelman, J. R., Ramsey, M. S., Ayalew, D., and Yirgu, G., 2014, The protracted development of focused magmatic intrusion during continental rifting: *Tectonics*, v. 33, doi: 10.1002/2013TC003514.
- Rosendahl, B. R., 1987, Architecture of continental rifts with special reference to East Africa: *Annual Review of Earth and Planetary Sciences*, v. 15, p. 445-503, doi: 10.1146/annurev.ea.15.050187.002305.
- Ross, P. S., and White, J. D. L., 2005, Mafic, large-volume, pyroclastic density current deposits from phreatomagmatic eruptions in the Ferrar large igneous province, Antarctica: *Journal of Geology*, v. 113, p. 627-649, doi.
- Ross, P. S., and White, J. D. L., 2006, Debris jets in continental phreatomagmatic volcanoes: A field study of their subterranean deposits in the Coombs Hills vent complex, Antarctica: *Journal of Volcanology and Geothermal Research*, v. 149, p. 62-84, doi: 10.1016/j.jvolgeores.2005.06.007.
- Ross, P. S., and White, J. D. L., 2012, Quantification of vesicle characteristics in some diatreme-filling deposits, and the explosivity levels of magma-water interactions within diatremes: *Journal of Volcanology and Geothermal Research*, v. 245, p. 55-67, doi: 10.1016/j.jvolgeores.2012.07.006.
- Ross, P. S., Peate, I. U., McClintock, M. K., Xu, Y. G., Skilling, I. P., White, J. D. L., and Houghton, B. F., 2005, Mafic volcanoclastic deposits in flood basalt provinces: A review: *Journal of Volcanology and Geothermal Research*, v. 145, p. 281-314, doi: 10.1016/j.jvolgeores.2005.02.003.

- Ross, P. S., White, J. D. L., and McClintock, M., 2008, Geological evolution of the Coombs-Allan Hills area, Ferrar large igneous province, Antarctica: Debris avalanches, mafic pyroclastic density currents, phreatocauldrons: *Journal of Volcanology and Geothermal Research*, v. 172, p. 38-60, doi: 10.1016/j.jvolgeores.2005.11.011.
- Rotella, M. D., Wilson, C. J. N., Barker, S. J., Cashman, K. V., Houghton, B. F., and Wright, I. C., 2014, Bubble development in explosive silicic eruptions: insights from pyroclast vesicularity textures from Raoul volcano (Kermadec arc): *Bulletin of Volcanology*, v. 76, doi: 10.1007/s00445-014-0826-6.
- Rowland, J. V., and Sibson, R. H., 2001, Extensional fault kinematics within the Taupo Volcanic Zone, New Zealand: soft-linked segmentation of a continental rift system: *New Zealand Journal of Geology and Geophysics*, v. 44, p. 271-283, doi.
- Rowland, J. V., and Sibson, R. H., 2004, Structural controls on hydrothermal flow in a segmented rift system, Taupo Volcanic Zone, New Zealand: *Geofluids*, v. 4, p. 259-283, doi: 10.1111/j.1468-8123.2004.00091.x.
- Rowland, J. V., and Simmons, S. F., 2012, Hydrologic, Magmatic, and Tectonic Controls on Hydrothermal Flow, Taupo Volcanic Zone, New Zealand: Implications for the Formation of Epithermal Vein Deposits: *Economic Geology*, v. 107, p. 427-457.
- Rowland, J. V., Baker, E., Ebinger, C. J., Keir, D., Kidane, T., Biggs, J., Hayward, N., and Wright, T. J., 2007, Fault growth at a nascent slow-spreading ridge: 2005 Dabbahu rifting episode, Afar: *Geophysical Journal International*, v. 171, p. 1226-1246, doi: 10.1111/j.1365-246X.2007.03584.x.
- Rowland, J. V., Wilson, C. J. N., and Gravley, D. M., 2010, Spatial and temporal variations in magma-assisted rifting, Taupo Volcanic Zone, New Zealand: *Journal of Volcanology and Geothermal Research*, v. 190, p. 89-108, doi: 10.1016/j.jvolgeores.2009.05.004.
- Rubin, A. M., 1995, Propagation of magma-filled cracks: *Annual Review of Earth and Planetary Sciences*, v. 23, p. 287-336.
- Rubin, A. M., and Pollard, D. D., 1988, Dike-induced faulting in rift zones of Iceland and Afar: *Geology*, v. 16, p. 413-417.
- Ryan, M. P., 1988, The mechanics and 3-dimensional internal structure of active magmatic systems: Kilauea volcano, Hawaii: *Journal of Geophysical Research*, v. 93, p. 4213-4248, doi: 10.1029/JB093iB05p04213.
- Saffer, D. M., and Tobin, H. J., 2011, Hydrogeology and Mechanics of Subduction Zone Forearcs: Fluid Flow and Pore Pressure: *Annual Review of Earth and Planetary Sciences*, Vol 39, v. 39, p. 157-186, doi: 10.1146/annurev-earth-040610-133408.
- Saggerson, E. P., 1991, *Geology of the Nairobi Area: Geological Survey of Kenya Report 98*, 60 p.
- San'kov, V., Deverchere, J., Gaudemer, Y., Houdry, F., and Filippov, A., 2000, Geometry and rate of faulting in the North Baikal Rift, Siberia: *Tectonics*, v. 19, p. 707-722.
- San'kov, V. A., Likhnev, A. V., Miroshnichenko, A. I., Ashurkov, S. V., Byzov, L. M., Dembelov, M. G., Calais, E., and Deverchere, J., 2009, Extension in the Baikal rift: Present-day kinematics of passive rifting: *Doklady Earth Sciences*, v. 425, p. 205-209, doi: 10.1134/s1028334x09020056.
- Sano, Y., and Marty, B., 1995, Origin of carbon in fumarolic gas from island arcs: *Chemical Geology*, v. 119, p. 265-274.

- Saria, E., Calais, E., Stamps, D. S., Delvaux, D., and Hartnady, C. J. H., 2014, Present-day kinematics of the East African Rift: *Journal of Geophysical Research*, v. 119, p. 3584-3600, doi: 10.1002/2013jb010901.
- Sawyer, G. M., Carn, S. A., Tsanev, V. I., Oppenheimer, C., and Burton, M., 2008, Investigation into magma degassing at Nyiragongo volcano, Democratic Republic of the Congo: *Geochemistry, Geophysics, Geosystems*, v. 9, p. Q02017, doi: 10.1029/2007gc001829.
- Schirnick, C., van den Bogaard, P., and Schmincke, H. U., 1999, Cone sheet formation and intrusive growth of an oceanic island - The Miocene Tejada complex on Gran Canaria (Canary Islands): *Geology*, v. 27, p. 207-210.
- Schlische, R. W., 1993, Anatomy and evolution of the Triassic-Jurassic continental rift system, eastern North America: *Tectonics*, v. 12, p. 1026-1042, doi: 10.1029/93tc01062.
- Schlische, R. W., Young, S. S., Ackermann, R. V., and Gupta, A., 1996, Geometry and scaling relations of a population of very small rift-related normal faults: *Geology*, v. 24, p. 683-686.
- Schofield, N., Stevenson, C., and Reston, T., 2010, Magma fingers and host rock fluidization in the emplacement of sills: *Geology*, v. 38, p. 63-66, doi: 10.1130/g30142.1.
- Schofield, N., Heaton, L., Holford, S. P., Archer, S. G., Jackson, C. A. L., and Jolley, D. W., 2012a, Seismic imaging of 'broken bridges': linking seismic to outcrop-scale investigations of intrusive magma lobes: *Journal of the Geological Society of London*, v. 169, p. 421-426, doi: 10.1144/0016-76492011-150.
- Schofield, N. J., Brown, D. J., Magee, C., and Stevenson, C. T., 2012b, Sill morphology and comparison of brittle and non-brittle emplacement mechanisms: *Journal of the Geological Society of London*, v. 169, p. 127-141, doi: 10.1144/0016-76492011-078.
- Scholz, C. H., and Cowie, P. A., 1990, Determination of total strain from faulting using slip measurements: *Nature*, v. 346, p. 837-839, doi: 10.1038/346837a0.
- Scholz, C. A., Rosendahl, B. R., and Scott, D. L., 1990, Development of coarse-grained facies in lacustrine rift basins: examples from East Africa: *Geology*, v. 18, p. 140-144.
- Schultz, R. A., Okubo, C. H., and Wilkins, S. J., 2006, Displacement-length scaling relations for faults on the terrestrial planets: *Journal of Structural Geology*, v. 28, p. 2182-2193, doi: 10.1016/j.jsg.2006.03.034.
- Schultz, R. A., Soliva, R., Okubu, C. H., and Mege, D., 2010, Fault populations, *in* Watters, R., and Schultz, R. A., eds., *Planetary Tectonics*: New York, Cambridge University Press, p. 457-510.
- Segall, P., 2013, Volcano deformation and eruption forecasting: *Remote Sensing of Volcanoes and Volcanic Processes: Integrating Observation and Modelling*, v. 380, p. 85-106, doi: 10.1144/sp380.4.
- Self, S., Thordarson, T., and Keszthelyi, L., 1997, Emplacement of continental flood basalt lava flows, *in* Mahoney, J. J., and Coffin, M. F., eds., *Large igneous provinces: continental, oceanic, and planetary flood volcanism*, American Geophysical Union Geophysical Monograph 100, p. 381-410.
- Self, S., Gertisser, R., Thordarson, T., Rampino, M. R., and Wolff, J. A., 2004, Magma volume, volatile emissions, and stratospheric aerosols from the 1815 eruption of Tambora: *Geophysical Research Letters*, v. 31, p. L20608, doi: 10.1029/2004gl020925.

- Self, S., Widdowson, M., Thordarson, T., and Jay, A. E., 2006, Volatile fluxes during flood basalt eruptions and potential effects on the global environment: A Deccan perspective: *Earth and Planetary Science Letters*, v. 248, p. 518-532, doi: 10.1016/j.epsl.2006.05.041.
- Self, S., Jay, A. E., Widdowson, M., and Keszthelyi, L. P., 2008, Correlation of the Deccan and Rajahmundry Trap lavas: Are these the longest and largest lava flows on Earth?: *Journal of Volcanology and Geothermal Research*, v. 172, p. 3-19, doi: 10.1016/j.jvolgeores.2006.11.012.
- Sengor, A. M. C., and Burke, K., 1978, Relative timing of rifting and volcanism on Earth and its tectonic implications: *Geophysical Research Letters*, v. 5, p. 419-421.
- Seno, T., and Saito, A., 1994, Recent East-African earthquakes in the lower crust: *Earth and Planetary Science Letters*, v. 121, p. 125-136, doi: 10.1016/0012-821x(94)90036-1.
- Seward, T. M., and Kerrick, D. M., 1996, Hydrothermal CO₂ emission from the Taupo Volcanic Zone, New Zealand: *Earth and Planetary Science Letters*, v. 139, p. 105-113, doi: 10.1016/0012-821x(96)00011-8.
- Shelly, D. R., Taira, T., Prejean, S. G., Hill, D. P., and Dreger, D. S., 2015, Fluid-faulting interactions: Fracture-mesh and fault-valve behavior in the February 2014 Mammoth Mountain, California earthquake swarm: *Geophysical Research Letters*, v. 42, p. 5803-5812, doi: 10.1002/2015gl064325.
- Sherrod, D. R., Magigita, M. M., and Kwelwa, S., 2013, Geologic map of Oldonyo Lengai (Oldoinyo Lengai) and surroundings, Arusha Region, United Republic of Tanzania: US Geological Survey Open-File Report 2013-1306, scale 1:50,000, 1 sheet, 50 p.
- Sheth, H. C., and Canon-Tapia, E., 2015, Are flood basalt eruptions monogenetic or polygenetic?: *International Journal of Earth Sciences*, v. 104, p. 2147-2162, doi: 10.1007/s00531-014-1048-z.
- Sibson, R. H., 1985, A note on fault reactivation: *Journal of Structural Geology*, v. 7, p. 751-754, doi: 10.1016/0191-8141(85)90150-6.
- Sibson, R. H., 2000, Fluid involvement in normal faulting: *Journal of Geodynamics*, v. 29, p. 469-499.
- Sigmundsson, F., Einarsson, P., Bilham, R., and Sturkell, E., 1995, Rift-transform kinematics in south Iceland: deformation from global positioning system measurements, 1986 to 1992: *Journal of Geophysical Research*, v. 100, p. 6235-6248, doi: 10.1029/95jb00155.
- Sigmundsson, F., Hreinsdottir, S., Hooper, A., Arnadottir, T., Pedersen, R., Roberts, M. J., Oskarsson, N., Auriac, A., Decriem, J., Einarsson, P., Geirsson, H., Hensch, M., Ofeigsson, B. G., Sturkell, E., Sveinbjornsson, H., and Feigl, K. L., 2010, Intrusion triggering of the 2010 Eyjafjallajokull explosive eruption: *Nature*, v. 468, doi: 10.1038/nature09558.
- Sigmundsson, F., Hooper, A., Hreinsdottir, S., Vogfjord, K. S., Ofeigsson, B. G., Heimisson, E. R., Dumont, S., Parks, M., Spaans, K., Gudmundsson, G. B., Drouin, V., Arnadottir, T., Jonsdottir, K., Gudmundsson, M. T., Hognadottir, T., Fridriksdottir, H. M., Hensch, M., Einarsson, P., Magnusson, E., Samsonov, S., Brandsdottir, B., White, R. S., Agustsdottir, T., Greenfield, T., Green, R. G., Hjartardottir, A. R., Pedersen, R., Bennett, R. A., Geirsson, H., La Femina, P. C., Bjornsson, H., Palsson, F., Sturkell, E., Bean, C. J., Mollhoff, M., Braiden, A. K., and Eibl, E. P. S., 2015, Segmented lateral

- dyke growth in a rifting event at Bardarbunga volcanic system, Iceland: *Nature*, v. 517, doi: 10.1038/nature14111.
- Simiyu, S. M., and Keller, G. R., 2001, An integrated geophysical analysis of the upper crust of the southern Kenya rift: *Geophysical Journal International*, v. 147, p. 543-561, doi: 10.1046/j.0956-540x.2001.01542.x.
- Skilling, I. P., White, J. D. L., and McPhie, J., 2002, Peperite: a review of magma-sediment mingling: *Journal of Volcanology and Geothermal Research*, v. 114, p. 1-17, doi: 10.1016/s0377-0273(01)00278-5.
- Smets, B., Wauthier, C., and d'Oreye, N., 2010, A new map of the lava flow field of Nyamulagira (D.R. Congo) from satellite imagery: *Journal of African Earth Sciences*, v. 58, p. 778-786, doi: 10.1016/j.jafrearsci.2010.07.005.
- Smets, B., d'Oreye, N., Kervyn, F., Kervyn, M., Albino, F., Arellano, S. R., Bagalwa, M., Balagizi, C., Carn, S. A., Darrah, T. H., Fernandez, J., Galle, B., Gonzalez, P. J., Head, E., Karume, K., Kavotha, D., Lukaya, F., Mashagiro, N., Mavonga, G., Norman, P., Osodundu, E., Pallero, J. L. G., Prieto, J. F., Samsonov, S., Syauswa, M., Tedesco, D., Tiampo, K., Wauthier, C., and Yalire, M. M., 2014, Detailed multidisciplinary monitoring reveals pre- and co-eruptive signals at Nyamulagira volcano (North Kivu, Democratic Republic of Congo): *Bulletin of Volcanology*, v. 76, doi: 10.1007/s00445-013-0787-1.
- Smith, M., 1994, Stratigraphic and structural constraints on mechanisms of active rifting in the Gregory Rift, Kenya: *Tectonophysics*, v. 236, p. 3-22, doi: 10.1016/0040-1951(94)90166-x.
- Smith, M., and Mosley, P., 1993, Crustal heterogeneity and basement influence on the development of the Kenya Rift, East Africa: *Tectonics*, v. 12, p. 591-606, doi: 10.1029/92tc01710.
- Sneddon, I. N., and Lowengrub, M., 1969, *Crack problems in the classical theory of elasticity*: New York, John Wiley, 221 p.
- Soliva, R., and Schultz, R. A., 2008, Distributed and localized faulting in extensional settings: Insight from the North Ethiopian Rift-Afar transition area: *Tectonics*, v. 27, doi: 10.1029/2007tc002148.
- Sparks, R. S. J., 1978, The dynamics of bubble formation and growth in magmas: a review and analysis: *Journal of Volcanology and Geothermal Research*, v. 3, p. 1-37.
- Sparks, R. S. J., 2003, Forecasting volcanic eruptions: *Earth and Planetary Science Letters*, v. 210, p. 1-15, doi: 10.1016/s0012-821x(03)00124-9.
- Sparks, R. S. J., Biggs, J., and Neuberg, J. W., 2012, *Monitoring Volcanoes*: *Science*, v. 335, p. 1310-1311, doi: 10.1126/science.1219485.
- Spiegel, C., Kohn, B. P., Belton, D. X., and Gleadow, A. J. W., 2007, Morphotectonic evolution of the central Kenya rift flanks: Implications for late Cenozoic environmental change in East Africa: *Geology*, v. 35, p. 427, doi: 10.1130/g23108a.1.
- Stammler, K., 1993, SeismicHandler - programmable multichannel data handler and automatic processing of seismological analysis: *Computational Geosciences*, v. 19, p. 135-140.
- Stamps, D. S., Calais, E., Saria, E., Hartnady, C., Nocquet, J. M., Ebinger, C. J., and Fernandes, R. M., 2008, A kinematic model for the east African rift: *Geophysical Research Letters*, v. 35, p. L05304, doi: 10.1029/2007gl032781.

- Stamps, D. S., Flesch, L. M., Calais, E., and Ghosh, A., 2014, Current kinematics and dynamics of Africa and the East African Rift System: *Journal of Geophysical Research*, v. 119, p. 5161-5186, doi: 10.1002/2013jb010717.
- Stamps, D. S., Iaffaldano, G., and Calais, E., 2015, Role of mantle flow in Nubia-Somalia plate divergence: *Geophysical Research Letters*, v. 42, p. 290-296, doi: 10.1002/2014gl062515.
- Steiger, R. H., and Jager, E., 1977, Subcommittee on geochronology: convention on the use of decay constants in geochronology and cosmochronology: *Earth and Planetary Science Letters*, v. 36, p. 359-362, doi: 10.1016/0012-821x(77)90060-7.
- Stein, R. S., and Barrientos, S. E., 1985, Planar high-angle faulting in the Basin and Range: geodetic analysis of the 1983 Borah Peak, Idaho, earthquake: *Journal of Geophysical Research*, v. 90, p. 1355-1366, doi: 10.1029/JB090iB13p11355.
- Stein, R. S., King, G. C. P., and Rundle, J. B., 1988, The growth of geological structures by repeated earthquakes 2. Field examples of continental dip-slip faults: *Journal of Geophysical Research*, v. 93, p. 13319-13331, doi: 10.1029/JB093iB11p13319.
- Stein, R. S., Briole, P., Ruegg, J. C., Tapponnier, P., and Gasse, F., 1991, Contemporary, Holocene, and Quaternary deformation of the Asal Rift, Djibouti: implications for the mechanics of slow spreading ridges: *Journal of Geophysical Research*, v. 96, p. 21789-21806, doi: 10.1029/91jb02118.
- Stipp, M., Tullis, J., and Behrens, H., 2006, Effect of water on the dislocation creep microstructure and flow stress of quartz and implications for the recrystallized grain size piezometer: *Journal of Geophysical Research*, v. 111, p. B04201, doi: 10.1029/2005jb003852.
- Stollhofen, H., and Stanistreet, I. G., 2012, Plio-Pleistocene synsedimentary fault compartments, foundation for the eastern Olduvai Basin paleoenvironmental mosaic, Tanzania: *Journal of Human Evolution*, v. 63, p. 309-327, doi: 10.1016/j.jhevol.2011.10.002.
- Strecker, M., and Bosworth, W., 1991, Quaternary stress-field change in the Gregory rift, Kenya: *Eos Transactions, American Geophysical Union*, v. 72, p. 21-22.
- Tarasewicz, J., Brandsdottir, B., White, R. S., Hensch, M., and Thorbjarnardottir, B., 2012, Using microearthquakes to track repeated magma intrusions beneath the Eyjafjallajökull stratovolcano, Iceland: *Journal of Geophysical Research*, v. 117, p. B00C06, doi: 10.1029/2011jb008751.
- Tentler, T., 2003, Analogue modeling of overlapping spreading centers: insights into their propagation and coalescence: *Tectonophysics*, v. 376, p. 99-115, doi: 10.1016/j.tecto.2003.08.011.
- Tepp, G., Ebinger, C. J., and Yun, S.-H., 2016, Spectral analysis of dike-induced earthquakes in Afar, Ethiopia: *Journal of Geophysical Research*, v. 121, doi: 10.1002/2015jb012658.
- Thomas, A. L., and Pollard, D. D., 1993, The geometry of echelon fractures in rock - implications from laboratory and numerical experiments: *Journal of Structural Geology*, v. 15, p. 323-334, doi: 10.1016/0191-8141(93)90129-x.
- Thomson, K., 2007, Determining magma flow in sills, dykes and laccoliths and their implications for sill emplacement: *Bulletin of Volcanology*, v. 70, p. 183-201.

- Thomson, K., and Hutton, D., 2004, Geometry and growth of sill complexes: insights using 3D seismic from the North Rockall Trough: *Bulletin of Volcanology*, v. 66, p. 364-375, doi.
- Thomson, K., and Schofield, N., 2008, Lithological and structural controls on the emplacement and morphology of sills in sedimentary basins, *in* Thomson, K., and Petford, N., eds., *Structure and Emplacement of High-Level Magmatic Systems.*, Geological Society of London Special Publications, v. 302, p. 31-44.
- Thordarson, T., and Self, S., 1996, Sulfur, chlorine and fluorine degassing and atmospheric loading by the Roza eruption, Columbia River Basalt Group, Washington, USA: *Journal of Volcanology and Geothermal Research*, v. 74, p. 49-73, doi: 10.1016/s0377-0273(96)00054-6.
- Thordarson, T., and Self, S., 1998, The Roza Member, Columbia River Basalt Group: A gigantic pahoehoe lava flow field formed by endogenous processes?: *Journal of Geophysical Research*, v. 103, p. 27411-27445, doi: 10.1029/98jb01355.
- Thordarson, T., Self, S., Oskarsson, N., and Hulsebosch, T., 1996, Sulfur, chlorine, and fluorine degassing and atmospheric loading by the 1783-1784 AD Laki (Skaftar fires) eruption in Iceland: *Bulletin of Volcanology*, v. 58, p. 205-225, doi: 10.1007/s004450050136.
- Tibaldi, A., 1995, Morphology of pyroclastic cones and tectonics: *Journal of Geophysical Research*, v. 100, p. 24521-24535, doi: 10.1029/95jb02250.
- Tibaldi, A., 2015, Structure of volcano plumbing systems: A review of multi-parametric effects: *Journal of Volcanology and Geothermal Research*, v. 298, p. 85-135, doi: 10.1016/j.jvolgeores.2015.03.023.
- Tibaldi, A., Bonali, F. L., and Corazzato, C., 2014, The diverging volcanic rift system: *Tectonophysics*, v. 611, p. 94-113, doi: 10.1016/j.tecto.2013.11.023.
- Tullis, J., and Yund, R. A., 1989, Hydrolytic weakening of quartz aggregates: the effects of water and pressure on recovery: *Geophysical Research Letters*, v. 16, p. 1343-1346, doi: 10.1029/GL016i011p01343.
- Turcotte, D., and Schubert, G., 1982, *Geodynamics: Applications of continuum physics to geological problems*: New York, John Wiley & Sons, 450 p.
- Turnbull, I. M., Allibone, A., H., Forsyth, P. J., and Heron, D. W., 1994, *Geology of the Bull Pass-St Johns Range area, southern Victoria Land, Antarctica*: Institute of Geological & Nuclear Sciences geological map 14, 1:50 000, 1 sheet.
- Valentine, G. A., and Krogh, K. E. C., 2006, Emplacement of shallow dikes and sills beneath a small basaltic volcanic center - The role of pre-existing structure (Paiute Ridge, southern Nevada, USA): *Earth and Planetary Science Letters*, v. 246, p. 217-230, doi: 10.1106/j.epsl.2006.04.031.
- Valentine, G. A., and Cortes, J. A., 2013, Time and space variations in magmatic and phreatomagmatic eruptive processes at Easy Chair (Lunar Crater Volcanic Field, Nevada, USA): *Bulletin of Volcanology*, v. 75, doi: 10.1007/s00445-013-0752-z.
- Valkiers, S., Vendelbo, D., Berglund, M., and de Podesta, M., 2010, Preparation of argon Primary Measurement Standards for the calibration of ion current ratios measured in argon: *International Journal of Mass Spectrometry*, v. 291, p. 41-47, doi: 10.1016/j.ijms.2010.01.004.

- Vanderkluyzen, L., Mahoney, J. J., Hooper, P. R., Sheth, H. C., and Ray, R., 2011, The Feeder System of the Deccan Traps (India): Insights from Dike Geochemistry: *Journal of Petrology*, v. 52, p. 315-343, doi: 10.1093/petrology/egq082.
- Vauchez, A., Dineur, F., and Rudnick, R., 2005, Microstructure, texture and seismic anisotropy of the lithospheric mantle above a mantle plume: Insights from the Labait volcano xenoliths (Tanzania): *Earth and Planetary Science Letters*, v. 232, p. 295-314, doi: 10.1016/j.epsl.2005.01.024.
- Vening Meinesz, F., 1950, Les grabens africains, resultat de compression ou de tension dans la croûte terrestre?: *Insitut Royal Colonial Belge, Bulletin des Seances*, v. 21, p. 539-552.
- Versfelt, J., and Rosendahl, B. R., 1989, Relationships between pre-rift structure and rift architecture in Lakes Tanganyika and Malawi, East Africa: *Nature*, v. 337, p. 354-357, doi: 10.1038/337354a0.
- Vetel, W., Le Gall, B., and Walsh, J. J., 2005, Geometry and growth of an inner rift fault pattern: The Kino Sogo Fault Belt, Turkana Rift (North Kenya): *Journal of Structural Geology*, v. 27, p. 2204-2222, doi: 10.1016/j.jsg.2005.07.003.
- Villamor, P., and Berryman, K.R., 2001, A late Quaternary extension rate in the Taupo Volcanic Zone, New Zealand, derived from fault slip data: *New Zealand Journal of Geology and Geophysics*, v. 44, p. 243-269, doi: 10.1080/00288306.2001.9514937.
- Villamor, P., and Berryman, K. R., 2006, Evolution of the southern termination of the Taupo Rift, New Zealand: *New Zealand Journal of Geology and Geophysics*, v. 49, p. 23-37, doi: 10.1080/00288306.2006.9515145.
- Wadge, G., and Burt, L., 2011, Stress field control of eruption dynamics at a rift volcano: Nyamuragira, DR Congo: *Journal of Volcanology and Geothermal Research*, v. 207, p. 1-15, doi: 10.1016/j.jvolgeores.2011.06.012.
- Walker, R. J., 2016, Controls on transgressive sill growth: *Geology*, v. 44, p. 99-102, doi: 10.1130/g37144.1.
- Walsh, J. J., and Watterson, J., 1988, Analysis of the relationship between displacements and dimensions of faults: *Journal of Structural Geology*, v. 10, p. 239-247, doi: 10.1016/0191-8141(88)90057-0.
- Walsh, J. J., and Watterson, J., 1991, Geometric and kinematic coherence and scale effects in normal fault systems: *Geological Society of London Special Publications*, v. 56, p. 193-203.
- Walsh, J. J., Bailey, W. R., Childs, C., Nicol, A., and Bonson, C. G., 2003, Formation of segmented normal faults: a 3-D perspective: *Journal of Structural Geology*, v. 25, p. 1251-1262, doi: 10.1016/s0191-8141(02)00161-x.
- Watkinson, A. J., and Ward, E. M. G., 2006, Reactivation of pressure-solution seams by a strike-slip fault-sequential, dilational jog formation and fluid flow: *AAPG Bulletin*, v. 90, p. 1187-1200, doi: 10.1306/03060604088.
- Wauthier, C., 2011, InSAR applied to the study of active volcanic and seismic areas in Africa [Ph.D, thesis]: Belgium, University of Liege, 209 p.
- Wauthier, C., Cayol, V., Kervyn, F., and d'Oreye, N., 2012, Magma sources involved in the 2002 Nyiragongo eruption, as inferred from an InSAR analysis: *Journal of Geophysical Research*, v. 117, p. B05411, doi: 10.1029/2011jb008257.
- Wauthier, C., Cayol, V., Poland, M., Kervyn, F., D'Oreye, N., Hooper, A., Samsonov, S., Tiampo, K., and Smets, B., 2013, Nyamulagira's magma plumbing system inferred

- from 15 years of InSAR: Remote Sensing of Volcanoes and Volcanic Processes: Geological Society of London Special Publications, v. 380, p. 39-65, doi: 10.1144/sp380.9.
- Wauthier, C., Smets, B., and Keir, D., 2015, Diking-induced moderate-magnitude earthquakes on a youthful rift border fault: The 2002 Nyiragongo-Kalehe sequence, DR Congo: *Geochemistry, Geophysics, Geosystems*, v. 16, p. 4280-4291, doi: 10.1002/2015gc006110.
- Weinstein, A., Oliva, S. J., Ebinger, C., Roecker, S., and Tiberi, C., 2015, Seismicity patterns around Oldoinyo Lengai and Gelai volcanoes, Africa: Abstract T51G-3012 presented at 2015 Fall Meeting, San Francisco, California, 14-18 December.
- Werner, C., and Cardellini, C., 2006, Comparison of carbon dioxide emissions with fluid upflow, chemistry, and geologic structures at the Rotorua geothermal system, New Zealand: *Geothermics*, v. 35, p. 221-238, doi: 10.1016/j.geothermics.2006.02.006.
- Whaler, K. A., and Hautot, S., 2006, The electrical resistivity structure of the crust beneath the northern Main Ethiopian Rift: Geological Society of London Special Publications, v. 259, p. 293-305, doi: 10.1144/gsl.sp.2006.259.01.22.
- Wheeler, W. H., and Karson, J. A., 1994, Extension and subsidence adjacent to a weak continental transform: an example from the Rukwa Rift, East Africa: *Geology*, v. 22, p. 625-628.
- White, J. D. L., 1990, Depositional architecture of a maar-pitted playa - sedimentation in the Hopi Buttes volcanic field, northeastern Arizona, USA: *Sedimentary Geology*, v. 67, p. 55-84, doi: 10.1016/0037-0738(90)90027-q.
- White, J. D. L., 1991, Maar-diatreme phreatomagmatism at Hopi Buttes, Navajo Nation (Arizona), USA: *Bulletin of Volcanology*, v. 53, p. 239-258, doi: 10.1007/bf00414522.
- White, J. D. L., 1992, Pliocene subaqueous fans and gilbert-type deltas in maar crater lakes, Hopi Buttes, Navajo Nation (Arizona), USA: *Sedimentology*, v. 39, p. 931-946, doi: 10.1111/j.1365-3091.1992.tb02160.x.
- White, J. D. L., and McClintock, M. K., 2001, Immense vent complex marks flood-basalt eruption in a wet failed rift: Coombs Hills, Antarctica: *Geology*, v. 29, p. 935-938.
- White, J. D. L., and Ross, P. S., 2011, Maar-diatreme volcanoes: A review: *Journal of Volcanology and Geothermal Research*, v. 201, p. 1-29, doi: 10.1016/j.jvolgeores.2011.01.010.
- White, J. D. L., Thordarson, T., McClintock, M. K., and Ross, P.-S., 2005, Cracking the Lid - dike emplacement above large sills of the Ferrar Province, Antarctica: Abstract V23A-0690 presented at 2013 Fall Meeting, AGU, San Francisco, California, 5-9 December.
- White, J. D. L., Bryan, S. E., Ross, P.-S., Self, S., and Thordarson, T., 2009, Physical volcanology of continental large igneous provinces: update and review: Geological Society of London Special Publications of IAVCEI, v. 2, p. 291-321.
- White, R. S., and McKenzie, D. P., 1989, Magmatism at rift zones: the generation of volcanic continental margins and flood basalts: *Journal of Geophysical Research*, v. 94, p. 7685-7729.
- White, R. S., Smith, L. K., Roberts, A. W., Christie, P. A. F., Kuszniir, N. J., and i, S. T., 2008, Lower-crustal intrusion on the North Atlantic continental margin: *Nature*, v. 452, p. 460-U466, doi: 10.1038/nature06687.

- Whitmarsh, R. B., Manatschal, G., and Minshull, T. A., 2001, Evolution of magma-poor continental margins from rifting to seafloor spreading: *Nature*, v. 413, p. 150-154, doi: 10.1038/35093085.
- Wilkinson, M., Roberts, G. P., McCaffrey, K., Cowie, P. A., Faure Walker, J. P., Papanikolaou, I., Phillips, R. J., Michetti, A. M., Vittori, E., Gregory, L., Wedmore, L., and Watson, Z. K., 2015, Slip distributions on active normal faults measured from LiDAR and field mapping of geomorphic offsets: an example from L'Aquila, Italy, and implications for modelling seismic moment release: *Geomorphology*, v. 237, p. 130-141, doi: 10.1016/j.geomorph.2014.04.026.
- Wilkinson, P., Mitchell, J. G., Cattermole, P. J., and Downie, C., 1986, Volcanic chronology of the Meru-Kilimanjaro region, northern Tanzania: *Journal of the Geological Society of London*, v. 143, p. 601-605, doi: 10.1144/gsjgs.143.4.0601.
- Willemse, E. J. M., Pollard, D. D., and Aydin, A., 1996, Three-dimensional analyses of slip distributions on normal fault arrays with consequences for fault scaling: *Journal of Structural Geology*, v. 18, p. 295-309, doi: 10.1016/s0191-8141(96)80051-4.
- Willemse, E. J. M., Peacock, D. C. P., and Aydin, A., 1997, Nucleation and growth of strike-slip faults in limestones from Somerset, UK: *Journal of Structural Geology*, v. 19, p. 1461-1477, doi: 10.1016/s0191-8141(97)00056-4.
- Wilson, C. J. N., and Rowland, J. V., 2016, The volcanic, magmatic and tectonic setting of the Taupo Volcanic Zone, New Zealand, reviewed from a geothermal perspective: *Geothermics*, v. 59, p. 168-187, doi: 10.1016/j.geothermics.2015.06.013.
- Wilson, C. J. N., Houghton, B. F., McWilliams, M. O., Lanphere, M. A., Weaver, S. D., and Briggs, R. M., 1995, Volcanic and structural evolution of Taupo Volcanic Zone, New Zealand: a review: *Journal of Volcanology and Geothermal Research*, v. 68, p. 1-28, doi: 10.1016/0377-0273(95)00006-g.
- Wilson, T. J., 1993, Jurassic faulting and magmatism in the Transantarctic Mountains: Implications for Gondwana breakup, in Findlay, R.H. et al., eds., *Gondwana 8 - Assembly, Evolution and Dispersal*: Rotterdam, AA Balkema, p. 563-572.
- WoldeGabriel, G., Aronson, J. L., and Walter, R. C., 1990, Geology, geochronology, and rift basin development in the central sector of the Main Ethiopia Rift: *Geological Society of America Bulletin*, v. 102, p. 439-458.
- Wolfenden, E., Ebinger, C., Yirgu, G., Deino, A., and Ayalew, D., 2004, Evolution of the northern Main Ethiopian rift: birth of a triple junction: *Earth and Planetary Science Letters*, v. 224, p. 213-228, doi: 10.1016/j.epsl.2004.04.022.
- Wolfenden, E., Ebinger, C., Yirgu, G., Renne, P. R., and Kelley, S. P., 2005, Evolution of a volcanic rifted margin: Southern Red Sea, Ethiopia: *Geological Society of America Bulletin*, v. 117, p. 846-864, doi: 10.1130/1325516.1.
- Wood, C. A., 1980, Morphometric evolution of cinder cones: *Journal of Volcanology and Geothermal Research*, v. 7, p. 387-413, doi: 10.1016/0377-0273(80)90040-2.
- Woolfe, K. J., Kirk, P. A., and Sherwood, A. M., 1989, The geology of the Knobhead area, southern Victoria Land, Antarctica: Wellington Department of Scientific and Industrial Research New Zealand Geological Survey miscellaneous series map 19, scale 1:50 000, 1 sheet.
- Wright, T. J., Ebinger, C., Biggs, J., Ayele, A., Yirgu, G., Keir, D., and Stork, A., 2006, Magma-maintained rift segmentation at continental rupture in the 2005 Afar dyking episode: *Nature*, v. 442, p. 291-294, doi: 10.1038/nature04978.

- Wright, T. J., Sigmundsson, F., Pagli, C., Belachew, M., Hamling, I. J., Brandsdottir, B., Keir, D., Pedersen, R., Ayele, A., Ebinger, C., Einarsson, P., Lewi, E., and Calais, E., 2012, Geophysical constraints on the dynamics of spreading centres from rifting episodes on land: *Nature Geoscience*, v. 5, p. 242-250, doi: 10.1038/ngeo1428.
- Yardley, B. W. D., Harlov, D. E., and Heinrich, W., 2010, Rates of retrograde metamorphism and their implications for crustal rheology: *Geofluids*, v. 10, p. 234-240, doi: 10.1111/j.1468-8123.2010.00286.x.
- Youash, Y., 1969, Tension tests on layered rocks: *Geological Society of America Bulletin*, v. 80, p. 303-306.
- Zhang, P. Z., Mao, F. Y., and Slemmons, D. B., 1999, Rupture terminations and size of segment boundaries from historical earthquake ruptures in the Basin and Range Province: *Tectonophysics*, v. 308, p. 37-52, doi: 10.1016/s0040-1951(99)00089-x.
- Zoback, M. L., 1992, 1st-order and 2nd-order patterns of stress in the lithosphere: the world stress map project: *Journal of Geophysical Research*, v. 97, p. 11703-11728, doi: 10.1029/92jb00132.

APPENDIX A

Supplementary data for Chapter 2

Data used in this study can be accessed in the accompanying CD-ROM, or, online at the following website:

<http://onlinelibrary.wiley.com/doi/10.1002/2015GC005918/full>

Summary of content:

The 4 tables provided summarize all data used in this study. These tables are available as Excel spreadsheets.

Table A1. Locations and lineament trends produced by volcanic cones in this study.

Table A2. Vent alignment locations and orientations.

Table A3. Fault locations, lengths and orientations.

Table A4. Focal mechanism data for the North Tanzanian Divergence.

APPENDIX B

*Supplementary data tables for Chapter 3*Table B1. Diffuse CO₂ flux data (in g m⁻² d⁻¹) for different structural zones in the Magadi and Natron basin study areas.

	Magadi basin			Natron basin		
	fault zone	hanging wall	footwall	fault zone	hanging wall	footwall
number of data	174	186	93	71	24	17
mean flux	36.6	8.8	1.9	17.2	11.7	1.1
error (95% conf.)	11	2.6	1.4	5	6.8	0.8

Table B2. Summary of diffuse CO₂ flux for the Magadi-Natron basin, including mean and total flux from different structural zones, and estimated annual flux from each study area.

study area	structural zone	mean flux (g m ⁻² d ⁻¹)	area (km ²)	total flux (g d ⁻¹)	annual flux (Mt yr ⁻¹)
Magadi	fault zones	36.6 ± 11.0	72.9	2.7 x 10 ⁹	0.98 ± 0.29
	hanging walls	8.8 ± 2.6	150.7	1.3 x 10 ⁹	0.48 ± 0.14
	footwalls	1.9 ± 1.4	183.8	3.5 x 10 ⁸	0.13 ± 0.10
	total		407.5		1.59 ± 0.53
Natron	fault zones	17.2 ± 5.0	33.1	5.7 x 10 ⁸	0.21 ± 0.06
	hanging walls	11.7 ± 6.8	526.5	6.2 x 10 ⁹	2.25 ± 1.31
	footwalls	1.1 ± 0.8	14.4	1.6 x 10 ⁷	< 0.01
	total		574		2.46 ± 1.37

Mean and annual flux values are within 95% confidence

Table B3. Locations, temperatures, and pH of springs in the Magadi-Natron basin.

	ID	latitude (S°)	longitude (E°)	Temperature (°C)	pH
Magadi	KN14-S01	1.85744	36.21900	48.4	8.9
	KN14-S02	1.86319	36.21983	47.7	9.3
	KN14-S03	1.83581	36.21839	46.4	9.1
	KN14-S04	1.84329	36.21583	34.1	-
	KN14-S05	2.00228	36.23148	44.7	9.8
	KN14-S06	1.99825	36.23131	44.6	9.9
	KN14-S07	2.00284	36.22848	39	9.8
	KN14-S08	1.72756	36.28086	83.5	9.5
	KN14-S09	1.72547	36.27828	82.3	9.3
	KN14-S10	1.72461	36.27308	-	-
	KN14-S11	1.85989	36.30636	35	10
Natron	TZ14-S01	2.37314	35.90581	50.7	10.3
	TZ14-S02	2.39228	35.89828	51.2	10.3
	TZ14-S03	2.45581	36.08842	43.1	9.5
	TZ14-S04	2.52733	36.04928	-	-
	TZ14-S05	2.52733	36.04928	38.1	9.3
	TZ14-S06	2.59283	36.01597	36.8	9.2

Table B4. Locations, gas compositions, carbon isotope values ($\delta^{13}\text{C-CO}_2$), and structural divisions of measured gas samples from the Magadi and Natron basin study areas and Oldoinyo Lengai North Crater.

Area	sample ID	location		Ar	N ₂	O ₂	CO ₂	zone	H ₂	CH ₄	CO	$\delta^{13}\text{C-CO}_2$ ‰ vs. PDB	zone
		latitude (S°)	Longitude (E°)										
Magadi	A1P44	1.828625	36.167317	0.70	83.19	16.02	944.42	6.84	8.26	b.d.	b.d.	-8.5	FZ
	A1P63	1.84275	36.165028	0.70	83.28	15.94	832.00	7.11	5.45	b.d.	b.d.	-9.2	FZ
	A1P43	1.828289	36.167503	0.85	82.27	16.79	824.71	2.21	6.14	b.d.	16.03	-7.7	FZ
	A1P39	1.829833	36.165639	0.71	83.64	15.56	863.52	7.23	5.47	b.d.	b.d.	-9.6	HW
	A1P67	1.845944	36.164417	0.67	78.47	20.78	800.38	7.44	5.63	b.d.	b.d.	-8.7	FZ
	A2P82	1.838444	36.200167	0.66	80.61	18.66	642.53	6.49	5.35	b.d.	b.d.	-8.1	FZ
	A2P76	1.843972	36.198778	0.69	81.51	17.74	645.68	6.82	9.16	b.d.	16.32	-8.0	FZ
	A2P69	1.848028	36.1975	0.68	80.45	18.78	869.88	6.60	6.07	b.d.	b.d.	-10.1	FZ
	A2P86	1.834333	36.201639	0.66	80.85	18.42	688.76	7.29	5.62	b.d.	b.d.	-7.8	FW
	A3P5	1.859028	36.216361	0.76	78.94	20.22	803.95	0.96	5.86	b.d.	b.d.	-8.4	FZ
	A3P13	1.8575	36.218989	0.70	82.03	17.15	1223.27	9.21	4.26	b.d.	b.d.	-9.1	FZ
	A3P9	1.856528	36.216472	0.81	76.97	22.15	698.69	1.49	5.40	b.d.	b.d.	-9.9	HW
	A3P18	1.859328	36.219308	0.59	79.38	19.84	1882.03	13.47	4.37	b.d.	b.d.	-7.6	FZ
	A3P8	1.856833	36.216667	0.70	81.43	17.81	544.99	10.88	8.60	b.d.	b.d.	-7.2	FZ
	A3P21	1.85575	36.218472	0.70	83.55	15.36	3803.59	7.51	6.70	b.d.	b.d.	-7.9	FZ
	A4P27	1.835535	36.21852	0.86	82.60	16.46	768.65	1.47	4.57	b.d.	b.d.	-8.5	FZ
	A4P94	1.834439	36.222847	0.66	80.38	18.86	994.93	5.74	8.15	b.d.	15.77	-7.5	HW
	A4P82	1.844181	36.219661	0.86	82.32	16.70	1201.33	1.41	13.01	b.d.	b.d.	-7.1	HW
	A4P101	1.834103	36.220825	0.68	80.96	18.23	1314.96	6.61	6.58	b.d.	b.d.	-7.3	HW
	A4P111	1.836356	36.219469	0.82	81.82	17.31	578.11	7.43	6.45	b.d.	b.d.	-7.3	HW
	A4P113	1.8369	36.220089	0.71	80.05	19.14	990.99	7.67	6.11	b.d.	b.d.	-7.1	HW
	A4P81	1.844089	36.219269	0.65	81.23	17.99	1223.57	6.45	12.23	b.d.	18.19	-6.5	HW
	A4P90	1.844239	36.222794	0.68	82.28	16.95	919.84	5.70	8.27	b.d.	b.d.	-7.5	FZ
	A4P99	1.834244	36.221225	0.81	80.60	18.49	1025.56	2.30	5.75	b.d.	b.d.	-7.4	HW
	A4P108	1.835656	36.218458	0.82	80.51	18.62	464.87	10.02	4.94	b.d.	b.d.	-7.9	FZ
	A4P115	1.837517	36.220681	0.70	81.67	17.53	988.54	7.20	6.40	b.d.	b.d.	-5.9	HW
	A4P120	1.838653	36.221867	0.69	82.52	16.68	1053.10	11.22	4.88	b.d.	b.d.	-7.5	FZ
	A5P19	1.815472	36.205722	0.79	79.51	19.65	520.77	8.36	6.44	b.d.	b.d.	-8.3	HW
	A5P24	1.816417	36.207694	0.68	82.31	16.91	958.17	10.92	3.74	b.d.	b.d.	-7.8	FZ
	A5P34	1.824361	36.203278	0.69	80.32	18.91	835.54	9.20	9.12	b.d.	11.93	-8.6	HW
A5P21	1.815889	36.2065	0.79	82.61	16.53	663.78	8.99	4.47	b.d.	b.d.	-7.4	HW	

A6P54	1.830889	36.22075	0.61	79.55	19.77	710.90	13.86	4.32	b.d.	b.d.	-8.0	FZ
A6P50	1.829417	36.221194	0.67	80.95	18.29	873.04	6.04	5.84	b.d.	13.99	-11.1	FZ
A6P52	1.831139	36.220667	0.69	82.27	16.89	1360.76	7.29	10.39	b.d.	b.d.	-6.5	FZ
A7P30	1.921111	36.288222	0.74	82.89	16.29	784.68	11.22	9.06	b.d.	10.48	-5.8	HW
A7P26	1.922417	36.288417	0.80	80.20	18.94	617.14	13.02	4.59	b.d.	b.d.	-10.2	HW
A7P14	1.922694	36.3	1.08	80.64	18.22	573.68	8.71	5.69	b.d.	b.d.	-7.4	FZ
A7P4	1.920306	36.289306	0.71	80.22	18.99	759.74	9.05	9.89	b.d.	b.d.	-6.4	HW
A7P22	1.922611	36.292944	0.70	80.63	18.58	915.98	6.14	7.09	b.d.	15.99	-7.7	FW
A7P12	1.921056	36.300694	0.68	80.72	18.51	881.32	6.31	17.93	b.d.	16.64	-8.9	FZ
A7P5	1.920361	36.292444	0.83	82.34	16.78	484.60	7.68	7.52	b.d.	13.83	-7.1	HW
A7P19	1.922639	36.294639	0.71	82.14	17.07	834.17	7.29	6.63	b.d.	16.45	-6.7	FZ
A7P11	1.920778	36.300111	0.67	81.11	18.13	818.68	6.94	6.21	b.d.	b.d.	-6.9	HW
A7P8	1.920528	36.294722	0.69	82.46	16.79	543.74	7.94	5.11	b.d.	b.d.	-8.1	FZ
A7P29	1.922139	36.28775	0.86	82.56	16.51	659.63	9.54	4.19	b.d.	b.d.	-7.6	FZ
A8P35	1.988944	36.264167	0.69	82.05	17.19	686.65	10.77	4.64	b.d.	b.d.	-6.2	FZ
A8P40	2.000389	36.25275	0.72	81.21	17.97	969.67	8.67	12.59	b.d.	b.d.	-7	HW
A8P50	2.00225	36.231458	0.68	82.23	16.98	1021.22	7.66	11.89	b.d.	b.d.	-7.3	FZ
A8P42	1.999722	36.249889	0.67	82.17	17.09	662.11	6.05	7.51	b.d.	b.d.	-8.5	HW
A9P9	1.730319	36.298964	0.70	82.11	17.11	842.79	6.70	6.90	b.d.	17.19	-9.3	FZ
A9P5	1.732603	36.291972	0.86	81.06	18.03	497.51	2.31	8.45	b.d.	b.d.	-9.6	HW
A9P4	1.733103	36.291111	0.67	81.21	18.05	676.82	5.91	6.32	b.d.	15.89	-8.6	HW
A11P36	1.789639	36.268178	0.94	82.83	16.05	1735.20	2.00	9.37	b.d.	19.63	-5.7	FZ
A11P29	1.791111	36.271242	0.66	82.73	16.53	776.27	12.62	6.91	b.d.	b.d.	-4.3	FZ
A11P32	1.790764	36.269622	0.69	82.19	17.01	1107.14	9.93	5.06	b.d.	14.95	-3.8	FZ
A11P22	1.785847	36.278933	0.69	81.18	18.05	779.67	8.95	5.99	b.d.	15.39	-9.1	FW
A12P7	1.801833	36.359917	0.85	83.54	15.56	527.89	2.15	7.77	b.d.	b.d.	-9.3	HW
A12P4	1.804222	36.364472	0.84	80.77	18.32	618.92	1.47	9.79	b.d.	18.57	-6.8	HW
A12P17	1.780528	36.351111	0.85	80.56	18.52	666.84	1.66	5.89	b.d.	b.d.	-9.3	HW
A12P9	1.799083	36.355278	0.70	82.78	16.43	822.19	7.42	6.65	b.d.	15.84	-8.5	HW
A12P19	1.779556	36.347639	0.78	80.08	19.05	893.78	0.84	5.58	b.d.	16.00	-6.9	HW
A12P1	1.802944	36.362472	0.71	82.26	16.98	487.25	7.25	7.51	b.d.	b.d.	-9.8	HW
A13P38	1.855694	36.30675	0.87	82.01	17.01	1106.85	2.09	10.20	b.d.	b.d.	-7.4	FZ
A13P37	1.860667	36.306194	0.85	82.04	17.00	981.63	9.35	10.16	b.d.	b.d.	-9.3	FZ
A13P31	1.860861	36.309583	0.69	82.00	17.24	687.88	7.39	6.63	b.d.	18.52	-8.1	HW
A14P6	1.734694	36.283478	0.68	81.40	17.81	1103.97	7.41	8.97	b.d.	19.51	-6.3	FZ
A14P20	1.723619	36.271606	0.67	80.63	18.58	1107.60	6.94	5.47	b.d.	b.d.	-7.3	FZ
A14P18	1.724681	36.273306	0.68	80.81	18.34	1647.35	7.41	5.82	b.d.	16.39	-6.5	FZ

	A14P7	1.735419	36.283494	0.65	77.72	21.51	1202.78	6.02	6.74	b.d.	b.d.	-8.3	FZ	
	A14P10	1.730081	36.281619	0.69	81.60	17.49	2058.20	6.80	6.23	b.d.	16.86	-8.6	FZ	
	A14P21	1.719167	36.269775	0.85	80.44	18.56	1420.52	32.71	10.04	b.d.	17.82	-8.9	FZ	
	A14P1	1.727233	36.283283	0.68	80.96	18.28	787.91	6.45	5.72	b.d.	b.d.	-9.6	FW	
	A14P4	1.731719	36.283842	0.68	82.13	17.11	771.18	5.77	11.76	b.d.	b.d.	-9.1	HW	
Natron	T1P1	2.373139	35.905806	0.67	81.78	17.47	773.14	8.26	5.42	b.d.	0.00	-9.3	FZ	
	T1P2	2.373083	35.905278	0.69	82.51	16.69	1068.13	7.57	6.23	b.d.	14.40	-7.5	FZ	
	T1P5	2.372639	35.904167	0.74	84.09	15.08	872.89	8.48	7.14	b.d.	24.81	-7.8	FZ	
	T1P12	2.375583	35.904111	0.73	83.41	15.78	779.56	8.27	9.96	b.d.	20.67	-7.9	FZ	
	T1P18	2.385	35.905194	0.73	83.83	15.34	988.28	8.04	5.96	b.d.	0.00	-8.8	FZ	
	T1P23	2.392278	35.898278	0.73	84.07	15.12	879.30	7.98	6.49	b.d.	0.00	-8.3	FZ	
	T3P12	2.679528	35.882139	0.72	83.73	15.46	807.21	7.87	10.21	b.d.	0.00	-7.5	FZ	
	T3P13	2.6795	35.882389	0.70	83.83	15.38	882.85	7.37	6.17	b.d.	16.22	-8.1	FZ	
	T3P14	2.6795	35.882722	0.72	81.05	18.13	961.39	6.20	6.24	b.d.	18.98	-7.9	FZ	
	T3P17	2.679833	35.882667	0.76	83.66	15.49	872.08	7.40	6.11	b.d.	15.45	-8.0	FZ	
	T3P22	2.680667	35.882889	0.70	81.08	18.15	699.21	6.90	11.90	b.d.	0.00	-7.7	FZ	
	T3P26	2.680694	35.884056	0.71	83.61	15.56	1183.75	7.05	5.76	b.d.	0.00	-9.9	FZ	
	T3P28	2.680657	35.884472	0.72	80.80	18.38	865.70	7.09	5.55	b.d.	0.00	-9.8	FZ	
	T3P34	2.679583	35.8855	0.61	83.67	15.66	683.20	7.73	6.55	b.d.	0.00	-7.7	FZ	
	T3P35	2.678889	35.88525	0.68	82.19	17.02	1033.39	7.66	9.76	b.d.	15.90	-10.6	FZ	
	T5P45	2.767	36.044861										-11.7	HW
	T6P7	2.453806	36.086861	0.85	77.64	21.39	1214.85	5.82	8.35	b.d.	21.70	-6.4	FZ	
	T6P9	2.453944	36.087556	0.81	81.12	17.97	908.40	8.30	5.94	b.d.	0.00	-7.4	FZ	
	T6P3	2.453556	36.086111	0.82	81.65	17.44	922.00	7.89	5.80	b.d.	0.00	-7.7	FZ	
	T6P6	2.453778	36.086611	0.80	79.00	20.06	1414.51	7.18	6.25	b.d.	0.00	-7.2	FZ	
	T6P11	2.453889	36.088278	0.84	80.19	18.87	1034.56	8.78	7.39	b.d.	16.76	-7.8	FZ	
	T6P2	2.453	36.085944	0.86	83.62	15.43	879.47	13.15	11.22	b.d.	19.29	-8.6	HW	
	T6P13	2.45425	36.088667	0.83	79.15	19.93	872.40	9.54	9.50	b.d.	0.00	-8.7	FZ	
	T6P16	2.454972	36.088806	0.88	83.85	15.19	829.02	9.58	12.10	b.d.	14.96	-8.7	FW	
	T7P27	2.526639	36.045278	0.85	81.60	17.33	1012.82	9.62	10.44	125 0.0 3	0.00	-6.2	FZ	
	T7P31	2.5265	36.046583	0.88	82.90	16.14	795.65	9.74	6.41	b.d.	15.62	-6.4	FZ	
	T7P29	2.526083	36.046111	0.88	83.97	15.06	808.82	9.74	6.33	b.d.	22.35	-6.5	FZ	
	T7P24	2.526639	36.044278	0.81	82.33	16.76	957.88	9.78	10.15	b.d.	0.00	-7.7	FZ	
	T7P22	2.526361	36.043667	0.84	83.75	15.31	995.48	9.32	11.58	b.d.	18.75	-8.8	FZ	
	T7P23	2.526389	36.043972	0.87	83.36	15.68	888.45	9.57	9.78	b.d.	0.00	-8.7	FZ	
T7P35	2.527333	36.049278	0.87	83.75	15.29	762.89	9.52	10.10	b.d.	19.22	-8.1	FW		

	T8P42	2.59325	36.015889	0.90	81.56	17.44	925.20	10.26	6.20	b.d.	15.73	-7.8	FZ
	T8P36	2.592333	36.014194	0.92	83.52	15.43	1224.22	10.44	6.37	b.d.	0.00	-8.2	FZ
	T8P38	2.592472	36.014778	0.84	79.33	19.74	853.63	9.65	5.44	b.d.	0.00	-8.6	FZ
	T8P40	2.592889	36.015333	0.93	83.36	15.60	1072.86	11.80	5.72	b.d.	0.00	-9.1	FZ
	T9P47	2.610667	35.989583	0.87	83.67	15.37	887.28	10.64	6.16	b.d.	19.08	-9.1	HW
	T9P49	2.606694	35.971306	0.83	82.24	16.86	669.92	9.44	5.91	b.d.	0.00	-10.6	HW
	T9P52	2.618306	35.927556	0.64	77.08	22.19	788.17	6.82	6.94	b.d.	15.86	-9.8	HW
	T9P53	2.620972	35.908028	0.69	83.42	15.78	1040.75	7.79	6.72	b.d.	16.62	-9.7	HW
Oldoinyo Lengai North Crater	OL21	2.761513	35.91533									-5.7	
	OL23	2.761339	35.915594	0.83	83.16	15.14	8655.19	9.82	6.49	b.d.	21.48	-3.0	
	OL24	2.761322	35.915638	0.83	83.16	15.29	7091.05	9.79	12.26	b.d.	20.51	-2.2	

FZ: fault zone. HW: hanging wall. FW: footwall. b.d.: below detection limit. No gas

chemistry data for T5P45 and OL21.

APPENDIX C

Supplementary data for Chapter 4

Data used in this study can be accessed in the accompanying CD-ROM.

Summary of content:

Table C1. Supplementary Geological Map of the Natron and Magadi region.

Table C2. Incremental-heating $^{40}\text{Ar}/^{39}\text{Ar}$ data for newly analyzed Natron and Magadi volcanic rocks.

APPENDIX D

*Supplementary data tables for Chapter 6***Summary of content:**

Data used in this study come from 644 dike intrusions in South Victoria Land, Antarctica. Data have been collected and compiled from number maps, publications, and theses released over the past 30 years. The newly compiled data set has been supplemented by an additional 136 dikes observed and measured using DigitalGlobe images (1-2 m pixel resolution) courtesy of Google Earth (Table D1). Field measurements of dike dip and mean dike-segment thickness come from 5 previous studies (Tables D2 & D3). The total exposure area of Beacon Supergroup and Mawson Formation rocks in the study area was measured from 8 published maps in the South Victoria Land region (Table D4).

Table D1. Strikes, lengths and coordinates (WGS 84) of all dikes in South Victoria Land from this study.

ID	Area	Long. °E (dike start)	Lat. °S (dike start)	Long. °E (dike end)	Lat. °S (dike end)	Length (m)	Strike (degrees)	Reference
1	Beacon Heights	161.040	77.853	161.033	77.867	1841	2	Cox et al. (2012)
2	Beacon Heights	161.139	77.846	161.171	77.856	1317	141	Cox et al. (2012)
3	Beacon Heights	161.150	77.865	161.197	77.866	1098	92	Cox et al. (2012)
4	Beacon Heights	161.197	77.866	161.242	77.870	1183	107	Cox et al. (2012)
5	Olympus Range	160.788	77.473	160.869	77.466	2119	64	Cox et al. (2012)
6	Olympus Range	160.874	77.487	160.900	77.487	614	86	Cox et al. (2012)
7	Olympus Range	160.929	77.494	160.933	77.498	459	163	Cox et al. (2012)
8	Olympus Range	160.980	77.494	161.010	77.505	2381	145	Cox et al. (2012)
9	Olympus Range	160.986	77.504	161.027	77.518	1879	144	Cox et al. (2012)
10	Olympus Range	160.701	77.516	160.733	77.516	782	85	Cox et al. (2012)

11	Head Mountains	161.055	77.389	161.088	77.388	876	76	Cox et al. (2012)
12	Head Mountains	160.516	77.354	160.534	77.355	436	101	Cox et al. (2012)
13	Head Mountains	159.741	77.199	159.756	77.202	548	133	Cox et al. (2012)
14	Head Mountains	160.041	77.187	160.038	77.198	1206	178	Cox et al. (2012)
15	Head Mountains	160.298	77.203	160.302	77.196	717	4	Cox et al. (2012)
16	Head Mountains	160.317	77.181	160.333	77.183	455	112	Cox et al. (2012)
17	Head Mountains	160.297	77.191	160.321	77.191	612	80	Cox et al. (2012)
18	Head Mountains	160.374	77.224	160.372	77.229	567	180	Cox et al. (2012)
19	Head Mountains	160.315	77.219	160.358	77.235	2056	144	Cox et al. (2012)
20	Head Mountains	160.567	77.244	160.610	77.234	1496	42	Cox et al. (2012)
21	Head Mountains	160.600	77.183	160.606	77.188	602	160	Cox et al. (2012)
22	Beacon Heights	161.040	77.853	161.026	77.865	1556	9	Cox et al. (2012)
23	Cruzen Range	161.197	77.332	161.210	77.326	824	19	Cox et al. (2012)
24	Cruzen Range	161.167	77.337	161.194	77.334	739	59	Cox et al. (2012)
25	Cruzen Range	161.177	77.338	161.189	77.336	345	56	Cox et al. (2012)
26	Cruzen Range	161.196	77.335	161.193	77.341	604	5	Cox et al. (2012)
27	Insel Range	161.352	77.392	161.379	77.394	700	102	Cox et al. (2012)
28	Insel Range	161.391	77.406	161.390	77.410	475	178	Cox et al. (2012)
29	Insel Range	161.441	77.386	161.512	77.394	2277	113	Cox et al. (2012)
30	Insel Range	161.390	77.391	161.473	77.389	2069	79	Cox et al. (2012)
31	Olympus Range	161.283	77.466	161.292	77.482	1810	169	Cox et al. (2012)
32	Olympus Range	161.256	77.496	161.282	77.489	1013	35	Cox et al. (2012)
33	Olympus Range	161.285	77.501	161.329	77.492	1436	44	Cox et al. (2012)
34	Olympus Range	161.391	77.473	161.391	77.481	917	176	Cox et al. (2012)
35	Olympus Range	161.402	77.481	161.426	77.479	627	68	Cox et al. (2012)
36	Olympus Range	161.426	77.479	161.465	77.476	1019	65	Cox et al. (2012)
37	Olympus Range	161.426	77.479	161.431	77.486	893	169	Cox et al. (2012)
38	Olympus Range	161.558	77.465	161.587	77.486	2488	160	Cox et al. (2012)
39	Olympus Range	161.585	77.466	161.615	77.484	2126	156	Cox et al. (2012)
40	Cruzen Range	161.275	77.322	161.350	77.330	2073	112	Cox et al. (2012)
41	Olympus Range	161.055	77.474	161.336	77.480	7001	92	Cox et al. (2012)
42	Wright Valley	161.215	77.553	161.253	77.543	1428	36	Cox et al. (2012)
43	Wright Valley	161.227	77.552	161.256	77.547	930	45	Cox et al. (2012)
44	Wright Valley	161.328	77.556	161.343	77.552	611	35	Cox et al. (2012)
45	Asgard Range	161.331	77.599	161.336	77.599	119	87	Cox et al. (2012)
46	Asgard Range	161.127	77.607	161.147	77.602	742	37	Cox et al. (2012)
47	Asgard Range	161.109	77.621	161.124	77.616	615	34	Cox et al. (2012)
48	Asgard Range	161.274	77.598	161.331	77.599	1401	92	Cox et al. (2012)
49	Asgard Range	161.336	77.599	161.346	77.600	241	104	Cox et al. (2012)
50	Asgard Range	161.336	77.599	161.333	77.612	1461	179	Cox et al. (2012)
51	Asgard Range	161.302	77.618	161.331	77.599	2261	15	Cox et al. (2012)
52	Asgard Range	161.397	77.611	161.338	77.600	1971	126	Cox et al. (2012)

53	Asgard Range	161.190	77.626	161.172	77.602	2763	167	Cox et al. (2012)
54	Asgard Range	161.149	77.635	161.145	77.630	541	166	Cox et al. (2012)
55	Asgard Range	161.244	77.681	161.244	77.679	252	177	Cox et al. (2012)
56	Asgard Range	161.272	77.663	161.277	77.658	586	7	Cox et al. (2012)
57	Asgard Range	161.285	77.673	161.291	77.670	315	23	Cox et al. (2012)
58	Asgard Range	161.364	77.672	161.380	77.668	555	40	Cox et al. (2012)
59	Fenrir Valley	161.719	77.607	161.728	77.610	345	137	Cox et al. (2012)
60	Fenrir Valley	161.717	77.605	161.733	77.606	429	108	Cox et al. (2012)
61	Fenrir Valley	161.716	77.601	161.727	77.604	397	132	Cox et al. (2012)
62	Fenrir Valley	161.719	77.599	161.739	77.602	566	117	Cox et al. (2012)
63	Fenrir Valley	161.735	77.592	161.750	77.598	800	150	Cox et al. (2012)
64	Fenrir Valley	161.745	77.589	161.771	77.592	738	119	Cox et al. (2012)
65	Fenrir Valley	161.895	77.622	161.903	77.622	212	68	Cox et al. (2012)
66	Fenrir Valley	161.556	77.699	161.558	77.696	374	6	Cox et al. (2012)
67	Olympus Range	161.231	77.483	161.243	77.494	1260	163	Cox et al. (2012)
68	Insel Range	161.416	77.379	161.429	77.375	568	31	Cox et al. (2012)
69	Fenrir Valley	161.712	77.605	161.719	77.607	313	146	Cox et al. (2012)
70	Fenrir Valley	161.709	77.609	161.719	77.607	306	50	Cox et al. (2012)
71	Fenrir Valley	161.719	77.607	161.729	77.606	260	67	Cox et al. (2012)
72	Odin Valley	161.831	77.789	161.861	77.793	817	118	Cox et al. (2012)
73	Asgard Range	161.352	77.597	161.368	77.591	781	25	Cox et al. (2012)
74	Odin Valley	161.959	77.792	161.974	77.792	369	75	Cox et al. (2012)
75	Beacon Heights	160.054	77.844	160.070	77.848	577	134	Cox et al. (2012)
76	Beacon Heights	160.057	77.839	160.075	77.842	512	116	Cox et al. (2012)
77	Beacon Heights	160.062	77.836	160.076	77.840	571	139	Cox et al. (2012)
78	Beacon Heights	160.442	77.926	160.441	77.930	460	178	Cox et al. (2012)
79	Beacon Heights	160.439	77.934	160.440	77.940	662	174	Cox et al. (2012)
80	Beacon Heights	160.553	77.910	160.564	77.909	256	83	Cox et al. (2012)
81	Beacon Heights	160.922	77.899	160.947	77.899	578	84	Cox et al. (2012)
82	Beacon Heights	160.939	77.869	160.922	77.899	3353	3	Cox et al. (2012)
83	Beacon Heights	160.750	77.871	160.740	77.885	1492	4	Cox et al. (2012)
84	Beacon Heights	160.926	77.854	160.970	77.854	1043	88	Cox et al. (2012)
85	Beacon Heights	160.970	77.854	160.984	77.853	350	67	Cox et al. (2012)
86	Beacon Heights	160.883	77.841	160.961	77.833	2058	59	Cox et al. (2012)
87	Beacon Heights	160.964	77.825	160.963	77.830	533	178	Cox et al. (2012)
88	Beacon Heights	160.854	77.800	160.857	77.813	1422	173	Cox et al. (2012)
89	Beacon Heights	160.587	77.811	160.598	77.804	859	13	Cox et al. (2012)
90	Beacon Heights	160.875	77.887	160.881	77.885	196	44	Cox et al. (2012)
91	Beacon Heights	160.878	77.885	160.890	77.883	382	42	Cox et al. (2012)
92	Beacon Heights	160.904	77.879	160.918	77.877	421	49	Cox et al. (2012)
93	Beacon Heights	160.918	77.876	160.930	77.873	429	37	Cox et al. (2012)
94	Beacon Heights	160.907	77.874	160.915	77.871	359	29	Cox et al. (2012)

95	Beacon Heights	160.920	77.869	160.923	77.868	216	17	Cox et al. (2012)
96	Beacon Heights	160.916	77.867	160.923	77.864	328	28	Cox et al. (2012)
97	Beacon Heights	160.991	77.846	161.018	77.842	770	51	Cox et al. (2012)
98	Beacon Heights	161.029	77.833	161.036	77.841	951	165	Cox et al. (2012)
99	Beacon Heights	161.036	77.832	161.057	77.835	648	125	Cox et al. (2012)
100	Beacon Heights	160.959	77.860	160.970	77.854	738	18	Cox et al. (2012)
101	Beacon Heights	160.896	77.899	160.922	77.899	635	86	Cox et al. (2012)
102	Beacon Heights	160.903	77.901	160.928	77.901	593	87	Cox et al. (2012)
103	Beacon Heights	160.821	77.928	160.817	77.932	470	7	Cox et al. (2012)
104	Beacon Heights	160.544	77.834	160.568	77.831	736	53	Cox et al. (2012)
105	Beacon Heights	160.576	77.784	160.635	77.782	1600	79	Cox et al. (2012)
106	Beacon Heights	160.616	77.789	160.611	77.792	436	11	Cox et al. (2012)
107	Beacon Heights	160.584	77.794	160.550	77.793	821	91	Cox et al. (2012)
108	Beacon Heights	160.550	77.793	160.564	77.797	593	140	Cox et al. (2012)
109	Beacon Heights	160.535	77.798	160.582	77.801	1167	103	Cox et al. (2012)
110	Asgard Range	161.037	77.644	161.092	77.627	2273	32	Cox et al. (2012)
111	Asgard Range	160.988	77.587	160.989	77.594	719	174	Cox et al. (2012)
112	Asgard Range	160.733	77.582	160.794	77.579	1510	73	Cox et al. (2012)
113	Asgard Range	160.806	77.585	160.819	77.580	577	28	Cox et al. (2012)
114	Asgard Range	161.044	77.640	161.140	77.600	5143	23	Cox et al. (2012)
115	Beacon Heights	160.569	77.765	160.610	77.763	1066	69	Cox et al. (2012)
116	Beacon Heights	160.590	77.761	160.615	77.761	592	85	Cox et al. (2012)
117	Beacon Heights	160.960	77.820	160.964	77.825	618	168	Cox et al. (2012)
118	Beacon Heights	160.970	77.819	160.964	77.825	711	8	Cox et al. (2012)
119	Convoy Range	161.118	76.977	161.140	76.976	575	73	Cox et al. (2012)
120	Convoy Range	160.940	76.898	160.949	76.900	287	124	Cox et al. (2012)
121	Convoy Range	160.957	76.901	160.973	76.906	670	138	Cox et al. (2012)
122	Beacon Heights	160.671	77.927	160.706	77.929	885	103	Cox et al. (2012)
123	Beacon Heights	160.712	77.787	160.678	77.795	1187	40	Cox et al. (2012)
124	Head Mountains	160.083	77.186	160.098	77.186	365	84	Google Earth
125	Head Mountains	160.298	77.202	160.304	77.208	637	162	Google Earth
126	Head Mountains	160.269	77.184	160.271	77.186	195	161	Google Earth
127	Head Mountains	160.278	77.203	160.283	77.205	280	145	Google Earth
128	Head Mountains	160.159	77.214	160.149	77.216	362	41	Google Earth
129	Head Mountains	160.133	77.186	160.114	77.185	485	93	Google Earth
130	Head Mountains	160.084	77.185	160.099	77.188	536	131	Google Earth
131	Head Mountains	160.338	77.192	160.326	77.192	321	77	Google Earth
132	Head Mountains	160.323	77.189	160.339	77.188	415	64	Google Earth
133	Head Mountains	160.339	77.188	160.330	77.187	227	90	Google Earth
134	Head Mountains	160.333	77.184	160.333	77.187	339	176	Google Earth
135	Olympus Range	161.563	77.485	161.552	77.479	735	156	Google Earth
136	Shapeless Mountain	160.457	77.409	160.438	77.409	474	79	Google Earth

137	Shapeless Mountain	160.449	77.409	160.442	77.411	293	37	Google Earth
138	Shapeless Mountain	160.434	77.405	160.488	77.402	1360	72	Google Earth
139	Shapeless Mountain	160.446	77.405	160.460	77.405	358	78	Google Earth
140	Olympus Range	161.429	77.487	161.418	77.484	419	134	Google Earth
141	Olympus Range	161.430	77.487	161.420	77.484	393	134	Google Earth
142	Olympus Range	161.533	77.466	161.518	77.468	445	51	Google Earth
143	Olympus Range	161.424	77.485	161.421	77.484	114	121	Google Earth
144	Olympus Range	161.602	77.489	161.614	77.484	630	24	Google Earth
145	Olympus Range	160.613	77.471	160.637	77.508	4223	168	Google Earth
146	Olympus Range	161.039	77.473	160.985	77.465	1599	120	Google Earth
147	Olympus Range	161.461	77.467	161.413	77.473	1323	57	Google Earth
148	Olympus Range	161.297	77.505	161.298	77.498	730	179	Google Earth
149	Olympus Range	161.222	77.469	161.232	77.473	564	151	Google Earth
150	Asgard Range	161.157	77.619	161.154	77.624	632	2	Google Earth
151	Olympus Range	161.285	77.480	161.290	77.484	467	159	Google Earth
152	Olympus Range	161.273	77.481	161.341	77.479	1719	76	Google Earth
153	Olympus Range	161.233	77.487	161.249	77.487	403	86	Google Earth
154	Olympus Range	161.268	77.491	161.264	77.490	160	148	Google Earth
155	Olympus Range	160.936	77.515	160.930	77.504	1315	169	Google Earth
156	Olympus Range	161.337	77.476	161.317	77.477	520	72	Google Earth
157	Olympus Range	160.984	77.500	160.963	77.498	541	102	Google Earth
158	Olympus Range	161.015	77.500	160.983	77.500	793	86	Google Earth
159	Asgard Range	161.144	77.650	161.153	77.649	264	47	Google Earth
160	Asgard Range	161.418	77.588	161.506	77.592	2160	98	Google Earth
161	Asgard Range	161.459	77.585	161.463	77.590	599	166	Google Earth
162	Asgard Range	161.462	77.591	161.472	77.596	606	151	Google Earth
163	Asgard Range	161.444	77.599	161.425	77.600	448	83	Google Earth
164	Asgard Range	161.447	77.594	161.449	77.599	643	173	Google Earth
165	Asgard Range	161.430	77.600	161.413	77.600	404	91	Google Earth
166	Asgard Range	161.402	77.603	161.409	77.608	553	159	Google Earth
167	Asgard Range	161.442	77.603	161.421	77.601	567	114	Google Earth
168	Asgard Range	161.315	77.602	161.313	77.604	238	7	Google Earth
169	Asgard Range	161.311	77.607	161.311	77.609	324	177	Google Earth
170	Asgard Range	161.327	77.587	161.319	77.596	1023	6	Google Earth
171	Asgard Range	161.150	77.650	161.148	77.650	89	42	Google Earth
172	Beacon Heights	160.839	77.808	160.841	77.805	407	5	Google Earth
173	Asgard Range	161.155	77.645	161.160	77.643	217	31	Google Earth
174	Asgard Range	161.177	77.633	161.169	77.634	209	69	Google Earth
175	Asgard Range	161.157	77.636	161.177	77.633	549	58	Google Earth
176	Asgard Range	161.142	77.610	161.151	77.625	1804	169	Google Earth
177	Asgard Range	161.140	77.608	161.147	77.604	427	20	Google Earth
178	Asgard Range	161.141	77.608	161.135	77.613	579	10	Google Earth

179	Asgard Range	161.137	77.600	161.141	77.608	940	170	Google Earth
180	Asgard Range	161.134	77.587	161.136	77.599	1319	174	Google Earth
181	Asgard Range	161.146	77.590	161.145	77.592	202	3	Google Earth
182	Asgard Range	161.130	77.596	161.122	77.595	206	118	Google Earth
183	Asgard Range	161.135	77.597	161.109	77.595	708	111	Google Earth
184	Asgard Range	161.089	77.589	161.103	77.593	575	140	Google Earth
185	Asgard Range	161.069	77.602	161.116	77.596	1323	54	Google Earth
186	Asgard Range	161.208	77.598	161.183	77.597	600	92	Google Earth
187	Asgard Range	161.185	77.597	161.187	77.597	73	149	Google Earth
188	Asgard Range	161.133	77.605	161.120	77.611	792	20	Google Earth
189	Asgard Range	161.266	77.628	161.257	77.623	537	155	Google Earth
190	Asgard Range	161.264	77.629	161.259	77.627	208	143	Google Earth
191	Asgard Range	161.263	77.628	161.255	77.626	259	133	Google Earth
192	Asgard Range	161.031	77.633	161.035	77.636	320	162	Google Earth
193	Fenrir Valley	161.937	77.623	161.934	77.622	171	152	Google Earth
194	Fenrir Valley	161.934	77.621	161.939	77.623	243	150	Google Earth
195	Fenrir Valley	161.912	77.622	161.936	77.622	588	84	Google Earth
196	Fenrir Valley	161.900	77.605	161.908	77.609	504	154	Google Earth
197	Fenrir Valley	161.932	77.620	161.926	77.617	373	156	Google Earth
198	Fenrir Valley	161.932	77.618	161.934	77.620	312	172	Google Earth
199	Fenrir Valley	161.929	77.617	161.932	77.620	343	165	Google Earth
200	Fenrir Valley	161.922	77.621	162.039	77.604	3537	52	Google Earth
201	Fenrir Valley	162.055	77.595	162.051	77.598	288	19	Google Earth
202	Fenrir Valley	162.057	77.596	162.030	77.598	689	66	Google Earth
203	Fenrir Valley	161.971	77.607	162.050	77.607	1909	87	Google Earth
204	Fenrir Valley	161.993	77.607	161.995	77.615	812	174	Google Earth
205	Fenrir Valley	162.014	77.615	161.981	77.620	955	55	Google Earth
206	Fenrir Valley	162.015	77.621	162.033	77.621	425	95	Google Earth
207	Fenrir Valley	162.023	77.616	162.038	77.616	353	81	Google Earth
208	Fenrir Valley	162.108	77.616	162.086	77.617	552	83	Google Earth
209	Fenrir Valley	162.111	77.620	162.111	77.617	281	177	Google Earth
210	Fenrir Valley	162.098	77.619	162.083	77.618	374	92	Google Earth
211	Fenrir Valley	162.091	77.617	162.096	77.619	271	151	Google Earth
212	Fenrir Valley	161.960	77.607	161.989	77.621	1679	152	Google Earth
213	Knobhead Mountain	161.349	77.908	161.305	77.911	1067	73	Google Earth
214	Knobhead Mountain	161.319	77.914	161.350	77.914	828	92	Google Earth
215	Knobhead Mountain	161.411	77.905	161.446	77.903	843	73	Google Earth
216	Knobhead Mountain	161.325	77.904	161.444	77.895	3089	66	Google Earth
217	Beacon Heights	161.179	77.854	161.183	77.848	584	4	Google Earth
218	Beacon Heights	161.187	77.850	161.184	77.852	170	17	Google Earth
219	Beacon Heights	161.165	77.849	161.176	77.848	289	66	Google Earth
220	Beacon Heights	161.173	77.847	161.155	77.852	752	33	Google Earth

221	Beacon Heights	161.166	77.844	161.149	77.852	915	22	Google Earth
222	Beacon Heights	161.159	77.845	161.164	77.844	143	46	Google Earth
223	Beacon Heights	161.159	77.844	161.147	77.849	568	27	Google Earth
224	Beacon Heights	161.136	77.844	161.144	77.842	305	37	Google Earth
225	Beacon Heights	161.130	77.842	161.137	77.840	277	31	Google Earth
226	Beacon Heights	161.156	77.842	161.143	77.845	423	43	Google Earth
227	Beacon Heights	161.158	77.841	161.138	77.846	674	39	Google Earth
228	Beacon Heights	161.203	77.865	161.257	77.867	1279	96	Google Earth
229	Beacon Heights	161.217	77.866	161.217	77.865	109	3	Google Earth
230	Beacon Heights	161.172	77.866	161.173	77.874	970	176	Google Earth
231	Beacon Heights	161.196	77.866	161.188	77.873	993	10	Google Earth
232	Beacon Heights	161.145	77.867	161.151	77.863	485	11	Google Earth
233	Beacon Heights	161.071	77.839	161.073	77.837	241	9	Google Earth
234	Beacon Heights	161.040	77.840	161.075	77.835	977	52	Google Earth
235	Beacon Heights	161.072	77.840	161.040	77.831	1188	137	Google Earth
236	Beacon Heights	160.933	77.846	160.902	77.840	979	129	Google Earth
237	Asgard Range	161.138	77.616	161.150	77.619	488	141	Google Earth
238	Asgard Range	160.816	77.588	160.806	77.580	920	161	Google Earth
239	Asgard Range	160.993	77.600	160.992	77.597	406	171	Google Earth
240	Asgard Range	160.991	77.597	160.992	77.600	402	173	Google Earth
241	Asgard Range	161.096	77.620	161.100	77.618	289	14	Google Earth
242	Asgard Range	161.047	77.628	161.057	77.621	807	14	Google Earth
243	Asgard Range	161.053	77.623	161.053	77.618	600	176	Google Earth
244	Asgard Range	161.089	77.624	161.045	77.621	1094	100	Google Earth
245	Allan Hills	159.847	76.627	159.848	76.628	108	154	Google Earth
246	Allan Hills	159.835	76.630	159.838	76.632	270	159	Google Earth
247	Allan Hills	159.842	76.630	159.853	76.629	323	64	Google Earth
248	Allan Hills	159.856	76.630	159.848	76.630	205	82	Google Earth
249	Allan Hills	159.857	76.630	159.853	76.630	120	38	Google Earth
250	Allan Hills	159.883	76.638	159.876	76.639	228	46	Google Earth
251	Allan Hills	159.878	76.640	159.884	76.638	213	41	Google Earth
252	Allan Hills	159.844	76.651	159.824	76.645	853	137	Google Earth
253	Allan Hills	159.880	76.654	159.872	76.654	219	76	Google Earth
254	Allan Hills	159.859	76.662	159.845	76.662	408	74	Google Earth
255	Fenrir Valley	161.644	77.627	161.642	77.624	342	167	Google Earth
256	Fenrir Valley	161.657	77.624	161.640	77.625	419	73	Google Earth
257	Fenrir Valley	161.678	77.610	161.665	77.611	350	67	Google Earth
258	Fenrir Valley	161.671	77.605	161.678	77.608	338	146	Google Earth
259	Fenrir Valley	161.682	77.605	161.670	77.605	287	88	Google Earth
260	Terra Cotta Mountain	161.354	77.882	161.197	77.890	3788	72	Google Earth
261	Allan Hills	159.836	76.622	159.838	76.627	499	168	Airoldi et al. (2012)
262	Allan Hills	159.833	76.629	159.825	76.631	365	30	Airoldi et al. (2012)

263	Allan Hills	159.839	76.624	159.855	76.636	1494	159	Airoldi et al. (2012)
264	Allan Hills	159.871	76.640	159.854	76.638	487	109	Airoldi et al. (2012)
265	Allan Hills	159.823	76.661	159.827	76.665	476	160	Airoldi et al. (2012)
266	Allan Hills	159.817	76.667	159.816	76.669	325	2	Airoldi et al. (2012)
267	Allan Hills	159.803	76.668	159.811	76.673	670	154	Airoldi et al. (2012)
268	Allan Hills	159.838	76.671	159.818	76.667	691	124	Airoldi et al. (2012)
269	Allan Hills	159.814	76.672	159.847	76.676	1062	111	Airoldi et al. (2012)
270	Allan Hills	159.847	76.672	159.857	76.671	293	70	Airoldi et al. (2012)
271	Allan Hills	159.844	76.675	159.853	76.675	348	92	Airoldi et al. (2012)
272	Allan Hills	159.919	76.674	159.896	76.672	667	102	Airoldi et al. (2012)
273	Allan Hills	159.906	76.677	159.925	76.674	614	50	Airoldi et al. (2012)
274	Allan Hills	159.906	76.677	159.888	76.684	986	25	Airoldi et al. (2012)
275	Allan Hills	159.885	76.678	159.893	76.681	387	139	Airoldi et al. (2012)
276	Allan Hills	159.791	76.672	159.797	76.675	349	150	Airoldi et al. (2012)
277	Allan Hills	159.815	76.683	159.793	76.673	1182	147	Airoldi et al. (2012)
278	Allan Hills	159.818	76.681	159.803	76.678	495	126	Airoldi et al. (2012)
279	Allan Hills	159.808	76.679	159.789	76.673	834	138	Airoldi et al. (2012)
280	Allan Hills	159.813	76.682	159.787	76.674	1074	135	Airoldi et al. (2012)
281	Allan Hills	159.808	76.686	159.791	76.682	602	129	Airoldi et al. (2012)
282	Allan Hills	159.802	76.684	159.799	76.680	378	164	Airoldi et al. (2012)
283	Allan Hills	159.793	76.679	159.791	76.678	112	151	Airoldi et al. (2012)
284	Allan Hills	159.798	76.680	159.786	76.675	695	147	Airoldi et al. (2012)
285	Allan Hills	159.793	76.680	159.785	76.675	547	151	Airoldi et al. (2012)
286	Allan Hills	159.795	76.682	159.785	76.676	735	154	Airoldi et al. (2012)
287	Allan Hills	159.796	76.682	159.788	76.679	397	142	Airoldi et al. (2012)
288	Allan Hills	159.794	76.684	159.789	76.681	409	156	Airoldi et al. (2012)
289	Allan Hills	159.785	76.678	159.782	76.677	225	156	Airoldi et al. (2012)
290	Allan Hills	159.786	76.681	159.778	76.677	493	148	Airoldi et al. (2012)
291	Allan Hills	159.778	76.678	159.777	76.677	98	174	Airoldi et al. (2012)
292	Allan Hills	159.792	76.687	159.791	76.682	557	173	Airoldi et al. (2012)
293	Allan Hills	159.788	76.687	159.784	76.681	676	165	Airoldi et al. (2012)
294	Allan Hills	159.786	76.686	159.769	76.678	1089	150	Airoldi et al. (2012)
295	Allan Hills	159.784	76.686	159.784	76.685	138	176	Airoldi et al. (2012)
296	Allan Hills	159.784	76.687	159.774	76.682	629	151	Airoldi et al. (2012)
297	Allan Hills	159.772	76.681	159.766	76.678	364	150	Airoldi et al. (2012)
298	Allan Hills	159.765	76.678	159.769	76.679	134	129	Airoldi et al. (2012)
299	Allan Hills	159.768	76.681	159.758	76.679	353	125	Airoldi et al. (2012)
300	Allan Hills	159.779	76.688	159.775	76.685	346	154	Airoldi et al. (2012)
301	Allan Hills	159.768	76.684	159.750	76.680	646	127	Airoldi et al. (2012)
302	Allan Hills	159.763	76.682	159.747	76.683	415	79	Airoldi et al. (2012)
303	Allan Hills	159.764	76.684	159.760	76.682	224	149	Airoldi et al. (2012)
304	Allan Hills	159.765	76.685	159.760	76.685	150	103	Airoldi et al. (2012)

305	Allan Hills	159.880	76.694	159.873	76.697	329	29	Airoldi et al. (2012)
306	Allan Hills	159.837	76.707	159.825	76.705	413	122	Airoldi et al. (2012)
307	Allan Hills	159.799	76.708	159.798	76.698	1092	174	Airoldi et al. (2012)
308	Allan Hills	159.800	76.702	159.797	76.698	487	164	Airoldi et al. (2012)
309	Allan Hills	159.799	76.698	159.797	76.693	525	170	Airoldi et al. (2012)
310	Allan Hills	159.811	76.701	159.840	76.697	870	57	Airoldi et al. (2012)
311	Allan Hills	159.803	76.698	159.806	76.703	667	166	Airoldi et al. (2012)
312	Allan Hills	159.772	76.709	159.781	76.702	970	10	Airoldi et al. (2012)
313	Allan Hills	159.782	76.688	159.788	76.699	1280	168	Airoldi et al. (2012)
314	Allan Hills	159.789	76.698	159.787	76.700	226	7	Airoldi et al. (2012)
315	Allan Hills	159.786	76.698	159.784	76.698	115	27	Airoldi et al. (2012)
316	Allan Hills	159.785	76.696	159.772	76.698	419	50	Airoldi et al. (2012)
317	Allan Hills	159.781	76.695	159.771	76.703	1026	10	Airoldi et al. (2012)
318	Allan Hills	159.770	76.702	159.779	76.702	237	88	Airoldi et al. (2012)
319	Allan Hills	159.764	76.703	159.764	76.695	981	175	Airoldi et al. (2012)
320	Allan Hills	159.753	76.699	159.751	76.692	759	170	Airoldi et al. (2012)
321	Allan Hills	159.782	76.695	159.751	76.692	875	107	Airoldi et al. (2012)
322	Allan Hills	159.776	76.699	159.758	76.691	1034	147	Airoldi et al. (2012)
323	Allan Hills	159.759	76.699	159.756	76.691	831	169	Airoldi et al. (2012)
324	Allan Hills	159.749	76.706	159.746	76.690	1789	172	Airoldi et al. (2012)
325	Allan Hills	159.748	76.691	159.747	76.688	286	165	Airoldi et al. (2012)
326	Allan Hills	159.747	76.692	159.745	76.690	224	162	Airoldi et al. (2012)
327	Allan Hills	159.760	76.688	159.757	76.687	213	147	Airoldi et al. (2012)
328	Allan Hills	159.764	76.689	159.748	76.684	810	142	Airoldi et al. (2012)
329	Allan Hills	159.758	76.689	159.747	76.684	611	146	Airoldi et al. (2012)
330	Allan Hills	159.742	76.690	159.747	76.683	739	4	Airoldi et al. (2012)
331	Allan Hills	159.800	76.715	159.780	76.719	751	39	Airoldi et al. (2012)
332	Allan Hills	159.785	76.715	159.773	76.716	368	61	Airoldi et al. (2012)
333	Allan Hills	159.771	76.717	159.782	76.713	525	28	Airoldi et al. (2012)
334	Allan Hills	159.727	76.715	159.707	76.713	553	109	Airoldi et al. (2012)
335	Allan Hills	159.717	76.723	159.707	76.723	249	81	Airoldi et al. (2012)
336	Allan Hills	159.679	76.720	159.605	76.715	2003	99	Airoldi et al. (2012)
337	Allan Hills	159.567	76.713	159.570	76.707	677	2	Airoldi et al. (2012)
338	Allan Hills	159.616	76.738	159.564	76.733	1518	109	Airoldi et al. (2012)
339	Allan Hills	159.595	76.737	159.561	76.747	1614	31	Airoldi et al. (2012)
340	Allan Hills	159.798	76.739	159.725	76.738	1955	88	Airoldi et al. (2012)
341	Allan Hills	159.751	76.729	159.746	76.730	233	30	Airoldi et al. (2012)
342	Allan Hills	159.726	76.723	159.720	76.726	349	21	Airoldi et al. (2012)
343	Allan Hills	159.714	76.728	159.729	76.727	390	71	Airoldi et al. (2012)
344	Allan Hills	159.621	76.666	159.608	76.663	452	129	Airoldi et al. (2012)
345	Allan Hills	159.613	76.666	159.609	76.665	200	149	Airoldi et al. (2012)
346	Allan Hills	159.608	76.667	159.600	76.661	747	158	Airoldi et al. (2012)

347	Allan Hills	159.607	76.667	159.600	76.662	644	158	Airoldi et al. (2012)
348	Allan Hills	159.599	76.665	159.596	76.662	290	162	Airoldi et al. (2012)
349	Allan Hills	159.624	76.661	159.609	76.659	474	122	Airoldi et al. (2012)
350	Allan Hills	159.628	76.660	159.613	76.657	508	124	Airoldi et al. (2012)
351	Allan Hills	159.622	76.657	159.615	76.656	226	112	Airoldi et al. (2012)
352	Allan Hills	159.627	76.654	159.634	76.652	321	29	Airoldi et al. (2012)
353	Allan Hills	159.607	76.627	159.596	76.629	357	48	Airoldi et al. (2012)
354	Mt Kuipers	Not specified	68	Airoldi (2011)				
355	Mt Kuipers	Not specified	180	Airoldi (2011)				
356	Mt Kuipers	Not specified	157	Airoldi (2011)				
357	Mt Kuipers	Not specified	80	Airoldi (2011)				
358	Terra Cotta Mountain	Not specified	5	Muirhead et al. (2012)				
359	Terra Cotta Mountain	Not specified	18	Muirhead et al. (2012)				
360	Terra Cotta Mountain	Not specified	20	Muirhead et al. (2012)				
361	Terra Cotta Mountain	Not specified	32	Muirhead et al. (2012)				
362	Terra Cotta Mountain	Not specified	40	Muirhead et al. (2012)				
363	Terra Cotta Mountain	Not specified	44	Muirhead et al. (2012)				
364	Terra Cotta Mountain	Not specified	45	Muirhead et al. (2012)				
365	Terra Cotta Mountain	Not specified	50	Muirhead et al. (2012)				
366	Terra Cotta Mountain	Not specified	52	Muirhead et al. (2012)				
367	Terra Cotta Mountain	Not specified	Not specified	Not specified	Not specified	1409	55	Morisson (1989)
368	Terra Cotta Mountain	Not specified	56	Muirhead et al. (2012)				
369	Terra Cotta Mountain	Not specified	Not specified	Not specified	Not specified	1474	62	Morisson (1989)
370	Terra Cotta Mountain	Not specified	62	Muirhead et al. (2012)				
371	Terra Cotta Mountain	Not specified	Not specified	Not specified	Not specified	1674	65	Morisson (1989)
372	Terra Cotta Mountain	Not specified	Not specified	Not specified	Not specified	1477	65	Morisson (1989)
373	Terra Cotta Mountain	Not specified	Not specified	Not specified	Not specified	1482	65	Morisson (1989)
374	Terra Cotta Mountain	Not specified	Not specified	Not specified	Not specified	867	65	Morisson (1989)
375	Terra Cotta Mountain	Not specified	65	Muirhead et al. (2012)				

376	Terra Cotta Mountain	Not specified	65	Muirhead et al. (2012)				
377	Terra Cotta Mountain	Not specified	66	Muirhead et al. (2012)				
378	Terra Cotta Mountain	Not specified	66	Muirhead et al. (2012)				
379	Terra Cotta Mountain	Not specified	Not specified	Not specified	Not specified	1114	67	Morisson (1989)
380	Terra Cotta Mountain	Not specified	Not specified	Not specified	Not specified	1099	67	Morisson (1989)
381	Terra Cotta Mountain	Not specified	67	Muirhead et al. (2012)				
382	Terra Cotta Mountain	Not specified	69	Muirhead et al. (2012)				
383	Terra Cotta Mountain	Not specified	70	Muirhead et al. (2012)				
384	Terra Cotta Mountain	Not specified	77	Muirhead et al. (2012)				
385	Terra Cotta Mountain	Not specified	84	Muirhead et al. (2012)				
386	Terra Cotta Mountain	Not specified	91	Muirhead et al. (2012)				
387	Terra Cotta Mountain	Not specified	92	Muirhead et al. (2012)				
388	Terra Cotta Mountain	Not specified	102	Muirhead et al. (2012)				
389	Terra Cotta Mountain	Not specified	108	Muirhead et al. (2012)				
390	Terra Cotta Mountain	Not specified	148	Muirhead et al. (2012)				
391	Terra Cotta Mountain	Not specified	150	Muirhead et al. (2012)				
392	Terra Cotta Mountain	Not specified	150	Muirhead et al. (2012)				
393	Terra Cotta Mountain	Not specified	150	Muirhead et al. (2012)				
394	Terra Cotta Mountain	Not specified	154	Muirhead et al. (2012)				
395	Terra Cotta Mountain	Not specified	156	Muirhead et al. (2012)				
396	Terra Cotta Mountain	Not specified	158	Muirhead et al. (2012)				
397	Terra Cotta Mountain	Not specified	173	Muirhead et al. (2012)				
398	Terra Cotta Mountain	Not specified	175	Muirhead et al. (2012)				
399	Shapeless Mtn	Not specified	Not specified	Not specified	Not specified	40	159	Korsch (1984)
400	Shapeless Mtn	Not specified	Not specified	Not specified	Not specified	1000	103	Korsch (1984)
401	Coombs Hills	159.941	76.755	159.926	76.757	433	56	Guegan (2006)
402	Coombs Hills	159.956	76.754	159.952	76.755	297	24	Guegan (2006)

403	Coombs Hills	159.955	76.754	159.948	76.755	225	62	Guegan (2006)
404	Coombs Hills	159.947	76.755	159.950	76.756	159	140	Guegan (2006)
405	Coombs Hills	159.965	76.758	159.973	76.758	220	106	Guegan (2006)
406	Coombs Hills	159.960	76.758	159.963	76.758	111	121	Guegan (2006)
407	Coombs Hills	159.972	76.759	159.974	76.760	89	147	Guegan (2006)
408	Coombs Hills	159.955	76.758	159.963	76.759	228	114	Guegan (2006)
409	Coombs Hills	159.958	76.759	159.961	76.761	218	148	Guegan (2006)
410	Coombs Hills	159.930	76.761	159.938	76.761	199	93	Guegan (2006)
411	Coombs Hills	159.936	76.761	159.942	76.763	242	133	Guegan (2006)
412	Coombs Hills	159.928	76.762	159.933	76.763	171	125	Guegan (2006)
413	Coombs Hills	159.937	76.764	159.941	76.764	106	90	Guegan (2006)
414	Coombs Hills	159.947	76.762	159.955	76.761	209	57	Guegan (2006)
415	Coombs Hills	159.958	76.761	159.959	76.762	55	126	Guegan (2006)
416	Coombs Hills	159.964	76.762	159.969	76.762	163	120	Guegan (2006)
417	Coombs Hills	159.970	76.761	159.970	76.762	99	170	Guegan (2006)
418	Coombs Hills	159.851	76.762	159.854	76.763	129	136	Guegan (2006)
419	Coombs Hills	159.973	76.762	159.970	76.764	230	12	Guegan (2006)
420	Coombs Hills	159.973	76.764	159.971	76.765	70	35	Guegan (2006)
421	Coombs Hills	159.973	76.764	159.982	76.765	316	123	Guegan (2006)
422	Coombs Hills	159.974	76.764	159.982	76.766	266	123	Guegan (2006)
423	Coombs Hills	159.976	76.763	159.987	76.765	344	121	Guegan (2006)
424	Coombs Hills	159.961	76.766	159.963	76.766	99	128	Guegan (2006)
425	Coombs Hills	159.967	76.766	159.963	76.766	114	63	Guegan (2006)
426	Coombs Hills	159.988	76.765	159.984	76.766	151	38	Guegan (2006)
427	Coombs Hills	159.990	76.766	159.981	76.769	367	40	Guegan (2006)
428	Coombs Hills	159.989	76.767	159.983	76.769	241	36	Guegan (2006)
429	Coombs Hills	159.970	76.768	159.961	76.767	261	115	Guegan (2006)
430	Coombs Hills	160.035	76.770	160.023	76.768	414	125	Guegan (2006)
431	Coombs Hills	159.954	76.766	159.949	76.770	425	14	Guegan (2006)
432	Coombs Hills	159.912	76.764	159.919	76.766	303	136	Guegan (2006)
433	Coombs Hills	159.908	76.766	159.912	76.767	159	126	Guegan (2006)
434	Coombs Hills	159.845	76.771	159.842	76.772	213	16	Guegan (2006)
435	Coombs Hills	159.840	76.771	159.843	76.771	102	119	Guegan (2006)
436	Coombs Hills	159.832	76.771	159.830	76.772	98	30	Guegan (2006)
437	Coombs Hills	159.831	76.770	159.830	76.773	335	179	Guegan (2006)
438	Coombs Hills	159.792	76.772	159.786	76.776	511	13	Guegan (2006)
439	Coombs Hills	159.801	76.773	159.797	76.775	260	19	Guegan (2006)
440	Coombs Hills	159.790	76.776	159.788	76.777	125	19	Guegan (2006)
441	Coombs Hills	159.788	76.777	159.784	76.777	132	40	Guegan (2006)
442	Coombs Hills	159.834	76.775	159.834	76.778	292	176	Guegan (2006)
443	Coombs Hills	159.817	76.777	159.819	76.779	205	161	Guegan (2006)
444	Coombs Hills	159.808	76.780	159.812	76.780	96	106	Guegan (2006)

445	Coombs Hills	159.815	76.779	159.817	76.780	67	139	Guegan (2006)
446	Coombs Hills	159.823	76.779	159.823	76.780	163	1	Guegan (2006)
447	Coombs Hills	159.822	76.780	159.820	76.781	68	34	Guegan (2006)
448	Coombs Hills	159.829	76.780	159.821	76.781	280	47	Guegan (2006)
449	Coombs Hills	159.830	76.780	159.829	76.781	181	180	Guegan (2006)
450	Coombs Hills	159.846	76.774	159.849	76.774	124	135	Guegan (2006)
451	Coombs Hills	159.847	76.773	159.847	76.774	81	176	Guegan (2006)
452	Coombs Hills	159.850	76.775	159.851	76.775	67	145	Guegan (2006)
453	Coombs Hills	159.879	76.774	159.880	76.774	79	140	Guegan (2006)
454	Coombs Hills	159.977	76.769	159.981	76.770	153	136	Guegan (2006)
455	Coombs Hills	159.979	76.770	159.983	76.771	166	136	Guegan (2006)
456	Coombs Hills	159.983	76.771	159.986	76.772	122	133	Guegan (2006)
457	Coombs Hills	159.989	76.772	159.991	76.773	52	136	Guegan (2006)
458	Coombs Hills	159.950	76.773	159.954	76.775	217	152	Guegan (2006)
459	Coombs Hills	160.034	76.773	160.042	76.776	465	150	Guegan (2006)
460	Coombs Hills	160.045	76.776	160.044	76.778	209	5	Guegan (2006)
461	Coombs Hills	160.041	76.776	160.037	76.779	348	13	Guegan (2006)
462	Coombs Hills	160.040	76.781	160.037	76.780	133	132	Guegan (2006)
463	Coombs Hills	160.021	76.775	160.026	76.777	239	142	Guegan (2006)
464	Coombs Hills	160.026	76.777	160.024	76.778	125	26	Guegan (2006)
465	Coombs Hills	160.020	76.776	160.021	76.777	133	154	Guegan (2006)
466	Coombs Hills	160.022	76.777	160.020	76.777	56	60	Guegan (2006)
467	Coombs Hills	160.019	76.777	160.010	76.777	218	83	Guegan (2006)
468	Coombs Hills	160.013	76.778	160.005	76.777	236	117	Guegan (2006)
469	Coombs Hills	160.023	76.778	160.019	76.779	133	37	Guegan (2006)
470	Coombs Hills	160.029	76.778	160.026	76.779	185	14	Guegan (2006)
471	Coombs Hills	160.022	76.779	160.024	76.779	65	137	Guegan (2006)
472	Coombs Hills	160.023	76.779	160.024	76.780	75	158	Guegan (2006)
473	Coombs Hills	160.024	76.780	160.030	76.780	160	98	Guegan (2006)
474	Coombs Hills	160.017	76.779	160.016	76.780	137	3	Guegan (2006)
475	Coombs Hills	160.019	76.780	160.019	76.780	66	175	Guegan (2006)
476	Coombs Hills	160.033	76.781	160.030	76.781	92	44	Guegan (2006)
477	Coombs Hills	160.030	76.782	160.030	76.783	79	163	Guegan (2006)
478	Coombs Hills	160.032	76.783	160.040	76.783	213	89	Guegan (2006)
479	Coombs Hills	160.037	76.784	160.046	76.784	227	83	Guegan (2006)
480	Coombs Hills	160.012	76.781	160.015	76.781	92	133	Guegan (2006)
481	Coombs Hills	160.010	76.781	160.012	76.782	72	133	Guegan (2006)
482	Coombs Hills	160.008	76.781	160.004	76.782	168	40	Guegan (2006)
483	Coombs Hills	160.012	76.781	160.014	76.781	85	136	Guegan (2006)
484	Coombs Hills	160.011	76.781	160.013	76.781	75	130	Guegan (2006)
485	Coombs Hills	159.997	76.776	159.999	76.777	76	135	Guegan (2006)
486	Coombs Hills	160.004	76.777	159.997	76.779	317	33	Guegan (2006)

487	Coombs Hills	159.993	76.780	159.994	76.780	36	135	Guegan (2006)
488	Coombs Hills	159.976	76.779	159.980	76.779	110	108	Guegan (2006)
489	Coombs Hills	159.949	76.780	159.953	76.780	122	112	Guegan (2006)
490	Coombs Hills	159.949	76.780	159.952	76.781	79	111	Guegan (2006)
491	Coombs Hills	160.061	76.784	160.055	76.785	166	70	Guegan (2006)
492	Coombs Hills	160.053	76.785	160.020	76.784	876	91	Guegan (2006)
493	Coombs Hills	160.007	76.783	160.011	76.784	105	100	Guegan (2006)
494	Coombs Hills	160.018	76.784	160.013	76.784	144	97	Guegan (2006)
495	Coombs Hills	160.012	76.784	160.003	76.785	298	53	Guegan (2006)
496	Coombs Hills	159.995	76.785	159.995	76.786	94	173	Guegan (2006)
497	Coombs Hills	159.979	76.785	159.981	76.785	60	81	Guegan (2006)
498	Coombs Hills	159.985	76.786	159.982	76.786	90	73	Guegan (2006)
499	Coombs Hills	159.987	76.786	159.984	76.786	92	76	Guegan (2006)
500	Coombs Hills	159.990	76.787	159.986	76.789	277	16	Guegan (2006)
501	Coombs Hills	159.984	76.787	159.975	76.787	263	110	Guegan (2006)
502	Coombs Hills	159.976	76.789	159.974	76.788	68	124	Guegan (2006)
503	Coombs Hills	159.972	76.788	159.975	76.789	96	132	Guegan (2006)
504	Coombs Hills	159.976	76.790	159.978	76.791	80	134	Guegan (2006)
505	Coombs Hills	159.979	76.790	159.981	76.791	176	159	Guegan (2006)
506	Coombs Hills	159.980	76.791	159.982	76.792	108	143	Guegan (2006)
507	Coombs Hills	159.980	76.792	159.978	76.793	90	18	Guegan (2006)
508	Coombs Hills	159.979	76.792	159.976	76.794	230	16	Guegan (2006)
509	Coombs Hills	159.969	76.791	159.970	76.791	34	118	Guegan (2006)
510	Coombs Hills	159.962	76.789	159.965	76.789	77	113	Guegan (2006)
511	Coombs Hills	159.958	76.791	159.960	76.791	65	112	Guegan (2006)
512	Coombs Hills	159.966	76.792	159.969	76.792	107	118	Guegan (2006)
513	Coombs Hills	159.966	76.792	159.967	76.792	50	115	Guegan (2006)
514	Coombs Hills	159.963	76.791	159.964	76.792	82	160	Guegan (2006)
515	Coombs Hills	159.961	76.791	159.963	76.792	60	141	Guegan (2006)
516	Coombs Hills	159.962	76.793	159.963	76.794	90	150	Guegan (2006)
517	Coombs Hills	159.943	76.784	159.941	76.785	155	13	Guegan (2006)
518	Coombs Hills	159.940	76.785	159.937	76.785	78	122	Guegan (2006)
519	Coombs Hills	159.937	76.787	159.939	76.788	101	145	Guegan (2006)
520	Coombs Hills	159.949	76.790	159.951	76.792	201	159	Guegan (2006)
521	Coombs Hills	160.047	76.790	160.048	76.792	149	167	Guegan (2006)
522	Coombs Hills	160.045	76.790	160.039	76.791	196	52	Guegan (2006)
523	Coombs Hills	160.047	76.793	160.044	76.794	97	58	Guegan (2006)
524	Coombs Hills	160.044	76.793	160.044	76.794	48	177	Guegan (2006)
525	Coombs Hills	160.034	76.789	160.020	76.805	1897	6	Guegan (2006)
526	Coombs Hills	160.019	76.805	160.022	76.806	125	138	Guegan (2006)
527	Coombs Hills	160.022	76.806	160.026	76.808	278	151	Guegan (2006)
528	Coombs Hills	160.028	76.807	160.001	76.803	847	119	Guegan (2006)

529	Coombs Hills	160.020	76.805	160.012	76.804	200	102	Guegan (2006)
530	Coombs Hills	160.015	76.804	160.012	76.805	69	55	Guegan (2006)
531	Coombs Hills	160.009	76.804	160.008	76.806	133	6	Guegan (2006)
532	Coombs Hills	160.006	76.804	160.005	76.805	106	6	Guegan (2006)
533	Coombs Hills	160.039	76.807	160.041	76.809	257	164	Guegan (2006)
534	Coombs Hills	160.040	76.808	160.035	76.809	148	58	Guegan (2006)
535	Coombs Hills	160.042	76.802	160.039	76.801	108	118	Guegan (2006)
536	Coombs Hills	160.040	76.801	160.024	76.800	495	113	Guegan (2006)
537	Coombs Hills	160.025	76.799	160.023	76.799	47	89	Guegan (2006)
538	Coombs Hills	160.023	76.800	160.012	76.799	296	109	Guegan (2006)
539	Coombs Hills	159.998	76.799	159.995	76.802	297	11	Guegan (2006)
540	Coombs Hills	159.997	76.801	159.995	76.802	124	17	Guegan (2006)
541	Coombs Hills	160.002	76.801	160.003	76.800	169	0	Guegan (2006)
542	Coombs Hills	160.014	76.797	160.011	76.797	65	84	Guegan (2006)
543	Coombs Hills	160.017	76.793	160.018	76.794	106	174	Guegan (2006)
544	Coombs Hills	160.003	76.795	160.008	76.795	114	73	Guegan (2006)
545	Coombs Hills	160.012	76.794	160.012	76.795	67	174	Guegan (2006)
546	Coombs Hills	160.013	76.795	160.018	76.795	127	79	Guegan (2006)
547	Coombs Hills	160.018	76.794	160.023	76.794	119	84	Guegan (2006)
548	Coombs Hills	159.971	76.797	159.969	76.799	204	4	Guegan (2006)
549	Coombs Hills	159.974	76.796	159.970	76.796	103	84	Guegan (2006)
550	Coombs Hills	159.970	76.796	159.967	76.798	226	13	Guegan (2006)
551	Coombs Hills	159.965	76.798	159.966	76.797	193	2	Guegan (2006)
552	Coombs Hills	159.965	76.797	159.962	76.796	142	139	Guegan (2006)
553	Coombs Hills	159.965	76.796	159.966	76.797	67	144	Guegan (2006)
554	Coombs Hills	159.966	76.796	159.967	76.797	44	143	Guegan (2006)
555	Coombs Hills	159.958	76.796	159.963	76.797	202	136	Guegan (2006)
556	Coombs Hills	159.969	76.799	159.967	76.801	173	12	Guegan (2006)
557	Coombs Hills	159.958	76.800	159.968	76.800	248	93	Guegan (2006)
558	Coombs Hills	159.956	76.799	159.956	76.801	158	172	Guegan (2006)
559	Coombs Hills	159.948	76.800	159.935	76.800	346	100	Guegan (2006)
560	Coombs Hills	159.936	76.799	159.940	76.800	142	141	Guegan (2006)
561	Coombs Hills	159.942	76.798	159.944	76.799	104	135	Guegan (2006)
562	Coombs Hills	159.952	76.801	159.954	76.802	190	158	Guegan (2006)
563	Coombs Hills	159.968	76.803	159.956	76.804	379	57	Guegan (2006)
564	Coombs Hills	159.952	76.805	159.954	76.806	176	157	Guegan (2006)
565	Coombs Hills	159.903	76.805	159.902	76.806	152	11	Guegan (2006)
566	Coombs Hills	159.916	76.806	159.914	76.807	93	33	Guegan (2006)
567	Coombs Hills	159.920	76.804	159.918	76.806	239	9	Guegan (2006)
568	Coombs Hills	159.921	76.808	159.925	76.808	87	82	Guegan (2006)
569	Coombs Hills	159.919	76.810	159.917	76.811	74	38	Guegan (2006)
570	Coombs Hills	159.939	76.808	159.936	76.810	160	24	Guegan (2006)

571	Coombs Hills	159.939	76.809	159.941	76.809	62	125	Guegan (2006)
572	Coombs Hills	159.943	76.809	159.937	76.810	203	48	Guegan (2006)
573	Coombs Hills	159.953	76.807	159.953	76.808	184	174	Guegan (2006)
574	Coombs Hills	159.958	76.807	159.970	76.806	352	64	Guegan (2006)
575	Coombs Hills	159.964	76.807	159.955	76.810	388	31	Guegan (2006)
576	Coombs Hills	159.955	76.808	159.950	76.810	213	33	Guegan (2006)
577	Coombs Hills	159.928	76.812	159.932	76.812	95	88	Guegan (2006)
578	Coombs Hills	159.928	76.812	159.933	76.813	123	101	Guegan (2006)
579	Coombs Hills	159.958	76.808	159.954	76.810	178	31	Guegan (2006)
580	Coombs Hills	159.953	76.809	159.956	76.812	305	163	Guegan (2006)
581	Coombs Hills	159.956	76.810	159.955	76.811	75	29	Guegan (2006)
582	Coombs Hills	159.950	76.813	159.957	76.813	182	70	Guegan (2006)
583	Coombs Hills	159.957	76.812	159.961	76.815	366	157	Guegan (2006)
584	Coombs Hills	159.955	76.815	159.953	76.815	62	62	Guegan (2006)
585	Coombs Hills	159.959	76.809	159.960	76.811	191	169	Guegan (2006)
586	Coombs Hills	159.959	76.811	159.959	76.811	72	7	Guegan (2006)
587	Coombs Hills	159.989	76.805	159.991	76.808	350	169	Guegan (2006)
588	Coombs Hills	159.991	76.812	159.999	76.811	231	63	Guegan (2006)
589	Coombs Hills	160.003	76.809	160.001	76.810	98	27	Guegan (2006)
590	Coombs Hills	160.001	76.810	160.009	76.809	269	44	Guegan (2006)
591	Coombs Hills	160.009	76.810	160.015	76.809	201	56	Guegan (2006)
592	Coombs Hills	159.805	76.797	159.817	76.799	394	120	Guegan (2006)
593	Coombs Hills	159.823	76.800	159.831	76.802	253	120	Guegan (2006)
594	Coombs Hills	159.833	76.800	159.833	76.803	382	174	Guegan (2006)
595	Coombs Hills	159.841	76.794	159.843	76.795	88	128	Guegan (2006)
596	Coombs Hills	159.844	76.794	159.844	76.795	100	165	Guegan (2006)
597	Coombs Hills	159.844	76.795	159.847	76.795	111	121	Guegan (2006)
598	Coombs Hills	159.878	76.800	159.879	76.799	35	36	Guegan (2006)
599	Coombs Hills	159.883	76.798	159.882	76.799	64	27	Guegan (2006)
600	Coombs Hills	159.881	76.798	159.881	76.799	46	0	Guegan (2006)
601	Coombs Hills	159.881	76.797	159.880	76.797	50	72	Guegan (2006)
602	Coombs Hills	159.872	76.794	159.871	76.793	51	141	Guegan (2006)
603	Coombs Hills	159.873	76.793	159.871	76.793	89	131	Guegan (2006)
604	Coombs Hills	159.877	76.793	159.875	76.792	61	127	Guegan (2006)
605	Coombs Hills	159.881	76.791	159.875	76.789	277	142	Guegan (2006)
606	Coombs Hills	159.882	76.790	159.883	76.789	63	9	Guegan (2006)
607	Coombs Hills	159.890	76.789	159.884	76.789	166	102	Guegan (2006)
608	Coombs Hills	159.882	76.788	159.879	76.788	109	128	Guegan (2006)
609	Coombs Hills	159.890	76.788	159.882	76.787	241	101	Guegan (2006)
610	Coombs Hills	159.886	76.787	159.881	76.785	246	138	Guegan (2006)
611	Coombs Hills	159.887	76.785	159.884	76.786	89	43	Guegan (2006)
612	Coombs Hills	159.869	76.785	159.861	76.784	240	108	Guegan (2006)

613	Coombs Hills	159.882	76.784	159.879	76.784	81	93	Guegan (2006)
614	Coombs Hills	159.877	76.784	159.875	76.784	48	116	Guegan (2006)
615	Coombs Hills	159.874	76.784	159.873	76.784	49	131	Guegan (2006)
616	Coombs Hills	159.880	76.781	159.883	76.781	69	105	Guegan (2006)
617	Coombs Hills	159.885	76.781	159.886	76.782	31	114	Guegan (2006)
618	Coombs Hills	159.887	76.782	159.888	76.782	27	130	Guegan (2006)
619	Coombs Hills	159.888	76.780	159.889	76.780	43	112	Guegan (2006)
620	Coombs Hills	159.888	76.779	159.891	76.780	77	112	Guegan (2006)
621	Coombs Hills	159.851	76.787	159.846	76.784	430	156	Guegan (2006)
622	Coombs Hills	159.847	76.784	159.852	76.786	342	150	Guegan (2006)
623	Coombs Hills	159.848	76.785	159.840	76.785	214	62	Guegan (2006)
624	Coombs Hills	159.844	76.784	159.839	76.784	139	80	Guegan (2006)
625	Coombs Hills	159.794	76.786	159.789	76.787	171	40	Guegan (2006)
626	Coombs Hills	159.781	76.787	159.778	76.787	86	137	Guegan (2006)
627	Coombs Hills	159.793	76.787	159.791	76.787	56	119	Guegan (2006)
628	Coombs Hills	159.798	76.786	159.809	76.785	286	66	Guegan (2006)
629	Mt Fleming	160.019	77.568	160.023	77.573	592	166	Pyne (1984)
630	Mt Fleming	160.116	77.557	160.118	77.559	232	162	Pyne (1984)
631	Mt Fleming	160.105	77.554	160.114	77.551	356	33	Pyne (1984)
632	Mt Fleming	160.145	77.553	160.166	77.551	552	66	Pyne (1984)
633	Mt Fleming	160.263	77.528	160.248	77.531	479	44	Pyne (1984)
634	Mt Fleming	160.238	77.542	160.251	77.548	698	148	Pyne (1984)
635	Mt Fleming	160.218	77.544	160.244	77.549	870	128	Pyne (1984)
636	Mt Fleming	160.261	77.545	160.260	77.547	270	180	Pyne (1984)
637	Mt Fleming	160.309	77.545	160.306	77.550	556	3	Pyne (1984)
638	Mt Fleming	160.285	77.553	160.292	77.557	503	155	Pyne (1984)
639	Mt Fleming	160.310	77.557	160.315	77.560	410	157	Pyne (1984)
640	Mt Fleming	160.289	77.561	160.299	77.563	315	127	Pyne (1984)
641	Mt Fleming	160.262	77.554	160.284	77.560	897	140	Pyne (1984)
642	Mt Fleming	160.264	77.556	160.272	77.559	389	143	Pyne (1984)
643	Mt Fleming	160.268	77.556	160.289	77.566	1184	150	Pyne (1984)
644	Mt Fleming	160.245	77.562	160.276	77.565	851	113	Pyne (1984)

Table D2. Field measurements of dike attitudes from Allan Hills, Terra Cotta Mountain and Mt Kuipers (South Victoria Land).

Location	Strike	Dip	Sense	Reference
Allan Hills (Set A)	138	60	S	Muirhead et al. (2012)
Allan Hills (Set A)	112	52	S	Muirhead et al. (2012)
Allan Hills (Set A)	90	17	N	Muirhead et al. (2012)
Allan Hills (Set A)	6	14	E	Muirhead et al. (2012)
Allan Hills (Set A)	155	34	S	Muirhead et al. (2012)
Allan Hills (Set A)	140	68	S	Muirhead et al. (2012)
Allan Hills (Set A)	130	78	S	Muirhead et al. (2012)
Allan Hills (Set A)	148	78	S	Muirhead et al. (2012)
Allan Hills (Set A)	136	78	S	Muirhead et al. (2012)
Allan Hills (Set A)	113	80	S	Muirhead et al. (2012)
Allan Hills (Set A)	120	21	S	Muirhead et al. (2012)
Allan Hills (Set A)	139	40	S	Muirhead et al. (2012)
Allan Hills (Set A)	151	39	S	Muirhead et al. (2012)
Allan Hills (Set A)	165	30	S	Muirhead et al. (2012)
Allan Hills (Set A)	151	31	W	Muirhead et al. (2012)
Allan Hills (Set A)	153	40	W	Muirhead et al. (2012)
Allan Hills (Set A)	146	38	W	Muirhead et al. (2012)
Allan Hills (Set A)	155	28	W	Muirhead et al. (2012)
Allan Hills (Set A)	160	30	W	Muirhead et al. (2012)
Allan Hills (Set A)	162	50	W	Muirhead et al. (2012)
Allan Hills (Set A)	149	34	W	Muirhead et al. (2012)
Allan Hills (Set A)	141	52	W	Muirhead et al. (2012)
Allan Hills (Set A)	146	48	W	Muirhead et al. (2012)
Allan Hills (Set A)	122	44	W	Muirhead et al. (2012)
Allan Hills (Set A)	136	42	W	Muirhead et al. (2012)
Allan Hills (Set A)	126	44	W	Muirhead et al. (2012)
Allan Hills (Set A)	112	50	W	Muirhead et al. (2012)
Allan Hills (Set A)	124	45	W	Muirhead et al. (2012)
Allan Hills (Set A)	142	45	W	Muirhead et al. (2012)
Allan Hills (Set A)	140	48	W	Muirhead et al. (2012)
Allan Hills (Set A)	140	48	W	Muirhead et al. (2012)
Allan Hills (Set A)	146	40	W	Muirhead et al. (2012)
Allan Hills (Set A)	105	40	W	Muirhead et al. (2012)

Allan Hills (Set A)	134	55	W	Muirhead et al. (2012)
Allan Hills (Set A)	166	80	W	Muirhead et al. (2012)
Allan Hills (Set A)	148	40	W	Muirhead et al. (2012)
Allan Hills (Set A)	140	21	W	Muirhead et al. (2012)
Allan Hills (Set A)	106	24	w	Muirhead et al. (2012)
Allan Hills (Set A)	25	35	w	Muirhead et al. (2012)
Allan Hills (Set A)	129	7	W	Muirhead et al. (2012)
Allan Hills (Set A)	6	18	W	Muirhead et al. (2012)
Allan Hills (Set A)	155	36	W	Muirhead et al. (2012)
Allan Hills (Set A)	162	41	W	Muirhead et al. (2012)
Allan Hills (Set A)	138	60	W	Muirhead et al. (2012)
Allan Hills (Set A)	148	78	W	Muirhead et al. (2012)
Allan Hills (Set A)	120	21	W	Muirhead et al. (2012)
Allan Hills (Set A)	114	41	W	Muirhead et al. (2012)
Allan Hills (Set A)	138	35	W	Muirhead et al. (2012)
Allan Hills (Set A)	151	39	W	Muirhead et al. (2012)
Allan Hills (Set A)	139	40	W	Muirhead et al. (2012)
Allan Hills (Set A)	130	78	W	Muirhead et al. (2012)
Allan Hills (Set A)	116	55	S	Muirhead et al. (2012)
Allan Hills (Set A)	151	31	W	Muirhead et al. (2012)
Allan Hills (Set A)	153	40	W	Muirhead et al. (2012)
Allan Hills (Set A)	146	38	W	Muirhead et al. (2012)
Allan Hills (Set A)	155	28	W	Muirhead et al. (2012)
Allan Hills (Set A)	154	80	W	Muirhead et al. (2012)
Allan Hills (Set A)	130	60	S	Muirhead et al. (2012)
Allan Hills (Set A)	124	60	S	Muirhead et al. (2012)
Allan Hills (Set A)	133	58	S	Muirhead et al. (2012)
Allan Hills (Set A)	147	78	S	Muirhead et al. (2012)
Allan Hills (Set A)	130	62	S	Muirhead et al. (2012)
Allan Hills (Set A)	177	58	S	Muirhead et al. (2012)
Allan Hills (Set A)	175	60	S	Muirhead et al. (2012)
Allan Hills (Set A)	151	39	S	Muirhead et al. (2012)
Allan Hills (Set A)	165	30	S	Muirhead et al. (2012)
Allan Hills (Set A)	176	68	W	Muirhead et al. (2012)
Allan Hills (Set A)	154	64	W	Muirhead et al. (2012)
Allan Hills (Set A)	174	63	W	Muirhead et al. (2012)
Allan Hills (Set A)	168	70	W	Muirhead et al. (2012)

Allan Hills (Set A)	1	60	W	Muirhead et al. (2012)
Allan Hills (Set A)	158	56	W	Muirhead et al. (2012)
Allan Hills (Set A)	168	58	W	Muirhead et al. (2012)
Allan Hills (Set A)	165	57	W	Muirhead et al. (2012)
Allan Hills (Set A)	150	20	W	Muirhead et al. (2012)
Allan Hills (Set A)	154	34	W	Muirhead et al. (2012)
Allan Hills (Set A)	170	17	W	Muirhead et al. (2012)
Allan Hills (Set A)	142	50	W	Muirhead et al. (2012)
Allan Hills (Set A)	136	48	W	Muirhead et al. (2012)
Allan Hills (Set A)	176	70	W	Muirhead et al. (2012)
Allan Hills (Set A)	162	76	W	Muirhead et al. (2012)
Allan Hills (Set A)	3	48	W	Muirhead et al. (2012)
Allan Hills (Set A)	172	52	W	Muirhead et al. (2012)
Allan Hills (Set A)	164	66	W	Muirhead et al. (2012)
Allan Hills (Set A)	162	75	W	Muirhead et al. (2012)
Allan Hills (Set A)	169	70	W	Muirhead et al. (2012)
Allan Hills (Set A)	164	60	W	Muirhead et al. (2012)
Allan Hills (Set A)	168	52	W	Muirhead et al. (2012)
Allan Hills (Set A)	170	57	W	Muirhead et al. (2012)
Allan Hills (Set A)	10	38	W	Muirhead et al. (2012)
Allan Hills (Set A)	24	40	W	Muirhead et al. (2012)
Allan Hills (Set A)	174	54	W	Muirhead et al. (2012)
Allan Hills (Set A)	160	47	W	Muirhead et al. (2012)
Allan Hills (Set A)	153	38	W	Muirhead et al. (2012)
Allan Hills (Set A)	159	45	W	Muirhead et al. (2012)
Allan Hills (Set A)	134	66	W	Muirhead et al. (2012)
Allan Hills (Set A)	6	64	W	Muirhead et al. (2012)
Allan Hills (Set A)	170	80	W	Muirhead et al. (2012)
Allan Hills (Set A)	167	66	W	Muirhead et al. (2012)
Allan Hills (Set A)	162	60	W	Muirhead et al. (2012)
Allan Hills (Set A)	172	70	W	Muirhead et al. (2012)
Allan Hills (Set A)	165	72	W	Muirhead et al. (2012)
Allan Hills (Set A)	166	84	W	Muirhead et al. (2012)
Allan Hills (Set A)	165	76	W	Muirhead et al. (2012)
Allan Hills (Set A)	158	66	W	Muirhead et al. (2012)
Allan Hills (Set A)	158	68	W	Muirhead et al. (2012)
Allan Hills (Set A)	169	80	W	Muirhead et al. (2012)

Allan Hills (Set A)	151	73	W	Muirhead et al. (2012)
Allan Hills (Set A)	178	90	S	Muirhead et al. (2012)
Allan Hills (Set A)	153	70	W	Muirhead et al. (2012)
Allan Hills (Set A)	152	82	W	Muirhead et al. (2012)
Allan Hills (Set A)	160	78	W	Muirhead et al. (2012)
Allan Hills (Set A)	144	53	W	Muirhead et al. (2012)
Allan Hills (Set A)	150	63	W	Muirhead et al. (2012)
Allan Hills (Set A)	134	50	W	Muirhead et al. (2012)
Allan Hills (Set A)	150	42	W	Muirhead et al. (2012)
Allan Hills (Set A)	148	42	W	Muirhead et al. (2012)
Allan Hills (Set A)	136	40	W	Muirhead et al. (2012)
Allan Hills (Set A)	123	50	W	Muirhead et al. (2012)
Allan Hills (Set A)	132	50	W	Muirhead et al. (2012)
Allan Hills (Set A)	145	67	W	Muirhead et al. (2012)
Allan Hills (Set A)	142	66	W	Muirhead et al. (2012)
Allan Hills (Set A)	139	68	W	Muirhead et al. (2012)
Allan Hills (Set A)	142	45	W	Muirhead et al. (2012)
Allan Hills (Set A)	148	55	W	Muirhead et al. (2012)
Allan Hills (Set A)	136	65	W	Muirhead et al. (2012)
Allan Hills (Set A)	134	68	W	Muirhead et al. (2012)
Allan Hills (Set A)	118	16	W	Muirhead et al. (2012)
Allan Hills (Set A)	125	64	W	Muirhead et al. (2012)
Allan Hills (Set A)	145	75	W	Muirhead et al. (2012)
Allan Hills (Set A)	136	73	W	Muirhead et al. (2012)
Allan Hills (Set A)	158	75	W	Muirhead et al. (2012)
Allan Hills (Set A)	164	63	W	Muirhead et al. (2012)
Allan Hills (Set A)	166	60	W	Muirhead et al. (2012)
Allan Hills (Set A)	6	40	W	Muirhead et al. (2012)
Allan Hills (Set A)	25	62	W	Muirhead et al. (2012)
Allan Hills (Set A)	160	68	W	Muirhead et al. (2012)
Allan Hills (Set A)	161	86	W	Muirhead et al. (2012)
Allan Hills (Set A)	164	76	W	Muirhead et al. (2012)
Allan Hills (Set A)	163	74	W	Muirhead et al. (2012)
Allan Hills (Set A)	21	64	W	Muirhead et al. (2012)
Allan Hills (Set A)	16	68	W	Muirhead et al. (2012)
Allan Hills (Set A)	26	34	W	Muirhead et al. (2012)
Allan Hills (Set A)	51	52	W	Muirhead et al. (2012)

Allan Hills (Set A)	112	46	S	Muirhead et al. (2012)
Allan Hills (Set A)	109	40	S	Muirhead et al. (2012)
Allan Hills (Set A)	121	48	S	Muirhead et al. (2012)
Allan Hills (Set A)	122	65	S	Muirhead et al. (2012)
Allan Hills (Set A)	136	76	S	Muirhead et al. (2012)
Allan Hills (Set A)	157	82	S	Muirhead et al. (2012)
Allan Hills (Set A)	168	76	S	Muirhead et al. (2012)
Allan Hills (Set A)	28	30	W	Muirhead et al. (2012)
Allan Hills (Set A)	160	38	N	Muirhead et al. (2012)
Allan Hills (Set A)	184	22	W	Muirhead et al. (2012)
Allan Hills (Set A)	50	82	W	Muirhead et al. (2012)
Allan Hills (Set A)	5	40	W	Muirhead et al. (2012)
Allan Hills (Set A)	15	40	W	Muirhead et al. (2012)
Allan Hills (Set A)	171	46	W	Muirhead et al. (2012)
Allan Hills (Set A)	178	65	W	Muirhead et al. (2012)
Allan Hills (Set A)	24	53	W	Muirhead et al. (2012)
Allan Hills (Set A)	29	66	W	Muirhead et al. (2012)
Allan Hills (Set A)	171	52	W	Muirhead et al. (2012)
Allan Hills (Set A)	10	42	W	Muirhead et al. (2012)
Allan Hills (Set A)	12	56	W	Muirhead et al. (2012)
Allan Hills (Set A)	3	51	W	Muirhead et al. (2012)
Allan Hills (Set A)	0	52	W	Muirhead et al. (2012)
Allan Hills (Set A)	9	46	W	Muirhead et al. (2012)
Allan Hills (Set A)	172	26	W	Muirhead et al. (2012)
Allan Hills (Set A)	175	70	W	Muirhead et al. (2012)
Allan Hills (Set A)	29	52	W	Muirhead et al. (2012)
Allan Hills (Set A)	162	30	W	Muirhead et al. (2012)
Allan Hills (Set A)	163	69	W	Muirhead et al. (2012)
Allan Hills (Set A)	211	48	W	Muirhead et al. (2012)
Allan Hills (Set A)	188	76	W	Muirhead et al. (2012)
Allan Hills (Set A)	224	66	N	Muirhead et al. (2012)
Allan Hills (Set A)	209	52	W	Muirhead et al. (2012)
Allan Hills (Set A)	190	32	W	Muirhead et al. (2012)
Allan Hills (Set A)	193	38	W	Muirhead et al. (2012)
Allan Hills (Set A)	162	30	W	Muirhead et al. (2012)
Allan Hills (Set A)	53	45	W	Muirhead et al. (2012)
Allan Hills (Set A)	70	58	N	Muirhead et al. (2012)

Allan Hills (Set A)	138	47	W	Muirhead et al. (2012)
Allan Hills (Set A)	182	48	W	Muirhead et al. (2012)
Allan Hills (Set A)	166	43	W	Muirhead et al. (2012)
Allan Hills (Set A)	20	30	N	Muirhead et al. (2012)
Allan Hills (Set A)	18	50	N	Muirhead et al. (2012)
Allan Hills (Set A)	6	39	W	Muirhead et al. (2012)
Allan Hills (Set A)	4	46	W	Muirhead et al. (2012)
Allan Hills (Set A)	92	62	S	Muirhead et al. (2012)
Allan Hills (Set A)	106	60	S	Muirhead et al. (2012)
Allan Hills (Set A)	100	69	S	Muirhead et al. (2012)
Allan Hills (Set A)	80	30	S	Muirhead et al. (2012)
Allan Hills (Set A)	70	33	S	Muirhead et al. (2012)
Allan Hills (Set A)	92	40	S	Muirhead et al. (2012)
Allan Hills (Set A)	100	32	S	Muirhead et al. (2012)
Allan Hills (Set A)	95	41	S	Muirhead et al. (2012)
Allan Hills (Set A)	84	30	S	Muirhead et al. (2012)
Allan Hills (Set A)	73	28	S	Muirhead et al. (2012)
Allan Hills (Set A)	116	30	S	Muirhead et al. (2012)
Allan Hills (Set A)	107	28	S	Muirhead et al. (2012)
Allan Hills (Set A)	120	55	S	Muirhead et al. (2012)
Allan Hills (Set A)	144	62	W	Muirhead et al. (2012)
Allan Hills (Set A)	160	66	W	Muirhead et al. (2012)
Allan Hills (Set A)	6	60	W	Muirhead et al. (2012)
Allan Hills (Set A)	113	58	W	Muirhead et al. (2012)
Allan Hills (Set A)	112	57	S	Muirhead et al. (2012)
Allan Hills (Set A)	177	54	W	Muirhead et al. (2012)
Allan Hills (Set A)	177	52	W	Muirhead et al. (2012)
Allan Hills (Set A)	82	72	S	Muirhead et al. (2012)
Allan Hills (Set A)	110	53	S	Muirhead et al. (2012)
Allan Hills (Set B)	45	48	S	Airoldi et al. (2011)
Allan Hills (Set B)	35	62	S	Airoldi et al. (2011)
Allan Hills (Set B)	53	50	S	Airoldi et al. (2011)
Allan Hills (Set B)	63	55	S	Airoldi et al. (2011)
Allan Hills (Set B)	57	57	S	Airoldi et al. (2011)
Allan Hills (Set B)	43	88	S	Airoldi et al. (2011)
Allan Hills (Set B)	36	53	S	Airoldi et al. (2011)
Allan Hills (Set B)	74	65	S	Airoldi et al. (2011)

Allan Hills (Set B)	46	60	S	Airoldi et al. (2011)
Allan Hills (Set B)	65	47	S	Airoldi et al. (2011)
Allan Hills (Set B)	65	70	S	Airoldi et al. (2011)
Allan Hills (Set B)	44	46	E	Airoldi et al. (2011)
Allan Hills (Set B)	10	36	E	Airoldi et al. (2011)
Allan Hills (Set B)	82	52	S	Airoldi et al. (2011)
Allan Hills (Set B)	196	68	W	Airoldi et al. (2011)
Allan Hills (Set B)	188	79	W	Airoldi et al. (2011)
Allan Hills (Set B)	199	71	W	Airoldi et al. (2011)
Allan Hills (Set B)	165	60	W	Airoldi et al. (2011)
Allan Hills (Set B)	184	74	W	Airoldi et al. (2011)
Allan Hills (Set B)	195	66	W	Airoldi et al. (2011)
Allan Hills (Set B)	179	74	W	Airoldi et al. (2011)
Allan Hills (Set B)	186	86	W	Airoldi et al. (2011)
Allan Hills (Set B)	178	70	W	Airoldi et al. (2011)
Allan Hills (Set B)	174	79	W	Airoldi et al. (2011)
Allan Hills (Set B)	185	78	W	Airoldi et al. (2011)
Allan Hills (Set B)	194	82	W	Airoldi et al. (2011)
Allan Hills (Set B)	199	72	W	Airoldi et al. (2011)
Allan Hills (Set B)	174	52	W	Airoldi et al. (2011)
Allan Hills (Set B)	197	64	W	Airoldi et al. (2011)
Allan Hills (Set B)	186	68	W	Airoldi et al. (2011)
Allan Hills (Set B)	194	68	W	Airoldi et al. (2011)
Allan Hills (Set B)	181	90	W	Airoldi et al. (2011)
Allan Hills (Set B)	185	78	W	Airoldi et al. (2011)
Allan Hills (Set B)	207	67	W	Airoldi et al. (2011)
Allan Hills (Set B)	191	68	W	Airoldi et al. (2011)
Allan Hills (Set B)	176	57	W	Airoldi et al. (2011)
Allan Hills (Set B)	185	52	W	Airoldi et al. (2011)
Allan Hills (Set B)	194	59	W	Airoldi et al. (2011)
Allan Hills (Set B)	175	58	W	Airoldi et al. (2011)
Allan Hills (Set B)	192	65	W	Airoldi et al. (2011)
Allan Hills (Set B)	138	63	W	Airoldi et al. (2011)
Allan Hills (Set B)	167	73	W	Airoldi et al. (2011)
Allan Hills (Set B)	179	70	W	Airoldi et al. (2011)
Allan Hills (Set B)	184	67	W	Airoldi et al. (2011)
Allan Hills (Set B)	182	72	W	Airoldi et al. (2011)

Allan Hills (Set B)	195	38	W	Airoldi et al. (2011)
Allan Hills (Set B)	185	64	W	Airoldi et al. (2011)
Allan Hills (Set B)	346	89	E	Airoldi et al. (2011)
Allan Hills (Set B)	185	89	W	Airoldi et al. (2011)
Allan Hills (Set B)	234	52	N	Airoldi et al. (2011)
Allan Hills (Set B)	200	51	W	Airoldi et al. (2011)
Allan Hills (Set B)	324	52	E	Airoldi et al. (2011)
Allan Hills (Set B)	343	46	E	Airoldi et al. (2011)
Allan Hills (Set B)	206	66	W	Airoldi et al. (2011)
Allan Hills (Set B)	214	50	W	Airoldi et al. (2011)
Allan Hills (Set B)	213	40	W	Airoldi et al. (2011)
Allan Hills (Set B)	174	58	W	Airoldi et al. (2011)
Allan Hills (Set B)	207	84	W	Airoldi et al. (2011)
Allan Hills (Set B)	132	78	S	Airoldi et al. (2011)
Allan Hills (Set B)	214	48	W	Airoldi et al. (2011)
Allan Hills (Set B)	176	67	W	Airoldi et al. (2011)
Allan Hills (Set B)	192	54	W	Airoldi et al. (2011)
Allan Hills (Set B)	152	58	W	Airoldi et al. (2011)
Allan Hills (Set B)	178	58	W	Airoldi et al. (2011)
Allan Hills (Set B)	181	68	W	Airoldi et al. (2011)
Allan Hills (Set B)	161	82	W	Airoldi et al. (2011)
Allan Hills (Set B)	198	42	W	Airoldi et al. (2011)
Allan Hills (Set B)	182	50	W	Airoldi et al. (2011)
Allan Hills (Set B)	199	40	W	Airoldi et al. (2011)
Allan Hills (Set B)	275	28	N	Airoldi et al. (2011)
Allan Hills (Set B)	175	75	W	Airoldi et al. (2011)
Allan Hills (Set B)	184	28	W	Airoldi et al. (2011)
Allan Hills (Set B)	180	48	W	Airoldi et al. (2011)
Allan Hills (Set B)	184	58	W	Airoldi et al. (2011)
Allan Hills (Set B)	166	63	W	Airoldi et al. (2011)
Allan Hills (Set B)	186	60	W	Airoldi et al. (2011)
Allan Hills (Set B)	179	60	W	Airoldi et al. (2011)
Allan Hills (Set B)	203	70	W	Airoldi et al. (2011)
Allan Hills (Set B)	204	39	W	Airoldi et al. (2011)
Allan Hills (Set B)	175	75	W	Airoldi et al. (2011)
Allan Hills (Set B)	24	78	W	Airoldi et al. (2011)
Allan Hills (Set B)	166	36	W	Airoldi et al. (2011)

Allan Hills (Set B)	108	25	W	Airoldi et al. (2011)
Allan Hills (Set B)	108	62	S	Airoldi et al. (2011)
Allan Hills (Set B)	112	30	S	Airoldi et al. (2011)
Allan Hills (Set B)	134	38	S	Airoldi et al. (2011)
Allan Hills (Set B)	100	25	S	Airoldi et al. (2011)
Allan Hills (Set B)	8	10	W	Airoldi et al. (2011)
Allan Hills (Set B)	148	40	W	Airoldi et al. (2011)
Allan Hills (Set B)	139	46	W	Airoldi et al. (2011)
Allan Hills (Set B)	44	30	W	Airoldi et al. (2011)
Allan Hills (Set B)	214	74	W	Airoldi et al. (2011)
Allan Hills (Set B)	226	54	N	Airoldi et al. (2011)
Allan Hills (Set B)	246	67	N	Airoldi et al. (2011)
Allan Hills (Set B)	223	53	W	Airoldi et al. (2011)
Allan Hills (Set B)	241	74	N	Airoldi et al. (2011)
Allan Hills (Set B)	226	54	N	Airoldi et al. (2011)
Allan Hills (Set B)	210	76	W	Airoldi et al. (2011)
Allan Hills (Set B)	229	63	N	Airoldi et al. (2011)
Allan Hills (Set B)	214	76	W	Airoldi et al. (2011)
Allan Hills (Set B)	184	70	W	Airoldi et al. (2011)
Allan Hills (Set B)	199	61	W	Airoldi et al. (2011)
Allan Hills (Set B)	202	59	W	Airoldi et al. (2011)
Allan Hills (Set B)	184	70	W	Airoldi et al. (2011)
Allan Hills (Set B)	192	70	W	Airoldi et al. (2011)
Allan Hills (Set B)	220	76	W	Airoldi et al. (2011)
Allan Hills (Set B)	210	79	W	Airoldi et al. (2011)
Allan Hills (Set B)	190	80	W	Airoldi et al. (2011)
Allan Hills (Set B)	198	62	W	Airoldi et al. (2011)
Allan Hills (Set B)	210	80	W	Airoldi et al. (2011)
Allan Hills (Set B)	220	83	W	Airoldi et al. (2011)
Allan Hills (Set B)	219	60	W	Airoldi et al. (2011)
Allan Hills (Set B)	213	60	W	Airoldi et al. (2011)
Allan Hills (Set B)	209	50	W	Airoldi et al. (2011)
Allan Hills (Set B)	189	56	W	Airoldi et al. (2011)
Allan Hills (Set B)	214	74	W	Airoldi et al. (2011)
Allan Hills (Set B)	218	62	W	Airoldi et al. (2011)
Allan Hills (Set B)	230	63	N	Airoldi et al. (2011)
Allan Hills (Set B)	218	61	W	Airoldi et al. (2011)

Allan Hills (Set B)	219	79	W	Airoldi et al. (2011)
Allan Hills (Set B)	212	67	W	Airoldi et al. (2011)
Allan Hills (Set B)	217	88	W	Airoldi et al. (2011)
Allan Hills (Set B)	211	59	W	Airoldi et al. (2011)
Allan Hills (Set B)	225	58	N	Airoldi et al. (2011)
Allan Hills (Set B)	187	43	W	Airoldi et al. (2011)
Allan Hills (Set B)	168	71	W	Airoldi et al. (2011)
Allan Hills (Set B)	165	62	W	Airoldi et al. (2011)
Allan Hills (Set B)	170	48	W	Airoldi et al. (2011)
Allan Hills (Set B)	208	65	W	Airoldi et al. (2011)
Allan Hills (Set B)	158	66	W	Airoldi et al. (2011)
Allan Hills (Set B)	196	59	W	Airoldi et al. (2011)
Allan Hills (Set B)	209	68	W	Airoldi et al. (2011)
Allan Hills (Set B)	215	81	W	Airoldi et al. (2011)
Allan Hills (Set B)	208	38	W	Airoldi et al. (2011)
Allan Hills (Set B)	161	39	W	Airoldi et al. (2011)
Allan Hills (Set B)	200	81	W	Airoldi et al. (2011)
Allan Hills (Set B)	186	47	W	Airoldi et al. (2011)
Allan Hills (Set B)	210	44	W	Airoldi et al. (2011)
Allan Hills (Set B)	210	68	W	Airoldi et al. (2011)
Allan Hills (Set B)	182	60	W	Airoldi et al. (2011)
Allan Hills (Set B)	185	59	W	Airoldi et al. (2011)
Allan Hills (Set B)	180	62	W	Airoldi et al. (2011)
Allan Hills (Set B)	195	68	W	Airoldi et al. (2011)
Allan Hills (Set B)	185	74	W	Airoldi et al. (2011)
Allan Hills (Set B)	185	69	W	Airoldi et al. (2011)
Allan Hills (Set B)	192	69	W	Airoldi et al. (2011)
Allan Hills (Set B)	182	65	W	Airoldi et al. (2011)
Allan Hills (Set B)	207	80	W	Airoldi et al. (2011)
Allan Hills (Set B)	216	77	W	Airoldi et al. (2011)
Allan Hills (Set B)	222	81	W	Airoldi et al. (2011)
Allan Hills (Set B)	219	76	W	Airoldi et al. (2011)
Allan Hills (Set B)	79	85	S	Airoldi et al. (2011)
Allan Hills (Set B)	8	70	N	Airoldi et al. (2011)
Allan Hills (Set B)	140	14	W	Airoldi et al. (2011)
Allan Hills (Set B)	160	62	W	Airoldi et al. (2011)
Allan Hills (Set B)	36	61	W	Airoldi et al. (2011)

Allan Hills (Set B)	46	51	W	Airoldi et al. (2011)
Allan Hills (Set B)	52	66	W	Airoldi et al. (2011)
Allan Hills (Set B)	11	62	W	Airoldi et al. (2011)
Allan Hills (Set B)	40	50	w	Airoldi et al. (2011)
Allan Hills (Set B)	158	44	w	Airoldi et al. (2011)
Allan Hills (Set B)	136	76	w	Airoldi et al. (2011)
Allan Hills (Set B)	132	72	s	Airoldi et al. (2011)
Allan Hills (Set B)	50	70	w	Airoldi et al. (2011)
Allan Hills (Set B)	42	22	w	Airoldi et al. (2011)
Allan Hills (Set B)	171	52	w	Airoldi et al. (2011)
Allan Hills (Set B)	136	60	w	Airoldi et al. (2011)
Allan Hills (Set B)	162	56	w	Airoldi et al. (2011)
Allan Hills (Set B)	37	60	w	Airoldi et al. (2011)
Allan Hills (Set B)	11	71	w	Airoldi et al. (2011)
Allan Hills (Set B)	157	75	w	Airoldi et al. (2011)
Allan Hills (Set B)	159	70	w	Airoldi et al. (2011)
Allan Hills (Set B)	156	68	w	Airoldi et al. (2011)
Allan Hills (Set B)	78	55	w	Airoldi et al. (2011)
Allan Hills (Set B)	146	70	W	Airoldi et al. (2011)
Allan Hills (Set B)	21	68	W	Airoldi et al. (2011)
Allan Hills (Set B)	6	55	W	Airoldi et al. (2011)
Allan Hills (Set B)	169	50	W	Airoldi et al. (2011)
Allan Hills (Set B)	144	52	W	Airoldi et al. (2011)
Allan Hills (Set B)	160	40	W	Airoldi et al. (2011)
Allan Hills (Set B)	150	40	W	Airoldi et al. (2011)
Allan Hills (Set B)	179	54	W	Airoldi et al. (2011)
Allan Hills (Set B)	165	56	W	Airoldi et al. (2011)
Allan Hills (Set B)	146	70	W	Airoldi et al. (2011)
Allan Hills (Set B)	183	25	W	Airoldi et al. (2011)
Allan Hills (Set B)	177	30	W	Airoldi et al. (2011)
Allan Hills (Set B)	124	28	W	Airoldi et al. (2011)
Allan Hills (Set B)	174	52	W	Airoldi et al. (2011)
Allan Hills (Set B)	76	52	W	Airoldi et al. (2011)
Allan Hills (Set B)	108	24	W	Airoldi et al. (2011)
Allan Hills (Set B)	136	56	W	Airoldi et al. (2011)
Allan Hills (Set B)	153	64	W	Airoldi et al. (2011)
Allan Hills (Set B)	172	56	W	Airoldi et al. (2011)

Allan Hills (Set B)	179	60	W	Airoldi et al. (2011)
Allan Hills (Set B)	157	60	W	Airoldi et al. (2011)
Allan Hills (Set B)	217	23	W	Airoldi et al. (2011)
Allan Hills (Set B)	171	45	W	Airoldi et al. (2011)
Allan Hills (Set B)	220	34	W	Airoldi et al. (2011)
Allan Hills (Set B)	208	43	W	Airoldi et al. (2011)
Allan Hills (Set B)	123	64	W	Airoldi et al. (2011)
Allan Hills (Set B)	172	44	W	Airoldi et al. (2011)
Allan Hills (Set B)	135	60	W	Airoldi et al. (2011)
Allan Hills (Set B)	167	50	W	Airoldi et al. (2011)
Allan Hills (Set B)	134	20	W	Airoldi et al. (2011)
Allan Hills (Set B)	134	62	W	Airoldi et al. (2011)
Allan Hills (Set B)	165	30	W	Airoldi et al. (2011)
Allan Hills (Set B)	151	54	W	Airoldi et al. (2011)
Allan Hills (Set B)	154	42	W	Airoldi et al. (2011)
Allan Hills (Set B)	155	36	W	Airoldi et al. (2011)
Allan Hills (Set B)	140	32	W	Airoldi et al. (2011)
Allan Hills (Set B)	136	63	W	Airoldi et al. (2011)
Allan Hills (Set B)	32	66	w	Airoldi et al. (2011)
Allan Hills (Set B)	89	38	N	Airoldi et al. (2011)
Allan Hills (Set B)	83	65	N	Airoldi et al. (2011)
Allan Hills (Set B)	188	58	W	Airoldi et al. (2011)
Allan Hills (Set B)	182	70	W	Airoldi et al. (2011)
Allan Hills (Set B)	142	62	W	Airoldi et al. (2011)
Terra Cotta Mt. (SE slopes)	93	63	S	Muirhead et al. (2012)
Terra Cotta Mt. (SE slopes)	82	82	S	Muirhead et al. (2012)
Terra Cotta Mt. (SE slopes)	82	80	S	Muirhead et al. (2012)
Terra Cotta Mt. (SE slopes)	95	74	S	Muirhead et al. (2012)
Terra Cotta Mt. (SE slopes)	25	64	E	Muirhead et al. (2012)
Terra Cotta Mt. (SE slopes)	90	76	S	Muirhead et al. (2012)
Terra Cotta Mt. (SE slopes)	94	74	S	Muirhead et al. (2012)
Terra Cotta Mt. (SE slopes)	98	72	N	Muirhead et al. (2012)
Terra Cotta Mt. (SE slopes)	89	72	N	Muirhead et al. (2012)
Terra Cotta Mt. (SE slopes)	77	18	N	Muirhead et al. (2012)
Terra Cotta Mt. (SE slopes)	12	54	E	Muirhead et al. (2012)
Terra Cotta Mt. (SE slopes)	32	32	E	Muirhead et al. (2012)
Terra Cotta Mt. (SE slopes)	108	85	N	Muirhead et al. (2012)

Terra Cotta Mt. (SE slopes)	102	75	S	Muirhead et al. (2012)
Terra Cotta Mt. (SE slopes)	62	58	E	Muirhead et al. (2012)
Terra Cotta Mt. (SE slopes)	66	65	E	Muirhead et al. (2012)
Terra Cotta Mt. (SE slopes)	70	73	S	Muirhead et al. (2012)
Terra Cotta Mt. (SE slopes)	56	33	S	Muirhead et al. (2012)
Terra Cotta Mt. (SE slopes)	74	36	S	Muirhead et al. (2012)
Terra Cotta Mt. (SE slopes)	64	59	S	Muirhead et al. (2012)
Terra Cotta Mt. (SE slopes)	144	66	E	Muirhead et al. (2012)
Terra Cotta Mt. (SE slopes)	16	74	E	Muirhead et al. (2012)
Terra Cotta Mt. (SE slopes)	76	83	S	Muirhead et al. (2012)
Terra Cotta Mt. (SE slopes)	25	64	E	Muirhead et al. (2012)
Terra Cotta Mt. (SE slopes)	25	60	E	Muirhead et al. (2012)
Terra Cotta Mt. (SE slopes)	16	62	E	Muirhead et al. (2012)
Terra Cotta Mt. (SE slopes)	178	72	N	Muirhead et al. (2012)
Terra Cotta Mt. (SE slopes)	130	80	N	Muirhead et al. (2012)
Terra Cotta Mt. (SE slopes)	18	71	E	Muirhead et al. (2012)
Terra Cotta Mt. (SE slopes)	33	70	E	Muirhead et al. (2012)
Terra Cotta Mt. (SE slopes)	150	65	E	Muirhead et al. (2012)
Terra Cotta Mt. (SE slopes)	13	32	E	Muirhead et al. (2012)
Terra Cotta Mt. (SE slopes)	5	42	E	Muirhead et al. (2012)
Terra Cotta Mt. (SE slopes)	176	46	E	Muirhead et al. (2012)
Terra Cotta Mt. (SE slopes)	24	30	E	Muirhead et al. (2012)
Terra Cotta Mt. (SE slopes)	24	80	E	Muirhead et al. (2012)
Terra Cotta Mt. (SE slopes)	5	60	E	Muirhead et al. (2012)
Terra Cotta Mt. (SE slopes)	17	57	E	Muirhead et al. (2012)
Terra Cotta Mt. (SE slopes)	150	56	E	Muirhead et al. (2012)
Terra Cotta Mt. (SE slopes)	54	40	N	Muirhead et al. (2012)
Terra Cotta Mt. (SE slopes)	25	78	S	Muirhead et al. (2012)
Terra Cotta Mt. (SE slopes)	5	38	E	Muirhead et al. (2012)
Terra Cotta Mt. (SE slopes)	62	84	S	Muirhead et al. (2012)
Terra Cotta Mt. (SE slopes)	25	60	E	Muirhead et al. (2012)
Terra Cotta Mt. (SE slopes)	10	51	E	Muirhead et al. (2012)
Terra Cotta Mt. (SE slopes)	45	89	E	Muirhead et al. (2012)
Terra Cotta Mt. (SE slopes)	98	63	N	Muirhead et al. (2012)
Terra Cotta Mt. (SE slopes)	92	72	N	Muirhead et al. (2012)
Terra Cotta Mt. (SE slopes)	178	42	E	Muirhead et al. (2012)
Terra Cotta Mt. (SE slopes)	173	47	E	Muirhead et al. (2012)

Terra Cotta Mt. (SE slopes)	178	54	E	Muirhead et al. (2012)
Terra Cotta Mt. (SE slopes)	162	37	E	Muirhead et al. (2012)
Terra Cotta Mt. (SE slopes)	40	48	E	Muirhead et al. (2012)
Terra Cotta Mt. (SE slopes)	94	51	S	Muirhead et al. (2012)
Terra Cotta Mt. (SE slopes)	40	36	E	Muirhead et al. (2012)
Terra Cotta Mt. (SE slopes)	30	47	E	Muirhead et al. (2012)
Terra Cotta Mt. (SE slopes)	102	50	S	Muirhead et al. (2012)
Terra Cotta Mt. (SE slopes)	90	37	S	Muirhead et al. (2012)
Terra Cotta Mt. (SE slopes)	35	68	E	Muirhead et al. (2012)
Terra Cotta Mt. (SE slopes)	54	61	E	Muirhead et al. (2012)
Terra Cotta Mt. (SE slopes)	175	36	E	Muirhead et al. (2012)
Terra Cotta Mt. (SE slopes)	5	30	E	Muirhead et al. (2012)
Terra Cotta Mt. (SE slopes)	164	66	E	Muirhead et al. (2012)
Terra Cotta Mt. (SE slopes)	14	46	E	Muirhead et al. (2012)
Terra Cotta Mt. (SE slopes)	18	46	E	Muirhead et al. (2012)
Terra Cotta Mt. (SE slopes)	50	60	E	Muirhead et al. (2012)
Terra Cotta Mt. (SE slopes)	24	34	E	Muirhead et al. (2012)
Terra Cotta Mt. (SE slopes)	42	45	E	Muirhead et al. (2012)
Terra Cotta Mt. (SE slopes)	113	17	E	Muirhead et al. (2012)
Terra Cotta Mt. (SE slopes)	167	30	E	Muirhead et al. (2012)
Terra Cotta Mt. (SE slopes)	158	19	E	Muirhead et al. (2012)
Terra Cotta Mt. (SE slopes)	159	52	N	Muirhead et al. (2012)
Terra Cotta Mt. (SE slopes)	1	21	E	Muirhead et al. (2012)
Terra Cotta Mt. (SE slopes)	163	55	E	Muirhead et al. (2012)
Terra Cotta Mt. (SE slopes)	6	85	E	Muirhead et al. (2012)
Terra Cotta Mt. (SE slopes)	177	45	E	Muirhead et al. (2012)
Terra Cotta Mt. (SE slopes)	176	52	E	Muirhead et al. (2012)
Terra Cotta Mt. (SE slopes)	25	75	E	Muirhead et al. (2012)
Terra Cotta Mt. (SE slopes)	44	55	E	Muirhead et al. (2012)
Terra Cotta Mt. (SE slopes)	67	45	N	Muirhead et al. (2012)
Terra Cotta Mt. (SE slopes)	154	20	N	Muirhead et al. (2012)
Terra Cotta Mt. (SE slopes)	160	75	E	Muirhead et al. (2012)
Terra Cotta Mt. (SE slopes)	154	60	E	Muirhead et al. (2012)
Terra Cotta Mt. (SE slopes)	158	56	E	Muirhead et al. (2012)
Terra Cotta Mt. (SE slopes)	148	54	E	Muirhead et al. (2012)
Terra Cotta Mt. (SE slopes)	86	60	E	Muirhead et al. (2012)
Terra Cotta Mt. (SE slopes)	60	38	E	Muirhead et al. (2012)

Terra Cotta Mt. (SE slopes)	63	28	E	Muirhead et al. (2012)
Terra Cotta Mt. (SE slopes)	140	83	E	Muirhead et al. (2012)
Terra Cotta Mt. (SE slopes)	131	84	E	Muirhead et al. (2012)
Terra Cotta Mt. (SE slopes)	178	75	E	Muirhead et al. (2012)
Terra Cotta Mt. (SE slopes)	85	77	S	Muirhead et al. (2012)
Terra Cotta Mt. (SE slopes)	82	79	S	Muirhead et al. (2012)
Terra Cotta Mt. (SE slopes)	110	12	W	Muirhead et al. (2012)
Terra Cotta Mt. (SE slopes)	100	36	N	Muirhead et al. (2012)
Terra Cotta Mt. (SE slopes)	30	8	E	Muirhead et al. (2012)
Terra Cotta Mt. (SE slopes)	165	86	W	Muirhead et al. (2012)
Terra Cotta Mt. (SE slopes)	89	61	S	Muirhead et al. (2012)
Terra Cotta Mt. (SE slopes)	95	10	N	Muirhead et al. (2012)
Terra Cotta Mt. (SE slopes)	158	57	E	Muirhead et al. (2012)
Terra Cotta Mt. (SE slopes)	94	18	N	Muirhead et al. (2012)
Terra Cotta Mt. (SE slopes)	155	64	E	Muirhead et al. (2012)
Terra Cotta Mt. (SE slopes)	24	60	S	Muirhead et al. (2012)
Terra Cotta Mt. (SE slopes)	24	78	S	Muirhead et al. (2012)
Terra Cotta Mt. (SE slopes)	13	70	E	Muirhead et al. (2012)
Terra Cotta Mt. (SE slopes)	12	65	E	Muirhead et al. (2012)
Terra Cotta Mt. (SE slopes)	44	55	E	Muirhead et al. (2012)
Terra Cotta Mt.(E slopes)	56	37	E	Muirhead et al. (2012)
Terra Cotta Mt.(E slopes)	133	78	E	Muirhead et al. (2012)
Terra Cotta Mt.(E slopes)	27	86	S	Muirhead et al. (2012)
Terra Cotta Mt.(E slopes)	142	60	N	Muirhead et al. (2012)
Terra Cotta Mt.(E slopes)	56	75	S	Muirhead et al. (2012)
Terra Cotta Mt.(E slopes)	50	58	E	Muirhead et al. (2012)
Terra Cotta Mt.(E slopes)	62	50	SE	Morrison (1989)
Terra Cotta Mt.(E slopes)	65	57	SE	Morrison (1989)
Terra Cotta Mt.(E slopes)	67	60	SE	Morrison (1989)
Terra Cotta Mt.(E slopes)	65	45	SE	Morrison (1989)
Terra Cotta Mt.(E slopes)	65	45	SE	Morrison (1989)
Terra Cotta Mt.(E slopes)	67	30	SE	Morrison (1989)
Terra Cotta Mt.(E slopes)	65	58	SE	Morrison (1989)
Terra Cotta Mt.(E slopes)	55	40	SE	Morrison (1989)
Terra Cotta Mt.(E slopes)	69	25	SE	Morrison (1989)
Terra Cotta Mt.(E slopes)	65	46	SE	Morrison (1989)
Terra Cotta Mt.(E slopes)	20	4	SE	Morrison (1989)

Mt Kuipers (west slopes)	58	75	N	Airoidi (2011)
Mt Kuipers (west slopes)	72	84	N	Airoidi (2011)
Mt Kuipers (west slopes)	72	78	N	Airoidi (2011)
Mt Kuipers (west slopes)	70	65	N	Airoidi (2011)
Mt Kuipers (west slopes)	40	24	NW	Airoidi (2011)
Mt Kuipers (west slopes)	114	15	NE	Airoidi (2011)
Mt Kuipers (west slopes)	123	24	NE	Airoidi (2011)
Mt Kuipers (west slopes)	55	32	NW	Airoidi (2011)
Mt Kuipers (west slopes)	38	60	W	Airoidi (2011)
Mt Kuipers (west slopes)	68	18	N	Airoidi (2011)
Mt Kuipers (west slopes)	35	78	W	Airoidi (2011)
Mt Kuipers (west slopes)	6	80	W	Airoidi (2011)
Mt Kuipers (west slopes)	11	84	W	Airoidi (2011)
Mt Kuipers (west slopes)	152	75	W	Airoidi (2011)
Mt Kuipers (west slopes)	22	62	E	Airoidi (2011)
Mt Kuipers (west slopes)	134	80	SW	Airoidi (2011)
Mt Kuipers (west slopes)	156	34	E	Airoidi (2011)
Mt Kuipers (west slopes)	162	89	E	Airoidi (2011)
Mt Kuipers (west slopes)	173	74	E	Airoidi (2011)
Mt Kuipers (west slopes)	136	68	SW	Airoidi (2011)
Mt Kuipers (west slopes)	172	87	E	Airoidi (2011)
Mt Kuipers (west slopes)	18	78	W	Airoidi (2011)
Mt Kuipers (west slopes)	68	18	N	Airoidi (2011)
Mt Kuipers (west slopes)	19	70	W	Airoidi (2011)
Mt Kuipers (west slopes)	159	72	W	Airoidi (2011)
Mt Kuipers (west slopes)	146	79	W	Airoidi (2011)
Mt Kuipers (west slopes)	161	65	W	Airoidi (2011)
Mt Kuipers (west slopes)	172	70	W	Airoidi (2011)
Mt Kuipers (west slopes)	165	70	W	Airoidi (2011)
Mt Kuipers (west slopes)	24	66	W	Airoidi (2011)
Mt Kuipers (west slopes)	150	85	S	Airoidi (2011)
Mt Kuipers (west slopes)	125	86	S	Airoidi (2011)
Mt Kuipers (west slopes)	127	82	S	Airoidi (2011)
Mt Kuipers (west slopes)	90	90	-	Airoidi (2011)
Mt Kuipers (west slopes)	84	75	N	Airoidi (2011)
Mt Kuipers (west slopes)	66	85	S	Airoidi (2011)

Table D3. Width measurements of dike segments from Allan Hills, Coombs Hills, Terra Cotta Mountain, and Mt Kuipers (South Victoria Land).

Segment width (m)	Area	Location	Reference
0.15	Allan Hills	North East Arm	Airoidi et al. (2011)
0.17	Allan Hills	North East Arm	Airoidi et al. (2011)
0.3	Allan Hills	North East Arm	Airoidi et al. (2011)
0.3	Allan Hills	North East Arm	Airoidi et al. (2011)
0.3	Allan Hills	North East Arm	Airoidi et al. (2011)
0.33	Allan Hills	North East Arm	Airoidi et al. (2011)
0.41	Allan Hills	North East Arm	Airoidi et al. (2011)
0.47	Allan Hills	North East Arm	Airoidi et al. (2011)
0.5	Allan Hills	North East Arm	Airoidi et al. (2011)
0.5	Allan Hills	North East Arm	Airoidi et al. (2011)
0.51	Allan Hills	North East Arm	Airoidi et al. (2011)
0.55	Allan Hills	North East Arm	Airoidi et al. (2011)
0.57	Allan Hills	North East Arm	Airoidi et al. (2011)
0.59	Allan Hills	North East Arm	Airoidi et al. (2011)
0.6	Allan Hills	North East Arm	Airoidi et al. (2011)
0.65	Allan Hills	North East Arm	Airoidi et al. (2011)
0.7	Allan Hills	North East Arm	Airoidi et al. (2011)
0.7	Allan Hills	North East Arm	Airoidi et al. (2011)
0.73	Allan Hills	North East Arm	Airoidi et al. (2011)
0.75	Allan Hills	North East Arm	Airoidi et al. (2011)
0.75	Allan Hills	North East Arm	Airoidi et al. (2011)
0.75	Allan Hills	North East Arm	Airoidi et al. (2011)
0.8	Allan Hills	North East Arm	Airoidi et al. (2011)
0.8	Allan Hills	North East Arm	Airoidi et al. (2011)
0.86	Allan Hills	North East Arm	Airoidi et al. (2011)
0.86	Allan Hills	North East Arm	Airoidi et al. (2011)
0.9	Allan Hills	North East Arm	Airoidi et al. (2011)
0.9	Allan Hills	North East Arm	Airoidi et al. (2011)
1	Allan Hills	North East Arm	Airoidi et al. (2011)
1	Allan Hills	North East Arm	Airoidi et al. (2011)
1	Allan Hills	North East Arm	Airoidi et al. (2011)
1.08	Allan Hills	North East Arm	Airoidi et al. (2011)
1.1	Allan Hills	North East Arm	Airoidi et al. (2011)

1.1	Allan Hills	North East Arm	Airoldi et al. (2011)
1.12	Allan Hills	North East Arm	Airoldi et al. (2011)
1.15	Allan Hills	North East Arm	Airoldi et al. (2011)
1.16	Allan Hills	North East Arm	Airoldi et al. (2011)
1.2	Allan Hills	North East Arm	Airoldi et al. (2011)
1.2	Allan Hills	North East Arm	Airoldi et al. (2011)
1.2	Allan Hills	North East Arm	Airoldi et al. (2011)
1.35	Allan Hills	North East Arm	Airoldi et al. (2011)
1.4	Allan Hills	North East Arm	Airoldi et al. (2011)
1.4	Allan Hills	North East Arm	Airoldi et al. (2011)
1.4	Allan Hills	North East Arm	Airoldi et al. (2011)
1.6	Allan Hills	North East Arm	Airoldi et al. (2011)
1.7	Allan Hills	North East Arm	Airoldi et al. (2011)
1.73	Allan Hills	North East Arm	Airoldi et al. (2011)
1.77	Allan Hills	North East Arm	Airoldi et al. (2011)
1.8	Allan Hills	North East Arm	Airoldi et al. (2011)
2	Allan Hills	North East Arm	Airoldi et al. (2011)
2.1	Allan Hills	North East Arm	Airoldi et al. (2011)
2.2	Allan Hills	North East Arm	Airoldi et al. (2011)
2.3	Allan Hills	North East Arm	Airoldi et al. (2011)
2.7	Allan Hills	North East Arm	Airoldi et al. (2011)
2.85	Allan Hills	North East Arm	Airoldi et al. (2011)
3	Allan Hills	North East Arm	Airoldi et al. (2011)
3.4	Allan Hills	North East Arm	Airoldi et al. (2011)
3.6	Allan Hills	North East Arm	Airoldi et al. (2011)
4.1	Allan Hills	North East Arm	Airoldi et al. (2011)
4.2	Allan Hills	North East Arm	Airoldi et al. (2011)
4.7	Allan Hills	North East Arm	Airoldi et al. (2011)
5	Allan Hills	North East Arm	Airoldi et al. (2011)
6	Allan Hills	North East Arm	Airoldi et al. (2011)
1.7	Allan Hills	North East Arm	Airoldi et al. (2011)
0.2	Allan Hills	North East Arm	Airoldi et al. (2011)
0.6	Allan Hills	North East Arm	Airoldi et al. (2011)
2.4	Allan Hills	North East Arm	Airoldi et al. (2011)
3	Allan Hills	North East Arm	Airoldi et al. (2011)
1.5	Allan Hills	North East Arm	Airoldi et al. (2011)
1.1	Allan Hills	North East Arm	Airoldi et al. (2011)

0.2	Allan Hills	North East Arm	Airoldi et al. (2011)
1.2	Allan Hills	North East Arm	Airoldi et al. (2011)
1	Allan Hills	North East Arm	Airoldi et al. (2011)
0.8	Allan Hills	North East Arm	Airoldi et al. (2011)
1	Allan Hills	North East Arm	Airoldi et al. (2011)
1	Allan Hills	North East Arm	Airoldi et al. (2011)
0.5	Allan Hills	North East Arm	Airoldi et al. (2011)
0.3	Allan Hills	North East Arm	Airoldi et al. (2011)
0.25	Allan Hills	North East Arm	Airoldi et al. (2011)
0.1	Allan Hills	North East Arm	Airoldi et al. (2011)
0.19	Allan Hills	North East Arm	Airoldi et al. (2011)
0.4	Allan Hills	North East Arm	Airoldi et al. (2011)
0.2	Allan Hills	North East Arm	Airoldi et al. (2011)
1	Allan Hills	North East Arm	Airoldi et al. (2011)
0.35	Allan Hills	North East Arm	Airoldi et al. (2011)
0.3	Allan Hills	North East Arm	Airoldi et al. (2011)
0.35	Allan Hills	North East Arm	Airoldi et al. (2011)
1.1	Allan Hills	North East Arm	Airoldi et al. (2011)
1.7	Allan Hills	North East Arm	Airoldi et al. (2011)
14	Terra Cotta Mountain	East Slopes	Morrison (1989)
3	Terra Cotta Mountain	East Slopes	Morrison (1989)
4	Terra Cotta Mountain	East Slopes	Morrison (1989)
22.5	Terra Cotta Mountain	East Slopes	Morrison (1989)
12	Terra Cotta Mountain	East Slopes	Morrison (1989)
4.5	Terra Cotta Mountain	East Slopes	Morrison (1989)
8	Terra Cotta Mountain	East Slopes	Morrison (1989)
3	Terra Cotta Mountain	East Slopes	Morrison (1989)
2.5	Terra Cotta Mountain	East Slopes	Morrison (1989)
18	Terra Cotta Mountain	East Slopes	Morrison (1989)
20	Terra Cotta Mountain	East Slopes	Morrison (1989)
0.21	Terra Cotta Mountain	East Slopes	Morrison (1989)
0.23	Terra Cotta Mountain	East Slopes	Morrison (1989)
0.31	Terra Cotta Mountain	East Slopes	Morrison (1989)
2	Terra Cotta Mountain	East Slopes	Morrison (1989)
2	Terra Cotta Mountain	East Slopes	Morrison (1989)
25	Terra Cotta Mountain	South East Slopes	Muirhead et al. (2012)
20	Terra Cotta Mountain	South East Slopes	Muirhead et al. (2012)

20	Terra Cotta Mountain	South East Slopes	Muirhead et al. (2012)
6	Terra Cotta Mountain	South East Slopes	Muirhead et al. (2012)
2.9	Terra Cotta Mountain	South East Slopes	Muirhead et al. (2012)
2.2	Terra Cotta Mountain	South East Slopes	Muirhead et al. (2012)
1.3	Terra Cotta Mountain	South East Slopes	Muirhead et al. (2012)
1.8	Terra Cotta Mountain	South East Slopes	Muirhead et al. (2012)
0.33	Terra Cotta Mountain	South East Slopes	Muirhead et al. (2012)
2.6	Terra Cotta Mountain	South East Slopes	Muirhead et al. (2012)
13	Terra Cotta Mountain	South East Slopes	Muirhead et al. (2012)
6	Terra Cotta Mountain	South East Slopes	Muirhead et al. (2012)
2.5	Terra Cotta Mountain	South East Slopes	Muirhead et al. (2012)
14	Terra Cotta Mountain	South East Slopes	Muirhead et al. (2012)
10	Terra Cotta Mountain	South East Slopes	Muirhead et al. (2012)
2.8	Terra Cotta Mountain	South East Slopes	Muirhead et al. (2012)
0.06	Terra Cotta Mountain	South East Slopes	Muirhead et al. (2012)
0.08	Terra Cotta Mountain	South East Slopes	Muirhead et al. (2012)
0.12	Terra Cotta Mountain	South East Slopes	Muirhead et al. (2012)
0.2	Terra Cotta Mountain	South East Slopes	Muirhead et al. (2012)
0.38	Terra Cotta Mountain	South East Slopes	Muirhead et al. (2012)
0.38	Terra Cotta Mountain	South East Slopes	Muirhead et al. (2012)
1.2	Terra Cotta Mountain	South East Slopes	Muirhead et al. (2012)
0.24	Terra Cotta Mountain	South East Slopes	Muirhead et al. (2012)
0.2	Terra Cotta Mountain	South East Slopes	Muirhead et al. (2012)
0.62	Terra Cotta Mountain	South East Slopes	Muirhead et al. (2012)
2	Terra Cotta Mountain	South East Slopes	Muirhead et al. (2012)
2	Terra Cotta Mountain	South East Slopes	Muirhead et al. (2012)
8.2	Terra Cotta Mountain	South East Slopes	Muirhead et al. (2012)
6.3	Terra Cotta Mountain	South East Slopes	Muirhead et al. (2012)
3.5	Terra Cotta Mountain	South East Slopes	Muirhead et al. (2012)
3.36	Terra Cotta Mountain	South East Slopes	Muirhead et al. (2012)
2.7	Terra Cotta Mountain	South East Slopes	Muirhead et al. (2012)
5.3	Terra Cotta Mountain	South East Slopes	Muirhead et al. (2012)
0.41	Terra Cotta Mountain	South East Slopes	Muirhead et al. (2012)
1.6	Terra Cotta Mountain	South East Slopes	Muirhead et al. (2012)
1	Shapeless Mountain		Korsch (1984)
0.8	Shapeless Mountain		Korsch (1984)
5	Shapeless Mountain		Korsch (1984)

24	Mt Kuipers	West Slopes	Airoidi (2011)
23	Mt Kuipers	West Slopes	Airoidi (2011)
0.5	Mt Kuipers	West Slopes	Airoidi (2011)
1.7	Mt Kuipers	West Slopes	Airoidi (2011)
1.81	Coombs Hills	Central Coombs Hills	Guegan (2006)
3	Coombs Hills	Central Coombs Hills	Guegan (2006)
1.75	Coombs Hills	Central Coombs Hills	Guegan (2006)
2	Coombs Hills	Central Coombs Hills	Guegan (2006)
3	Coombs Hills	Central Coombs Hills	Guegan (2006)
2	Coombs Hills	Central Coombs Hills	Guegan (2006)
1.9	Coombs Hills	Central Coombs Hills	Guegan (2006)
1.85	Coombs Hills	Central Coombs Hills	Guegan (2006)
1.8	Coombs Hills	Central Coombs Hills	Guegan (2006)
2.2	Coombs Hills	Central Coombs Hills	Guegan (2006)
2	Coombs Hills	Central Coombs Hills	Guegan (2006)
1.8	Coombs Hills	Central Coombs Hills	Guegan (2006)
1.6	Coombs Hills	Central Coombs Hills	Guegan (2006)
1	Coombs Hills	Central Coombs Hills	Guegan (2006)
0.5	Coombs Hills	Central Coombs Hills	Guegan (2006)
0.1	Coombs Hills	Central Coombs Hills	Guegan (2006)
0.6	Coombs Hills	Central Coombs Hills	Guegan (2006)
0.8	Coombs Hills	Central Coombs Hills	Guegan (2006)
2	Coombs Hills	Central Coombs Hills	Guegan (2006)
0.2	Coombs Hills	Central Coombs Hills	Guegan (2006)
0.1	Coombs Hills	Central Coombs Hills	Guegan (2006)
2	Coombs Hills	Central Coombs Hills	Guegan (2006)
0.1	Coombs Hills	Central Coombs Hills	Guegan (2006)
0.7	Coombs Hills	Central Coombs Hills	Guegan (2006)
0.1	Coombs Hills	Central Coombs Hills	Guegan (2006)
0.6	Coombs Hills	Central Coombs Hills	Guegan (2006)
0.4	Coombs Hills	Central Coombs Hills	Guegan (2006)
1.8	Coombs Hills	Central Coombs Hills	Guegan (2006)
0.1	Coombs Hills	Central Coombs Hills	Guegan (2006)
0.3	Coombs Hills	Central Coombs Hills	Guegan (2006)
1.2	Coombs Hills	Central Coombs Hills	Guegan (2006)
0.02	Coombs Hills	Central Coombs Hills	Guegan (2006)
0.5	Coombs Hills	Central Coombs Hills	Guegan (2006)

0.05	Coombs Hills	Central Coombs Hills	Guegan (2006)
0.5	Coombs Hills	Central Coombs Hills	Guegan (2006)
0.04	Coombs Hills	Central Coombs Hills	Guegan (2006)
0.5	Coombs Hills	Central Coombs Hills	Guegan (2006)
0.1	Coombs Hills	Central Coombs Hills	Guegan (2006)
1.4	Coombs Hills	Central Coombs Hills	Guegan (2006)
0.2	Coombs Hills	Central Coombs Hills	Guegan (2006)
1.2	Coombs Hills	Central Coombs Hills	Guegan (2006)
0.02	Coombs Hills	Central Coombs Hills	Guegan (2006)
0.15	Coombs Hills	Central Coombs Hills	Guegan (2006)
0.6	Coombs Hills	Central Coombs Hills	Guegan (2006)
1.6	Coombs Hills	Central Coombs Hills	Guegan (2006)
0.2	Coombs Hills	Central Coombs Hills	Guegan (2006)
1.2	Coombs Hills	Central Coombs Hills	Guegan (2006)
0.1	Coombs Hills	Central Coombs Hills	Guegan (2006)
0.03	Coombs Hills	Central Coombs Hills	Guegan (2006)
0.6	Coombs Hills	Central Coombs Hills	Guegan (2006)
0.1	Coombs Hills	Central Coombs Hills	Guegan (2006)
0.25	Coombs Hills	Central Coombs Hills	Guegan (2006)
0.1	Coombs Hills	Central Coombs Hills	Guegan (2006)
0.1	Coombs Hills	Central Coombs Hills	Guegan (2006)
0.1	Coombs Hills	Central Coombs Hills	Guegan (2006)
0.03	Coombs Hills	Central Coombs Hills	Guegan (2006)
0.05	Coombs Hills	Central Coombs Hills	Guegan (2006)
0.2	Coombs Hills	Central Coombs Hills	Guegan (2006)
0.55	Coombs Hills	Central Coombs Hills	Guegan (2006)
1.4	Coombs Hills	Central Coombs Hills	Guegan (2006)
1.6	Coombs Hills	Central Coombs Hills	Guegan (2006)
0.1	Coombs Hills	Central Coombs Hills	Guegan (2006)
0.25	Coombs Hills	Central Coombs Hills	Guegan (2006)
0.1	Coombs Hills	Central Coombs Hills	Guegan (2006)
0.1	Coombs Hills	Central Coombs Hills	Guegan (2006)
10	Coombs Hills	Central Coombs Hills	Guegan (2006)
3	Coombs Hills	Central Coombs Hills	Guegan (2006)
1	Coombs Hills	Central Coombs Hills	Guegan (2006)
3.5	Coombs Hills	Central Coombs Hills	Guegan (2006)
4	Coombs Hills	Central Coombs Hills	Guegan (2006)

0.4	Coombs Hills	Central Coombs Hills	Guegan (2006)
0.15	Coombs Hills	Central Coombs Hills	Guegan (2006)
0.1	Coombs Hills	Central Coombs Hills	Guegan (2006)
0.6	Coombs Hills	Central Coombs Hills	Guegan (2006)
0.1	Coombs Hills	Central Coombs Hills	Guegan (2006)
0.1	Coombs Hills	Central Coombs Hills	Guegan (2006)
0.25	Coombs Hills	Central Coombs Hills	Guegan (2006)
1.5	Coombs Hills	Central Coombs Hills	Guegan (2006)
0.1	Coombs Hills	Central Coombs Hills	Guegan (2006)
0.1	Coombs Hills	Central Coombs Hills	Guegan (2006)
0.14	Coombs Hills	Central Coombs Hills	Guegan (2006)
1.11	Coombs Hills	Central Coombs Hills	Guegan (2006)
5	Coombs Hills	Central Coombs Hills	Guegan (2006)
0.11	Coombs Hills	Central Coombs Hills	Guegan (2006)
0.11	Coombs Hills	Central Coombs Hills	Guegan (2006)
0.11	Coombs Hills	Central Coombs Hills	Guegan (2006)
0.8	Coombs Hills	Central Coombs Hills	Guegan (2006)
4	Coombs Hills	Central Coombs Hills	Guegan (2006)
7	Coombs Hills	Central Coombs Hills	Guegan (2006)
1.5	Coombs Hills	Central Coombs Hills	Guegan (2006)
0.3	Coombs Hills	Central Coombs Hills	Guegan (2006)
1	Coombs Hills	Central Coombs Hills	Guegan (2006)
2.5	Coombs Hills	Central Coombs Hills	Guegan (2006)
2.8	Coombs Hills	Central Coombs Hills	Guegan (2006)
1.5	Coombs Hills	Central Coombs Hills	Guegan (2006)
0.9	Coombs Hills	Central Coombs Hills	Guegan (2006)
1.5	Coombs Hills	Central Coombs Hills	Guegan (2006)
1.4	Coombs Hills	Central Coombs Hills	Guegan (2006)
1	Coombs Hills	Central Coombs Hills	Guegan (2006)
0.6	Coombs Hills	Central Coombs Hills	Guegan (2006)
1	Coombs Hills	Central Coombs Hills	Guegan (2006)
6	Coombs Hills	Central Coombs Hills	Guegan (2006)
5	Coombs Hills	Central Coombs Hills	Guegan (2006)
5	Coombs Hills	Central Coombs Hills	Guegan (2006)
4	Coombs Hills	Central Coombs Hills	Guegan (2006)
1	Coombs Hills	Central Coombs Hills	Guegan (2006)
0.4	Coombs Hills	Central Coombs Hills	Guegan (2006)

0.3	Coombs Hills	Central Coombs Hills	Guegan (2006)
0.5	Coombs Hills	Central Coombs Hills	Guegan (2006)
1	Coombs Hills	Central Coombs Hills	Guegan (2006)
0.1	Coombs Hills	Central Coombs Hills	Guegan (2006)
1.5	Coombs Hills	Central Coombs Hills	Guegan (2006)
2.4	Coombs Hills	Central Coombs Hills	Guegan (2006)
1.8	Coombs Hills	Central Coombs Hills	Guegan (2006)
1.8	Coombs Hills	Central Coombs Hills	Guegan (2006)
3	Coombs Hills	Central Coombs Hills	Guegan (2006)
5	Coombs Hills	Central Coombs Hills	Guegan (2006)
3	Coombs Hills	Central Coombs Hills	Guegan (2006)
1.8	Coombs Hills	Central Coombs Hills	Guegan (2006)
1.5	Coombs Hills	Central Coombs Hills	Guegan (2006)
0.4	Coombs Hills	Central Coombs Hills	Guegan (2006)
0.13	Coombs Hills	Central Coombs Hills	Guegan (2006)
1	Coombs Hills	Central Coombs Hills	Guegan (2006)
0.5	Coombs Hills	Central Coombs Hills	Guegan (2006)
0.5	Coombs Hills	Central Coombs Hills	Guegan (2006)
0.7	Coombs Hills	Central Coombs Hills	Guegan (2006)
2.5	Coombs Hills	Central Coombs Hills	Guegan (2006)
0.25	Coombs Hills	Central Coombs Hills	Guegan (2006)
3	Coombs Hills	Central Coombs Hills	Guegan (2006)
0.1	Coombs Hills	Central Coombs Hills	Guegan (2006)
0.1	Coombs Hills	Central Coombs Hills	Guegan (2006)
0.1	Coombs Hills	Central Coombs Hills	Guegan (2006)
0.1	Coombs Hills	Central Coombs Hills	Guegan (2006)
0.1	Coombs Hills	Central Coombs Hills	Guegan (2006)
5	Coombs Hills	Central Coombs Hills	Guegan (2006)
0.1	Coombs Hills	Central Coombs Hills	Guegan (2006)
1.3	Coombs Hills	Central Coombs Hills	Guegan (2006)
0.1	Coombs Hills	Central Coombs Hills	Guegan (2006)
1.5	Coombs Hills	Central Coombs Hills	Guegan (2006)
0.1	Coombs Hills	Central Coombs Hills	Guegan (2006)
4.5	Coombs Hills	Central Coombs Hills	Guegan (2006)
1	Coombs Hills	Central Coombs Hills	Guegan (2006)
1	Coombs Hills	Central Coombs Hills	Guegan (2006)
0.1	Coombs Hills	Central Coombs Hills	Guegan (2006)

0.1	Coombs Hills	Central Coombs Hills	Guegan (2006)
0.1	Coombs Hills	Central Coombs Hills	Guegan (2006)
0.6	Coombs Hills	Central Coombs Hills	Guegan (2006)
0.5	Coombs Hills	Central Coombs Hills	Guegan (2006)
1	Coombs Hills	Central Coombs Hills	Guegan (2006)

Table D4. Total exposure area of Beacon Supergroup and Mawson Formation rocks in the study area.

Region	Area of Beacon-Mawson Fm (km²)	Map references
Beacon Heights	91.0	McElroy and Rose (1987)
Knobhead-Terra Cotta Mt.	17.5	Woolfe et al. (1989)
Thundergut Area	49.4	Allibone et al. (1991)
Bull Pass	6.1	Turnbull et al. (1995)
Olympus Range Area	165.6	Isaac et al. (1996)
Convoy Range	30.3	Pocknall et al. (1992)
Coombs Hills	45.0	Ross et al. (2008)
Allan Hills	53.5	Ross et al. (2008), Grapes et al. (1974)
Total	458.4	

APPENDIX E

Supplementary data for Chapter 7

Data used in this study can be accessed in the accompanying CD-ROM.

Summary of content:

Data tables in Appendix E summarize field and remoting sensing data collected from the Hopi Buttes in this study.

Table E1. Summary of data collected from remote sensing analyses of south Hopi Buttes using Google Earth. Included are the locations massifs and diatremes and their subsequent 3-point alignments, and the locations, dimensions, and trends of dikes and sills.

Table E2. Summary of field data collected in south Hopi Buttes. Included are the location of thickness and strike and dip measurements of dikes, joints and transgressive sills. Also included are field measurements collected by Re et al. (2015).

APPENDIX F

*Copyright permissions for Chapters 2, 6, and 7***JOHN WILEY AND SONS LICENSE
TERMS AND CONDITIONS**

Mar 28, 2016

This Agreement between James D Muirhead ("You") and John Wiley and Sons ("John Wiley and Sons") consists of your license details and the terms and conditions provided by John Wiley and Sons and Copyright Clearance Center.

License Number	3837741073397
License date	Mar 28, 2016
Licensed Content Publisher	John Wiley and Sons
Licensed Content Publication	Geochemistry, Geophysics, Geosystems
Licensed Content Title	Varying styles of magmatic strain accommodation across the East African Rift
Licensed Content Author	James D. Muirhead, Simon A. Kattenhorn, Nicolas Le Corvec
Licensed Content Date	Aug 25, 2015
Pages	21
Type of use	Dissertation/Thesis
Requestor type	Author of this Wiley article
Format	Print and electronic
Portion	Full article
Will you be translating?	No
Title of your thesis / dissertation	Tectonic-magmatic controls on volcanism, rifting, and volatile release
Expected completion date	Apr 2016
Expected size (number of pages)	300
Requestor Location	James D Muirhead 232 NE 53rd Avenue PORTLAND, OR 97213 United States Attn: James D Muirhead
Billing Type	Invoice
Billing Address	James D Muirhead 232 NE 53rd Avenue PORTLAND, OR 97213 United States Attn: James D Muirhead

**ELSEVIER LICENSE
TERMS AND CONDITIONS**

Mar 28, 2016

This is a License Agreement between James D Muirhead ("You") and Elsevier ("Elsevier") provided by Copyright Clearance Center ("CCC"). The license consists of your order details, the terms and conditions provided by Elsevier, and the payment terms and conditions.

All payments must be made in full to CCC. For payment instructions, please see information listed at the bottom of this form.

Supplier	Elsevier Limited The Boulevard, Langford Lane Kidlington, Oxford, OX5 1GB, UK
Registered Company Number	1982084
Customer name	James D Muirhead
Customer address	232 NE 53rd Avenue PORTLAND, OR 97213
License number	3837741241082
License date	Mar 28, 2016
Licensed content publisher	Elsevier
Licensed content publication	Earth and Planetary Science Letters
Licensed content title	Cracking the lid: Sill-fed dikes are the likely feeders of flood basalt eruptions
Licensed content author	James D. Muirhead, Giulia Airoidi, James D.L. White, Julie V. Rowland
Licensed content date	15 November 2014
Licensed content volume number	406
Licensed content issue number	n/a
Number of pages	11
Start Page	187
End Page	197
Type of Use	reuse in a thesis/dissertation
Intended publisher of new work	other
Portion	full article
Format	both print and electronic
Are you the author of this Elsevier article?	Yes
Will you be translating?	No
Title of your thesis/dissertation	Tectonic-magmatic controls on volcanism, rifting, and volatile release
Expected completion date	Apr 2016

**SPRINGER LICENSE
TERMS AND CONDITIONS**

Mar 28, 2016

This is a License Agreement between James D Muirhead ("You") and Springer ("Springer") provided by Copyright Clearance Center ("CCC"). The license consists of your order details, the terms and conditions provided by Springer, and the payment terms and conditions.

All payments must be made in full to CCC. For payment instructions, please see information listed at the bottom of this form.

License Number	3837731026990
License date	Mar 28, 2016
Licensed content publisher	Springer
Licensed content publication	Bulletin of Volcanology
Licensed content title	Monogenetic volcanoes fed by interconnected dikes and sills in the Hopi Buttes volcanic field, Navajo Nation, USA
Licensed content author	James D. Muirhead
Licensed content date	Jan 1, 2016
Volume number	78
Issue number	2
Type of Use	Thesis/Dissertation
Portion	Figures/tables/illustrations
Number of figures/tables /illustrations	19
Author of this Springer article	Yes and you are the sole author of the new work
Order reference number	Figures 1, 2, 3, 4, 5, 6, 7, 8, 9, 10, 11, 12, 13, 14, 15, S1, S2
Original figure numbers	Tables 1, 2
Title of your thesis / dissertation	Tectonic-magmatic controls on volcanism, rifting, and volatile release
Expected completion date	Apr 2016

**SPRINGER LICENSE
TERMS AND CONDITIONS**

Mar 28, 2016

This is a License Agreement between James D Muirhead ("You") and Springer ("Springer") provided by Copyright Clearance Center ("CCC"). The license consists of your order details, the terms and conditions provided by Springer, and the payment terms and conditions.

All payments must be made in full to CCC. For payment instructions, please see information listed at the bottom of this form.

License Number	3837730784772
License date	Mar 28, 2016
Licensed content publisher	Springer
Licensed content publication	Bulletin of Volcanology
Licensed content title	Monogenetic volcanoes fed by interconnected dikes and sills in the Hopi Buttes volcanic field, Navajo Nation, USA
Licensed content author	James D. Muirhead
Licensed content date	Jan 1, 2016
Volume number	78
Issue number	2
Type of Use	Thesis/Dissertation
Portion	Full text
Number of copies	1
Author of this Springer article	Yes and you are the sole author of the new work
Order reference number	None
Title of your thesis / dissertation	Tectonic-magmatic controls on volcanism, rifting, and volatile release
Expected completion date	Apr 2016